their study, the required nanofluid volumetric flow rate for a given heat duty was found to be lower than that of water causing lower pressure drop. Shortly, they concluded that the use of smaller equipment and less pumping power were required. Since the total volume of the equipment was the main issue, use of the nanofluids seemed to be a promising solution towards designing efficient heat exchanging systems. The only disadvantages were the high price and the possible instability of the nanoparticle suspensions.

Vajjha and Das [103] investigated the determination of the thermal conductivity of three nanofluids comprising aluminum oxide, copper oxide and zinc oxide nanoparticles dispersed in a base fluid of 60:40 (by mass) ethylene glycol and water mixture. According to evaluated particle volumetric concentration being up to 10% and the temperature range of the experiments varied from 298 to 363 K the results indicated an increase in the thermal conductivity of nanofluids compared to the base fluids with an increasing volumetric concentration of nanoparticles parallel with the thermal conductivity that also increased substantially with an increase in temperature. By using their experimental data for comparisons with various existing models to determine thermal conductivity they developed a model that was a refinement of an existing model, that incorporated the classical Maxwell model and the Brownian motion effect to account for the thermal conductivity of nanofluids as a function of temperature, particle volumetric concentration, the properties of nanoparticles, and the base fluid with these experimental data.

Wen *et al*. [104] carried out a critical review of research on heat transfer applications of nanofluids with the aim of identifying the limiting factors so as to boost their development.

Hadjov [105] studied spherical nanoparticles with a conductive interface in the self-consisted scheme for forecasting the thermal conductivity of nanofluids. They adopted a flux jump in the particle-fluid interface opposite to the temperature jump that was assumed in the case of thermal barrier resistance. Upper and lower bounds to the homogenized suspension thermal conductivity were gained by their working to the particle packing.

Ali *et al*. [106] numerically studied two-dimensional turbulent convective heat transfer behavior of alumina nanoparticle dispersed in water flow in a horizontal circular pipe at constant wall temperature. The finite-volume method was employed considering the full range of flow at the entrance length and at the fully developed region. They showed that the shear stress was observed to be increasing at any x station along the pipe as the concentration of nanoparticle increased and achieved its higher value at the beginning of the pipe at the entrance region and then dropped to an asymptotic value at the fully developed region. When the velocity increased, both Nusselt number and the shear stress were observed to be increasing. As a result Reynolds number was observed to decrease as the concentration increased at fixed inlet velocity.

Duangthongsuk and Wongwises [107] reported the thermal conductivity and dynamic viscosity of nanofluids experimentally. TiO_2 nanoparticles dispersed in water with volume concentration of 0.2-2 vol.% were used in their study. A transient hot-wire apparatus was used for measuring the thermal conductivity of nanofluids whereas the Bohlin rotational rheometer (Malvern Instrument) for measuring the viscosity of nanofluids. The data were collected for temperatures ranging from 15 °C to 35 °C. The results showed that the measured viscosity and thermal conductivity of nanofluids increased as the particle concentrations increased and were found to be higher than the values of the base liquids. Furthermore, thermal conductivity of nanofluids increased by increasing nanofluid temperatures and, conversely, the viscosity of nanofluids decreased by increasing temperature of nanofluids. Moreover, the measured thermal conductivity and viscosity of nanofluids were found to be quite different from the predicted values evaluated from the existing correlations and the data reported by other researchers. Finally, new thermophysical correlations were proposed for predicting the thermal conductivity and viscosity of nanofluids.

Duangthongsuk and Wongwises [108] reported an experimental study on the forced convective heat transfer and flow characteristics of a nanofluid consisting of water and 0.2 vol.% TiO_2 nanoparticles. The heat transfer coefficient and friction factor of the TiO_2-water nanofluid flowing in a horizontal double-tube counter flow heat exchanger under turbulent flow conditions were investigated. They utilized Degussa P25 TiO_2 nanoparticles of about 21 nm diameter in their study. The results showed that the convective heat transfer coefficient of nanofluid was found to be slightly higher than that of the base liquid by about 6-11%. The heat transfer coefficient of the nanofluid increased with an increase in the mass flow rate of the hot water and nanofluid, and it also increased with a decrease in the nanofluid temperature, and the temperature of the heating fluid showed no significant effect on the heat transfer coefficient of the nanofluid. It was also noted that the Gnielinski equation failed to predict the heat transfer coefficient of the nanofluid. Finally, the use of the nanofluid presented a little penalty in pressure drop.

3e. Somestudies of 2008

Bi *et al*. [109] studied nanoparticles in the working fluid for observing domestic refrigerator's reliability and performance. They utilized from mineral oil/TiO_2 nanoparticle mixtures such as the lubricant instead of Polyol-ester (POE) oil in the 1,1,1,2-tetrafluoroethane (HFC134a) used in refrigerator. Researchers analyzed that the refrigerator performance regarding the energy consumption and freezing capacity was enhanced with the use of nanoparticles. Their results showed that HFC134a and mineral oil with TiO_2 nanoparticles worked normally and securely in the refrigerator. They also observed that the refrigerator had higher performance than the HFC134a and POE oil system,and the use of nanoparticles with 0.1% mass fraction reduced energy consumption 26.1% compared to the HFC134a and POE oil system.

Hwang *et al*. [110] tested homogeneous dispersion of nanoparticles in nanofluids. They investigated various physical treatment techniques based on two step methods comprising ultrasonic bath, ultrasonic disruptor and high-pressure homogenizer to confirm their versatility for preparing stable nanofluids. They used CB (carbon black) and Ag nanoparticles with the diameter of 330nm to 585nm. Their results indicated that Ag nanoparticle, which was generated by the modified magnetron sputtering system, dispersed homogeneously and sustained its stability in the silicon oil based fluid.

Karthikeyan *et al*. [111] studied on synthesizing of CuO nanoparticles having average diameter of 8 nm by using a simple precipitation technique and observed thermal properties of the suspensions. They utilized from water and ethylene glycol as based fluids and 1 vol.% CuO nanoparticles. Their results showed that thermal conductivity increased with increasing finer particle size and mono dispersity of nanoparticles. They obtained some results from experiments that of thermal conductivity being significantly affected from the nanoparticles size, polydispersity, cluster size and the volume fraction of particles.

Khandekar *et al*. [112] studied on a closed two-phase thermosyphon's overall thermal resistance. They selected pure water and various water based nanofluids (of Al_2O_3, CuO and laponite clay) as working fluids. The results indicated that all these nanofluids had worse thermal performance than pure water. In additionto all nanofluids on copper substrate, having the same average roughness as that of the thermo syphon container pipe was greater than that of pure water.

Lee *et al*. [113] synthesized and characterized aqueous nanofluids including low volume concentrations of Al_2O_3 nanoparticles from 0.01 to 0.3 vol.%. Their results pointed out that those alumina nanoparticles had the highest dispersion and stabilization performance in DI water at 5 h of ultrasonic vibration. They observed that

the temperature increased with decreasing the Al_2O_3-water nano fluids' viscosity. In addition, Al_2O_3-water nano fluids' viscosity indicated a nonlinear correlation with the concentration even in the low volume concentration (from0.01 to 0.3 vol.%.).

Murshed *et al*. [114] searched the existing theories in the literature on thedetermination of nanofluids' properties such as synthesis methods, potential application areas, experimental and analytical studies on the effective thermal conductivity, effective thermal diffsivity, convective heat transfer, and electrokinetic properties and compared them with each other.

Oh *et al*. [115] investigated 3-omega (3 w) method as new application to measure the thermal conductivity of nanofluids and they provided information about it. Their new theoretical model was proposed instead of the transient hot wire method for the determination of thermal conductivity. They tested the effective thermal conductivity of Al_2O_3 nanofluids in DI water and EG at room temperature. Furthermore, thermal response showed interesting effects owing to agglomeration and sedimentation of nanoparticles.

Kang *et al*. [116] studied on measuring the vapor absorption rate and heat transfer rate for falling film flow of binary nanofluids, being tested at the same conditions with pure water, and tried to observe the changes of heat and mass transfer. They used some parameters such as base fluid concentration of LiBr, the concentration of nanoparticles in weight %, and nano-particle constituents. They prepared the mixture of H_2O/LiBr solution with nanoparticles of Fe and Carbon nanotubes (CNT). Their results illustrated that the mass transfer increase was more than the heat transfer augmentationin the binary nanofluids with Fe and CNT and the properties of mass transfer of CNT nanoparticles were better than those of Fe nanoparticles.

Lu and Fan [117] studied on molecular dynamics (MD) simulation method, applicable for a stationary nanofluids of the volume fractions less than 8%. They used this method to simulate nanofluids' thermophysical properties such as thermal conductivity and viscosity. They compared experimental data with numerical results and obtained good results. They found it very useful to estimate some thermal properties of nanofluids. Their results also showed that thermal conductivity and the viscosity of nanofluids depended on the volume fraction and the size of nanoparticles.

Nguyen *et al*. [118] focused on the temperature and particle volume concentration's impact on the dynamic viscosity for the water-Al_2O_3 mixture experimentally. They benefited from piston-type device used as a commercial viscometer for temperatures at room condition. Their results indicated an enhancement on the nanofluid dynamic viscosity in respect with particle volume fraction; however temperature increase showed a negative effect on it.

Chen *et al*. [119] presented the properties of the effective thermal conductivity, their rheological behavior and forced convective heat transfer of the nanofluids. They found that thermal conductivity increased as 3% at 25 °C and 5% at 40 °C for the 2.5 wt.% nanofluid. They observed that nanofluidsincluding spherical titanium nanoparticles had better properties of thermal conductivity and convective heat transfer coefficient. They also suggested new systems to increase the convective heat transfer coefficient.

3f. Somestudies of 2007

Ding *et al*. [120] experimentally studied on the forced convective heat transfer using aqueous and ethylene glycol-based spherical titanium nanofluids, and aqueous-based titanate nanotubes, carbon nanotubes and nano-diamond nanofluids.. They accomplished to formulate these nanofluid's specifications. They indicated that all the formulated nanofluids performed a higher effective thermal conductivity than those predicted by the conventional theories. Apart from the ethylene glycol-based titanium nanofluids, all other nanofluids were observed to be non-Newtonian. They reported that the convective heat transfer coefficient enhancement was substantially higher than the thermal conduction enhancement. However, they indicated deterioration of the convective heat transfer for ethylene glycol-based titanium nanofluids at low Reynolds numbers. They recommended the effective thermal conductivity as to be responsible for the experimental observations.

Zhang *et al*. [121] accomplished to measure the effective thermal conductivity and thermal diffusivity of Au/toluene, Al_2O_3/water, TiO_2/water, CuO/water and CNT/water nanofluids by utilizing from the transient short-hot-wire technique. In their study, the average diameters of Au, Al_2O_3, TiO_2 and CuO spherical particles were 1.65, 20, 40 and 33 nm, respectively. Also the average length and diameter of CNFs were 10 l m and 150 nm, respectively. According to results obtained, the effective thermal conductivities of the nanofluids indicated no abnormal enhancements.

Ko *et al*. [122] published an experimental investigation on the flow characteristics of the aqueous suspensions of carbon nanotubes (CNTs). They tried to measure pressure drop to obtain stable nanotube suspensions by utilizing two methods. They studied the effects of CNT loading and various preparation methods and measured the pressure drops in a horizontal tube and viscosities of nanofluids. They found that the CNT nanofluids prepared by the acid treatment had much smaller viscosity than the ones made with surfactant at the same volume fraction. They indicated that the friction factor of stabilized CNT nanofluids (by adding surfactant) was much greater than that of CNT nanofluids prepared by acid treatment, and nanofluids had greater friction factors than distilled water under laminar flow conditions. It was found that the friction factors of nanofluids were inversely similar to that of the base fluids. As the flow rate improved under turbulent flow conditions,they noticed that nanofluids had low friction factors than pure water flows at definite range of flow rates.

Mansour *et al*. [123] studied the uncertainty impacts regarding with the physical properties of water-Al_2O_3 nanofluid on the determination of the thermohydraulic performance for both laminar and turbulent fully developed forced convection in a tube with uniform wall heat flux. They suggested many experimental data necessary to determine the real potential of nanofluid.

Hong *et al*. [124] firstly reported that the thermal conductivity (TC) and heat transfer of nanofluids could be enhanced by the external magnetic field. The nanofluids contained carbon nanotubes (CNTs) and magnetic-field-sensitive nanoparticles of Fe_2O_3. The sensible explanation for these interesting determinations was that the Fe_2O_3 particles formed aligned chains under applied magnetic field that helped to connect the nanotubes. In that magnetic field, the particles slowly moved and formedlarge clumps of particles, and caused clumping of CNTs, then decreased the TC.

Li and Peterson [125] pointed out the Brownian motion of the nanoparticles in these suspensions as one of the potential contributors to this enhancement and the mechanisms that could contribute considerable discussion and debate to this subject. The mixing effect of the base fluid in the immediate vicinity of the nanoparticles caused by the Brownian motion was examined, modeled and was also compared with the experimental data in the literature. Moreover, simulation results showed the effective thermal conductivity of nanofluids being affected by this mixing effect.

Yoo *et al*. [126] prepared some nanofluids such as T_iO_2, Al_2O_3, F_e, and WO_3compounds in a two-step procedure by dispersing in a base fluid. The transient hot wire method was used for the calculation of thermal conductivity. These nanofluids' thermal conductivities were analyzed and then compared with each other.

Avsec and Oblak [127] proposed a mathematical model for the calculation of thermophysical properties of nanofluids on the basis of statistical nanomechanics. In this study, they indicated two calculation methods to describe the properties such as classical and statistical mechanics. It was reported that the classical mechanics had no insight into the microstructure of the substance. On the other

hand, it calculated the properties of state both on the basis of molecular motions in a space and on the basis of the intermolecular interactions. On the contrary to the classical mechanics, they suggested that the statistical mechanics calculated the thermomechanic properties of state on the basis of intermolecular interactions between particles in the same system of molecules. They illustrated that the systems were composed of a very large number of particles. The results of the analysis were compared with experimental data that indicated a relatively good agreement.

He *et al*. [128] studied different particle (agglomerate) sizes in stable aqueous TiO_2 nanofluids and calculated their static thermal conductivity and rheological behavior. Heat transfer and flow behavior were investigated in a vertical pipe during both laminar and turbulent flow regimes. Thermal conduction was observed to increase with addition of nanoparticles into the base liquid but decreased with increasing particle (agglomerate) size. Increasing particle (agglomerate) size and particle concentration caused to grow the constant viscosity. In both the laminar and turbulent flow regimes, convective heat transfer coefficient increased with increasing nanoparticle concentrations.

Lee and Mudawar [129] experimentally studied water-based nanofluids containing small concentrations of Al_2O_3 in the microchannel cooling. They investigated the high thermal conductivity of nanoparticles in the single-phase heat transfer coefficient, especially for laminar flow. In the entrance region of micro-channels, maximum heat transfer coefficients were obtained. Greater sensitivity to heat flux was caused by higher concentrations.

Wang and Mujumdar [130] reviewed convective heat transfer using suspensions of nanometer-sized solid particles in base liquids. The transport properties and heat transfer characteristics of the suspension were found to be significantly dependable to the suspended nanoparticles.

Trisaksri and Wongwises [131] reviewed the literature on the general heat transfer characteristics of nanofluids. It was found that only a few papers had discussed on the convective heat transfer of nanofluids. The purpose of this article was to review the literature mentioning convective heat transfer of nanofluids, such as the experimental and theoretical investigations.

Daungthongsuk and Wongwises [132] reviewed suspension of ultrafine particles in a conventional base fluid which tremendously enhanced the heat transfer characteristics of the original fluid. They reported that nanofluids were expected to be ideally suited in practical applications as their use incurred little or no penalty in pressure drop because the nanoparticles were ultrafine, therefore, appearing to behave more like a single-phase fluid than a solid-liquid mixture. The purpose of their article was to summarize the published subjects respectively with the investigating forced convective heat transfer of the nanofluids both experimentally and numerically.

3g. Somestudies of 2006

Hwang *et al*. [133] showed the higher effective thermal conductivity of nanofluid consisting of nanoparticles dispersed in base fluid than those dispersed in its pure fluid. They used four kinds of nanofluids such as multiwalled carbon nanotube (MWCNT) in water, CuO in water, SiO_2 in water, and CuO in ethylene glycol. They used transient hot-wire method to measure the thermal conductivities. They reported that the increase in thermal conductivity enhancement of water-based MWCNT nanofluid was 11.3% at a volume fraction of 0.01. According to their results, the thermal conductivities of both particles and the base fluid affected the thermal conductivity enhancement of nanofluids.

Hwang *et al*. [134] used the nanoparticles of multi-walled carbon nanotube (MWCNT), fullerene, copper oxide, silicon dioxide and silver to improve the thermal conductivity and lubrication. DI water, ethylene glycol, oil, silicon oil and poly-a-olefinoil (PAO) were taken as the base fluids. They measured the thermal conductivity and kinematic viscosity to investigate the thermo-physical properties of nanofluids. UV-vis spectrophotometer was used to check the stability estimation of nanofluid. They found that the increase in particle volume fraction displayed a positive effect on the increase in thermal conductivity of nanofluid that increased with increasing particle volume fraction.

Liu *et al*. [135] presented a study on the enhancement of the thermal conductivity of water in the presence of copper (Cu) using the chemical reduction method. They reported that their method was used firstly for the synthesis of nanofluids containing Cu nanoparticles in water. Their results showed that Cu-water nanofluids having low concentration of nanoparticles had higher thermal conductivities than those of the water base fluid without Cu. Beside this, thermal conductivity was improved up to 23.8% for Cu nanoparticles at a volume fraction of 0.001 (0.1 vol.%).

Palm *et al*. [136] investigated the heat transfer enhancement capabilities of coolants' laminar forced convection flow with suspended metallic nanoparticles inside typical radial flow cooling systems. They obtained significant heat transfer enhancement with the use of these fluid/solid particle mixtures. They also indicated the noticeable differences between the use of constant property of nanofluids (temperature independent) and nanofluids with temperature dependent properties.

Heris *et al*. [137] investigated the laminar flow convective heat transfer of nanofluids containing CuO and Al_2O_3 oxide nanoparticles in water through circular tube with constant wall temperature boundary condition. They experimentallyshowed that homogeneous model should be used for the prediction of nanofluids properties concerning the determination of the single phase heat transfer coefficient enhancement. Al_2O_3-water nanofluids were noted to have higher heat transfer enhancement with the increase in the volume fraction.

3h. Somestudies of 2005

Xuan *et al*. [138] determined heat transfer process and flow properties of Cu-water nanofluid flowing inside a channel by using the thermal Lattice Boltzmann model. Because they took into consideration the molecular dynamics and bridged the gap of macroscopic or microscopic challenge of the nanofluids, this method showed a significant advantage. Two existing methods used for application of this method to model the thermal fluid flow problem were the multispeed (MS) and the double-distribution-function (DDF). In this study, double-distribution-function (DDF) was used that led to two separate distribution functions as follows: The temperature was treated as a passive diffusing scalar, that was simulated by a distribution function notdependent on density distribution, respectively. The feature point of the Lattice Boltzmann method was the assumption that the particles mesoscopically located at a series of lattices and their distributions corresponding to the Boltzmann distribution. The viscosity dissipation term in the Lattice Boltzmann equation for energy transport was neglected in order to simulate heat transfer characteristics of the nanofluid. According to numerical results, for 1% volume fraction the Nusselt number of Cu-water nanofluid was calculated 27% higher than that of pure water at the same Reynolds number. Furthermore, random motion of the particles suspended in the fluid could be seen along the main flow direction because of fluctuations of the Nusselt number of the nanofluid.

Liu *et al*. [139] studied thermal conductivity enhancements in ethylene glycol and synthetic engine oil using multiwalled carbon nanotubes (MWNTs). The volume concentration of CNT-ethylene glycol suspensions and synthetic engine oil suspensionswere below 1.0 and 2.0 vol.% respectively. They used a modified transient hot wire method to measure the thermal conductivities of the CNT suspensions and observed significant increase in CNT-ethylene glycol suspensions' thermal conductivities in comparison to the ethylene glycol base fluid without CNT. They noted that CNT–

synthetic engine oil suspensions gave the similar results with CNT-ethylene glycol suspensions. They obtained 12.4% enhancement on thermal conductivity for CNT-ethylene glycol suspensions at a volume fraction of 0.01 (1 vol.%) and 30% enhancement at a volume fraction of 0.02 (2 vol.%) for CNT-synthetic engine oil suspension, thermal conductivity was enhanced by 30% at a volume fraction of 0.02 (2 vol.%). As a result of their analysis, the thermal conductivity ratio of CNT-synthetic engineoil suspension was found to be having a noticeably higher value than that of the CNT-ethylene glycolsuspension.

Maiga *et al*. [140] used two particular geometrical configurations, namely a uniformly heated tube and a system of parallel, coaxial and heated disks to study the laminar forced convection flow of nanofluids numerically. By using the mixtures of water-γAl_2O_3 and Ethylene Glycol-γAl_2O_3they obtained a significant increase in the heat transfer coefficient in the presence of nanoparticles dispersed into the base fluids. They also illustrated that the heat transfer coefficient increased with increasing the particle concentration having severe effects on the wall shear stress that increased considerably with the particle loading. The Ethylene Glycol-γAl_2O_3 nanofluids were found to have a better heat transfer enhancement and adverse effects on the wall shear stress than water-γAl_2O_3.

3i. Somestudies of 2004

Wen and Ding [141] performed experiments in order to calculate the convective heat transfer coefficient of γ-Al_2O_3 nanoparticles suspended in deionized water in a copper tube for laminar flow. Under a constant wall heat flux condition, nanoparticles having 0.6 %, 1.0 %, and 1.6 % concentrations were tested in their study. In the experiments, straight copper tube with 4.5±0.02 mm inner diameter, 6.4±0.05 mm outer diameter and 970 mm length was used as a test section. A flexible silicon rubber having 300W heating capacity was used to maintain a constant heat flux boundary condition. A peristaltic pump was used to deliver a maximum flow rate of 10 l/min. The flow rate was controlled by adjusting rotational speed of the pump. Sodium dodecylbenzene sulfonate (SDBS) was used as a dispersant in order to stabilize the nanoparticles.

Maiga *et al*. [142] reported numerical method and a mathematical formulation for water-γAl_2O_3 and ethylene glycol-γAl_2O_3 to determine the forced convective heat transfer and wall shear stress for the laminar and turbulent regions of water-γAl_2O_3 and ethylene glycol-γAl_2O_3 flowing inside a uniformly heated tube. The solid-liquid mixture was considered as a single-phase, so the slip velocity between the phases was neglected. Moreover, symmetry in flow and the local thermal equilibrium of the mixture were considered. To define heat flux and stresses of the nanofluids for the turbulent flow, the Reynolds-averaged Navier-Stokes equation and κ-ε turbulent model were used. In the numerical simulations, the heated tube having 0.01m diameter and 1.0 m length was used. The conditions of laminar flow were as follows: the Reynolds number was fixed at 250 and the constant heat flux was varied between 10-250 W/m^2. The conditions of turbulent flow were as follows: the constant heat flux was fixed at 500,000 W/m^2 and the Reynolds number was varied in the range of 10,000-50,000.

Roy *et al*. [143] performed a numerical investigation to analyze the heat transfer and wall shear stress for radial laminar flow in a cooling system of water-γAl_2O_3 nanofluids compared with some base fluids such as water, glycol, and oil. All assumptions used in this study being similar to those reported by Maiga *et al*. [142] marked the nanofluid as an incompressible fluid.

Nguyen *et al*. [144] introduced a numerical simulation to determine the efficiency of water-γAl_2O_3 and ethylene glycol-γAl_2O_3 nanofluids for the cooling of a high-heat output microprocessor under laminar forced flow inside a heat sink. The simulation set-up comprised of a 50x50x10 mm rectangular slot having a 3x48 mm fluid flow cross-section. In this article, assumptions were uniform velocity and temperature profile at the inlet section and laminar flow. The contact area for exchange heat was 10x10 mm. The numerical results showed that Reynolds number and the volume fraction were mainly parameters affecting average heat transfer coefficient of nanofluids and ethylene glycol-γAl_2O_3 nanofluid had higher heat transfer coefficient than that of the water-γAl_2O_3 nanofluid.

Ali *et al*. [145] reported the mathematical and numerical formulation to determine heat and mass transfer between air and falling solution film in a cross-flow heat exchanger for the dehumidification and cooling process. Effect of Cu nanoparticles to the heat and mass transfer process were tested by adding them into the solution. In this study, two models from available literature were used. Moreover, the assumptions of this article were laminar and steady state flow. Constant film thickness, thermal properties of the air and the solution were constant except for the thermal conductivity of the solution, gravitational force of the air was neglected for fully developed velocity profile of fluids. According to he results of the study, the dehumidification and cooling process increased with high Cu particle volume fraction, low air Reynolds number, decrease in the channel width, increase in the height and length of the channel. In addition, it was revealed that an increase in Cu volume fraction led to more stability of the solution.

Ali and Vafai [146] suggested the numerical and mathematical formulations in order to analyze the effects of the inclination angel of parallel-and-counter-flow on heat and mass transfer between air and falling desiccant film having Cu nanoparticles suspended. They used the same assumptions in the two approach models as those used in the previous paper such as the simulated conditions used in this study being low and high air Reynolds number for the inclined parallel flow arrangement and low and high air Reynolds number for the inclined counter flow configuration.

Zhu *et al*. [147] developed a method for the preparation of copper nanofluids using the base fluid of ethylene glycol with $CuSO_4 \cdot 5H_2O$ with $NaH_2PO_2 \cdot H_2O$ under microwave irradiation. They investigated the effects of $CuSO_4$concentration with the addition of NaH_2PO_2 and microwave irradiation on the reaction rate and the properties of Cu nanofluids by transmission of electron microscopy, infrared analysis, and sedimentation measurements. They obtained nonagglomerated and stably suspended Cu nanofluids at the end of their analysis.

3j. Somestudies of 2003 and Previous Studies

Li and Xuan [148] and Xuan and Li [149] used an experimental set up in order to determine the convective heat transfer coefficient and friction factor parameters of nanofluids for laminar and turbulent flow in a tube. Deionized water with a dispersion of Cu particles with under 100nm diameter was used in this study. The effect of the nanoparticle concentration on the heat transfer coefficient was determined for different particle volume percentages being 0.3, 0.5, 0.8, 1, 1.5 and 2%. The Reynolds number of the nanofluids varied between 800 and 25,000. The experimental set up was consisted of a test section, a pipeline, a pump, a cooler, a fluid collection and a reservoir tank. A straight brass tube having 800 mm length and 10 mm inner diameter was used and a 3.5 kW electric heater was placed to test section for getting a constant wall heat flux boundary condition. A fatty acid was used to prevent the aggregation of the nanoparticles in the base fluid.

Xuan and Li [149] suggested a method for preparing some nanofluid samples and presented theoretical study of thermal conductivity. The transient hot-wire method was used for measurements in their study. For determining the heat transfer performance of nanofluids flowing in a tube, they proposed a single phase or dispersion model. Cu particles having a diameter of 100 nm were used as nanoparticles where base fluids are water and mineral oil. The particles in the mineral oil and water were stabilized by using oleic acid and laureate salt respectively. For Cu-mineral oil, suspension stabilization time was nearly 1 week and suspension had no sedimentation with a fill of 22 wt%. For Cu-water, suspension with 9

wt% laureate salt, vibrated by an ultrasonic vibrator, the results indicated that the nanoparticles could suspend more 30 h than in stationary state. This behavior implied that particle stability and dispersion were affected by fluid viscosity. Furthermore, this study showed that and Crosser model [150] and Wasp model [151] can be used for predicting thermal conductivity in the absence of a sophisticated formula. According to measurements obtained by using transient hot-wire method, the thermal conductivity was observed to be significantly varied with the volume fraction of the particles. The heat transfer enhancement was evaluated with two different ways the single-phase model and two-phase model. The single phase model assumed that both the liquid and particle phases being in thermal equilibrium were flowing at the same velocity. This model beingsimple required less computation time. The two-phase model provided opportunity to understand functions of liquid phase and solid phase in the heat transfer process but required a long time for computation and a high performance computer.

The purpose of their work aimed to develop a modified single-phase model to determine the heat transfer process of nanofluids flowing in tubes.

Xuan and Roetzel [152] presented two different approaches to define some fundamentals for predicting the convective heat transfer coefficient of nanofluids under the assumption that they behaved like a single-phase liquid rather than a normal solid-liquid mixture. In their study, the effects of thermal dispersion and transport properties of the nanofluid were covered. The first model treated as a single-phase and the other model treated as a multi-phase fluid and dispersed fluid. It was assumed that liquid phase and the particles being in thermal equilibrium state were devoid of slip velocity between them. The nanofluid acted as a common pure liquid. This implied that the all equation of energy continuity, and motion for a single-phase fluid had been applied directly to the nanofluid.

Similar to the Xuan and Li model [153], the Hamilton and Crosser model [150] and Wasp model [151] provided rough results for predicting the thermal conductivity of nanofluid. For a modified conventional approach, known as dispersion model, the slip velocity between the solid-liquid mixture could not be zero because of many factors such as gravity, Brownian force, friction force between the solid-liquid mixture, Brownian diffusion, sedimentation, and dispersion happening simultaneously in the main flow.

Xue [154] presented a model of the effective thermal conductivity for nanofluids, based on Maxwell theory and average polarization theory, considering the interface effect between the solid particles and the base fluid in nanofluids. They found that their theoretical results were in good agreement with the experimental data on the effective thermal conductivity of nanotube/oil nanofluid and Al_2O_3/water nanofluid.

4. CONCLUSIONS

Nanofluid has been classified as a new class of heat transfer fluids engineered by dispersing metallic or non-metallic nanoparticleswith a typical size of less than 100 nm in the conventional heat transfer fluids. Their use remarkably augments the heat transfer potential of the base liquids thus offering an opportunity to the engineers for the development of highly compact and effective heat transfer equipmentfor many industrial applications, nuclear reactors, transportation, electronics as well as biomedicine and food.

Nanofluid is consideredas an innovative heat transfer fluid with superior potential for enhancing the heat transfer performance of conventional fluids. This review presents the recent studies of single phase and two-phase nanofluid flows in tubes and channels and also helps to determine the physical properties of nanofluids chronologically. According to the most recent experimental papers, heat transfer performance of the base fluid can significantly be increased by the suspended nanoparticles since heat transfer coefficient of the nanofluid was found to be larger than that of its base fluid for the same Reynolds number. The volume fraction of nanoparticles increases the heat transfer feature of a nanofluid. Pressure drop and friction factors of nanofluids are also larger than its base fluids. Besides of many attempts made to determine the nanofluids' thermal conductivity and viscosity, being important thermophysical properties no definitive agreements have emerged on these properties. Moreover, there is a lack of studies on the mixture flows of nano particles with the refrigerants as pressurized flows in tubes or channels due to the hardness in the experimental conditions.

CONFLICT OF INTEREST

The authors confirm that this article content has no conflicts of interest.

ACKNOWLEDGEMENTS

The authors would like to thank King Mongkut's University of Technology Thonburi (KMUTT), the Thailand Research Fund, the Office of Higher Education Commission and the National Research University Project for the financial support. Especially, the first author wishes to thank KMUTT for providing him with a Post-doctoral fellowship.

REFERENCES

[1] Putra, N.; Roetzel W.; Das, S. K. Natural convection of nano-fluids. *Int. J. Heat Mass Transfer*., **2003**, *39*, 775-784.

[2] Tang, G.Y.; Yang, C.; Chai, J.C.; Gong, H.Q. Joule heating effect on electroosmotic flow and mass species transport in a microcapillary. *Int. J. Heat and Mass Transfer*., **2004**, *47*, 215-227.

[3] Tseng, W.J.; Chen, C.N. Effect of polymeric dispersant on rheological behavior of nickel–terpineol suspensions. *Mater. Sci. Eng*., **2003**, A *347* (1–2), 145-153.

[4] Chen, H.; Ding, Y.; He, Y.; Tan, C. Rheological behaviour of ethylene glycol based titania nanofluids. *Chem. Phys. Lett.*, **2007**, *444* (4–6), 333-337.

[5] Nguyen, C.; Desgranges, F.; Roy, G.; Galanis, N.; Mare, T.; Boucher, S.; Anguemintsa, H. Temperature and particle-size dependent viscosity data for water-based nanofluids – hysteresis phenomenon. *Int. J. Heat Fluid Flow*., **2007**, *28* (6), 1492-1506.

[6] Khanafer, K.; Vafai, K. A. critical synthesis of thermophysical characteristics of nanofluids. *Int. J. Heat Mass Transfer*, **2011**, *54,* 4410-4428.

[7] Duangthongsuk, W.; Wongwises, S. Measurement of temperature-dependent thermal conductivity and viscosity of TiO2–water nanofluids. *Exp. Therm. Fluid Sci*., **2009**, 33, 706–714.

[8] Yu, W.; Choi, S.U.S. The role of interfacial layers in the enhanced thermal conductivity of nanofluids: a renovated Maxwell model. *J. Nanopart. Res.*, **2003**, *5*, 167-171.

[9] Godson, L.; Raja, B.; Lal, M.D.; Wongwises, S. Experimental investigation on the thermal conductivity and viscosity of silver-deionized water nanofluid. *Exp. Heat Transfer.*, **2010**, *23*, 317-332.

[10] Prasher, R.; Bhattacharya, P.; Phelan, P.E. Thermal conductivity of nanoscale colloidal solutions (nanofluids). *Phys. Rev. Lett.*, **2005**, *94*, 025901-1–025901-4.

[11] Koo J., Kleinstreuer,C. A new thermal conductivity model for nanofluids. *J. Nanopart. Res.*, **2004**, *6*, 577-588.

[12] Li, C.H.; Peterson, G.P. Experimental investigation of temperature and volume fraction variations on the effective thermal conductivity of nanoparticle suspensions (nanofluids). *J. Appl. Phys.*, **2006**, *99*, 084314.

[13] Maiga, S.E.B.; Nguyen, C.T.; Galanis, N.; Roy, G. Heat transfer behaviours of nanofluids in a uniformly heated tube. *Superlattice. Microst.*,**2004**, *35*, 543-557.

[14] Bhattacharya, P.; Saha, S.K.; Yadav, A.; Phelan, P.E.; Prasher, R.S. Brownian dynamics simulation to determine the effective thermal conductivity of nanofluids. *J. Appl. Phys.*, **2004**, *95*, 6492-6494.

[15] Buongiorno, J. Convective transport in nanofluids. *J. Heat Transf.*, **2006**, *128*, 240-251.

[16] Kim, D.; Kwon, Y.; Cho, Y.; Li, C.; Cheong S., Hwang Y., Lee J., Hong D., Moon S., Convective heat transfer characteristics of nanofluids under laminar and turbulent flow conditions. *Curr. Appl. Phys.*, **2009**, *9* (2), 119-123.

[17] Timofeeva, E. V.; Gavrilov, A. N.;McCloskey, J.M.;Tolmachev, Y.V. Thermal conductivity and particle agglomeration in alumina nanofluids: Experiment and Theory. *Phys. Rev. E*, **2007,** *76*, 061203.

[18] Chon, C.H.; Kihm, K.D.; Lee, S.P.; Choi, S.U.S. Empirical correlation finding the role of temperature and particle size for nanofluid (Al2O3) thermal conductivity enhancement. *Appl. Phys. Lett.*, **2005**, *87*.

[19] Murshed, S.M.S.; Leong, K.C.; Yang, C. A model for predicting the effective thermal conductivity of nanoparticles–fluid suspensions, *Int. J. Nanosci*., **2006**, *5,* 23-33.

[20] Qiang, L.; Yimin, X. Convective heat transfer and flow characteristics of Cu-water nanofluid. *Sci. China Ser. E*, **2002**, *45*, 408-416.

[21] Yang, Y.; Zhang, Z.G.; Grulke, E.A.; Anderson, W.B.; Wu, G. Heat Transfer properties of nanoparticle-in-fluid dispersions (Nanofluids) in laminar flow. *Int. J. Heat Mass Transfer*., **2005**, *48*, 1107-1116.

[22] Monrad, C.C; Pelton, J.F. Heat transfer by convection in annular spaces. *Trans. Am. Inst. Chem. Eng.,* **1942**, *38*, 593-611.

[23] Sieder, E.N.; Tate, G.E. Heat transfer and pressure drop of liquids in tubes. *Ind. Eng. Chem.*, **1936**, *28*, 1429-1435.

[24] Choi, U.S. Enhancing thermal conductivity of fluids with nanoparticle. *ASME FED 231*, **1995**, *231*, 99-103.

[25] Alizad, K.; Vafai, K.; Shafahi M. Thermal performance and operational attributes of the startup characteristics of flat-shaped heat pipes using nanofluids. *Int. J. Heat Mass Transfer*, **2012,** *55*, 140-155.

[26] Bobbo, S.; Fedele, L.; Benetti, A.; Colla, L.; Fabrizio, M.; Pagura, C.; Barison, S. Viscosity of water based SWCNH and TiO_2 nanofluids. *Exp. Therm. Fluid Sci.*, **2012,** *36*, 65-71.

[27] Buschmann, M. H.; Thermal conductivity and heat transfer of ceramic nano fluids. *Int. J. Therm. Sci.*, **2011**, Article in Press-Corrected Proof.

[28] Yang, L.; Du, K.; Ding, Y. H.; Cheng, B.; Li, Y. J. Viscosity-prediction models of ammonia water nanofluids based on various dispersion types. *Powder Technol.,* **2012**, *215-216*, 210-218.

[29] Colangelo, G.; Favale E.; Risi A.; Laforgia, D. Results of experimental investigations on the heat conductivity of nanofluids based on diathermic oil for high temperature applications. *Appl. Energy*, **2011**, Article in Press-Corrected Proof..

[30] Jamshidi, N.; Farhadi, M.; Sedighi, K.; Ganji, D. D. Optimization of design parameters for nanofluids flowing inside helical coils. *Int. Commun. Heat Mass Trans.,* **2011***, 39*, 311-317.

[31] Giraldo, M.; Sanin, D.; Flórez, W. F. Heat transfer in nanofluids: A computational evaluation of the effects of particle motion. *Appl. Math. Comput.,* **2011**, Article in Press-Corrected Proof.

[32] S. Özerinç, A .G. Yazıcıoglu, S. Kakaç, Numerical analysis of laminar forced convection with temperature-dependent. *Int. J. Therm. Sci.*, **2011**, Article in Press-Corrected Proof.

[33] Yu, L.; Liu, D.; Botz, F. Laminar convective heat transfer of alumina-polyalphaolefin nanofluids containing spherical and non-spherical nanoparticles. *Exp. Therm. Fluid Sci*., **2011**, *37*, 72-83.

[34] Farahani, S.D.; Kowsary, F. Estimation local convective boiling heat transfer coefficient in mini channel. *Int. Commun. Heat Mass Trans.*, **2011**, *39*, 304-310

[35] Cimpean, D. S.; Pop, I. Fully developed mixed convection flow of a nanofluid through an inclined channel filled with a porous medium. *Int. J. Heat Mass Transfer*, **2012**, *55*, 907-914.

[36] Leong, K.Y.; Saidur, R.; Mahlia, T.M.I.; Yau, Y.H. Modeling of shell and tube heat recovery exchanger operated with nanofluid based coolants. *Int. J. Heat and Mass Transfer*, **2012**, *55*, 808-816.

[37] Mahbubul, I.M.; Saidur, R.; Amalina, M.A. Latest developments on the viscosity of nanofluids. *Int. J. Heat Mass Transfer,* **2012**, *55*, 874-885.

[38] Wenzheng, C.; Minli, B.; Jizu, L.; Xiaojie, Li. On the microscopic flow characteristics of nanofluids by molecular dynamics simulation on Couette Flow. *Open Fuels Energy Sci. J.*, **2012**, *5*, 21-27.

[39] Ahmed, M.A.; Shuaib, N.H.; Yusoff, M.Z.; Al-Falahi A.H. Numerical investigations of flow and heat transfer enhancement in a corrugated channel using nanofluid. *Int. Commun. Heat Mass Trans.,* **2011**, *38*, 1368-1375.

[40] Akbarinia, A.; Abdolzadeh, M.; Laur, R. Critical investigation of heat transfer enhancement using nanofluids in microchannels with slip and non-slip flow regimes. *Appl. Therm. Eng.*, **2011**, *31*, 556-565.

[41] Bianco, V.; Manca, O.; Nardini, S. Numerical investigation on nanofluids turbulent convection heat transfer inside a circular tube. *Int. J. Therm. Sci*., **2011**, *50*, 341-349.

[42] Corcione, M. Empirical correlating equations for predicting the effective thermal conductivity and dynamic viscosity of nanofluids. *Energy Convers. Manage.*, **2011**, *52*, 789-793.

[43] Firouzfar, E.; Soltanieh, M.; Noie, S.H.; Saidi, S.H. Energy saving in HVAC systems using nanofluid. *Appl. Therm. Eng*., **2011**, *31*, 1543-1545.

[44] Gherasim, I.; Roy; G., Nguyen, C.T.; Vo-Ngoc, D. Heat transfer enhancement and pumping power in confined radial flows using nanoparticle suspensions (nanofluids). *Int. J. Therm. Sci.,* **2011**, *50*, 369-377.

[45] Hojjat, M.; Etemad, S.Gh.; Bagheri, R.; Thibault. J. Convective heat transfer of non-Newtonian nanofluids through a uniformly heated circular tube. *Int. J. Therm. Sci.,* **2011**, *50*, 525-531.

[46] Hojjat, M.; Etemad, S.Gh.; Bagheri, R.; Thibault, J. Thermal conductivity of non-Newtonian nanofluids: Experimental data and modeling using neural network. *Int. J. Heat Mass Trans*., **2011**, *54*, 1017-1023.

[47] Hojjat, M.; Etemad, S.Gh.; Bagheri, R.; Thibault. Turbulent forced convection heat transfer of non-Newtonian nanofluids. *Exp. Therm. Fluid Sci.,* **2011***, 35*, 1351-1356.

[48] Huminic, G.; Huminic, A. Heat transfer characteristics in double tube helical heat exchangers using nanofluids. *Int. J. Heat Mass Tran.,* **2011***, 54*, 4280-4287.

[49] Huminic, G.; Huminic, A. Heat transfer characteristics of a two-phase closed thermosyphons using nanofluids. *Exp. Therm. Fluid Sci.,* **2011***, 35,* 550-557.

[50] Jung, J.Y.; Cho, C.; Lee, W.H.; Kang, Y.T. Thermal conductivity measurement and characterization of binary nanofluids. *Int. J. Heat Mass Trans.,* **2011***, 54*, 1728-1733.

[51] Khanafer, K.; Vafai, K. A critical synthesis of thermophysical characteristics of nanofluids. *Int. J. Heat Mass Trans.,* **2011***, 54*, 4410-4428.

[52] Lee, S.W.; Park, S.D.; Kang, S.; Bang, I.C.; Kim, J.H. Investigation of viscosity and thermal conductivity of SiC nanofluids for heat transfer applications. *Int. J. Heat Mass Trans.,* **2011**, *54*, 433-438.

[53] Asirvatham, L.G.; Raja, B.; Lal, D.M.; Wongwises, S., Convective heat transfer of nanofluids with correlations. *Particuology*, **2011**, *9*, 626-631.

[54] Ebrahimnia-Bajestan, E.; Niazmand, H.; Duangthongsuk, W; Wongwises, S. Numerical investigation of effective parameters in convective heat transfer of nanofluids flowing under a laminar flow regime. *Int. J. Heat Mass Trans.,* **2011***, 54*, 4376-4388.

[55] Raisi, A.; Ghasemi, B.; Aminossadati, S. M. A Numerical study on the forced fonvection of laminar nanofluid in a microchannel with both slip and No-slip conditions. *Numer. Heat Tr. A-Appl.*, **2011**, *59*, 114-129.

[56] Heris, S; Z.;Noie, S.H.; Talaii, E.; Sargolzaei, J. Numerical investigation of Al2O3/water nanofluid laminar convective heat transfer through triangular ducts. *Nanoscale Res. Lett.*,**2011**, *6*,1-10.

[57] Vincenzo, B.; Nardini, S.; Manca, O. Enhancement of heat transfer and entropy generation analysis of nanofluids turbulent convection flow in square section tubes. *Nanoscale Res. Lett.,* **2011**, *6*, 1-12.

[58] Demir, H.; Dalkilic, A.S.; Kürekci, N.A.; Wongwises, D. S. Numerical investigation on the single phase forced convection heat transfer characteristics of TiO_2 nanofluids in a double-tube counter flow heat exchanger. *Int. J. Commun. Heat Mass Trans*., **2011**, *38*, 218-228.

[59] Abareshi, M.; Goharshadi, E.; Zebarjad, S.M.; Fadafan, H.K.; Youssefi, A. Fabrication characterization and measurement of thermal conductivity of Fe_3O_4 nanofluids. *J. Magn. Magn.Mater*., **2010**, *322*, 3895-3901.

[60] Farajollahi, B. I; Etemad, S.Gh.; Hojjat, M. Heat transfer of nanofluids in a shell and tube heat exchanger. *Int. J. Heat Mass Trans*., **2010,** *53*, 12-17.

[61] Fard, H. M.; Esfahany, M.N.; Talaie, M.R. Numerical study of convective heat transfer of nanofluids in a circular tube two-phase model versus single-phase model. *Int. J. Commun. Heat Mass Trans*., **2010**, *37*, 91-97.

[62] Do, K.H.; Ha, H.J.; Jang, S.P. Thermal resistance of screen mesh wick heat pipes using the water-based Al_2O_3 nanofluids. *Int. J. Heat Mass Trans*., **2010**, *53*, 5888-5894.

[63] Henderson, K.; Park, Y.G.; Liu, L.; Jacobi, A.M. Flow-boiling heat transfer of R-134a-based nanofluids in a horizontal tube, *Int. J. Heat Mass Trans.*, **2010**, *53*, 944-951.

[64] Godson, L.; Raja, B.; Lal, D.M.; Wongwises, S. Enhancement of heat transfer using nanofluids-An overview. *Renew. Sust. Energ. Rev.*, **2010**, *14*, 629-641.

[65] Kima, S.J.; McKrella, T.; Buongiornoa, J.; Hu, L.W Subcooled flow boiling heat transfer of dilute alumina, zinc oxide, and diamond nanofluids at atmospheric pressure. *Nucl. Eng. Des.*, **2010**, *240*, 1186-1194.

[66] Lotfi, R.; Saboohi, Y.; Rashidi, A.M. Numerical study of forced convective heat transfer of Nanofluids: Comparison of different approaches. *Int. J. Commun. Heat Mass Trans.,* **2010***, 37*, 74-78.

[67] Meibodi, M.E.; Sefti, M.V.; Rashidi, A.M.; Amrollahi, A.; Tabasi, M.; Kalal, H.S. Simple model for thermal conductivity of nanofluids using resistance model approach . *Int. J. Commun. Heat Mass Trans. ,* **2010**, *37*, 555-559.

[68] Meibodi, M.E.; Sefti, M.V.; Rashidi, A.M.; Amrollahi, A.; Tabasi, M.; Kalal, H.S. An estimation for velocity and temperature profiles of nanofluids in fully developed turbulent flow conditions. *Int. J. Commun. Heat Mass Trans.,* **2010**, *37*, 895-900.

[69] Meibodi, M.E.; Sefti, M.V.; Rashidi, A.M.; Amrollahi, A.; Tabasi, M.; Kalal, H.S. The role of different parameters on the stability and thermal conductivity of carbon nanotube/water nanofluids. *Int. J. Commun. Heat Mass Trans.*, **2010***, 37*, 319-323.

[70] Paul, G.; Chopkar, M.; Manna, I.; Das, P.K. Techniques for measuring the thermal conductivity of nanofluids: A review. *Renew. Sust. Energ. Rev.*, **2010**, *14*, 1913-1924.

[71] Paul, G.; Pal, T.; Manna, I. Thermo-physical property measurement of nano-gold dispersed water based nanofluids prepared by chemical precipitation technique. *J. Colloid Interf. Sci.*, **2010**, *349*, 434-437.

[72] Qu, J.; Wu, H.Y.; Cheng, P. Thermal performance of an oscillating heat pipe with Al_2O_3-water nanofluids. *Int. J. Commun. Heat Mass Trans.,* **2010***, 37*, 111-115.

[73] Rao, Y. Nanofluids: Stability, phase diagram, rheology and applications, *Particuology*, **2010**, 549-555.

[74] Raykar, V.S.; Singh, A.K. Dispersibility dependence of thermal conductivity of carbon nanotube based nanofluids. *Phys. Lett. A*, **2010**, *374*, 4618-4621.

[75] Roberts, N.A.; Walker, D.G. Convective performance of nano fluids in commercial electronics cooling systems. *Appl. Therm. Eng.*, **2010**, *30*, 2499-2504.

[76] Rostamani, M.; Hosseinizadeh, S.F.; Gorji, M.; Khodadadi, J.M. Numerical study of turbulent forced convection flow of nano fluids in a long horizontal duct considering variable properties. *Int. J. Commun. Heat Mass Trans*., **2010**, *37*, 1426-1431.

[77] Singh, P.K.; Anoop, K.B.; Sundararajan, T.; Das, S. K. Entropy generation due to flow and heat transfer in nanofluids. *Int. J. Heat Mass Trans*., **2010**, *53*, 4757-4767.

[78] Sundar, L.S. R; Sharma, K.V. Turbulent heat transfer and friction factor of Al_2O_3 Nanofluid in circular tube with twisted tape inserts. *Int. J. Heat Mass Trans*., **2010**, *53*, 1409-1416.

[79] Vajjha, R. S.; Das, D. K.; Kulkarni, D.P. Development of new correlations for convective heat transfer and friction factor in turbulent regime for nanofluids. *Int. J. Heat Mass Trans*., **2010**, *53* 4607-4618.

[80] Vajjha, R.S.; Das, D.K.; Namburu, P. K. Numerical study of fluid dynamic and heat transfer performance of Al_2O_3 and CuO nanofluids in the flat tubes of a radiator. *Int. J. Heat Fluid Fl.*, **2010**, *31*, 613-621.

[81] Wei, X.; Kong, T.; Zhu, H.; Wang, L. CuS/Cu_2S nanofluids: Synthesis and thermal conductivity. *Int. J. Heat Mass Trans*., **2010**, *53*, 1841-1843.

[82] Wei, X.; Wang, L. Synthesis and thermal conductivity of microfluidic copper nanofluids. *Particuology*, **2010**, *8*, 262-271.

[83] Yang, Y.T.; Lai, F.H. Numerical study of heat transfer enhancement with the use of nanofluids in radial flow cooling system. *Int. J. Heat Mass Trans*., **2010**, *53*, 5895-5904.

[84] Yu W., Xie H., Chen L., Li Y. Investigation on the thermal transport properties of ethylene glycol-based nanofluids containing copper nanoparticles. *Powder Technol.*, **2010**, *197*, 218-221.

[85] Wong, K.V.; Leon, O.D. Applications of Nanofluids: Current and Future. *Adv. Mech. Eng*., **2010**, 1-11.

[86] Duangthongsuk, W; Wongwises, S. Comparison of the effects of measured and computed thermophysical properties of nanofluids on heat transfer performance. *Exp. Therm. Fluid Sci.,* **2010***, 34*, 616-624.

[87] Duangthongsuk, W; Wongwises, S. An experimental study on the heat transfer performance and pressure drop of TiO_2-water nanofluids flowing under a turbulent flow regime. *Int. J. Heat Mass Trans*., **2010**, *53*, 334-344.

[88] Bergman, T.L. Effect of reduced specific heats of nanofluids on single phase, laminar internal forced convection. *Int. J. Heat Mass Trans*., **2009**, *52*, 1240-1244.

[89] Bianco, V.; Chiacchio, F.; Manca, O.; Nardini, S. Numerical investigation of nanofluids forced convection in circular tubes. *Appl. Therm. Eng.*, **2009**, *29*, 3632-3642.

[90] He, Y.; Men, Y.; Zhao, Y.; Lu, H.; Ding, Y. Numerical investigation into the convective heat transfer of TiO2 nanofluids flowing through a straight tube under the laminar flow conditions. *Appl. Therm. Eng.,* **2009***, 29*, 1965-1972.

[91] Hwang, K.S.; Jang, S.P.; Choi, S.U.S. Flow and convective heat transfer characteristics of water-based Al2O3 nanofluids in fully developed laminar flow regime. *Int. J. Heat Mass Trans*., **2009**, *52*, 193-199.

[92] Jung, J.Y.; Oh, H.S; Kwak, H.Y. Forced convective heat transfer of nanofluids in microchannels. *Int. J. Heat Mass Trans*., **2009***, 52*, 466-472.

[93] Kakaç S., Pramuanjaroenkij, A., Review of convective heat transfer enhancement with nanofluids. *Int. J. Heat Mass Trans*., **2009**, *52*, 3187-3196.

[94] Kim, D.; Kwon, Y.; Cho, Y.; Li, C.; Cheong, S.; Hwang, Y.; Lee, J.; Hong, D.; Moon S. Convective heat transfer characteristics of nanofluids under laminar and turbulent flow conditions. *Curr. Appl. Phys*., **2009**, *9*, e119-e123.

[95] Kulkarni, D.P.; Das, D.K.; Vajjha, R.S. Application of nanofluids in heating buildings and reducing pollution. *Appl. Energ.*, **2009**, *86*, 2566-2573.

[96] Mintsa, H.A; Roy, G.; Nguyen, C.T.; Doucet, D. New temperature dependent thermal conductivity data for water-based nanofluids. *Int. J. Therm. Sci.*, **2009**, *48*, 363-371.

[97] Murshed, S.M.S.; Leong, K.C.; Yang, C. A combined model for the effective thermal conductivity of nanofluids. *Appl. Therm. Eng.*, **2009**, *29*, 2477-2483.

[98] Namburu, P.K.; Das D. K., Tanguturi, K.M.; Vajjha, R.S. Numerical study of turbulent flow and heat transfer characteristics of nanofluids considering variable properties*. Int. J. Therm. Sci.*, **2009**, *48*, 290-302.

[99] Rea, U.; McKrell, T.; Hu, L.W. Buongiorno J., Laminar convective heat transfer and viscous pressure loss of alumina-water and zirconia-water nanofluids. *Int. J. Heat Mass Trans*., **2009**, *52*, 2042-2048.

[100] Pantzali, M.N.; Mouza, A.A.; Paras, S.V. Investigating the efficacy of nanofluids as coolants in plate heat exchangers (PHE), *Chem. Eng. Sci*., **2009**, *64*, 3290-3300.

[101] Xie, H.; Chen, L. Adjustable thermal conductivity in carbon nanotube nanofluids. *Phys. Lett.*, **2009**, *373*, 1861-1864.

[102] Pantzali, M.N.; Kanaris, A.G.; Antoniadis, K.D.; Mouza, A.A.; Paras, S.V. Effect of nanofluids on the performance of a miniature plate heat exchanger with modulated surface. *Int. J. Heat Fluid Fl.*, **2009**, *30*, 691-699.

[103] Vajjha, R.S.; Das, D. K. Experimental determination of thermal conductivity of three nanofluids and development of new correlations. *Int. J. Heat Mass Trans*., **2009**, *52*, 4675-4682.

[104] Wen D., Lin G., Vafaei S., Zhang K., Review of nanofluids for heat transfer applications. *Particuology,* **2009**, *7*, 141-150.

[105] Hadjov, K.B. Modified self-consisted scheme to predict the thermal conductivity of nanofluids. *Int. J. Therm. Sci.,* **2009***,* 48, 2249-2254.

[106] Ali, M.; Zeitoun, O. Nanofluids forced convection heat transfer inside circular tubes. *Int. J. Nanoparticles*, **2009**, *2*, 164-172.

[107] Duangthongsuk, W.; Wongwises, S. Measurement of temperature-dependent thermal conductivity and viscosity of TiO2-water nanofluids.*Exp. Therm. Fluid Sci*., 2009, *33*,706-714.

[108] Duangthongsuk, W.; Wongwises, S. Heat transfer enhancement and pressure drop characteristics of TiO_2-water nanofluid in a double-tube counter flow heat exchanger. *Int. J. Heat Mass Trans*., **2009**, *52*, 2059-2067.

[109] Bi, S.S.; Shi, L.; Zhang, L.L Application of nanoparticles in domestic refrigerators. *Appl. Therm. Eng.*, **2008**, *28*, 1834-1843.

[110] Hwang, Y., Lee, J. K.; Lee, J.K.; Jeong, Y.M.; Cheong, S.; Ahn, Y.C.; Kim, S. H. Production and dispersion stability of nanoparticles in nanofluids. *Powder Technol*., **2008**, *186*, 145-153.

[111] Karthikeyan, N.R.; Philip, J.; Raj, B. Effect of clustering on the thermal conductivity of nanofluids. *Mater. Chem. Phys.,* **2008**, *109*, 50-55.

[112] Khandekar, S.; Joshi, Y.M.; Mehta, B. Thermal performance of closed two-phase thermosyphon using nanofluids. *Int. J. Therm. Sci.,* **2008***, 47*, 659-667.

[113] Lee, J.H; Hwang, K.S.; Jang, S.P; Lee, B.H.; Kim, Ho, J.; Choi, S.U.S. Effective viscosities and thermal conductivities of aqueous nanofluids containing low volume concentrations of Al_2O_3 nanoparticles. *Int. J. Heat Mass Trans*., **2008**, *51*, 2651-2656.

[114] Murshed, S.M.S.; Leong, K.C.; Yang, C. Thermophysical and electrokinetic properties of nanofluids - A critical review. *Appl. Therm. Eng.,* **2008**, *28*, 2109-2125.

[115] Oh, D.W.; Jain, A.; Eaton, J. K.; Goodson, K. E.; Lee, J. S. Thermal conductivity measurement and sedimentation detection of aluminum oxide nanofluids by using the 3 w method. *Int. J. Heat Fluid Fl*., **2008**, *29*, 1456-1461.

[116] Kang, Y.T.; Kim, H. J.; Lee, K.I. Heat and mass transfer enhancement of binary nanofluids for H_2O/LiBr falling film absorption process. *Int. J. Refrig.*,**2008**, *31*, 850-856.

[117] Lu, W.Q.; Fan, Q.M. Study for the particle's scale effect on some thermophysical properties of nanofluids, by a simplified molecular dynamics method. *Eng. Anal. Bound. Elem.*, **2008**, *32*, 282-289.

[118] Nguyen, C.T.; Desgranges, F.; Galanis, N.; Roy, G.; Maré, T.; Boucher, S.; Mintsa, H. A. Viscosity data for Al_2O_3–water nanofluid-hysteresis: is heat transfer enhancement using nanofluids reliable. *Int. J. Therm. Sci.,* **2008***, 47*, 103-111.

[119] Chen, H.; Yang, W.; He, Y.; Ding, Y.; Zhang, L.; Tan, C.; Lapkin, A. A.; Bavykin, D. V. Heat transfer and flow behavior of aqueous suspensions of titanate nanotubes (nanofluids). *Powder Technol.,* **2008**, *183*, 63-72.

[120] Ding, Y.; Chen, H.; He, Y.; Lapkin, A.; Yeganeh, M.; Šiller, L.; Butenko, Y. V. Forced convective heat transfer of nanofluids. *Adv. Powder Technol.*, **2007**, *18*, 813-824.

[121] Zhang, X.; Gu, H.; Fujii, M.; Effective thermal conductivity and thermal diffusivity of nanofluids containing spherical and cylindrical nanoparticles. *Exp. Therm. Fluid Sci.,* **2007***, 31*, 593-599.

[122] Ko, G.H.; Heo, K.; Lee, K.; Kim, D.S.; Kim, C.; Sohn, Y. Choi M., An experimental study on the pressure drop of nanofluids containing carbon nanotubes in a horizontal tube. *Int. J. Heat Mass Trans*., **2007**, *50*, 4749-4753.

[123] Mansour, R.B.; Galanis, N.; Nguyen, C.T. Effect of uncertainties in physical properties on forced convection heat transfer with nanofluids. *Appl. Therm. Eng.*, **2007**, *27*, 240-249.

[124] Hong, H.; Wright, B.; Wensel, J.; Jin, S.; Ye, X.R.; Roy, W. Enhanced thermal conductivity by the magnetic field in heat transfer nanofluids containing carbon nanotube. *Synthetic Met.*, **2007**, *157*, 437-440.

[125] Li, C.H.; Peterson, G.P. Mixing effect on the enhancement of the effective thermal conductivity of nanoparticle suspensions (nanofluids). *Int. J. Heat Mass Trans.*, **2007**, 50, 4668-4677.

[126] Yoo, D.H.; Hong, K.S.; Yang, H.S. Study of thermal conductivity of nanofluids for the application of heat transfer fluids. *Thermochim. Acta*, **2007**, *455*, 66-69.

[127] Avsec, J.; Oblak, M. The calculation of thermal conductivity, viscosity and thermodynamic properties for nanofluids on the basis of statistical nanomechanics. *Int. J. Heat Mass Trans.*, **2007**, *50*, 4331-4341.

[128] He, Y.; Jin, Yi; Chen, H.; Ding, Y.; Cang, D.; Lu, H. Heat transfer and flow behavior of aqueous suspensions of TiO_2 nanoparticles (nanofluids) flowing upward through a vertical pipe. *Int. J. Heat Mass Trans.*, **2007**, *50*, 2272-2281.

[129] Lee, J.; Mudawar, I. Assessment of the effectiveness of nanofluids for single-phase and two-phase heat transfer in micro-channels. *Int. J. Heat Mass Trans.*, **2007**, *50*, 452-463.

[130] Wang, X.Q.; Mujumdar, A.S. Heat transfer characteristics of nanofluids: a review. *Int. J. Therm. Sci.,* **2007***, 46*, 1-19.

[131] Trisaksri, V.; Wongwises S. Critical review of heat transfer characteristics of nanofluids. *Renew. Sust. Ener. Rev.,* **2007***, 11*, 512-523.

[132] Daungthongsuk W.; Wongwises S.; A critical review of convective heat transfer of nanofluids. *Renew. Sust. Ener. Rev.*, **2007**, *11*, 797-817.

[133] Hwang, Y.J.; Ahn, Y.C.; Shin, H.S.; C.G. Lee; G.T. Kim; H.S. Park; J.K. Lee Investigation on characteristics of thermal conductivity enhancement of nanofluids. *Curr. Appl. Phys.*, **2006**, *6*, 1068-1071.

[134] Hwang, Y.; Park, H.S.; Lee, J.K.; Jung, W.H. Thermal conductivity and lubrication characteristics of nanofluids. *Curr. Appl. Phys.*, **2006**, *6* S1, e67-e71.

[135] Liu, M.S.; Lin, M.C.C.; Tsai, C.Y.; Wang, C.C. Enhancement of thermal conductivity with Cu for nanofluids using chemical reduction method. *Int. J. Heat Mass Trans.*, **2006**, *49*, 3028-3033.

[136] Palm, S.J.; Roy, G.; Nguyen, C.T.; Heat transfer enhancement with the use of nanofluids in radial flow cooling systems considering temperature-dependent properties. *Appl. Therm. Eng.*, **2006**, *26*, 2209-2218.

[137] Heris, S. Z.; Etemad, S.G.; Esfahany, M.N. Experimental investigation of oxide nanofluids laminar flow convective heat transfer. *Int. J. Commun. Heat Mass Trans.*, **2006**, *33*, 529-535.

[138] Xuan, Y.; Yu, K.; Li, Q. Investigation on flow and heat transfer of nanofluids by the thermal Lattice Boltzmann model. *Prog. Comput. Fluid Dy.*, **2005**, *5*, 13-19.

[139] Liu, M.S.; Lin, M.C.C.; Huang, I.T. Wang C.C., Enhancement of thermal conductivity with carbon nanotube for nanofluids. *Int. J. Commun. Heat Mass Trans.*, **2005**, *32*, 1202-1210.

[140] Maiga, S.E.B.; Palm, S.J.; Nguyen, C.T.; Roy, G.; Galanis, N. Heat transfer enhancement by using nanofluids in forced convection flows. *Int. J. Heat Fluid Fl.,* **2005**, *26*, 530-546.

[141] Wen, D.; Ding, Y. Experimental investigation into convective heat transfer of nanofluids at the entrance region under laminar flow conditions. *Int. J. Heat Mass Trans.*, **2004**, *47*, 5181-5188.

[142] Maiga, S.E.B.; Nguyen, C.T.; Galanis, N.; Roy, G. Heat transfer behaviours of nanofluids in a uniformly heated tube. *Superlattice. Microst.,* **2004***, 35*, 543-557.

[143] Roy, G.; Nguyen, C.T.; Lajoie, P.R. Numerical investigation of laminar flow and heat transfer in a radial flow cooling system with the use of nanofluids. *Superlattice. Microst.*, **2004**, *35*, 497-511.

[144] Nguyen, C.T.; Roy, G.; Maiga, S.E.B.; Lajoie, P.R. Heat transfer enhancement by using nanofluidsfor cooling of high output microprocessor. *www.electronicscooling.com/html/ 2004_nov_techbrief.html*, **2004**.

[145] Ali, A.; Vafai, K.; Khaled, A.R.A. Analysis of heat and mass transfer between air and falling film in a cross flow Configuration. *Int. J. Heat Mass Trans.*, **2004**, *47*, 743-755.

[146] Ali, A.; Vafai K. An investigation of heat and mass transfer between air and desiccant film in an inclined parallel and counter flow channels. *Int. J. Heat Mass Trans.*, **2004**, *47*, 1745-1760.

[147] Zhu, H.T.; Lin, Y.S.; Yin, Y.S. A novel one-step chemical method for preparation of copper nanofluids. *J. Colloid Interf. Sci.,* **2004**, *277*, 100-103.

[148] Li Q., Xuan Y., Convective heat transfer and flow characteristics of cu-water nanofluid, *Sci. China Ser E*, **2002**, *45*, 408-416.

[149] Xuan Y., Li Q., Investigation on convective heat transfer and flow features of nanofluids. *ASME J. Heat Transfer*, **2003**, *125*, 151-155.

[150] Hamilton R.L., Crosser O.K., Thermal conductivity of heterogeneous two-component systems. *I & EC Fundamentals*, **1962**, *1*, 187-191.

[151] Wasp E.J., Solid-liquid flow slurry pipeline transportation. Trans Tech Publications, **1977**.

[152] Xuan, Y.; Roetzel, W. Conceptions for heat transfer correlation of nanofluids. *Int. J. Heat Mass Trans.*, **2000**, *43*, 3701-3707.

[153] Xuan Y., Li Q., Heat transfer enhancement of nanofluids. *Int. J. Heat Fluid Fl.*, **2000**, *21*, 58-64.

[154] Xue, Q.Z. Model for effective thermal conductivity of nanofluids. *Phys. Lett.*, **2003**, *307*, 313-317.

Received: January 22, 2012 **Revised: April 24, 2012** **Accepted: July 18, 2012**

Send Orders of Reprints at reprints@benthamscience.org

Current Nanoscience, **2012,** *8,* **939-944**

Measurement of Specific Heat of Nanofluids

T. Yiamsawasd[a], A.S. Dalkilic[b] and S. Wongwises[a,c*]

[a]*Fluid Mechanics, Thermal Engineering and Multiphase Flow Research Lab. (FUTURE), Department of Mechanical Engineering, Faculty of Engineering, King Mongkut's University of Technology Thonburi, Bangmod, Bangkok 10140, Thailand;* [b]*Heat and Thermodynamics Division, Department of Mechanical Engineering, Yildiz Technical University (YTU), Yildiz, Besiktas, Istanbul 34349, Turkey;* [c]*The Academy of Science, The Royal Institute of Thailand, Sanam Suea Pa, Dusit, Bangkok 10300, Thailand*

Abstract: This article reports an experiment on specific heat measurement of nanofluids using a calorimeter of the comparison type. The measurement is based on a differential thermal analysis technique. The studied TiO_2 and Al_2O_3 nanoparticles are dispersed in base fluids which are pure water and a mixture of ethylene glycol/water (20/80 wt.%). Concentrations between 0 and 8 vol.% and temperatures are between 15 and 65°C. Results show that the measured specific heat of nanofluids is lower than that of the base liquid decreases as the particle concentrations increases. Furthermore, the specific heat of nanofluids was found to increase with increasing temperatures. When compared with predicted values from existing correlations and data reported by other researchers, measurements are compatible with the prediction from the thermal equilibrium model presented by Xuan and Roetzel. Finally, new correlations are proposed for predicting the specific heat of Al_2O_3 and TiO_2 nanofluids.

Keywords: Specific heat, nanofluids, nano particle, base fluid.

INTRODUCTION

Nanofluids are innovative working fluids gained from dispersing nanometer-sized solid particles in common working fluids. These solid particles with high thermal conductivity are expected to enhance heat transfer with long-term stability in suspensions and minimal effect on pressure drop. The term 'nanofluids' was firstly defined by Choi in 1995 [1] and was widely used since then. Nanofluids are expected to be used in mini- and micro-scaled heat exchangers, such as electrical and electronic appliances and computers. However, their relevant properties should be studied, especially thermal properties. This will be very useful for the effective use of nanofluids and for further analysis and development thereof.

Past studies have shown great interest in nanofluids. Initially, most studies focused on thermal conductivity [1-10], viscosity [6-11], and convective heat transfer [12-17]. Unfortunately, there are only a few studies that are concerned with specific heat. Actually, specific heat is one of the most important basic thermal properties that deserves attention. It can be used to calculate for example, the sensible heat transfer rate, Prandtl numbers and thermal diffusivity for predicting heat transfer performance of heat exchangers. Therefore, specific heat of nanofluids should be studied together with other properties.

Below are recent experimental studies about specific heat of nanofluids.

Namburu *et al.* [11] conducted an experiment to measure specific heat and viscosity of silicon dioxide nanofluids suspended in 60/40 by weight mixture of ethylene glycol/water. Particles sizes of SiO_2 examined were 20, 50 and 100 nm, with concentration range of 0 to 10 vol. %. A specially designed electrical heater calorimeter was used to measure the specific heat of nanofluids. Their experiment showed that specific heat of silicon dioxide nanofluids decreased when concentration increased. At the concentration of 10 vol.%, the specific heat decreased by about 12% when compared to the base fluid.

*Address correspondence to this author at the Fluid Mechanics, Thermal Engineering and Multiphase Flow Research Lab. (FUTURE), Department of Mechanical Engineering, King Mongkut's University of Technology Thonburi, Bangmod, Bangkok 10140, Thailand; Tel: +662-470-9115; Fax: +662-470-9111; E-mail: somchai.won@kmutt.ac.th

Zhou and Ni [18] measured the specific heat of Al_2O_3-water nanofluids with an Al_2O_3 particle size of 45 nm at a temperature of 33°C and a concentration range of 0 to 21.7 vol.%. A differential scanning calorimeter was used for measurement. Their study revealed that when the concentration increased, the specific heat of Al_2O_3-water nanofluids decreased. When compared to the existing correlation, the experimental result was found to be compatible with the prediction from the thermal equilibrium model of Xuan and Roetzel [19], whereas the ideal gas mixtures model of Pak and Cho [5] provided different results.

Vajjha and Das [20] measured the specific heat of 3 types of nanofluids that consisted of Al_2O_3 (44 nm) and ZuO (77 nm) particles suspended in 60/40 % by mass of ethylene glycol-water mixture, and SiO_2 (20 nm) particles suspended in deionized water. A specially designed electrical heating calorimeter was used in a temperature range of 42 to 82°C and a concentration range of 0 to 10 vol.%. Results showed that the specific heat of all 3 types of nanofluids decreased when the concentration increased. On the contrary, the specific heat increased when the temperature increased. However, their results were found to be incompatible with results from the ideal gas mixtures of Pak and Cho and from the thermal equilibrium model of Xaun and Roetzel.

Nelson *et al.* [21] conducted an experiment on thermal properties, as well as flow and forced convection heat transfer characteristics, of exfoliated graphite nanoparticles suspended in polyalphaolfin. The specific heat was measured at the concentration of 0.6 wt.% with a particle diameter of 20 nm and a thickness of 100 nm in a temperature range of 45 to 90°C, using differential scanning calorimeter techniques. They found that the specific heat of nanofluids increased by about 50% when compared to the base fluid and increased with increasing temperature.

Zhou *et al.* [22] measured the specific heat and volumetric heat capacity of CuO-EG nanofluids at a concentration range of 0.1 to 0.6 vol.%. They concluded that when concentration increased, the specific heat of CuO-EG decreased gradually. Volumetric heat capacity was found to change minimally. Their results were compatible with the prediction from the thermal equilibrium model of Xuan and Roetzel, while the ideal gas mixtures model of Pak and Cho could not predict.

Shin and Bernejee [23] measured the specific heat of nanofluids which were used in solar thermal energy storage. Silica nanoparti-

1875-6786/12 $58.00+.00

cles (1 wt.%) suspended in a eutectic of lithium carbonate and potassium carbonate mixture (62/38 % by weight). The silica nanoparticles with an average size of 35 nm were tested in a temperature range of 525 to 555°C using a differential scanning calorimeter. They found that the specific heat of nanofluids increased by about 19–24% when compared with the base fluid. Temperature had little effect on the change of the specific heat of nanofluids used in this experiment.

It can be clearly seen from the study on the nanofluids mentioned above that there are various types of apparatus or measurement techniques used to determine the specific heat of nanofluids and the results obtained from those techniques were also different. Thus, other techniques could be developed to measure the specific heat of nanofluids in order to determine compatibility. To the best of the authors' knowledge, a differential thermal analysis technique has never been found before to be used with nanofluids. In the present study, this technique will be applied to measure the specific heat of nanofluids. The results will be compared with those reported in literature. The correlations for determining the specific heat of nanofluids are also proposed for practical applications.

PREPARATION OF NANOFLUIDS

The preparation of nanofluids is an important step. Generally, there are three methods of nanofluids preparation: pH control, addition of surfactants or dispersants, and use of ultrasonic vibration. The purpose of nanofluids preparation is to suspend nanoparticles stably in base fluids without precipitation of particles in short duration [2].

TiO_2 and Al_2O_3 nanofluids used in the present study were supplied by DEGUSSA Company. The average diameter of the TiO_2 particles is 21 nm and the average diameter of the Al_2O_3 particles is 120 nm. Table **1** shows the density and specific heat of nanoparticles used in the present study determined using Ref. [24] and Ref. [25] for density and specific heat, respectively. Both are suspended in water base fluid with concentrations of 13.8 and 10.6 vol.%. The base fluids used in this research are pure water and ethylene glycol-water mixture at 20/80 wt %. Before the experiment, the nanofluids supplied by the manufacturer were mixed and diluted by adding base fluid to reach the desired concentrations. Then, ultrasonic vibration was used for about 2 hours to create dispersion. Preparation by pH control and addition of surfactants was done discretely by the manufacturer.

Table 1. Properties of Nanoparticles

Nanoparticles	Density (kg/m^3)	Specific heat at 33 °C (kJ/kg K)
TiO_2	4157	0.715
Al_2O_3	3970	0.795

The photograph of TiO_2 nanoparticles taken from the transmission electron microscope (TEM) is shown in Fig. (**1**). The particle size distribution is also shown in Fig. (**2**). Initially, it was found that both nanoparticles have a circular shape, with an average diameter of 21 nm for TiO_2 and of 120 nm for Al_2O_3 which are very similar to the information provided by the manufacturer.

EXPERIMENTAL APPARATUS AND PROCEDURES

In this study, a calorimeter of the comparison type used to measure the specific heat of nanofluids was newly developed. The measurement was based on differential thermal analysis technique as shown in Fig. (**3**). Temperature differences obtained from heating between the reference liquid and the tested nanofluids together with known properties of the reference liquid can be used to determine the specific heat.

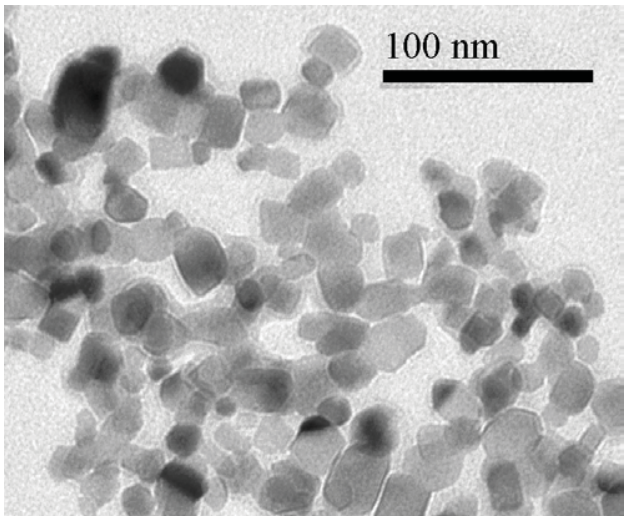

Fig. (1). TEM image of dispersed TiO_2 nanoparticles in water [From Suriyawong and Wongwises [26], with permission from Elsevier].

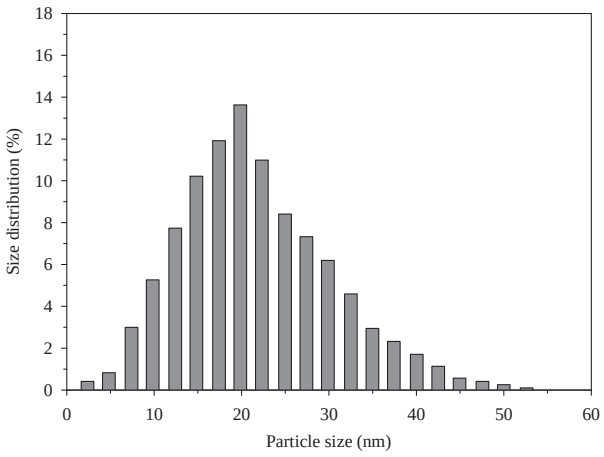

Fig. (2). Size distribution of TiO_2.

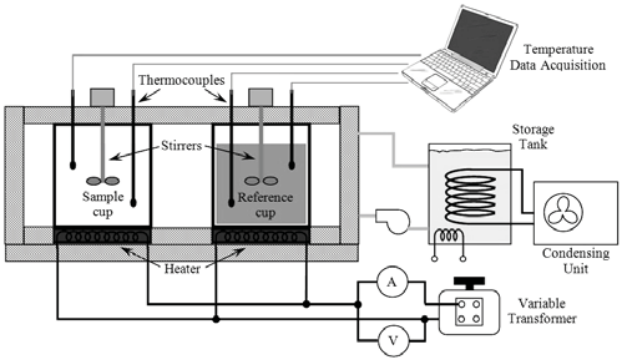

Fig. (3). Schematic diagram of experimental apparatus.

Important components shown in Fig. (**3**) are cups for sample and reference substances that are specially designed in symmetrical sizes. The cups are made from stainless steel with high conductivity

and high sensibility to temperature change. Both cups are placed in temperature control sleeves connected to a hot-cold water tank. Heat for each cup is fed from the bottom of each cup with a 30-watt electrical plate heater. The heater's coils are specially designed to have equal resistance. Heat can be controlled by variable transformers. Each cup has a small propeller with a low speed to create an evenly dispersed temperature and to prevent sedimentation and agglomeration of nanoparticles. The temperatures of both substances are measured with T-type thermocouples installed at the top and the bottom of the cup are recorded precisely via a computerized data logger every 3 seconds.

The experiment began by measuring an equal volume of the prepared nanofluids and reference substances. Both substances were weighed for use in calculation. Next, the substances were put in each cup carefully. The lids of the cups and the temperature control sleeves were then closed. Next, the level of the thermocouples, as well as the level and speed of the propeller, were adjusted and checked. Cooling water was put into the sleeves to adjust the starting temperature of both substances. When the desired starting temperature was reached, the cooling water was poured out of the sleeves and the heater was turned on. The temperature was recorded immediately. The temperature change of the nanofluids and reference substance were observed during the experiment. The experiment was stopped when the final temperature was reached. Both cups were cleaned, along with the other components that came in contact with nanofluids, before repeating the experiment.

Based on the differential thermal analysis, both sample and reference substances received an equal amount of heat. Therefore, specific heat of nanofluids $\left(C_{p,nf}\right)$ could be calculated from

$$Q_{nf} = Q_{ref}$$

$$m_{nf} C_{p,nf} \Delta T_{nf} = m_{ref} C_{p,ref} \Delta T_{ref}$$

$$C_{p,nf} = \frac{m_{ref} C_{p,ref} \Delta T_{ref}}{m_{nf} \Delta T_{nf}} \quad (1)$$

where $C_{p,ref}$ is the specific heat of reference substance; m_{nf} and m_{ref} are the masses of the nanofluids and the reference substances, respectively; and ΔT_{nf} and ΔT_{ref} are the temperature changes during the experiment of the nanofluids and the reference substances, respectively.

RESULTS AND DISCUSSION

Before the experiment, the developed apparatus was calibrated by measuring the specific heat of the water sample and a 20/80 % by weight mixture of ethylene glycol (EG)/water in the temperature range of 15 to 65°C. Results were then compared with the standard values from ASHRAE [27] and were found to be similar. The water sample had a maximum deviation of 1.4% with an average deviation of 1.36%. The EG/water mixture had maximum deviation of 3.21% with average deviation of 2.24%, as shown in Fig. (**4**).

This section discusses the effect of the concentration and temperature on the specific heat of nanofluids with water and mixture of ethylene glycol as base fluids, tested at concentrations of 1, 2, 4, 6 and 8 vol.% in a temperature range of 15 to 65°C. Fig. (**5**(a)) shows that the specific heat of Al_2O_3-water is a function of concentration and temperature. The experimental results indicated that specific heat decreased by about 20% when the concentration increased to 8 vol.%. In terms of temperature, the specific heat increased only slightly when the temperature increased. Fig. (**5**(b)) shows similar results of TiO_2-water. That is, the increasing concentration caused specific heat to decrease by about 5 to 23% at the concentrations of 1 to 8 vol.%. The increasing temperature also caused a slight increase in specific heat.

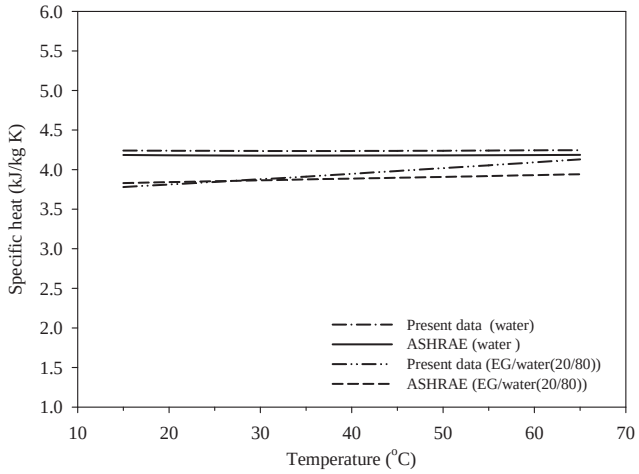

Fig. (4). Comparison of the measured specific heat with reference data.

This research also studied the effect of base fluid on the specific heat of nanofluids. Hence, apart from the water-based nanofluids, the EG/water (20/80)-based fluid was also examined. Al_2O_3-EG/water and TiO_2-EG/water at the concentrations of 1, 2 and 4 vol.% in a temperature range of 15 to 65°C were tested. Figs. (**6**(a) and **6**(b)) show that for both Al_2O_3-EG/water and TiO_2-EG/water the increasing concentrations caused the specific heat to decrease by about 3 to 11% in a concentration range of 1 to 4 vol.%. The specific heat tended to increase when the temperature increased.

From the experimental results of all four types of nanofluids mentioned above, the decrease of the specific heat of nanofluids when the concentration increased could directly result from the fact that the specific heat of nanoparticles mixed is much lower than that of the base fluid. As a result, the overall specific heat of nanofluids decreases. In terms of temperature, the increase of specific heat with the increasing temperature is similar to that of the base fluid. Basically, the specific heat of the base fluids increases when the temperature increases. Different from the base fluids, the specific heat of nanoparticles slightly increases with the increasing temperature. As a result the slope of the experimental lines shown in Figs. (**5** and **6**) are almost the same.

This section compares the experimental results with the prediction from existing models and data obtained from other researches. The widely used models of Pak and Cho [5] assume that nanofluids are homogeneous substances that could be calculated by mixing theory as follows:

$$C_{p,nf} = \phi C_{p,np} + (1-\phi) C_{p,b} \quad (2)$$

where $C_{p,nf}$ is the specific heat of nanofluids; $C_{p,np}$ is the specific heat of nanoparticles; $C_{p,b}$ is the specific heat of the base fluid; and ϕ is the concentration by volume.

Another widely used model of Xuan and Roetzel [19] assumes that the heat transfer process between nanoparticles and the base fluid is thermal equilibrium, as follows:

$$C_{p,nf} = \frac{\phi \rho_{np} C_{p,np} + (1-\phi) \rho_b C_{p,b}}{\phi \rho_{np} + (1-\phi) \rho_b} \quad (3)$$

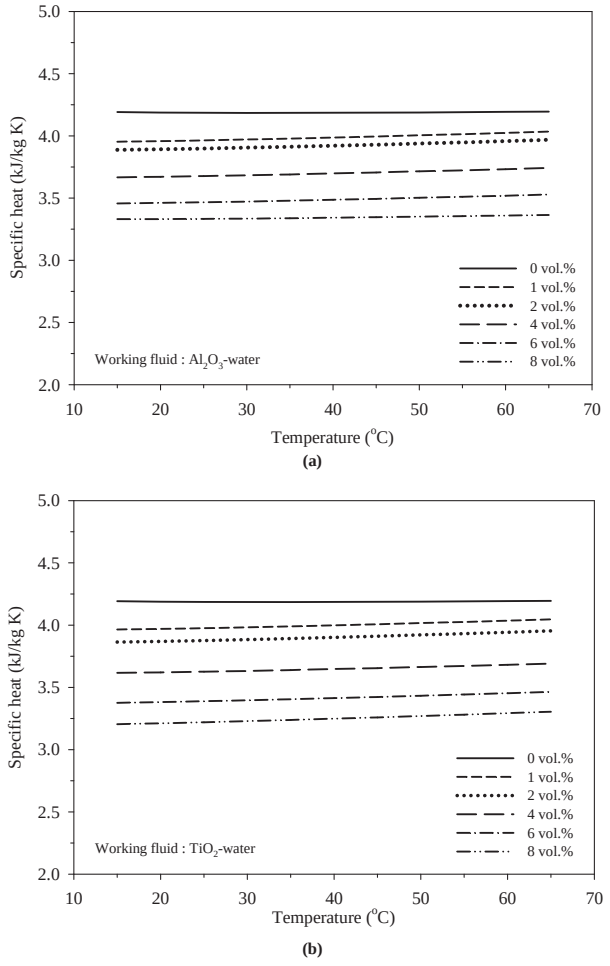

Fig. (5). The specific heat of water-base nanofluids as a function of temperature and volume fraction.

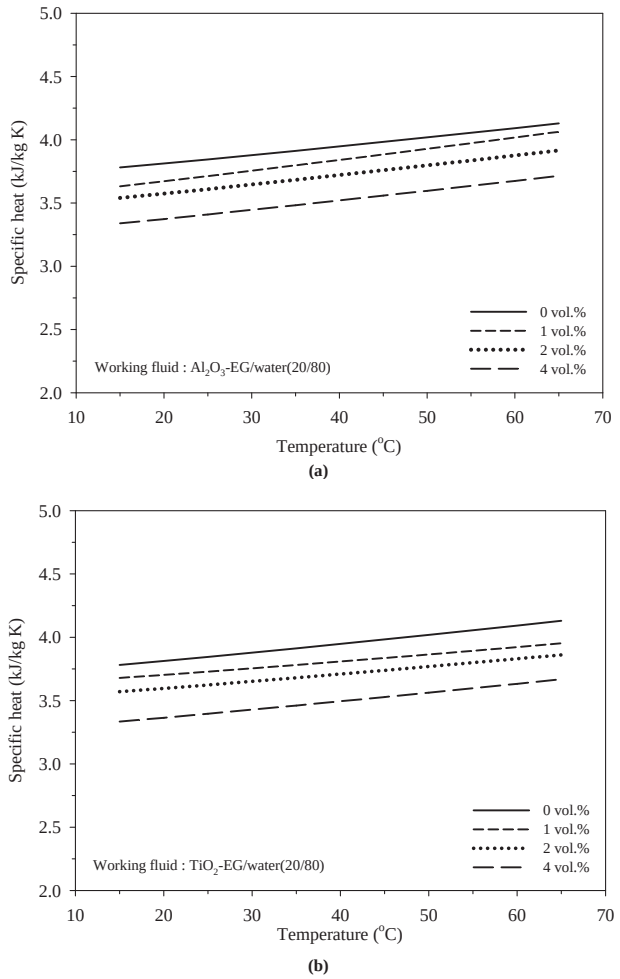

Fig. (6). The specific heat of EG/water (20/80)-base nanofluids as a function of temperature and volume fraction.

where ρ_{np} is the density of the nanoparticles, and ρ_b is the density of the base fluid.

Vajjha and Das [20] also present a correlation developed from the experiment to measure the specific heat of Al_2O_3, ZnO, and SiO_2 nanofluids as follows:

$$C_{p,nf} = \frac{\left((AT) + B(\frac{C_{p,np}}{C_{p,b}}) \right)}{C + \phi} \quad (4)$$

where *T* is the temperature of the nanofluids, and *A*, *B*, and *C* are coefficients shown in Table **2**.

Table 2. Coefficients in Vajjha and Das Model

Nanoparticle	Coefficients		
	A	**B**	**C**
Al_2O_3	0.0008911	0.5179	0.4250
SiO_2	0.001769	1.1937	0.8021
ZnO	0.0004604	0.9855	0.299

Fig. (**7**(a)) shows the specific heat of Al_2O_3-water nanofluids at various concentrations. Results are similar to those from the model of Xuan and Roetzel. However, the model of Pak and Cho could not be used to predict, particularly at high concentrations. On the other hand, the model of Vajjha and Das gave lower values, particularly at low concentrations. In terms of temperature, the experimental results are also similar to those from the model of Xuan and Roetzel. The model of Pak and Cho gave higher values, whereas the model of Vajjha and Das gave lower values, particularly in the lower temperature ranges, as shown in Fig. (**7**(b)). Similarly, the experimental results of TiO_2-water nanofluids, shown in Figs. (**8**(**a**) and **8**(**b**)), also correspond with the prediction from the model of Xuan and Roetzel, both in terms of concentration and temperature. From all comparisons, it could be said that the sample nanofluids used in this experiment are in a thermal equilibrium during the experiment. Therefore, the specific heat gained from the experiment is similar to the prediction of the thermal equilibrium model presented by Xuan and Roetzel. This could be confirmed with the experiment of Zhon and Ni, who measured Al_2O_3-water nanofluids and obtained similar results to the prediction from the model of Xuan and Roetzel, as shown in Fig. (**7**(a)). Moreover, Zhou *et al*. [21] also concluded from their experiment in measuring the specific heat of CuO-EG nanofluids that the specific heat of CuO-water was also similar to those predicted by the thermal equilibrium model.

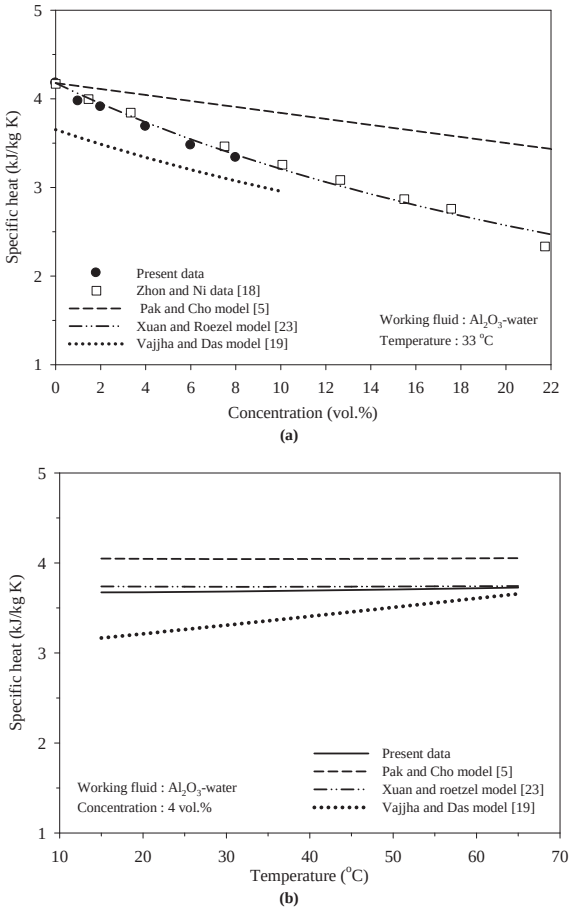

Fig. (7). Comparison of the measured specific heat with those obtained from various researchers.

This research presents a correlation to predict specific heat of Al_2O_3 and TiO_2 nanofluids in a form of specific heat ratio between nanofluids and base fluid $\left(C_{p,nf}/C_{p,b}\right)$ that could be applied to other base fluids. This model considers the effects of temperature, concentration, the specific heat of nanoparticles, and the specific heat of the base fluid as follows:

$$\frac{C_{p,nf}}{C_{p,b}} = A\phi^B T^C \left(\frac{C_{p,np}}{C_{p.b}}\right)^D \quad (5)$$

where A, B, C, and D are the coefficients shown in Table **3**. The model could be used in a temperature range of 15 to 65°C and a concentration range of 1 to 8 vol.%. Fig. (**9**) shows a comparison between experimental specific heat and predictions from the correlation (Eq. (5)). It could be seen that the predicted value is similar to the experimental value at a verifiable and acceptable level.

Table 3. The Coefficients in Presented Correlation for Different Nanofluids

Nanofluid	Coefficients				Max. error	Avg. error
	A	B	C	D		
Al_2O_3	1.249458	-0.05846	0.006467	-0.17236	1.77%	0.79%
TiO_2	1.387402	-0.06425	0.001124	-0.21159	1.82%	0.85%

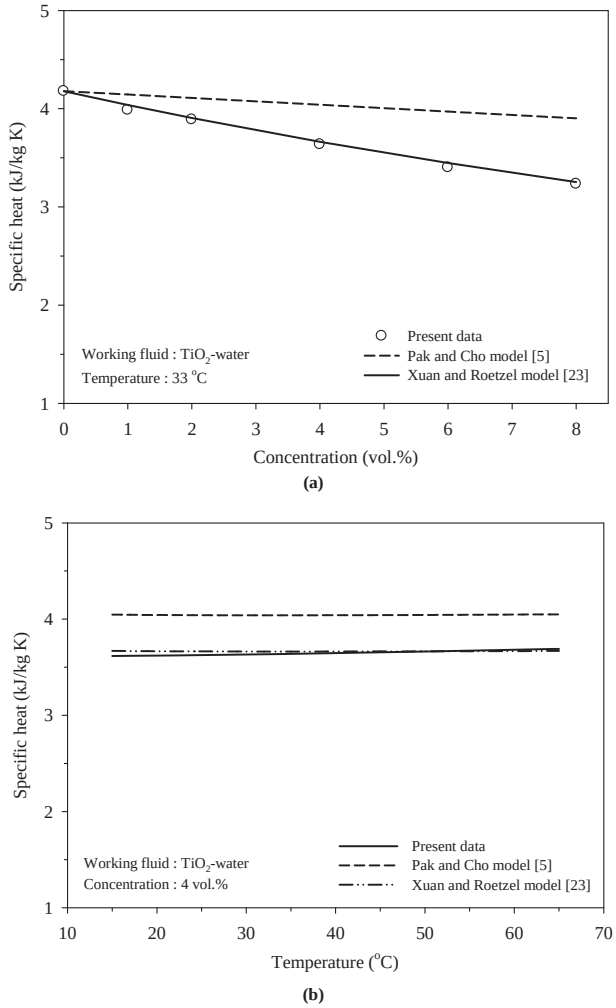

Fig. (8). Comparison of the measured specific heat of TiO_2-water nanofluids with those obtained from various researchers.

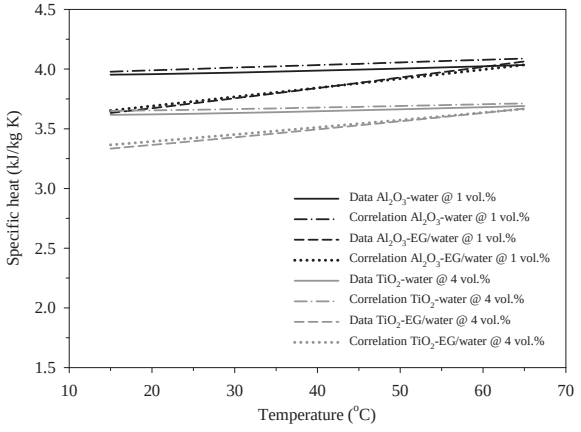

Fig. (9). Comparison of the measured specific heat with the proposed correlations.

CONCLUSIONS

From the calibration of measuring specific heat of water and ethylene glycol, the results are similar to the standard values from

ASHRAE. The developed specific heat measurement apparatus also has an acceptable precision level.

The experimental results indicate that the specific heat of nanofluids is lower than the base fluid and tends to decrease when concentration increases. On the other hand, the increasing temperature causes the specific heat of nanofluids to increase. These experimental results are compatible with the prediction from the thermal equilibrium model of Xuan and Roetzel. This research also presents a newly developed correlation to predict the specific heat of Al_2O_3 and TiO_2 nanofluids.

CONFLICT OF INTEREST

The authors confirm that this article content has no conflicts of interest.

ACKNOWLEDGEMENTS

The present study was supported by the Thailand Research Fund (TRF), the Office of the Higher Education Commission and the National Research University Project whose guidance and assistance are gratefully acknowledged.

REFERENCES

[1] Choi, S.U.S. Enhancing thermal conductivity of fluids with nanoparticles. *ASME FED*, **1995**, *231*, 99-103.

[2] Das, S.K.; Putta, N.; Thiesen, P.; Roetzel, W. Temperature Dependence of Thermal Conductivity Enhancement For Nanofluids. *ASME Trans. J. Heat Transfer*, **2003**, *125*, 567-574.

[3] Eastman, J.A.; Choi, S.U.S.; Li, S.; Yu, W.; Thomson, L.J. Anomalously increased effective thermal conductivities of ethylene glycol-based nanofluids containing copper nanoparticles. *Appl. Phys. Lett.*, **2001**, *78*, 718-720.

[4] Wang, X.; Xu, X.; Choi, S.U.S. Thermal Conductivity of Nanoparticles-Fluid Mixture. *J. Thermophys. Heat Transfer*, **1999**, *13*, 474-480.

[5] Pak, B. C.; Cho, Y. I. Hydrodynamic and Heat Transfer Study of Dispersed Fluids with Submicron Metallic Oxide Particles. *Exp. Heat Transfer*, **1998**, *11*, 151-170.

[6] Murshed, S.M.S.; Leong, K.C.; Yang, C. Investigations of Thermal Conductivity and Viscosity of Nanofluids. *Int. J. Therm. Sci.*, **2008**, *47*, 560-568.

[7] Duangthongsuk, W.; Wongwises, S. Measurement of temperature-dependent thermal conductivity and viscosity of TiO_2-water nanofluids. *Exp. Therm. Fluid Sci.*, **2009**, *33*, 706-714.

[8] Yu, W.; Xie, H.; Li, Y.; Chen, L. Experimental investigation on thermal conductivity and viscosity of aluminum nitride nanofluid. *China Particuol.*, **2011**, *9*, 187-191.

[9] Nguyen, C.T.; Desgranges, F.; Roy, G.; Galanis, N.; Mare, T.; Boucher, S.; Mintsa, H.A. Temperature and particle-size dependent viscosity data for water-based nanofluids – Hysteresis phenomenon. *Int. J. Heat Fluid Flow*, **2007**, *28*, 1492-1506.

[10] Masuda, H.; Ebata, A.; Teramae, K.; Hishinuma, N. Alteration of Thermal Conductivity and Viscosity of Liquid by Dispersing Ultra-Fine Particles (Dispersion of Al_2O_3, SiO_2 and TiO_2 Ultra-Fine Particles). *Netsu Bussei (Japan)*, **1993**, *7*, 227-233.

[11] Namburu, P.K.; Kulkarni, D.P.; Dandekar, A.; Das, D.K. Experimental investigation of viscosity and specific heat of silicon dioxide nanofluids. *Micro Nano Lett.*, **2007**, *2*, 67-71.

[12] Yang, Y.; Zhang, Z.G.; Grulke, E.A.; Anderson, W.B.; Wu, G. Heat Transfer Properties of Nanoparticle-in-Fluid Dispersions (Nanofluids) in Laminar Flow. *Int. J. Heat Mass Transfer*, **2005**, *48*, 1107-1116.

[13] Xuan, Y.; Li, Q. Investigation on Convective Heat Transfer and Flow Features of Nanofluids. *ASME J. Heat Transfer*, **2003**, *125*, 151-155.

[14] Nguyen, C.T.; Roy, G.; Gauthier, C.; Galanis, N. Heat Transfer Enhancement Using Al_2O_3-Water Nanofluid for Electronic Liquid Cooling System. *Appl. Therm. Eng.*, **2007**, *28*, 1501-1506.

[15] Heris, S.Z.; Etemad, S.G.; Esfahany, M.N. Experimental Investigation of Oxide Nanofluids Laminar Flow Convective Heat Transfer. *Int. Commun. Heat Mass Transfer*, **2006**, *33*, 529-535.

[16] He, Y.; Jin, Y.; Chen, H.; Ding, Y.; Cang, D.; Lu, H. Heat Transfer and Flow Behavior of Aqueous Suspensions of TiO_2 Nanoparticles (Nanofluids) Flowing Upward Through a Vertical Pipe. *Int. J. Heat Mass Transfer*, **2007**, *50*, 2272-2281.

[17] Duangthongsuk, W.; Wongwises, S. An experimental study on the heat transfer performance and pressure drop of TiO_2-water nanofluids flowing under a turbulent flow regime. *Int. J. Heat Mass Transfer*, **2010**, *53*, 334-344.

[18] Zhou, S.; Ni, R Measurement of the Specific Heat Capacity of Water-Based Al_2O_3 Nanofluid. *Appl. Phys. Lett.*, **2008**, *92*, 093123.

[19] Xuan, Y.; Roezel, W. Conceptions for Heat Transfer Correlations of Nanofluids. *Int. J. Heat Mass Transfer*, **2000**, *43*, 3701-3707.

[20] Vajjha, R.S.; Das, D.K. Specific Heat Measurement of Three Nanofluids and Development of New Correlations. *ASME J. Heat Transfer*, **2009**, *131*, 071601

[21] Nelson, I.C.; Banerjee, D.; Rengasamy, P. Flow Loop Experiments Using Polyalphaolefin Nanofluids. *J. Thermophys. Heat Transfer*, **2009**, *23*, 752-761.

[22] Zhou, L.P.; Wang, B.X.; Peng, X.F.; Du X.Z.; Yang Y.P. Research Article on The Specific Heat Capacity of CuO Nanofluid. *Adv. Mech. Eng.*, **2010**, *2010*, 172085.

[23] Shin, D.; Banerjee, D. Enhanced Specific Heat of Silica Nanofluid. *ASME J. Heat Transfer*, **2011**, *133*, 024501.

[24] Incropera, F.P.; DeWitt, D.P. *Introduction to Heat Transfer*, 3rd ed.; Wiley, New York: **1996**.

[25] Touloukian, Y.S.; Buyco, F.H. In: *Thermophysical Properties of Matter*; Specific Heat Nonmetallic Solids; IFI/Plenum, New York: **1970**; Vol. *5*

[26] Suriyawong, A.; Wongwises, S. Nucleate Pool Boiling Heat Transfer Characteristics of TiO_2-Water Nanofluids at Very Low Concentrations. *Exp. Therm. Fluid Sci.*, **2010**, *34*, 992-999.

[27] ASHRAE, *ASHRAE Handbook: Fundamentals*, American Society of Heating, Refrigerating and Air-Conditioning Engineers Inc., Atlanta, GA, **2005**.

Received: October 22, 2011 **Revised: June 17, 2012** **Accepted: July 11, 2012**

International Journal of Air-Conditioning and Refrigeration
Vol. 20, No. 4 (2012) 1230003 (20 pages)

DOI: 10.1142/S2010132512300030

World Scientific
www.worldscientific.com

A REVIEW ON THE HEAT-TRANSFER PERFORMANCE AND PRESSURE-DROP CHARACTERISTICS OF VARIOUS ENHANCED TUBES

S. LAOHALERTDECHA*, A. S. DALKILIC† and S. WONGWISES*,‡,§
*Fluid Mechanics, Thermal Engineering and Multiphase Flow Research Lab. (FUTURE)
Department of Mechanical Engineering, Faculty of Engineering
King Mongkut's University of Technology Thonburi (KMUTT) Bangmod
Bangkok, 10140, Thailand
†Heat and Thermodynamics Division, Department of Mechanical Engineering
Yildiz Technical University, Yildiz, Besiktas, Istanbul, 34349, Turkey
‡The Academy of Science, The Royal Institute of Thailand
Sanam Suea Pa, Dusit, Bangkok 10300, Thailand
§somchai.won@kmutt.ac.th

Received 11 May 2012
Revised 28 August 2012
Accepted 3 September 2012
Published 4 December 2012

The enhanced tube is a kind of the passive technique for improving the thermal performance of the heat exchangers with a little increase of the friction penalty. They have stated to use instead of the common smooth tubes for designing of the heat exchangers. The size of these heat exchangers can be reduced considerably by using the enhanced tubes instead of smooth tubes. Normally, they are divided into four groups: the corrugated tube, ribbed tube, grooved tube, and fluted tube. Compared with the common smooth tube, many researchers reported that use of the enhanced tubes dramatically increases the heat-transfer performance, both theoretically and experimentally. Focusing on the advantages of the enhanced tubes, this article summarizes the published studies on the heat-transfer and pressure-drop characteristics of the enhanced tubes, both experimental and quantitative investigations.

Keywords: Enhanced tubes; heat-transfer performance; pressure drop; heat exchanger.

Nomenclature

D : Diameter (m)
e : Corrugation depth (m)
f : Friction factor
G : Mass flux ($\mathrm{kg \cdot m^{-2} \cdot s}$)
h : Heat transfer coefficient ($\mathrm{W \cdot m^{-2} \cdot K}$)
L : Length of the test tube (m)
Nu : Nusselt number
p : Corrugation pitch (m)
Pr : Prandtl number
Re : Reynolds number

§Corresponding author.

t : Corrugation width (m)
x : Quality

Greek Letters

β : Helix angle (degree)

Subscripts

avg : Average
i : Inside
o : Outside

1. Introduction

The surface area of heat exchangers has a directly significant effect on their heat-transfer performance. Improvements to make heat transfer equipment more energy-efficient would need to focus on miniaturization on the one hand and an astronomical increase in heat flux on the other. Normally, heat-transfer enhancement techniques necessarily reduce the thermal resistance in a conventional heat exchanger by promoting a higher convection heat-transfer coefficient in order to minimize the size of the heat exchanger.

In general, enhancement techniques can be divided into two categories — active and passive techniques. The active technique requires external forces such as an electric field or acoustic or surface vibration, whereas the passive technique requires special surface geometries, such as a rough surface, extended surface, or fluid additives. Enhanced heat-transfer surfaces or "enhanced tubes" are one of the passive techniques, in which the surface is modified in such a way as to promote turbulence in the flow field and increase the heat-transfer surface.

These tubes can be employed in many heat exchangers to enhance the heat-transfer performance of both the inside and outside tubes, by mixing and also limiting the fluid boundary layers close to the heat transfer surfaces. Nowadays, enhanced tubes such as spirally corrugated tubes, ribbed tubes, grooved tubes, and fluted corrugated tubes are typically selected to replace conventional smooth tubes in the designs of industrial heat exchangers. They are expected to increase the heat-transfer performance of the heat-transfer equipment with only a very small increase in the pressure-drop penalty.

The heat transfer and pressure drop characteristics of the various refrigerants flowing through different type of the enhanced tubes under condensation process were summarized and reported in Ref. 1. The effects of tube orientation, tube geometry, flow pattern, oil mixture and void fraction on the condensation heat transfer performance and pressure drop were presented.

The purpose of this article is to review the literature mentioning heat-transfer performance and pressure-drop characteristics of the enhanced tubes, both experimental and theoretical studies. Various categories of enhanced tubes will be investigated i.e., corrugated tubes, ribbed tubes, grooved tubes, and fluted tubes. In addition, heat transfer characteristics of a new type of enhanced tube named "Vipertubes" are also presented. Each type is described in detail in the following sections.

2. Corrugated Tubes

This type of tube has a corrugated surface. The overall heat-transfer coefficient has been remarkably improved because of the turbulent flow effect on the inner surface and outer surface of the tube caused by the corrugation. The details of corrugated tubes are shown in Fig. 1. Many experimental investigations have been performed to investigate the effects of corrugation pitch, corrugation depth, and tube diameter on the heat-transfer and pressure-drop characteristics of the corrugated tubes. The heat transfer and flow characteristics of corrugated tubes have been reviewed as described below.

Mimura and Isozaki[2] reported the effect of shapes of corrugated tubes on the experimentally observed heat-transfer and flow characteristics. For heat-transfer experiments, steam is condensed on the

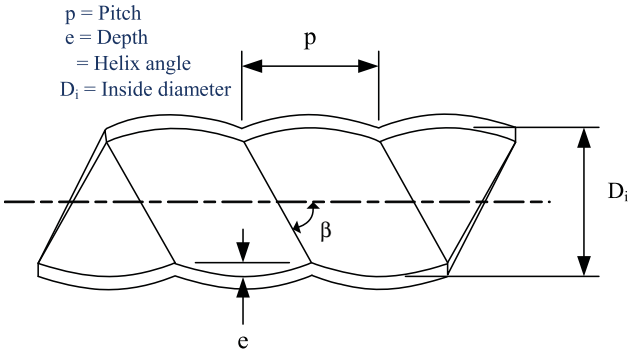

Fig. 1. Schematic diagram of the corrugated tubes.

outside of a horizontally corrugated tube made from 90−10 cupronickel. Similarly, pressure drop is measured under isothermal cold-flow conditions. The results indicated that the heat-transfer coefficient decreased with increasing corrugated pitch. At the ratio of depth to tube diameter of 0.05, the maximum heat-transfer coefficient was obtained. Moreover, the dual-start corrugated tubes gave a slightly higher heat-transfer coefficient than those of the single-start tubes. The friction factor equation was presented by considering the effect of pitch and depth. Finally, the correlation between the tube side heat-transfer coefficient and pressure drop in the corrugated tube was proposed.

Ganeshan and Rao[3] presented an experimental study on the heat-transfer behavior and friction characteristics of hot water flowing through a smooth tube and seven spirally corrugated tubes. The corrugated tubes of one to four helical starts and having constant helix angle of 65° were used as the test sections. They were different geometrical aspect ratios of e/d, p/e and p/d. The experimental data demonstrated that the heat-transfer coefficient of the four-start corrugated tube was larger than the smooth tube by about 100% at a Prandtl number of 4.3. Similarly, at a higher Prandtl number of 109, a 150% increase in the heat transfer coefficient was obtained.

Thien and Khan[4] reported the friction factor of an Oldroyd-type fluid flowing inside a sinusoidally corrugated tube, experimentally and quantitatively. The boundary element method was used to solve the problem and a Deborah number up to 20 was used in their study. The numerical results showed that the friction factor increased with the Deborah number. The results also gave reasonably agreement with the measured data.

Asako *et al.*[5] studied the heat transfer and flow characteristics of corrugated ducts with rounded corners, quantitatively. The results with the rounded corners were compared with the straight duct results. Three assigned corrugation angles and four aspect ratios of corrugated ducts are used as the test section. The simulation conditions were as follows: (1) Reynolds number between 100 and 1000 and (2) a fixed Prandtl number of 0.7. Their results indicated that rounding of the corners led to decreases in both the friction factor and the Nusselt number.

Honda and colleagues[6] investigated heat transfer and flow behaviors of R-11 and R-113 flowing in the annulus of a horizontal double-tube condenser during the condensation process. A corrugated tube with an outside diameter of 19.1 mm and installed with wire fins on the outer surface is used as the inner tube; three smooth tubes with inner diameter of 24.8, 27.2, and 29.9 mm are used as the outer tube. The mass velocity of working fluids were between 50 and $300\,\mathrm{kg}\cdot\mathrm{m}^{-2}\cdot\mathrm{s}$. The Lockhart−Martinelli parameters were used to calculate the frictional pressure gradient and then compared with the measured data. The experimental results showed that the local heat-transfer coefficient was two to 13 times higher than those for horizontal annuli with a smooth and corrugated inner tube. Moreover, the measured data was used to develop the correlation for predicting the local heat-transfer coefficient based on the surface tension controlled flow and the vapor shear controlled-flow model.

Burdette *et al.*[7] presented an upper-convected Maxell (UCM) model for predicting the flow behavior of working fluid flowing through an axisymmetric corrugated tube with a sinusoidally varying cross-section. The explicitly elliptic momentum equation (EEME) was used to solve the problem, and the results showed an agreement with the spectral/finite difference calculations.

Zimparov *et al.*[8] experimentally investigated the heat transfer and frictional pressure drop of a power plant condenser. One smooth tube and 25 spirally corrugated brass tubes were used as the test sections. The corrugated pitch varied from 6.5 to 16.9 mm, the ridge height varied from 0.44 to 1.18 mm, and the spiral angle ranged from 68° to 85°. Performance evaluation criteria were used to estimate the benefit of the spirally corrugated tubes.

Zimparov *et al.*[9] introduced a mixing-length model for predicting the heat-transfer coefficient and the Fanning friction factor of water flowing through a corrugated tube. A Reynolds number between 10^4 and 6×10^4 and a Prandtl number between 2.2 and 3.4 were used as the test conditions.

Gopalan and Ponnalagasamy[10] reported a steady laminar flow of a suspension in a corrugated tube with asymmetric and symmetric wavy wall, numerically. The effects of Reynolds number, Peclet number, wave number and the volume fraction of the particles on the flow were presented. The simulation results indicated that the mixing phenomenon due to secondary flow increased the flow of a relatively large volume fraction of low diffusive particles. In addition, their results also illustrated that

the pressure drop of corrugated tubes is higher than that of the smooth tube and decreased with increases in the diffusive particles.

Hinton and Conklin[11] experimentally studied the condensing heat-transfer and pressure drop characteristics of R-22 and non-azeotropic refrigerant mixture (NARM) of 75 wt.% R-143a and 25 wt.% R-124 flowing through a condenser made from common smooth tubes and then compared with the spirally corrugated tubes. The double-tube counter flow heat exchanger is used as the test section, in which refrigerant flows inside the internal tube and the water circulates in the annulus. Their results showed that the average heat transfer coefficient for the corrugated tube was higher than that for the smooth tube by about 40% for R-22 and 70% for NARM. Similarly, the pressure drop of the corrugated tube working with R-22 and NARM was roughly 23% and 36% larger than that of the smooth tube, respectively.

Chen *et al.*[12] experimentally investigated the heat-transfer and friction characteristics of four-start spirally corrugated tubes. A double-pipe counter flow heat exchanger was used as the test section. In their study, the non-symmetric nature of the corrugation angles along the longitudinal direction was reported. Then, the measured data were compared with the neural network analysis. The differences in heat transfer and friction loss due to effect of the corrugation angles were observed. Moreover, the heat transfer coefficient correlation based on a neural network model was proposed by considering the effect of the corrugation angles.

Dong *et al.*[13] reported the heat transfer and friction characteristics of water and oil flowing through four spirally corrugated tubes under turbulent flow, experimentally. The dimensions of the test tubes are shown in Table 1. The test conditions were conducted for the Reynolds number between 6000 and 93,000 for water and 3200 and 19,000 for oil. Compared with the common smooth tube, the experimental data indicated that the spirally corrugated tubes gave higher heat-transfer coefficient and friction factor by about 30% to 120% and 60% to 160%, respectively, as shown in Fig. 2. Moreover, the increase of e/d has a greater effect on the increase of the friction factor and heat transfer coefficient than the increase of p/d.

Table 1. The dimensions of the corrugated tubes.[13] [From Ref. 13, with permission from Elsevier.]

Number	p (mm)	e (mm)	β (degree)	D_i (mm)	L (mm)
1	10	0.39	78.8	16.04	500
2	10	0.32	78.8	16.12	500
3	10	0.69	82.1	22.82	500
4	12	0.7	79.0	20.08	500

Zimparov[14,15] experimentally investigated the heat-transfer and pressure-drop characteristics of water flow in single-start and three-start spirally corrugated tubes combined with five twisted tape inserts. The effects of height to diameter ratio and relative pitch were presented. The extended performance evaluation criteria equation was used to evaluate the multiplicative effect. At a given condition, the measured data illustrated that the heat-transfer coefficient and friction factor of spirally corrugated tubes combined with twisted tape inserts were higher than those for the conventional smooth tube.

Rainieri and Pagliarini[16] presented experimental study on the convective heat-transfer performance of corrugated wall tubes with axial symmetrical and helical corrugations with various pitch values. The effects of the wall roughness and fluid property variation were determined. Figure 3 presents a photo of the corrugated tubes. The Reynolds number ranged from 90 to 800, and ethylene glycol was used as the working fluid. The experimental data showed that the helical corrugation promoted a significant swirl component. However, an as much significant heat-transfer enhancement was not associated. Moreover, variation of fluid properties with temperature promoted the transition to an unstable flow.

Barba *et al.*[17] reported an experimental study on heat-transfer and pressure-drop characteristics of ethylene glycol flowing through a corrugated tube. The corrugated tube was obtained from a circular SS AISI 304 smooth tube, through a cold mechanical bucking, indenting the smooth tube without abrasion and mass removal as shown in Fig. 4. A Reynolds number ranging from 100 to 800 was tested. In comparison to the smooth tube, their results showed that the Nusselt number of the corrugated tube was significantly increased throughout the test run. However, for pressure drop consideration, the results also showed that using the corrugated tube caused increases in the friction factor by about 1.83 to 2.45. Moreover, the Nusselt number and friction factor correlations were proposed.

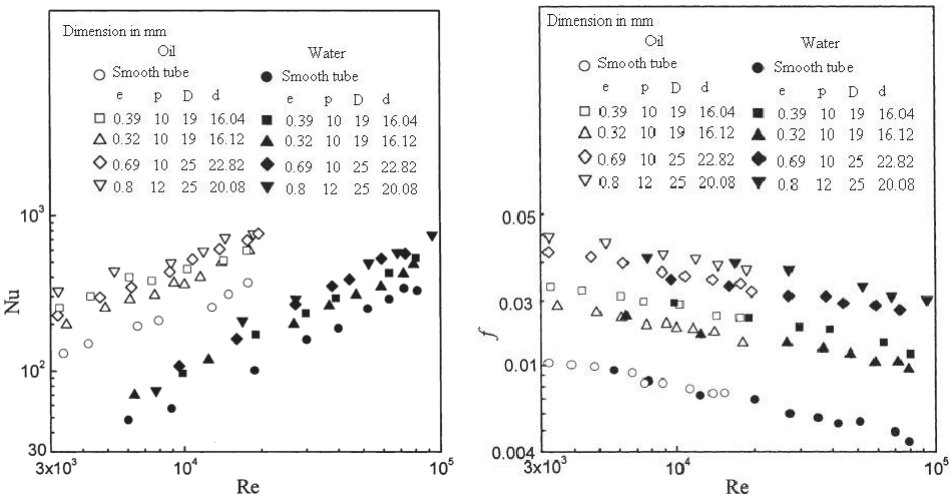

Fig. 2. Nusselt number and friction factor versus Reynolds number.[13] [From Ref. 13, with permission from Elsevier.]

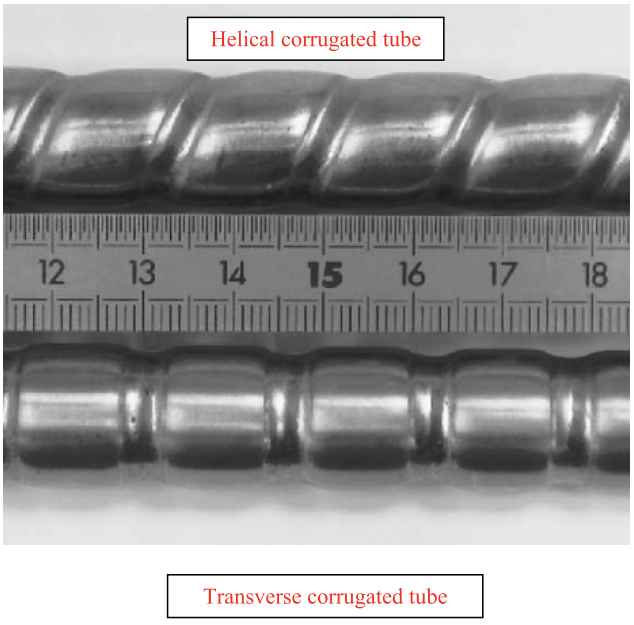

Fig. 3. Helical and transverse corrugated tubes.[16] [From Ref. 16, with permission from Elsevier (color online).]

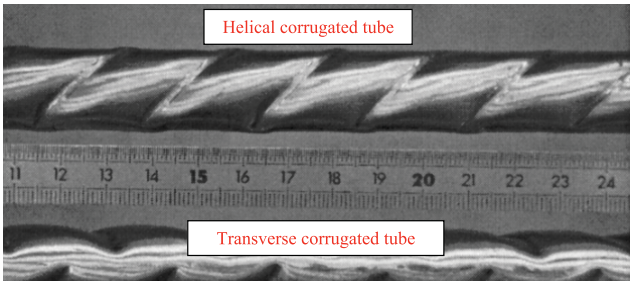

Fig. 4. Helical and transverse corrugated tubes.[17] [From Ref. 17, with permission from Elsevier (color online).]

Vicente and colleagues[18] determined the heat-transfer performance and friction characteristics of water and ethylene glycol flow in 10 corrugated tubes under turbulent flow. In this study, the Prandtl number was in the range of 2.5 to 100. The effect of rib height and spiral pitch was also investigated. Their data indicated that the severity index can be used to identify the effects of roughness on flow behaviors. Moreover, based on the experimental data, the Nusselt number and Fanning friction factor correlations were proposed as function of flow and geometry dimensionless parameters.

Zimparov[18] proposed a simple mathematical model for predicting the friction factor in the case of a spirally corrugated tube combined with a twisted tape insert under a fully developed turbulent flow region. This model was first suggested by Smithberg and Landis. In this study, the flow field was divided into two regions: (1) a helicoidal core flow and (2) a twisting boundary layer flow. Their simulation results demonstrated that the wall roughness had a significant effect on both the axial velocity and tangential velocity, which led to swirl-mixing phenomena. Moreover, their data were compared with 570 experimental data points obtained from the testing of 57 tubes. The results also indicated that the majority of the data falls within $\pm 15\%$ of the proposed model. This means that the proposed model can be used to predict the friction factor in the cases of smooth pipe, smooth pipe with a twisted tape inserts, a corrugated tube, and a corrugated tube combined with twisted tape inserts for turbulent flow regime.

The ongoing work of Zimparov[20] was to present a simple mathematical model created by Smithberg and Landis for predicting the heat-transfer coefficients of a spirally corrugated tube combined with a twisted tape insert in fully developed turbulent flow regime. The effects of both axial and tangential boundary layer were considered. Their results demonstrated that the wall roughness had simultaneous effects on the axial velocity and secondary fluid motion. Similar to the case of friction factor, the proposed model was compared with the 544 measured data obtained from Bergles *et al.*[21] for heat-transfer coefficient. The results showed that the proposed model gave reasonably good agreement with the measured data and deviations of $\pm 15\%$ were obtained.

Vicente *et al.*[18] reported an experimental study on the heat-transfer and pressure-drop characteristics of water and ethylene glycol flowing through corrugated tubes under laminar and transition flow regime. For laminar flow condition, their results indicated that the Nusselt number depended on both the natural convection and the entrance effect, and corrugated tube increases heat-transfer performance by about 30% at high Rayleigh numbers. Similarly, the friction factors in corrugated tubes were 25% larger than those of a smooth tube. Moreover, they reported that roughness of the corrugated tube accelerated the transition to a critical Reynolds number below 1300.

Targanski and Cieslinski[22] studied the evaporation heat-transfer coefficient and pressure drop of pure R407C and R407C/oil mixtures flow in two smooth tubes, corrugated tube and micro-finned tube, experimentally. The dimensions of the test sections are shown in Table 2. The experiments were conducted at saturation temperature of 0°C and mass flux varied between 250 and 500 $\mathrm{kg \cdot m^{-2} \cdot s}$. Their experimental data showed that two enhanced tubes gave a larger heat-transfer coefficient than the smooth tube, as well as a pressure drop. The average heat-transfer coefficient in the micro-finned tube and corrugated tube was up to 50% and 20%, respectively, higher than in the smooth tube. Similarly, pressure drop in the micro-finned tube and corrugated tube was up to 40% and 80%, respectively, higher than in the smooth tube, as shown in Fig. 5. Moreover, compared with pure R407C and R407C/oil mixtures, higher heat-transfer coefficients for pure R407C were obtained.

Table 2. The dimensions of the corrugated tubes[22] (from Ref. 22, with permission from Elsevier).

Number	Tube description	h (mm)	D_i (mm)	L (mm)
1	Smooth	—	8	2000
2	Smooth	—	8.8	2000
3	Corrugated	0.45	8.8	2000
4	Micro-fin	0.2	8.92	2000

Rozzi *et al.*[23] presented an experimental investigation on the convective heat transfer and friction losses in helically corrugated tubes. A shell and tube heat exchanger was used as the test apparatus. Whole milk, cloudy orange juice, apricot, and apple puree were tested under heating and cooling conditions. The experimental data showed that the use of helically corrugated tube had no effect on the heat-transfer performance for a Reynolds number less than 800. For a Reynolds number ranging from 800 to the limit of the transition flow regime, larger heat-transfer coefficients for corrugated tubes were obtained. Moreover, the results indicated that heat-transfer coefficients for corrugated tubes were moderately higher than those for smooth tubes and very high pressure drops were also obtained.

Dalkilic *et al.*[24] showed an experimental comparison of the laminar film condensation heat transfer coefficients of R134a in vertical smooth and micro-fin tubes having inner diameters of 7 mm and lengths of 500 mm at a mass flux of 29 $\mathrm{kg\,m^{-2}\,s^{-1}}$ and the pressures between 0.8 and 0.9 MPa. The original smooth tube heat transfer model was modified by a well-known friction factor to account for the heat transfer enhancement effects due to the presence of micro-fins, shown in Fig. 6(a), on the internal wall surface during annular flow regime conditions. Alterations of the local heat transfer coefficient, and condensation rate along the tube length during downward condensing film were determined. Their results show that the interfacial shear stress is found to have significance for the laminar condensation heat transfer of R134a under the given conditions due to its better predictive performance than the classical solution neglecting the interfacial shear stress effect. A comparison of the convective heat transfer coefficients was done according to the condensing pressures as shown in Fig. 6(b).

In 2010 and 2011, the work of Laohalertdecha and Wongwises[25–29] presented an experimental investigation on the heat-transfer coefficient and pressure-drop characteristics of refrigerant R134a flowing through the corrugated tubes under evaporation and condensation processes. The dimensions of the corrugated tubes are shown in Table 3, while

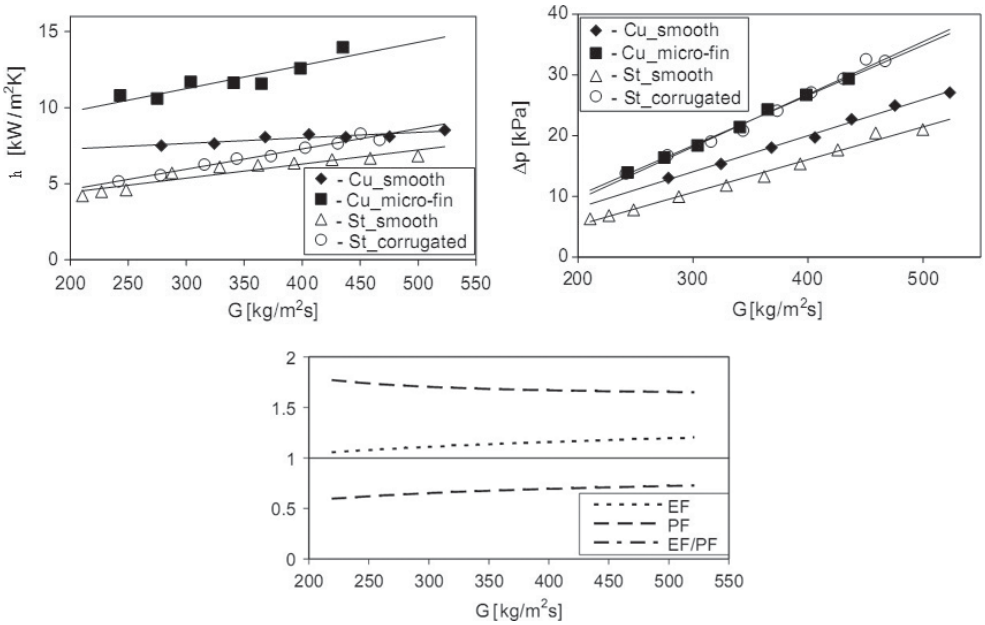

Fig. 5. Average heat transfer coefficient, pressure drop, enhancement factor and penalty factor versus mass flux for R407C.[22] [From Ref. 22, with permission from Elsevier.]

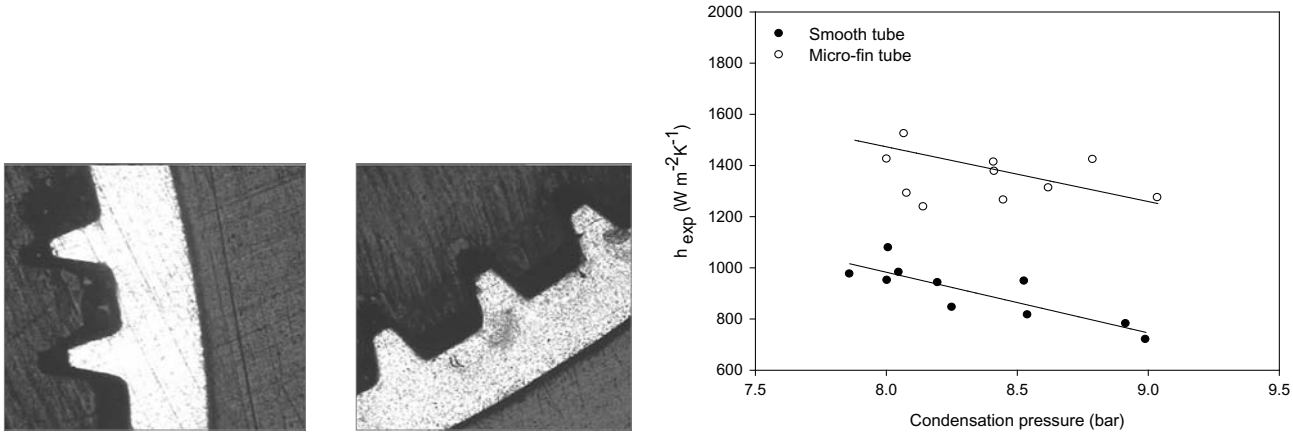

(a) (b)

Fig. 6. Cross-section of the micro-fin tube by electron microscope (100×) (a) and Comparison of average experimental convective heat transfer coefficients of the smooth and micro-fin tubes for the mass flux of 29 kg $m^{-2}s^{-1}$ at pressures of 0.77−0.90 MPa (b)[24] [From Ref. 24, with permission from Turk Isı Bilimi Teknigi Dernegi.]

Table 3. The dimensions of the corrugated tubes.[25−29] [From Refs. 25−27 and 29 with permission from Elsevier and Ref. 28, with permission from ASME.]

Number	p (mm)	e (mm)	β (degree)	β (degree)	D_i (mm)	L (mm)
1	5.08	1	79.47	79.47	8.7	2000
2	5.08	1.25	79.47	79.47	8.7	2000
3	5.08	1.5	79.47	79.47	8.7	2000
4	8.46	1.5	74.20	74.20	8.7	2000
5	6.35	1.5	76.56	76.56	8.7	2000

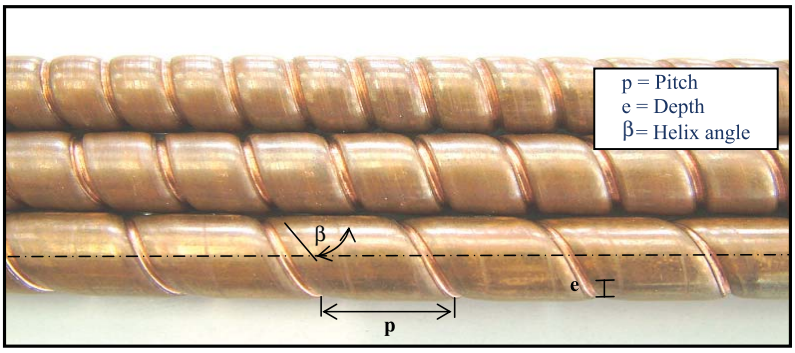

Fig. 7. The photograph of the corrugated tubes.[25–29] [From Refs. 25–29, with permission from Elsevier (color online).]

the photograph of corrugated tubes is displayed in Fig. 7. The tube-in-tube heat exchanger was used as the test section, in which R134a flows inside the corrugated tube and water flows in the annulus. The experimental results demonstrated that the corrugated tube gave higher heat-transfer performance and pressure drop than those of the smooth tube, by about 50% and 70%, respectively. The effect of pitch and depth on the heat-transfer performance and friction characteristics were reported and then compared with the common smooth tube, as illustrated in Fig. 8. Moreover, the new heat transfer and two-phase friction factor correlations were proposed for predicting the Nusselt number and two-phase friction factor for corrugated tubes. Moreover, the two-phase heat transfer coefficient and friction factor correlations were also proposed based on the measured data of R134a flowing through the corrugated tubes under evaporation process.

Aroonrat and Wongwises[30] studied the heat-transfer and friction characteristics of the pure refrigerant HFC-134a during evaporation inside a vertical corrugated tube, experimentally. The double-tube test sections were 0.5 m long with refrigerant flowing in the inner tube and hot water flowing in the annulus. The inner tubes were one smooth tube and two corrugated tubes, which were constructed from smooth copper tube with 8.7 mm inner diameter. The test runs were performed at evaporating temperatures of 10°C, 15°C, and 20°C, heat fluxes of 20, 25, and 30 $kW \cdot m^{-2}$, and mass fluxes of 200, 300, and 400 $kg \cdot m^{-2} \cdot s$. The effects of heat flux, mass flux, and evaporation temperature on the heat-transfer coefficient and two-phase friction factor were also discussed. It was found that the percentage increases of the heat-transfer coefficient and the two-phase friction factor of the corrugated tubes compared with those of the smooth tube are approximately zero to 10% and 70% to 140%, respectively.

Khoeiki *et al.*[31] studied the effect of inclination angle on the heat transfer performance of R134a flows inside a corrugated tube under condensation condition. Inclination angle ranging between −90° and 90°, mass flux varied from 87 to 253 kg/m^2s were tested. The experimental data illustrated that the inclination angle of the test section had a significant effect on the condensation heat transfer coefficient. The highest condensation heat transfer coefficient was obtained at inclination of 30° which was about 140% larger than that at the inclination of −90°. Moreover, a new empirical correlation of the heat-transfer coefficient of R134a flowing inside the corrugated tube with different inclination angles was proposed.

Rainieri *et al.*[32] presented an experimental investigation on the convective heat transfer performance of coiled corrugated tubes for highly viscous fluids such as glycerol and ethylene glycol. The test tube with diameter of 14 mm, curvature ratio of 0.06, corrugation depth of 1 mm, and pitch of 16 mm was used as the test section. The results indicated that the wall curvature could increase the heat transfer performance. Moreover, the wall corrugation had significant effect on the heat transfer performance for only the higher Reynolds number (150–1500).

Garcia *et al.*[33] reported the artificial roughness shape affecting the heat transfer enhancement of corrugated tubes, dimpled tubes and wire coils. The experimental data from their previous works for heat transfer and pressure drop in laminar, transition and turbulent flow regimes were used to compare with the analytical results. The results showed

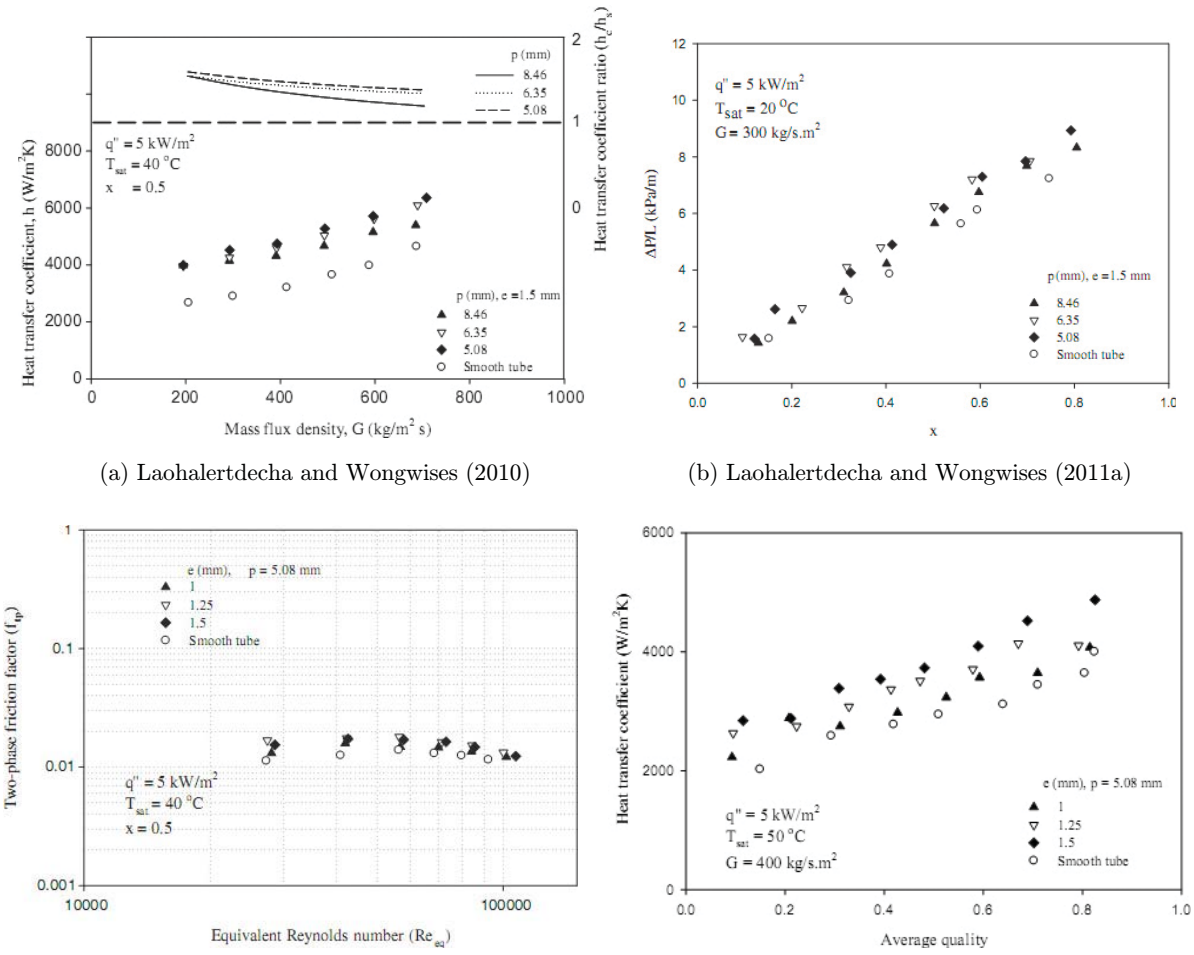

(a) Laohalertdecha and Wongwises (2010)

(b) Laohalertdecha and Wongwises (2011a)

(c) Laohalertdecha and Wongwises (2011b)

(d) Laohalertdecha and Wongwises (2011c)

Fig. 8. The effects of pitch and depth on heat transfer and flow characteristics. [From Refs. 25–28, with permission from Elsevier and ASME.]

that the shape of the artificial roughness had larger effect on the pressure drop than the heat transfer performance. Moreover, they also recommended that the smooth tube should be used for Reynolds number less than 200, wire coil for Reynolds number ranging between 200 and 2000. For Reynolds number larger than 2000, the employment of corrugated and dimpled tubes gave an advantage over the wire coils.

As mentioned above, it is clearly seen that numerous papers are currently available on the single-phase behavior, both experimentally and quantitatively. There are only a few research works that attempt to study the heat-transfer and flow characteristics of the refrigerant two-phase flow. Thus, the research works with respect to the thermal performance and flow characteristics of the refrigerant two-phase flow flowing through fluted tubes with different configurations are required in order to address their performance.

3. Ribbed Tubes

The schematic diagram of an internally finned or ribbed tube is shown in Fig. 9. In an internally finned or ribbed tube, it is difficult to geometrically identify a difference between fin and rib. Normally, both names are assumed to refer to the same geometry. The internal fin or rib geometry is defined by the fin height, the mean fin thickness, pitch of the fin and the apex angle, and the helix angle of the fin. Publications on the heat-transfer and flow characteristics of fluid flow in ribbed tubes are summarized as follows.

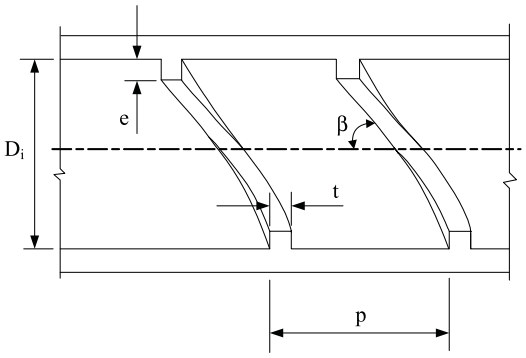

Fig. 9. Schematic diagram of the ribbed tube.

Morris and Rahmat-Asadi[34] conducted an experimental study to investigate the forced convection heat transfer in rotating ribbed tubes. The effect of internal ribs and orthogonal mode rotation on heat transfer was presented. The dimensions of the ribbed tubes are shown in Table 4. Typical three-rib geometries used in turbine rotor blade cooling channels were used as the test tubes. Their experimental data indicated that rotating ribbed tubes increase the heat-transfer performance compared with a common smooth tube as shown in Fig. 10. This behavior is due to the rotation Coriolis-induced secondary flows, which led to the increase in heat-transfer performance on the trailing edge of the tube compared with the leading edge. Finally, the effects of centripetal buoyancy and Coriolis forces were investigated.

Ravigururajan and Bergles[35] use generalized ribbed tube correlations to optimize the thermal performance of heat exchangers based on performance evaluation criteria (PEC). At a given pumping power and surface area, the maximum heat transfer was considered. Similarly, the minimum surface area was taken into account for the case of constant heat load and pumping power. The PEC with their relayed constraint equations were calculated by using a simple iterative procedure. Their simulation results indicated that the Reynolds number and

Table 4. The dimensions of the ribbed tubes.[34] [From Ref. 34, with permission from Elsevier.]

Number	p (mm)	e (mm)	D_i (mm)	L (mm)
1	20	2	10	130
2	15	1.5	10	130
3	10	1	10	130

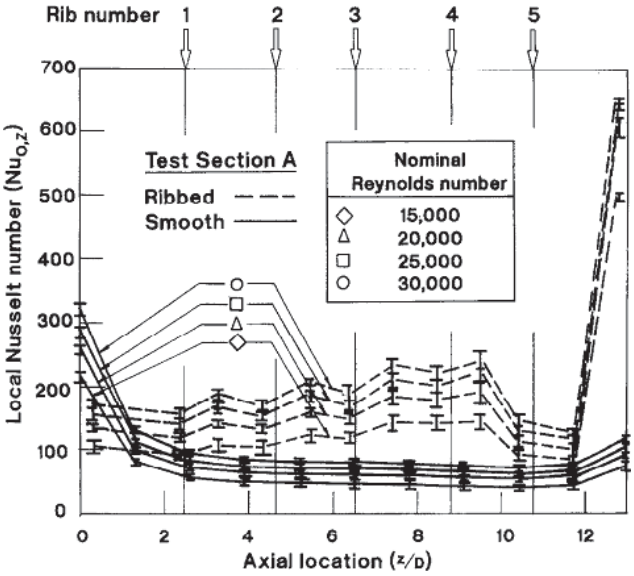

Fig. 10. The effect of ribs on measured local Nusselt number distribution.[34] [From Ref. 34, with permission from Elsevier.]

Prandtl number had a tiny effect on the heat-transfer enhancement. On the contrary, the use of the ribbed tubes can improve the thermal performance, which is useful for designing the enhanced heat exchangers.

Cho and Liu[36] presented an experimental study to investigate the possibility of the electronic anti-fouling (EAF) technique to control precipitation fouling in a spirally ribbed tube used in a common refrigerator. Two new tubes, one with the EAF treatment and another without EAF treatment, were used for testing the fouling tendency of the test tubes. Their measured data showed that the EAF technique could be used to control precipitation fouling that takes place in a spirally ribbed tube.

Chang and Su[37] experimentally investigated the heat-transfer performance of a reciprocating helical tube fitted with full circumferential ribs, which is commonly used in piston designs for a marine diesel engine. The effects of the Reynolds number, Dean number, pulsating number, buoyancy number, and five different reciprocating frequencies on the local heat transfer were tested. The results demonstrated that the presence of Dean vortices caused the increase in local heat-transfer coefficient on the outer surface, even with the agitated flow field caused by ribs under a reciprocating environment. Moreover, the pulsating force and reciprocating buoyancy had also significant effects on the heat-transfer coefficient due to the modified vortex flow

Table 5. The dimensions of the ribbed tubes.[38] [From Ref. 38, with permission from Elsevier.]

Number	p (mm)	e (mm)	D_i (mm)	L (mm)
1	9	0.4–0.6	11.69	1620

structures in the ribbed coils. Finally, an empirical correlation for predicting the heat transfer in the ribbed coils was proposed by considering the effect of pulsating force and reciprocating buoyancy force.

Cheng and Xia[38] presented the critical heat flux (CHF) for water flow in a conventional smooth tube and a four-head spiral internally ribbed tube, experimentally. The test tubes were located in the vertical direction and were heated by an electric power supply. The dimensions of the test tubes are shown in Table 5. The effects of mass flux and pressure on the CHF were investigated. The measured data demonstrated that the increase of wall temperature at which CHF occurs in the spirally internally ribbed tube is less than that of the smooth tube. For both the smooth tube and the spirally internally ribbed tube, fluid enthalpy decreases with the increase of pressure as shown in Fig. 11.

Li and Webb[39] presented long-term cooling tower water fouling data for seven helically ribbed tubes with inner diameter of 15.54 mm, experimentally. The effects of rib starts, helix angle, and height were determined. Based on internal dimensions, there are only two ranges of fouling characteristics, the linear range and nonlinear range. The experimental results showed that the ratio of the enhanced-to-plain tube fouling resistance rose with increases in the product of area indexes and efficiency indexes in the linear range, and the linear relationship fell in a nonlinear range. In addition, the semi-theoretical fouling correlations as a function of the product of area indexes and efficiency indexes and the linear multiple regression correlations as a function of geometric variables and Reynolds number were proposed. These correlations could be used to evaluate the fouling potential of enhanced tubes in actual cooling water situations.

Kim *et al.*[40] experimentally investigated the CHF for flow boiling of R-134a flowing through rifled tubes with four heads and six heads in vertical direction. The test section was shown in Fig. 12. The results were then compared with the data for smooth tube and calculated values from Bowing and Katto correlations. The inner diameters of both the rifled tube and the smooth tube were 17.04 mm. The experimental test runs were conducted at outlet pressure ranging from 13 to 23.9 bar, mass flux ranging from 285 to 1300 $\mathrm{kg \cdot m^{-2} \cdot s}$, and inlet subcooling temperature of five to 40°C. The experimental data showed that the CHF in the rifled tube was approximately 40% to 60% greater than that of the smooth tube and rose with increasing mass flux as well as outlet pressure as shown in Fig. 13.

Naphon and co-workers[41] reported the heat-transfer and pressure-drop characteristics of helical rib tubes, experimentally. The double-tube counter flow heat exchanger was used as the test section, in which hot water flowed inside the test tube and cold water flowed in the annulus. The effects of helical rib height and helical rib pitch were presented. Their results indicated that the heat-transfer coefficient

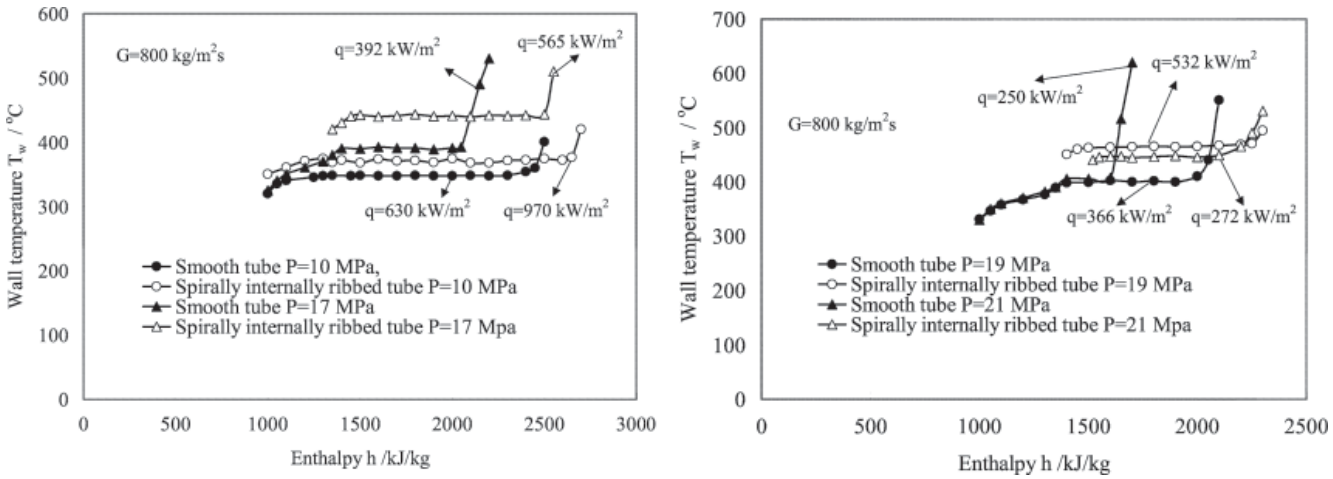

Fig. 11. Variation of wall temperatures with enthalpy.[38] [From Ref. 38, with permission from Elsevier.]

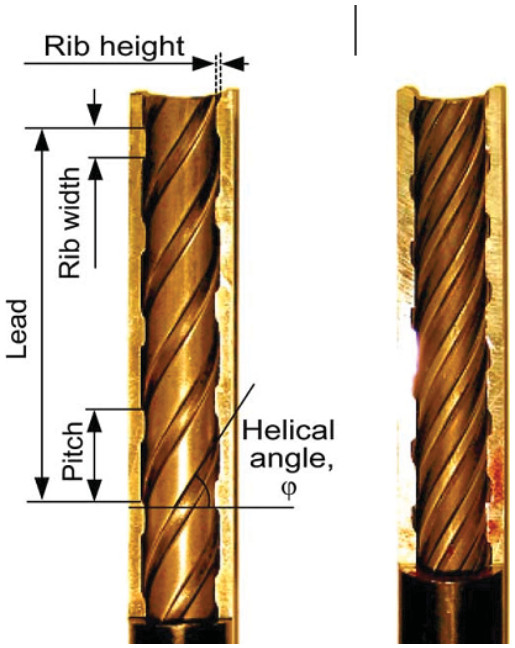

Fig. 12. Cross sectional view of rifled tubes and geometric parameters.[40] [From Ref. 40, with permission from Elsevier (color online).]

and pressure of helical rib tube were significantly higher than that of the smooth tube approximately 10% to 70% and 10% to 280%, respectively. The heat-transfer coefficient rose with increases in the Reynolds number and the helical rib depth, and also rose with decreases in the helical rib pitches. Similarly, the friction factor of the helical ribbed tube rose with an increase in helical rib depth and decreased with increases in the Reynolds number and helical rib pitch. Moreover, they also proposed the heat transfer and friction factor correlation for predicting the Nusselt number and friction characteristics of the helical ribbed tube as a function of helical rib dept and helical rib pitch. The proposed correlations gave good agreement between measured data and calculated values, and the majority of the data fell within $\pm 15\%$ of the proposed equations.

Recently, Ji *et al.*[42] presented an experimental investigation on the heat transfer and friction factor of 16 internal helically ribbed tubes with different geometrical parameters under turbulent flow regime. Reynolds number ranged from 10,000 to 100,000 and Prandtl number varied between 4.98 and 8.22 were tested. A correlation for predicting the average heat transfer coefficient of the ribbed tubes was proposed based on the Gnielinski correlation by replacing the friction factor with the measured friction factor of the internally ribbed tubes. The results indicated that the proposed equation was very appropriate for practical engineering design and gave vary good accuracy.

Similar to the corrugated tubes, a number of researchers reported on the heat-transfer and flow features of ribbed tubes with single-phase flow of

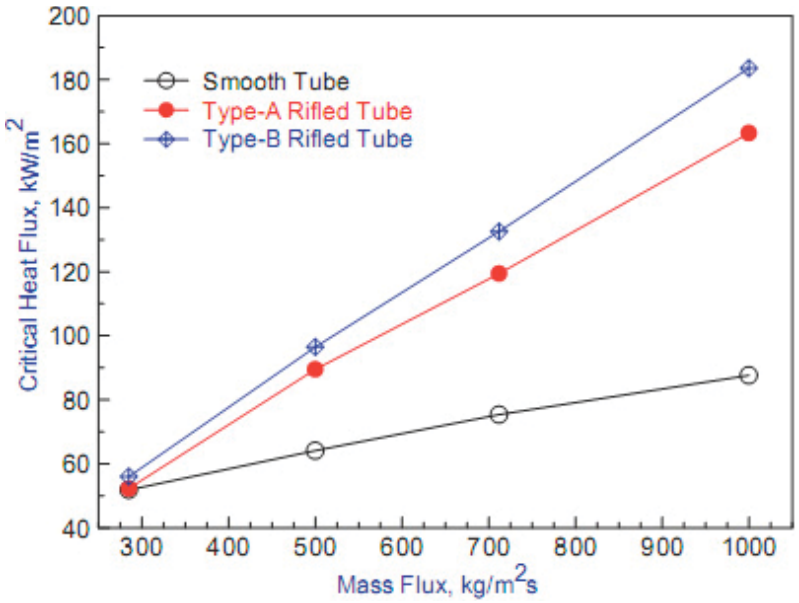

Fig. 13. CHF versus mass flux for one smooth tube and two rifled tubes at 16.5 bar.[40] [From Ref. 40, with permission from Elsevier (color online).]

liquids, both experimentally and quantitatively. Therefore, the two-phase flow data are required to certify the heat transfer and flow characteristics of ribbed tubes.

4. Grooved Tubes

As shown in Fig. 14, internally grooved tubes having an internal surface including many grooves to increase the heat-transfer performance have been used in many applications. The internal surface of an internally grooved tube includes many ribs helically extending along the tube in an axial direction and a groove is formed between each adjacent pair of ribs. Publications on the heat-transfer and flow characteristics of single-phase flow in internally grooved tubes are summarized as follows.

Graham *et al.*[43] presented an experimental study on the heat-transfer and pressure-drop characteristics of R-134a flowing through an axially grooved tube during the condensation process. The measured data were compared with the data for a smooth tube and a common grooved tube with an 18° helix angle. A grooved tube with an inner diameter of 8.91 mm was used as the test section and tested at the mass flux range from 75 to 450 $\mathrm{kg \cdot m^{-2} \cdot s}$. At a mass flux of 75 $\mathrm{kg \cdot m^{-2} \cdot s}$, their results showed that the axially grooved tube gave higher heat-transfer performance than that of a smooth tube smaller than the common grooved tube with an 18° helix angle. In contrast, at a mass flux of 150 $\mathrm{kg \cdot m^{-2} \cdot s}$, the results indicated that the heat-transfer performance of axially grooved tubes was larger than those of both smooth tubes and helically ribbed tubes. For the pressure drop, their data showed that the pressure drops of axially grooved tubes agreed well with those of the helically ribbed tubes.

Herman and Kang[44] presented an experimental study on the unsteady temperature field in the grooved channel with curved vanes (GCV) using holographic interferometry. The heat-transfer performance of GCV was compared with the basic grooved channel (BGC). Their experimental data indicated that addition of the curved vane above the downstream end of the heated block gave higher heat-transfer performance than that of BGC by a factor of approximately 1.5 to 3.5 times. This behavior due to the GCV tube accelerated the flow between the curved vane and the heated block and the large recirculation region in the groove was eliminated. At the Reynolds number of 450, flow transition from steady to oscillatory regime took place. Moreover, their data also showed that the pressure drop for the GCV tube was three to five times greater than those of the BGC tube.

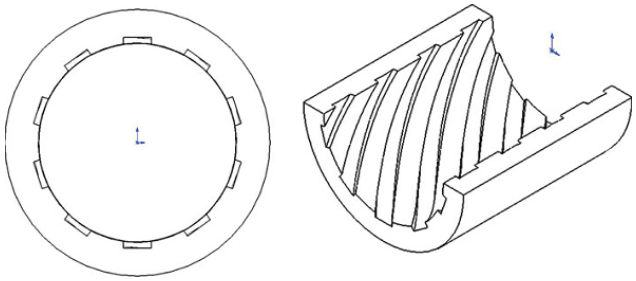

Fig. 14. Schematic diagram of the grooved tube.[51] [From Ref. 51, with permission from Springer.]

Goto *et al.*[45,46] investigated the local condensation and evaporation heat-transfer coefficient of R410A and R22 flow inside the five different kinds of internally grooved tubes placed in the horizontal direction. The test conditions were conducted at a refrigerant mass flow rate ranging from 130 to 400 $\mathrm{kg \cdot m^{-2} \cdot s}$ for both R410A and R22 and the vapor pressures of 2.41 MPa for R410A and 1.53 MPa for R22. The measured data indicated that the local heat-transfer coefficients of the herringbone grooved tube were two times larger than those of the helical tube for both R410A and R22. Moreover, they also proposed the new heat-transfer correlations for predicting the Nusselt number of R410A and R22 flowing in the helical micro-finned tube and herringbone micro-finned tube. Compared with the measured data, good correspondence between the experimental values and the calculated values by the proposed equations were obtained and the majority of the data fell within ± 20% of the proposed equation.

Zhang *et al.*[47] reported the evaporation heat-transfer characteristics of R417A flowing inside horizontal two internally grooved tubes with various geometrical parameters compared with common smooth tube and micro-finned tube correlations, experimentally. The experimental conditions used in their study were summarized as follows: mass flow rate ranged from 176 to 344 $\mathrm{kg \cdot m^{-2} \cdot s}$; heat flux ranged from 11 to 32 $\mathrm{kW \cdot m^{-2}}$; evaporation temperatures ranged from 0°C to 5.5°C; and vapor quality ranged from 0.2 to 1. The effects of the above parameters were presented. The results demonstrated that the evaporation heat-transfer coefficient of R417A was lower than that of the R22 and

significantly smaller in internally grooved tubes than the conventional smooth tube. This means that the heat-transfer enhancement was more effective for pure refrigerant than that for the non-azeotropic refrigerant mixtures. Compared with the calculated values from the existing correlations, the results indicated that the modified Kattan model gave better agreement with the measured data than the standard Kattan model. Moreover, the Koyama and Wellsandt model for micro-finned tubes overestimated the evaporation heat-transfer coefficient, especially for R417A.

Zhang *et al.*[48] presented an experimental investigation on the local heat-transfer coefficient of R417A flowing through internally grooved tubes during the evaporation process, experimentally. Two internally grooved tubes with different geometrical parameters were tested and then compared with the common smooth tube and the existing correlations. Their data showed that the existing micro-finned tube correlations could not be used to predict the local evaporation heat-transfer coefficient of the internally grooved tubes. They also proposed a new correlation based on the modified Kattan model for computing the heat-transfer coefficient of non-azeotropic refrigerant R417A. Compared with the measured data, a deviation of $\pm 30\%$ was obtained for vapor quality less than 0.8.

Bilen *et al.*[49] experimentally studied the heat-transfer and friction characteristics of air flowing inside internally grooved tubes with circular, trapezoidal and rectangular configurations under turbulent flow regime. The geometrical parameters of the grooved tubes are shown in Fig. 15. A Reynolds number ranging from 10,000 to 38,000 was tested. At the highest Reynolds number, the results indicated that the Nusselt number for internally grooved tubes was larger than that for a common smooth tube by about 47% for a rectangular groove, 58% for a trapezoidal groove, and 63% for a circular groove. Moreover, the thermal performance for all internally grooved tubes was shown to be higher than that of a smooth tube — approximately 1.24−1.28 times for a circular groove, 1.22−1.25 times for a trapezoidal groove, and 1.13−1.26 times for a rectangular groove. In addition, the friction factors of all grooved tubes were nearly the same, and the friction factor was independent of the Reynolds number for grooved tubes as shown in Fig. 16.

Bharadwaj *et al.*[50] presented an experimental study on the heat-transfer and pressure-drop characteristics of water flowing through a 75-start spirally grooved tube with twisted tape insert under laminar and turbulent flow regimes. Their results showed that the Nusselt number of the spirally grooved tube without twisted tape insert was 400% and 140% higher than that of a smooth tube for laminar and turbulent flow regime, respectively. Similarly, for the spirally grooved tube with twisted tape insert, maximum heat-transfer enhancements of 600% and 140% were obtained for laminar and

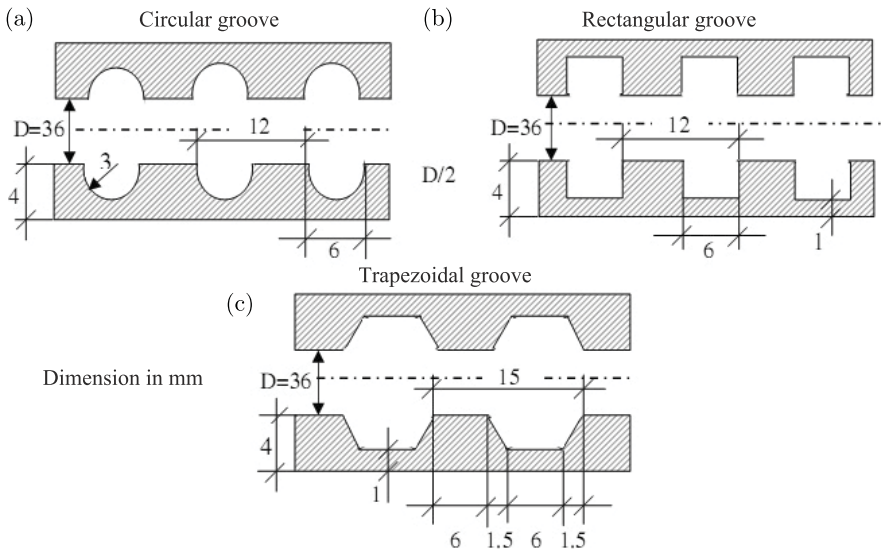

Fig. 15. The geometric shapes of the grooved tubes.[49] [From Ref. 49, with permission from Elsevier.]

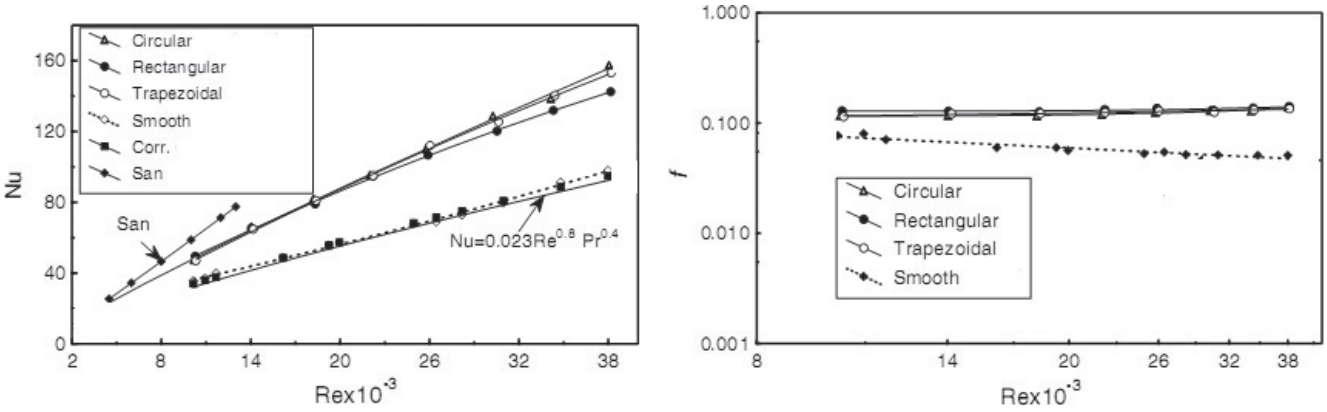

Fig. 16. Variation of the Nusselt number and friction factor with the Reynolds number.[49] [From Ref. 49, with permission from Elsevier (color online).]

turbulent flow regime, respectively. Moreover, the pressure drop of internally grooved tubes was larger than that of the smooth conventional smooth tube.

Wongwises *et al.*[51] reported the evaporation heat-transfer coefficient and pressure drop of R-134a flowing inside internally grooved tubes, experimentally. Four grooved tubes with different configurations made from stainless steel were tested under a condition of constant heat flux. The effects of groove pitch, mass flux, heat flux, and saturation temperature on heat-transfer coefficient and frictional pressure drop were presented. The measured data showed that the grooved tubes gave higher heat-transfer coefficient and frictional pressure drop than those of the common smooth tube.

As mentioned above, many researchers have been focused on the heat-transfer and friction characteristics of two-phase refrigerants flowing through horizontal internally grooved tubes under both evaporation and condensation processes. However, heat-transfer and pressure-drop characteristics of internally grooved tubes in other directions should be studied.

5. Fluted Tubes

From the configuration of the fluted tube, it is evident that they are quite similar to the corrugated tubes. However, from the point view of the authors, there are small differences between the two enhanced tubes. If the ratio of corrugation to cross-sectional area is greater than one, it is a fluted tube; however, if this ratio is less than one, it is a corrugated tube. The published articles describe the heat-transfer enhancements of the fluted tubes as follows.

Aly and Bedrose[52] introduced a theoretical study of heat-transfer performance of stagnant water vapor condensed on both vertical and horizontal spirally fluted tubes. In this study, two regions of fluted tubes, namely the valley and the crest, were separately considered; the condensation process was started on the flute crest and then ran down to the valley by gravity and surface tension. The motion equation and energy balance equation were taken into account to examine the relationships between condensate flow rate and film thickness. Their simulation results indicated that the spirally fluted tube gave five times higher heat-transfer performance than a smooth tube in the case of horizontal direction and about three times higher in the case of vertical direction. Moreover, the calculated Nusselt number from the proposed model coincided well with the experimental results for integral finned tubes and the majority of the data fell within $\pm 20\%$ of the proposed model. Similarly, for vertical tubes, an agreement between the predicted value and the measured data can be seen and the majority of the data fell within $\pm 5\%$ of the proposed model.

Kang *et al.*[53] presented an experimental system to formulate the new flooding correlations for both vertical and horizontal directions as a function of declination angle for a fluted tube with a twisted insert. Figure 17 depicts the sketch of the fluted tube and geometrical parameters. In their study, twisted tubes made from plastic were inserted inside the fluted tube to accelerate the absorption rate in counter-current absorption. Water−ethyl alcohol solution flows downward in the fluted tube, whereas air flows counter-current in an upward direction. For the inclination angle less than 60°, the results

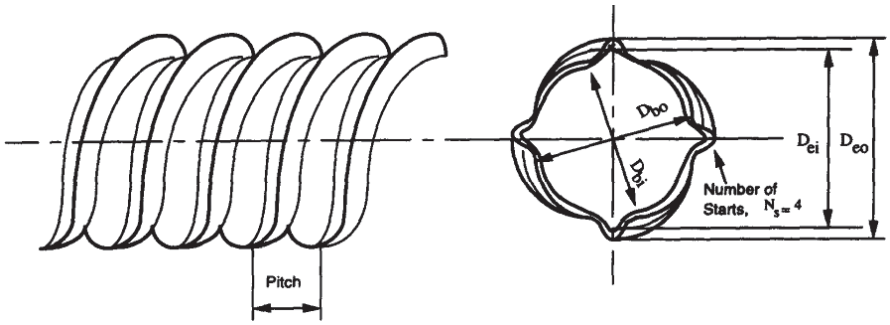

Fig. 17. Schematic diagram of the fluted tube.[53] [From Ref. 53, with permission from Elsevier.]

indicated that flooding was created from the top of the tube. On the contrary, it was initiated from the bottom of the tube for an inclination angle greater than 60°. The position of the twisted insert had no significant effect on the flooding mechanism in the case of a horizontal tube, whereas it had a small effect in the case of a vertical tube. Moreover, for the fluted tube with a twisted insert, the results indicated that the flooding vapor velocity reached a maximum for the inclination angle between 40° and 60° and superficial liquid velocities less than $0.01178\,\mathrm{m}\cdot\mathrm{s}^{-1}$. However, in the case of superficial liquid velocities greater than $0.01178\,\mathrm{m}\cdot\mathrm{s}^{-1}$, the superficial flooding vapor velocity increased with the inclination angle.

Wang and colleagues[54] reported experimental results that illustrated the heat-transfer performance of carbon-steel spirally fluted tubes replacing the conventional copper smooth tubes that corrode easily due to the feed water of boiler. The dimensions of the fluted tubes are shown in Table 6. Compared with the common carbon-steel smooth tube, the experimental results showed that the heat-transfer coefficient of the carbon-steel spirally fluted tube was 10% to 17% higher than that of the smooth tube and it was very close to that of the copper smooth tubes, as shown in Fig. 18.

Qi *et al.*[55] presented an experimental study that evaluated the drag reduction and heat-transfer

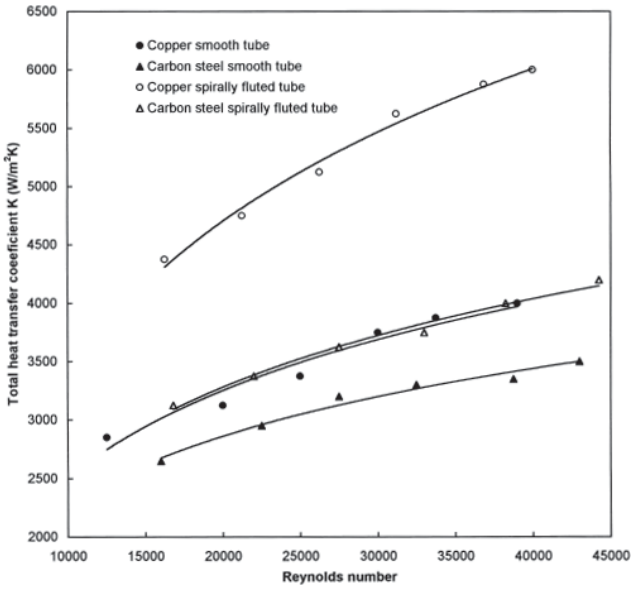

Fig. 18. Heat transfer coefficient versus Reynolds number.[54] [From Ref. 54, with permission from Elsevier.]

enhancement of a fluted tube. Tube-in-tube heat exchanger was used as the test section for cationic surfactant solution Ethoquad T13-50/NaSal (5 mM/8.75 mM) and zwitterionic/anionic reduction surfactant solution SPE98330 (1500 ppm). The results indicated that use of the fluted inner tube increased the heat-transfer coefficient for both surfactant solutions. Moreover, cationic surfactant solution

Table 6. The dimensions of the fluted tubes.[54] [From Ref. 54, with permission from Elsevier.]

Number	Tube description	e (mm)	p (mm)	D_o (mm)	D_i (mm)	β (degree)	L (mm)
1	Copper (Smooth)	—	—	16	13	—	650
2	Carbon steel (Smooth)	—	—	16	13	—	650
3	Copper (Fluted)	0.25	15.6	16	13	40	650
4	Carbon steel (Fluted)	0.25	15.6	16	13	40	650

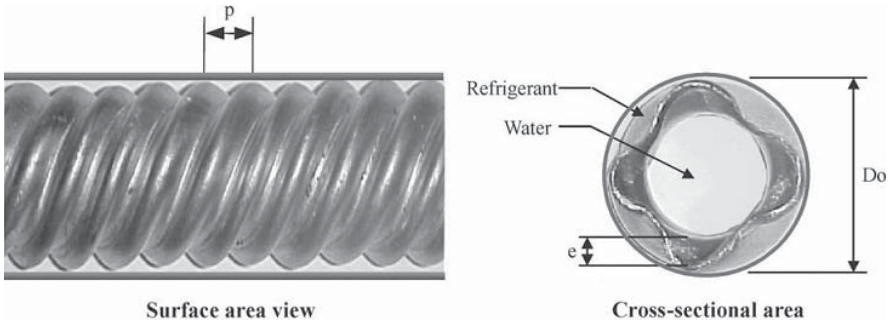

Fig. 19. Photograph of the fluted tube.[56] [From Ref. 56, with permission from Elsevier.]

gave a higher pressure-drop penalty than the zwitterionic/anionic solution.

Rousseau and co-workers[56] presented a mathematical formulation and numerical method to investigate the heat-transfer and pressure-drop characteristics of fluted-tube refrigerant-to-water condensers. Figure 19 shows the photo of the fluted tube. In this model, the surface area was divided into three regions: superheated, two-phase, and subcooled regions, in which all properties of refrigerant and water can be calculated. The proposed model was formulated based on the effectiveness-NTU method. For the water side, the existing empirical correlations for friction factor and heat-transfer coefficient were used. Unfortunately, for the refrigerant side, they reported that there are no available correlations for calculating the friction factor and heat-transfer coefficient of the fluted tube-in-tube condenser. Thus, the existing correlations for smooth tubes, combined with an enhancement ratio based on available correlations for helical coils, as well as an enhancement factor based on empirical data for fluted tube condenser were employed. Data for two commercial fluted tube heat exchangers were used to validate the proposed model. The average difference between the measured and the predicted pressure drop was about 7.27%. Similarly, the difference in the log mean temperature was roughly 4.41%.

As mentioned above, for the fluted tube, a number of researches studied the single-phase heat transfer and flow behaviors for conventional heat transfer fluids. The heat-transfer and pressure-drop characteristics for two-phase flow of refrigerants in the fluted tubes are required for practical applications.

6. Vipertubes

Vipertube is a new type of enhanced tube which produced by Vipertex^{TM} company under ASTM standard. The configuration of the Vipertubes is shown in Fig. 20. Kukulka *et al.*[57] was the first research group who presented the heat-transfer enhancement and fouling characteristics of a series of the Vipertubes. These tubes were made from stainless steel tube (Type 304L) with outer diameter of 1.905 cm and length of 0.9144 m. From their experiment with water, the measured data illustrated that the enhancement ratio of the Vipertubes was

Fig. 20. Photograph of the Vipertube.[57] [From Ref. 57, with permission from Elsevier (color online).]

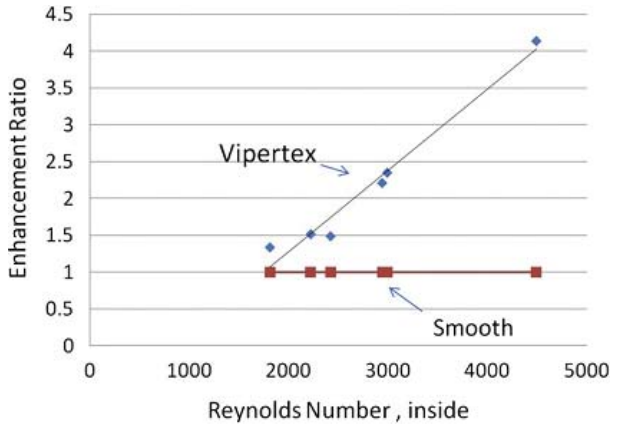

Fig. 21. Heat transfer enhancement ratio versus Reynolds number.[57] [From Ref. 57, with permission from Elsevier (color online).]

varied between 1 and 4, for Reynolds number ranging from 2000 to 5000. This enhancement is due to several factors such as increasing of fluid turbulence, secondary flow, disturbing of the thermal boundary layer and increasing of the heat transfer area. Moreover, the Vipertubes was designed to minimize the effect of fouling. Some results were shown in Fig. 21.

7. Conclusions

As discussed, different types of the enhanced tubes (corrugated tube, ribbed tube, grooved tube and fluted tube) have great potential for heat-transfer enhancement and are highly suited to applications in practical heat-transfer processes. This offers an opportunity for engineers to develop highly compact and effective heat-transfer equipment. Several published articles show that the heat-transfer coefficients of the enhanced tubes are much higher than the conventional smooth tubes and give only marginal drops in pressure. An important reason for the heat-transfer enhancement of the enhanced tubes is the modified rough surface, which causes increases in the turbulence mixing intensity in the flow field, and also by limiting the growth of fluid boundary layers close to the heat transfer surfaces, which leads to increases in heat-transfer performance. Moreover, from the review of the published literature, many researchers reported the heat-transfer performance and pressure-drop characteristics of the enhanced tubes working with single-phase fluids. Only some researchers reported on the use of two-phase flow refrigerants as working fluids for both evaporation and condensation processes. Many researchers suggested that the enhanced tubes have higher potential for replacing the conventional smooth tubes normally used in heat-transfer equipment. This is a great opportunity for researchers to discover new ways for increasing the heat-transfer performance of the enhanced tubes in order to meet high compactness and high heat flux of the heat exchangers. Moreover, new types of enhanced tubes such as Vipertube should be investigated in order to meet highest heat transfer performance and lowest. This is a challenge task of researchers and heat exchanger manufacturer.

Acknowledgments

The authors would like to express their appreciation to the Thailand Research Fund, the Office of the Higher Education Commission and the National Research University Project for providing financial support. Especially, the second author wishes to thank KMUTT for providing him with a Post-doctoral fellowship.

References

1. A. S. Dalkilic and S. Wongwises, Intensive literature review of condensation inside smooth and enhanced tubes, *Int. J. Heat Mass Transfer* **52** (2009) 3409−3426.
2. K. Mimura and A. Isozaki, Heat transfer and pressure drop of corrugated tubes, *Desalination* **22** (2001) 131−139.
3. S. Ganeshan and M. R. Rao, Studies on themohydraulics of single and multi-start spirally corrugated tubes for water and time independent power law fluids, *Int. J. Heat Mass Transfer* **25** (1982) 1013−1022.
4. P. P. Thien and M. M. K. Khan, Flow of an Oldroyd-type fluid through a sinusoidally corrugated tube, *J. Non-Newtonian Fluid Mech.* **24** (1987) 203−220.
5. Y. Asako, H. Nakamura and M. Faghri, Heat transfer and pressure drop characteristics in a corrugated duct with rounded corners, *Int. J. Heat Mass Transfer* **31** (1988) 1237−1245.
6. H. Honda, S. Nozu, Y. Matsuoka, T. Aoyama and H. Nakata, Condensation of R-11 and R-113 in the annuli of horizontal double-tube condensers with an enhanced inner tube, *Exp. Ther. Fluid Sci.* **2** (1989) 173−182.

7. S. R. Burdette, P. J. Coates, R. C. Armstrong and R. A. Brown, Calculations of viscoelastic flow through an axisymmetric corrugated tube using the explicitly elliptic momentum equation formulation (EEME), *J. Non-Newtonian Fluid Mech.* **33** (1989) 1−23.
8. V. Zimparov, N. L. Vulchanov and L. B. Delov, Heat transfer and friction characteristics of spirally corrugated tubes for power plant condensers-1. Experimental investigation and performance evaluation, *Int. J. Heat Mass Transfer* **34** (1991a) 2187−2197.
9. V. Zimparov, N. L. Vulchanov and L. B. Delov, Heat transfer and friction characteristics of spirally corrugated tubes for power plant condensers-2. A mixing-length model for predicting fluid friction and heat transfer, *Int. J. Heat Mass Transfer* **34** (1991b) 2199−2206.
10. N. P. Gopalan and R. Ponnalagasamy, Investigation on laminar flow of a suspension in corrugated straight tubes, *Int. J. Eng. Sci.* **30** (1992) 631−644.
11. D. L. Hinton and J. C. Conklin, Condensation of refrigerants flowing inside smooth and corrugated tubes, *Fourth ASME/JSME Thermal Engineering Joint Conference*, Hawaii, March 1995, pp. 19−24.
12. X. D. Chen, S. K. Nguang and A. E. Bergles, Characterization of the effect of corrugation angles on hydrodynamic and heat transfer performance of four-start spiral tubes, *J. Heat Transfer* **123** (2001) 1149−1158.
13. Y. Dong, L. Huixiong and C. Tingkuan, Pressure drop, heat transfer and performance of single phase turbulent flow in spirally corrugated tubes, *Exp. Therm. Fluid Sci.* **24** (2001) 131−138.
14. V. Zimparov, Enhancement of heat transfer by a combination of three-start spirally corrugated tubes with a twisted tape, *Int. J. Heat Mass Transfer* **44** (2001) 551−574.
15. V. Zimparov, Enhancement of heat transfer by a combination of single-start spirally corrugated tubes with a twisted tape, *Exp. Therm. Fluid Sci.* **25** (2002) 535−546.
16. S. Rainieri and G. Pagliarini, Convective heat transfer to temperature dependent property fluids in the entry region of corrugated tubes, *Int. J. Heat Mass Transfer* **45** (2002) 4525−4536.
17. A. Barba, S. Rainieri and M. Spica, Heat transfer enhancement in a corrugated tube, *Int. Comm. Heat Mass Transfer* **29** (2002) 313−322.
18. P. G. Vicente, A. Garcia and A. Viedma, Mixed convection heat transfer and isothermal pressure drop in corrugated tubes for laminar and transition flow, *Int. Comm. Heat Mass Transfer* **31** (2004a) 651−662.
19. V. Zimparov, Prediction of friction factor and heat transfer coefficients for turbulent flow in corrugated tubes combined with twisted tape inserts. Part 1: Friction factor, *Int. J. Heat Mass Transfer* **47** (2004) 589−599.
20. V. Zimparov, Prediction of friction factor and heat transfer coefficients for turbulent flow in corrugated tubes combined with twisted tape inserts. Part 2: Heat transfer coefficients, *Int. J. Heat Mass Transfer* **47** (2004) 385−393.
21. A. E. Bergles, R. A. Lee and B. B. Mikic, Heat transfer in rough tubes with twisted tape swirl flow, *Trans. ASME, J. Heat Transfer* **91** (1969) 443−445.
22. W. Targanski and J. T. Cieslinski, Evaporation of R407C/Oil mixtures inside corrugated and micro-fin tubes, *Appl. Therm. Eng.* **27** (2007) 2226−2232.
23. S. Rozzi, R. Massini, G. Paciello, G. Pagliarini, S. Raineiri and A. Trifiro, Heat treatment of fluid foods in a shell and tube heat exchanger: Comparison between smooth and helically corrugated wall tubes, *J. Food Eng.* **79** (2007) 249−254.
24. A. S. Dalkiliç, İ. Teke, S. Wongwises, Heat transfer enhancement during downward laminar flow condensation of R134a in vertical smooth and micro-fin tubes, *Isi Bilimi Ve Teknigi Dergisi/Journal of Thermal Science and Technology* **32** (2012) 19v31.
25. S. Laohalertdecha and S. Wongwises, The effects of corrugation pitch on the condensation heat transfer coefficient and pressure drop of R-134a inside horizontal corrugated tube, *Int. J. Heat Mass Transfer* **53** (2010) 2924−2931.
26. S. Laohalertdecha and S. Wongwises, An experimental study into the evaporation heat transfer and flow characteristics of R-134a refrigerant flowing through corrugated tubes, *Int. J. Ref.* **34** (2011a) 280−291.
27. S. Laohalertdecha and S. Wongwises, Condensation heat transfer and flow characteristics of R-134a flowing through corrugated tubes, *Int. J. Heat Mass Transfer* **54** (2011b) 2673−2682.
28. S. Laohalertdecha and S. Wongwises, Effects of pitch and depth on the condensation heat transfer of R-134a flowing through corrugated tubes, *Proc. ASME/JSME 2011 8th Therm. Eng. Con.*, Hawaii, USA (2011c).
29. S. Laohalertdecha, A. S. Dalkilic and S. Wongwises, Correlations for evaporation heat transfer coefficient and two-phase friction factor for R-134a flowing through horizontal corrugated tubes, *Int. J. Heat Mass Transfer* **38** (2011d) 1406−1413.
30. K. Aroonrat and S. Wongwises, Evaporation heat transfer and friction characteristics of R-134a flowing downward in a vertical corrugated tube, *Exp. Therm. Fluid Sci.* **35** (2011) 20−28.
31. D. Khoeiki, M. A. Akhavan-Behabadi and A. Saboonchi, Experimental study on condensation heat transfer of R-134a flow in corrugated tubes with

different inclinations, *Int. Comm. Heat Mass Transfer* **39** (2012) 138−143.
32. S. Rainieri, F. Bozzoli and G. Pagliarini, Experimental investigation on the convective heat transfer in straight and coiled corrugated tubes for highly viscous fluids: Preliminary results, *Int. J. Heat Mass Transfer* **55** (2012) 498−504.
33. A. Garcia, J. P. Solano, P. G. Vicente and A. Viedma, The influence of artificial roughness shape on heat transfer enhancement: Corrugated tubes, dimpled tubes and wire coils, *App. Therm. Eng.* **35** (2012) 196−201.
34. W. D. Morris and W. F. Rahmat-Asadi, Convective heat transfer in rotating ribbed tubes, *Int. J. Heat Mass Transfer* **39** (1996) 2253−2266.
35. T. S. Ravigururajan and A. E. Bergles, Optimization of fin-tube enhancement for large evaporation and condensers, *Energy* **39** (1996) 421−432.
36. Y. I. Cho and R. Liu, Control of fouling in a spirally-ribbed water chilled tube with electronic anti-fouling technology, *Int. J. Heat Mass Transfer* **42** (1999) 3037−3046.
37. S. W. Chang and L. M. Su, Heat transfer of reciprocating helical tube fitted with full circumferential ribs, *Int. J. Heat Mass Transfer* **44** (2001) 3025−3042.
38. L. Cheng and G. Xia, Experimental study of CHF in a vertical spirally internally ribbed tube under the condition of high pressures, *Int. J. Therm. Sci.* **41** (2002) 396−400.
39. W. Li and R. L. Webb, Fouling characteristics of internal helical-rib roughness tubes using low-velocity cooling tower water, *Int. J. Therm. Sci.* **45** (2002) 1685−1691.
40. C. H. Kim, I. C. Bang and S. H. Chang, Critical heat flux performance for flow boiling of R-134a in vertical uniformly heated smooth tube and rifled tubes, *Int. J. Heat Mass Transfer* **48** (2005) 2868−2877.
41. P. Naphon, M. Nuchjapo and J. Kurujareon, Tube side heat transfer coefficient and friction factor characteristics of horizontal tubes with helical rib, *Energ. Convers. Manag.* **47** (2006) 3031−3044.
42. W. T. Ji, D. C. Zhang, Y. L. He and W. Q. Tao, Prediction of fully developed turbulent heat transfer of internal helically ribbed tubes — an extension of gnielinski equation, *Int. J. Heat Mass Transfer* **55** (2012) 1375−1384.
43. D. Graham, J. C. Chato and T. A. Newell, Heat transfer and pressure drop during condensation of refrigerant 134a in an axially grooved tube, *Int. J. Heat Mass Transfer* **42** (1999) 1935−1944.
44. C. Herman and E. Kang, Heat transfer enhancement in a grooved channel with curved vanes, *Int. J. Heat Mass Transfer* **45** (2002) 3741−3757.
45. M. Goto, N. Inoue and N. Ishiwatari, Condensation and evaporation heat transfer of R410A inside internally grooved horizontal tubes, *Int. J. Ref.* **24** (2001) 628−638.
46. M. Goto, N. Inoue and R. Yonemoto, Condensation heat transfer of R410a inside internally grooved horizontal tubes, *Int. J. Ref.* **26** (2003) 410−416.
47. X. Zhang, X. Zhang, Y. Chen and X. Yuan, Heat transfer characteristics for evaporation of R417a flowing inside horizontal smooth and internally grooved tubes, *Energ. Convers. Manag.* **49** (2008) 1731−1739.
48. X. Zhang, C. Ji and X. Yuan, Prediction method for evaporation heat transfer of non-azeotropic refrigerant mixtures flowing inside internally grooved tubes, *Appl. Therm. Eng.* **28** (2008) 1974−1983.
49. K. Bilen, M. Cetin, H. Gul and T. Balta, The investigation of groove geometry effect on heat transfer for internally grooved tubes, *Appl. Therm. Eng.* **29** (2009) 753−761.
50. P. Bharadwaj, A. D. Khondge and A. W. Date, Heat transfer and pressure drop in a spirally grooved tube with twisted tape insert, *Int. J. Heat Mass Transfer* **52** (2009) 1938−1944.
51. S. Wongwises, J. Kaew-On, S. Laohalertdecha, W. Duangthongsuk and K. Sakamatapan, Evaporation Heat Transfer and Flow Characteristics of R-134a Flowing Through Internally Grooved Tubes. Heat Mass Transfer DOI 10.1007/s00231-010-0748-6 (2010).
52. N. H. Aly and S. D. Bedrose, Enhanced film condensation of steam on spirally fluted tubes, *Desalination* **101** (1995) 295−301.
53. Y. T. Kang, R. Stout and R. N. Christensen, The effects of inclination angle on flooding in a helically fluted tube with a twisted insert, *Int. J. Mult. Flow.* **23** (1997) 1111−1129.
54. L. Wang, D. W. Sun, P. Liang, L. Zhuang and Y. Tan, Heat transfer characteristics of carbon steel spirally fluted tube for high pressure preheaters, *Energ. Convers. Manag.* **41** (2000) 993−1005.
55. Y. Qi, Y. Kawaguchi, Z. Lin, M. Ewing, R. N. Christensen and J. L. Zakin, Enhanced heat transfer of drag reducing surfactant solutions with fluted tube-in-tube heat exchanger, *Int. J. Heat Mass Transfer* **44** (2001) 1495−1505.
56. P. G. Rousseau, M. V. Eldik and G. P. Greyvenstein, Detailed simulation of fluted tube water heating condenser, *Int. J. Ref.* **26** (2003) 232−239.
57. P. J. Kukulka, R. Smith and K. G. Fuller, Development and evaluation of enhanced heat transfer tubes, *Appl. Therm. Eng.* **31** (2011) 2141−2145.
58. P. G. Vicente, A. Garcia and A. Viedma, Experimental investigation on heat transfer and frictional characteristics of spirally corrugated tubes in turbulent flow at different Prandtl number, *Int. J. Heat Mass Transfer* **47** (2004b) 671−681.

International Journal of Air-Conditioning and Refrigeration
Vol. 20, No. 4 (2012) 1250019 (11 pages)

DOI: 10.1142/S2010132512500198

World Scientific
www.worldscientific.com

NUMERICAL AND EXPERIMENTAL INVESTIGATION OF THE FLOW CHARACTERISTICS OF R134a FLOWING THROUGH ADIABATIC HELICAL CAPILLARY TUBES

SUKKARIN CHINGULPITAK[*,‡], JATUPORN KAEW-ON[†,‡] and SOMCHAI WONGWISES[‡,§]

[*]*The Joint Graduate School of Energy and Environment*
King Mongkut's University of Technology Thonburi
Bangmod, Bangkok 10140, Thailand

[†]*Physics Department, Faculty of Science*
Thaksin University, Papayom, Phattalung 93110, Thailand

[‡]*Fluid Mechanics, Thermal Engineering and Multiphase Flow Research Lab. (FUTURE)*
Department of Mechanical Engineering
Faculty of Engineering
King Mongkut's University of Technology Thonburi
Bangmod, Bangkok 10140, Thailand
[§]*somchai.won@kmutt.ac.th*

Received 10 July 2012
Accepted 1 October 2012
Published 14 December 2012

This paper presents numerical and experimental results of the flow characteristics of R134a flowing through adiabatic helical capillary tubes. The local pressure distribution along the length of the capillary tubes is measured at inlet pressures ranging from 10 to 14 bar, mass flow rates from 8 to 20 kg h^{-1}, and degrees of subcooling from 0.5°C to 15°C. The theoretical model is based on conservation of mass, energy and the momentum of the fluids in the capillary tube. The model is divided into three regions: subcooled liquid region, metastable liquid region and equilibrium two-phase region and can be applied for various tube geometries, new alternative refrigerants and critical or noncritical flow conditions. The model is validated by comparing results from the present experimental data with that of the available literature. Based on the comparison results, the model used in the present study provides reasonable agreement with the experimental data.

Keywords: Capillary; expansion valve; R134a; vapor pressure; two-phase flow.

[§]Corresponding author.

Nomenclature

A : Cross-sectional area of capillary tube, m^2
d_i : Capillary tube internal diameter, m
D_C : Coil diameter, m
f : Friction factor
g : Gravitational acceleration, $m\,s^{-2}$
G : Mass flow rate per unit area, $kg\,s^{-1}\,m^{-2}$
h : Specific enthalpy, $J\,kg^{-1}$
k : Entrance loss coefficient
L : Length, m
m : Mass flow rate, $kg\,h^{-1}$
P : Pressure, bar
Re : Reynolds number
s : Specific entropy, $J\,kg^{-1}\,K^{-1}$
T : Temperature, °C
V : Velocity, $m\,s^{-1}$
x : Quality

Greek Letters

ΔT_{sub} : Degree of subcooling, °C
ε : Roughness, m
ν : Specific volume, $m^3\ kg^{-1}$
μ : Dynamic viscosity, $kg\,m^{-1}\ s^{-1}$
ρ : Density, $kg\,m^{-3}$

Subscripts

evap : Evaporator
f : Liquid phase
g : Gas phase
i : Capillary inlet condition
in : Inlet
ml : Metastable liquid
sp : Single-phase
tp : Two-phase
vap : Vaporization

1. Introduction

A capillary tube is an important device in small vapor-compression refrigeration and air conditioning systems used to reduce refrigerant pressure from the condenser to the evaporator. The nominal size of the capillary tube typically ranges between 0.5 and 2.0 mm in diameter and 1−6 m in length. This type of tube is widely used in household refrigerators due to its simplicity, cost-effectiveness, no maintenance requirement, no moving parts and low starting torque. For several decades, the flow characteristics of various refrigerants flowing through capillary tubes have been studied both experimentally and theoretically and primarily for straight capillary tubes. However, in practical applications, household refrigerator systems use a helical capillary tube in order to reduce installation space. To the best of the authors' knowledge, there has been minimal experimental investigation of the differences that might exist for straight and helical tube structures. The available papers regarding numerical and experimental investigations of refrigerant flow in coiled capillary tubes are summarized as follows:

Kim *et al.*[1] presented experimental results of mass flow rate and proposed the mass flow rate correlation based on the Buckingham π theorem. They performed tests at condensing temperatures of 40°C, 45°C and 50°C and subcooling temperature of 1.5°C, 5°C and 10°C. They concluded that the mass flow rates of R22 were lower than those of R407C and R410A by about 4% and 23%, respectively. Moreover, the mass flow rates of the coiled capillary tubes were lower than those of straight capillary tubes, especially at smaller coil diameters. In the case of a 40 mm coil diameter, the mass flow rates of the coiled capillary tubes were approximately 9% lower than those for straight capillary tubes.

Zhou and Zhang[2] theoretically and experimentally investigated the performance of coiled adiabatic capillary tubes and compared the results with straight capillary data for R22. They found that the mass flow rate of a straight capillary tube was approximately 10% more than that of a coiled adiabatic capillary tube with a coil diameter of 40 mm. Moreover, the results showed that the mass flow rate of the refrigerant increased significantly with increases in the coil diameter. However, little change was observed for coil diameters larger than 300 mm.

Valladares[3] presented a numerical simulation describing the flow characteristics of coiled adiabatic capillary tubes based on a finite volume formulation. The numerical model was evaluated for various aspects such as type of fluid (pure substances and mixtures), geometry, metastable regions, critical or noncritical flow conditions and transient behavior. The prediction showed 97.7% agreement of 211 data points evaluated within an error of ± 10%.

Park *et al.*[4] studied the flow characteristics of coiled capillary tubes for R22 and proposed a mass flow rate correlation for coiled capillary tubes. In the same operating conditions, the results showed that the mass flow rates of the coiled capillary tubes decreased by about 5−16% less than those of the straight capillary tubes. The correlation was

developed on the basis of experimental data such as the effects of inlet condition, refrigerant properties and coiled tube geometry. For both straight and coiled capillary tubes, the results showed that the proposed correlation gave reasonable agreement with the experimental data for R22, R407C and R410A.

Mittal *et al.*[5] presented an experimental investigation of coiling effect on the flow characteristics of R407C in an adiabatic helical capillary tube. They observed that the coiling of capillary tubes (coil diameters of 60, 100 and 140 mm) significantly influenced the mass flow rate. From the experimental results, the mass flow rates through the coiled capillary tubes decreased about 5−10% less than those through the straight capillary tubes. In addition, the authors also proposed correlations to predict the mass flow rate of R407C flowing through straight and helical capillary tubes. When compared with experimental data, the majority of the results fell within 10% of their proposed correlation.

Chingulpitak and Wongwises[6] applied a mathematical model to study the flow characteristics of alternative refrigerants in adiabatic helical capillary tube. The model presented is based on conservation of mass, energy and momentum of fluids in the capillary tube. The developed model is validated by comparison with the experimental data from Kim *et al.*[1] for R22, R407C and R410A and Zhou and Zhang for R22.[2,7] The results obtained from the present model show reasonable agreement with the experiment data. Chingulpitak and Wongwises[8,9] studied the effects of various geometries of helical capillary tubes and compared the flow characteristics of refrigerants in straight and helical capillary tubes. The results show that for coil diameters of 40 to 300 mm, the mass flow rate of refrigerants increases rapidly by about 6−7%. For coil diameters between 300 and 600 mm, the increase in mass flow rate of refrigerant is small (about 1−2%). The comparison between the straight and helical capillary tubes showed that the length of the helical capillary tube was 20% shorter than that of the straight capillary tube under the same operating conditions.

Zhou and Zhang[10] studied the inlet pressure fluctuation characteristics of R22 in adiabatic helical and straight capillary tubes. Their results show that the pressure fluctuation for straight capillary tubes is less prominent than for helical ones. In the case of a small coil diameter, the inlet pressure fluctuation is weak. Moreover, the results show that the fluctuation amplitude decreases as the preset inlet pressure increases.

Up to now, as described above, there have been only two works, carried out by Zhou and Zhang[2] and Valladares,[3] dealing with the metastable region in the simulation of refrigerant flow in coil capillary tube. Although some information is currently available, there still remains room to discuss, for example, there are no information regarding local pressure and temperature distributions obtained from either simulation or experiment available yet, the effects of various relevant parameters on flow characteristics also remain unstudied. In this paper, the main concern is to present an experimental and theoretical study for predicting the refrigerant flow characteristics including metastable region in adiabatic helical capillary tubes. R134a which is current widely used but has never been investigated before in helical capillary tube, is studied. The influence of parameters such as inlet pressure, degree of subcooling, capillary tube diameters and coil diameters on local pressure and mass flow rate along the capillary tube length are also investigated. Flashing process behavior and the delay of refrigerant vaporization are also discussed.

2. Experimental Apparatus and Method

A schematic diagram of experimental apparatus is shown in Fig. 1. The main refrigeration system components consist of a compressor, condenser, capillary tube, evaporator and other accessory parts, including the oil separator, liquid receiver, filter/drier, sight glass, subcooler and accumulator. A two-cylinder single stage reciprocating compressor, driven by an electric motor, was used to circulate the refrigerant. The speed of the motor was varied so as to provide a wide range of mass flow rates by means of an inverter. More details of the experimental apparatus are available from Kaew-on *et al.*[11]

The details of the test capillary tube dimensions are presented in Fig. 2. The inlet pressure and inlet temperature were measured at the inlet header. Similarly, the outlet pressure and outlet temperature were obtained from the outlet header. Seven points of the capillary tube were drilled for the installation of pressure taps. Also, seven T-type

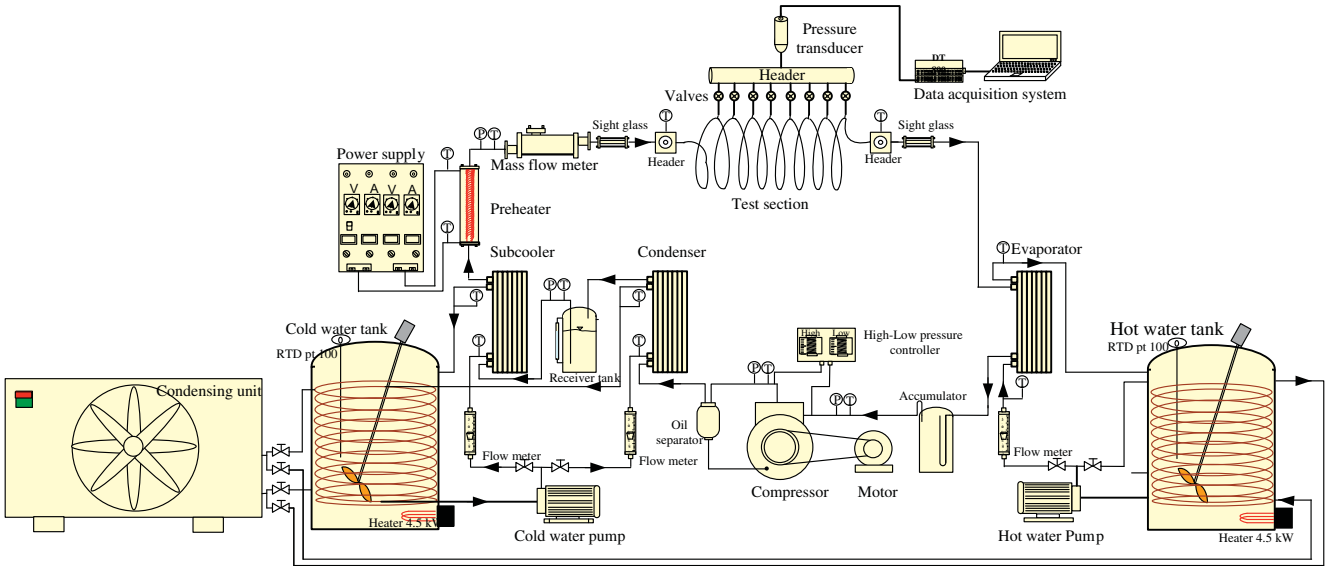

Fig. 1. Schematic diagram of the experimental apparatus.[11]

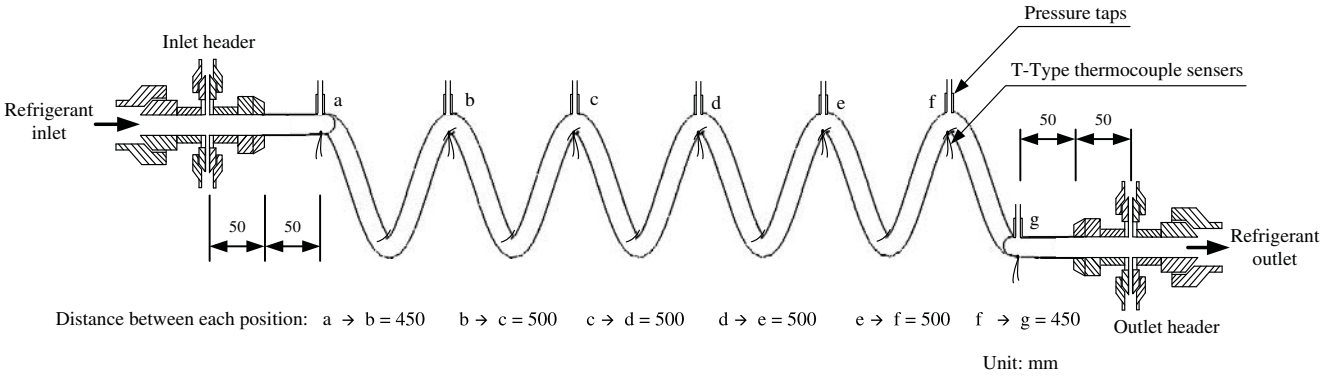

Fig. 2. Schematic diagram of the test section.

thermocouples were installed in the same sections as the pressure taps. The thermocouples were insulated with an Aeroflex standard sheet to reduce the effect of heat transfer on measurement. The range of experimental conditions and the details of test sections are listed in Table 1.

Table 1. The details of test sections and experimental conditions.

Items	Details
Refrigerant	R134a
Capillary diameter, d_i, mm	1.07, 1.27, 1.62
Coil diameter, D_c, mm	25, 50, 100
Capillary length, L, m	3.05
Inlet pressure, P_{in}, bar	10, 12, 14
Degree of subcooling, ΔT_{sub}, °C	0.5−10.5
Mass flow rate, m, kg/h	7−18

3. Mathematical Modeling

In mathematical modeling, the flow characteristics of refrigerant are analyzed by applying the fundamental principles of thermodynamics and fluid mechanics.[6,12] The proposed model assumes that the helical capillary tube is a horizontal capillary tube with constant coil diameter, inner diameter and roughness. Also, the flow inside is considered to be adiabatic, one-dimensional, steady, metastable region and homogeneous two-phase flow. The flow characteristics of refrigerant in a helical capillary tube can be divided into a single-phase flow region,

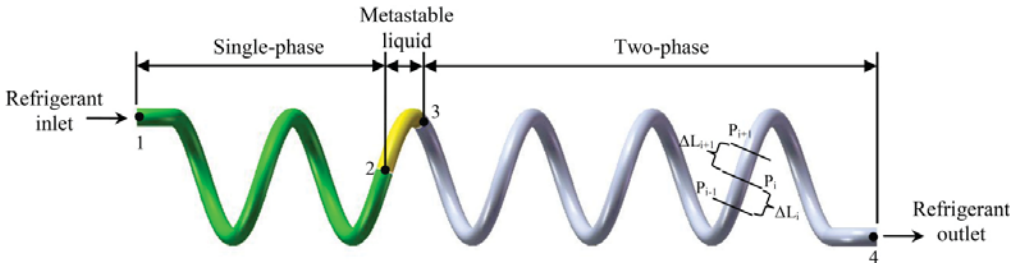

Fig. 3. Schematic diagram of an adiabatic helical capillary tube.

metastable liquid region and a two-phase flow region. The theoretical flow model of refrigerant through the capillary tube is based on the conservation of mass, energy and momentum of fluids in the helical capillary tube. For convenience, the developed model is briefly reviewed.

3.1. *Single-phase flow region*

The single-phase flow region represents the position from the inlet of the capillary tube to the position where the pressure drops to the saturated pressure (points 1 and 2 in Fig. 3). From our previous work,[6] the single-phase length is calculated as follows:

$$L_{\mathrm{sp}} = \frac{d_i}{f_{\mathrm{sp}}}\left[\frac{2}{\rho V^2}(P_1 - P_3) - k - 1\right], \tag{1}$$

where f_{sp} is the single-phase friction factor and k is the entrance loss coefficient (for square edged, $k = 0.5$).

The friction factor of coil capillary tube (f_c) proposed by Mori and Nakayama[13] presented in Eq. (2), is used to calculate the single-phase friction factor.

$$f_c = \frac{C_1(d_i/D_c)^{0.5}}{[\mathrm{Re}(d_i/D_c)^{2.5}]^{1/6}}\left\{1 + \frac{C_2}{[\mathrm{Re}(d_i/D_c)^{2.5}]^{1/6}}\right\}, \tag{2}$$

where

$$\begin{aligned} C_1 &= 1.88411177 \times 10^{-1} + 85.2472168(\varepsilon/d_i) \\ &\quad - 4.63030629 \times 10^{4}(\varepsilon/d_i)^2 \\ &\quad + 1.31570014 \times 10^{7}(\varepsilon/d_i)^3, \\ C_2 &= 6.79778633 \times 10^{-2} + 25.3880380(\varepsilon/d_i) \\ &\quad - 1.06133140 \times 10^{4}(\varepsilon/d_i)^2 \\ &\quad + 2.54555343 \times 10^{6}(\varepsilon/d_i)^3, \end{aligned}$$

and

$$\mathrm{Re} = \frac{\rho V d_i}{\mu}. \tag{3}$$

3.2. *Metastable-liquid flow region*

The metastable phenomenon occurs when the pressure of the liquid approaches the saturation pressure, but the fluid is still in the liquid phase (points 2 and 3 in Fig. 3). The pressure of vaporization (P_{vap}) is calculated using the correlation proposed by Chen *et al.*,[14] as follows;

$$\frac{(P_{\mathrm{sat}} - P_{\mathrm{vap}})\sqrt{kT_{\mathrm{sat}}}}{\sigma^{1.5}} = 0.679\left(\frac{\nu_g}{\nu_g - \nu_l}\right)\mathrm{Re}^{0.914}\left(\frac{\Delta T_{sc}}{T_c}\right)^{-0.208}\left(\frac{d_i}{D'}\right)^{-3.18}, \tag{4}$$

where D' is the reference length $\left(\sqrt{\frac{kT_{\mathrm{sat}}}{\sigma}} \times 10^4\right)$, and k is the Boltzmann constant ($1.380662 \times 10^{-23}\,\mathrm{J\,K^{-1}\,mol^{-1}}$).

According to the recommendation by Zhou and Zhang,[2] the metastable liquid region length is evaluated in the same way as the single-phase region.

3.3. *Two-phase flow region*

The flow in this region is assumed to be homogeneous flow. The fundamental equations used for this section are conservation of mass, energy and momentum. The following equations are based on the control volume considerations in the two-phase region. Also, calculation of the two-phase length can be followed from our previous model.[6]

$$dL = \frac{2d_i}{f_{\mathrm{tp}}}\left[-\frac{\rho dP}{\rho V^2} + \frac{d\rho}{\rho}\right]. \tag{5}$$

The two-phase friction factor can be calculated using Eq. (2), in the same way as the single-phase region, where the Reynolds number in the two-phase region is determined by

$$\mathrm{Re}_{\mathrm{tp}} = \frac{Vd_i}{\mu_{\mathrm{tp}}\nu_{\mathrm{tp}}}\,, \tag{6}$$

where

$$V = G\nu_{\mathrm{tp}} = G\big(x\nu_g + (1-x)\nu_f\big)\,. \tag{7}$$

The two-phase dynamic viscosity correlation proposed by McAdams *et al.*[15] is presented as follows:

$$\frac{1}{\mu_{\mathrm{tp}}} = \frac{x}{\mu_g} + \frac{1-x}{\mu_f}\,. \tag{8}$$

4. Solution Methodology

The solution methodology used in the present stydy is modified from Wongwises and Pirompak,[12] Bansal and Rupasingh.[16]

For the two-phase region, as shown in Fig. 3, the capillary tube between points 3 and 4 can be divided into numerous sections. Since P_3 is known (the pressure of vaporization, P_{vap}), the pressure in any section, i, can be expressed as

$$P_i = P_3 - i\Delta P\,. \tag{9}$$

The entropy of each section can be calculated from

$$s_i = s_{if}(1-x) + s_{ig}\,x\,. \tag{10}$$

The calculation is done section by section along the capillary tube until the entropy reaches its maximum value. At this point, the fluid velocity is equal to the local speed of sound and the flow is choked. The pressure of the element, where the entropy has the maximum value, $(P_i)_{s\,\max}$, is then compared to the evaporator pressure, P_{evap}, as follows:

if $P_{i,s\max} > P_{\mathrm{evap}}$ then $P_4 = P_{i,s\max}$ and if $P_{i,s\max} < P_{\mathrm{evap}}$ then $P_4 = P_{\mathrm{evap}}$.

Thus, from Eq. (5) the two-phase length (L_{tp}) can be expressed as follows:

$$L_{\mathrm{tp}} = d_i\left[\frac{-2}{G^2}\int_{P_3}^{P_{s\max}}\frac{\rho}{f_{\mathrm{tp}}}dp + 2\int_{P_3}^{P_{s\max}}\frac{d\rho}{\rho f_{\mathrm{tp}}}\right]. \tag{11}$$

Finally, the total length of the capillary tube is a summation of the single-phase, metastable liquid region and two-phase lengths, which is defined as follows:

$$L_{\mathrm{total}} = L_{\mathrm{sp}} + L_{\mathrm{ml}} + L_{\mathrm{tp}}\,. \tag{12}$$

All refrigerant properties are taken from the REFPROP version 6.01 computer program,[17] and are developed in the pressure function.

5. Results and Discussion

5.1. *Mathematical model verification*

To validate the present model, comparison is made with the available experimental data from Ref. 7. As shown in Fig. 4, a comparison between the present numerical result and experimental data from Ref. 7 for R22 was used to validate the temperature distribution along the capillary tube length. In the subcooled liquid region, the temperature remains nearly constant along the tube, while rapidly decreasing after the refrigerant flashes. This is due to the delay of vaporization. However, the actual point of inception of vaporization did not occur at the end of the subcooled liquid region. The result shows that the calculated tube length of R22 deviates from the experimental results. However, the results also indicate that the tendency of temperature distribution along the capillary tube length obtained from the present model shows reasonable agreement with previous data.

5.2. *Comparison of the present model and the Chingulpitak and Wongwises model*[6]

Figure 5 shows the comparison of simulation results of our previous model[6] with the present model. It is

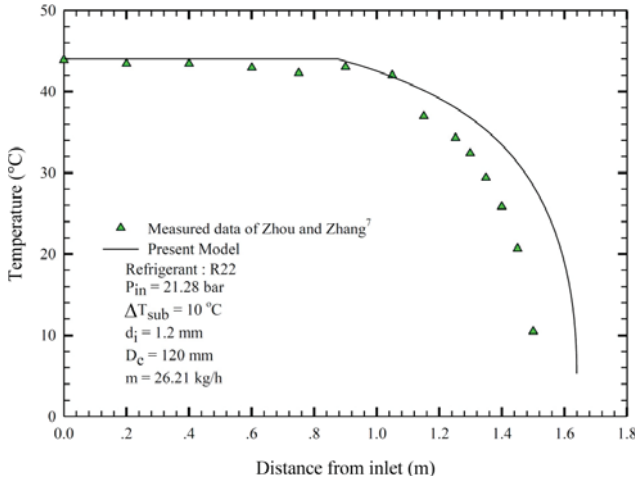

Fig. 4. Comparison of present numerical results with experimental data.

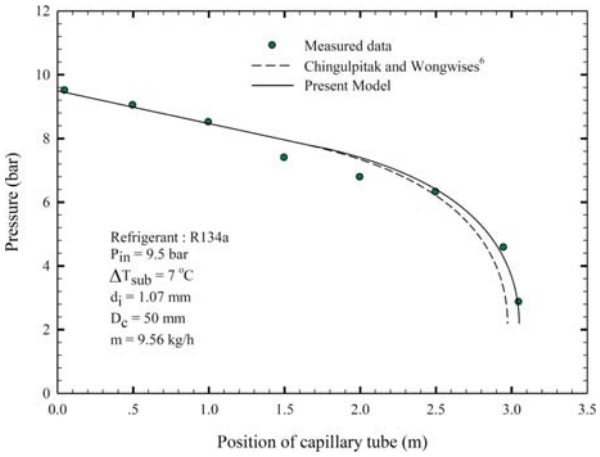

(a)

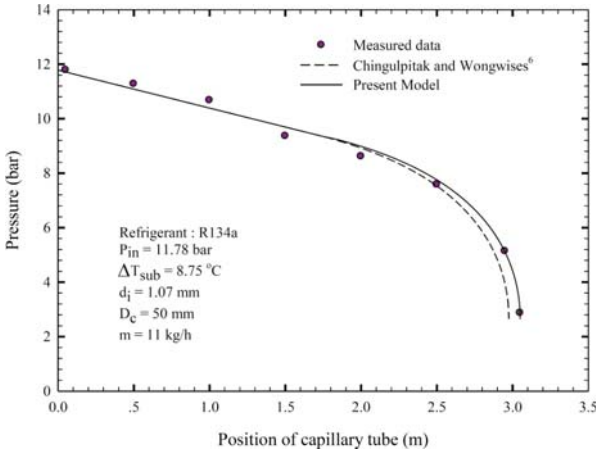

(b)

Fig. 5. Comparison of the present model and nonmetastable region model proposed by Chingulpitak and Wongwises[6] with experimental data.

clear that the pressure distribution along the helical capillary tube obtained from the present model gives a better prediction than those of our previous model.[6] This is due to the fact that the previous model was developed excluding a metastable liquid region. The metastable phenomenon is an effect on increasing the capillary tube's length in the single-phase region.

5.3. *Pressure distributions*

5.3.1. *Effect of inlet pressure on pressure distribution*

The variations of refrigerant pressure along the capillary tube at different inlet pressures are depicted in Fig. 6. It is apparent that the pressure drop of

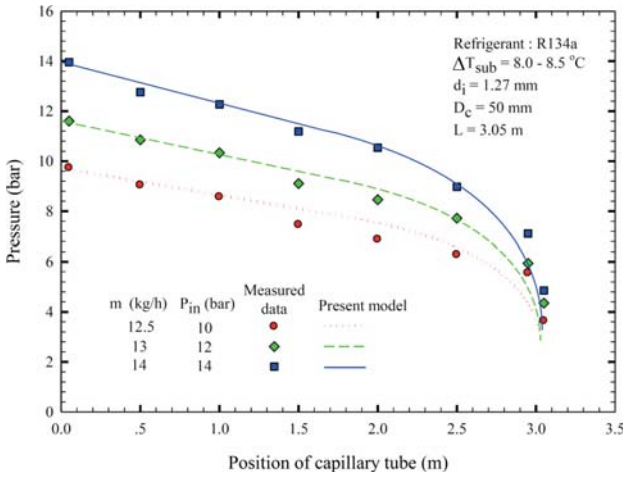

Fig. 6. Effect of inlet pressure on the pressure distribution along the capillary tube length.

refrigerant increases as the inlet pressure increases. The enlargement of inlet pressure led to an increased difference between inlet and outlet pressure, resulting in an increase of refrigerant mass flow rate and velocity. Therefore, the frictional and accelerational pressure drop inside the capillary tube increased.

5.3.2. *Effect of coil and inner diameters on pressure distribution*

The effects of coil and inner diameters on pressure distribution are presented in Fig. 7. In Fig. 7(a), the results show that decreases in pressure for all conditions have similar profiles. Thus, it can be concluded that coil diameter has no significant effect on pressure distribution in the range of the present study. However, in terms of inner diameter, the pressure drop along the capillary tube decreased with increasing capillary tube diameter, as shown in Fig. 7(b).

5.3.3. *Effect of degree of subcooling on pressure distribution*

At the same inlet pressure and dimensions of capillary tube, the effect of degree of subcooling on pressure distribution along the capillary tube is presented in Fig. 8. It is evident from this data that the single-phase length increases with increasing subcooling temperature. In the subcooled liquid region, the pressure drop remains nearly constant along the tube, while it decreases rapidly after the refrigerant flashes.

From the comparison results, the present model gives a good tendency of pressure distribution along

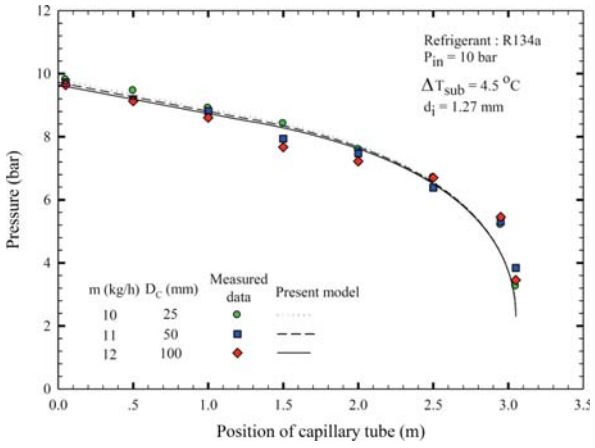

(a)

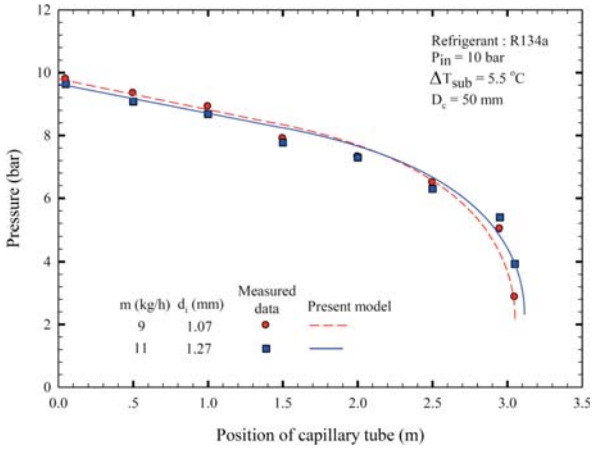

(b)

Fig. 7. Effect of the relevant parameters on pressure distribution of the R134a through the capillary tubes (a) effect of coil diameters and (b) effect of inner diameters.

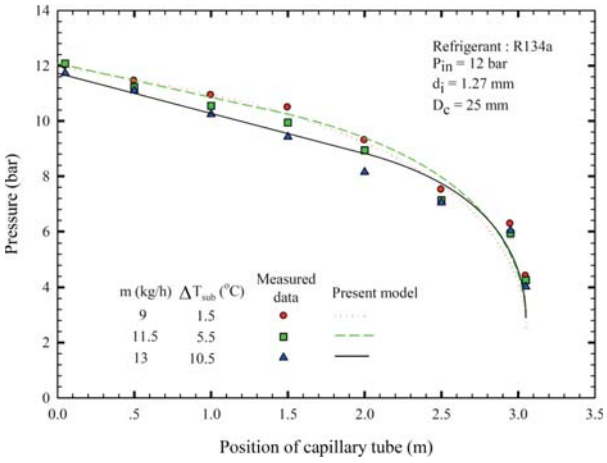

Fig. 8. Effect of degree of subcooling on pressure distribution of the R134a through the capillary tube.

the tube's length compared with experimental data. The present model can be used to predict the flow characteristics of R134a flowing through adiabatic helical capillary tube.

5.4. *The mass flow rate*

5.4.1. *Effect of inlet pressure on mass flow rate*

In Fig. 9(a), the variation of mass flow rates for capillary inlet pressures of 10 and 12 bar with varying degrees of subcooling is presented. The results show that for a given capillary diameter, the mass flow rate increased with an increase of inlet pressure. At higher inlet pressures, the driving force was also higher and resulted in an increase of mass flow rate. Moreover, the comparison of the predicted mass flow rates with the measured data at inlet pressure 10 and 12 bar shows that the present model gives a mean absolute error of 2.1% and 4.1%, respectively.

5.4.2. *Effect of coil diameters on mass flow rate*

As shown in Fig. 9(b), the variation of mass flow rates with coil diameters of 50 and 100 mm is presented. Here, the refrigerant mass flow rate increased with an increase in coil diameter. At 4.5°C of subcooling, the refrigerant mass flow rate of the helical capillary tube from coil diameters of 50 to 100 mm, increased by 9%. Comparison of mass flow rates obtained from the present model with the measured data at coil diameter 50 and 100 mm shows that the present model gives a mean absolute error of 5.9% and 2.1%, respectively.

5.4.3. *Effect of degree of subcooling and inner diameter on mass flow rate*

Figure 9(c) shows mass flow rates and degrees of subcooling for capillary tube diameters of 1.07 and 1.27 mm, inlet pressure of 10 bar and coil diameter of 50 mm. The results show that the mass flow rate increased with increasing degree of subcooling. This phenomenon can be explained by the fact that the increase in mass flow rate was a result of increased liquid length for high inlet subcooling. Moreover, the results also indicate that the effect of capillary tube diameter on the refrigerant mass flow rate is clear and significant. The results show that the mass flow

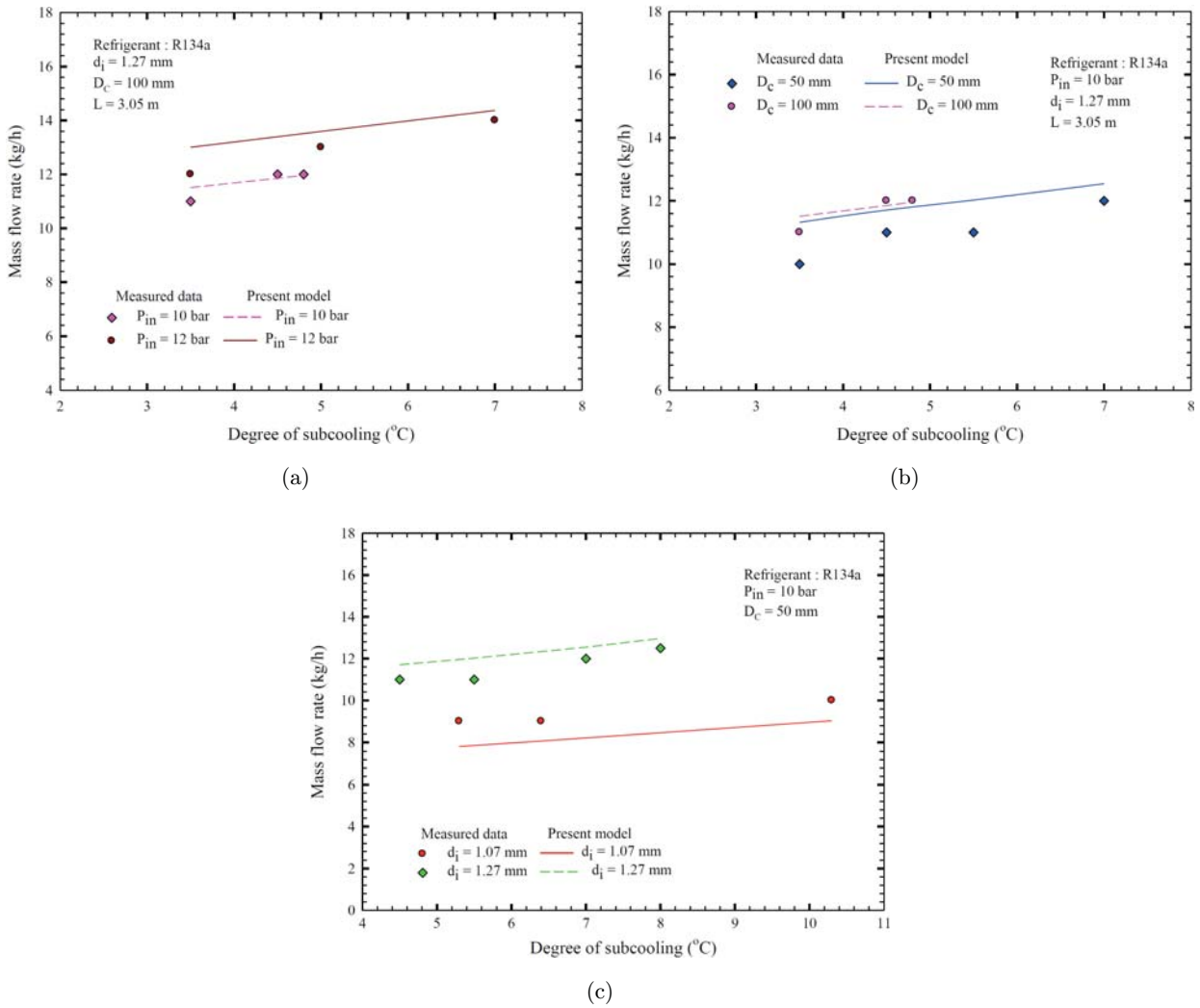

Fig. 9. Effect of the relevant parameter on the mass flow rate of the R134a through the capillary tubes (a) effect of inlet pressure, (b) effect of coil diameter and (c) effect of degree of subcooling and capillary tube diameter.

rates dramatically increased with an increase in capillary tube diameter.

5.5. *Effect of the choked flow condition on pressure distribution and total capillary tube length*

As shown in Fig. 10, with an inner diameter of 1.62 mm, the pressure distribution along capillary tube length of the present model with a mass flow rate 18.1 kg h^{-1} fits very well with the measured data, although the numerical result gives the total capillary tube length longer than that of the measured data by about 11.14%. On the other hand, a mass flow rate of 19.1 kg h^{-1} gives the best result for the total capillary tube length but this mass flow

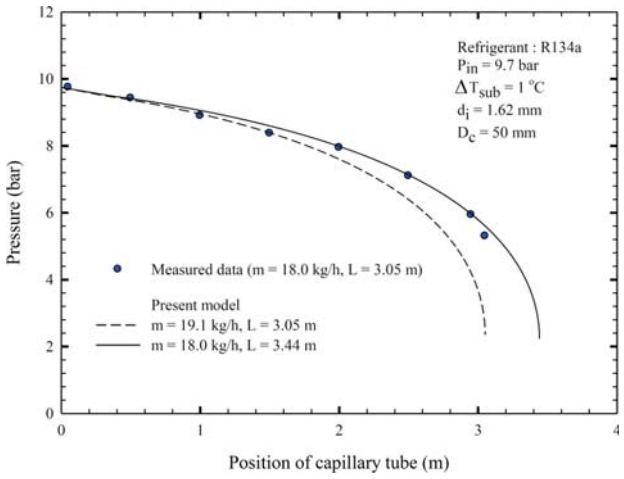

Fig. 10. Comparison of measured pressure distribution with present numerical results at different mass flow rate.

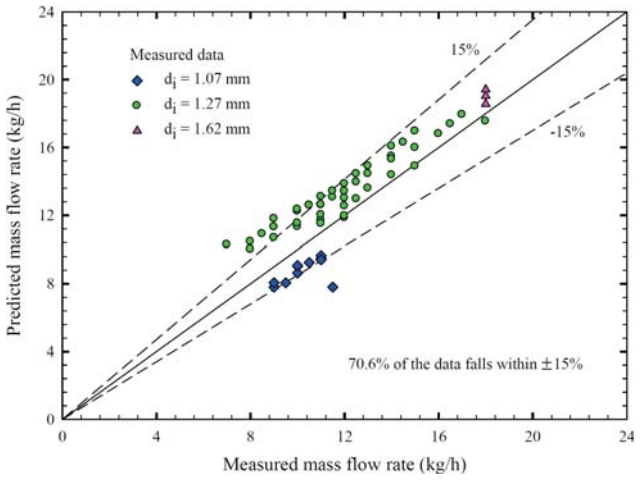

Fig. 11. Comparison of mass flow rate obtained from the present model with measured data for R134a.

rate failed with the tendency of pressure distribution inside the helical capillary tube. This is due to the fact that the present model is limited at the choked flow condition for any computation. Therefore, the pressure profile of refrigerant in the capillary tube should be considered for accuracy of the comparison between the simulation and experiment results. In addition, considering the pressure distribution at any position along capillary tube length is one of the main purposes of the present experiment.

In Fig. 11, the comparison of the predicted mass flow rates with all of the present measured data for R134a shows that 70.6% of the 58 data points are within $\pm 15\%$.

6. Conclusion

In this study, the flow characteristics of R134a flowing through adiabatic helical capillary tubes were theoretically and experimentally investigated. From the measured mass flow rate data, the capillary tube diameter has a more significant effect on mass flow rate than the other variables. For example, at 5.5°C of subcooling, as the capillary tube diameter increased from 1.07 mm to 1.27 mm, the refrigerant mass flow rate increased by 22.2%. Similarly, at 4.5°C of subcooling, the refrigerant mass flow rate of the helical capillary tube from coil diameters of 50 mm to 100 mm increased by 9%. In terms of the theoretical study, the present model was validated by comparing its results with the experimental data. The comparison results show that the proposed model, including metastable liquid region, can be used to predict the flow characteristics of R134a flowing through an adiabatic helical capillary tube, and specifically, local pressure distribution along the tube's length.

Acknowledgments

The authors are indebted to the Thailand Research Fund, the Office of the Higher Education Commission and the National Research University Project for supporting this study.

References

1. S. G. Kim, M. S. Kim and S. T. Ro, Experimental investigation of the performance of R22 R407C and R410A in several capillary tubes for air-conditioners, *Int. J. Ref.* **25** (2002) 521−531.
2. G. Zhou and Y. Zhang, Numerical and experimental investigations on the performance of coiled adiabatic capillary tubes, *Appl. Therm. Eng.* **26** (2006) 1106−1114.
3. O. G. Valladares, Numerical simulation and experimental validation of coiled adiabatic capillary tubes, *Appl. Therm. Eng.* **27** (2007) 1062−1071.
4. C. Park, S. Lee, H. Kang and Y. Kim, Experimentation and modeling of refrigerant flow through coiled capillary tubes, *Int. J. Ref.* **30** (2007) 1168−1175.
5. M. K. Mittal, R. Kumar and A. Gupta, An experimental study of the flow of R-407C in an adiabatic helical capillary tube, *Int. J. Ref.* **33** (2010) 840−847.
6. S. Chingulpitak and S. Wongwises, Two-phase flow model of refrigerants flowing through helically coiled capillary tubes, *Appl. Therm. Eng.* **30** (2010) 1927−1936.
7. G. Zhou and Y. Zhang, Experimental investigation on hysteresis effect of refrigerant flowing through a coiled adiabatic capillary tube, *Energy Convers. Manage.* **47** (2006) 3084−3093.
8. S. Chingulpitak and S. Wongwises, Effects of coil diameter and pitch on the flow characteristics of alternative refrigerants flowing through adiabatic helical capillary tubes, *Int. Commun. Heat Mass Transfer* **37** (2010) 1305−1311.
9. S. Chingulpitak and S. Wongwises, A comparison of flow characteristics of refrigerants flowing through adiabatic straight and helical capillary tubes, *Int. Commun. Heat Mass Transfer* **38** (2011) 398−404.
10. G. Zhou and Y. Zhang, Inlet pressure fluctuation characteristics of coiled adiabatic capillary tubes, *Appl. Therm. Eng.* **33–34** (2012) 183−189.

11. J. Kaew-on, K. Nilpuang, S. Chingulpitak and S. Wongwises, Experimental investigation of R134A flowing through adiabatic helically coiled capillary tubes, *Int. J. Air-conditioning Ref.* **20** (2012) 1−11.
12. S. Wongwises and W. Pirompak, Flow characteristics of pure refrigerants and refrigerant mixtures in adiabatic capillary tubes, *Appl. Therm. Eng.* **21** (2001) 845−861.
13. Y. Mori and W. Nakayama, Study on forced convective heat transfer in curved pipes (2nd, report turbulent region), *Int. J. Heat Mass Transfer* **10** (1967) 37−59.
14. Z. H. Chen, R. Y. Li, S. Lin and Z. Y. Chen, A correlation for metastable flow of refrigerant 12 through capillary tubes, *ASHRAE Trans.* **96** (1990) 550−554.
15. W. H. McAdams, W. K. Wood and R. L. Bryan, Vaporization inside horizontal tubes. II, Benzence-oil mixture, *Trans. ASME* **64** (1942) 193.
16. P. K. Bansal and A.S. Rupasinghe, A homegeneous model for adiabatic capillary tubes, *Appl. Therm. Eng.* **18** (1998) 207−219.
17. M. O. McLinden, S. A. Klein and E. W. Lemmon, REFPROP — thermodynamic and transport properties of refrigerants and refrigerant mixtures, NIST Standard Reference Database — version 6.01 (1998).

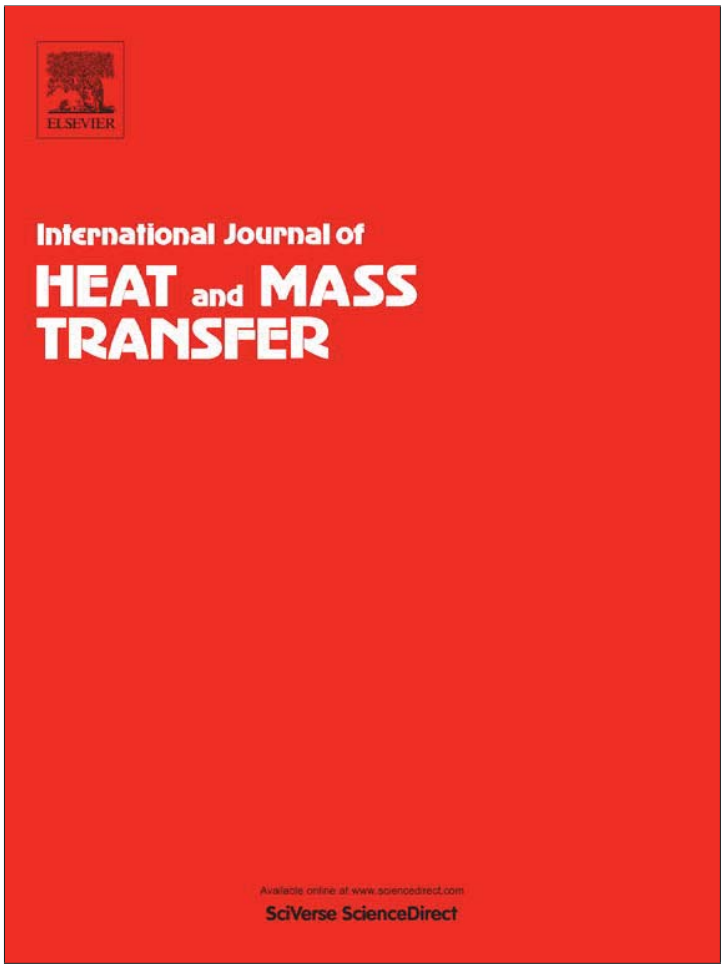

(This is a sample cover image for this issue. The actual cover is not yet available at this time.)

International Journal of Heat and Mass Transfer 57 (2013) 582–594

Contents lists available at SciVerse ScienceDirect

International Journal of Heat and Mass Transfer

journal homepage: www.elsevier.com/locate/ijhmt

A review of the applications of nanofluids in solar energy

Omid Mahian [a], Ali Kianifar [a], Soteris A. Kalogirou [b], Ioan Pop [c,*], Somchai Wongwises [d,e]

[a] Department of Mechanical Engineering, Engineering Faculty, Ferdowsi University of Mashhad, Mashhad, Iran
[b] Department of Mechanical Engineering and Materials Science and Engineering, Cyprus University of Technology, Cyprus
[c] Department of Mathematics, Babeş-Bolyai University, 400084 Cluj-Napoca, CP 325, Romania
[d] Fluid Mechanics, Thermal Engineering and Multiphase Flow Research Lab. (FUTURE), Department of Mechanical Engineering, Faculty of Engineering, King Mongkut's University of Technology Thonburi, Bangmod, Bangkok 10140, Thailand
[e] The Academy of Science, The Royal Institute of Thailand, Sanam Suea Pa, Dusit, Bangkok 10300, Thailand

ARTICLE INFO

Article history:
Received 27 May 2012
Received in revised form 26 August 2012
Accepted 11 October 2012

Keywords:
Nanofluids
Solar energy
Efficiency
Economic and environmental considerations
Challenges

ABSTRACT

Utilizing nanofluids as an advanced kind of liquid mixture with a small concentration of nanometer-sized solid particles in suspension is a relatively new field, which is less than two decades old. The aim of this review paper is the investigation of the nanofluids' applications in solar thermal engineering systems. The shortage of fossil fuels and environmental considerations motivated the researchers to use alternative energy sources such as solar energy. Therefore, it is essential to enhance the efficiency and performance of the solar thermal systems. Nearly all of the former works conducted on the applications of nanofluids in solar energy is regarding their applications in collectors and solar water heaters. Therefore, a major part of this review paper allocated to the effects of nanofluids on the performance of solar collectors and solar water heaters from the efficiency, economic and environmental considerations viewpoints. In addition, some reported works on the applications of nanofluids in thermal energy storage, solar cells, and solar stills are reviewed. Subsequently, some suggestions are made to use the nanofluids in different solar thermal systems such as photovoltaic/thermal systems, solar ponds, solar thermoelectric cells, and so on. Finally, the challenges of using nanofluids in solar energy devices are discussed.

Contents

* Corresponding author. Tel.: +40 264405300; fax: +40 264591906.
E-mail address: popm.ioan@yahoo.co.uk (I. Pop).

0017-9310/$ - see front matter © 2012 Elsevier Ltd. All rights reserved.
http://dx.doi.org/10.1016/j.ijheatmasstransfer.2012.10.037

1. Introduction

Common fluids such as water, ethylene glycol, and heat transfer oil play an important role in many industrial processes such as power generation, heating or cooling processes, chemical processes, and microelectronics. However, these fluids have relatively low thermal conductivity and thus cannot reach high heat exchange rates in thermal engineering devices. A way to overcome this barrier is using ultra fine solid particles suspended in common fluids to improve their thermal conductivity. The suspension of nano-sized particles (1–100 nm) in a conventional base fluid is called a nanofluid. Choi first used the term "nanofluid" in 1995 [1]. Nanofluids, compared to suspensions with particles of millimeter-or-micrometer size, show better stability, rheological properties, and considerably higher thermal conductivities.

In recent years, many researchers have investigated the effects of nanofluids on the enhancement of heat transfer in thermal engineering devices, both experimentally and theoretically. Researchers have also applied a variety of preparation methods, characteristics, and different models used for the calculation of thermophysical properties of nanofluids (i.e., thermal conductivity, viscosity, density, specific heat capacity) [2–9]. Some investigators have also summarized the effects of nanofluids on flow and heat transfer in natural and forced convection in different systems [10–13]. The enhanced thermal behavior of nanofluids could provide a basis for an enormous innovation for heat transfer intensification, which is of major importance to a number of industrial sectors including transportation, power generation, micromanufacturing, thermal therapy for cancer treatment, chemical and metallurgical sectors, as well as heating, cooling, ventilation and air-conditioning. Nanofluids are also important for the production of nanostructured materials for the engineering of complex fluids as well as for cleaning oil from surfaces due to their excellent wetting and spreading behavior (Ding et al. [14]). Another application of the nanofluid flow is in the delivery of nano-drug as suggested by Kleinstreuer et al. [15].

Saidur et al. [16] reviewed the potential of nanofluids in the improvement of heat transfer in refrigeration systems. The authors concluded that more studies are required to find the reasons behind the considerable improvements in heat transfer whereas an insignificant increase in pressure occurs. Thomas and Sobhan [17] presented experimental studies on nanofluids, with emphasis on the techniques of measuring the effective thermal conductivity. Escher et al. [18] investigated the applications of nanofluids in cooling electronics. Recently, applications of computer simulations and computational fluid dynamics (CFD) used to model systems employing nanofluids were reviewed and analyzed by Abouali and Ahmadi [19] and Kamyar et al. [20]. Ahn and Kim [21] also published a review on the critical heat flux of nanofluids for both convective flow boiling and pool boiling applications. In another publication, Saidur et al. [22] reviewed the general applications of nanofluids in some fields such as cooling of electronics, heat exchangers, medical applications, fuel cells, nuclear reactors, and many more. They also mentioned briefly the applications of nanofluids in solar water heaters. They investigated challenges in using nanofluids, including an increased pressure drop and pumping power, long-term stability of nanoparticles dispersion, and the high cost of nanofluids.

In recent years, the use of solar energy has had a remarkable edge. The perceived shortage of fossil fuels as well as environmental considerations will constrain the use of fossil fuels in the future. Therefore, researchers are motivated to find alternative sources of energy. This has become even more popular as the price of fossil fuels continues to rise. The earth receives in just about 1 h more energy from the sun than that consumed by the entire world for 1 year. Most solar energy applications are financially viable while small systems for individual use require just a few kilowatts of power [23,24]. It is important to apply solar energy to a wide range of applications and provide solutions through the modification of the energy proportion, improving energy stability, increasing energy sustainability, and enhancing system efficiency [25]. This paper presents a review of former studies on the application of nanofluids in solar thermal engineering systems. The former works on applications of nanofluids in solar energy are mainly related to their applications in collectors. Therefore, this review mainly investigates the effects of nanofluids on the efficiency improvement of solar collectors as well as on economic and environmental considerations regarding the usage of these systems. Other applications of nanofluids in thermal energy storage, solar cells, and solar stills are also reviewed. Some suggestions also are made for future works in this field. In addition, the existing challenges of using nanofluids in solar energy applications are discussed. Finally, the authors wish to mention that in contrast with the comprehensive references on nanofluids mentioned above much less is known about the application of nanofluids in solar energy applications. It should be reiterated here that, as this is the first systematic review paper on this subject, it is desirable to provide as complete details as possible. However, in an attempt to reduce the overall length of the paper, without compromising the technical quality, only some very important questions for problems of practical applications have been briefly described.

2. Applications of nanofluids in solar energy

Initially, the application of nanofluids in collectors and water heaters are investigated from the efficiency, economic, and environmental aspects. Some studies conducted on thermal conductivity and optical properties of nanofluids are also briefly reviewed, because these parameters can determine the capability of nanofluids to enhance the performance of solar systems.

2.1. Collectors and solar water heaters

Solar collectors are particular kind of heat exchangers that transform solar radiation energy into internal energy of the transport medium. These devices absorb the incoming solar radiation, convert it into heat, and transfer the heat to a fluid (usually air, water, or oil) flowing through the collector. The energy collected is carried from the working fluid, either directly to the hot water or space conditioning equipment or to a thermal energy storage tank, from which it can be drawn for use at night or on cloudy days [26]. Solar water heaters are the most popular devices in the field of solar energy. As mentioned in the introduction, the nanofluid-based solar collectors are investigated in two aspects. In the first, these devices are studied from the efficiency viewpoint, and in the second, from economic and environmental viewpoints.

2.1.1. Efficiency of nanofluid-based solar collectors

Tyagi et al. [27] investigated theoretically the effects of different parameters on the efficiency of a low-temperature nanofluid-based direct absorption solar collector (DAC) where the working fluid is a mixture of water and aluminum nanoparticles. A schematic of the direct absorption collector is shown in Fig. 1. The upper side of this collector is covered by a glass while the lower side is well insulated, so it is adiabatic. The efficiency of the collector is obtained by the following equation:

$$\eta = \frac{useful\ gain}{available\ energy} = \frac{\dot{m}c_p(\overline{T}_{out} - \overline{T}_{in})}{AG_T} \quad (1)$$

where $\dot{m}$ is the mass flow rate of the fluid flowing through the collector; c_p is the specific heat; and $\overline{T}_{in}$ and $\overline{T}_{out}$ are the mean fluid inlet and outlet temperatures, respectively. A is the cover area of the collector, and G_T is the solar flux incident on the solar collector. In the analysis, they assumed that the values of $\overline{T}_{in}$, G_T, and $\dot{m}$ to be 35 °C, 1000 W/m^2, and 1.2 kg/s, respectively.

Tyagi et al. [27] plotted the variation of collector efficiency as a function of the particle volume fraction (%), where the volume fraction varies from 0.1% to 5% (see Fig. 2). Their results showed that by adding nanoparticles to the working fluid, the efficiency increases remarkably for low values of volume fraction of nanoparticles. They attributed the increase of collector efficiency to the increase in attenuation of sunlight passing through the collector due to the nanoparticles addition that leads to the increase of collector efficiency. However, for a volume fraction higher than 2%, the efficiency remains nearly constant, so adding more nanoparticles is not beneficial. Tyagi et al. [27] also investigated the effects of nanoparticles size on the collector efficiency where the volume fraction is equal to 0.8%. The results revealed that the efficiency increases slightly with an increase in the size of nanoparticles (see Fig. 3).

Otanicar et al. [28] investigated both experimentally and numerically the effects of different nanofluids (carbon nanotubes, graphite, and silver) on the performance of a micro scale direct absorption solar collector (DASC). The schematic of the experimental set up showing also the dimensions of the collector is presented in Fig. 4. Fig. 5 shows the variation of collector efficiency with volume fraction for different materials, estimated using Eq. (1). The DASC data are compared to a conventional collector configuration where the solar energy is absorbed on a black plate surface. As

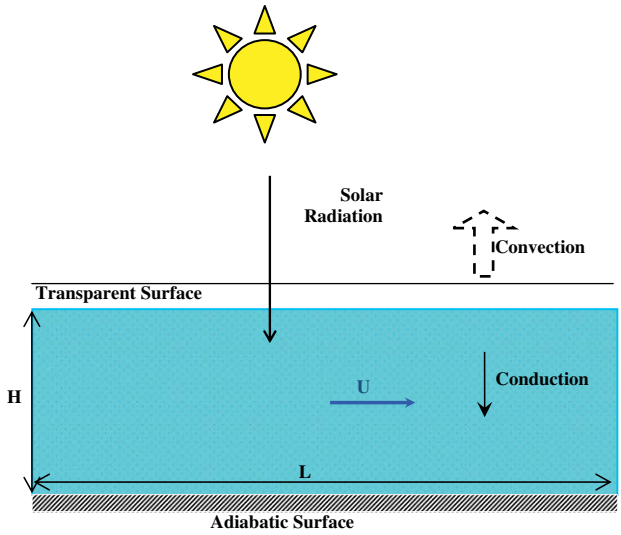

Fig. 1. Schematic of the nanofluid-based direct absorption solar collector (Reprinted from Tyagi et al. [27], with permission from ASME).

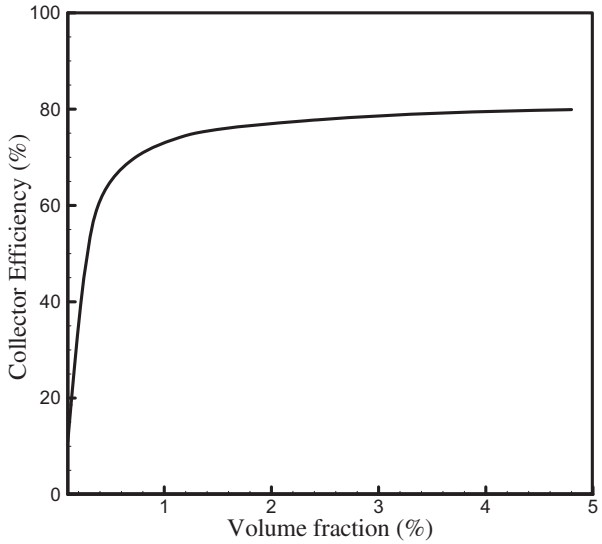

Fig. 2. Effect of particle volume fraction on collector efficiency (Reprinted from Tyagi et al. [27], with permission from ASME).

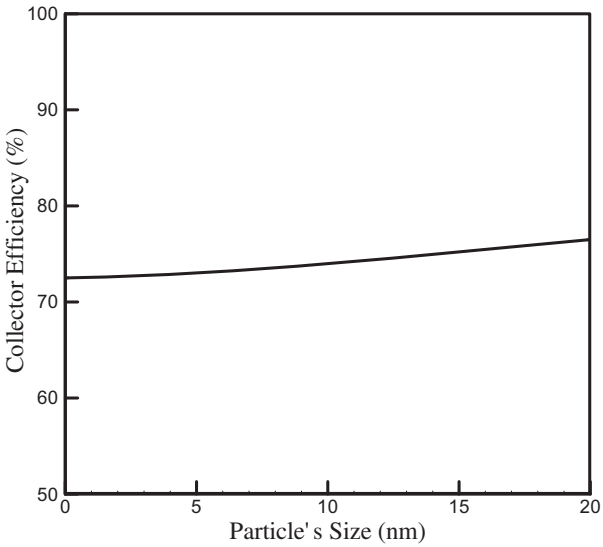

Fig. 3. Effect of nanoparticles size on collector efficiency (Reprinted from Tyagi et al. [27], with permission from ASME).

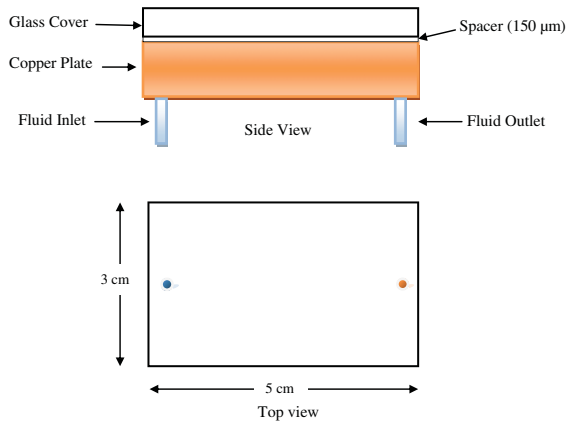

Fig. 4. Experimental schematic of the microsolar thermal collector (Reprinted with permission from Otanicar et al. [28]. Copyright 2010, American Institute of Physics).

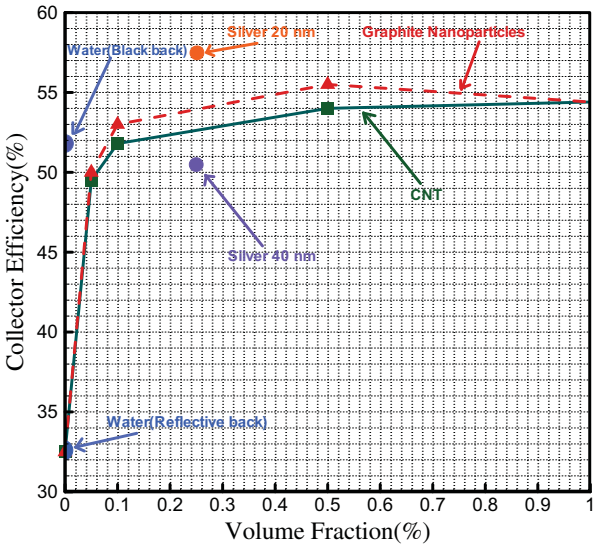

Fig. 5. Experimental microsolar thermal collector: steady-state collector efficiency (Reprinted with permission from Otanicar et al. [28]. Copyright 2010, American Institute of Physics).

shown, adding small quantities of nanoparticles leads to the remarkable enhancement of the efficiency until a volume fraction of approximately 0.5%. After a volume fraction of 0.5%, the efficiency begins to level off and even decrease slightly with increasing volume fraction. The authors attributed this reduction to the high increase of the fluid absorption at high particle loadings. The main difference in the steady-state efficiency between nanofluids occurs in silver particles when the size of the particles is between 20 and 40 nm. When halving the size from 40 to 20 nm, a 6% efficiency increase is found. The effect of particle size on efficiency is shown in Fig. 6 for silver nanoparticles. Unlike the results obtained by Tyagi et al. [27], with increase in size of nanoparticles, the efficiency of the collector decreases.

Taylor et al. [29] compared a nanofluid-based concentrating solar thermal system with a conventional one. Their results show that the use of a nanofluid in the receiver can improve the

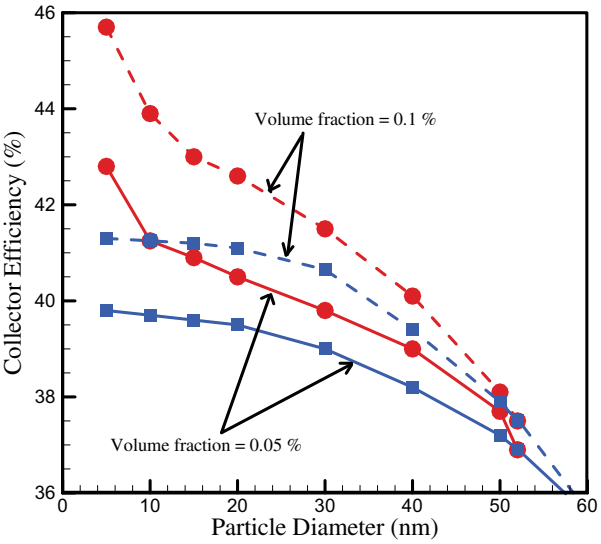

Fig. 6. Collector efficiency as a function of silver nanoparticle diameter (squares: bulk properties; circles: size-dependent properties and volume fraction (Reprinted with permission from Otanicar et al. [28]. Copyright 2010, American Institute of Physics).

efficiency by 10%. They also concluded that for 10–100 MWe power plants, using graphite/therminol VP-1 nanofluid with volume fractions approximately to 0.001% or less could be beneficial. The authors estimated that combining a nanofluid receiver with a solar thermal power tower with the capacity of 100 MWe operating in a solar resource like Tucson, Arizona, could generate $3.5 million more per year. Taylor et al. [29] considered two notional designs of potential nanofluid receivers, designated as A and B, as shown in Fig. 7.

He et al. [30] investigated the light-heat conversion characteristics of two nanofluids, water–TiO_2 and water–carbon nanotube (CNT), in a vacuum tube solar collector under sunny and cloudy weather conditions. The experimental results show a very good light heat conversion characteristic of the CNT–H_2O nanofluid with the weight concentration of 0.5%. Because of the better light-heat conversion characteristics of the CNT–H_2O nanofluid compared to the TiO_2–H_2O nanofluid, the temperature of the CNT–H_2O nanofluid is higher than that of the TiO_2–H_2O one. This means that the CNT–H_2O nanofluid is more suitable than the TiO_2–H_2O to be utilized in a vacuum tube solar collector.

Li et al. [31] studied the effects of three different nanofluids, Al_2O_3/water, ZnO/water, and MgO/water, on the performance of a tubular solar collector. Their results show that ZnO–H_2O nanofluid with 0.2% volume concentration is the best selection for the collector. Taylor et al. [32] investigated the optical property characterization of graphite, silver, copper, gold, and aluminum nanoparticles in water and VP1 as the based fluids to determine their potential to be used in direct absorption solar collectors. They revealed that over 95% of incoming sunlight can be absorbed (in a nanofluid thickness $\geqslant$10 cm) with very low nanoparticle volume fractions (less than 1×10^{-5}, or 10 ppm).

Khullar et al. [33] investigated theoretically a nanofluid-based concentrating parabolic solar collector (NCPSC) and compared the results obtained with the experimental results of conventional concentrating parabolic solar collectors operating under similar conditions. They used Aluminum nanoparticles with 0.05 vol.% suspended in Therminol VP-1 as the base fluid for the analysis. Fig. 8 shows the schematic of the nanofluid-based concentrating parabolic solar collector (NCPSC) that they considered in their work. They found that the thermal efficiency of NCPSC compared to a conventional parabolic solar collector is about 5–10% higher under the same weather conditions (see Fig. 9).

Yousefi et al. [34] experimentally investigated the effects of Al_2O_3/water nanofluid on the efficiency of a flat-plate solar collector. They examined the effects of two different weight fractions of the nanofluid, including 0.2% and 0.4%, where the diameter of particles was 15 nm. In addition, they studied the effects on efficiency of Triton X-100 used as a surfactant. The photograph and specifications of the flat-plate collector tested are presented in Fig. 10 and Table 1, respectively.

Yousefi et al. [34] conducted the experiments using a schematic setup shown in Fig. 11. Their findings are as follows:

1. The efficiency of the solar collector with 0.2% weight fraction (wt.) nanofluid is greater than that with water by 28.3% (see Fig. 12).
2. For a wide range of the reduced temperature parameter $(T_i - T_a)/G_T$, the efficiency of collector with 0.2% wt.% nanofluid is higher compared to 0.4 wt.% (see Fig. 12).
3. Using surfactant leads to a 15.63% enhancement of the efficiency.

Later, Yousefi et al. [35], using the same experimental setup as in their previous work [34], examined the effects of water–Multi wall carbon nanotubes (MWCNT) – Water nanofluid on the efficiency of the flat plate collector. They observed that:

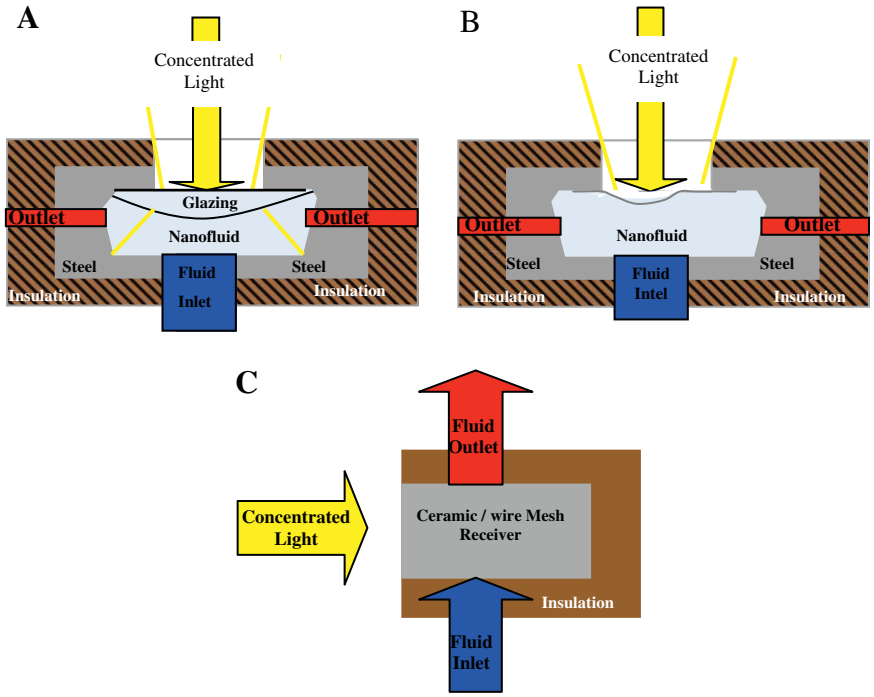

Fig. 7. (a) Conceptual design of a nanofluid concentrating collector with glazing. (b) Conceptual design of a nanofluid concentrating collector without glazing. (c) Conceptual drawing of a conventional power tower solid surface absorber (Reprinted with permission from Taylor et al. [29]. Copyright 2011, American Institute of Physics).

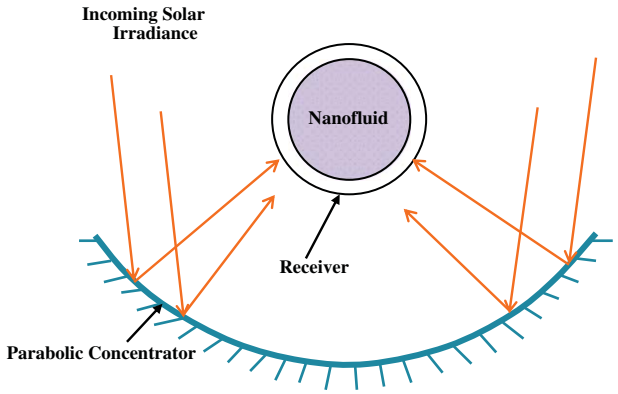

Fig. 8. Schematic of nanofluid-based concentrated parabolic solar collector (NCPSC) (Reprinted from Khullar et al. [33], with permission from ASME).

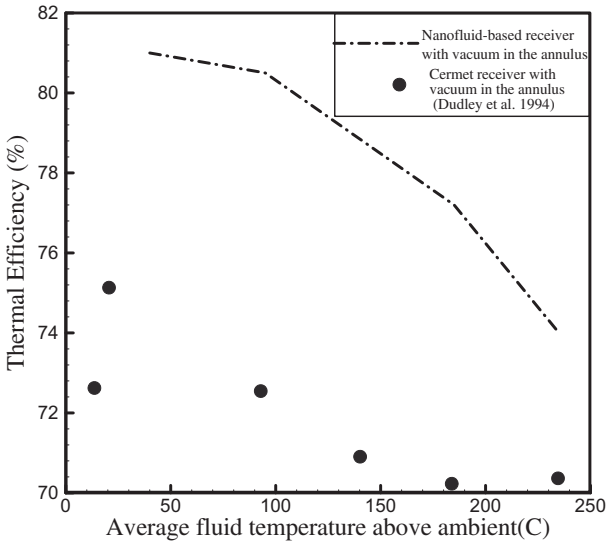

Fig. 9. Comparison of thermal efficiency as a function of average fluid temperature above ambient for NCPSC with conventional linear parabolic solar collector (Reprinted from Khullar et al. [33], with permission from ASME).

1. The efficiency of the collector by using of MWCNT–water nanofluid without surfactant is remarkably increased for 0.4 wt.% nanofluid, whereas with 0.2 wt.% the efficiency reduces compared to water as the working fluid.
2. For 0.2 wt.% nanofluid, using surfactant increases the efficiency of the collector compared to water.

In another study, Yousefi et al. [36], investigated the effects of pH variation of the MWCNT–water nanofluid on the efficiency of the flat plate collector. They used 0.2 wt.% MWCNT with various pH values −3.5, 6.5, and 9.5 – and Triton X-100 as an additive. They found that a bigger difference between the pH of nanofluid and pH of isoelectric point leads to higher efficiency. The isoelectric point is the point at which the molecules carry no electrical charge. For MWCNT, the pH of the isoelectric point is 7.4. The effects of pH variation of H_2O–MWCNT nanofluid on the efficiency of the flat plate collector are presented in Fig. 13.

In the following, some previous works are reviewed in which the potential of nanofluids for use in solar energy system is performed through the study of optical properties and thermal conductivity of nanofluids. Link and El-Sayed [37] reviewed the optical properties of gold nanoparticles. Particularly, they studied the shape and size dependence of radiative, and photothermal properties of gold nanocrystals. Khlebtsov et al. [38] investigated the effects of the size, shape, and structure of gold and silver nanoparticles on the optical properties of the nanofluids and perceived that the shape and size of the nanoparticle have great effect on the optical properties of a nanofluid. Sani et al. [39] reported the

Fig. 10. Flat-plate collector used by Yousefi et al. (Reprinted from Yousefi et al. [34], with permission from Elsevier).

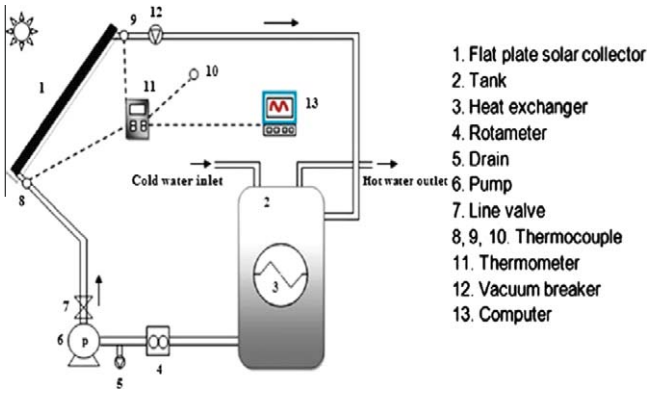

Fig. 11. Schematic of the experiment used by Yousefi et al. (Reprinted from Yousefi et al. [34], with permission from Elsevier).

Table 1
The specifications of the flat-plate collector (Reprinted from Yousefi et al. [34], with permission from Elsevier).

Specification	Dimension/value	Unit
Occupied area	200 × 94 × 9.5	cm
Absorption area	1.51	m^2
Weight	38.5	kg
Frame (Al6063 extruded)	–	–
Glass (float)	$t = 4$	mm
Header pipe (Cu)	Ø22, $t = 0.9$	mm
Connector riser pipe to absorber sheet (Cu)	Ø10, $t = 0.9$	mm
Absorption sheet:	–	–
Thermal emission:	7	%
Solar absorption:	96.2	%
Coating method:	Vacuum magnetron sputtering	–

optical characterization of a new fluid consisting of single-wall carbon nanohorns and ethylene glycol for solar energy applications. They concluded that carbon nanohorns could enhance remarkably the sunlight absorption with respect to pure base-fluid. The results obtained are compared with those obtained for fluids suspending more conventional carbon forms, i.e., carbon-black particles. They found that nanohorn spectral features are considerably more favorable than those of amorphous carbon for a specific application. This result shows that using carbon nanohorn-based nanofluids in thermal solar devices leads to the enhancement of efficiency and compactness in the systems. Mercatelli et al. [40,41] investigated the potential of single-wall carbon nanohorns nanoparticles with two different base fluids including water and glycol. Their measurements showed that these nanofluids are very suitable for direct absorption solar devices because only about 5% of the total extinction is scattered by SWCNH particles. In another work, Mercatelli et al. [42] applied a simple spectrophotometric to estimate the spectral scattering albedo of SWCNHs/water nanofluid. Recently, Saidur et al. [43] investigated the potential of Aluminum/water nanofluid to use in direct absorption solar collectors. They concluded that Aluminum/water nanofluid with 1% volume fraction improves considerably the solar absorption so that it is a fine solution for a direct solar collector. To use of the nanofluid they suggested, although the particle size has no effect on the extinction coefficient of nanofluid, in order to have Rayleigh scattering the size of nanoparticles should be less than 20 nm. They also found that the extinction coefficient varies linearly with volume fraction. Lenert and Wang [44] and Lenert [45] presented a combined theoretical and experimental work to optimize the efficiency of liquid-based solar receivers seeded with carbon-coated absorbing nanoparticles. They concluded that the efficiency of nanofluid volumetric receivers increases with increasing solar concentration and nanofluid height. Colangelo et al. [46] measured the thermal conductivities of CuO, Al_2O_3, ZnO and Cu with different shapes and volume fraction by 3%, where water and diathermic oil are as the base fluids, to evaluate their potential to use for high temperature applications such as in solar collectors. They found that the thermal conductivity enhancement of the nanofluids with diathermic oil is higher than that with water, with the same nanoparticles and at the same conditions. They also concluded that the thermal conductivity is reduced with increasing the size of particles. Kameya and Hanamura [47] found experimentally that the solar radiation absorption for the nanofluid of Ni/alkyl naphthalene with 0.1% volume fraction is much higher than the base fluid. Gan and Qiao [48] investigated the optical properties of ethanol-based nanofluids containing multiwalled carbon nanotubes (MWCNTs), carbon and aluminum nanoparticles. They concluded that MWCNTs leads to more absorption than aluminum and carbon nanoparticles. Finally, Gan and Qiao [49] found that for ethanol-based nanofluids, the radiation absorption for nanofluids

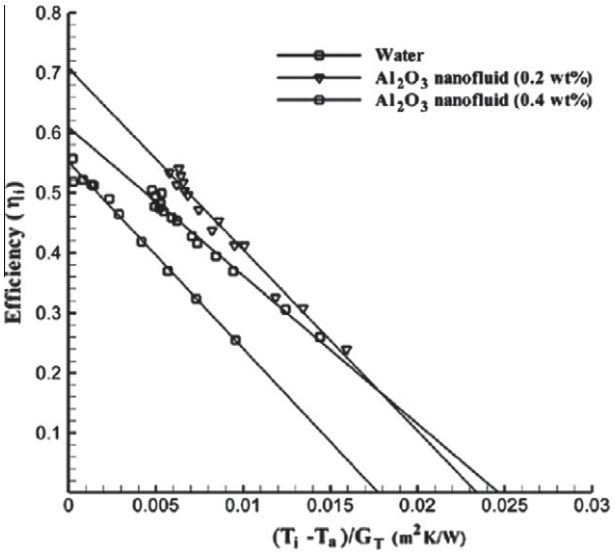

Fig. 12. The efficiencies of solar collectors for Al_2O_3 nanofluid without surfactant and for water (Reprinted from Yousefi et al. [34], with permission from Elsevier).

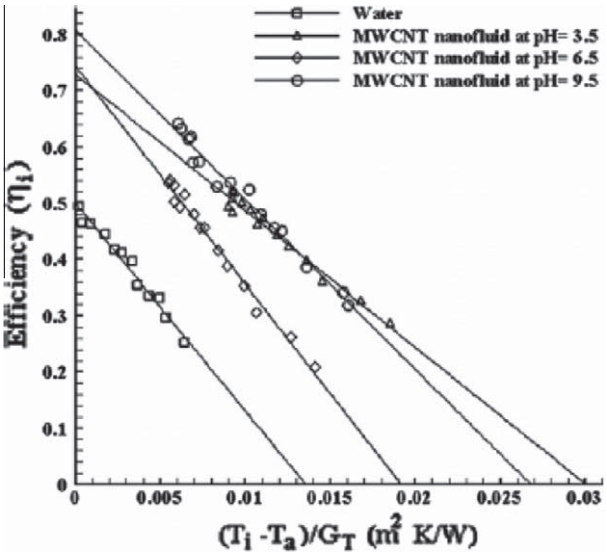

Fig. 13. The efficiency of the flat-plate solar collector with MWCNT nanofluid as a base fluid at three pH values compared water at a 0.0333 kg/s mass flow rate (Reprinted from Yousefi et al. [36], with permission from Elsevier).

containing Al_2O_3 nanoparticles is higher than nanofluids containing aluminum nanoparticles.

2.1.2. Economic and environment considerations

An accepted way to determine the economic and environmental impacts of a product is life cycle assessment [50]. This section presents the economic and environment considerations of nanofluid-based collectors. Otanicar and Golden [50] compared the environmental and economic aspects of using a conventional solar collector against a nanofluid based collector located in Phoenix, Arizona. The economic analysis shows that the capital cost and maintenance costs of the nanofluid-based solar collector compared to the conventional one are $120 and $20 higher, respectively (see Table 2). However, because of the higher efficiency and annual solar fraction of the nanofluid-based solar collector, the fuel cost savings per year, for both electricity and natural gas, is greater than that of the conventional solar collector. Moreover, due to the high cost of nanofluids compared the conventional collector, the payback period for a nanofluid-based collector is longer, but at the end of its useful life, it has the same life cycle savings as a conventional collector.

Embodied energy for both solar collectors, including conventional and nanofluid-based collectors, are compared in Table 3. The embodied energy for the nanofluid-based collector is about 9% lower. Additionally, from an environmental point of view, as shown in Table 4, the manufacturing of the nanofluid-based solar collector leads to 34 kg fewer CO_2 emissions while during its operation it saves 50 kg year when compared to the conventional solar collector. The magnitudes of other emissions including SO_x and NO_x are very small, so the differences are not considerable. Over the 15-year expected lifetime of the solar collectors, the nanofluid-based solar collector would offset more than 740 kg of CO_2 in comparison to a conventional collector. The authors concluded that more than one million metric tons of CO_2 could be offset per year if the usage of nanofluid-based solar collector systems for hot water heating increases by 50% in Phoenix, Arizona.

Khullar and Tyagi [51] examined the potential of the nanofluid-based concentrating solar water heating system (NCSWHS) as an alternative for systems based on fossil fuels. Using NCSWHS leads to annual electricity and liquefied petroleum gas (LPG) savings of approximately 1716 kWh/household/year and 206 kg/household /year, respectively, which produces significant economic benefits. In addition, they concluded that based on the annual estimation, CO_2 emissions are reduced by about 2.2×10^3 kg of CO_2/household/year. The use of nanofluid-based collectors is beneficial to reduce the environment problems. Table 5 summarizes the most important results obtained from the former works concerning the application or potential of nanofluids to use in solar collectors.

2.2. Other applications

In this section, other applications of nanofluids in solar energy systems including their applications in thermal energy storage materials, solar cells, and solar stills are reviewed. It should be noted that the reported works in this field are very scarce.

2.2.1. Thermal energy storage

Typical solar thermal-energy storage facilities require the storage medium to have high heat capacity and thermal conductivity. However, few materials are available with these properties and applicable in high temperatures. Recently, Shin and Banerjee [52] reported the anomalous enhancement of specific heat capacity of high-temperature nanofluids. They found that Alkali metal chloride salt eutectics when is doped with silica nanoparticles at 1% mass concentration increases the specific heat capacity of the nanofluid by 14.5%, so that this material can be a suitable one to use in solar thermal-energy storage facilities. One of techniques of storing solar energy is the application of PCMs. Among lots of PCMs available, paraffin is the most suitable due to its desirable characteristics, including large latent heat capacity, negligible super cooling and low cost. However, the inherent low thermal conductivity (0.21–0.24 W/mK) strongly prevents possible applications [53]. Wua et al. [53] numerically investigated the melting processes of Cu/paraffin nanofluids PCMs. Their results revealed that with 1 wt.% Cu/paraffin, the melting time can be saved by 13.1%. Therefore, they concluded that adding nanoparticles is an efficient technique to enhance the heat transfer in latent heat thermal energy storage system.

Table 2
Economic comparisons for conventional and nanofluid-based solar collectors (Reprinted with permission from Otanicar and Golden [50]. Copyright (2009) American Chemical Society).

Parameter	Conventional solar collector {$}	Nanofluid solar collector {$}
Independent costs	200.00	200.00
Area based costs	397.80	327.80
Nanoparticles		188.79
Total capital (one time cost)	597.80	716.59
Total maintenance (for 15 year life)	96.23	115.35
Total costs	694.03	831.94
Electricity cost saving per year	270.13	278.95
Years until electricity savings = costs	2.57	2.98
Natural gas cost saving per year	80.37	83.02
Years until natural gas savings = costs	8.64	10.02
Electricity price		
November_March (per kWh)	0.08	0.08
May_October (per kWh)	0.09	0.09
Daily service charge	0.25	0.25
Gas price		
Rate (per therm)	0.74	0.74
Monthly service charge	9.70	9.70

Table 3
Embodied energy comparisons for conventional and nanofluid-based solar collectors (Reprinted with permission from Otanicar and Golden [50]. Copyright (2009) American Chemical Society).

Description	Embodied energy index (MJ/kg)	Conventional solar collector		Nanofluid-based solar collector	
		Mass (kg)	Embodied energy content (MJ)	Mass (kg)	Embodied energy (MJ)
Insulation					
Polyester	53.7	1.74	93.22	1.74	93.22
Fiberglass	30.3	3.26	98.75	3.26	98.75
Glass	15.9	14.20	225.76	28.40	451.52
Copper pipe					
Collector	70.6	4.97	350.72	0.00	0.00
Manifold	70.6	3.48	245.57	3.48	245.57
Aluminum extrusion	201.0	0.56	111.58	0.56	111.58
Aluminum backplate	199.0	2.12	421.75	2.12	421.75
Steel backplate	34.8	0.00	0.00	5.97	207.65
Sealant	87.0	0.70	60.90	0.70	60.90
Black paint	90.4	0.30	27.12	0.30	27.12
Casing paint	90.4	0.90	81.36	0.90	81.36
Screws	34.8	0.00	0.04	0.00	0.04
Copper absorber	70.6	4.05	285.80	0.00	0.00
Nanoparticles	246.8	0.00	0.00	0.06	15.55
Thermal fluid	17.0	5.84	99.28	5.84	99.28
Conversion rate (27%)			567.50		516.86
Total		42.10	2669.34	53.32	2431.14

Table 4
Embodied energy emissions and consumer phase operational energy (Reprinted with permission from Otanicar and Golden [50]. Copyright (2009) American Chemical Society).

Emissions	Pollution from collector embodied energy		Saving of solar energy	
	Conventional (kg)	Nanofluid-based (kg)	Conventional (kg/year)	Nanofluid-based (kg/year)
Carbon dioxide (CO_2)	599.77	564.94	1500.89	1550.33
Sulfur oxides (SO_x)	0.51	0.48	0.83	0.85
Nitrogen oxides (NO_x)	0.84	0.79	1.53	1.58

2.2.2. Solar cells

Cooling of solar cells can improve the efficiency of such solar devices. Nanofluids can be used as a solution to cool the solar cells. Elmir et al. [54] simulated the cooling of a silicon solar cell using the finite element method. They considered the solar panel as an inclined cavity (with a slope of 30°) and solved the equations in Cartesian coordinate system. They used Al_2O_3/water nanofluid for their analysis, where the thermal conductivity and viscosity of the nanofluid are estimated using the models of Wasp [55] and Brinkman [56], respectively. As seen in Fig. 14, they concluded that using nanofluids leads to the increase of the average Nusselt number, and, hence, the rate of cooling increases with increases in volume fraction. Of course, it should be noted that the thermophysical properties, which are used in this study, are old and they do not predict the thermal conductivity and viscosity of nanofluids correctly. Therefore, it is suggested that in the future works, temperature-dependent models, or at least newer temperature-independent models are used to calculate the thermophysical properties of nanofluids. For example, to calculate the viscosity of nanofluids, the models and relation presented by Maiga et al. [57], Buongiorno [58], Nguyen et al. [59], Koo and Kleinstreuer [60], and Duangthongsuk and Wongwises [61] can be used. To estimate the thermal conductivity of nanofluids, the relations presented by Maiga et al. [57], Xuan et al. [62], Jang and Choi [63], Koo and Kleinstreuer [64], Chon et al. [65], Duangthongsuk and Wongwises [61] and Yiamsawasd et al. [66] can be applied.

2.2.3. Solar stills

Potable water demand is increasing due to rapid population increase and due to uncontrolled pollution of freshwater resources. According to the World Health Organization, nearly 2.8 billion people (approximately 40% of the world population) currently have no access to safe drinking water, and water-borne diseases account for 90% of all infectious diseases in the developing world [67]. In arid remote regions in the world, the provision of fresh water is more critical. In these regions, solar desalination systems can solve part of the problem where solar energy is available. Solar stills can be used to avoid the greenhouse gas emissions from the production of fresh water [68]. Many researches have carried out research on solar stills, and different methods are applied to improve their productivity. Recently, Gnanadason et al. [69] reported that using nanofluids in a solar still can increase its productivity. The schematic of their experimental set-up is shown in Fig. 15. They investigated the effects of adding carbon nanotubes (CNTs) to the water inside a single basin solar still. Their results revealed that adding nanofluids increases the efficiency by 50%. Nevertheless, they have not mentioned the amount of nanofluid added to the water inside the solar still. Regarding the addition of nanofluids to the solar still, the economic viability should be considered. In literature, some works reported that adding dyes to solar stills could improve the efficiency. For instance, Nijmeh et al. [70] concluded that adding violet dye to the water inside the solar still increases the efficiency by 29%, which is considerable. On the other hand, it is evident that nanofluids (especially CNTs) compared to dyes are more expensive, hence this may be a challenge on using nanofluids in solar stills, because in this type of use of nanofluids in solar stills the nanofluids have no flow in a closed loop so that they could be recovered.

3. Future work

The above review shows that the application of nanofluids in solar energy applications is still in its infancy. Nanofluids can be used in many fields of solar energy. Here, some suggestions are presented for future work in the area. The authors hope that these

Table 5
Summary of former works on the application or potential of nanofluids to use in solar collectors.

Author(s) and type of study	Collector type	Nanofluid type and nanoparticle size	Results
Tyagi et al. [27] (Theoretically)	Non-concentrating direct absorption	Aluminum/water (0–20 nm)	–Efficiency remarkably increases for volume fraction less than 2% –Efficiency remains nearly constant for volume fraction higher than 2% –Efficiency increases slightly with an increase in the size of nanoparticles
Otanicar et al. [28] (Theoretically and experimentally)	Non-concentrating micro scale direct absorption	Graphite/water (30 nm) silver/water (20 and 40 nm) carbon nanotube/water (6–20 nm diameter, 1000–5000 nm length)	–Efficiency considerably increases for volume fractions less than 0.5% –Efficiency for volume fractions higher than 0.5% may even decrease –Efficiency increases by 6%, with decreasing the nanoparticle size in Silver/Water nanofluid
Taylor et al. [29] (Theoretically and experimentally)	Concentrating direct absorption	Graphite/therminol VP-1 aluminum/therminol VP-1 silver/therminol VP-1 copper/therminol VP-1 (10–100 nm)	–Efficiency increases up to 10% by using a nanofluid in the receiver –Using graphite/therminol VP-1 nanofluid with volume fractions less than 0.001% is beneficial for 10–100 MWe power plants
He et al. [30] (Experimentally)	Vacuum tube	TiO_2/water (5–10 nm) CNT/water (10–50 nm diameter, 100–1000 nm length)	–CNT/water nanofluid is more suitable than the TiO_2/water to be used in a vacuum tube solar collector
Li et al. [31] (Experimentally)	Tubular	Al_2O_3/water ZnO/water MgO/water(size < 20 nm)	–ZnO/water nanofluid with 0.2% volume concentration is the best selection for the collector
Taylor et al. [32] (Theoretically and experimentally)	Direct absorption	Graphite/water and graphite/VP1 aluminum/water and aluminum/VP1 copper/water and copper/VP1 silver/water and silver/VP1 gold/water and silver/VP1	–Over 95% of incoming sunlight can be absorbed for nanofluid thickness $\geqslant$ 10 and nanoparticle volume fractions less than 1×10^{-5}
Khullar et al. [33] (Theoretically)	Concentrating Parabolic	Aluminum/therminol VP-1 (5 nm)	–Thermal efficiency of nanofluid concentrating parabolic collectors compared to a conventional parabolic solar collector is about 5–10% higher
Yousefi et al. [34] (Experimental)	Flat plate	Al_2O_3/water (15 nm) Triton X-100 is used as a surfactant	–Efficiency of the solar collector with 0.2% weight fraction (wt) nanofluid is higher than that with water by 28.3%. –Efficiency increases by15.63% using the surfactant
Yousefi et al. [35] (Experimental)	Flat plate	Water-Multi wall carbon nanotubes (MWCNT)/water (10–30 nm) Triton X-100 is used as a surfactant	–Efficiency of the collector increases remarkably for 0.4 wt.% nanofluid, whereas with 0.2 wt.% the efficiency reduces compared to water –For 0.2 wt.% nanofluid, using surfactant increases the efficiency of the collector compared to water
Yousefi et al. [36] (Experimental)	Flat plate	Water-Multi wall carbon nanotubes (MWCNT)/water with various pH values: 3.5, 6.5, and 9.5 Triton X-100 is used as a surfactant	–A bigger difference between the pH of nanofluid and pH of isoelectric point leads to higher efficiency
Otanicar and Golden [50] (Theoretical)	Direct absorption	Graphite/water and propylene glycol	–Using a nanofluid-based solar collector leads to fewer CO_2 emissions compared to the conventional solar collector
Khullar and Tyagi [51] (Theoretical)	Concentrating direct absorption	Aluminum/water	–Using this type of collector leads to fewer CO_2 emissions by 2.2×10^3 kg in 1 year

proposals will be helpful for the development on the use of nanofluids in the solar thermal devices.

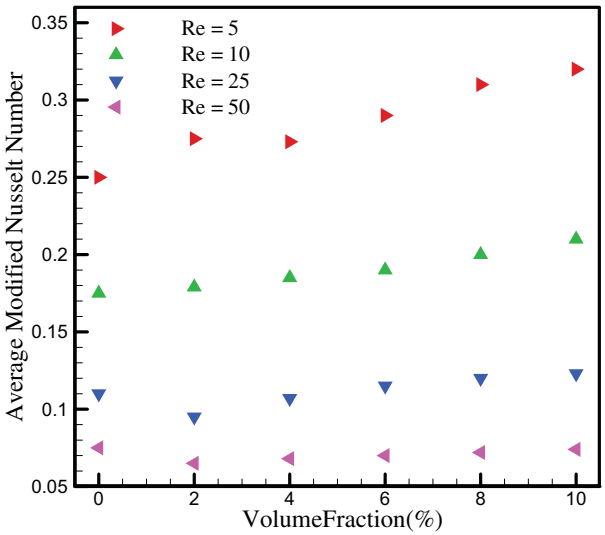

Fig. 14. Effects of volume fraction on Nusselt number for cooling a solar cell (Reprinted from Elmir et al. [54], with permission from Elsevier).

3.1. Parabolic trough systems

As mentioned, only a theoretical work has been done on parabolic trough collectors, therefore some experimental studies can be performed on the effects of nanofluids on the efficiency of parabolic trough systems.

3.2. Photovoltaic/thermal systems

A photovoltaic/thermal (PV/T) system is a hybrid structure that converts part of the sun's radiation to electricity and part to thermal energy [71]. One can investigate experimentally the effects of using different nanofluids on the cooling rate, and, hence, the efficiency of the PV/T systems. In this area, the effects of different volume fractions, nanoparticle size on the efficiency of the system can be studied. A review of the literature shows that many researches have been carried out on the potential of nanofluids for cooling of different thermal systems such as electronic devices [72–74], automobile radiator [75], and micro channel heat sinks [76]. Therefore, using nanofluids to cool the PV/T system may be reasonable.

3.3. Solar thermoelectric cells

In recent years, interest in the development of solar thermoelectric systems has been considerably increased [77]. The

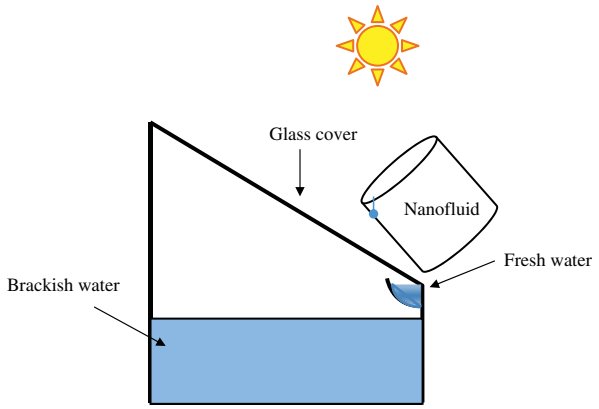

Fig. 15. Schematic of the experimental set up used by Gnanadason et al. [69].

thermoelectric cells can be used to convert the solar energy to electricity due to the temperature difference between two hot and cold surfaces. A greater temperature difference between the hot and cold surfaces of the thermoelectric cell leads to a bigger electricity production. The authors would like to suggest an experimental set-up to investigate the effects of nanofluids on the performance of such systems. Fig. 16 shows the schematic of the set-up, which is a development of the work done by Fan et al. [77]. In this work, a dish concentrates the solar radiation on the thermoelectric cells installed on the focal point of the dish. In this way the effects of different nanofluids with various mass flow rates on the efficiency of the solar thermoelectric cell can be studied.

3.4. Solar ponds

Salinity gradient solar ponds are great bodies of water between 2–5 m deep, which could collect solar radiation and store it in the form of heat [78,79].

Heat can be extracted from the solar ponds and has been used for industrial process heating, space heating, and power generation. In all these applications heat is extracted from the bottom of the solar pond which is at a temperature of about 50–60 °C higher than the top surface of the solar pond [80,81]. Concerning the application of nanofluids in solar ponds an experimental set up is proposed in Fig. 17. As seen, a nanofluid flows through a heat exchanger mounted at the bottom of the solar pond to absorb the heat. It expects that nanofluids could enhance the rate of heat removal from the bottom of the solar pond.

3.5. Other possibilities

The above suggestions are only a few of the possible applications relating to the use of nanofluids in solar energy. Besides the above ideas, nanofluids also can be used in solar cooling systems, solar absorption refrigeration systems, and a combination of different solar devices. Here, for instance, the authors would like to suggest some Refs. [82–86], in which there is a potential to use a nanofluid as the working fluid. In addition, in numerical studies such as the simulation of solar cell cooling, which it is mentioned in Section 2.2.2, new models can be used to calculate the thermophysical properties. Additionally, the nanofluid can be considered as a two-phase mixture [87].

4. Challenges

The possible challenges for the application of nanofluids in solar thermal devices are mentioned briefly in the following sections.

4.1. High cost

The first possible challenge in the use of nanofluids in solar thermal devices is the high cost of nanofluids because of difficulties in production. The high cost of nanofluids to use in thermal engineering systems such as heat exchangers is emphasized as a disadvantage in some works [88,89].

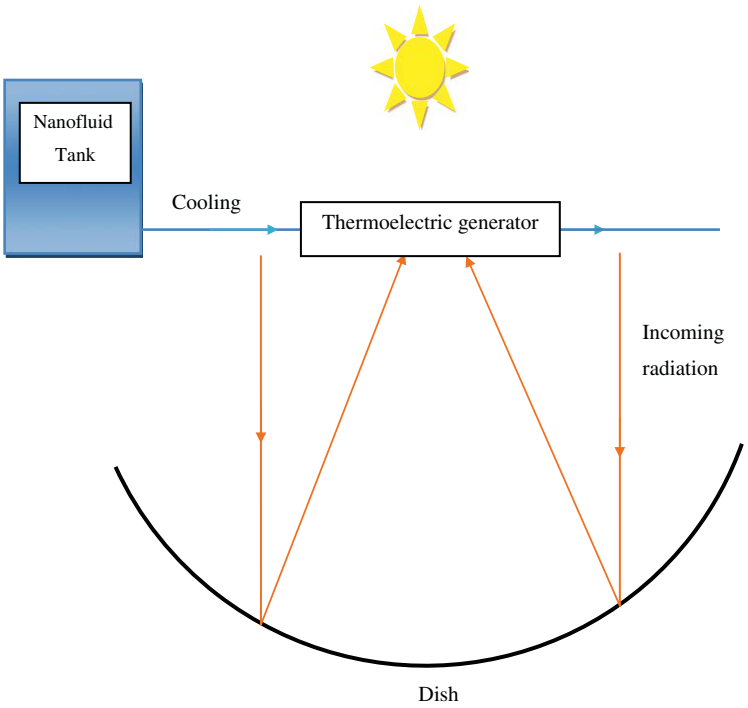

Fig. 16. The experimental set-up proposed for using nanofluids in thermoelectric cells.

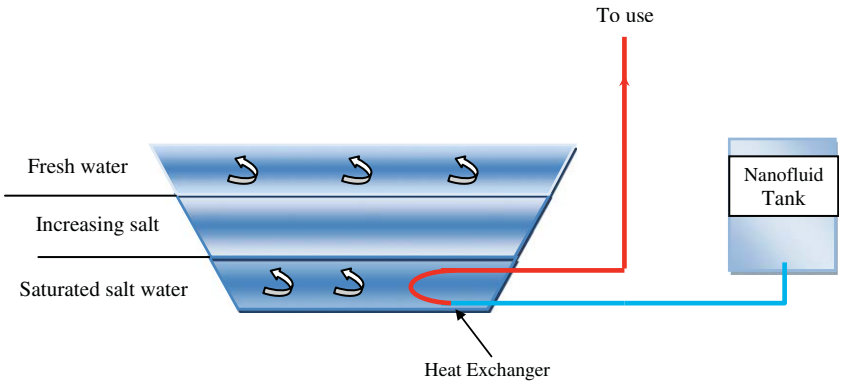

Fig. 17. The experimental set-up proposed for using nanofluids in solar ponds.

4.2. Instability and agglomerating

Instability and agglomerating of the nanoparticles is another problem. Therefore, using nanofluids in solar systems with natural circulation (such as thermosiphons) where there is no pump to circulate the fluid, is not reasonable. It should be also noted that for high temperature gradients the agglomeration of nanoparticles seems to be more serious [90]. Therefore, exact investigations are needed for an appropriate selection of a nanofluid for applications in high temperatures.

4.3. Pumping power and pressure drop

Using a nanofluid with higher viscosity compared to the base fluid leads to the increase of pressure drop and consequently the increases in the required power for pumping. For example, Duangthongsuk and Wongwises [91] found during their experiments that the pressure drop under a turbulent regime increases with an increase in volume fraction of TiO_2/water nanofluid. In another experimental research, Razi et al. [92] also concluded that using CuO/oil nanofluid increases the pressure drop under a laminar regime.

4.4. Erosion and corrosion of components

Existing of nanoparticles in nanofluid may lead to corrosion and erosion of thermal devices in a long time. Celata et al. [93] recently investigated the effects of nanofluid flow effects on erosion and corrosion of metal surfaces. They conducted their experiments for TiO_2, Al_2O_3, SiC, ZrO_2 nanoparticles with water as the base fluid where the nanofluids flow in pipes with three different materials, i.e., aluminum, copper and stainless. They concluded that the nanofluids have no effect on the erosion of the stainless pipe, while the aluminum pipe has highest erosion. They also found that ZrO_2 and TiO_2 nanoparticles lead to highest erosion while SiC nanoparticles results in lowest erosion.

5. Conclusion

Nanofluids are advanced fluids containing nano-sized particles that have emerged during the last two decades. Nanofluids are used to improve system performance in many thermal engineering systems. This paper presented a review of the applications of nanofluids in solar thermal engineering. The experimental and numerical studies for solar collectors showed that in some cases, the efficiency could increase remarkably by using nanofluids. Of course, it is found that using a nanofluid with higher volume fraction always is not the best option (Yousefi et al. [34]). Therefore, it is suggested that the nanofluids in different volume fractions should be tested to find the optimum volume fraction. It is also seen that the available theoretical works give different results on the effects of particle size on the efficiency of the collectors (see Refs. [27,28]). It is worth to carry out an experimental work on the effect of particle size on the collector efficiency. It is also concluded that some factors such as adding surfactant to nanofluid and a suitable selection of the pH of nanofluid are effective in the collector efficiency. From the economic and environmental point of view, the previous studies showed that using nanofluids in collectors leads to a reduction in CO_2 emissions and annual electricity and fuel savings. Some other reported works of applications of nanofluids in solar cells, solar thermal energy storage, and solar stills are also reviewed. It is also stressed that for the numerical study of solar systems (for example cooling of solar cells), it is better to use the new thermophysical (temperature-dependent) models and two phase mixture models for the nanofluid to have a more exact prediction of the system performance. This review reveals that the application of nanofluids in solar energy is yet in its infancy. Therefore, some proposals are presented to develop the use of nanofluids in different solar systems such as solar ponds, solar thermoelectric cells, and so on. Finally, the most important challenges on the use of nanofluids in solar systems including high costs of production, instability and agglomeration problems, increased pumping power and erosion are mentioned. These challenges may be reduced with the development of nanotechnology in the future.

Acknowledgments

The fifth author wishes to thank the Thailand Research Fund, and the National Research University Project for support for his study. Also, the valuable help of Prof. Akbarzadeh and Dr. Singh from RMIT University, Australia, and Dr. Tyagi from the School of Mechanical, Materials and Energy Engineering, Indian Institute of Technology Ropar, India is appreciated.

References

[1] U.S. Choi, Enhancing thermal conductivity of fluids with nanoparticles, ASME FED 231 (1995) 99–103.
[2] Y. Li, J. Zhou, S. Tung, E. Schneider, S. Xi, A review on development of nanofluid preparation and characterization, Powder Technol. 196 (2009) 89–101.
[3] J.H. Lee, S.H. Lee, C.J. Choi, S.P. Jang, S.U.S. Choi, A review of thermal conductivity data, mechanics and models for nanofluids, Int. J. Micro–Nano Scale Transport 1 (2010) 269–322.
[4] A. Ghadimi, R. Saidur, H.S.C. Metselaar, A review of nanofluid stability properties and characterization in stationary conditions, Int. J. Heat Mass Transfer 54 (2011) 4051–4068.

[5] G. Ramesh, N.K. Prabhu, Review of thermo-physical properties, wetting and heat transfer characteristics of nanofluids and their applicability in industrial quench heat treatment, Nanoscale Res. Lett. 6 (2011) 334.
[6] K. Khanafer, K. Vafai, A critical synthesis of thermophysical characteristics of nanofluids, Int. J. Heat Mass Transfer 54 (2011) 4410–4428.
[7] J. Fan, L. Wang, Review of heat conduction in nanofluids, ASME J. Heat Transfer 133 (2011) 040801.
[8] R.S. Vajjha, D.K. Das, A review and analysis on influence of temperature and concentration of nanofluids on thermophysical properties, heat transfer and pumping power, Int. J. Heat Mass Transfer (2012), http://dx.doi.org/10.1016/j.ijheatmasstransfer.2012.03.048.
[9] V. Trisaksri, S. Wongwises, Critical review of heat transfer characteristics of nanofluids, Renew. Sustain. Energy Rev. 11 (2007) 512–523.
[10] W. Daungthongsuk, S. Wongwises, A critical review of convective heat transfer of nanofluids, Renew. Sustain. Energy Rev. 11 (2007) 797–817.
[11] S. Kakaç, Pramuanjaroenkij, Review of convective heat transfer enhancement with nanofluids, Int. J. Heat Mass Transfer 52 (2009) 3187–3196.
[12] L. Godson, B. Raja, D. Mohan, S. Wongwises, Enhancement of heat transfer using nanofluids – An overview, Renew. Sustain. Energy Rev. (2009), http://dx.doi.org/10.1016/j.rser.2009.10.004.
[13] J. Sarkar, A critical review on convective heat transfer correlations of nanofluids, Renew. Sustain. Energy Rev. 11 (2011) 3271–3277.
[14] Y. Ding, H. Chen, L. Wang, C.-Y. Yang, Y. He, W. Yang, W.P. Lee, L. Zhang, R. Huo, Heat transfer intensification using nanofluids, Kona, Nr. 25 (2007) 23–38.
[15] C. Kleinstreuer, J. Li, J. Koo, Microfluidics of nano-drug delivery, Int. J. Heat Mass Transfer 51 (2008) 5590–5597.
[16] R. Saidur, S.N. Kazi, M.S. Hossain, M.M. Rahman, H.A. Mohammed, A review on the performance of nanoparticles suspended with refrigerants and lubricating oils in refrigeration systems, Renew. Sustain. Energy Rev. 15 (2011) 310–323.
[17] S. Thomas, C. Sobhan, A review of experimental investigations on thermal phenomena in nanofluids, Nanoscale Res. Lett. 6 (2011) 377.
[18] W. Escher, T. Brunschwiler, N. Shalkevich, A. Shalkevich, T. Burgi, B. Michel, D. Poulikakos, On the cooling of electronics with nanofluids, ASME J. Heat Transfer 133 (2011) 051401.
[19] O. Abouali, G. Ahmadi, Computer simulations of natural convection of single phase nanofluids in simple enclosures: a critical review, Appl. Therm. Eng. 36 (2012) 1–13.
[20] A. Kamyar, R. Saidur, M. Hasanuzzaman, Application of computational fluid dynamics (CFD) for nanofluids, Int. J. Heat Mass Transfer (2012), http://dx.doi.org/10.1016/j.ijheatmasstransfer.2012.03.052.
[21] H.S. Ahn, M.H. Kim, A review on critical heat flux enhancement with nanofluids and surface modification, ASME J. Heat Transfer 134 (2012) 024001.
[22] R. Saidur, K.Y. Leong, H.A. Mohammad, A review on applications and challenges of nanofluids, Renew. Sustain. Energy Rev. 15 (2011) 1646–1668.
[23] M. Thirugnanasambandam, S. Iniyan, R. Goic, A review of solar thermal technologies, Renew. Sustain. Energy Rev. 14 (2010) 312–322.
[24] A. Sharma, A comprehensive study of solar power in India and World, Renew. Sustain. Energy Rev. 15 (2011) 1767–1776.
[25] S. Mekhilef, R. Saidur, A. Safari, A review on solar energy use in industries, Renew. Sustain. Energy Rev. 15 (2011) 1777–1790.
[26] S.A. Kalogirou, Solar Energy Engineering: Processes and Systems, Elsevier, Oxford, 2009.
[27] H. Tyagi, P. Phelan, R. Prasher, Predicted efficiency of a low-temperature nanofluid – based direct absorption solar collector, J. Solar Energy Eng. 131 (2009) 041004.
[28] T.P. Otanicar, P.E. Phelan, R.S. Prasher, G. Rosengarten, R.A. Taylor, Nanofluid-based direct absorption solar collector, J. Renew. Sustain. Energy 2 (2010) 033102.
[29] R.A. Taylor, P.E. Phelan, T.P. Otanicar, C.A. Walker, M. Nguyen, S. Trimble, R. Prasher, Applicability of nanofluids in high flux solar collectors, J. Renew. Sustain. Energy 3 (2011) 023104.
[30] Y. He, S. Wang, J. Ma, F. Tian, Y. Ren, Experimental study on the light-heat conversion characteristics of nanofluids, Nanosci. Nanotechnol. Lett. 3 (2011) 494–496.
[31] Y. Li, H. Xie, W. Yu, J. Li, Investigation on heat transfer performances of nanofluids in solar collector, Mater. Sci. Forum 694 (2011) 33–36.
[32] R.A. Taylor, P.E. Phelan, T.P. Otanicar, R. Adrian, R.P. Prasher, Nanofluid optical property characterization: towards efficient direct absorption solar collectors, Nanoscale Res. Lett. 6 (2011) 225.
[33] V. Khullar, H. Tyagi, P.E. Phelan, T.P. Otanicar, H. Singh, R.A. Taylor, Solar energy harvesting using nanofluids-based concentrating solar collector, in: Proceedings of MNHMT2012 3rd Micro/Nanoscale Heat & Mass Transfer International Conference on March 3–6, Atlanta, Georgia, USA, 2012.
[34] T. Yousefi, F. Veysi, E. Shojaeizadeh, S. Zinadini, An experimental investigation on the effect of Al_2O_3–H_2O nanofluid on the efficiency of flat-plate solar collectors, Renew. Energy 39 (2012) 293–298.
[35] T. Yousefi, F. Veysi, E. Shojaeizadeh, S. Zinadini, An experimental investigation on the effect of MWCNT–H_2O nanofluid on the efficiency of flat-plate solar collector, Exp. Therm. Fluid Sci. 39 (2012) 207–212.
[36] T. Yousefi, F. Veysi, E. Shojaeizadeh, S. Zinadini, An experimental investigation on the effect of pH variation of MWCNT–H2O nanofluid on the efficiency of a flat-plate solar collector, Solar Energy 86 (2012) 771–779.
[37] S. Link, M.A. El-Sayed, Shape and size dependence of radiative, non-radiative and photothermal properties of gold nanocrystals, Int. Rev. Phys. Chem. 19 (2000) 409–453.
[38] N. Khlebtsov, L. Trachuk, A. Mel'nikov, The effect of the size, shape, and structure of metal nanoparticles on the dependence of their optical properties on the refractive index of a disperse medium, Optics Spectrosc. 98 (1) (2005) 77–83.
[39] E. Sani, L. Mercatelli, S. Barison, C. Pagura, F. Agresti, L. Colla, P. Sansoni, Potential of carbon nanohorn-based suspensions for solar thermal collectors, Solar Energy Mater. Solar Cells 95 (2011) 2994–3000.
[40] L. Mercatelli, E. Sani, G. Zaccanti, F. Martelli, D.P. Ninni, S. Barison, C. Pagura, F. Agresti, D. Jafrancesco, Absorption and scattering properties of carbon nanohorn-based nanofluid for direct sunlight absorbers, Nanoscale Res. Lett. 6 (1) (2011) 282.
[41] L. Mercatelli, E. Sani, D. Fontani, G. Zaccanti, F. Martelli, D.P. Ninni, Scattering and absorption properties of carbon nanohorn-based nanofluids for solar energy applications, J. Euro. Optical Soc. 6 (2011) 11025.
[42] L. Mercatelli, E. Sani, A. Giannini, D.P. Ninni, F. Martelli, G. Zaccanti, Carbon nanohorn-based nanofluids: characterization of the spectral scattering albedo, Nanoscale Res. Lett. 7 (2012) 96.
[43] R. Saidur, T.C. Meng, Z. Said, M. Hasanuzzaman, A. Kamyar, Evaluation of the effect of nanofluid-based absorbers on direct solar collector, Int. J. Heat Mass Transfer 55 (2012) 589–5907.
[44] A. Lenert, E.N. Wang, Optimization of nanofluid volumetric receivers for solar thermal energy conversion, Solar Energy (2011).
[45] A. Lenert, Nanofluid-based receivers for high-temperature, high-flux direct solar collectors. M.Sc. Thesis, Massachusetts Institute of Technology, 2010.
[46] G. Colangelo, E. Favale, A. de Risi, D. Laforgia, Results of experimental investigations on the heat conductivity of nanofluids based on diathermic oil for high temperature applications, Appl. Energy 97 (2012) 828–833.
[47] Y. Kameya, K. Hanamura, Enhancement of solar radiation absorption using nanoparticle suspension, Solar Energy 85 (2011) 299–307.
[48] Y. Gan, L. Qiao, Optical properties and radiation-enhanced evaporation of nanofluid fuels containing carbon-based nanostructures, Energy Fuels 26 (2012) 4224–4230.
[49] Y. Gan, L. Qiao, Radiation-enhanced evaporation of ethanol fuel containing suspended metal nanoparticles, Int. J. Heat Mass Transfer 55 (2012) 5777–5782.
[50] T.P. Otanicar, J. Golden, Comparative environmental and economic analysis of conventional and nanofluid solar hot water technologies, Environ. Sci. Technol. 43 (2009) 6082–6087.
[51] V. Khullar, H. Tyagi, A study on environmental impact of nanofluid based concentrating solar water heating system, Int. J. Environ. Studies 69 (2012) 220–232.
[52] D. Shin, D. Banerjee, Enhancement of specific heat capacity of high-temperature silica-nanofluids synthesized in alkali chloride salt eutectics for solar thermal-energy storage applications, Int. J. Heat Mass Transfer 54 (2011) 1064–1070.
[53] S. Wua, H. Wanga, S. Xiaoa, D. Zhub, Numerical simulation on thermal energy storage behavior of Cu/paraffin nanofluids PCMs, Energy Procedia 31 (2012) 240–244.
[54] M. Elmir, R. Mehdaoui, A. Mojtabi, Numerical simulation of cooling a solar cell by forced convection in the presence of a nanofluid, Energy Procedia 18 (2012) 594–603.
[55] F.J. Wasp, Solid–Liquid Slurry Pipeline Transportation, Trans. Tech, Berlin, 1977.
[56] H.C. Brinkman, The viscosity of concentrated suspensions and solutions, J. Chem. Phys. 20 (1952) 571.
[57] S. Maiga, S.J. Palm, C.T. Nguyen, G. Roy, N. Galanis, Heat transfer enhancement by using nanofluids in forced convection flows, Int. J. Heat Fluid Flow 26 (2005) 530–546.
[58] J. Buongiorno, Convective transport in nanofluids, ASME J. Heat Transfer 128 (2006) 240–250.
[59] C.T. Nguyen, F. Desgranges, G. Roy, N. Galanis, T. Maŕe, S. Boucher, H.A. Mintsa, Temperature and particle-size dependent viscosity data for waterbased nanofluids– hysteresis phenomenon, Int. J. Heat Fluid Flow 28 (2007) 1492–1506.
[60] J. Koo, C. Kleinstreuer, Laminar nanofluid flow in microheat-sinks, Int. J. Heat Mass Transfer 48 (2005) 2652–2661.
[61] W. Duangthongsuk, S. Wongwises, Measurement of temperature-dependent thermal conductivity and viscosity of TiO2–water nanofluids, Exp. Therm. Fluid Sci. 33 (2009) 706–714.
[62] Y. Xuan, Q. Li, W. Hu, Aggregation structure and thermal conductivity of nanofluids, AIChE J. 49 (2003) 1038–1043.
[63] S.P. Jang, S.U.S. Choi, Role of Brownian motion in the enhanced thermal conductivity of nanofluids, Appl. Phys. Lett. 84 (2004) 4316–4318.
[64] J. Koo, C. Kleinstreuer, A new thermal conductivity model for nanofluids, J. Nanopart. Res. 6 (2004) 577–588.
[65] C.H. Chon, K.D. Kihm, S.P. Lee, S.U.S. Choi, Empirical correlation finding the role of temperature and particle size for nanofluid (Al_2O_3) thermal conductivity enhancement, Appl. Phys. Lett. 87 (2005) 153107.
[66] T. Yiamsawasd, A. Dalkilic, S. Wongwises, Measurement of the thermal conductivity of titania and alumina nanofluids, Thermochim. Acta 545 (2012) 48–56.
[67] O. Mahian, A. Kianifar, Mathematical modeling and experimental study of a solar distillation system, Proc. Inst. Mech. Eng., Part C J. Mech. Eng. Sci. 225 (2011) 1203–1212.
[68] A. Kianifar, S. Zeinali Heris, O. Mahian, Exergy and economic analysis of a pyramid shaped solar water purification system: active and passive cases, Energy 38 (2012) 31–36.

[69] M.K. Gnanadason, P.S. Kumar, S. Rajakumar, M.H.S. Yousuf, Effect of nanofluids in a vacuum single basin solar still, I.J.AERS 1 (2011) 171–177.
[70] S. Nijmeh, S. Odeh, B. Akash, Experimental and theoretical study of a single-basin solar still in Jordan, Int. Commun. Heat Mass Transfer 32 (2005) 565–572.
[71] A. Bouzoukas, New approaches for cooling photovoltaic/thermal (PV/T) systems, Ph.D Thesis, University of Nottingham, 2008.
[72] C.T. Nguyen, G. Roy, C. Gauthier, N. Galanis, Heat transfer enhancement using Al_2O_3–water nanofluid for an electronic liquid cooling system, Appl. Therm. Eng. 27 (2007) 1501–1506.
[73] M. Elmir, R. Mehdaoui, A. Mojtabi, A vertical magneto-convection in square cavity containing Al_2O_3/water nanofluid: cooling of electronic compounds, Energy Procedia 18 (2012) 724–732.
[74] A. Ijam, R. Saidur, Nanofluid as a coolant for electronic devices (cooling of electronic devices, Appl. Therm. Eng. 32 (2012) 76–82.
[75] S.M. Peyghambarzadeh, S.H. Hashemabadi, M. Seifi Jamnani, S.M. Hoseini, Improving the cooling performance of automobile radiator with Al_2O_3/water nanofluid, Appl. Therm. Eng. 31 (2011) 1833–1838.
[76] T. Hung, W. Yan, Enhancement of thermal performance in double-layered microchannel heat sink with nanofluids, Int. J. Heat Mass Transfer 55 (2012) 3225–3238.
[77] H. Fan, R. Singh, A. Akbarzadeh, Electric power generation from thermoelectric cells using a solar dish concentrator, J. Electron. Mater. 40 (2011). pages !.
[78] H. Tabor, Z. Weinberger, Nonconvecting solar ponds, in: J.F. Kreider, F. Kreith (Eds.), Solar Energy Handbook, McGraw-Hill, New York, 1980.
[79] J. Hull, C.E. Nielsen, P. Golding, Salinity Gradient Solar Ponds, CRC Press, Boca Raton, FL, 1989.
[80] J. Andrews, A. Akbarzadeh, Enhancing the thermal efficiency of solarponds by extracting heat from the gradient layer, Solar Energy 78 (2005) 704–716.
[81] R. Singh, S. Tundee, A. Akbarzadeh, Electric power generation from solar pond using combined thermosyphon and thermoelectric modules, Solar Energy 85 (2011) 371–378.
[82] M. Ozgoren, M. Bilgili, O. Babayigit, Hourly performance prediction of ammoniaewater solar absorption refrigeration, Appl. Therm. Eng. 40 (2012) 80–90.
[83] M. Balghouthi, M.H. Chahbani, A. Guizani, Investigation of a solar cooling installation in Tunisia, Appl. Energy 98 (2012) 138–148.
[84] T.S. Ge, Y.J. Dai, Y. Li, R.Z. Wang, Simulation investigation on solar powered desiccant coated heat exchanger cooling system, Appl. Energy 93 (2012) 532–540.
[85] Z.S. Lu, R.Z. Wang, Z.Z. Xia, X.R. Lu, C.B. Yang, Y.C. Ma, G.B. Ma, Study of a novel solar adsorption cooling system and a solar absorption cooling system with new CPC collectors, Renew. Energy 50 (2013) 299–306.
[86] Y.J. Dai, R.Z. Wang, L. Ni, Experimental investigation and analysis on a thermoelectric refrigerator driven by solar cells, Solar Energy Mater. Solar Cells 77 (2003) 377–391.
[87] M. Alinia, D.D. Ganji, M. Gorji-Bandpy, Numerical study of mixed convection in an inclined two sided lid driven cavity filled with nanofluid using two-phase mixture mode, Int. Commun. Heat Mass Transfer 38 (2011) 1428–1435.
[88] M.N. Pantzali, A.A. Mouza, S.V. Paras, Investigating the efficacy of nanofluids as coolants in plate heat exchangers (PHE), Chem. Eng. Sci. 64 (2009) 3290–3300.
[89] J. Lee, I. Mudawar, Assessment of the effectiveness of nanofluids for singlephase and two-phase heat transfer in micro-channels, Int. J. Heat Mass Transfer 50 (2007) 452–463.
[90] R.A. Taylor, P.E. Phelan, R.J. Adrian, A. Gunawan, T.P. Otanicar, Characterization of light-induced, volumetric steam generation in nanofluids, Int. J. Therm. Sci. 56 (2012) 1–11.
[91] W. Duangthongsuk, S. Wongwises, An experimental study on the heat transfer performance and pressure drop of TiO_2–water nanofluids flowing under a turbulent flow regime, Int. J. Heat Mass Transfer 53 (2010) 334–344.
[92] P. Razi, M.A. Akhavan-Behabadi, M. Saeedinia, Pressure drop and thermal characteristics of CuO-base oil nanofluid laminar flow in flattened tubes under constant heat flux, Int. Commun. Heat Mass Transfer 38 (2011) 964–971.
[93] G.P. Celata, F.D. Annibale, A. Mariani, Nanofluid Flow Effects on metal surfaces, Energia Ambiente e Innovazione 4–5 (2011) 94–98.

Experimental Thermal and Fluid Science 45 (2013) 8–15

Contents lists available at SciVerse ScienceDirect

Experimental Thermal and Fluid Science

journal homepage: www.elsevier.com/locate/etfs

An experimental investigation of the heat transfer and pressure drop characteristics of a circular tube fitted with rotating turbine-type swirl generators

Weerapun Duangthongsuk [a,b], Somchai Wongwises [b,c,*]

[a] Department of Mechanical Engineering, South-East Asia University, Bangkok, Thailand
[b] Fluid Mechanics, Thermal Engineering and Multiphase Flow Research Lab. (FUTURE), Department of Mechanical Engineering, Faculty of Engineering, King Mongkut's University of Technology Thonburi, Bangmod, Bangkok 10140, Thailand
[c] The Academy of Science, The Royal Institute of Thailand, Sanam Suea Pa, Dusit, Bangkok 10300, Thailand

ARTICLE INFO

Article history:
Received 17 March 2012
Received in revised form 6 July 2012
Accepted 9 September 2012
Available online 2 November 2012

Keywords:
Heat transfer coefficient
Pressure drop
Swirl generator
Passive technique

ABSTRACT

Heat transfer enhancement and flow behaviors in horizontal circular tubes installed with five rotating turbine-type swirl generators (RTSG) are presented experimentally. This type of RTSG is an innovative design that has not been seen in the previous research. Deionized water is used as a working fluid and flows through the test section under turbulent flow conditions. A smooth, stainless steel tube 9.2 mm in ID, 0.4 mm in thickness, and 2.3 m in length is used as the test section. RTSG made from aluminum, with a twisted angle of 60° and a length of 2 cm, are located at 0.46 m equally distant along the test section. When fluid flows through the RTSG, continuously free rotations are observed, and swirl flow after RTSG is created. A DC power supply is used to supply heat load to the test section. Compared with a common, plain tube (without rotating swirl devices), the experimental results indicate that the local heat transfer coefficient of the tube with RTSG inserts is higher than that of the common, plain tube, and they increase when the working fluid flows through the RTSG. Similarly, the wall temperatures of the tube with RTSG inserts are lower than those of the common tube. However, the pressure drop of the tube fitted with RTSG is significantly greater than that of the common, plain tube.

1. Introduction

Heat transfer enhancement techniques are ways to increase heat transfer performance and minimize the size and cost of heat exchangers. A variety of approaches is concluded by Goldstein et al. [1]. Normally, there are two heat transfer enhancement techniques. The first is a passive technique, and the other is an active technique. The passive technique requires special surface geometries, such as a rough surface, an extended surface, fluid additives, displaced insert devices, or swirl flow devices, whereas the active technique requires external forces, such as an electrical field, stirring of the fluid, fluid and surface vibration, or jet impingement. Focusing on passive techniques, displaced insert devices or swirl flow devices can be equipped inside and outside of the tubes to generate swirl flow, thereby reducing the thermal boundary layer thickness, which leads to an increase in heat transfer performance. However, the addition of some devices into the main flow can cause an increase in the natural pressure drop. A significant increase in heat transfer performance and reduction of the pressure drop to the minimum value are the most suitable ways to improve the heat transfer performance of heat exchangers. As a result, a number of researchers have tried to investigate the heat transfer performance and flow characteristics of conventional tubes with the insertion of swirl flow devices. Several existing articles describing these attempts follow.

Garcia et al. [2] reported on an experimental investigation of heat transfer enhancement of a circular tube with different helical-wire-coil inserts. Water and water-propylene glycol were used as working fluids, along with flowing under laminar, transition, and turbulent flow regimes. Under turbulent flow conditions, their results showed that heat transfer performance and the pressure of wire coils were four times and nine times higher, respectively, than those for plain tubes. However, at a low Reynolds number, the wire coils behaved like smooth tubes. Under transition flow conditions, the heat transfer rate of the wire coils was 200% higher than that of the smooth tube, without a decrease in pumping power. Correlations for predicting the Fanning friction factor and Nusselt number were also proposed.

Tandiroglu [3] reported on the effect of flow geometry parameters on transient forced convective heat transfer of an experimental round tube with baffle inserts. Air was used as a working fluid, and flowing took place under constant heat flux and turbulent flow regimes. Time-averaged Nusselt number and time-averaged pressure drop correlations were also proposed.

* Corresponding author at: Fluid Mechanics, Thermal Engineering and Multiphase Flow Research Lab. (FUTURE), Department of Mechanical Engineering, King Mongkut's University of Technology Thonburi, Bangmod, Bangkok 10140, Thailand.
E-mail address: somchai.won@kmutt.ac.th (S. Wongwises).

0894-1777/$ - see front matter © 2012 Elsevier Inc. All rights reserved.
http://dx.doi.org/10.1016/j.expthermflusci.2012.09.009

Nomenclature

A	area, m^2
C_p	specific heat, J/kg K
D	diameter, m
f	friction factor
h	heat transfer coefficient, W/m^2 K
I	electric current (A)
k	thermal conductivity, W/m K
L	length of the test tube, m
$\dot{m}$	mass flow rate, kg/s
Nu	Nusselt number
Pr	Prandtl number
ΔP	Pressure drop, Pa
Q	heat transfer rate, W
Re	Reynolds number
T	temperature, °C
u	velocity, m/s
V	electric voltage, V

Greek symbols

ε	roughness, m
ρ	density, kg/m^3
μ	viscosity, kg/ms

Subscript

ave	average
elec	electric
f	fluid
in	inlet
m	mean
out	outlet
s	surface
w	tube wall
x	local distance

Sivashanmugam and Suresh [4] experimentally investigated the heat transfer performance and friction factor of a round tube fitted with a full-length helical screw element with different twist ratios and spacer lengths. Their data indicated that the helical screw inserts with spacers provided higher heat transfer enhancement than those in the round tube only under turbulent flow conditions, and less of a reduction in pumping power was observed. Moreover, the empirical equations for Nusselt number and friction factor were performed.

Chang et al. [5] reported on an experimental study on the local heat transfer coefficient and pressure drop characteristics of a circular tube with a broken twisted tape insert. The data showed that the use of the broken twisted tape insert could increase the heat transfer coefficient and friction factor. Finally, the local Nusselt number and Fanning friction factor correlations for the tube fitted with broken twisted tape were presented.

Garcia et al. [6] reported on the heat transfer performance and pressure drop characteristics of an experimental smooth tube with three different wire coils inserts. The test fluids flowed under laminar and transition conditions. Their results indicated that the use of wire coils did not increase the heat transfer performance at a Reynolds number less than 200. However, at a Reynolds number ranging between 200 and 1000, the heat transfer coefficients of the wire coil inserts were much larger than those of the conventional smooth tube. At a Reynolds number of 1000, eight times the heat transfer coefficient over the smooth tube was obtained.

Kurtbas et al. [7] investigated the effects of propeller-type turbulators fitted into a circular tube on the entropy generation rate and exergy loss rate. The experimental data indicated that the Nusselt number and exergy loss rate of a round tube with propeller-type turbulator inserts were higher than those of a smooth tube.

Sarac and Bali [8] reported on an experimental investigation into the heat transfer and pressure drop characteristics of a circular tube fitted with a decaying swirl flow. Their data showed that a round tube with decaying swirl flow inserts provided higher heat transfer performance than a smooth tube by approximately 18.1–163%.

Gul and Evin [9] reported on an experimental investigation of the heat transfer and friction characteristics under decaying turbulent swirl flow conditions generated by a short helical tape fitted at the entrance of the test section. Their measured data demonstrated that the use of helical tape inserted into the tube led to a significant increase in the heat transfer rate, compared with a circular tube. Moreover, the number of helical channels and the helical angle had no significant effects on heat transfer performance.

Akhavan-Behabadi et al. [10] carried out an experimental study on the heat transfer enhancement and pressure drop characteristics due to twisted tape inserts in a horizontal evaporator of R-134a. The experiments were carried out for four tubes with different twist ratios and refrigerant mass flux.

Kurtbas et al. [11] experimentally investigated the heat transfer performance and pressure drop characteristics of a circular tube fitted with a conical injector-type swirl generator (CITSG). The results demonstrated that the heat transfer enhancement ratio of CITSG decreased with increasing Reynolds number. The director angle and the director diameter and width decreased with increasing CITSG angle.

Akhavan-Behabadi et al. [12] studied the heat transfer coefficient and pressure drop of a round tube with coiled wire inserts during the heating of engine oil. The results showed that the use of coiled wire inserted into the round tube provided higher heat transfer augmentation than the plain tube, by approximately 2.2–3.2 times, and there was an increase in the friction factor. Heat transfer correlations for coiled wire inserts were proposed.

Khali et al. [13] experimentally studied the heat transfer and pressure drop characteristics of turbulent swirling air flow through a sudden expansion pipe. Their data showed that the sudden expansion pipe with a swirl generator inserts remarkably 40% increased the heat transfer performance of the tested pipe. Moreover, the Nusselt number and friction factor correlations for swirl flow were proposed.

In the last year, Zohir et al. [14] examined the heat transfer enhancement and pressure drop characteristics of a sudden expansion pipe experimentally implanted with a propeller-type swirl generator and a spiral spring for turbulent air flow. The measured data showed that the tube with the propeller inserts provided a higher heat transfer rate and a larger pressure drop than the plain tube, by roughly 1.69 times and 1.5 times, respectively. The Nusselt number correlations for propeller inserts were also presented.

Ibrahim [15] presented an experimental investigation on the heat transfer and friction factor characteristics of flat tubes with full-length helical screw-tape inserts. The results indicated that the Nusselt number and friction factor of a flat tube decreased with increasing spacer length, as did the twist ratio. The Nusselt number and friction factor correlations were also presented.

Patil and Babu [16] experimentally studied the heat transfer and pressure drop characteristics of a double-pipe counter flow

heat exchanger fitted with full-length twisted tape and full-length screw tape inserts. Their data indicated that the Nusselt number of the screw tape and twisted tape inserts was higher than that of the plain tube, by approximately 5.3 and 2.85 times, respectively. Similarly, the friction factor of the screw tape and twisted tape inserts was found to be 14 and 7.7 times, respectively, that of the plain duct.

As mentioned above, it has been seen that the use of some devices inserted in plain tubes resulted in better heat transfer performance than with a common plain tube. These devices also generate higher pressure drops than that of plain tubes, by roughly four to five times, due to their being fixed or their not freely rotating. Only the research of Kurtbas et al. [7], and Zohir et al. [14] has been concerned with freely rotating swirl devices. However, the sizes of their test tubes have varied from 40 to 100 mm, which are rather large and the fluid used in their studies are air. This research aimed to investigate the heat transfer performance and pressure drop characteristics of a small, round tube (ID = 9.2 mm) fitted with rotating turbine-type swirl generators (RTSGs) at five positions along the test section. These types of RTSG inserts are new designs that have never been seen before in the available literature. Five RTSG with twist angles of 60° were made from aluminum. The length of each RTSG was 2 cm, with thickness of 0.5 mm and diameter of 6.6 mm, and each RTSG had four blades. When the working fluid flowed through the RTSG, continuously free rotation took place, and swirl flow after each RTSG was created. They were expected to improve the heat transfer performance and result in a small decrease in pressure drop. The experimental data for the RTSG inserts were compared with conventional plain tubes.

2. Experimental apparatus and procedures

The experimental apparatus used in this research is shown schematically in Fig. 1. It mainly consisted of two test sections: the first section was the common plain tube, and the other was the tube with RTSG inserts. Moreover, it consisted of two cooling tanks, a pump with a speed controller, and a rotameter. De-ionized water was used as the working fluid flowing under constant heat flux and turbulent flow conditions. The test section was made from stainless steel and was 2.3 m in length, 10 mm in outer diameter, and 0.4 mm in thickness. For the test section with RTSG inserts, five RTSG were mounted at x/L of 0.0, 0.2, 0.4, 0.6 and 0.8, respectively. RTSG with twist angles of 60° were made from aluminum material with 2 cm in length, 0.5 mm thickness, and 6.6 mm in outer diameter, and each RTSG had four blades. Each RTSG was installed inside the transparency tube for observation of the rotation of the RTSG. When the fluid was forced through the RTSG, continuously free rotation was observed, and swirl flow was produced after the RTSG. The detail of the RTSG is shown in Fig. 2. To measure the pressure drop and the bulk temperature of the de-ionization, the differential pressure transmitter and a T-type thermocouple were mounted at both ends of the test section. Similarly, 10 T-type thermocouples were mounted at different longitudinal positions on the outer surface to measure the wall temperature along the test tube. For the thermocouple fixations at the outer wall of the test section, the thermal insulation tape was used to bind the thermocouple end around the tube. The positions of the wall temperature measurements and the RTSG locations are depicted in Fig. 3. A DC power supply was used to supply the heat load to the test section. Cooling tank No. 1, with a 3.52 kW cooling capacity, a 4 kW electric heater, and an RTD with a temperature controller were used to keep the water temperature constant at a desired value. Similarly, cooling tank No. 2, with an 5.28 kW cooling capacity, and an RTD with a temperature controller was used to cool the water temperature leaving from the test section to the setting temperature of tank No. 1. The water flow rate was measured by a rotameter and was controlled by adjusting the rotation speed of the pump. Finally, in order to minimize the

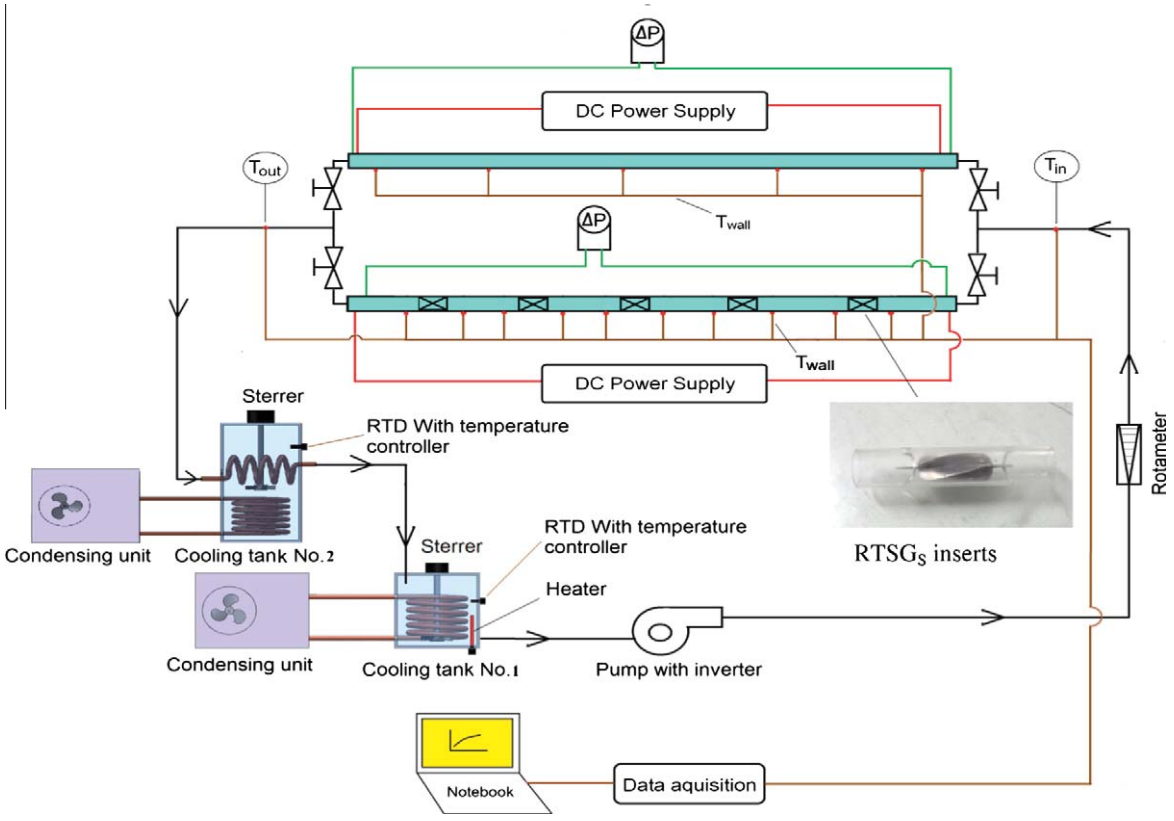

Fig. 1. Schematic diagram of the experimental apparatus used in the present study.

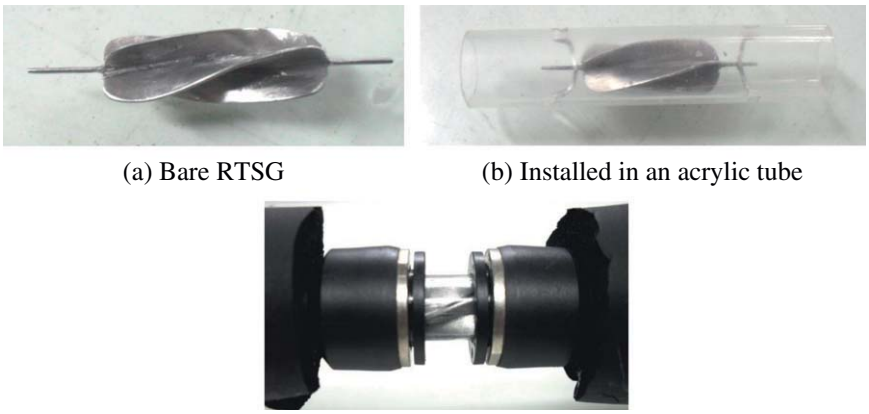

(a) Bare RTSG (b) Installed in an acrylic tube

(c) After fitting in the experimental system

Fig. 2. Configuration of the RTSG used in this study.

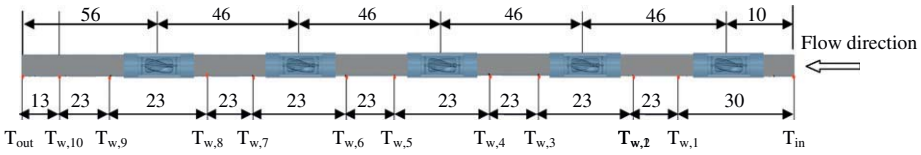

Fig. 3. Position of the wall temperature measurement and the $RTSG_S$ insert (Unit: cm).

Table 1
The dimensions of the test section and testing conditions used in the present study.

Parameter	Quantity
1. Tube length (m)	2.3
2. Outside diameter (mm)	10
3. Tube thickness (mm)	0.4
4. Inlet fluid temperature (°C)	15
5. Wall heat flux (kW/m^2)	15
6. Reynolds number	4500–9500
7. Volume flow rate (LPM)	2–4

heat loss along the test section, the elastomer type insulator with thickness of 20 mm and thermal conductivity of 0.04 W/mK was used to insulate the outer surface of the tube. The dimensions of the test tube and operating conditions are shown in Table 1.

In the present study, the differential pressure transmitter was calibrated using an air-operated dead weight tester. The uncertainty of the pressure measurement was ±0.030 kPa. All of the temperature-measuring devices were well calibrated in a controlled temperature bath, using standard precision mercury glass thermometers. The uncertainty of the temperature measurements as recorded by the data acquisition system was ±0.1 °C. The rotameter was specially calibrated by the manufacturer, and its accuracy was ±7% of full scale. In the present study, the root mean sum square method was used to estimate the uncertainty of the measured data. Therefore, the uncertainty of the measured heat transfer coefficient was approximately 5%.

The experiments were conducted with various flow rates of water. A Reynolds number ranging between 4500 and 9500 was employed. Heat flux was kept at 15 kW/m^2. The inlet water temperature was kept at 15 °C. During each experiment, the heat transferred from the test section was kept at a desired value by adjusting the voltage regulator. The system was allowed to approach a steady state before any data were recorded. After stabilization, the wall temperatures and the inlet and outlet temperatures of the water and the pressure drop across the test section and flow rates of water were all recorded.

3. Data reduction

The accuracy and reliability of the experimental system were tested before measuring the convective heat transfer coefficient and the pressure drop of the round tube fitted with RTSG. Thus, a plain circular tube was tested. The experimental results of the convective heat transfer coefficient and pressure drop were compared with the predicted values obtained from Gnielinski's equation and Colebrook's equation, respectively, which are defined as follows.

The Gnielinski equation [17] is defined as:

$$Nu = \frac{(f/8)(\mathrm{Re}-1000)\mathrm{Pr}}{1+12.7(f/8)^{0.5}(\mathrm{Pr}^{2/3}-1)}, \quad (1)$$

where Nu is the Nusselt number, Re is the Reynolds number, Pr is the Prandtl number, and f is the friction factor.

The Colebrook equation [18] is defined as:

$$\frac{1}{\sqrt{f}} = -2.0\log\left(\frac{\varepsilon/D}{3.7}+\frac{2.51}{\mathrm{Re}\sqrt{f}}\right), \quad (2)$$

The pressure drop across the test section is defined as:

$$\Delta P = f\frac{Lu_m^2}{2D}g, \quad (3)$$

where ΔP is the measured pressure drop, L is the length of the tube, D is the inner diameter of the tube, and u_m is the mean velocity of fluid.

Then, the heat transfer performance of RTSG could be computed from the following equation.

The heat supplied to the test section can be calculated from:

$$Q_{elec} = VI, \quad (4)$$

The heat transfer rate into the fluid was computed from:

$$Q_f = \dot{m}Cp(T_{out}-T_{in}), \quad (5)$$

The average heat transfer rate was described as follows:

$$Q_{ave} = \frac{Q_{elec} + Q_f}{2}, \tag{6}$$

where Q_{elec} and Q_f are the heat transfer rate of electric power and the fluid, respectively, Q_{ave} is the average heat transfer rate, V is the electric voltage, I is the electric current, $\dot{m}$ is the mass flow rate of the fluid, Cp is the specific heat, and T_m and T_{out} are the temperature of the water at the inlet and exit, respectively, of the test section. However, the difference between electric power input and energy absorbed by working fluids is approximately less than 2.0%.

The local heat transfer coefficient and the local Nusselt number are evaluated from the following equations:

$$h_x = \frac{q}{(T_w - T_f)_x}, \tag{7}$$

$$Nu_x = \frac{h_x D}{k}, \tag{8}$$

The bulk fluid temperature along the test section is calculated from:

$$T_{f,2} = T_{f,1} + \frac{q\pi Dx}{\dot{m}C_P}, \tag{9}$$

where h_x is the local heat transfer coefficient, T_{wall} is the average wall temperature of the tube, q is the wall heat flux, T_f is the bulk temperature of the fluid at each section, x is the length of the each section, Nu_x is the local Nusselt number, A_S is the surface area of the test tube, and k is the thermal conductivity of the fluid.

The average heat transfer coefficient (h_{ave}) can be computed by using the following equation:

$$h_{ave} = \frac{1}{L}\int_{x_1}^{x_2} h_x dx = \frac{1}{L}\sum_{i=1}^{n}\frac{1}{2}(h_{x,i} + h_{x,i+1})x_i, . \tag{10}$$

Moreover, the Reynolds number can be calculated by using the following equation:

$$\mathrm{Re} = \frac{\rho u_m D}{\mu}, \tag{11}$$

where ρ is the density, and μ is the viscosity of the fluids.

Similarly, the Prandtl number is defined as:

$$\mathrm{Pr} = \frac{\mu Cp}{k}. \tag{12}$$

For cases of pressure drop, the measured pressure drops of RTSG were compared with the conventional plain tube.

4. Results and discussion

As shown in Figs. 4 and 5, an agreement between the experimental results and the calculated values for the common, plain tube could be seen.

Fig. 6a and b shows the variation of the wall temperature along the test section for the common, plain tube and the RTSG inserts, respectively. For common plain tube, the results showed that the wall temperature increased with the increasing distance of the test section. This result was due to the heat from the electric power continuously transmitted to the test section, which resulted in an increase of the wall temperature. However, for the case of the RTSG inserts, abnormal behavior was obtained. As shown in Fig. 6b, the wall temperature of the test tube decreased after the fluid flowed past the RTSG. This result might due to fluid swirl flow freely rotating after each RTSG, which led to higher heat transfer rate from the tube wall. Thus, the lower wall temperature after the RTSG was obtained.

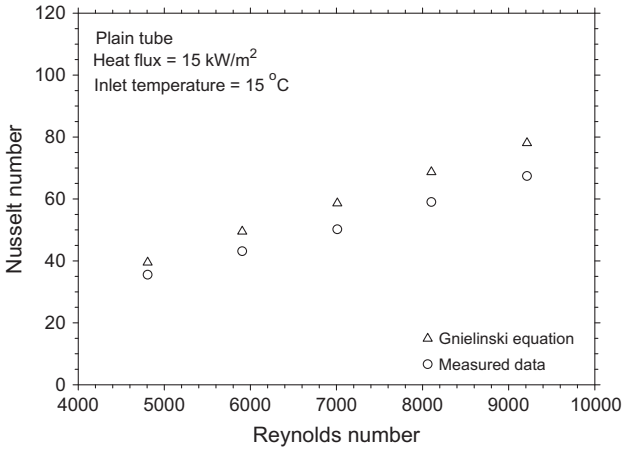

Fig. 4. Comparison between the measured Nusselt number and that calculated from Gnielinski equation.

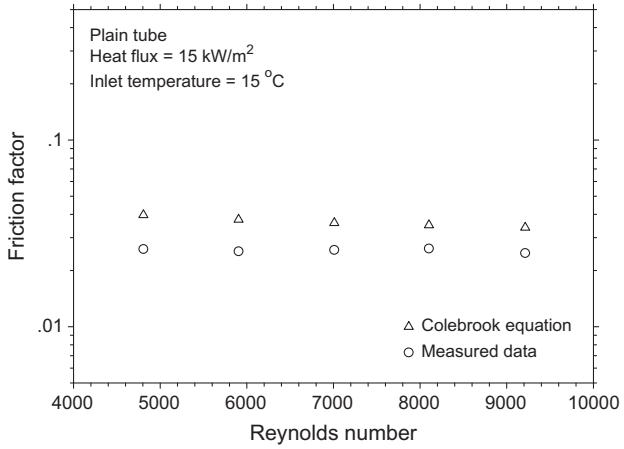

Fig. 5. Comparison between the measured friction factor and that calculated from Colebrook equation.

Fig. 7 shows the comparisons between the local wall temperatures obtained from the common, plain tube and those obtained from the RTSG inserts. The results showed that the wall temperature of the RTSG inserts was lower than that of the common, round tube. This result means that the use of RTSG inserted inside the round tube provide better thermal performance than the conventional plain tube.

Similarly, the variation of the water temperatures along the test tube for the common round tube and the tube fitted with $RTSG_S$ was shown in Fig. 8a and b, respectively. The data indicated that the water temperature along the test section increases with increasing the tube length and varied linearly with the length of the test section. This result was caused from heat supplied to the test tube continuously transferring to the fluid, which led to increase in the water temperature.

Comparison of the water temperature along the test section between common plain tube and RTSG inserts was shown in Fig. 9. The results showed that the tube with RTSG inserts gave lower water temperature than those of the common plain tube. This behavior caused from use of the RTSG inserted into the common tube led to decrease in the wall temperature which resulted decrease in the water temperature at the same time which described in Fig. 7.

Fig. 10a and b shows the variation in the local heat transfer coefficient along the test tube as a function of the volume flow

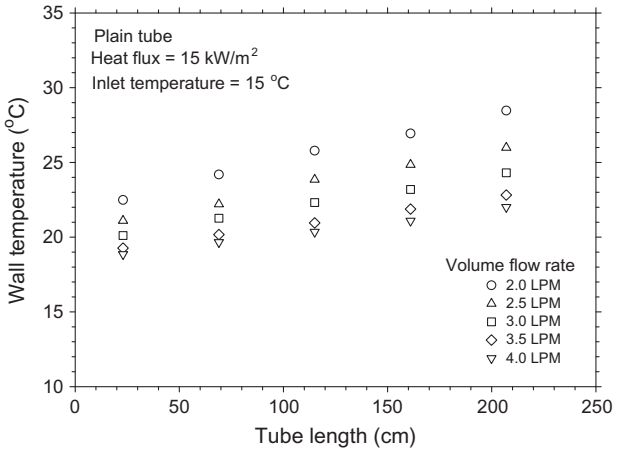

(a) For the common plain tube

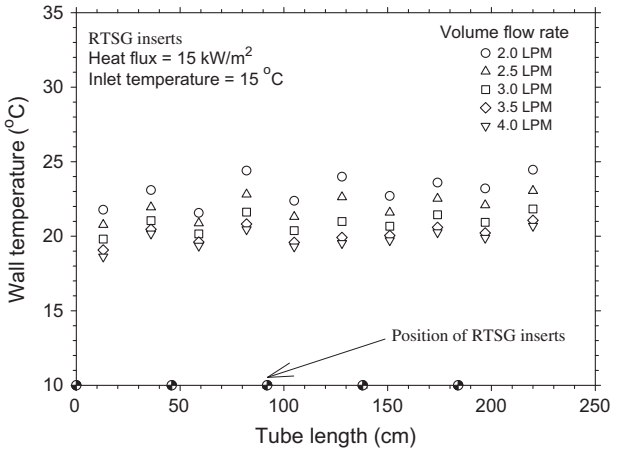

(b) For RTSG inserts

Fig. 6. Variation of the wall temperatures along the test section.

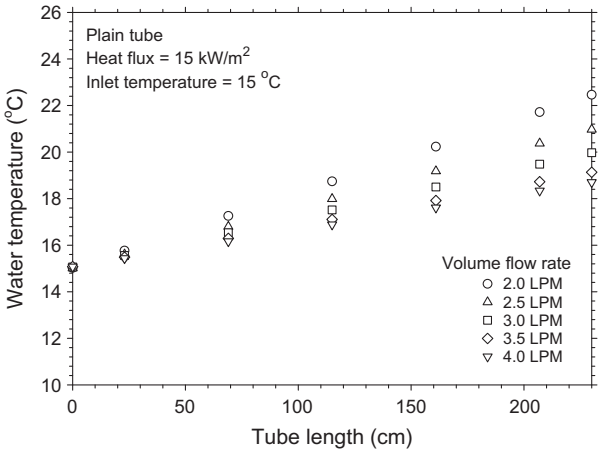

(a) For the common plain tube

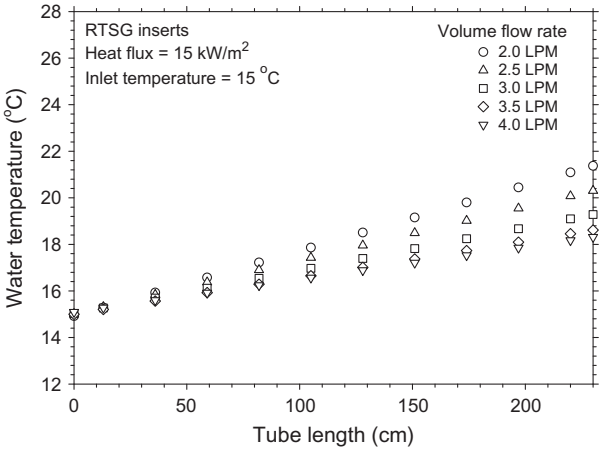

(b) For RTSG inserts

Fig. 8. Variation of the water temperatures along the test section.

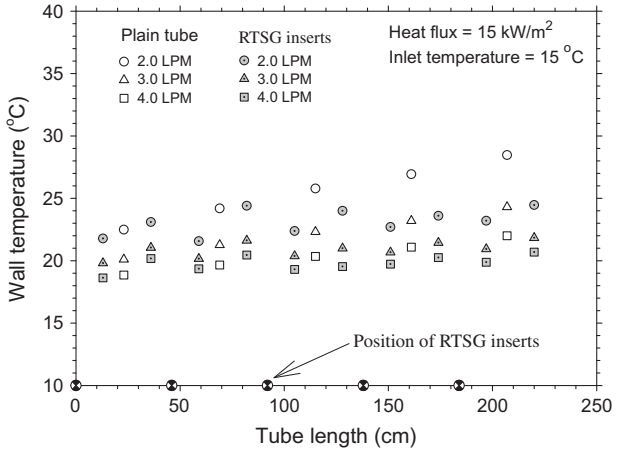

Fig. 7. Comparison of the wall temperature along the test section between the plain tube and the tube fitted with RTSG.

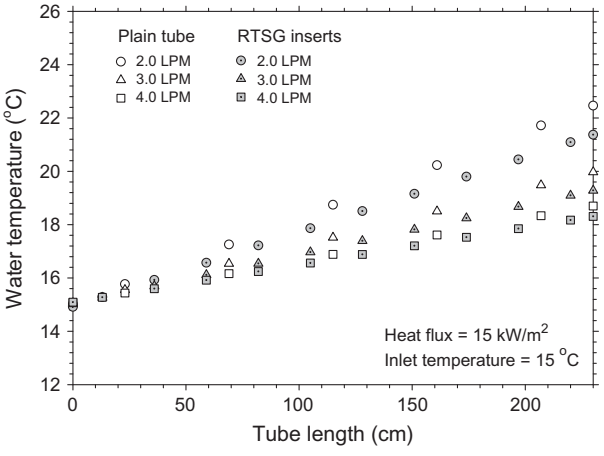

Fig. 9. Comparison of the water temperature along the test section between the plain tube and the RTSG inserts.

rates for the common, plain tube and the RTSG inserts, respectively. For the common, plain tube, the results indicated that the local heat transfer coefficient increased with the increasing volume flow rate and remained constant along the tube length. However, for the case of RTSG inserts, abnormal heat transfer behavior could be clearly seen. From the measured data, it was seen that the heat transfer coefficient of the round tube fitted with RTSG increased with increasing tube length. Moreover, focusing on the position behind the RTSG, a significantly higher heat transfer coefficient is obtained. This result was due to the swirling flow after the RTSG, creating higher heat transfer performance.

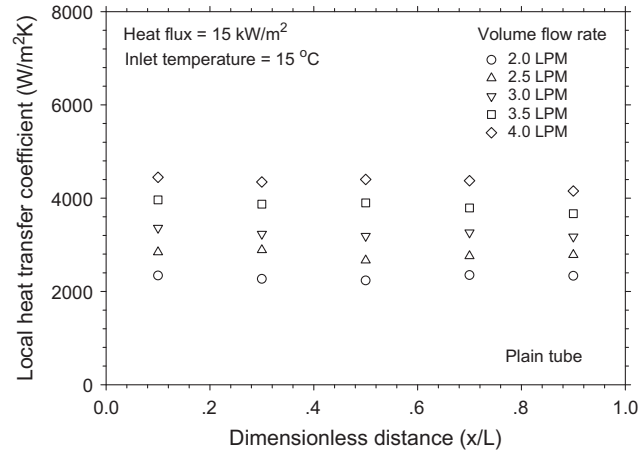

(a) For the common plain tube

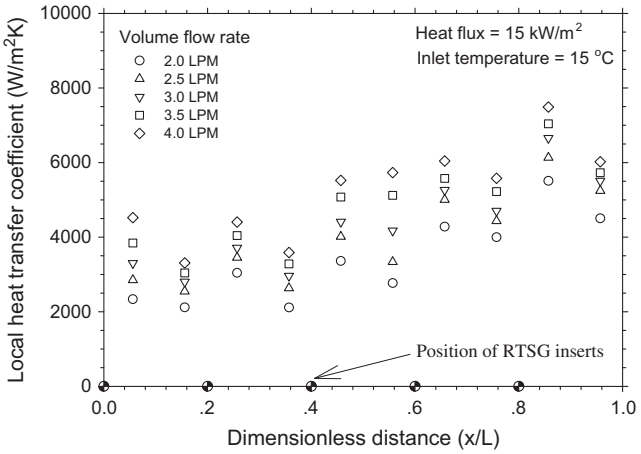

(b) For RTSG inserts

Fig. 10. Local heat transfer coefficient along the test section at different volume flow rates.

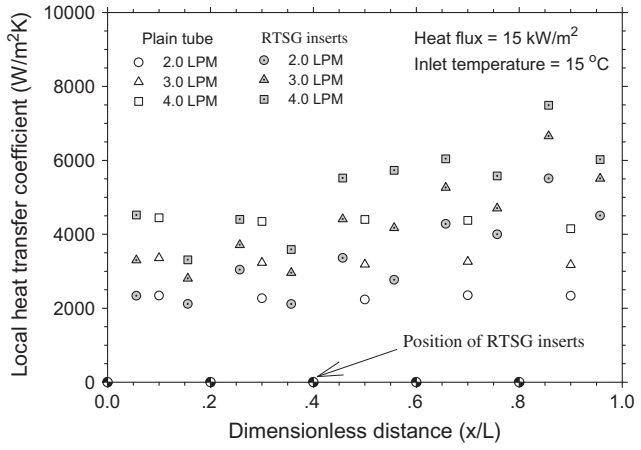

Fig. 11. Comparison of the local heat transfer coefficient between the plain tube and the RTSG inserts.

Fig. 11 also shows comparisons between the local heat transfer coefficients obtained from the common, plain tube and those obtained from the tube fitted with RTSG. The results indicated that the use of RTSG inserted inside a common, round tube provided

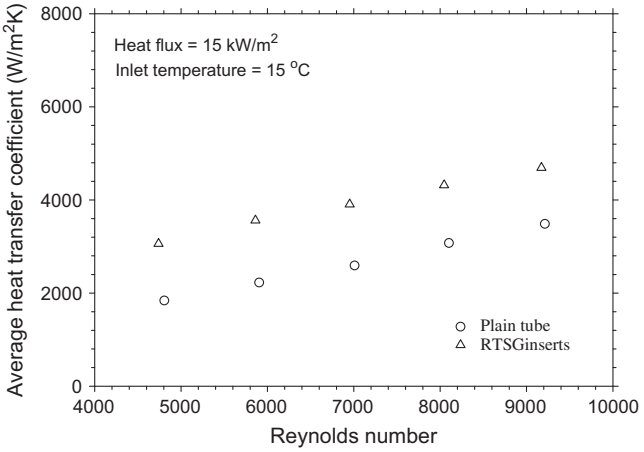

Fig. 12. Comparison of the average heat transfer coefficient between the plain tube and the RTSG inserts.

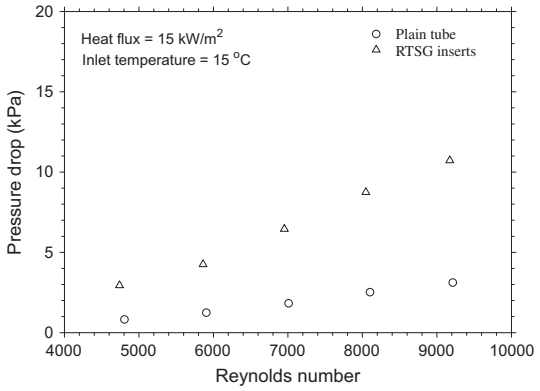

Fig. 13. Comparison of the pressure drop obtained from the common, plain tube and that of the RTSG inserts.

significantly higher heat transfer performance than the plain tube. The results were described in the above sub-section.

Similarly, a comparison of the average heat transfer coefficient between the common, plain tube and the RTSG inserts, as a function of the Reynolds number, is shown in Fig. 12. The measured results showed that the average heat transfer coefficient of the RTSG inserts was approximately 35–37% higher than that of the plain tube and increases with increasing Reynolds number. The reason for this was given in the preceding section. This result was due to the fact that the swirl flow was created after the RTSG in which led to enhance the heat transfer performance.

The pressure drops of the common plain, tube and the tube fitted with RTSG are shown in Fig. 13. The results show that the pressure drop of the RTSG inserts was larger than that of the plain tube by roughly 2.5 times. However, this value was still smaller than in the previous work of other researchers. This behavior, due to a freely rotating device, was used in the present study. Moreover, different distances (short-length tabulators) of RTSG were installed in the round tube, and its configuration could not resist the flow as could a propeller.

5. Conclusions

The heat transfer enhancement and pressure drop characteristics of a plain tube fitted with a rotating turbine-type swirl generator (RTSG) were experimentally investigated. This type of RTSG is

an innovative design that has not been seen in the previous research. The measured data for RTSG inserts were compared with the data for the common, plain tube. Important conclusions have been obtained and summarized as follows:

- The tube with RTSG inserts creates abnormal behaviors of the local heat transfer coefficients which increase after the flow passes the RTSG;
- the use of RTSG inserted into the round tube at different locations provided a significantly higher average heat transfer coefficient than that of the common, plain tube by roughly 35%;
- the wall temperatures and water temperature of the round tube with RTSG inserts were lower than those of the common, plain tube, and they significantly decreased after the fluid flowed past the RTSG; and
- the pressure drops of the tube with RTSG inserted were higher than those of the conventional, plain tube by approximately 2.5 times. However, this value was less than that seen in the previous literature, due to the freely rotating device used in the present study.

Acknowledgments

The authors would like to express their appreciation to the Office of Research, South-East Asia University, the Thailand Research Fund, the Office of the Higher Education Commission and the National Research University Project for providing financial support. The authors also wish to thank Mr. Arnont Kamlangsuea and Mr. Theindham Kaenak for their help during our study.

References

[1] R.J. Goldstein, W.E. Ibele, S.V. Patankar, T.W. Simon, T.H. Kuehn, P.J. Strykowski, K.K. Tamma, J.V.R. Heberlein, J.H. Davidson, J. Bischof, F.A. Kulacki, U. Kortshagen, S. Garrick, V. Srinivasan, Heat transfer—A review of 2003 literature, International Journal of Heat and Mass Transfer 49 (2006) 451–534.
[2] A. Garcia, P.G. Vicente, A. Viedma, Experimental study of heat transfer enhancement with wire coil inserts in laminar-transition-turbulent regimes at different Prandtl numbers, International Journal of Heat and Mass Transfer 48 (2005) 4640–4651.
[3] A. Tandiroglu, Effect of flow geometry parameters on transient heat transfer for turbulent flow in a circular tube with baffle inserts, International Journal of Heat and Mass Transfer 49 (2006) 1559–1567.
[4] P. Sivashanmugam, S. Suresh, Experimental studies on heat transfer and friction factor characteristics of turbulent flow through a circular tube fitted with regularly spaced helical screw-tape inserts, Applied Thermal Engineering 27 (2007) 1311–1319.
[5] S.W. Chang, T.L. Yang, J.S. Liou, Heat transfer and pressure drop in tube with broken twisted tape insert, Experimental Thermal and Fluid Science 32 (2007) 489–501.
[6] A. Garcia, J.P. Solano, P.G. Vicente, A. Viedma, Enhancement of laminar and transitional flow heat transfer in tubes by means of wire coil inserts, International Journal of Heat and Mass Transfer 50 (2007) 3176–3189.
[7] I. Kurtbas, A. Durmus, H. Eren, E. Turgut, Effect of propeller type swirl generators on the entropy generation and efficiency of heat exchangers, International Journal of Thermal Sciences 46 (2007) 300–307.
[8] B.A. Sarac, T. Bali, An experimental study on heat transfer and pressure drop characteristics of decaying swirl flow through a circular pipe with a vortex generator, Experimental Thermal and Fluid Science 32 (2007) 158–165.
[9] H. Gul, D. Evin, Heat transfer enhancement in circular tubes using helical swirl generator insert at the entrance, International Journal of Thermal Sciences 46 (2007) 1297–1303.
[10] M.A. Akhavan-Behabadi, R. Kumar, A. Mohammadpour, M. Jamali-Asthiani, Effect of twisted tape insert on heat transfer and pressure drop in horizontal evaporators for the flow of R-134a, International Journal of Refrigeration 32 (2009) 922–930.
[11] I. Kurtbas, F. Gulcimen, A. Akbulut, D. Buran, Heat transfer augmentation by swirl generators inserted into a tube with constant heat flux, International Communications in Heat and Mass Transfer 36 (2009) 865–871.
[12] M.A. Akhavan-Behabadi, R. Kumar, M.R. Salimpour, R. Azimi, Pressure drop and heat transfer augmentation due to coiled wire inserts during laminar flow of oil inside a horizontal tube, International Journal of Thermal Sciences 49 (2010) 373–379.
[13] A. Khali, A.E. Zohir, A.M. Farid, Heat transfer characteristics and friction of turbulent swirling air flow through abrupt expansion, American Journal of Scientific and Industrial Research 1 (2) (2010) 364–374.
[14] A.E. Zohir, A.A. Abdel Aziz, M.A. Habib, Heat transfer characteristics in a sudden expansion pipe equipped with swirl generators, International Journal of Heat and Fluid Flow 32 (2011) 352–361.
[15] E.Z. Ibrahim, Augmentation of laminar flow and heat transfer in flat tubes by means of helical screw-tape inserts, Energy Conversion and Management 52 (2011) 250–257.
[16] S.V. Patil, P.V. Vijay Babu, Performance comparison of twisted tape inserts in square duct, in: Proceedings of the International Conference on Advanced Science, Engineering and Information Technology (Malaysia), 2011, pp. 50–55.
[17] V. Gnielinski, New equations for heat and mass transfer in turbulent pipe and channel flow, International Chemical Engineering 16 (1976) 359–368.
[18] C.F. Colebrook, Turbulent flow in pipes, with particular reference to the transition between the smooth and rough pipe laws, Journal of the Institution of Civil Engineers, London 11 (1939) 133–156.

International Communications in Heat and Mass Transfer 40 (2013) 32–35

Contents lists available at SciVerse ScienceDirect

International Communications in Heat and Mass Transfer

journal homepage: www.elsevier.com/locate/ichmt

Application of two-phase vapor chamber technique for hard disk drive cooling of PCs ☆

P. Naphon [a,*], S. Wongwises [b], S. Wiriyasart [a]

[a] Thermo-Fluids and Heat Transfer Enhancement Lab. (TFHT), Department of Mechanical Engineering, Faculty of Engineering, Srinakharinwirot University, 63 Rangsit-Nakhornnayok Rd., Ongkharak, Nakhorn-Nayok, 26120, Thailand

[b] Fluid Mechanics, Thermal Engineering and Multiphase Flow Research Lab. (FUTURE), Department of Mechanical Engineering, King Mongkut's University of Technology Thonburi, 91 Suksawas 48, Bangmod, Bangkok 10140, Thailand

ARTICLE INFO

Available online 22 October 2012

Keywords:
Vapor chamber
Electronics cooling
Hard disk drive

ABSTRACT

The internal mechanism of the hard disk drive is seriously damaged if it is subjected to forces outside the environmental specifications. The results of the investigation on the thermal cooling of vapor chamber for cooling hard disk drive of the personal computer are presented. It was found that the vapor chamber cooling technique has a significant effect on the thermal cooling of a hard disk drive. The average hard disk drive temperature with the vapor chamber cooling system is 15.21%, which is lower than those without the vapor chamber cooling system. The results of this study are of technological importance for the efficient design of cooling systems of personal computers or electronic devices to enhance cooling performance.

1. Introduction

In recent years, the generated heat of PCs or electronic devices has been increasing along with the enhancement of CPU performance, memory capacity, and other devices. Therefore, the cooling system cools not only the CPU, but also others devices such as the HDD. In order to ensure the specified lifetime guarantee, most HDD suppliers do not allow the case temperature of the HDD to exceed 60 °C. For effective cooling the heat must spread to a larger surface area and away from those devices, as there is usually restricted space available. The heat transfer characteristics of the vapor chamber have been widely studied by researchers. Liu et al. [1] investigated on the startup of a novel two-phase cooling loop. Wang et al. [2] studied on the micro capillary pumped loop system for cooling high power devices. Xie et al. [3] experimentally investigated on a novel high-performance integrated heat pipe–heat sink for high-flux chip cooling. Hsieh et al. [4] examined the spreading thermal resistance of a flat vapor chamber. Vin and Astrain [5] studied on the development of a thermoelectric refrigerator with two-phase thermosyphons. Chang et al. [6] experimentally investigated the effects of the evaporation surfaces, fill ratios of working fluid and input heating powers on the thermal performance of the heat pipe cooling system with the thermal resistance model. Chen et al. [7] presented a numerical investigation of a plate-fin heat sink embedded with a vapor chamber, subject to the influence of concentrated heat sources. Zhang et al. [8] numerically and experimentally investigated on the flat two-phase thermosyphon. Vasiliev et al. [9] studied on the loop heat pipe for cooling of high-power electronic components. Ming et al. [10] experimentally and numerically investigated on the grooved vapor chamber. Tsai et al. [11] experimentally investigated on the effects of heat source, fill ratio of working fluid, and evaporator surface structure on the thermal performance of the vapor chamber. Wang et al. [12] considered the thermal performance of the vapor chamber for high-power LEDs. Wong et al. [13] studied on a novel vapor chamber with an inner groove surface. Wang et al. [14] analyzed the thermal characteristics for a board-level high performance package equipped with a vapor chamber. Li et al. [15,16] investigated the effects of the width, height and number of fins on the thermal performance of the vapor chamber. Reyes et al. [17] experimentally and theoretically studied on the vapor chamber based heat spreader. Attia et al. [18] experimentally investigated the effects of different working fluids, and different charge ratios on the thermal performance of the vapor chamber. Ji et al. [19] studied on the vapor chamber performance with sintering of the copper foam pieces. Choi et al. [20] studied a new CPU cooler design based on an active cooling heat sink combined with heat pipes.

As mentioned above, the numerous papers present studies on the heat transfer characteristics of the vapor chamber for cooling electronics devices. However, there are no researches present for the study on the thermal cooling of the hard disk drive (HDD). Therefore, the purpose of this paper is to study the thermal cooling of hard disk drives of personal computers with the vapor chamber. For computer applications, the operating temperatures are normally between 50 and 100 °C. Effects of the operating condition of a PC, and the fill ratio on the hard disk drive temperature are considered.

2. Experimental apparatus and method

The test loop consists of a set of PCs, and a set of vapor chamber cooling system and data acquisition system. A schematic diagram of

☆ Communicated by W.J. Minkowycz.

* Corresponding author.
E-mail address: paisarnn@swu.ac.th (P. Naphon).

0735-1933/$ – see front matter © 2012 Elsevier Ltd. All rights reserved.
http://dx.doi.org/10.1016/j.icheatmasstransfer.2012.10.014

the vapor chamber cooling system is shown in Fig. 1. The vapor chamber cooling system consists of the vapor chamber, the heat sink unit, and the axial fan unit. The vapor chamber is fabricated from a copper plate which consists of a bottom copper plate, a wick sheet, a sinter column, and a top copper plate. The wick sheet and the sinter column are fabricated from the copper powder. The bottom copper plate is the evaporator section that may be mounted on the hard disk drive of the PC to absorb the generated heat, and the other is the condenser section in which heat is transferred to the heat sink and air, respectively. In order to minimize thermal resistance between the HDD-vapor chamber and vapor chamber-heat sink unit, a thin film of high thermal conductivity grease is applied at their junction interface. The working fluid (de-ionized water) is evaporated on the heated side and condensed on the cooling side and then returns to the evaporator section under gravity. Type T copper-constantan thermocouples with an accuracy of 0.1% of full scale are employed to measure the temperatures. Four type T copper-constantan thermocouples are applied to measure the vapor chamber temperature (T_{vc}). Two thermocouples are applied to observe the air temperature in the computer case (T_{case}). A groove within the chamber walls is machined and the high conductivity cement is utilized to embed the thermocouples within the chamber wall. The hard disk drive temperature is measured by four type-T copper-constantan thermocouples (T_{hdd}). All thermocouples are pre-calibrated with a dry box temperature calibrator.

Experiments were conducted with various fill ratios and operating conditions of the PC. The supplied load into the hard disk drive was adjusted to achieve the desired level by setting the operating conditions of the hard disk drive: no load, 50%, and 100% operating loads. The temperatures at each position were recorded in a time period of 200 min. Data collection was carried out using a data acquisition system.

3. Results and discussion

The hard disk drive, with a 5.5-in. size, and two rotating disks with a nominal speed of 15,000 rpm, is tested in the present study. The hard disk drive was supported with insulation blocks under each corner.

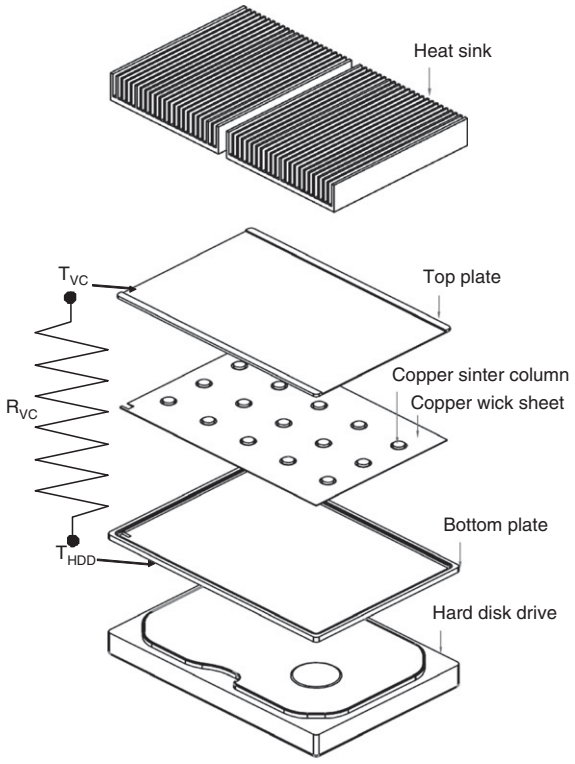

Fig. 1. Schematic diagram of the vapor chamber cooling system.

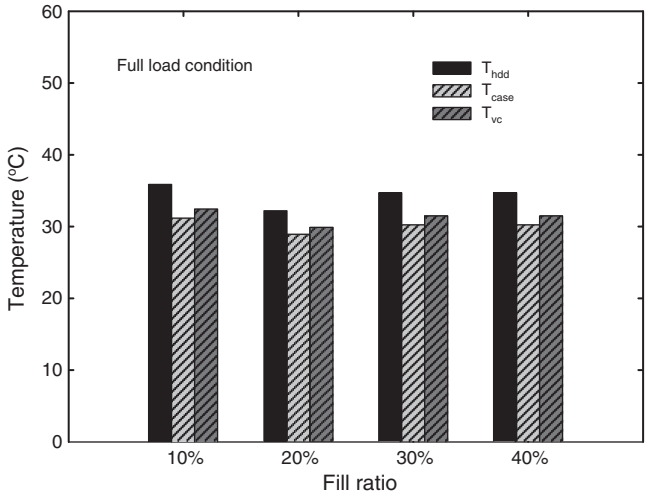

Fig. 2. Variation of HDD, vapor chamber and air temperatures for different fill ratios.

Both the top and bottom surfaces of the hard disk drive were exposed to the quiescent environment of the laboratory room with constant temperature of 26 °C. Initially experiments are performed without the vapor chamber cooling system which forms the basis for comparison of the results with the vapor chamber cooling technique. In order to ensure long life and reliable operations, hard disk drives are all designed to function only in specific temperature ranges. Fig. 2 shows the variation of the temperature of the HDD, vapor chamber and air in the computer temperatures for the different of fill ratios of the working fluid. For all fill ratios of the working fluid, it can be seen that the HDD temperatures are higher than those of the vapor chamber and air on the computer temperature. The full load operation of the HDD can be done by setting the writing data into both partitions of the HDD.

Fig. 3 shows the variation of the hard disk drive temperature for different fill ratios of the working fluid. It can be seen the HDD without the vapor chamber the cooling system gives a temperature higher than those with the vapor chamber cooling system. The values of the heat input to the system by various components depend on the operating condition of the hard disk drive. In general, the heat within the hard disk drive operation is mainly generated by the spindle motor, voice coil motor, magnetic read/write head sensor, and windage loss. Therefore, the HDD temperatures without the operating load are lower than those with the operating load. At a lower operating load, however, the heat is mainly transferred through natural

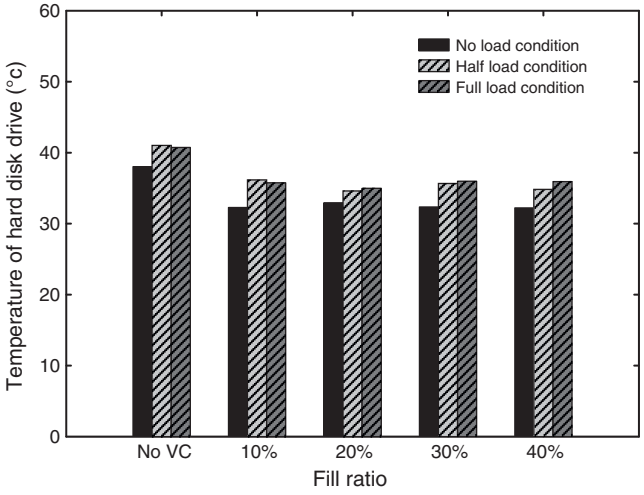

Fig. 3. Variation of HDD temperatures for different fill ratios.

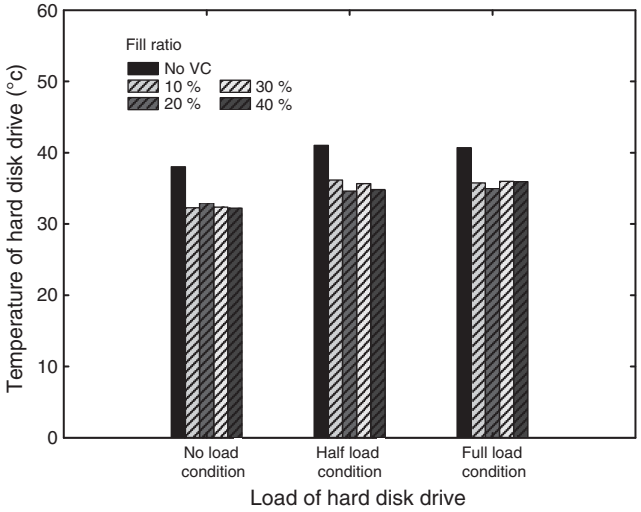

Fig. 4. Variation of HDD temperatures for different operating conditions of HDD.

convection. The increasing operating load induces a larger superheat, which activates and intensifies nucleate boiling and consequently leads to higher heat transfer efficiency. Therefore, a higher operating load of the hard disk drive has a slight effect on the hard disk drive temperature.

Fig. 4 shows the variation of hard disk drive temperature for different operating conditions of HDD. For a given operating load, it can be seen that the HDD temperatures of the HDD with the vapor chamber cooling system are lower than those without the vapor chamber cooling system. In addition, the hard disk drive with a fill ratio of 20% gives the lowest HDD temperature among the other fill ratios. It may be due to the low fill ratio that the dry out phenomenon might happen. The condensing liquid cannot promptly reflow at this operating load. For a higher fill ratio, there is a thin liquid film in the heat input region. The thermal resistance of the phase change heat transfer will also increase with the thickness of the liquid film. Therefore, the vapor chamber with a 20% fill ratio of the vapor chamber gives the lowest HDD temperature among the other fill ratios.

Fig. 5 shows the variation of vapor chamber temperature for different operating conditions of HDD. The average vapor chamber temperature is obtained from the top plate temperature and the bottom plate temperature of the vapor chamber. It can be seen that the fill

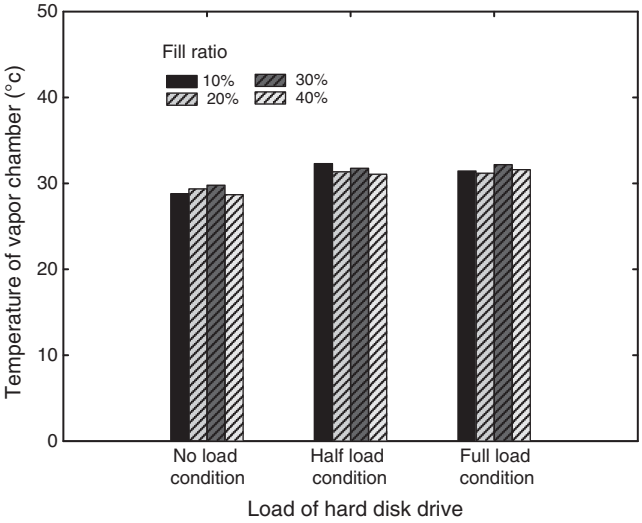

Fig. 5. Variation of vapor chamber temperatures for different operating conditions of HDD.

Table 1
Comparison of the energy consumption and hard disk drive temperature between the hard disk drive with and without vapor chamber cooling system.

Hard disk condition	Energy consumption	Hard disk drive temperature (°C)
HDD with 20% fill ratio for no load condition	+28.57%	−14.16%
HDD with 20% fill ratio for full load condition	+14.81%	−16.21%

ratio of the working fluid has a significant effect on the vapor chamber temperature. The heat phenomenon by the working fluid in the vapor chamber shows how the working fluid absorbs heat from heat source (HDD) and evaporates in the evaporator (bottom plate). The evaporating fluid moves toward the condenser, and then condenses in the condenser (top plate).

The HDD temperature and the energy consumption obtained from the HDD with the vapor chamber cooling system are compared with those without the vapor chamber cooling system. As seen in Table 1, the plus symbol represents the higher values while the minus symbol is represents the lower values as compared with those without the vapor chamber cooling system. It can be seen that the HDD temperatures obtained from the HDD with vapor chamber cooling system are lower than those without vapor chamber cooling system and with the same explanation as mentioned above. However, the energy consumption also increases.

4. Conclusions

Temperature is often quoted as the most important environmental factor affecting hard disk drive reliability. However, the space limitation and air cooling limitation are the encountered problems of the cooling system development of the hard disk drive or electronic devices. The vapor chambers have many advantages as compared to other cooling devices such as fans, thermoelectric modules, and liquid pump loop devices, which are that it has a simple structure, no moving parts and does not use electricity. In addition, selection of the working fluid is based on the operating temperature range of the applications. It is found that the HDD with the vapor chamber cooling system gives HDD temperatures lower than those without the vapor chamber cooling system.

Acknowledgments

The authors would like to express their appreciation to the Excellent Center for Sustainable Engineering (ECSE) of the Srinakharinwirot University (SWU) and the King Mongkut's University of Technology Thonburi (KMUTT) for providing financial support for this study. The authors also wish to acknowledge Fujikura Electronics (Thailand) Ltd. for their assistance in some of the vapor chamber samples.

References

[1] J. Liu, N.Q. Pei, K.H. Guo, Z.H. He, T.X. Li, J.M. Gu, Experimental investigation on startup of a novel two-phase cooling loop, Experimental Thermal and Fluid Science 32 (2008) 939–946.
[2] C.T. Wang, T.S. Leu, T.M. Lai, Micro capillary pumped loop system for a cooling high power device, Experimental Thermal and Fluid Science 32 (2008) 1090–1095.
[3] X.L. Xie, Y.L. He, W.Q. Tao, H.W. Yang, An experimental investigation on a novel high-performance integrated heat pipe–heat sink for high-flux chip cooling, Applied Thermal Engineering 28 (2008) 433–439.
[4] S.S. Hsieh, R.Y. Lee, J.C. Shyu, S.W. Chen, Thermal performance of flat vapor chamber heat spreader, Energy Conversion and Management 49 (2008) 1774–1784.
[5] J.G. Vin, D. Astrain, Development of a thermoelectric refrigerator with two-phase thermosyphons and capillary lift, Applied Thermal Engineering 28 (2008) 1514–1521.
[6] Y.W. Chang, C.H. Cheng, J.C. Wang, S.L. Chen, Heat pipe for cooling of electronic equipment, Energy Conversion and Management 49 (2008) 3398–3404.
[7] Y.S. Chen, K.H. Chien, T.C. Hung, C.C. Wang, Y.M. Ferng, B.S. Pei, Numerical simulation of a heat sink embedded with a vapor chamber and calculation of effective

thermal conductivity of a vapor chamber, Applied Thermal Engineering 29 (2009) 2655–2664.
[8] M. Zhang, Z. Liu, G. Ma, S. Cheng, Numerical simulation and experimental verification of a flat two-phase thermosyphon, Energy Conversion and Management 50 (2009) 1095–1100.
[9] L. Vasiliev, D. Lossouarn, C. Romestant, A. Alexandre, Y. Bertin, Y. Piatsiushyk, V. Romanenkov, Loop heat pipe for cooling of high-power electronic components, International Journal of Heat and Mass Transfer 52 (2009) 301–308.
[10] Z. Ming, L. Zhongliang, M. Guoyuan, The experimental and numerical investigation of a grooved vapor chamber, Applied Thermal Engineering 29 (2009) 422–430.
[11] T.E. Tsai, H.H. Wu, C.C. Chang, S.L. Chen, Two-phase closed thermosyphon vapor-chamber system for electronic cooling, International Communications in Heat and Mass Transfer 37 (2010) 484–489.
[12] J.C. Wang, R.T. Wang, T.L. Chang, D.S. Hwang, Development of 30 Watt high-power LEDs vapor chamber-based plate, International Journal of Heat and Mass Transfer 53 (2010) 3990–4001.
[13] S.C. Wong, K.C. Hsieh, J.D. Wu, W.L. Han, A novel vapor chamber and its performance, International Journal of Heat and Mass Transfer 53 (2010) 2377–2384.
[14] T.H. Wang, C.C. Lee, Y.S. Lai, Thermal characteristics evaluation for board-level high performance flip-chip package equipped with vapor chamber as heat spreader, Microelectronic Engineering 87 (2010) 2463–2467.
[15] H.Y. Li, M.H. Chiang, C.I. Lee, W.J. Yang, Thermal performance of plate-fin vapor chamber heat sinks, International Communications in Heat and Mass Transfer 37 (2010) 731–738.
[16] H.Y. Li, M.H. Chiang, Effects of shield on thermal-fluid performance of vapor chamber heat sink, International Journal of Heat and Mass Transfer 54 (2011) 1410–1419.
[17] M. Reyes, D. Alonso, J.R. Arias, A. Velazquez, Experimental and theoretical study of a vapour chamber based heat spreader for avionics applications, Applied Thermal Engineering 37 (2012) 51–59.
[18] A.A.A. Attia, B.T.A. El-Assal, Experimental investigation of vapor chamber with different working fluids at different charge ratios, Ain Shams Engineering Journal, 2 (2012) 289–297.
[19] X. Ji, J. Xu, A.M. Abanda, Copper foam based vapor chamber for high heat flux dissipation, Experimental Thermal and Fluid Science 40 (2012) 93–102.
[20] J. Choi, M. Jeong, J. Yoo, M. Seo, A new CPU cooler design based on an active cooling heat sink combined with heat pipes, Applied Thermal Engineering 44 (2012) 50–56.

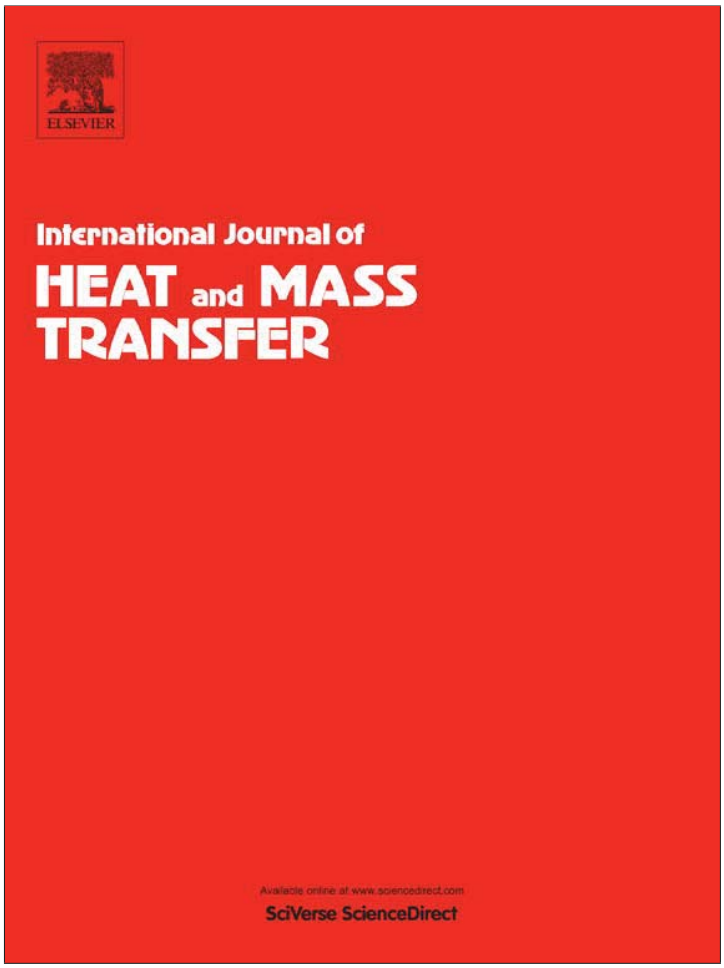

(This is a sample cover image for this issue. The actual cover is not yet available at this time.)

International Journal of Heat and Mass Transfer 59 (2013) 75–82

Contents lists available at SciVerse ScienceDirect

International Journal of Heat and Mass Transfer

journal homepage: www.elsevier.com/locate/ijhmt

Effect of fin pitches on the air-side performance of L-footed spiral fin-and-tube heat exchangers

Parinya Pongsoi [a], Patcharapit Promoppatum [a], Santi Pikulkajorn [b], Somchai Wongwises [a,c,*]

[a] Fluid Mechanics, Thermal Engineering and Multiphase Flow Research Lab (FUTURE), Department of Mechanical Engineering, Faculty of Engineering, King Mongkut's University of Technology Thonburi, Bangmod, Bangkok 10140, Thailand
[b] Somchai Industry Co., Ltd., Bangkok 10150, Thailand
[c] The Academy of Science, The Royal Institute of Thailand, Sanam Suea Pa, Dusit, Bangkok 10300, Thailand

ARTICLE INFO

Article history:
Received 24 August 2012
Received in revised form 15 November 2012
Accepted 21 November 2012

Keywords:
L-footed fin
Heat transfer
Heat exchanger
Air–water
Extended surface

ABSTRACT

The purpose of this experimental investigation is to investigate the effects of fin pitch (i.e., f_p of 2.4, 3.2, and 4.2 mm) on the air-side heat transfer performance and frictional characteristics of L-footed spiral fin-and-tube heat exchangers at high Reynolds numbers (Re_{dc}) of 4000–15,000. A determinant of the parallel cross-flow and the counter cross-flow is the flow arrangement of the test heat exchangers. Ambient air and hot water are used as a working fluid on the air- and the tube-side, respectively. The results indicate that the air-side heat transfer coefficient and Colburn factor are independent of fin pitch. However, fin pitch does have an influential effect on the average heat transfer rate, pressure drop, and friction factor. In terms of industrial applications, the correlation of the Colburn factor and friction factor are proposed for practical applications.

1. Introduction

The heat exchangers are used in two main methods of heat transfer (convection and conduction modes). Many types of heat exchangers are used in industrial applications, such as intercoolers, boilers, economizers, air and liquid pre-heaters, evaporating and condensing heat exchangers, etc. Fin and tube heat exchangers are among the more favored types of heat exchangers. This kind of heat exchanger is designed for enhancing heat transfer performance. This enhancement is very important for thermo-economic analysis. Moreover, this heat transfer enhancement is normally limited by the thermal resistance on the heat exchanger's air-side. Arguably, fin configuration improvement is one of the most effective ways to augment the heat transfer rate on heat exchangers' air-side.

Over the years, the spiral fin has been studied by a number of researchers. Some examples related to this subject can be found in [1–13].

Nuntaphan et al. [1] tested crimped spiral fin-and-tube heat exchangers to analyze the effect of tube arrangement, transverse tube pitch, fin pacing, tube diameter, and they proposed heat transfer and friction characteristics correlations under wet conditions at low Reynolds numbers. Wongwises and Naphon [2,3] studied the heat transfer characteristics and the performance of a spirally coiled finned tube heat exchanger under dry-surface and wet surface conditions. Moreover, they tested heat exchangers that rely on a crimped spiral finned tube. Then, Srisawad and Wongwises [4] tested the helically coiled crimped spiral finned tube heat exchanger, aiming on the heat transfer performance in dry-surface conditions. Pongsoi et al. [5–7] studied the effect of number of tube rows and fin pitches on the air-side heat transfer characteristics and the optimized fin pitch of crimped spiral fin-tube heat exchangers having multipass parallel and counter cross-flow under sensible heating conditions and purpose the ε-*NTU* relation equation for this new water flow arrangement. In addition, the correlation of Colburn factor (j) and friction factor (f) of crimped spiral fin-and-tube heat exchangers at high Reynolds number were proposed in this study. Hamakawa et al. [8] investigated the flow around the fin and vortex shedding from the fin tube by using smoke wire technique. According to results, the spiral fin seemed to have more heat transfer over the conventional circular fin by the influence of downstream rotational vortices. Lee et al. [9,10] studied the air-side heat transfer characteristics of spiral-type circular fin-tube heat exchangers under frosting and non-frosting conditions. They measured these characteristics by varying the fin pitches, the number of tube rows and the fin alignments. Kawaguchi et al. [11] studied the effects of fin pitches on the serrated finned tube bank on

* Corresponding author at: Fluid Mechanics, Thermal Engineering and Multiphase Flow Research Lab (FUTURE), Department of Mechanical Engineering, Faculty of Engineering, King Mongkut's University of Technology Thonburi, Bangmod, Bangkok 10140, Thailand. Tel.: +66 24709115.
E-mail address: somchai.won@kmutt.ac.th (S. Wongwises).

0017-9310/$ - see front matter © 2012 Elsevier Ltd. All rights reserved.
http://dx.doi.org/10.1016/j.ijheatmasstransfer.2012.11.071

Nomenclature

A	area, m^2
A_{min}	minimum free flow area, m^2
A_o	total surface area, m^2
A_p	cross-sectional or profile area of fin, m^2
Al	aluminum
c_P	specific heat at constant pressure, J/(kg K)
d_c	fin collar outside diameter, m
d_f	fin outside diameter, m
d_i	tube inside diameter, m
d_o	tube outside diameter, m
f	Fanning friction factor, dimensionless
f_p	fin pitch, m
f_t	fin thickness, m
G_c	mass flux of the air based on minimum free flow area, kg/m^2 s
H	height, m
h	heat transfer coefficient, $W/(m^2 K)$
I_0	modified Bessel function solution of the first kind, order 0
I_1	modified Bessel function solution of the first kind, order 1
j	Colburn factor, dimensionless
k	thermal conductivity, W/(m K)
K_0	modified Bessel function solution of the second kind, order 0
K_1	modified Bessel function solution of the second kind, order 1
L	length, m
m	mass flow rate, kg/s
M	data point
n_t	number of tubes in row
N_{row}	number of tube rows
NTU	number of transfer units, dimensionless
Nu	Nusselt number, dimensionless
P_L	longitudinal tube pitch, m
P_T	transverse tube pitch, m
Pr	Prandtl number, dimensionless
Q	heat transfer rate, W
r_o	radius of tip fin, m
r_i	radius of base fin, m
R	radius function in terms of the radius ratio, dimensionless
Re_{dc}	Reynolds number based on fin collar outside diameter (d_c)
T	temperature, °C
U	overall heat transfer coefficient, $W/(m^2 K)$
V_{fr}	air frontal velocity, m/s
V_{max}	maximum velocity across heat exchanger, m/s

Greek symbols

ε	heat exchanger effectiveness
η	fin efficiency
η_o	overall surface effectiveness
ρ	density, kg/m^3
σ	contraction ratio of cross-sectional area
μ	dynamic viscosity of air, Pa s
ϕ	combination of terms, dimensionless;
ψ	radius ratio
ΔP	pressure drop, Pa

Subscripts

1	air-side inlet
2	air-side outlet
a	air
ave	average
corr	correlation
c	multipass counter cross flow or cold fluid
exp	experiment
f	fin
h	hot fluid
i	tube-side
m	mean value
max	maximum
o	air-side
p	multipass parallel cross flow
pc	multipass parallel-and-counter cross flow
t	tube
w	water

the pressure drop characteristics for higher improvement of heat transfer than circular spiral finned tube. Næss [12] investigated the effects of tube layout and fin geometry on the heat transfer and pressure drop performance of serrated fin and tube heat exchangers. Moreover, Lemouedda et al. [13] studied the optimization of fin serration, fin twisting and the number of segments by numerical calculations for serrated spiral fin-and-tube heat exchangers.

The L-footed spiral fin is one of several types of fin configurations. The base of the fin has an L-shape, which provides a large contact area, ensuring a good path for heat transfer from the tube surface to the fin. The spiral fin seems to have a greater heat transfer coefficient than the conventional circular fin. The L-footed spiral fin-and-tube heat exchanger may be suitable for industrial processes that present a high risk of tube corrosion. Despite its importance in many applications, the air-side performance of L-footed spiral fin-and-tube heat exchangers has received little attention in the literature. To the best of our knowledge, Pongsoi et al. [14] is the only work dealing with this issue. In the present study, the primary concern is to study the heat transfer performance and frictional characteristics of L-footed spiral fin-and-tube heat exchangers at high Reynolds numbers in industrial applications. The effect of fin pitch on the performance of the L-footed spiral fin and tube heat exchangers, which have not yet appeared in the available literature, are presented.

2. Data reduction

In this experimental work, air and hot water were used as working fluids. The main components of the system were the heat exchanger, water flow loop, air supply, and the instrumentation and data acquisition system. In addition, detailed descriptions of the essential components are available from Pongsoi et al. [7].

The test samples are a type of fin-and-tube cross-flow heat exchanger. The copper tube is finned with an aluminum fin. Fig. 1 details the water-side circuit and the dimensions of the tested fin-and-tube heat exchangers. Additionally, the schematic diagram of the heat exchangers algorithm for multi-pass parallel cross-flow, multi-pass counter cross-flow, and multi-pass parallel and counter cross-flows ($N_{row} = 2$) are shown in the previous figure. For the present flow configuration, the heat exchanger's effectiveness lies between the multi-pass parallel cross-flow and the counter cross-flow. Finally, the geometric parameters of the heat exchangers are

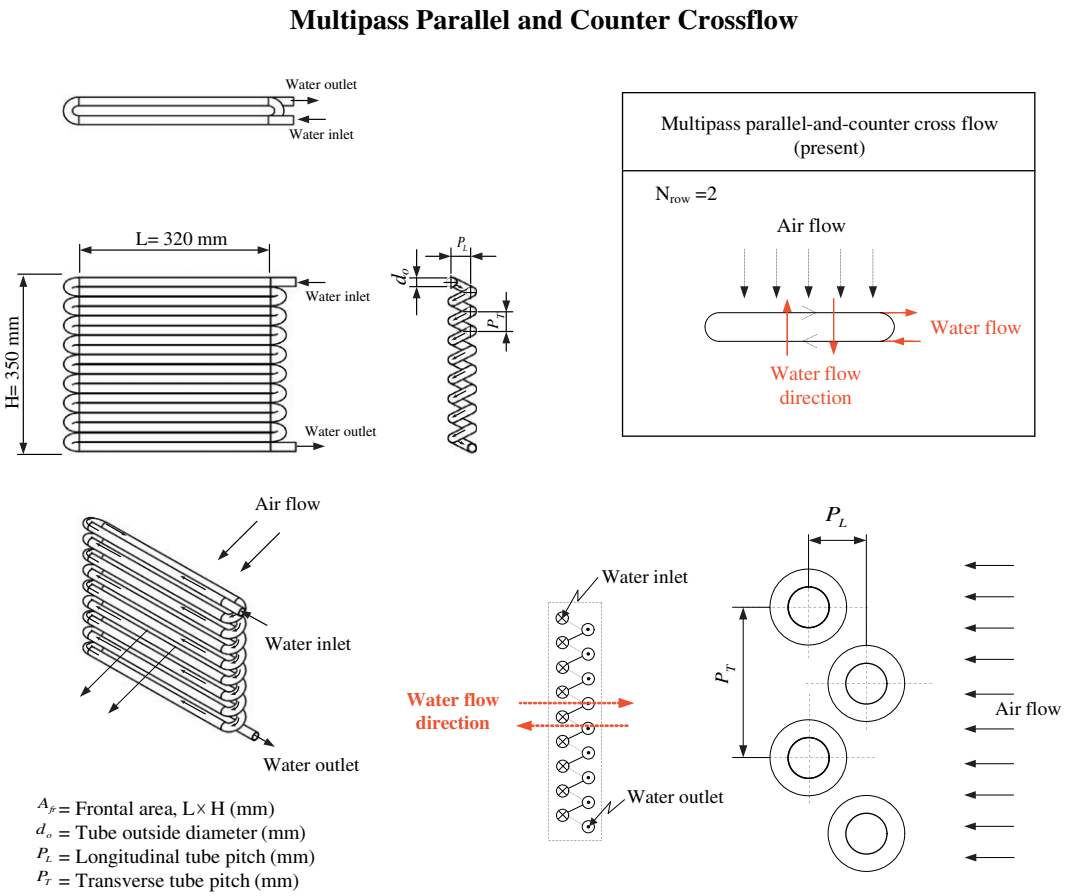

Fig. 1. Geometric details and schematic diagram of the heat exchangers algorithm for multipass parallel cross flow, multipass counter cross flow and multipass parallel-and-counter cross flow (× and ● signs indicate that water flows into or out of the paper, respectively).

Table 1
Detailed geometric parameters of the test samples.

No.	Fin type	d_i (mm)	d_c (mm)	d_f (mm)	P_L (mm)	P_T (mm)	f_t (mm)	n_t	N_{row}	Fin material	f_p (mm)
1	L-footed	13.5	16.85	34.8	35	39	0.25	9	2	Al	**2.4**
2	L-footed	13.5	16.85	34.8	35	39	0.25	9	2	Al	**3.2**
3	L-footed	13.5	16.85	34.8	35	39	0.25	9	2	Al	**4.2**

Remarks: d_f = Outside diameter of fin; d_i = Tube inside diameter; d_c = fin collar outside diameter; f_p = Fin pitch; f_t = Fin thickness; P_L = Longitudinal tube pitch; P_T = Transverse tube pitch; n_t = number of tubes in row; N_{row} = number of tube rows.
Notes: Tube layouts of all heat exchangers are staggered layout and all test sections have a tube outside diameter (d_o) of 16.35 mm.

summarized in Table 1, while the photographs and schematic diagram of L-footed spiral finned tube are shown in Fig. 2.

In the experiment, at a specific inlet water temperature, the water flow rate was fixed while the air flow rate was increased. The system was allowed to approach a steady state before any data was recorded under the experimental conditions shown in Table 2. After the system reached a steady state, the inlet and outlet temperatures of the air passing across the heat exchanger and the water flow rates were determined.

The overall heat transfer coefficient can be written in terms of the total resistance to heat transfer. This total resistance is the sum of the individual resistance values, as follows:

$$\frac{1}{UA} = \frac{1}{h_i A_i} + \frac{ln(d_o/d_i)}{2\pi k_t L} + \frac{ln(d_c/d_o)}{2\pi k_f L} + \frac{1}{\eta_o h_o A_o} \tag{1}$$

The multipass parallel and counter cross-flow used in this experiment is a combination of multipass parallel cross-flow and counter cross-flow. It may be suitable to use the average value of the heat exchanger effectiveness relations shown in Eq. (4). The air-side working fluid and the tube-side working fluid (water) are defined as fluid *A* and fluid B, respectively. It should be noted that the minimum heat capacity rate (C_{min}) is on the air-side (Fluid *A*). Therefore, the following relations are applied in the present calculation.

Multipass parallel cross-flow

For (N_{row} = 2);

$$\varepsilon_p = \left(1 - \frac{K}{2}\right)\left(1 - e^{-2K/C_A^*}\right), \quad K = 1 - e^{-NTU_A(C_A^*/2)} \tag{2}$$

Multipass counter cross-flow

For (N_{row} = 2);

$$\varepsilon_c = 1 - \left[\frac{K}{2} + \left(1 - \frac{K}{2}\right)e^{2K/C_A^*}\right]^{-1}, \quad K = 1 - e^{-NTU_A(C_A^*/2)} \tag{3}$$

where

$$\varepsilon_A = \frac{\varepsilon_p + \varepsilon_c}{2} \tag{4}$$

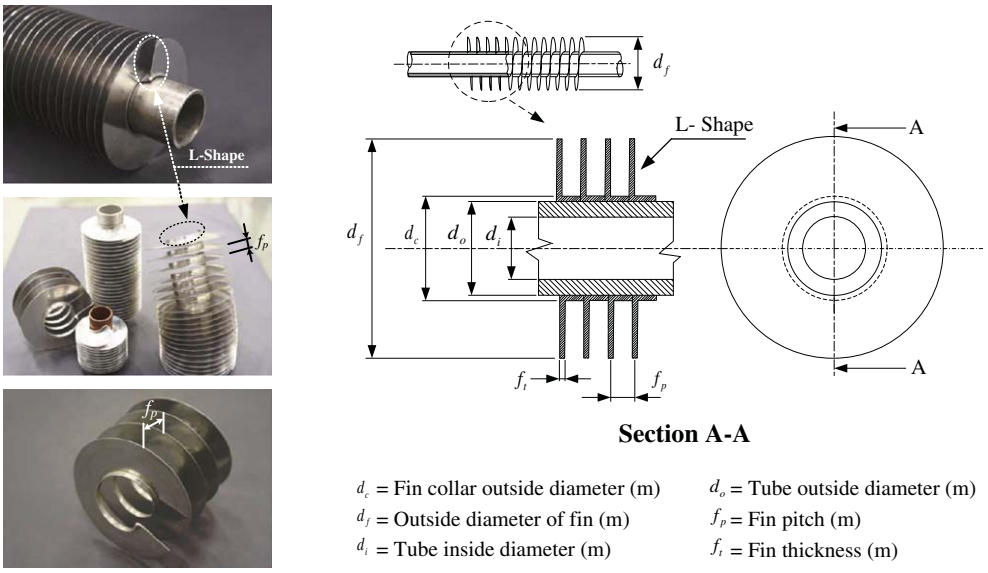

Fig. 2. Photographs and schematic diagram of L-footed spiral finned tube.

Table 2
Experimental conditions.

Inlet-air-dry bulb temperature, °C	31.5 ± 0.5
Inlet-air frontal velocity, m/s	2–8 or Re_{dc} (4000–15000)
Inlet-water temperature, °C	55–70
Water flow rate, LPM	12–14 or (0.2–0.233 kg/s)

Fluid A is mixed (C_{min}); Fluid B is unmixed (C_{max}).

$$\varepsilon_A = \varepsilon_B / C_A^* \tag{5}$$

$$C_A^* = \frac{C_A}{C_B} = \frac{1}{C_B^*}; \quad C^* \leqslant 1 \tag{6}$$

$$NTU_A = \frac{NTU_B}{C_A^*} \tag{7}$$

where $C^* = C_{min}/C_{max}$ is equal to C_c/C_h or C_h/C_c, depending on the value of the hot and cold fluid heat capacity rates.

$$C_{min} = C_h; \quad C_h < C_c \tag{8}$$

or

$$C_{min} = C_c; \quad C_c < C_h \tag{9}$$

as

$$Q_{max} = (mc_P)_c (T_{h1} - T_{c1}) \text{ if } C_c < C_h \tag{10}$$

or

$$Q_{max} = (mc_P)_h (T_{h1} - T_{c1}) \text{ if } C_h < C_c \tag{11}$$

$$\varepsilon = \frac{Q_{ave}}{Q_{max}} \tag{12}$$

The UA term in Eq. (1) is calculated by using Eq. (13):

$$UA = C_{min}(NTU) \tag{13}$$

The efficiency of a radial fin with a rectangular profile is determined by Gardner's [15] proposed method:

$$\eta = \frac{2\psi}{\phi(1+\psi)} \frac{I_1(\phi R_o)K_1(\phi R_i) - I_1(\phi R_i)K_1(\phi R_o)}{I_0(\phi R_i)K_1(\phi R_o) + I_1(\phi R_o)K_0(\phi R_i)} \tag{14}$$

where

$$\phi = (r_o - r_i)^{3/2} \left(\frac{2h_o}{k_f A_p}\right)^{1/2} \tag{15}$$

and where A_p is the area in the profile of the fin, as shown in Fig. 8:

$$A_p = f_t(r_o - r_i) \tag{16}$$

The parameters R_o, R_i are given in terms of the radius ratio (ψ):

$$R_o = \frac{1}{1-\psi} \tag{17}$$

and

$$R_i = \frac{\psi}{1-\psi} \tag{18}$$

where

$$\psi = \frac{r_i}{r_o} \tag{19}$$

The tube-side heat transfer coefficient (h_i) is calculated from the semi-empirical correlation of Gnielinski [16]:

$$h_i = \left(\frac{k_w}{d_i}\right) \frac{(Re_{di} - 1000)Pr(f_i/2)}{1 + 12.7\sqrt{f_i/2}\left(Pr^{2/3} - 1\right)} \tag{20}$$

where the friction factor is given by:

$$f_i = (1.58 \ln Re_{di} - 3.28)^{-2} \tag{21}$$

where $Re_{di} = \rho V d_i/\mu$.

The air-side heat transfer coefficient (h_o) can then be calculated from Eq. (1).

The heat transfer characteristics of the heat exchanger are presented in terms of non-dimensional groups:

$$Re_{dc} = \frac{\rho_a V_{max} d_c}{\mu} \tag{22}$$

$$j = \frac{Nu}{Re_{dc} Pr^{1/3}} = \frac{h_o}{\rho_a V_{max} c_P} (Pr)^{2/3} \tag{23}$$

The flow characteristics determined from the equation proposed by Kays and London [17] are given in terms of the fanning friction factor. The equation includes the entrance and exit pressure losses:

$$f = \left(\frac{A_{min}}{A_o}\right)\left(\frac{\rho_m}{\rho_1}\right)\left[\frac{2\Delta P \rho_1}{G_c^2} - (1+\sigma^2)\left(\frac{\rho_1}{\rho_2} - 1\right)\right] \tag{24}$$

where σ is the ratio of minimum free flow area to frontal area, A_o is the total heat transfer area, and A_{min} is the minimum free flow area.

The uncertainties are calculated from the root mean sum square method. The maximum uncertainties are 11% for the j-factor and 10% for the f-factor. The highest uncertainties were associated with the lowest Reynolds numbers.

3. Results and discussion

The primary analysis of the experimental data involved the energy balance between air and water. The energy balance related to systems, which investigated both heat transfer rates. The energy balance between the air and water associated with the L-footed spiral fin-and-tube heat exchangers had relative errors less than 5% (or $|Q_a - Q_w|/Q_{ave} < 0.05$). In addition, it is found that the ranges of the fin efficiency (η) and the heat exchanger effectiveness (ε) are 0.87–0.94 and 0.14–0.36, respectively. The air-side heat transfer and friction characteristics of all heat exchangers were examined in this experiment, which were presented in terms of the average heat transfer rate (Q_{ave}), air-side heat transfer coefficient (h_o), and pressure drop (ΔP) with air frontal velocity (V_{fr}). Moreover, the terms of a dimensionless number included the Colburn factor (j)

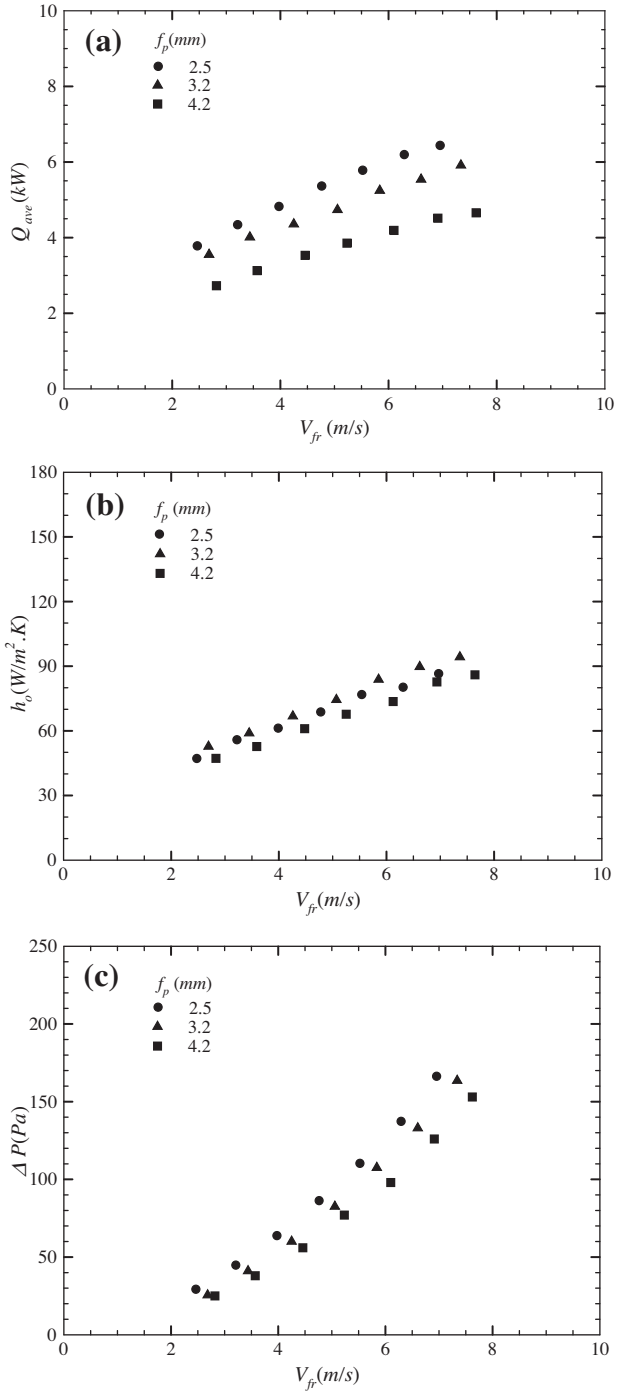

Fig. 3. Effect of fin pitches on the average heat transfer rate (a), heat transfer coefficient (b) and pressure drop (c) of L-footed spiral fin and tube heat exchangers. ($T_{w,in}$ = 65 °C/$m_{w,in}$ = 0.2 kg/s).

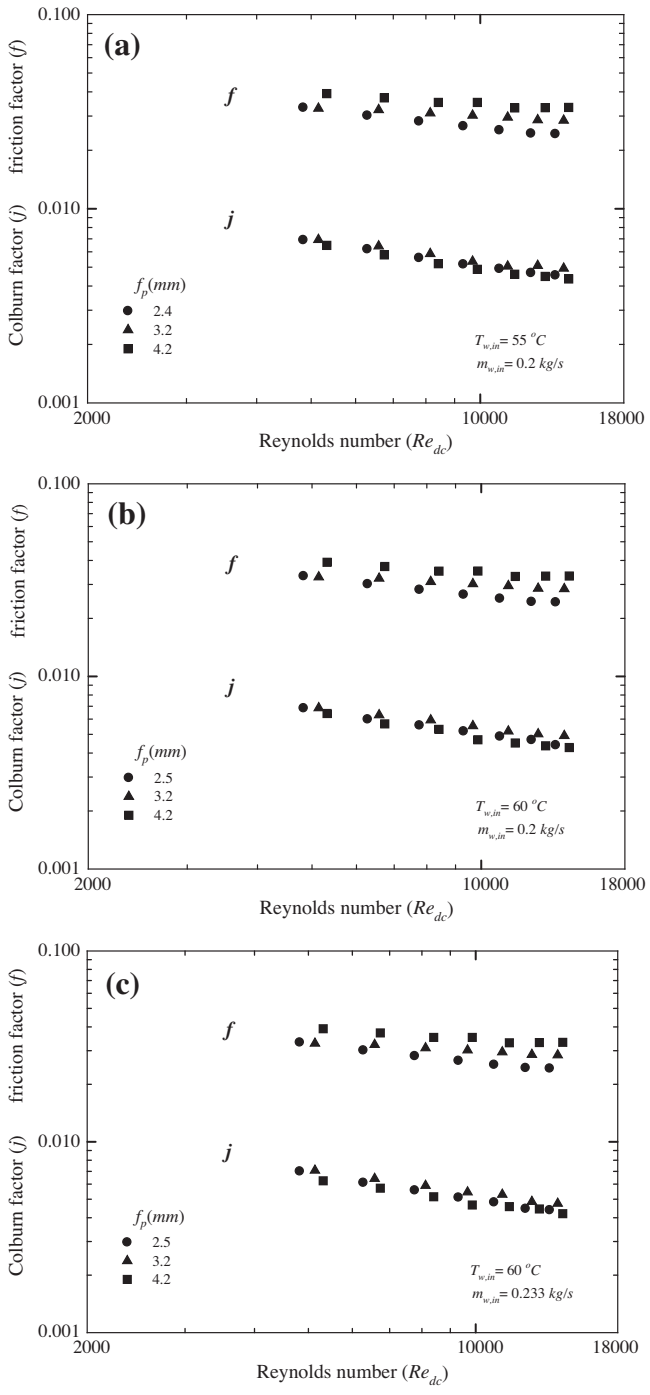

Fig. 4. Effect of fin pitches on the Colburn factor and friction factor at $T_{w,in}$ = 55 °C/$m_{w,i}$ = 0.2 kg/s (a), $T_{w,in}$ = 60 °C/$m_{w,in}$ = 0.2 kg/s (b) and $T_{w,in}$ = 60 °C/$m_{w,in}$ = 0.233 kg/s (c).

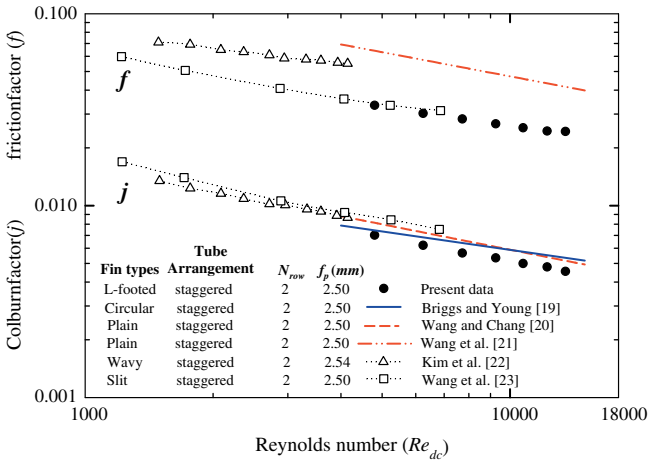

Fig. 5. Comparison of Colburn factor and friction factor between present data with correlational and experimental data of several fin types.

and friction factor (f) plotted against Re_{dc}, which was the Reynolds number based on the fin collar's outside diameter ($d_o + 2f_t$).

Fig. 3 shows the effect of the fin pitches on the average heat transfer rate, air-side heat transfer coefficient, and pressure drop for an aluminum fin with an outside fin collar diameter of 16.85 mm and outside fin diameter of 34.8 mm. This study has extended the fin pitches of 2.4, 3.2, and 4.2 mm. The results show that the average heat transfer rate, air-side heat transfer coefficient, and pressure drop increase with increasing air frontal velocity. Fig. 3(a) depicts the effect of fin pitches on average heat transfer rate. It was found that the average heat transfer rate of $f_p = 2.4$ and 3.2 mm are higher than that for $f_p = 4.2$ mm by about 37% and 26%, respectively, over the range of air frontal velocities. This is be because the surface heat transfer area of the smaller fin pitch is generally higher than that of larger ones which leads to the increasing of the average heat transfer rate.

However, Fig. 3(b) shows that the fin pitches had an insignificant effect on the air-side heat transfer coefficient. The present data correspond with Pongsoi et al. [5], who studied the effect of fin pitch on the air-side performance of the crimped spiral fin. Furthermore, as illustrated in Fig. 3(c), when f_p decreases from 4.2 to 2.4 mm, the pressure drop increases by about 18% (for $f_p = 3.2$) and 38% (for $f_p = 2.4$). The reason for this is increasing pressure blocking the flow area due to decreasing fin pitch.

The examination on the effect of fin pitch in the dimensionless terms is shown in Fig. 4. As expected, both the Colburn factor (j) and the friction factor (f) decrease with increasing Reynolds number over the range of operating conditions. The result shows that the fin pitch has a negligible effect on the Colburn factor (j), which is supported by findings in other research [5,6,18]. This phenomenon occurs because the high Reynolds number accentuates the good mixing, leading to better heat transfer performance, regardless of fin pitch changes.

In terms of the friction factor, it is clear that at Reynolds numbers greater than 6000, fin pitch has a significant effect (i.e., the friction factor is higher for a larger fin pitch than for a smaller fin pitch). According to Eq. (24), the ratio of minimum free-flow area and the total heat transfer area (A_{min}/A_o) and mass flux of air (G_c) showed that A_o significantly increases as fin pitch is changed from 4.2 to 3.2 or 2.4 mm. Conversely, the reduction of A_{min} is comparatively small. For these reasons, the friction factor signals a detectable rise for greater fin pitch. In summary, a large fin pitch increases the ratio of minimum free-flow area and the total heat transfer area (A_{min}/A_o), but decreases mass flux of the air (G_c). A low value of G_c will make the friction factor higher. It should be noted that the dynamic effects (A_{min}/A_o and G_c) have a more pronounced effect upon the friction factor than the air-side pressure drop (ΔP). Nevertheless, the effect of fin pitch on the friction factor tends to vanish at Reynolds numbers less than about 6000.

Initial validation comparison for the air-side heat transfer and flow characteristics of the performance of an L-footed spiral fin contrast with the performance of several plate fin types (circular [19], plain [20,21], wavy [22], and slit [23] fin) at high Reynolds numbers, as shown in Fig. 5. It was found that the present data and other fin types produce similar trends and slopes of the Colburn factor, which decrease with an increasing Reynolds number. However,

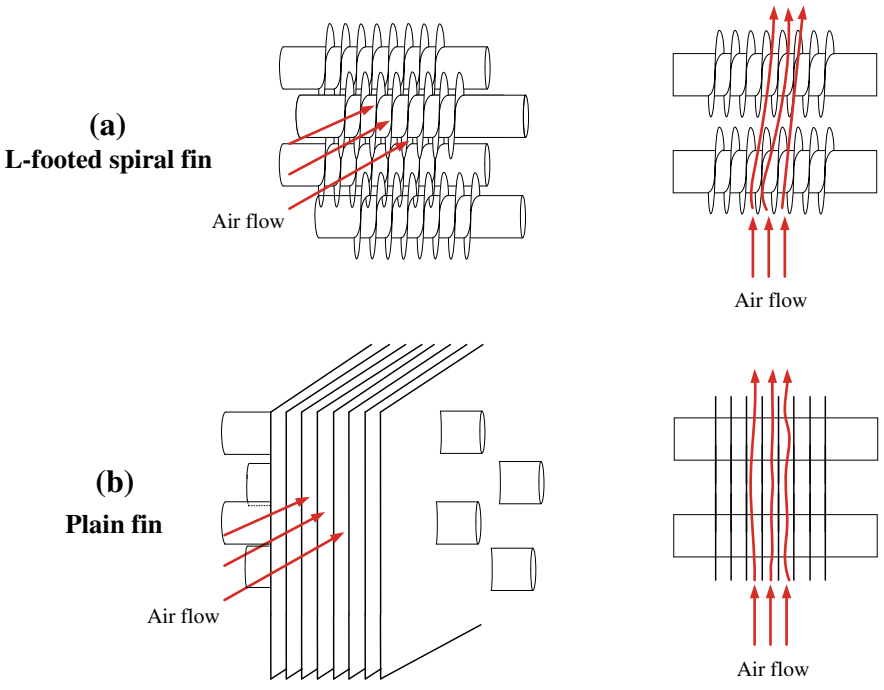

Fig. 6. Schematic showing the flow distribution (a) L-footed spiral fin (b) plain fin.

significant difference existed between an L-footed fin and plain fin on the friction factor. The authors found that the friction factor of L-footed spiral fins is about 80–90% different from the plain fin (conventional heat exchanger). As demonstrated in Fig. 6, the plain fin experiences single flow though channels. Therefore, this phenomenon might occur from the geometry of the plain fin that leads to contact surface friction greater than that of L-footed spiral fins.

Finally, empirical correlations for the Colburn factor (j) and the friction factor (f) are proposed in this study which parallel actual industrial applications operated at high Reynolds numbers. It must be noted that fin pitches have a negligible influence on the Colburn factor, as mentioned above. Thus, the fin pitch is not included in the Colburn factor correlation. The present data is correlated as suggested by Pongsoi et al. [6] in the form of $j = aRe_{dc}^{b}$ and $f = aRe_{dc}^{b}\left(\frac{f_p}{d_c}\right)^{c}$, where a, b, and c are the empirical constants obtained from least-square fitting of the experimental data. According to the data analysis, friction factor correlation was also associated with fin pitch. Therefore, the present correlation for f factor is modified by including the dimensionless fin pitch (f_p) normalized by the tube's outside diameter (d_c). The computable correlations for the Colburn and friction factors were suggested according to the form:

$$j_{corr} = 0.2150Re_{dc}^{-0.4059} \tag{25}$$

$$f_{corr} = 0.4852Re_{dc}^{-0.2156}\left(\frac{f_p}{d_c}\right)^{0.4771} \tag{26}$$

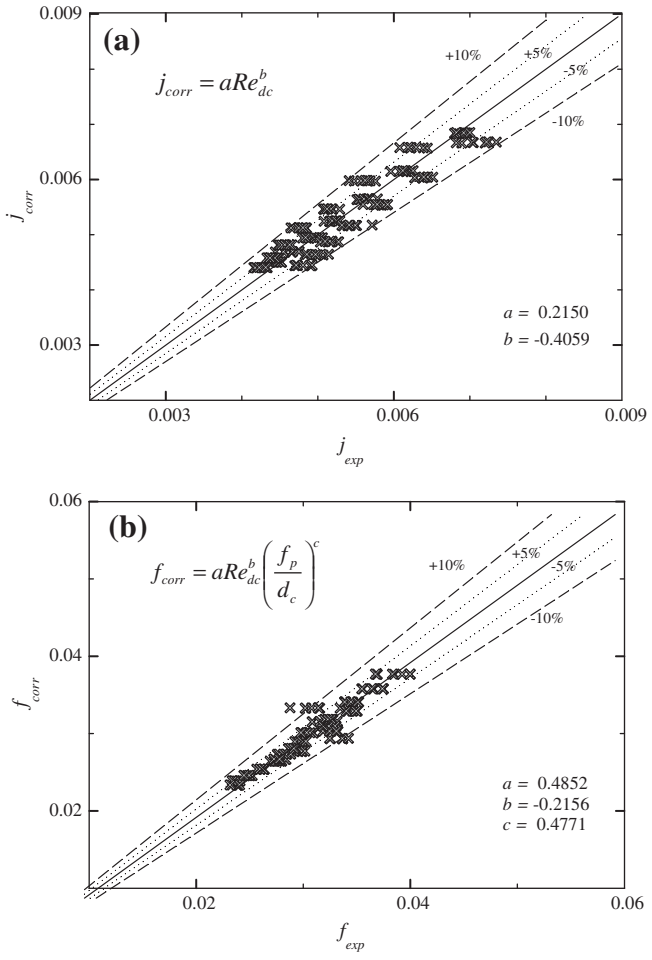

Fig. 7. Comparison of the proposed correlations with experimental data: (a) Colburn factor and (b) friction factor.

$$\text{Mean deviations} = \frac{1}{M}\left[\sum_{1}^{M}\frac{|\Phi_{corr} - \Phi_{exp}|}{\Phi_{exp}}\right] \times 100\% \tag{27}$$

Fig. 7 shows the comparison of the proposed correlations with experimental data. The correlation Eqs. (25) and (26) describe 100% and 95% of the j and f factors, respectively, to be within ±10%. The proposed heat transfer and friction correlations have mean deviations in Eq. (27) of 4.29% and 2.12%, respectively. However, these correlations can be used not only for parallel-and-counter cross-flow types of water flow arrangements, but also used for parallel cross-flow, counter cross-flow, and pure cross-flow.

4. Conclusions

This research determined the extent of the probable effect of fin pitch on the heat transfer performance of L-footed spiral fin-and-tube heat exchangers. Total test sections have a fin thickness of 0.25 mm, outside fin diameter (d_f) of 34.8 mm, two tube rows (N_{row}) and various fin pitches from 2.4, 3.2, and 4.2 mm (i.e., 10, 8, and 6 fpi, respectively), which are the manufacturing limitations for this kind of fin. The test samples were multi-pass parallel-and-counter cross-flows arrangement under sensible heating conditions and examined at a high Reynolds number (4000–15,000) based on the fin collar's outside diameter. In summary, the following major conclusions emerged from this study:

- It was confirmed that the average heat transfer rate, air-side heat transfer coefficient, and pressure drop increase with increasing Reynolds numbers. In addition, the effect of fin pitch on average heat transfer rate and pressure drop were considered significant. On the contrary, results suggest that the air-side heat transfer coefficient is independent of fin pitch.
- Fin pitch has no significant effect on the Colburn factor (j factor) at high Reynolds numbers (4000–15,000).
- The effect of fin pitch on the friction factor is negligible at Reynolds numbers lower than 6000. In other words, a detectable increment in friction factor is found for greater fin pitch when the Reynolds number is more than 6000.
- A correlation is proposed for the Colburn factor (j) and friction factor (f) for L-footed spiral fin-and-tube heat exchangers at high Reynolds number. The mean deviations of the proposed Colburn and friction factors correlations are 4.29% and 2.12%, respectively.
- The authors hope that future research will use this study as a foundation for enhancing our understanding of the effect of fin pitch on L-footed spiral fin-and-tube heat exchangers.

Acknowledgments

The authors are indebted to the Thailand Research Fund, the Office of the Higher Education Commission and the National Research University Project for supporting this study.

References

[1] A. Nuntaphan, T. Kiatsiriroat, C.C. Wang, Heat transfer and friction characteristics of crimped spiral finned heat exchangers with dehumidification, Appl. Therm. Eng. 25 (2005) 327–340.
[2] S. Wongwises, P. Naphon, Heat transfer characteristics of a spiral-coil, finned tube heat exchanger under dry-surface conditions, Heat Transfer Eng. 27 (1) (2006) 25–34.
[3] S. Wongwises, P. Naphon, Thermal performance of a spiral-coil finned tube heat exchanger under wet-surface conditions, J. Mech. Sci. Technol. 20 (2) (2006) 212–226.
[4] K. Srisawad, S. Wongwises, Heat transfer characteristics of a new helically coiled crimped spiral finned tube heat exchanger, Heat Mass Transfer 45 (4) (2009) 381–391.

[5] P. Pongsoi, S. Pikulkajorn, C.C. Wang, S. Wongwises, Effect of fin pitches on the air-side performance of crimped spiral fin-and-tube heat exchangers with a multipass parallel and counter cross-flow configuration, Int. J. Heat Mass Transfer 54 (9–10) (2011) 2234–2240.
[6] P. Pongsoi, S. Pikulkajorn, C.C. Wang, S. Wongwises, Effect of number of tube rows on the air-side performance of crimped spiral fin-and-tube heat exchangers with a multipass parallel and counter cross-flow configuration, Int. J. Heat Mass Transfer 55 (4) (2012) 1403–1411.
[7] P. Pongsoi, S. Pikulkajorn, S. Wongwises, Effect of fin pitches on the optimum heat transfer performance of crimped spiral fin-and-tube heat exchangers, Int. J. Heat Mass Transfer 55 (23–24) (2012) 6555–6566.
[8] H. Hamakawa, K. Nakashima, T. Kudo, E. Nishida, T. Fukano, Vortex shedding from a circular cylinder with spiral fin, J. Fluid Sci. Technol. 3 (6) (2008) 787–795.
[9] M. Lee, T. Kang, Y. Kim, Air-side heat transfer characteristics of spiral-type circular fin-and-tube heat exchangers, Int. J. Refrig. 33 (2) (2010) 313–320.
[10] M. Lee, T. Kang, Y. Joo, Y. Kim, Heat transfer characteristics of spirally-coiled circular fin-tube heat exchangers operating under frosting conditions, Int. J. Refrig. 34 (1) (2011) 328–336.
[11] K. Kawaguchi, K. Okui, Y. Asai, Y. Hasegawa, Effects of serrated fin and fin pitch on pressure drop of the finned tube banks, Turbomachinery 32 (2004) 551–559.
[12] E. Næss, Experimental investigation of heat transfer and pressure drop in serrated-fin tube bundles with staggered tube layouts, Appl. Therm. Eng. 30 (2010) 1531–1537.
[13] A. Lemouedda, A. Schmid, E. Franz, M. Breuer, A. Delgado, Numerical investigations for the optimization of serrated finned-tube heat exchangers, Appl. Therm. Eng. 31 (2011) 1393–1401.
[14] P. Pongsoi, S. Pikulkajorn, S. Wongwises, Experimental study on the air-side performance of a multipass parallel and counter cross-flow L-footed spiral fin-and-tube heat exchanger, Heat Transfer Eng. 33 (15) (2012) 1251–1263.
[15] K.A. Gardner, Efficient of extended surface, ASME Trans. 67 (1945) 621.
[16] V. Gnielinski, New equation for heat and mass transfer in turbulent pipe and channel flow, Int. Chem. Eng. 16 (1976) 359–368.
[17] W.M. Kays, A. London, Compact Heat Exchangers, third ed., Mcgraw-Hill, New York, 1984.
[18] S. Wongwises, Y. Chokeman, Effect of fin pitch and number of tube rows on the air side performance of herringbone wavy fin and tube heat exchangers, Energy Convers. Manage. 46 (2005) 2216–2231.
[19] D.E. Briggs, E.H. Young, Convective heat transfer and pressure drop of air flowing across triangular pitch banks of finned tubes, Chem. Eng. Prog. Symp. Ser. 59 (41) (1963) 1–10.
[20] C.C. Wang, C.-T. Chang, Heat and mass transfer for plate fin-and-tube heat exchangers with and without hydrophilic coating, Int. J. Heat Mass Transfer 41 (1998) 3109–3120.
[21] C.C. Wang, Y.J. Chang, Y.C. Hsieh, Y.T. Lin, Sensible heat and friction characteristics of plate fin-and-tube heat exchangers having plane fins, Int. J. Refrig. 19 (4) (1996) 223–230.
[22] N.H. Kim, J.H. Ham, J.P. Cho, Experimental investigation on the airside performance of fin-and-tube heat exchangers having herringbone wave fins and proposal of a new heat transfer and pressure drop correlation, J. Mech. Sci. Technol. 22 (2008) 545–555.
[23] C.C. Wang, W.H. Tao, C.J. Chang, An investigation of the airside performance of the slit fin-and-tube heat exchangers, Int. J. Refrig. 22 (1999) 595–603.

Experimental Heat Transfer: A Journal of Thermal Energy Generation, Transport, Storage, and Conversion

Publication details, including instructions for authors and subscription information:
http://www.tandfonline.com/loi/ueht20

Experimental Study on Evaporative Heat Transfer and Pressure Drop of R-134a Flowing Downward Through Vertical Corrugated Tubes with Different Corrugation Pitches

K. Aroonrat [a] , A. S. Dalkilic [b] & S. Wongwises [a c]

[a] Fluid Mechanics, Thermal Engineering and Multiphase Flow Research Lab (FUTURE), Department of Mechanical Engineering, Faculty of Engineering, King Mongkut's University of Technology Thonburi, Bangmod, Bangkok, Thailand

[b] Heat and Thermodynamics Division, Department of Mechanical Engineering, Yildiz Technical University (YTU), Yildiz, Besiktas, Istanbul, Turkey

[c] The Academy of Science, The Royal Institute of Thailand, Sanam Suea Pa, Dusit, Bangkok, Thailand

To cite this article: K. Aroonrat , A. S. Dalkilic & S. Wongwises (2013): Experimental Study on Evaporative Heat Transfer and Pressure Drop of R-134a Flowing Downward Through Vertical Corrugated Tubes with Different Corrugation Pitches, Experimental Heat Transfer: A Journal of Thermal Energy Generation, Transport, Storage, and Conversion, 26:1, 41-63

To link to this article: http://dx.doi.org/10.1080/08916152.2011.631080

Experimental Heat Transfer, 26:41–63, 2013

ISSN: 0891-6152 print/1521-0480 online
DOI: 10.1080/08916152.2011.631080

EXPERIMENTAL STUDY ON EVAPORATIVE HEAT TRANSFER AND PRESSURE DROP OF R-134a FLOWING DOWNWARD THROUGH VERTICAL CORRUGATED TUBES WITH DIFFERENT CORRUGATION PITCHES

K. Aroonrat,[1] A. S. Dalkilic,[2] and S. Wongwises[1,3]

[1]Fluid Mechanics, Thermal Engineering and Multiphase Flow Research Lab (FUTURE), Department of Mechanical Engineering, Faculty of Engineering, King Mongkut's University of Technology Thonburi, Bangmod, Bangkok, Thailand

[2]Heat and Thermodynamics Division, Department of Mechanical Engineering, Yildiz Technical University (YTU), Yildiz, Besiktas, Istanbul, Turkey

[3]The Academy of Science, The Royal Institute of Thailand, Sanam Suea Pa, Dusit, Bangkok, Thailand

This study reports an experimental investigation of evaporative heat transfer and pressure drop of R-134a flowing downward inside vertical corrugated tubes with different corrugation pitches. The double tube test section is 0.5 m long with refrigerant flowing in the inner tube and hot water flowing in the annulus. The inner tubes are comprised of one smooth tube and three corrugated tubes with different corrugation pitches of 6.35, 8.46, and 12.7 mm. The test runs are performed at evaporating temperatures of 10°C, 15°C, and 20°C; heat fluxes of 20, 25, and 30 kW/m^2; and mass fluxes of 200, 300, and 400 kg/m^{2}s. The experimental data obtained from the smooth tube are plotted with flow pattern map for vertical flow. Comparisons between smooth and corrugated tubes on the heat transfer and pressure drop are also discussed. It is observed that the heat transfer coefficient and frictional pressure drop obtained from the corrugated tubes are higher than those from the smooth tube. Furthermore, the heat transfer coefficient and frictional pressure drop increase as the corrugation pitch decreases. The maximum heat transfer enhancement factor and penalty factor are up to 1.22 and 4.0, respectively.

Keywords vertical, evaporative, heat transfer, pressure drop, corrugated tube

INTRODUCTION

Heat exchangers are devices used to implement the exchange of heat between two fluids that are at different temperatures and separated by a solid wall. They are commonly used in a wide range of applications, such as refrigeration and air-conditioning systems, power plants, and the chemical process industry. The aim in designing a heat exchanger is to reduce the heat transfer surface area required for a given application and thus reduce the heat exchanger size and material cost or to increase the heat

Received 6 September 2011; accepted 13 September 2011.

Address correspondence to S. Wongwises, Department of Mechanical Engineering, Faculty of Engineering, King Mongkut's University of Technology Thonburi, 126 Pracha-utid Road, Bangmod, Bangkok 10140, Thailand. E-mail: somchai.won@kmutt.ac.th

NOMENCLATURE

A	surface area of the test section (m^2)
c_p	specific heat at constant pressure (J/kg K)
d	tube diameter (m)
e	depth of corrugation (mm)
f	friction factor
g	gravitational acceleration (m/s^2)
G	mass flux (kg/m^2s)
h	heat transfer coefficient (W/m^2K)
i	specific enthalpy (J/kg)
i_{fg}	specific enthalpy of vaporization (J/kg)
J_g	superficial gas velocity, Gx/ρ_g (m/s)
J_l	superficial liquid velocity, $G(1-x)/\rho_l$ (m/s)
k	thermal conductivity (W/m K)
m	mass flow rate (kg/s)
p	pitch of corrugation (mm)
P	pressure (Pa)
Q	heat transfer rate (W)
q''	heat flux (kW/m^2)
Re	Reynolds number
T	temperature (°C)
x	vapor quality
z	axial coordinate (m)

Greek Symbols

α	void fraction
ΔP	pressure drop (Pa/m)
θ	helix angle (°)
μ	dynamic viscosity (kg/m s)
ρ	density (kg/m^3)

Subscripts

avg	average
eq	equivalent
F	frictional term
g	gas/vapor
G	gravitational term
i	inside
in	inlet
l	liquid
M	momentum term
o	outside
out	outlet
ph	pre-heater
ref	refrigerant
sat	saturation
tp	two-phase
TS	test section
w	water
wi	inner wall

exchanger effectiveness for a given surface area. In recent years, many researchers use the heat transfer enhancement techniques to improve the performance of the heat exchanger. In general, heat transfer enhancement techniques can be categorized as active and passive methods. Active methods are those that use the addition of external power—such as electric field, mechanical vibration, and injection—to facilitate the desired flow modification and concomitant improvement in the rate of heat transfer. Passive methods employ special surface geometries, such as rough surfaces, extended surfaces, and swirl flow devices. Rough surfaces are utilized in many configurations to promote turbulence rather than increase the heat transfer area. A corrugated tube has corrugation on the surface to increase the heat transfer coefficient by mixing the flow boundary layer and increasing the turbulence level of fluid flow.

In past decades, many researchers have thoroughly analyzed the heat transfer and flow characteristics of refrigerants in a horizontal smooth tube. Heat transfer enhancement of refrigerant using horizontal enhanced tubes has been the subject of some research, for example, Thors and Bogart [1]. However, there are not many investigations concerning the heat transfer and pressure drop of refrigerant in vertical tubes. Several experimental studies have been performed on condensation heat transfer and flow characteristics of refrigerant in vertical tube (Briggs et al. [2], Ma et al. [3], and Dalkilic et al. [4–8]). Publications on boiling heat transfer and flow characteristics of refrigerant flow in vertical tubes are summarized as follows.

Shah [9] proposed equations to fit his chart correlation, used for the estimation of heat transfer coefficients during saturated boiling of water, R-11, R-12, R-22, R-113, and cyclohexanein tubes and annuli. The correlation was shown to be applicable to both horizontal and vertical tubes. Gungor and Winterton [10] presented a new general correlation for forced-convection boiling that has been developed with a large data bank. This data bank consists of more than 4,300 data points for water, refrigerants, and ethylene glycol, covering 7 fluids and 28 authors, mostly for saturated boiling in vertical and horizontal tubes. Kandlikar [11] proposed the correlation for predicting saturated flow boiling heat transfer coefficients inside horizontal and vertical tubes. The correlation has been developed with 5,246 data points for water, refrigerants, and cryogenic fluids from 24 experimental investigations. Lee and Chang [12] investigated the heat transfer characteristics in the post-dryout region for the boiling of up-flow of R-134a in vertical smooth tubes and rifled tubes. Aroonrat and Wongwises [13] investigated the heat transfer and friction characteristics of pure refrigerant R-134a during evaporation inside vertical corrugated tubes. One smooth tube and two corrugated tubes were tested.

Among the above-described works, most experimental investigations focused on the heat transfer and flow characteristics of refrigerant flow inside vertical smooth tubes. There have been some works dealing with the flow in vertical enhanced tubes. In addition, there has been only one work—Aroonrat and Wongwises [13]—concerning the heat transfer and flow characteristics of R-134a during downward evaporation inside vertical corrugated tubes. Although some information is currently available, there still remains room for further research. In particular, the effects of corrugation pitch on the evaporative heat transfer and pressure drop characteristics of R-134a flow through vertical corrugated tubes remain unstudied. As a consequence, the objective of this current work is to study the effect of corrugation pitch on the evaporative heat transfer and pressure drop characteristics of R-134a flowing downward through vertical corrugated tubes. This article presents experimental data that have never been seen before on heat transfer and pressure drop.

EXPERIMENTAL APPARATUS AND METHOD

Figure 1 shows a schematic diagram of the test apparatus. The refrigerant loop consists of a pre-heating loop, test section, heating loop, and chilling loop. The refrigerant is forced by a gear pump controlled by an inverter. The refrigerant then passes through a filter/dryer, a refrigerant flow meter, a pre-heater, and a sight glass, and then enters the test section. The pre-heater controls the inlet quality before entering the test section; it consists of a spiral counter-flow tube-in-tube heat exchanger that is designed to supply heat to prepare an inlet quality for the vaporization of the refrigerant. Leaving the test section, the refrigerant vapor then condenses inside a sub-cooler and is collected in a receiver. After exiting the chilling loop, the refrigerant returns from a two-phase refrigerant to a sub-cooled state. Finally, the refrigerant returns to the refrigerant pump, completing the cycle.

Details of the test section are shown schematically in Figure 2. The test section is a vertical counter-flow double-tube heat exchanger with refrigerant flowing downward in the inner tube and heating water flowing upward in the annulus. Four different inner copper tubes, which are one smooth tube and three corrugated tubes having different corrugation pitches, are tested. The inner diameter and outer diameter of the inner tube

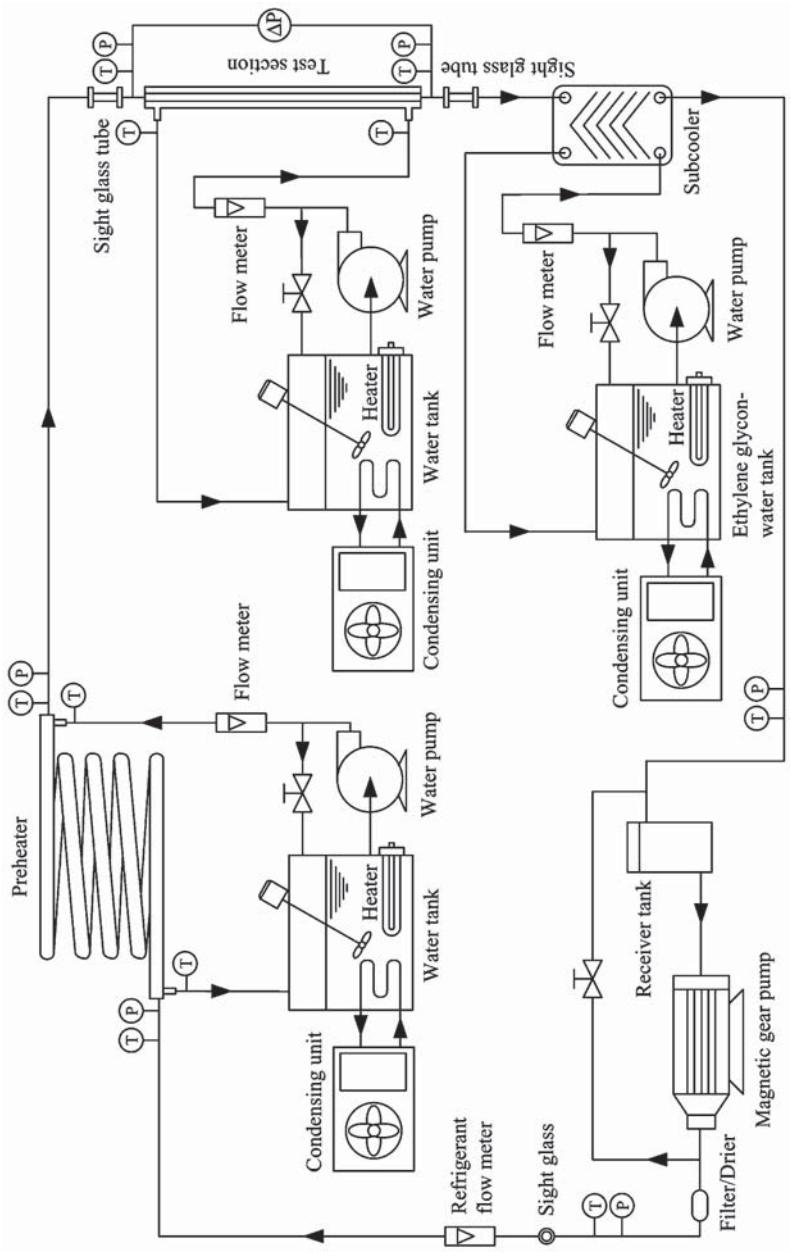

Figure 1. Schematic diagram of the experimental apparatus.

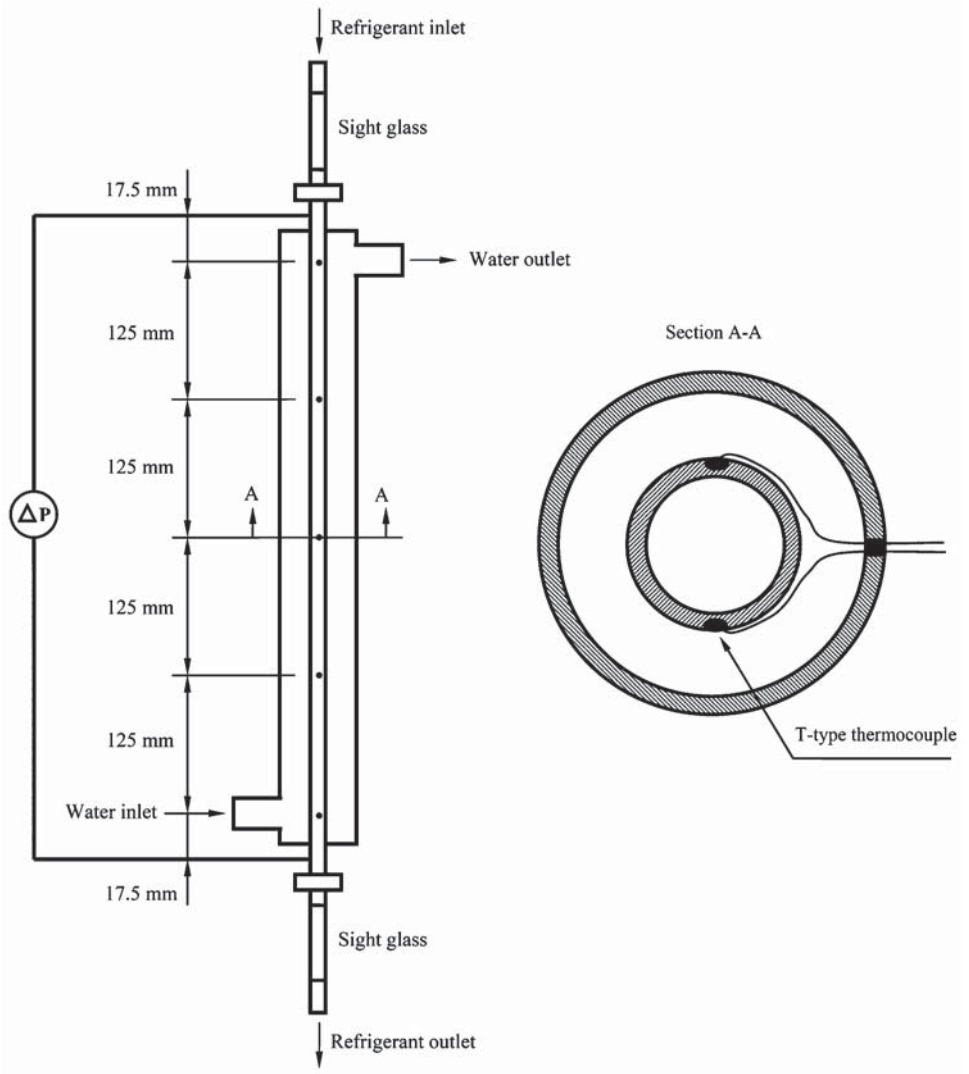

Figure 2. Schematic diagram of the test section.

are 8.7 and 9.52 mm, respectively. The length of the test section is 500 mm. Figure 3 shows the sketch and the actual photograph of the corrugated tube. The dimensions of the test section are listed in Table 1. T-type thermocouples are installed at the inlet and outlet of the test section to measure the saturation temperature of the refrigerant. Similarly, the differential pressure transducer is installed to measure the pressure drop across the test section. The length between the pressure taps is 850 mm. There are ten thermocouples located at five positions along the test section; all of the wall thermocouples are affixed with special glue having low thermal conductivity. The test section is well insulated with a proper material to minimize the heat loss. All of the thermocouples are well calibrated

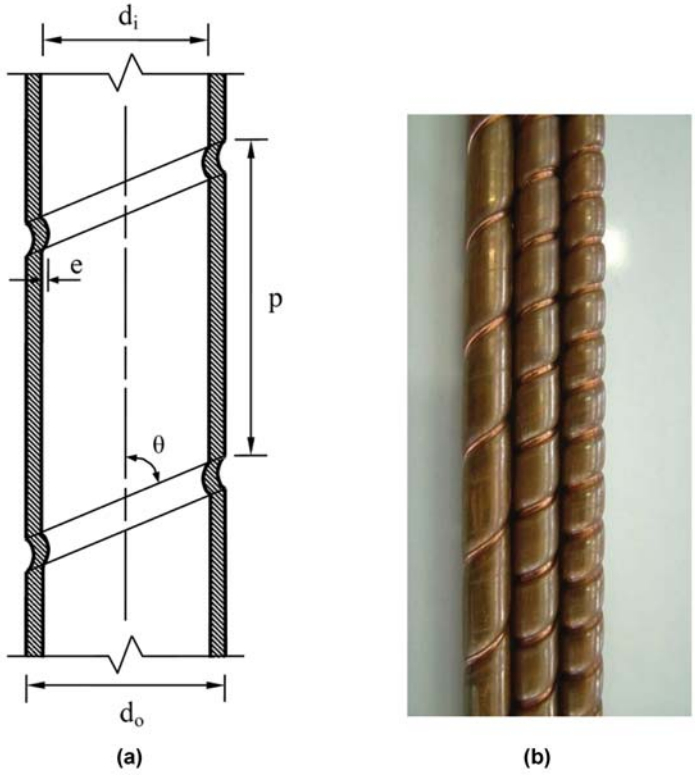

Figure 3. Corrugated tube: (a) sketch and (b) actual photograph. (color figure available online)

by standard thermometers with a precision of 0.1°C. The refrigerant flow meter is a variable area type and is specially calibrated in the range of 0.2–3.4 liters per minute (LPM) for R-134a by the manufacturer, as is the differential pressure transducer.

In the experiments, the inlet quality of the test section is varied by small increments. The imposed heat flux, mass flux, and saturation temperature are kept constant at the

Table 1. Dimensions of the test sections

		Corrugated tube		
Parameters	Smooth tube	Corrugation pitch 1	Corrugation pitch 2	Corrugation pitch 3
Outer diameter (mm)	9.52	9.52	9.52	9.52
Inner diameter (mm)	8.7	8.7	8.7	8.7
Length of test section (mm)	500	500	500	500
Inside tube area (mm^2)	13,665.9	15,362.2	15,951.1	16,582.8
Corrugation pitch (mm)	—	12.7	8.46	6.35
Corrugation depth (mm)	—	1	1	1
Helix angle (°)	—	53.875	64.07	69.95

Table 2. Experimental conditions

Controlled variable	Evaporation
Mass flux (kg/m^{2}s)	200, 300, 400
Heat flux (kW/m^2)	20, 25, 30
Saturation temperature (°C)	10, 15, 20
Tested tube material	Copper
Refrigerant	R-134a
Average vapor quality	0.2–0.8

desired values. The system is allowed to approach a steady state before any data are recorded. During experiments, the temperature and pressure are continuously recorded along the test section by the data acquisition system. The range of experimental conditions tested in this study is listed in Table 2. The uncertainties of measured quantities and calculated parameters calculated from the root mean sum square method are shown in Table 3.

DATA REDUCTION

The following calculation is employed to determine the vapor quality of the refrigerant entering and exiting the test section, heat transfer coefficient, and two-phase friction factor from the data recorded during each test run at steady-state conditions.

The Inlet Vapor Quality of the Test Section ($x_{TS,in}$)

The inlet vapor quality of the test section ($x_{TS,in}$) can be defined as

$$x_{TS,in} = \frac{i_{TS,in} - i_{lT_{TS,in}}}{i_{fgT_{TS,in}}}, \tag{1}$$

where $i_{lT_{TS,in}}$ and $i_{fgT_{TS,in}}$ are the enthalpy of the saturated liquid and the enthalpy of vaporization, respectively, based on the temperature at the test section inlet; $i_{TS,in}$ is

Table 3. Uncertainties of measured quantities and calculated parameters

Parameter	Uncertainty
Temperature, T	± 0.1
Frictional pressure drop, ΔP_F	± 10 %
Mass flow rate of refrigerant, m_{ref}	± 2% Full scale
Heat transfer rate of test section, Q_{TS}	± 15 %
Heat transfer rate of pre-heater, Q_{ph}	± 10 %
Average heat transfer coefficient, h_{avg}	± 15 %
Two-phase friction factor, f_{tp}	± 13 %
Average quality, x_{avg}	± 8 %
Equivalent Reynolds number, Re_{eq}	± 6 %

the enthalpy of refrigerant at the test section inlet, which is calculated by the following equation:

$$i_{TS,in} = i_{ph,in} + \frac{Q_{ph}}{m_{ref}}, \tag{2}$$

where $i_{ph,in}$ is the inlet enthalpy of the liquid refrigerant before entering the pre-heater, m_{ref} is the mass flow rate of the refrigerant, and Q_{ph} is the heat transfer rate in the pre-heater:

$$Q_{ph} = m_{w,ph} c_{p,w} (T_{w,in} - T_{w,out})_{ph}, \tag{3}$$

with $m_{w,ph}$ as the mass flow rate of water entering the pre-heater.

The Outlet Vapor Quality of the Test Section ($x_{TS,out}$)

The outlet vapor quality of the test section ($x_{TS,out}$) can be defined as

$$x_{TS,out} = \frac{i_{TS,out} - i_{lT_{TS,out}}}{i_{fgT_{TS,out}}}, \tag{4}$$

where $i_{TS,out}$ is the refrigerant enthalpy at the test section outlet, $i_{lT_{TS,out}}$ is the enthalpy of the saturated liquid based on the temperature at the test section outlet, and $i_{fgT_{TS,out}}$ is the enthalpy of vaporization based on the temperature at the test section outlet. As a consequence, the outlet enthalpy of the refrigerant flow is calculated as

$$i_{TS,out} = i_{TS,in} + \frac{Q_{TS}}{m_{ref}}, \tag{5}$$

where the heat transfer rate Q_{TS} in the test section is obtained from

$$Q_{TS} = m_{w,TS} c_{p,w} (T_{w,in} - T_{w,out})_{TS}, \tag{6}$$

where $m_{w,TS}$ is the mass flow rate of the water entering the test section, and $(T_{w,in} - T_{w,out})_{TS}$ is the difference in water temperature between the outlet and inlet positions.

Average Heat Transfer Coefficient (h_{avg})

The average heat transfer coefficient (h_{avg}) can be calculated using the following equation:

$$h_{avg} = \frac{Q_{TS}}{A_i (T_{i,avg,wi} - T_{avg,sat})}, \tag{7}$$

where $T_{avg,sat}$ is the average temperature of the refrigerant at the test section inlet and outlet, $T_{i,avg,wi}$ is the average temperature of the inner wall, and A_i is the inside surface area of the test section.

Nusselt Number (Nu)

The Nusselt number is calculated as follows:

$$\mathrm{Nu} = \frac{h_{avg} d_i}{k_l}, \tag{8}$$

where k_l is thermal conductivity of liquid refrigerant.

Two-Phase Friction Factor (f_{tp})

The total pressure gradient is the sum of three contributions: the gravitational pressure gradient, the momentum pressure gradient, and the frictional pressure gradient, as follows:

$$\left(\frac{dP}{dz}\right)_T = \left(\frac{dP}{dz}\right)_F + \left(\frac{dP}{dz}\right)_G + \left(\frac{dP}{dz}\right)_M. \tag{9}$$

Pressure drop due to gravity can be determined from

$$\left(\frac{dP}{dz}\right)_G = -g\left[(1-\alpha)\rho_l + \alpha\rho_g\right], \tag{10}$$

where the void fraction α can be determined from the Zivi correlation [14], as follows:

$$\alpha = \frac{1}{1 + \dfrac{(1-x)}{x}\left(\dfrac{\rho_g}{\rho_l}\right)^{2/3}}. \tag{11}$$

The momentum pressure gradient can be defined as follows:

$$\left(\frac{dP}{dz}\right)_M = G^2 \frac{d}{dz}\left[\frac{(1-x)^2}{\rho_l(1-\alpha)} + \frac{x^2}{\rho_g \alpha}\right]. \tag{12}$$

The two-phase frictional pressure gradient can be obtained by subtracting the gravitational and momentum terms from the total measured pressure drop, as follows:

$$\left(\frac{dP}{dz}\right)_F = \left(\frac{dP}{dz}\right)_T - \left(\frac{dP}{dz}\right)_G - \left(\frac{dP}{dz}\right)_M. \tag{13}$$

The two-phase friction factor is calculated by the following equation based on the equivalent Reynolds number:

$$f_{tp} = \left(\frac{dP}{dz}\right)_F \frac{\rho_l d_i^3}{2\,\mathrm{Re}_{eq}^2\,\mu_l^2}, \tag{14}$$

where the equivalent Reynolds number is determined from

$$\mathrm{Re}_{eq} = \frac{G_{eq} d_i}{\mu_l}, \tag{15}$$

and equivalent mass flux is defined as

$$G_{eq} = G\left[(1-x) + x\sqrt{\frac{\rho_l}{\rho_g}}\right]. \tag{16}$$

RESULTS AND DISCUSSION

The present study is performed to investigate the effect of corrugation pitch on the heat transfer coefficient and pressure drop of R-134a during evaporation inside vertical corrugated tubes. The experimental data obtained from this work are not from the dry-out region. Before measuring the two-phase heat transfer coefficient and pressure drop during evaporation of refrigerant in the test section, the experimental results obtained from the smooth tube are checked by sight glass at the inlet and outlet of the test section, and they are also checked with the flow pattern maps for vertical flow. Figures 4–6 show the flow pattern map of Hewitt and Roberts [15], Taitel et al. [16], and Mishima and Ishii [17] with the plotted experimental data of the current study, respectively. They are observed that more than 90% of the data points locate in the region of annular flow regime.

Heat Transfer Coefficient

The experimental data obtained from the smooth tube are validated by comparing the present heat transfer coefficient data with the correlations for vertical flow proposed by Shah [9], Gungor and Winterton [10], Kandlikar [11], Wright [18], Schrock and

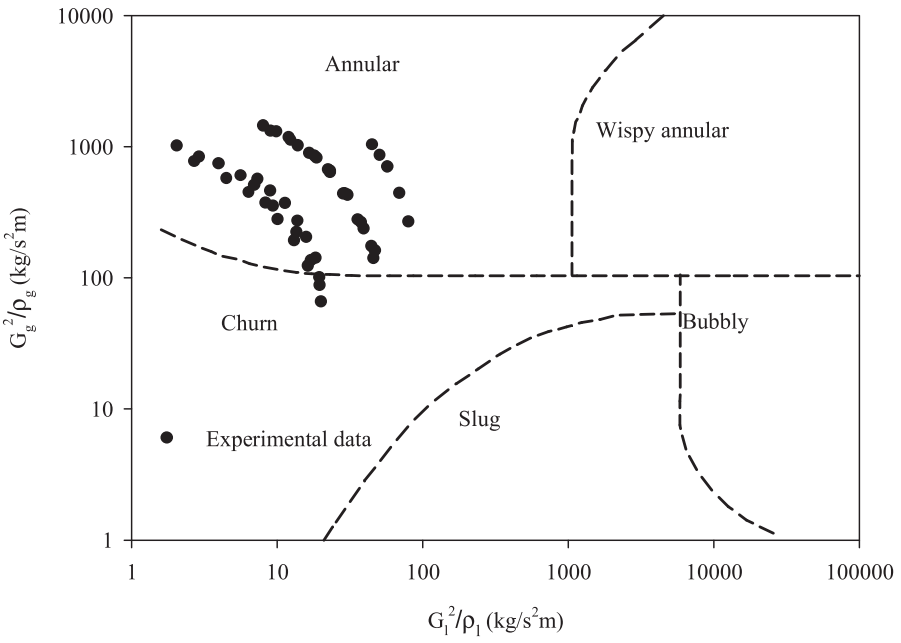

Figure 4. Flow pattern identification of the experimental data by means of Hewitt and Roberts [15] flow regime map.

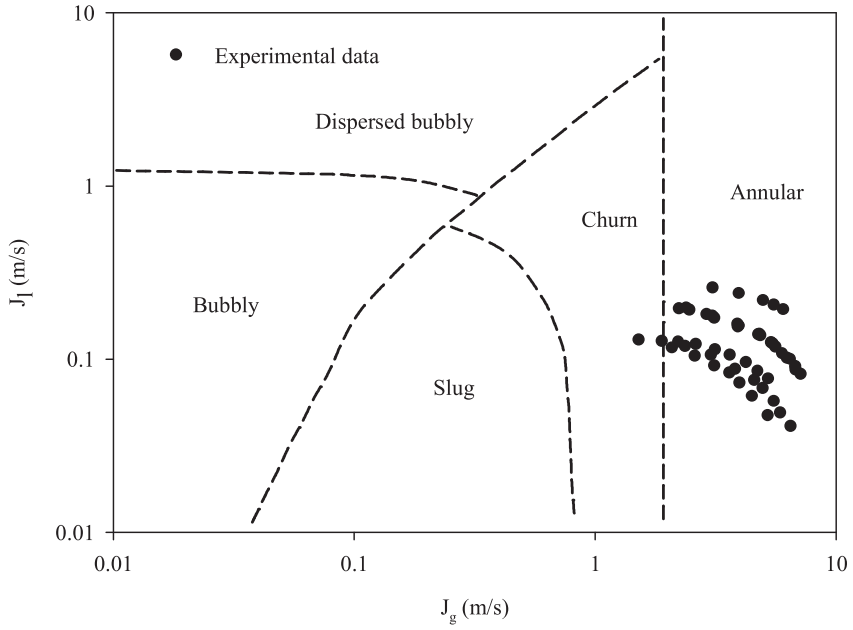

Figure 5. Flow pattern identification of the experimental data by means of Taitel et al. [16] flow regime map.

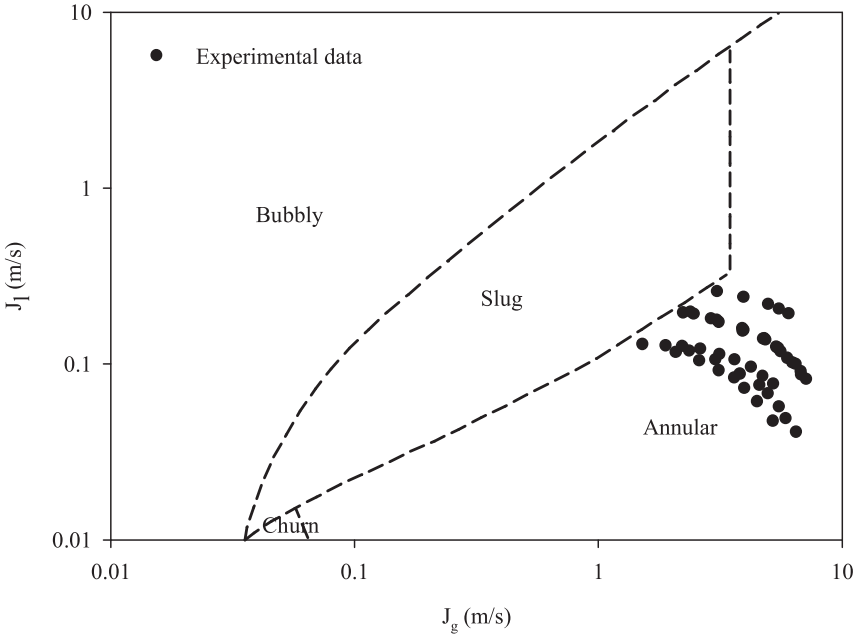

Figure 6. Flow pattern identification of the experimental data by means of Mishima and Ishii [17] flow regime map.

Grossman [19], and Pujol and Stenning [20], as shown in Figure 7. It is observed that almost all of data correlate within the deviation of ± 30%.

Figure 8 shows the relationship between average heat transfer coefficient and average quality in the smooth tube and corrugated tube having different corrugation pitches of 6.35, 8.46, and 12.7 mm at heat flux of 20 kW/m^2, saturation temperature of 20°C, and mass fluxes of 200 kg/m^{2}s. It can be observed that higher average vapor quality results in a higher average heat transfer coefficient. This occurs because at high vapor quality, the velocity of the vapor flow is high, resulting in high shear stress at the interface between the vapor and liquid film. The increasing shear stress causes more entrainment of droplets, making the liquid film thinner. As a result, thermal resistance is decreased. In addition, during evaporation, the liquid film boils and turns to vapor, which, in turn, increases the velocity of two-phase flow. For these reasons, the average heat transfer coefficient tends to increase as the average vapor quality increases.

Figure 9 shows the variation of the average heat transfer coefficient as a function of the mass flux at the heat flux of 20 kW/m^2, the average vapor quality of 0.35, and the saturation temperature of 20°C. It is observed that the average heat transfer coefficient increases with increasing mass flux. This occurs because the velocity of the vapor and liquid film increase as the mass flux increases, and therefore, the average heat transfer coefficient also increases.

As seen from these figures, the heat transfer coefficients obtained from the corrugated tubes are higher than those from the smooth tube. This can be explained by the fact that the corrugated surface promotes more turbulence by increasing the mixing of the refrigerant flow. Further, it is speculated that the rotational flow produced by the

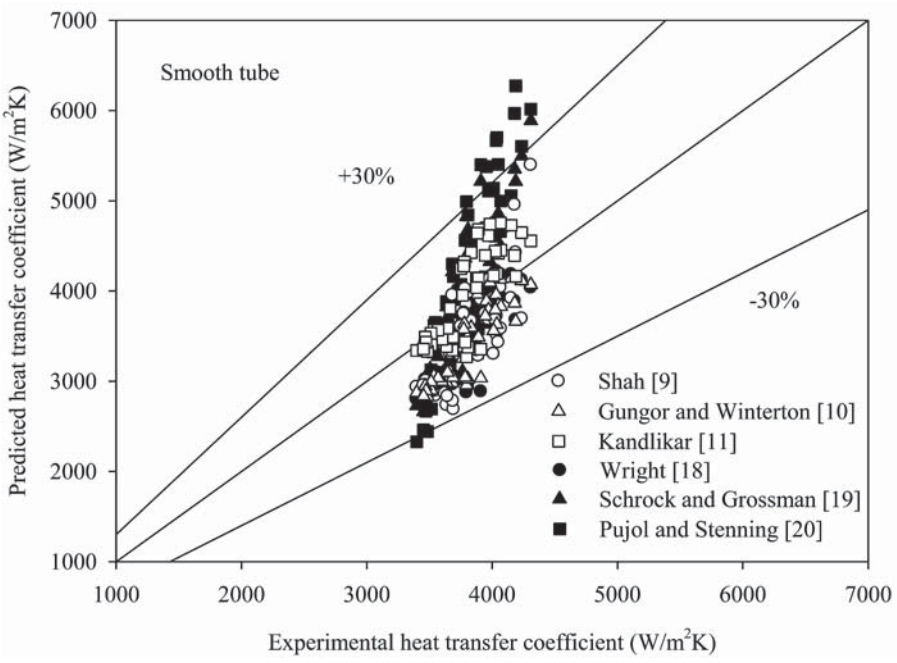

Figure 7. Comparison of experimental heat transfer coefficient data with existing correlations.

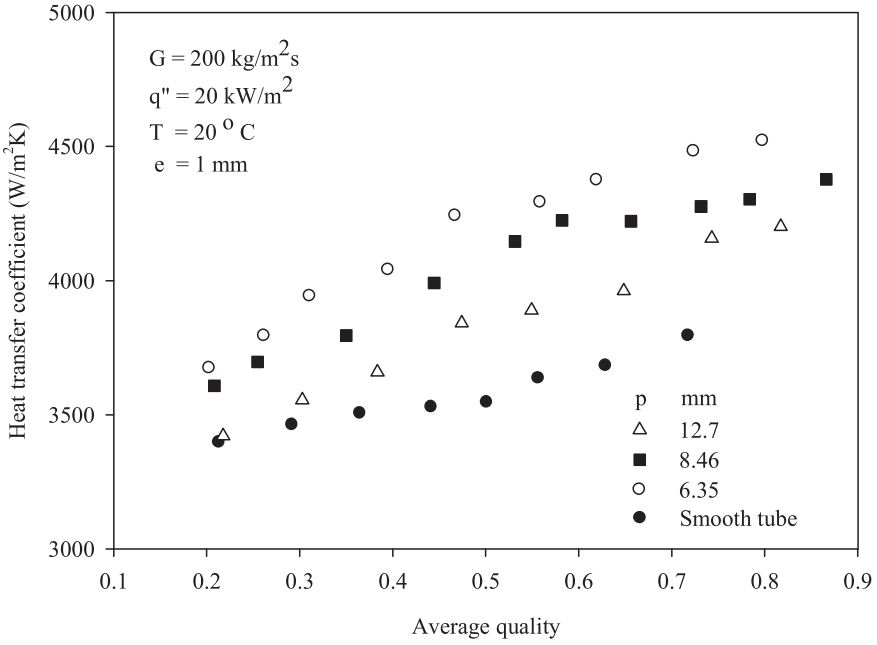

Figure 8. Average heat transfer coefficient as a function of average quality for $G = 200$ kg/m^{2}s, $q'' = 20$ kW/m^2, and $T = 20$°C.

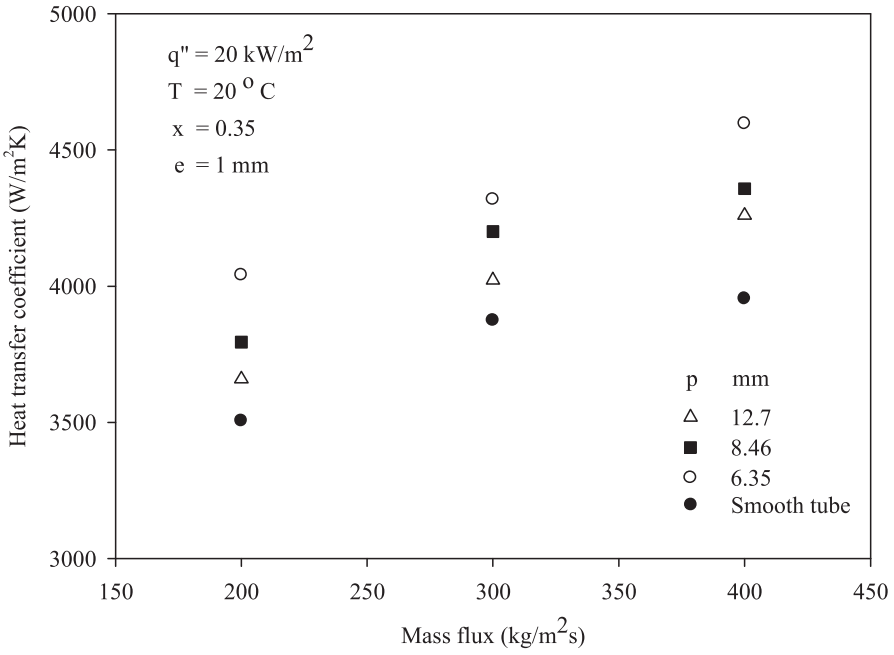

Figure 9. Average heat transfer coefficient as a function of mass flux for $x = 0.35$, $q'' = 20$ kW/m^2, and $T = 20$°C.

corrugation causes the liquid film to become thinner as a result of enhancing heat transfer. Moreover, the heat transfer coefficient increases with the decrease of corrugation pitch. This occurs because the tube with lower corrugation pitch produces more turbulence of the fluid flow and increases the heat transfer area. Hence, the highest heat transfer coefficient is achieved by the tube with the lowest corrugation pitch. The maximum heat transfer enhancement is obtained up to 22% for a pitch of 6.35 mm, 16% for a pitch of 8.46 mm, and 11% for a pitch of 12.7 mm in comparison with the smooth tube at the mass flux of 200 kg/m^{2}s, the heat flux of 20 kW/m^2, and the saturation temperature of 20°C.

The heat transfer enhancement factors as a function of vapor quality are shown in Figures 10 and 11, defined as the ratio of the heat transfer coefficient for a corrugated tube to that of a comparable smooth tube. The heat transfer enhancement factor is calculated by a linear regression analysis using a least-squares method to determine the best-fitting straight line. It is found that the heat transfer enhancement factor increases as the average vapor quality increases. This can be explained by the effect of corrugation on the heat transfer coefficient, which is weak in low vapor quality region but becomes stronger at high vapor quality. At low vapor quality, the liquid film thickness is higher than that at high vapor quality, and, as a result, the turbulence effects produced by the corrugation depth are reduced. When the liquid film thickness is close to the corrugation depth, the periodic liquid wave caused by corrugation pitch produces an unstable liquid flow, which maximizes thermal efficiency and turbulent effects [21]. The heat transfer enhancement factor varies from 1.09 to 1.22 for a pitch of 6.35 mm, 1.06 to 1.16 for a pitch of

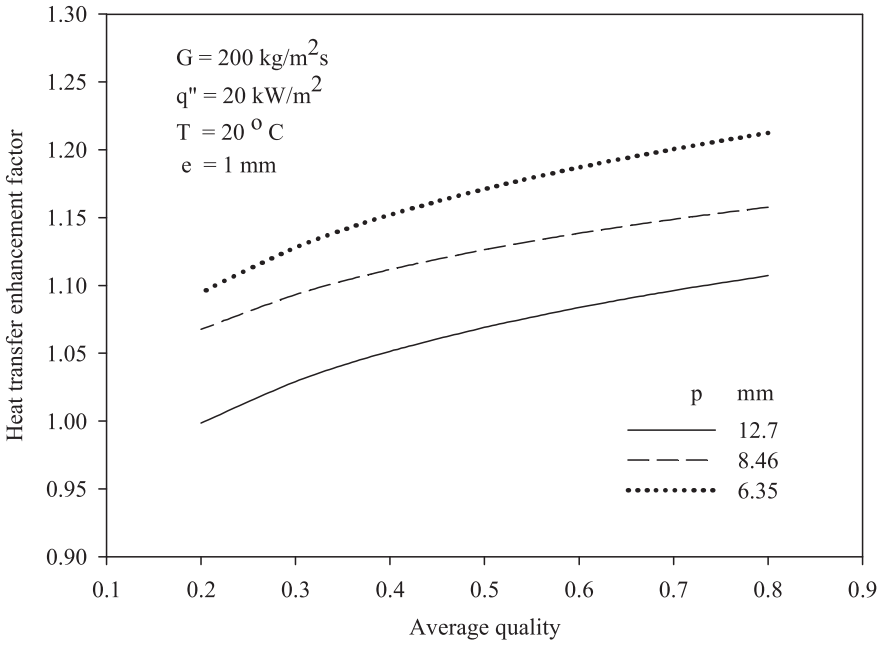

Figure 10. Heat transfer enhancement factors as a function of average quality for $G = 200$ kg/m^{2}s, $q'' = 20$ kW/m^2, and $T = 20$°C.

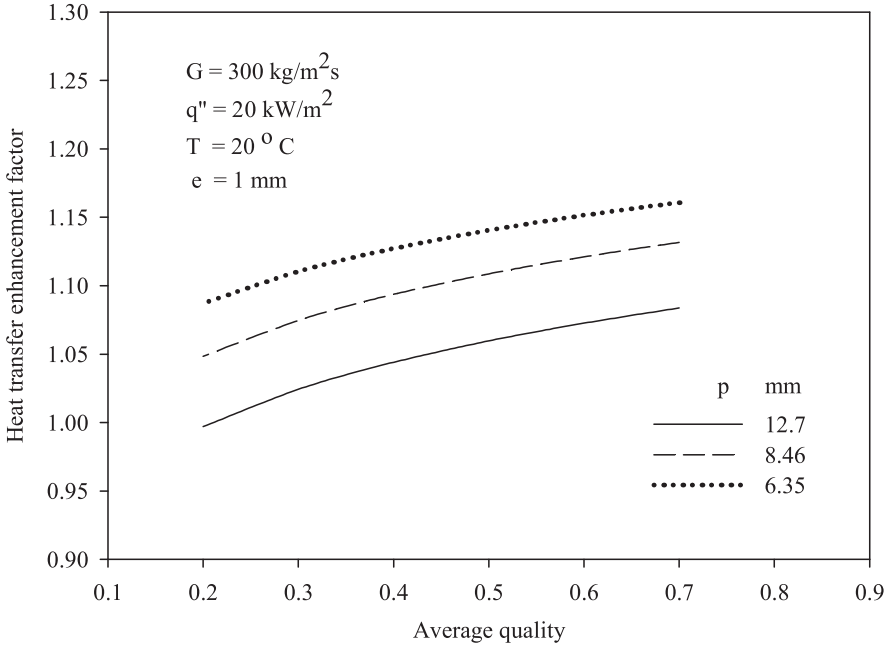

Figure 11. Heat transfer enhancement factors as a function of average quality for $G = 300$ kg/m^{2}s, $q'' = 20$ kW/m^2, and $T = 20$°C.

8.46 mm, and 1.00 to 1.11 for a pitch of 12.7 mm at the mass flux of 200 kg/m^{2}s, heat flux of 20 kW/m^2, and saturation temperature of 20°C.

Figure 12 shows a comparison of the experimental data for the corrugated tube with the proposed correlations. The correlation is expressed as a function of Nusselt number, equivalent Reynolds number, corrugation pitch, and inside diameter as follows:

$$\mathrm{Nu} = 35.948\,\mathrm{Re}_{eq}^{0.237}\left(\frac{p}{d_i}\right)^{-0.114}. \tag{17}$$

As shown in Figure 12, the results show that more than 95% of data fall within a deviation of ± 5%.

Pressure Drop

Figure 13 compares the frictional pressure drop for the smooth tube with the correlations from literature. The correlations proposed by Lockhart and Martinelli [22] and Chisholm [23] are in agreement with the present data within 30%. About 70% of the data are captured within 30% by Laohalertdecha et al.'s [24] correlation, while the Friedel [25], and Quibén and Thome [26] correlations underestimate the data by more than 30%.

The variation of the frictional pressure drop with average quality in smooth and corrugated tubes is illustrated in Figure 14. The frictional pressure drop increases with increasing vapor quality. This occurs because at higher vapor quality, the higher velocity

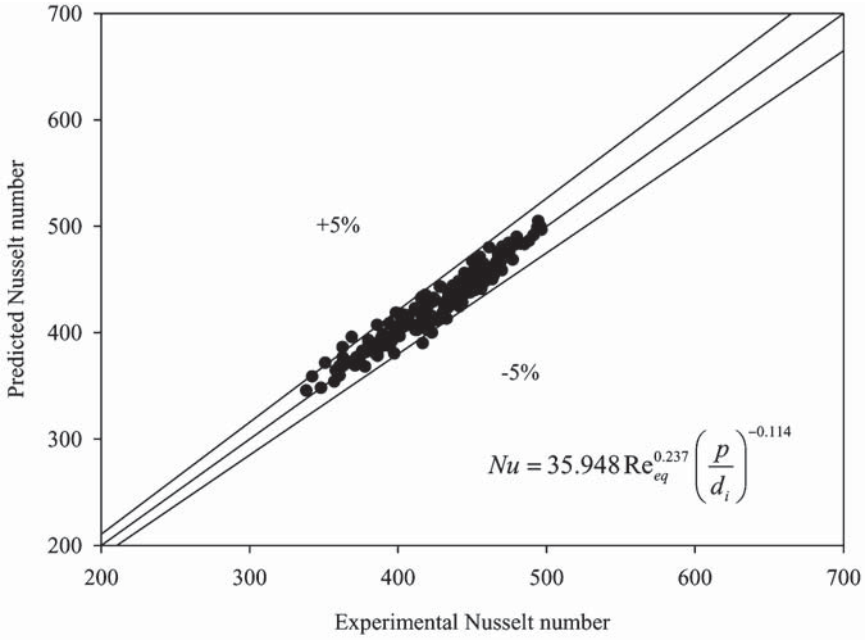

Figure 12. Predicted Nusselt number using the proposed correlation versus the experimental data.

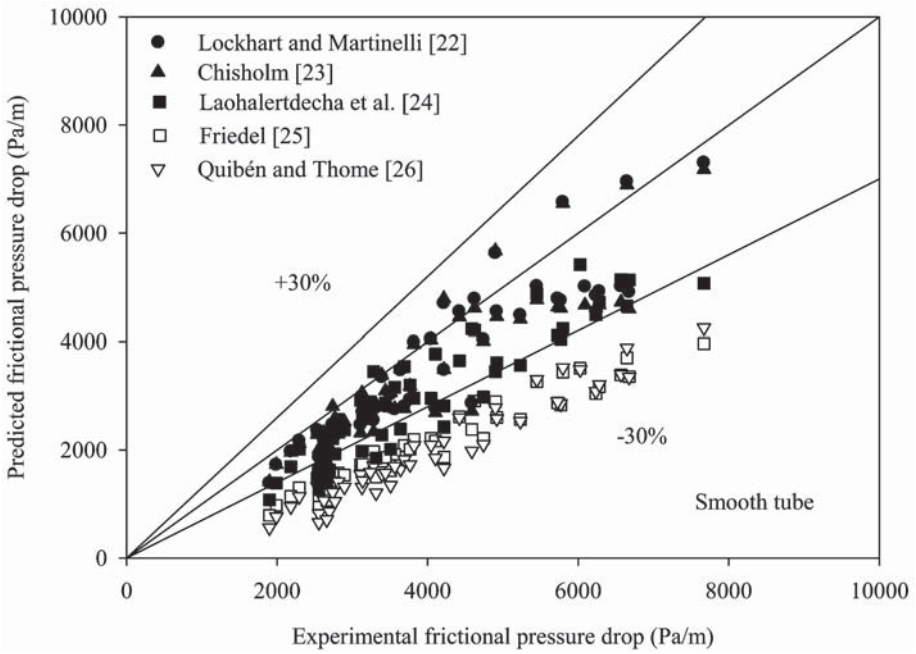

Figure 13. Comparison of experimental frictional pressure drop data with existing correlations.

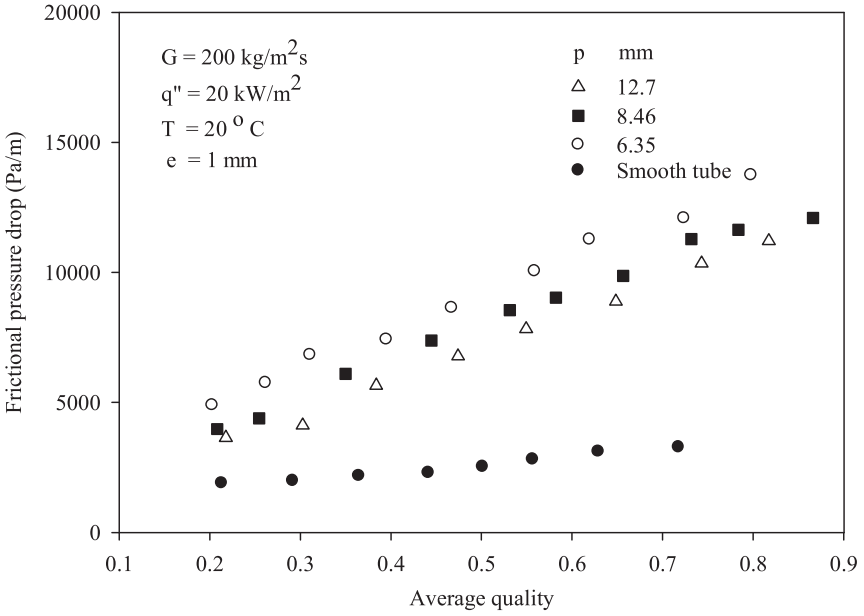

Figure 14. Frictional pressure drop as a function of average quality for $G = 200$ kg/m^{2}s, $q'' = 20$ kW/m^2, and $T = 20°$C.

of vapor flow causes more shear stress at the interface of the vapor and liquid film. Moreover, the secondary flow that becomes stronger at higher vapor velocity will produce more entrainment and redeposition of droplets, causing more flow turbulence.

Figure 15 illustrates the variation of the frictional pressure drop as a function of the saturation temperature at the heat flux of 20 kW/m^2, average vapor quality of 0.45, and mass flux of 200 kg/m^{2}s. The frictional pressure drop decreases significantly as the evaporating temperature increases. This is because when the evaporating temperature increases, the viscosity of liquid film decreases, resulting in lower flow resistance. Consequently, the frictional pressure drop decreases as the evaporating temperature increases.

As shown in Figures 14 and 15, the frictional pressure drops for the corrugated tubes are higher than those for the smooth tube. This is due to the pressure-drop augmentation in corrugated tubes that is produced by (1) drag forces exerted on the flow field by the corrugation, (2) flow blockage due to area reduction, (3) turbulence augmentation, and (4) rotational flow produced by the corrugation [27]. The figures also show the effect of the corrugation pitch at constant corrugation depth of 1 mm on the frictional pressure drop. These plots show that the higher frictional pressure drop is obtained from the tube with lower corrugation pitch; lower corrugation pitch results in increased corrugation surface, more turbulence of the fluid flow, and more pressure loss. The maximum value of frictional pressure drop is obtained from the tube having a corrugation pitch of 6.35 mm up to 300% in comparison with the smooth tube at the mass flux of 200 kg/m^{2}s, heat flux of 20 kW/m^2, and saturation temperature of 20°C.

The relationship between the two-phase friction factor and the equivalent Reynolds number is demonstrated in Figure 16. The two-phase friction factor decreases with

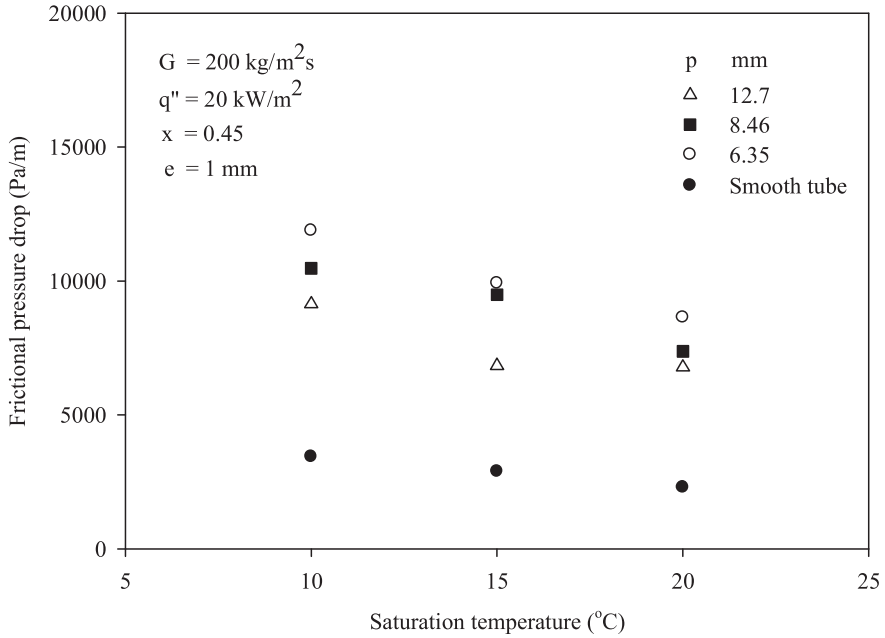

Figure 15. Frictional pressure drop as a function of saturation temperature for $G = 200$ kg/m^{2}s, $q'' = 20$ kW/m^2, and $x = 0.45$.

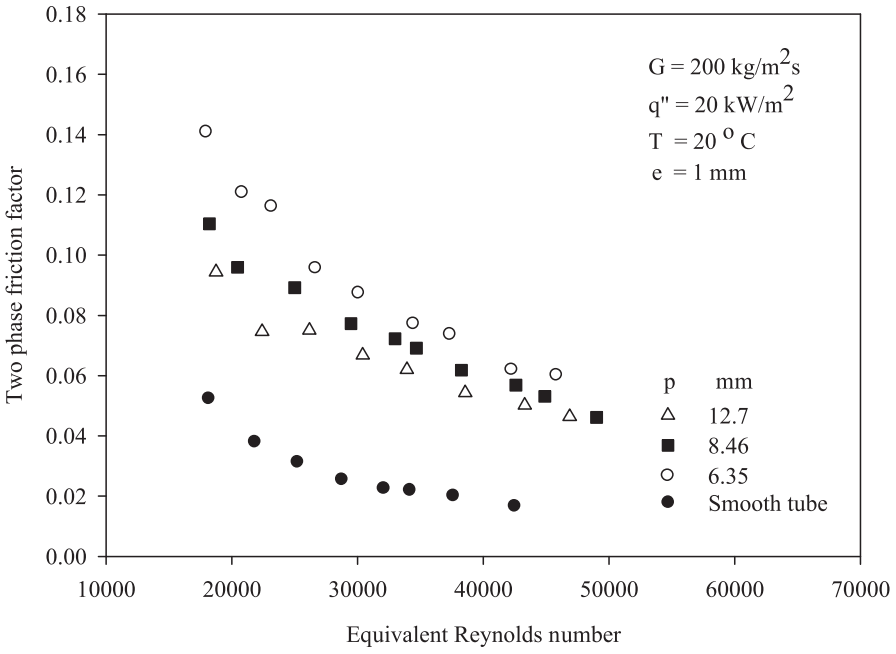

Figure 16. Two-phase friction factor as a function of equivalent Reynolds number for $G = 200$ kg/m^{2}s, $q'' = 20$ kW/m^2, and $T = 20°$C.

increasing equivalent Reynolds number. This is because both the frictional pressure drop and equivalent Reynolds number increase with increasing vapor quality. According to Eq. (14), the equivalent Reynolds number dominates the two-phase friction factor. Therefore, the increase in average quality causes the two-phase friction factor to decrease. Figure 16 also shows that the two-phase friction factor for the corrugated tubes is higher than that for the smooth tube. In addition, the two-phase friction factor tends to increase as the corrugation pitch decreases. The reason for this is similar to the above-mentioned explanation concerning the frictional pressure drop.

Figures 17 and 18 illustrate the variation of the penalty factor with the average vapor quality. The penalty factor is defined as the ratio of the frictional pressure drop for a corrugated tube to that of a comparable smooth tube. The penalty factor increases with a rise of the average vapor quality. This is because the turbulence effects produced by corrugation depth are strong at high vapor quality as a result of more pressure loss. The penalty factor ranges from 2.8 to 4.0 for a pitch of 6.35 mm, 2.2 to 3.5 for a pitch of 8.46 mm, and 1.8 to 3.2 for a pitch of 12.7 mm at the mass flux of 200 kg/m^{2}s, heat flux of 20 kW/m^2, and saturation temperature of 20°C.

Figure 19 shows the experimental two-phase friction factor plotted against predicted two-phase friction factor obtained from Eq. (18). It is found that about 90% of the data fall within a deviation of ± 15%:

$$f_{tp} = 37.337\,\mathrm{Re}_{eq}^{-0.594}\left(\frac{p}{d_i}\right)^{-0.301} . \tag{18}$$

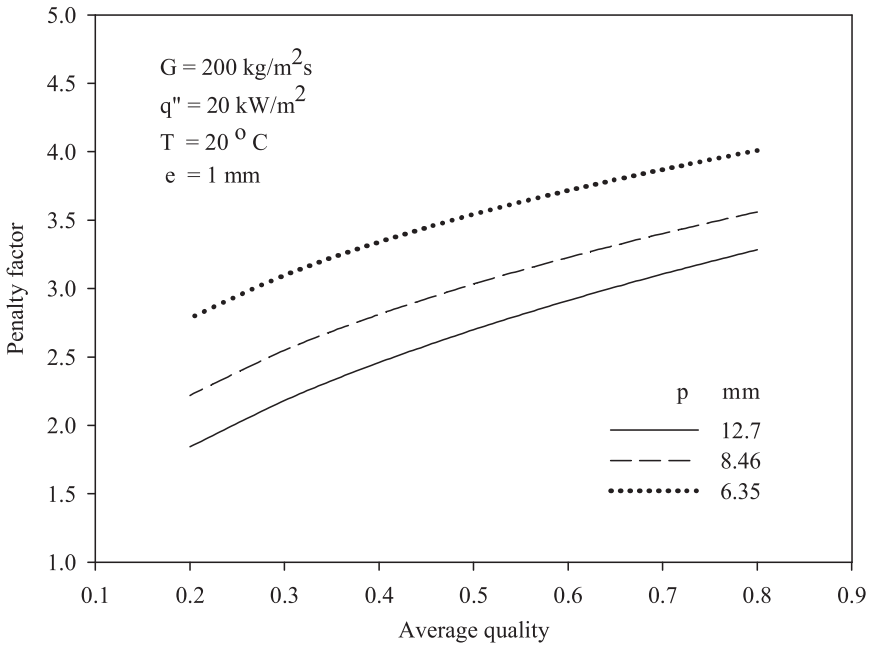

Figure 17. Penalty factors as a function of average quality for $G = 200$ kg/m^{2}s, $q'' = 20$ kW/m^2, and $T = 20$°C.

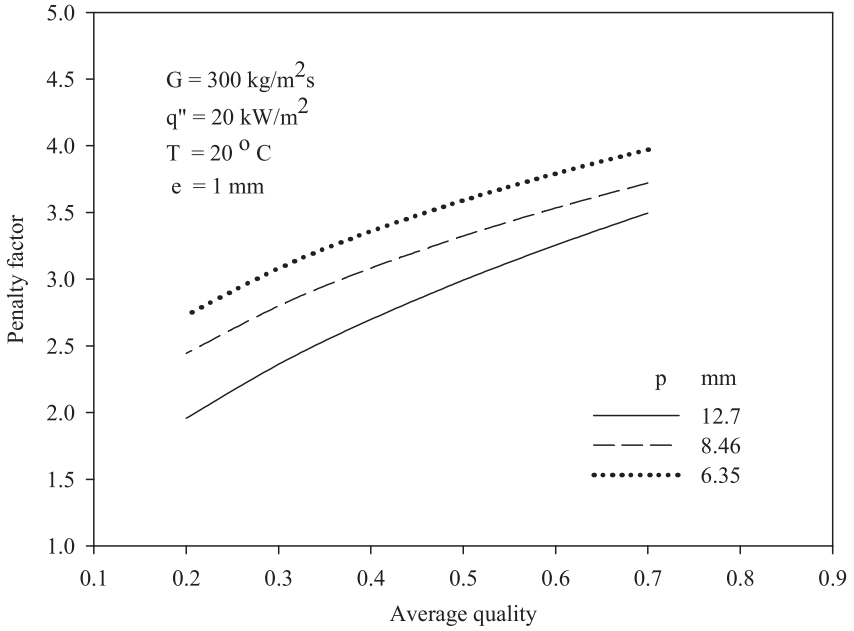

Figure 18. Penalty factors as a function of average quality for $G = 300$ kg/m^{2}s, $q'' = 20$ kW/m^2, and $T = 20$°C.

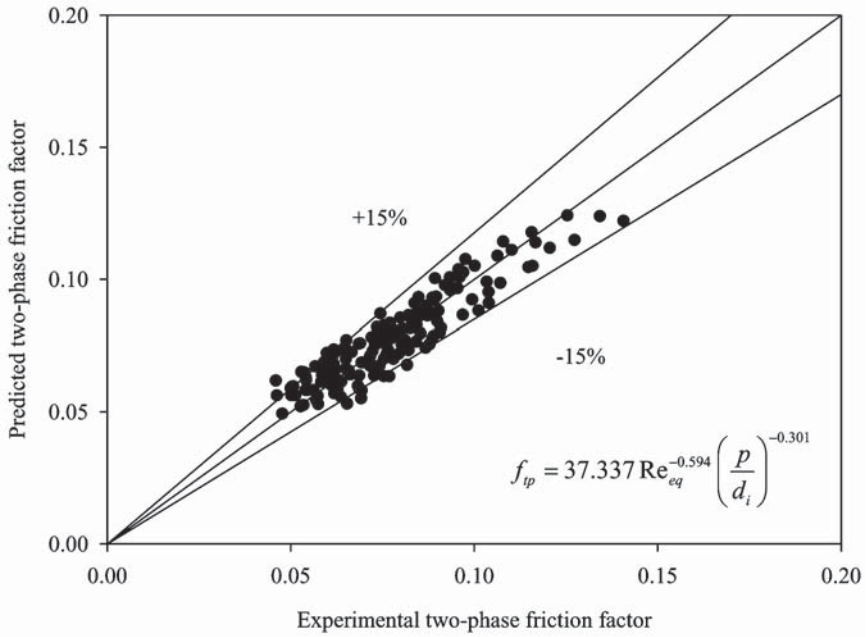

Figure 19. Predicted two-phase friction factor using the proposed correlation versus the experimental data.

CONCLUSION

This study is conducted to investigate the evaporative heat transfer and pressure drop characteristics of R-134a flow through vertical smooth and corrugated tubes with different corrugation pitches. The conclusions follow.

1. The experimental data obtained from the smooth tube are plotted with a flow pattern map for vertical flow proposed by Hewitt and Roberts [15], Taitel et al. [16], and Mishima and Ishii [17]. It is observed that more than 90% of the data points locate in the region of annular flow regime.
2. The heat transfer coefficient tends to increase with increasing average vapor quality and mass flux. The heat transfer coefficient obtained from the corrugated tube is higher than that from the smooth tube. Moreover, the heat transfer coefficient increases with the decrease of corrugation pitch.
3. The frictional pressure drop increases with increasing vapor quality, while it decreases significantly as the evaporating temperature increases. The two-phase friction factor decreases with increasing equivalent Reynolds number. The frictional pressure drops for the corrugated tube is higher than that for the smooth tube. In addition, the higher frictional pressure drop is obtained from the tube with lower corrugation pitch.
4. The heat transfer enhancement factor and penalty factor increase with a rise of the average vapor quality. The heat transfer enhancement factor varies from 1.09 to 1.22, 1.06 to 1.16, and 1.00 to 1.11, while the penalty factor ranges from 2.8 to 4.0, 2.2 to 3.5, and 1.8 to 3.2 for a pitch of 6.35 mm, 8.46 mm, and 12.7 mm, respectively.

ACKNOWLEDGMENTS

The present study was supported financially by the Thailand Research Fund and the National Research University Project, whose guidance and assistance are gratefully acknowledged.

REFERENCES

1. P. Thors and J. Bogart, In Tube Evaporation of HCFC-22 with Enhanced Tubes, *J. Enhanced Heat Transf.*, vol. 1, pp. 365–377, 1994.
2. A. Briggs, C. Kelemenis, and J. W. Rose, Condensation of CFC-113 with Downflow in Vertical Internally Enhanced Tubes, *Proceedings of 11th IHTC*, Keongju, Korea, pp. 23–28, August 23–28, 1998.
3. X. Ma, A. Briggs, and J. W. Rose, Heat Transfer and Pressure Drop Characteristics for Condensation of R113 in a Vertical Micro-Finned Tube with Wire Insert, *Int. Commun. Heat Mass Transf.*, vol. 31, pp. 619–627, 2004.
4. A. S. Dalkilic, S. Laohalertdecha, and S. Wongwises, Two-Phase Friction Factor in Vertical Downward Flow in High Mass Flux Region of Refrigerant HFC-134a During Condensation, *Int. Commun. Heat Mass Transf.*, vol. 35, pp. 1147–1152, 2008.

5. A. S. Dalkilic, S. Laohalertdecha, and S. Wongwises, Effect of Void Fraction Models on the Two-Phase Friction Factor of R134a During Condensation in Vertical Downward Flow in a Smooth Tube, *Int. Commun. Heat Mass Transf.*, vol. 35, pp. 921–927, 2008.
6. A. S. Dalkilic, S. Laohalertdecha, and S. Wongwises, Effect of Void Fraction Models on the Film Thickness of R134a During Downward Condensation in a Vertical Smooth Tube, *Int. Commun. Heat Mass Transf.*, Vol. 36, pp. 172–179, 2009.
7. A. S. Dalkilic, S. Laohalertdecha, and S. Wongwises, Experimental Investigation of Heat Transfer Coefficient of R134a During Condensation in Vertical Downward Flow at High Mass Flux in a Smooth Tube, *Int. Commun. Heat Mass Transf.*, vol. 36, pp. 1036–1043, 2009.
8. A. S. Dalkilic, S. Yildiz, and S. Wongwises, Experimental Investigation of Convective Heat Transfer Coefficient During Downward Laminar Flow Condensation of R134a in a Vertical Smooth Tube, *Int. J. Heat Mass Transf.*, vol. 52, pp. 142–150, 2009.
9. M. M. Shah, Chart Correlation for Saturated Boiling Heat Transfer Equation and Further Study, *ASHRAE Trans.*, vol. 88, pp. 185–196, 1982.
10. K.E. Gungor and R. H. S. Winterton, A General Correlation for Flow Boiling in Tubes and Annuli, *Int. J. Heat Mass Transf.*, vol. 29, pp. 351–358, 1986.
11. S. G. Kandlikar, A General Correlation for Saturated Two-Phase Flow Boiling Heat Transfer Inside Horizontal and Vertical Tubes, *ASME J. Heat Transf.*, vol. 112, pp. 219–228, 1990.
12. S. K. Lee and S. H. Chang, Experimental Study of Post-Dryout with R-134a Upward Flow in Smooth Tube and Rifled Tubes, *Int. J. Heat Mass Transf.*, vol. 51, pp. 3153–3163, 2008.
13. K. Aroonrat and S. Wongwises, Evaporation Heat Transfer and Friction Characteristics of R-134a Flowing Downward in a Vertical Corrugated Tube, *Exp. Thermal Fluid Sci.*, vol. 35, pp. 20–28, 2011.
14. S. M. Zivi, Estimation of Steady-State Steam Void-Fraction by Means of the Principle of Minimum Entropy Production, *ASME J. Heat Transf.*, vol. 86, pp. 247–252, 1975.
15. G. F. Hewitt and D. N. Roberts, *Studies of Two-Phase Flow Patterns by Simultaneous X-Ray and Flash Photography*, AERE-M 2159, Her Majesty's Stationery Office, London, 1969.
16. Y. Taitel, D. Barnea, and A. E. Dukler, Modelling Flow Pattern Transitions for Steady Upward Gas-Liquid Flow in Vertical Tubes, *AIChE J.*, vol. 26, pp. 345–354, 1980.
17. K. Mishima and M. Ishii, Flow Regime Transition Criteria for Upward Two-Phase Flow in Vertical Tubes, *Int. J. Heat Mass Transf.*, vol. 27, pp.723–737, 1984.
18. R. M. Wright, *Down Flow Forced Convection Boiling of Water in Uniformly Heated Tubes*, UCRL-9744, University of California, Berkeley, CA, 1961.
19. V. E. Schrock and L. M. Grossman, Forced Convection Boiling in Tubes, *Nuclear Sci. Eng.*, vol. 12, pp. 474–481, 1962.
20. L. Pujol and A. H. Stenning, Effects of Flow Directions on the Boiling Heat Transfer Coefficients in Vertical Tubes, in E. R. Rhodes and D. S. Scott (Eds.), *Co-Current Gas-Liquid Flow*, Plenum Press, New York, pp. 401–453, 1969.
21. R. Yun, Y. Kim, K. Seo, and H. Y. Kim, A Generalized Correlation for Evaporation Heat Transfer of Refrigerants in Micro-Fin Tubes, *Int. J. Heat Mass Transf.*, vol. 45, pp. 2003–2010, 2002.
22. R. W. Lockhart and R. C. Martinelli, Proposed Correlation of Data for Isothermal Two-Phase Two Component Flow in Pipes, *Chem. Eng. Progress*, vol. 45, pp. 39–48, 1949.
23. D. Chisholm, Pressure Gradients Due to Friction During the Flow of Evaporating Two-Phase Mixtures in Smooth Tubes and Channels, *Int. J. Heat Mass Transf.*, vol. 16, pp. 347–358, 1973.
24. S. Laohalertdecha, A. S. Dalkilic and S. Wongwises, Correlations for Evaporation Heat Transfer Coefficient and Two-Phase Friction Factor for R-134a Flowing Through Horizontal Corrugated Tubes, *Int. Commun. Heat Mass Transf.*, vol. 38, pp. 1406–1413, 2011.

25. L. Friedel, Improved Friction Pressure Drop Correlations for Horizontal and Vertical Two-Phase Pipe Flow, Paper E2, *The European Two-Phase Flow Group Meeting*, Ispra, Italy, June 5–8, 1979.
26. J. M. Quibén and J. R. Thome, Flow Pattern Based Two-Phase Frictional Pressure Drop Model for Horizontal Tubes, Part II: New Phenomenological Model, *Int. J. Heat Fluid Flow*, vol. 28, pp. 1060–1072, 2007.
27. P. G. Vicente, A. Garcia, and A. Viedma, Experimental Investigation on Heat Transfer and Friction Factor Characteristics of Spirally Corrugated Tubes in Turbulent Flow at Different Prandtl Number, *Int. J. Heat Mass Transf.*, vol. 47, pp. 671–681, 2004.

Technical Note

Performance of Two-Stage Upflow Anaerobic Sludge Blanket Reactor Treating Wastewater from Latex-Processing Factory

S. Phoolphundh[1]; K. Hathaisamit[2]; and S. Wongwises[3]

Abstract: In this study, a relatively high-rate treatment (hydraulic retention time ≤2.5 days) of latex-processing wastewater was achieved in a two-stage upflow anaerobic sludge blanket reactor. A maximum acid production rate of 1.8 $g\,L^{-1}\,d^{-1}$ acetic acid was obtained when the acidogenic reactor was operated over a hydraulic retention time (HRT) of 4 hr. Total chemical oxygen demand (COD) and sulfate removal efficiencies of the system were 51.6 and 75.9%, respectively, when the methanogenic reactor was operated over an HRT of 24 h. The specific acidogenic activity of granular sludge in the acidogenic and methanogenic reactor varied between 1.33–2.02 g COD g volatile suspended solids $(VSS)^{-1}\,d^{-1}$, and the specific methanogenic activity ranged from 0.0078 to 0.0138 $g\,COD\text{-}CH_4\,g\,VSS^{-1}\,d^{-1}$. Microbial diversity monitoring using the denaturing gradient gel electrophoresis technique revealed that there was more sulfate-reducing bacteria in both reactors than *archea* bacteria. **DOI: 10.1061/(ASCE)EE.1943-7870.0000604.** © *2013 American Society of Civil Engineers.*

CE Database subject headings: Reactors; Wastewater management; Sludge.

Author keywords: Acidogenic reactor; Latex-processing wastewater; Methanogenic reactor; Sulfate reduction; Two-stage upflow anaerobic sludge blanket system.

Introduction

Thailand is the leading natural rubber producer in the world. According to a report from the Thailand Office of Agricultural Economics (2009), there are approximately 27,200 square kilometres of rubber tree plantations in Thailand, 75% of which are located in the southern region. Latex concentrate, which is produced by centrifugation of rubber latex (sap), is generally used as a raw material for an enormous variety of products, e.g., sheet rubber, gloves, and tires. Wastewater from concentrated latex factories is a significant source of pollution because of its high organic content and sulphate concentration. Rubber latex wastewater is widely treated by an anaerobic process. A major problem associated with the anaerobic treatment of sulfate-rich wastewater is the production of sulfide by sulphate-reducing bacteria (SRB), which may lead to process failure. One of the strategies to accomplish the successful treatment of sulfate-containing wastewater is the separation of sulfide production and methanogenesis through a two-stage anaerobic digestion process (Lens et al. 1998). The resulting sulfide will be removed during the first stage (acidification) via stripping that can easily occur as a result of the low pH (approximately 5.0–6.5) in the reactor. This reduces the toxicity of sulfide to methane-producing bacteria (MPB) and acetogenic bacteria (AB) in the second stage (methanogenesis). This study attempted to determine the effect of hydraulic retention time (HRT) in an acidogenic reactor and methanogenic reactor on volatile fatty acid (VFA) production, chemical oxygen demand (COD) removal, sulfate reduction, and biogas production, to evaluate the performance of a two-stage upflow anaerobic sludge blanket (UASB) reactor on treating wastewater from a concentrated latex-processing factory.

Materials and Methods

Experimental Setup and Operation

A laboratory-scale two-stage UASB system, consisting of an acidogenic (A) reactor and a methanogenic reactor (M), was used in this study. The working volume of the A and M reactors was 2.9 and 4.1 L, with an inner diameter of 5 cm and a height of 96 and 120 cm, respectively. Fig. 1 is a schematic diagram of the two-stage UASB system. Both reactors were separated by an effluent tank that received the effluent from the A reactor and provided the feed for the M reactor. A water displacement-type gas meter was connected to the M reactor to measure the volume of produced biogas. One-third of each reactor was inoculated with granular sludge from a full-scale UASB reactor belonging to a beverage company (Sermsuk Co., Ltd., Pathumthani province, Thailand). The concentration of total suspended solids (TSS) and volatile suspended solids (VSS) of the seed sludge were 39 and 36 g/L, respectively. The latex-processing wastewater used in this study was taken from the first anaerobic pond at the wastewater treatment plant of Srithepthai Latex Co., Ltd. (Rayong province, Thailand), and was stored at 4°C before use. The characteristics of this latex-processing wastewater are shown in Table 1.

During the start-up period, seed sludge in both reactors was acclimatized by continuously fed with diluted latex-processing wastewater

[1]Dept. of Microbiology, Faculty of Science, King Mongkut's Univ. of Technology Thonburi, 126 Prachauthid Rd., Thungkru, Bangkok 10140, Thailand (corresponding author). E-mail: sivawan.pho@kmutt.ac.th

[2]Environmental Science, Faculty of Science and Technology, Bansomdejchaopraya Rajabhat Univ., Isaraphab Rd., Dhonburi, Bangkok 10600, Thailand.

[3]Dept. of Mechanical Engineering, Faculty of Engineering, King Mongkut's Univ. of Technology Thonburi, 126 Prachauthid Rd., Thungkru, Bangkok 10140, Thailand.

Note. This manuscript was submitted on September 21, 2011; approved on June 11, 2012; published online on August 3, 2012. Discussion period open until June 1, 2013; separate discussions must be submitted for individual papers. This technical note is part of the ***Journal of Environmental Engineering***, Vol. 139, No. 1, January 1, 2013. © ASCE, ISSN 0733-9372/2013/1-141-146/$25.00.

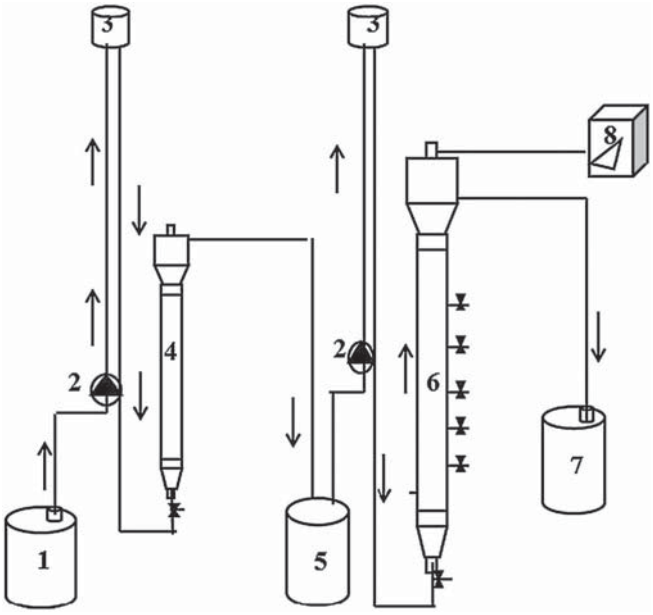

Fig. 1. Schematic diagram of two-stage UASB system: (1) influent tank, (2) feed pump, (3) control level tank, (4) acidogenic reactor, (5) effluent tank 1, (6) methanogenic reactor, (7) effluent tank 2, (8) gas meter

Table 1. Characteristics of Latex-Processing Wastewater in the First Anaerobic Pond of Srithepthai Latex Co., Ltd.

Parameters	Units	Value
pH	—	4.8–7.1
COD	mg/L	5,240–12,450
Sulfate	mg/L as SO_4^{-2}	1,889–4,210
Ammonia-N	mg/L as N	523–1,435
TKN	mg/L as N	816–1,970
Phosphate	mg/L as P	80–164
SS	mg/L	840–1,125
VSS	mg/L	670–924

(30% of the designated concentration, ≅6,000 mg COD/L) and the reactors were operated at HRT of 24 h. A stepwise increase of influent COD concentration from 30 to 50, 70, and 100% was conducted when ≥70% of COD removal efficiency at each dilution was attained. Tap water was used to prepare diluted wastewater and sodium bicarbonate solution was added to increase the pH of wastewater to neutral values (6.5–7.2). After the acclimation period, the pH and COD concentration of the influent were controlled at 5.5–6.0 and 6,000 mg/L, respectively. In Phase I of the experiment, the A reactor was first operated at HRT of 8 h and then was stepwise decreased to 6 and 4 h, respectively, while the M reactor was operated at HRT of 18 h. The steady state of each HRT was defined by the constant effluent COD and VFA concentrations. The HRT that permitted the highest VFA production rate will be used as the HRT for the A reactor of the two-stage UASB system in Phase II of the experiment. The HRT of the M reactor will be varied from 24, 32, and 56 h to maintain the HRT of the system at 28, 36, and 60 h, respectively.

Analysis

The measurement of COD, Total Kjeldahl Nitrogen (TKN), SO_4^{2-}, TSS, VSS, pH, and alkalinity in influent and effluent samples from both reactors was performed according to the *Standard Methods for Examination of Water and Wastewater* [American Public Health Association (APHA) 1992]. The VFA was determined by both direct titration and the use of a gas chromatograph (PerkinElmer, Auto System XL) equipped with a flame ionization detector (FID) and capillary column (Aquawax). The temperatures of the column, the injection port and the FID detector were 120, 180, and 250°C, respectively. The contents of CH_4 and CO_2 in the biogas was analyzed by another gas chromatograph (Shimadzu, GC-148) equipped with a thermal conductivity detector and a stainless-steel column (Porapak Q). The temperatures of the column, the injection port, and the detector were 45, 100, and 120°C, respectively. At the end of each HRT, sludge was taken from the A and M reactors to assess the specific acidogenic activity (SAA) and specific methanogenic activity (SMA) in a 120-mL serum bottle using glucose and acetic acid, respectively, as substrate (Soto et al. 1993). The external structure of the granular sludge from both reactors was examined using the JEOL scanning electron microscope (SEM), with the granules prepared according to Kalyuzhnyi et al. (1996). Sample sludge for DNA extraction was taken from the A and M reactors when each steady state was reached, and was stored in a refrigerator before use. Polymerase chain reaction-denaturing gel gradient electrophoresis (PCR-DGGE) was performed according to a previously published method (O-Thong et al. 2007).

Results and Discussion

Effect of HRT on Acidification in the UASB Reactor

Acidification and VFAs

The suitable HRT of A reactors in the two-stage anaerobic digestion process treating wastewater with a high COD concentration has been reported in the range of 6–24 h (Chathanee 1988). In the present study, it was found that the VFA concentration in the effluent decreased with the increasing HRT (Fig. 2) when the UASB reactors were operated at HRTs of 8 and 18 h. Because effluent VFA concentration is the sum of VFA production during acidification of the substrate and bacterial VFA degradation, this result indicated that the degradation of VFA in the reactor exceeded its production. Therefore, the HRTs of the experimental UASB reactors were lowered to 4 and 6 h in an attempt to achieve a high VFA concentration (especially of acetic acid) in the A reactor. The effluent VFA concentrations were found to be 8.9 and 2.67%, respectively, higher than those in the influent (Fig. 2). The concentration of each VFA, as determined by gas chromatography (data not shown), revealed that the acetic acid concentration in the

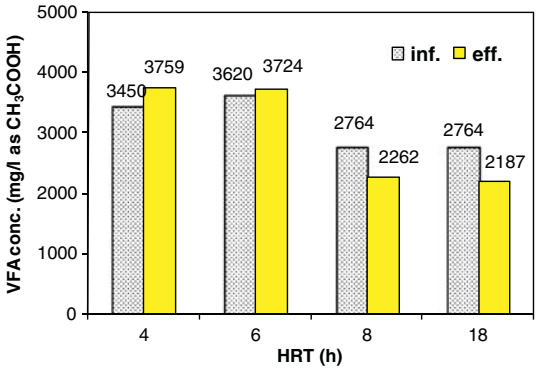

Fig. 2. VFA concentration in the influent and effluent at each HRT of the UASB reactor under acidogenic conditions

J. Environ. Eng. 2013.139:141-146.

effluent (1,783–2,907 mg/L) at each HRT was higher than the concentrations of propionic and butyric acids. This will be of benefit to the MPB in the second stage, because MPB can use acetic acid, formic acid, H_2, methanol, and methylamine as a substrate, but not VFAs that have a C atom > 2, e.g., propionic acid or butyric acid (Speece 1995). Butyrate is easily degraded to acetate by butyrate-oxidizing bacteria [Eq. (1)], whereas the degradation of propionate to acetate is thermodynamically infeasible unless the by-product, hydrogen, is removed by the hydrogen-consuming bacteria (Shin et al. 2001). However, the SRB are able to grow with a variety of organic carbon and sulfur compounds, including propionate [Eq. (2)]:

$$2\,\text{butyrate} + 4\,H_2O \longrightarrow 4\,\text{acetate} + H^+ + 4\,H_2 \quad (1)$$

$$4\,\text{propionate} + 3SO_4^{2-} \longrightarrow 4\,\text{acetate} + 4HCO_3^- + 3HS^- + H^+ \quad (2)$$

The reduction of propionic acid in the effluent, even for the short HRTs (4 and 6 h) observed in this study, may be attributable to the cooperation between propionate-degrading bacteria, hydrogen-consuming bacteria, and the activity of the SRB in the reactor.

COD removal and Sulfate Reduction

Generally, organic matter in sulfate-rich wastewater will be removed via sulfate reduction and methanogenesis in an anaerobic bioreactor (Hulshoff Pol et al. 1998). The SRBs obtain the energy for growth through oxidation of the organic substrate, and use sulfate as the terminal electron acceptor. The experimental results illustrate that COD and sulfate removal efficiency increased with the increasing HRT, in that 16–55% of COD and 23–35% of sulfate were removed (Fig. 3). The MPB and SRB were reported to be very competitive for substrate at a COD/SO_4^{2-} ratio of between 1.7 and 2.7, but which one will be dominant depends on the experimental conditions (Hao et al. 1996). Considering the COD/SO_4^{2-} ratio of this study (2.12–2.97) and the operating conditions of the reactor (pH 5.5, short HRT), which were not conducive to the optimal function of the MPB, it can be assumed that the reduction of COD concentration at each HRT was more because of the activity of the SRB than that of the MPB. The COD demand for SRB is in the range of 0.7 to 1.5 g $COD/g\,SO_4^{2-}$, depending on the C-source used as substrate (Hao et al. 1996). The increasing of alkalinity and pH (pH 7–8) in the effluent was observed although the influent pH was controlled at between pH 5.4–5.9. This may due to the degradation of protein and ammonia in latex-processing wastewater by the hydrolytic bacteria, which leads to the formation of NH_4HCO_3 [Eqs. (3) and (4)]. Moreover, the alkalinity could come from HCO_3^- alkalinity, HS^- alkalinity, and volatile acid alkalinity, which occur from sulfate reduction [Eqs. (5) and (6)]:

$$\text{Org-N} + H_2O \longrightarrow NH_3 + CO_2 \quad (3)$$

$$NH_3 + CO_2 + H_2O \longrightarrow NH_4HCO_3 \quad (4)$$

$$SO_4^{2-} + \text{organic matter} \xrightarrow{\text{SRB}} HS^- + H_2O + HCO_3^- \quad (5)$$

$$CH_3COO^- + SO_4^{2-} \xrightarrow{\text{SRB}} 2HCO_3^- + HS^- \quad (6)$$

Considering all the results, the suitable HRT for the acidification stage was 4 h, because a high degree of acidification and acetic acid concentration was achieved at this HRT. Although the COD removal efficiency at this HRT was rather low (<20%), the sulfate reduction efficiency was at the same level as it had been over HRTs of 6 and 8 h (Fig. 3). Moreover, effluent pH (6.5–7.5) and alkalinity

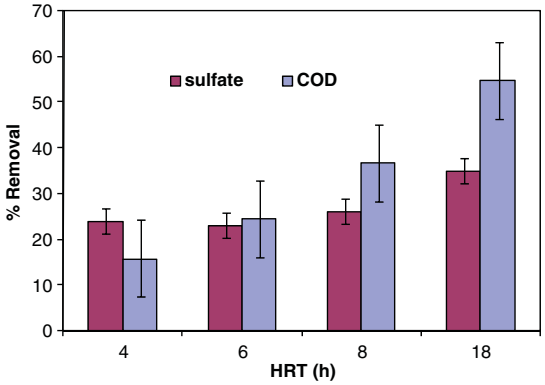

Fig. 3. COD and sulfate removal efficiency at each HRT of the UASB reactor under acidogenic conditions

at HRT of 4 h were optimal for the MPB; therefore, the effluent from the aforementioned conditions could feed directly to the methanogenic reactor without any alkaline addition.

Performance of the Two-stage UASB Reactor Treating Latex-Processing Wastewater

COD and Sulfate Removal Efficiency

The A reactor in the two-stage UASB system was constantly operated over an HRT of 4 h, while the HRTs of the M reactor were varied at 24, 32, and 56 h, respectively. The performance of the two-stage UASB system for each HRT, treating wastewater from a latex-processing factory, is shown in Table 2. The COD removal efficiency of the system was found to increase with the increasing HRT, in which 87.3% of COD was removed for HRT of 60 h [Fig. 4(a)]. A significantly decreased SS concentration was also observed after each stage of treatment. Suspended solids in the latex-processing wastewater are primarily rubber particles, which occur from the skim crepe recovery by adding H_2SO_4 to the skim latex. The decrease of SS concentration was presumably due to the degradation of the rubber particles, which resulted in the formation of rubber scum. It was noticed that most of the COD removal took place in the M reactor; however, the methane content of the biogas could be analyzed only at HRT of 28 h. It was found that the gas outlet in the gas-liquid-solid separator (GSS) of the methanogenic reactor was covered with a lot of rubber scum, which led to the loss of biogas with the effluent. The decrease in the VFA content was also consistent with the increase in efficiency of COD removal.

An increase in sulfate removal efficiency from 71 to 83% was observed when the HRT of the system increased from 28 to 36 h [Fig. 4(b)]. Corresponding to the COD removal, most of the sulfate reduction at those HRTs occurred in the M reactor. It can be presumed that the SRB shared contribution with MPB on COD removal in the M reactor, despite the presence of favorable conditions for the MPB in the reactor. Such results were not surprising, because in the anaerobic treatment of wastewater in the presence of sulfate, hydrogenotrophic SRB (HSRB) has a higher growth rate, substrate affinity, and cell yield than hydrogenotrophic MPB (HMPB) (Oude Elferink et al. 1994; Colleran et al. 1995). Acetate-utilizing SRB (ASRB) has a thermodynamic and kinetic advantage over acetate-utilizing MPB (AMPB) in its competition for acetate (Widdel 1988). In contrast to the COD removal, a remarkably low sulfate-reduction efficiency of only 17% was observed in the M reactor, operating for HRT of 56 h. A lower sulfate concentration in the A reactor (901 mg/L), which resulted in a

J. Environ. Eng. 2013.139:141-146.

Table 2. Performance of the Two-Stage UASB Reactor Treating Latex-Processing Wastewater at Each HRT

	HRT 28 h			HRT 36 h			HRT 60 h		
Parameters[a]	Influent	Acid tank (4 h)	Methane tank (24 h)	Influent	Acid tank (4 h)	Methane tank (32 h)	Influent	Acid tank (4 h)	Methane tank (56 h)
pH	5.41 ± 0.21	7.01 ± 0.3	8.00 ± 0.17	5.84 ± 0.22	7.83 ± 0.51	8.56 ± 0.13	6.2 ± 0.52	8.3 ± 0.24	8.9 ± 0.13
COD	6,394 ± 380	5,460 ± 449	3,093 ± 461	6,660 ± 817	5,230 ± 596	2,140 ± 499	5,821 ± 452	3,887 ± 373	742 ± 181
VFA	3,450 ± 329	3,759 ± 314	2,297 ± 236	3,385 ± 932	3,261 ± 1,081	1,260 ± 763	2,631 ± 567	2,217 ± 228	239 ± 74
Acetic acid	1,346	2,664	1,251	1,693	2,392	1,496	1,740	1,820	53
Propionic acid	1,032	309	n.d.[b]	1,062	284	40	878	141	n.d.[b]
Butyric acid	126	11	n.d.[b]	75	50	n.d.[b]	18	n.d.[b]	n.d.[b]
Alkalinity	2,220 ± 80	2,848 ± 206	4,120 ± 460	2,495 ± 699	2,903 ± 900	3,768 ± 1470	2,249 ± 609	2,971 ± 249	2,943 ± 286
Sulfate	2,987 ± 257	2,270 ± 82	859 ± 302	2,938 ± 999	2,037 ± 622	506 ± 333	1,767 ± 333	901 ± 185	807 ± 183
Sulfide	—	38 ± 15	132 ± 39	—	77 ± 28	139 ± 28	—	142 ± 25	56 ± 11
SS	955 ± 320	531 ± 304	252 ± 116	926 ± 157	344 ± 57	94 ± 16	742 ± 122	349 ± 98	66 ± 26
CH_4 (%)	—	7.14	48.98	—	n.a.[c]	n.a.[c]	—	n.a.[c]	n.a.[c]
CO_2 (%)	—	2.41	3	—	n.a.[c]	n.a.[c]	—	n.a.[c]	n.a.[c]

[a]The units of all parameters are mg/L, except pH, CH_4, CO_2.
[b]Not detected.
[c]Could not analyzed (because GSS was blocked by rubber scum).

Fig. 4. Removal efficiency of the two-stage UASB reactor at each HRT: (a) COD removal efficiency; (b) sulfate removal efficiency

COD/SO_4^{2-} ratio of 4.31, might be the reason for the low sulfate reduction efficiency, because MPB outcompeted SRB for available electron donors when the COD/SO_4^{2-} ratio of the wastewater was greater than 2.7 (Hao et al. 1996). Thus, it can be presumed that the degradation of COD in the M reactor operating at HRT of 56 h was primarily due to MPB.

Nevertheless, relatively low methane content in the biogas and low SMA were detected. Visser et al. (1996) found that sludge granules were 50% inhibited at H_2S concentrations of 250 and 90 mg L^{-1} at pH values of 6.4–7.2 and 7.8–8.0, respectively. The methane production of MPB was thought to be inhibited by sulfide toxicity, because the sulfide concentration in the effluent from the acidogenic reactor was 142 mg L^{-1} (Table 2). Moreover, it was noticeable that both the COD removal and sulfate reduction efficiency of the A reactor, even when it operated constantly for HRT of 4 h, increased as the HRT of the system increased from 28 to 36 and 60 h. This might be explained by two reasons: (1) the acclimation of microorganisms to the latex-processing wastewater; and (2) a rapid increase of SRB and acidogenic bacteria in the reactor, because the maximum specific growth rates (μ_{max}) of SRB and acidogenic bacteria were 0.85–2.0 and 0.05–7.2 day^{-1}, respectively (Speece 1995).

The COD removal efficiency of the two-stage UASB system in this study was compared to that of the anaerobic hybrid reactor (one stage) that treated latex-processing wastewater from the same source (Wongkittiwimol 2000). The average COD removal efficiencies when the anaerobic hybrid reactor was operated at HRTs of 36, 60, 96, and 144 h were 41, 59, 81, and 84%, respectively. It was found that the two-stage UASB system had higher removal efficiency than the anaerobic hybrid reactor for the same HRT. For example, a COD removal efficiency of 87.3% could be achieved by the two-stage UASB system at an HRT of 60 h, whereas the same level of efficiency was attained only when the anaerobic hybrid reactor was operated under HRT longer than

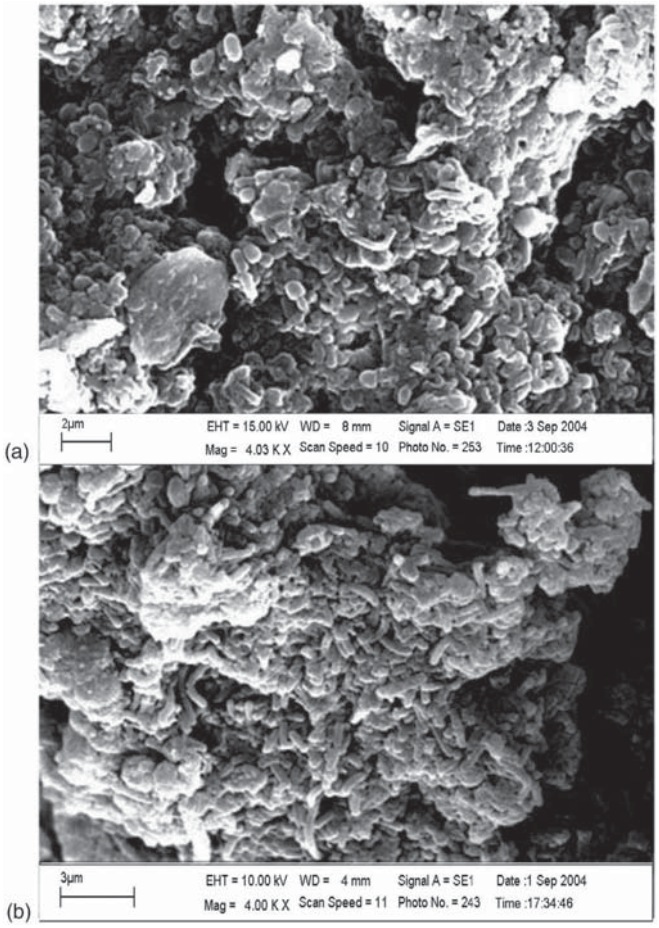

Fig. 5. Scanning electron micrograph of the surface of sludge from: (a) A reactor; (b) M reactor

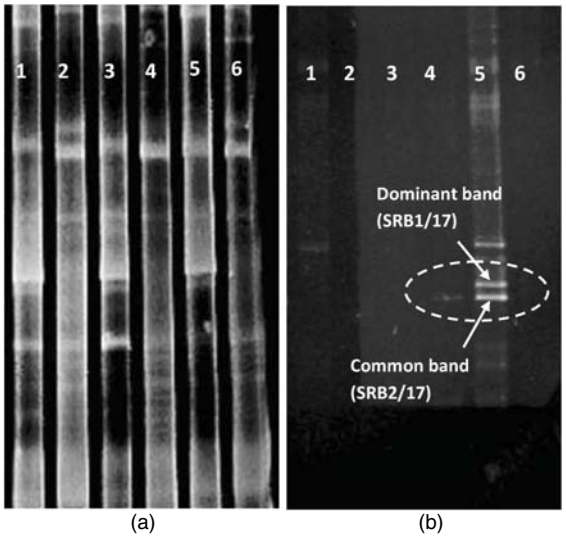

Fig. 6. DGGE profiles of 16S rRNA genes in sludge from the A reactor (columns 1, 3, 5: HRT 4 h) and the M reactor (column 2: HRT 24 h; column 4: HRT 32 h; column 6: HRT 56 h): (a) *archae* bacteria (571 bps); (b) sulfate reducing bacteria (522 bps)

4 days (96 h). This highlights the advantages of the two-stage UASB system, in which the accumulation of VFA and the interference or inhibition of the SRB in relation to the MPB could be reduced in the first stage of the system.

Sludge Morphology and Sludge Activity

The morphology of the sludge from both the acidogenic and the methanogenic reactor, as examined by SEM, revealed that the surfaces of most granules were covered by rubber polymer. A heterogeneous population of rod and filament bacteria was found on the surfaces of both types of sludge. Acidogenic granules predominantly consisted of short-rod bacteria [Fig. 5(a)], whereas networks of long multicellular filaments appeared to colonize the surface of the methanogenic sludge [Fig. 5(b)].

The SAA of sludge from the A reactor was between 1.705–1.835 g COD g VSS^{-1} d^{-1}, and the SAA of the M sludge was slightly broader (1.326–2.024 g COD g VSS^{-1} d^{-1}). Compared to the maximum acidogenic activity in pure cultures and in mixed cultures from anaerobic reactors in the literature (Henze and Harremoes 1983; Soto et al. 1993), the SAA of the tested sludge was 5–10 times lower. Unexpectedly low SMA in the range of 0.0078 to 0.0138 g COD-CH_4 g VSS^{-1} d^{-1}, accompanied by methane content of 25–36% in the biogas, was obtained from the acidogenic and the methanogenic sludge. It was hypothesized that the MPB in the UASB reactor, particularly the M reactor, were eliminated or inhibited by the other bacteria. The monitoring of the microbial community, using a denaturing gradient gel electrophoresis (DGGE) technique, revealed that MPB could still be detected in both the A and M reactors (Fig. 6), but were dominated by the SRB. This was clearly observed in the acidogenic sludge when the system was operated at HRT of 36 h. The ability of SRB to use several intermediates of the anaerobic process (e.g., propionate, butyrate, and acetate) as energy sources in the presence of sulfate, coupled with their high substrate affinity (Hao et al. 1996), were supposed to be the reasons for the overwhelming numbers of SRB in the M reactor. This assumption was confirmed by the SAA of the sludge from the M reactor, which was at the same level as the sludge from the A reactor, and by the high sulfate-reduction efficiency concomitant with the COD removal in the methanogenic reactor at HRTs of 28 and 36 h (Fig. 4).

Conclusions

Latex-processing wastewater was successfully treated in a two-stage UASB reactor. Maximum COD removal efficiency of 87% was achieved at HRT of 60 h and 83% sulfate reduction efficiency was observed at HRT of 36 h. Most of the COD removal was attributable to SRB rather than MPB. Not much difference was observed between the SAA of the acidogenic and methanogenic sludge, which indicates the existence of acetogenic, methanogenic, and sulfate-reducing bacteria in the methanogenic reactor. Microbial community monitoring by the DGGE technique confirmed the domination of SRB in both reactors.

Acknowledgments

The authors would like to express their acknowledgement to the Thailand Research Fund, the Office of the Higher Education Commission and the National Research University Project for the financial support. A grateful thank is also for Dr. Srisuda Dhamwichukorn for her helping hand in PCR-DGGE analysis and the Department of Microbiology, King Mongkut's University of Technology Thonburi for providing the facilities for this study.

J. Environ. Eng. 2013.139:141-146.

References

American Public Health Association (APHA). (1992). *Standard methods for the examination of water and wastewater*, 18th ed., APHA/American Water Works Association/Water Environment Federation, Washington DC.

Chathanee, C. (1988). "Tapioca wastewater treatment by two-stage anaerobic digestion process." Master's thesis, Biotechnology, Chulalongkorn Univ., Bangkok, Thailand, 35–46 (in Thai).

Colleran, E., Finnegan, S., and Lens, P. (1995). "Anaerobic treatment of sulphate-containing waste streams." *Antonie Leeuwenhoek*, 67(1), 29–46.

Hao, O. J., Chen, J. M., Huang, L., and Buglass, R. L. (1996). "Sulfate-reducing bacteria." *Crit. Rev. Env. Sci. Technol.*, 26(2), 155–187.

Henze, M., and Harremoes, P. (1983). "Anaerobic treatment of wastewater in fixed film reactors—A literature review." *Water Sci. Technol.*, 15, 1–101.

Hulshoff Pol, L. W., Lens, P. N. L., Stams, A. J. M., and Lettinga, G. (1998). "Anaerobic treatment of sulphate-rich wastewaters." *Biodegradation*, 9(3–4), 213–224.

Kalyuzhnyi, S. V., et al. (1996). "Organic removal and microbiological features of UASB-reactor under various organic loading rates." *Bioresour. Technol.*, 55(1), 47–54.

Lens, P. N. L., Visser, A., Janssen, A. J. H., Hulshoff Pol, L. W., and Lettinga, G. (1998). "Biotechnological treatment of sulfate-rich wastewaters." *Crit. Rev. Env. Sci. Tech.*, 28(1), 41–88.

O-Thong, S., Prasertsan, P., Intrasungkha, N., Dhamwichukorn, S., and Birkeland, N. (2007). "Improvement of biohydrogen production and treatment efficiency on palm oil mill effluent with nutrient supplementation at thermophilic condition using an anaerobic sequencing batch reactor." *Enzyme Microb. Technol.*, 41(5), 583–590.

Oude Elferink, S. J. W. H., Visser, A., Hulshoff Pol, L. W., and Stams, A. J. M. (1994). "Sulfate reduction in methanogenic bioreactors." *FEMS Microb. Rev.*, 15(2–3), 119–136.

Shin, H. S., Han, S. K., Song, Y. C., and Lee, C. Y. (2001). "Performance of UASB reactor treating leachate from acidogenic fermenter in the two-phase anaerobic digestion of food waste." *Water Res.*, 35(14), 3441–3447.

Soto, M., Mendez, R., and Lema, J. M. (1993). "Methanogenic and non-methanogenic activity tests: Theoretical basis and experimental set up." *Water Res.*, 27(8), 1361–1376.

Speece, R. E. (1995). *Anaerobic biotechnology for industrial wastewater*, Archae Press, Nashville, TN.

Thailand Office of Agricultural Economics. (2009). ⟨http://www.oae.go.th/download/prcai/Rubber09.xls⟩ (Jun. 27, 2011).

Visser, A., Hulshoff Pol, L. W., and Lettinga, G. (1996). "Competition of methanogenic and sulfidogenic bacteria." *Water Sci. Technol.*, 33(3), 99–110.

Widdel, F. (1988). "Microbiology and ecology of sulfate- and sulphur reducing bacteria." *Biology of anaerobic microorganisms*, A. J. B. Zehnder, ed., Wiley, New York, 469–586.

Wongkittiwimol, A. (2000). "Treatment of concentrated latex wastewater in the anaerobic hybrid reactor." Master's thesis, Faculty of Engineering, King Mongkut's Univ. of Technology Thonburi, Bangkok, Thailand.

J. Environ. Eng. 2013.139:141-146.

Send Orders of Reprints at bspsaif@emirates.net.ae

56 *Current Nanoscience,* **2013,** *9,* **56-60**

Pool-Boiling Heat Transfer Characteristics of Al_2O_3-Water Nanofluids on a Horizontal Cylindrical Heating Surface

Weerapun Duangthongsuk[a,b], Taklaew Yiamsawasd[a], Ahmet Selim Dalkilic[c] and Somchai Wongwises[a,d*]

[a]*Fluid Mechanics, Thermal Engineering and Multiphase Flow Research Lab. (FUTURE), Department of Mechanical Engineering, Faculty of Engineering, King Mongkut's University of Technology Thonburi, Bangmod, Bangkok 10140, Thailand;* [b]*Department of Mechanical Engineering, South-East Asia University, Bangkok, Thailand;* [c]*Heat and Thermodynamics Division, Department of Mechanical Engineering, Yildiz Technical University (YTU), Yildiz, Besiktas, Istanbul 34349, Turkey;* [d]*The Academy of Science, The Royal Institute of Thailand, SanamSueaPa, Dusit, Bangkok 10300, Thailand*

Abstract: This research involved conducting an experiment on pool boiling characteristics of Al_2O_3–water nanofluid. The experimental concentration ranged between 0.00005 and 0.03 %vol. The pressure used was at 1 and 2 atm. The boiling surface was a horizontal copper cylinder with a diameter of 28.5 mm, a length of 90 mm, and surface roughness of 3.14 μm. The main purpose of this research was to study the effect of the nanofluid's concentration and pressure on the heat transfer coefficient and on heat flux, by comparing with water. Calibration of the experimental apparatus with water revealed that the experimental results corresponded to the prediction by Rohsenow's equation. Results from the experiment on pool boiling of nanofluids indicated that the heat transfer coefficient of Al_2O_3–water nanofluid was lower than that of water and tended to decrease when the concentration was higher.

Keywords: Pool boiling, nanofluid, heat transfer coefficient, particle concentration.

1. INTRODUCTION

Heat exchangers are important energy devices commonly found in various industries. They include steamers, heat ventilators in mechanical or electronic devices, coolers, air-conditioners, and other types of devices. At present, the world is facing energy problems. Therefore, many researchers are interested in design and development of devices that use energy more efficiently, including heat exchangers. Working fluids used with heat exchangers include both phase-change (between liquid and vapor) and non phase-change types. The phase-change type produces better heat transfer, compared with the non-phase change type. Pool-boiling heat transfer is one of the mechanisms that occur in heat exchangers. Examples of pool-boiling heat exchangers are heat pipes in heat exchanger units of processors in mobile computers or military communication devices, and fire-tube steamers in industrial factories. Development of pool-boiling heat exchangers maybe carried out in two parts: 1) development of the heating surface and 2) development of the working substance used in the system. The first and most widely used for nucleate pool boiling was developed by Rohsenow [1]. The effects of the surface were taken into account in the correlation. The development of a working substance used in pool-boiling heat exchangers has been carried out in many ways. At present, one of the methods that many researchers are interested in is the addition of solid nanoparticles with high conductivity into base fluids in order to increase thermal conductivity of working fluids. Choi [2] termed the fluids obtained from the addition of solid nanoparticles into abase fluid as "Nanofluid." Regarding the use of nanofluids in forced heat transfer, many researchers have reported increases in the heat transfer coefficient by about 7% to 40% [3-10]. This is because nanofluids have higher conductivity than base fluids. However, only a few studies have used nanofluids with pool-boiling heat transfer, and their results are still inconsistent. Studies concerning specific characteristics of pool boiling of nanofluids in the past decade are summarized here.

*Address correspondence to this author at the Fluid Mechanics, Thermal Engineering and Multiphase Flow Research Lab. (FUTURE), Department of Mechanical Engineering, Faculty of Engineering, King Mongkut's University of Technology Thonburi, Bangmod, Bangkok 10140, Thailand;
Tel: +662-470-9115; Fax: +662-470-9111;
E-mail: somchai.won@kmutt.ac.th

Das *et al*. [11] studied specific characteristics of pool-boiling heat transfer of nanofluids by adding 58.4 mm Al_2O_3 particles to Al_2O_3–water nanofluid at a concentration of 0.1–4 vol.%. The heating surface was a horizontal tube with a diameter of 20 mm and surface roughness of 0.4 to 1.15 μm. Their experimental results showed that the pool boiling heat transfer performance was increased when level of surface roughness increased. However, when the concentration of the nanofluid was increased, the specific characteristics of the heat transfer decreased.

You *et al*. [12] studied the increase incritical heat flux caused by pool boiling of an Al_2O_3–water nanofluid with concentrations of 0.001–0.05 g/l. The heating surface was a horizontal 10x10 mm^2 square copper plate. During the experiment, pressure and temperature were fixed at 2.89 psi and 60°C, respectively. Their results showed that the critical heat flux of the nanofluid was higher than that of water and that it also increased with the increase of the nanofluid's concentration. They found that the critical heat flux increased by 200% at a concentration of 0.05 g/l.

Li *et al*. [13] studied pool-boiling heat transfer characteristics under atmospheric-pressured subcooled boiling of 25 mm silicon dioxide nanoparticles suspended in water at concentrations of 0.05–0.5 wt.%. The heating surface was platinum wire with a diameter of 0.1mm. They found that the pool-boiling heat transfer of SiO_2–water nanofluid was higher than that of water that it varied with the nanofluid's concentration level. In addition, they found that the critical heat flux also increased when the concentration increased.

Vassallo *et al*. [14] studied the pool-boiling heat transfer characteristics of a SiO_2–water nanofluid with Si-deionized size of 15 nm, 50 nm, and 3 μm, and with concentration levels of 0.5–9 vol.%. The heating surface was nickel-chromium wire with a diameter of 0.4 mm and a length of 75 mm. The experiment at atmospheric pressure showed that the critical heat flux of the nanofluid was higher than that of the base fluid, and that it increased when concentration levels of the particles increased.

Bang and Chang [15] studied specific characteristics of nucleate pool-boiling heat transfer of an Al_2O_3–water nanofluid with particle size of 47 nm and concentration levels of 0.5–4 vol.%. The heating surface consisted of 4×100 mm^2 rectangular copper plates placed both horizontally and vertically. Their results showed that increases in the nanofluid's concentration lowered the pool-boiling heat

1875-6786/13 $58.00+.00

transfer coefficient. However, the critical heat flux was higher than that of water. Analysis from photography revealed that at heat flux higher than 100 kW/m^2, the boiling pattern of the nanofluid was less vigorous than water. They also found that the horizontal heating surface produced higher heat flux than the vertical one.

Kim *et al*. [16] studied the critical heat flux of pool-boiling nanofluids at atmospheric pressure. The 85 nm TiO_2 particles were suspended in water at concentration levels of 0.00001–0.1 vol.%. The heating surface was 0.2 mm nickel-chromium wire. The effect of a heating surface covered with nanoparticles was also studied. They found that the critical heat flux of the nanofluid was higher than that of the base fluid and that the critical heat flux increased when the heating surface was covered with nanoparticles.

Nguyen *et al*. [17] studied specific characteristics of pool-boiling heat transfer of an Al_2O_3–distilledwater nanofluid at atmospheric pressure. The particle size was 47 nm and the concentration level was 0.5–2 vol.%. The heating surface was a horizontal 24 mm-diameter chromium-coated copper disc. Their results showed that when the nanofluid's concentration increased, its pool-boiling heat transfer capacity decreased, compared to water.

Kim *et al*. [18] studied the pool-boiling heat transfer of three-types of nanofluids: Al_2O_3, ZrO_2 and SiO_2 particles suspended in water at concentrations of 0.001–0.1 vol.%. Two types of heating surfaces were used: stainless steel wire with a diameter of 0.381mm and a length of 120mm, and a horizontal 5x45mm^2 plate. The experiment was carried out at atmospheric pressure. The researchers found that the critical heat flux increased with the increase of concentration and heat transfer coefficient was higher than that of water. For all nanofluids, the enhancement of critical heat flux (CHF) is obtained, up to 52% for alumina nanofluids, up to 75% for zirconia nanofluids and up to 80% for silica nanofluids.

Kiu *et al*. [19] studied pool-boiling heat transfer of nanofluids with 50nm CuO and 35 nm SiO_2 particles, each suspended in water and in ethyl alcohol with concentrations of 0.5 wt.%. The heating surface was a horizontal 20mm-diameter copper disc. Their results showed that the critical heat flux of nanofluids was higher than that of the base fluids.

Golubovic *et al*. [20] studied the effect of concentration levels on the critical heat flux of BiO_2–water and Al_2O_3–water nanofluids at a concentration range of 0.0005714–0.0064615 g/l. The heating surface was nickel-chromium wire with a diameter of 0.64 mm and a length of 50 mm, applied at atmospheric pressure. They found that the critical heat flux varied as concentration levels increased, and that it was overall higher than that of water. The CHF was increased by 50% when Al_2O_3 nanoparticles were suspended in pure distilled water and by 33% when BiO particles were suspended.

Trisaksri and Wongwises [21] studied the specific characteristics of pool-boiling heat transfer of a nanofluid with 21nm-diameter TiO_2 nanoparticles suspended in R141b refrigerant at concentrations of 0.01–0.05 vol.%. The heating surface was a horizontal cylinder with a diameter of 28.5 mm and length of 90mm,appliedat pressure levels of 200 to 500 kPa. The researchers concluded that the pool-boiling heat transfer coefficient decreased when the nanofluid's concentration increased, but it increased with increases in the pressure level.

Suriyawong and Wongwises [22] studied pool-boiling heat transfer characteristics of a TiO2–water nanofluid at very low concentration levels (0.00005–0.01 vol.%). The heating surface was made from copper and aluminum, with roughness of 0.2 and 4 μm, applied at atmospheric pressure. In the case of the copper surface, it was found that at concentrations of 0.00005–0.0001 vol.%, the heat transfer coefficient was higher than that of the base fluid. On the other hand, at concentrations higher than 0.0001 vol.%, the heat transfer coefficient was lower than that of the base fluid. In the case of the aluminum surface, the heat transfer coefficient was found to be lower than that of the base fluid at every concentration level. Regarding roughness, a surface roughness of 0.2μm produced a higher heat transfer than roughness of 4μm.

Cieslinski and Kaczmarczyk [23] studied pool-boiling heat transfer of Al_2O_3–water and Cu–water nanofluids at concentrations of 0.01%, 0.1% and 1% by weight. The heating surface was a horizontal smooth-surfaced tube made from copper and stainless steel with a diameter of 10 mm. The effects of concentration level and of surface material on heat transfer characteristics were studied at atmospheric pressure. They found that the concentration level had very little effect on the boiling heat transfer coefficient of Al_2O_3–water and Cu–water nanofluids on the copper heating surface. Additionally, the type of surface material used seemed to have no effect on boiling heat transfer of Cu–water at a concentration of 0.1 wt.%. However, at other concentration levels of both Al_2O_3–water and Cu–water, the boiling heat transfer coefficient on the stainless steel tube was higher than that onthe copper tube at the same heat flux.

From the above review of the literature, there are seemingly very few studies concerning the specific characteristics of pool-boiling heat transfer of nanofluids, and their results are inconsistent. Some researchers reported that the heat transfer coefficient varied with the concentration level of the nanofluid [12-14, 16, 18- 20], while some reported an inverse variation with concentration levels [11, 15, 17, 21, 22]. Every experiment was conducted at atmospheric pressure, except the experiment by Trisaksri and Wongwises [21], who also observed the effects of pressure. Thus, the researchers in the current study aimed to conduct additional experiments on pool-boiling heat transfer in order to clarify the inconsistent results mentioned above. This research uses a nanofluid with $A1_2O_3$ nanoparticles suspended in water at concentrations of 0.00005–0.03 vol.% and at pressure levels of 1 and 2 atm. The heating surface used is a horizontal copper cylinder.

2. PREPARATION OF THE NANOFLUID

The Al_2O_3–water nanofluidused in this study is a product supplied by DEGUSSA Company Limited (Thailand) under the code of AeroDisp. W630. The 120nm-diameter Al_2O_3 particles are suspended in water at a concentration of 30 wt.%. In order to study the effect of the concentration level, the fluidis diluted by addition of base water to obtain concentration levels of 0.00005, 0.0001, 0.005 and 0.03 vol.%. To attaineven dispersion of particles in the base fluid, an ultrasonic vibrator is used for sonication for 2 hours before every experiment. The preparation of the nanofluid with pH-control and the addition of surfactants were accomplished by the manufacturer without revealing information about the process.

3. EXPERIMENTAL APPARATUS AND PROCEDURES

The experimental apparatus includes a pressure vessel, a water-cooling unit, a boiling heating surface, and a DC power supply, as shown in Fig. (**1**).

The pressure vessel containing the nanofluid used in the experiment is made from stainless steel with a diameter of 10 cm, a height of 30 cm, and a thickness of 1 cm. Its outer surface is coated with insulator to prevent heat loss. A cooling coil and a pressure gauge are installed on top of the vessel to control the pressure level and to condense the upward flow of vapors into liquid, in order to maintain a stable concentration throughout the experiment. The control is done by adjusting the flow rate of cold water pumped from the cooling unit. A T-type thermocouple is also installed on top of the vessel to measure the temperature of the fluid mass.

The heating surface, as shown in Fig. (**2**), consists of a 2-kilowatt heater stick buried inside the copper cylinder (28.5 mm diameter and 90 mm length). Both ends of the copper cylinder are covered with insulators to force heat from the heater to the heating surface on its side only (radially). Four sets of T-type thermocouple are installed along the length at even intervals to measure surface

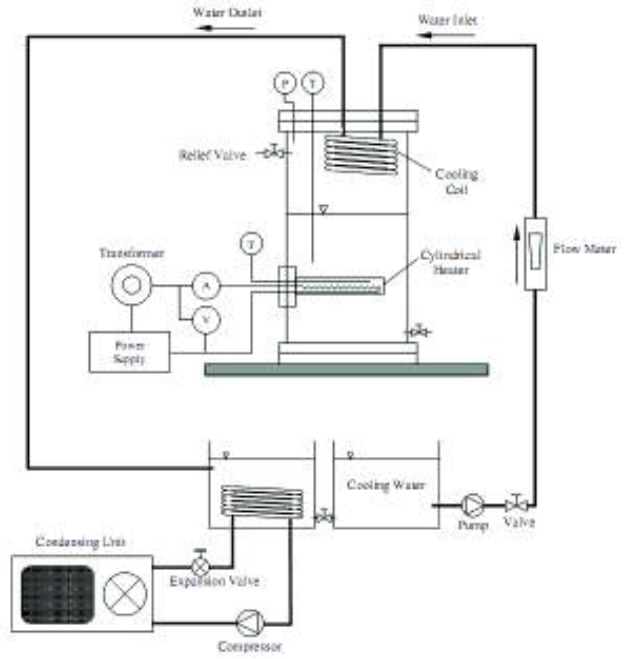

Fig. (1). Schematic diagram of experimental apparatus [Trisaksri and Wongwises [21], with permission from Elsevier].

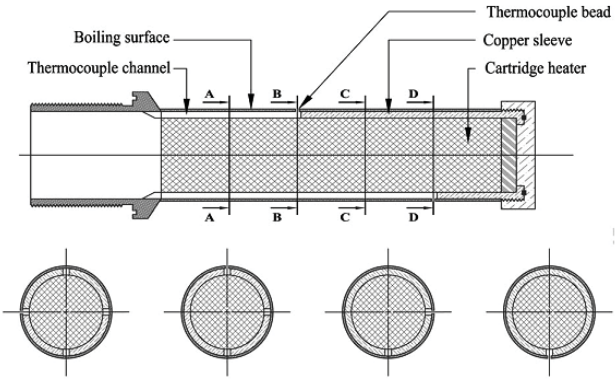

Fig. (2). Cross-sectional view of the heating surface [Trisaksri and Wongwises [21], with permission from Elsevier].

temperature of the tested unit. Each set is placed at an angle of 90 degrees radially. The thermocouples are specially designed so that only the small temperature gauge head is fixed directly onto the outer heating surface, while other signal wires are concealed inside to prevent interference on the heating surface and movement of vapor bubbles during the boiling process.

4. DATA REDUCTION

The heat transfer coefficient and the heat flux of pool boiling may be calculated with the following equations.

The heat flux q (W/m^2) maybe calculated with Eq. (1).

$$q = \frac{IV}{A} \tag{1}$$

where I is electrical current(Amp), V is voltage(Volt), and A is heating surface(m^2).

The average heat transfer coefficient of pool boiling, $h_b(W/m^2K)$ maybe calculated with Eq. (2).

$$h_b = \frac{q}{T_h - T_{sat}} \tag{2}$$

where T_{sat} is the saturated temperature of working fluids (^oC)and T_h is the average temperature of the heating surface, which maybe calculated with Eq. (3).

$$T_h = \frac{T_{h,top} + 2T_{h,side} + T_{h,bottom}}{4} \tag{3}$$

where $T_{h,top}$, $T_{h,side}$ and $T_{h,bottom}$ are temperatures at each location as shown in Fig. (**2**).

The uncertainties of the heat flux, heating surface temperature and heat transfer coefficient are ±2.92%, ±2.39% and ±5.89%, respectively.

Regarding calibration of the experimented apparatus, Rohsenow's equation [1] is used with water as the working fluid, as follows:

$$q = \mu_l h_{fg} \left[\frac{g(\rho_l - \rho_v)}{\sigma} \right]^{0.5} \left[\frac{C_p (T_h - T_{sat})}{C_{sf} h_{fg} \Pr_l^n} \right]^3 \tag{4}$$

where μ is viscosity of fluid, ρ is density of fluid, σ is surface tension of fluid, C_p is specific heat, h_{fg} is latent heat, Pr is Prandtl number, and C_{sf} and n are constants between heating surface and fluid. In the case of the copper surface and water, the constants are 0.031 and 1.0, respectively. The subscripts l and v represent the liquid phase and vapor phase, respectively.

5. RESULTS AND DISCUSSION

Before the experiment on boiling of the nanofluid, the invented apparatus was calibrated to confirm its accuracy by testing with water. The test results were compared with calculations from Rohsenow's equation [1] and data from the experiments of other researchers, as shown in Fig. (**3**). The calibration results confirmed that data gained from the invented apparatus were consistent with calculations from Rohsenow' sequation and with measurements by other researchers.

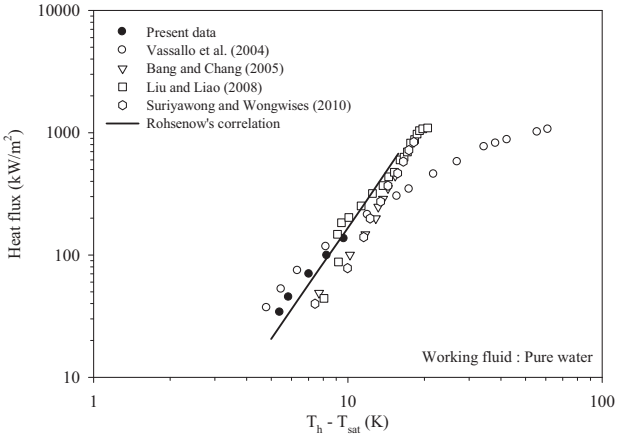

Fig. (3). Comparison of present data with Rohsenow's correlation and various researchers.

Fig. (**4**) shows boiling curves ofAl_2O_3–water nanofluidat various concentration levels. At the same heat flux, the boiling curves tend to move in a direction to the right when concentration levels of nanoparticles increased or when differences in temperature between the heating surface and the fluid increased. It could be said that the

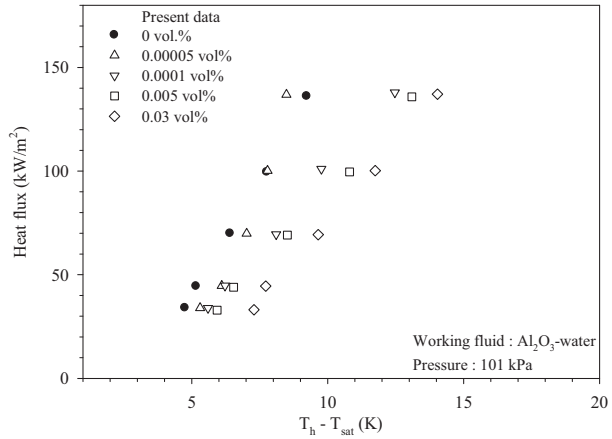

Fig. (4). Boiling curves for Al_2O_3-water nanofluid at 101 kPa.

onset of nucleate boiling is slower. That is, the heat transfer coefficient is lower than the water base fluid and decreases when the concentration increases, as clearly evident in Fig. (**5**). However, at a concentration of 0.00005 vol.%, it was found that at high heat flux, the heat transfer tended to be higher than that of the base fluid. Regarding heat flux, it was found that at the same concentration level, the heat transfer coefficient varied with heat flux in both water and nanofluidat every concentration level.

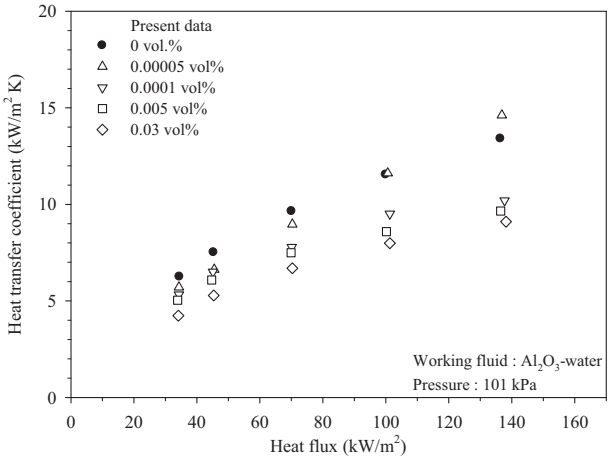

Fig. (5). Boiling heat transfer coefficient for Al_2O_3-water nanofluid at 101 kPa.

The results of the experiment on the pool-boiling heat transfer of an Al_2O_3–water nanofluid were compared with those of other studies, as shown in Fig. (**6**). Correspondence was found with the studies by Das *et al*. [11] and by Cieslinski and Kaczmarczyk [23]. Both of those studies used a horizontal copper cylinder boiling surface similar to that used in this research. It can be seen in the figure that when the concentration increases, the boiling curves tend to move in a direction to the right. In other words, the heat transfer coefficient tends to decrease and is lower than the base fluid. This could be clearly seen in Fig. (**7**), where the experimental results are presented in terms of heat transfer enhancement, which is a ratio between heat the transfer coefficient of nanofluid and the heat transfer coefficient of the base fluid. This figure also shows that at a low concentration level of 0.00005 vol.%, the heat transfer coefficientis higher than that of the base fluid. This is consistent with Suriyawong and Wongwises [22], who found that heat transfer

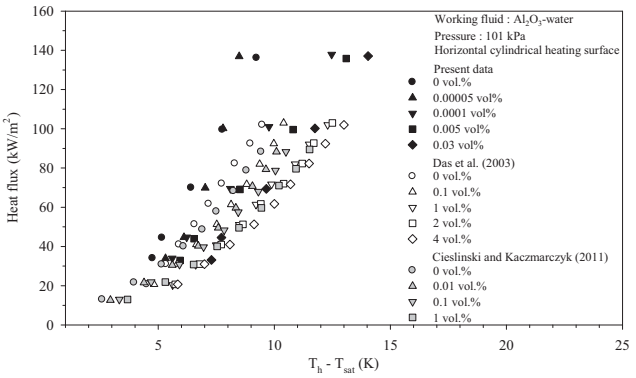

Fig. (6). Comparison of experimental boiling curves with those reported by various researchers.

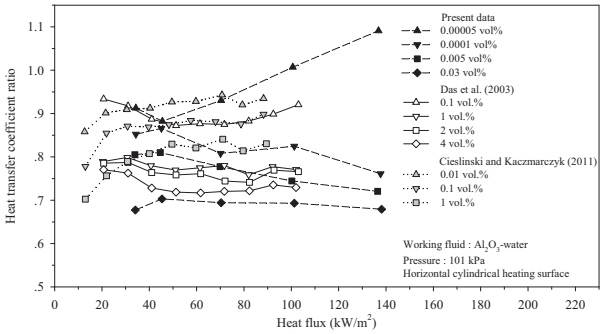

Fig. (7). Comparison of experimental pool boilingheat transfer enhancement with those reported by various researchers.

coefficient of TiO_2-water nanofluid was higher than the base fluid at low concentration levels (between 0.00005 to 0.01 vol.%), but decreased at high concentration level.

Fig. (**8**) shows the effect of pressure on the boiling curve of Al_2O_3–water nanofluid at a concentration of 0.00005 vol.%. The experiment reveals that when the pressure of a fluid increases, the boiling curvetends to move in the left direction, which means that the heat transfer coefficient is higher. Fig. (**9**) shows consistency with the study of Trisaksri and Wongwises [21] who found that the heat transfer coefficient of TiO_2–R141b decreased when the pressure decreased.

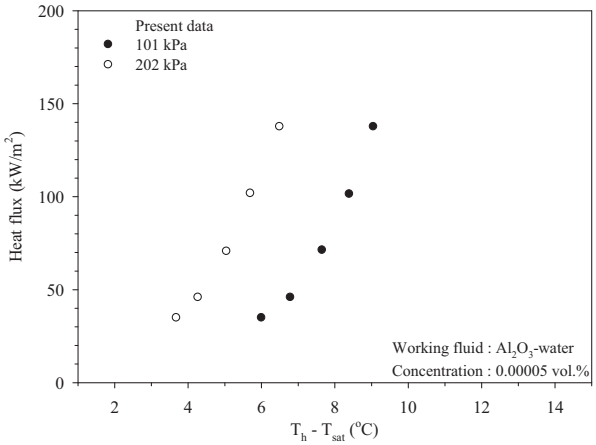

Fig. (8). Variation of boiling curves of nanofluid with pressures.

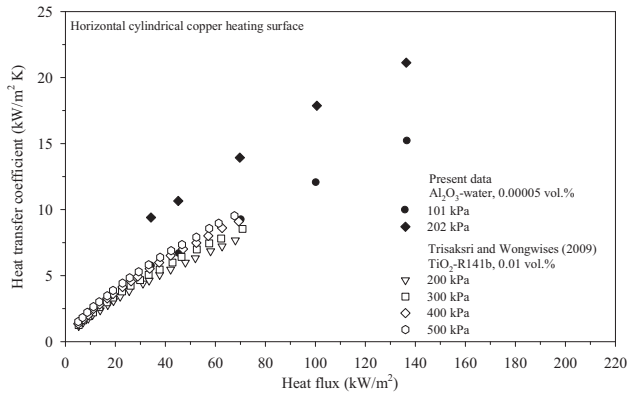

Fig. (9). Variation of heat transfer coefficient with heat flux at different pressures.

The fact that pool-boiling heat transfer coefficient of nanofluid used in this experiment is lower than the water base fluid and decreases when the concentration increases could occur because nanoparticles cover or clog up tiny pores on the heating surface and reduce nucleation site. Normally, these tiny pores produce nucleate bubbles which flow upward and help with circulation and turbulence of fluid that lead to better heat transfer. Moreover, the cover of nanoparticles on heating surface also increases thermal resistance which decreases its heat transfer coefficient.

6. CONCLUSIONS

This research studies pool-boiling heat transfer characteristics of Al_2O_3–water nanofluid with the concentration of 0.00005, 0.0001, 0.005 and 0.03 vol.% at the pressure levels of 1 and 2 atm. The heating surface used is a horizontal copper cylinder. The results from the experiment could be concluded as follows:

- The use ofAl_2O_3–water nanofluid does not help in increasing pool-boiling heat transfer coefficient when compared to water. It also decreases when the concentration increases.
- The heat transfer coefficient decreases when the pressure level decreases.

CONFLICT OF INTEREST

The authors confirm that this article content has no conflicts of interest.

ACKNOWLEDGEMENTS

The authors would like to express their appreciation to the Thailand Research Fund, the Office of the Higher Education Commission and the National Research University Project for providing financial support. The authors also thank Mr. Prawitt Kerdpermdee, Mr. Pumpat Jaturapattanapum and Mr. Theanthum Kaenak for their help in the experimental works.

REFERENCES

[1] Rohsenow, W.M. A method of correlation heat transfer data for surface boiling liquids. *ASME Transaction*, **1952**, *77,* 969.

[2] Choi, S.U.S. Enhancing thermal conductivity of fluids with nanoparticle. *ASME FED*, **1995**, *231*, 99-103.

[3] Duangthongsuk, W.; Wongwises, S. A critical review of convective heat transfer of nanofluids. *Renew. Sustain. Energy Rev.*, **2007**, *11*, 797-817.

[4] Pak, B. C.; Cho, Y. I. Hydrodynamic and heat transfer study of dispersed fluids with submicron metallic oxide particles. *Exp. Heat Transfer*, **1998**, *11*, 151-170.

[5] Xuan, Y.; Li, Q. Investigation on convective heat transfer and flow features of nanofluids. *ASME J. Heat Transfer*, **2003**, *125*, 151.

[6] Wen, D.; Ding, Y. Experimental investigation into convective heat transfer of nanofluids at the entrance region under laminar flow conditions. *Int. J. Heat Mass Transfer*, **2004**, *47*, 5181.

[7] He, Y.; Jin, Y.; Chen, H.; Ding, Y.; Cang, D.; Lu, H. Heat transfer and flow behavior of aqueous suspensions of TiO_2 nanoparticles (nanofluids) flowing upward through a vertical pipe. *Int. J. Heat Mass Transfer*, **2007**, *50*, 2272.

[8] Duangthongsuk, W.; Wongwises, S. Effect of thermophysical properties models on the prediction of the convective heat transfer coefficient for low concentration nanofluid. *Int. Commun. Heat Mass Transfer*, **2008**, *35*, 1320.

[9] Duangthongsuk, W.; Wongwises, S. Heat transfer enhancement and pressure drop characteristics of TiO_2-water nanofluid in a double-tube counter flow heat exchanger. *Int. J. Heat Mass Transfer*, **2009**, *52*, 2059.

[10] Duangthongsuk, W.; Wongwises, S. An experimental study on the heat transfer performance and pressure drop of TiO_2-water nanofluids flowing under a turbulent flow regime. *Int. J. Heat Mass Transfer*, **2010**, *53*, 334-344.

[11] Das, S.K.; Putra, N.; Roetzel, W. Pool boiling characteristics of nanofluids. *Int. J. Heat Mass Transfer*, **2003**, *46*, 851-862.

[12] You, S.M.; Kim, J.H.; Kim, K.H. Effect of nanoparticles on critical heat flux of water in pool boiling heat transfer. *Appl. Phys. Lett.*, **2003**, *83*, 3374-3376.

[13] Li, C.H.; Wang, B.X.; Peng, X.F. On the pool boiling of subcoolednano-particle suspensions. *paper presented in the 6th International Symposium on Heat Transfer*, Beijing, China, **2004**.

[14] Vassallo, P.; Kumar, R.; Amico, S.D. Pool boiling heat transfer experiments in silica–water nanofluids. *Int. J. Heat Mass Transfer*, **2004**, *47*, 407-411.

[15] Bang, I.C.; Chang, S.H. Boiling heat transfer performance and phenomena of Al_2O_3-water nanofluids from a plain surface in a pool. *Int. J. Heat Mass Transfer*, **2005**, *48*, 2407-2419.

[16] Kim, H.; Kim, J.; Kim, M. Experimental study on characteristics of water-TiO_2 nanofluids. *Nucl. Eng. Technol.*, **2006**, *38*, 61-68.

[17] Nguyen, C.T.; Galanis, N.; Roy, G.; Divoux, S.; Gillbert, D. Pool boiling characteristics of water-Al_2O_3 nanofluid, *paper presented in the 13th International Heat transfer conference*, Sydney, Australia, **2006**.

[18] Kim, S.J.; Bang, I.C.; Buongiorno, J.; Hu, L.W. Surface wettability change during pool boiling of nanofluids and its effect on critical heat flux. *Int. J. Heat Mass Transfer*, **2007**, *50*, 4105-4116.

[19] Liu, Z.; Liao, L. Sorption and agglutination phenomenon of nanofluids on a plain heating surface during pool boiling. *Int. J. Heat Mass Transfer*, **2008**, *51*, 2593-2602.

[20] Golubovic, M.N.; Madhawa, H.D.; Hettiarachchi, M.; Worek, W.M.; Minkowycz, W.J. Nanofluids and critical heat flux, experimental and analytical study. *Appl. Therm. Eng.*, **2009**, *29*, 1281-1288.

[21] Trisaksri, V.; Wongwises, S. Nucleate pool boiling heat transfer of TiO_2-R141b nanofluids. *Int. J. Heat Mass Transfer*, **2009**, *52*, 1582-1588.

[22] Suriyawong, S.; Wongwises, S. Nucleate pool boiling heat transfer characteristics of TiO_2-waternanofluids at very low concentrations. *Exp. Therm. Fluid Sci.*, **2010**, *34*, 992-999.

[23] Cieslinski, J.T.; Kaczmarczyk, T.Z. Pool boiling of water-Al_2O_3 and water-Cu nanofluids on horizontal smooth tubes. *Nanoscale Res. Lett.*, **2011**, *6*, 1-9.

Received: April 2, 2012 **Revised: September 13, 2012** **Accepted: October 14, 2012**

Send Orders of Reprints at bspsaif@emirates.net.ae

Current Nanoscience, **2013**, *9*, 61-80

Determination of the Single-Phase Forced Convection Heat Transfer Characteristics of TiO_2Nanofluids Flowing in Smooth and Micro-Fin Tubes by Means of CFD and ANN Analyses

N. Kayaci[1], M. Balcilar[2], M. Tabatabaei[1], A. Celen[1], O. Yıldız[3], A.S. Dalkilic*,[1] and S. Wongwises[4]

[1]*Heat and Thermodynamics Division, Department of Mechanical Engineering,Yildiz Technical University (YTU), Yildiz, Besiktas, Istanbul 34349, Turkey;* [2]*Computer Engineering Departmant, Yildiz Technical University (YTU), Davutpasa, Esenler, Istanbul 34220, Turkey;* [3]*Department of Mechanical Engineering, Kocaeli University, Umuttepe Campus, Kocaeli, 41380, Turkey;* [4]*Fluid Mechanics, Thermal Engineering and Multiphase Flow Research Lab. (FUTURE), Department of Mechanical Engineering, Faculty of Engineering, King Mongkut's University of Technology Thonburi (KMUTT), Bangmod, Bangkok 10140, Thailand*

Abstract: A numerical study including a validation process with experimental data was performed on the forced convection flows of nanofluids; the object of study was water containing TiO_2 nanoparticles in smooth and micro-fin tubes at a constant wall temperature. Constant heat flux and temperature-dependent properties were used to determine the hydrodynamics and thermal behaviors of the nanofluid flow;a single-phase numerical model was used to solve two-dimensional equations by means of a CFD program for the water flow, contained in a smooth tube and in various micro-fin tubes having various helix angles (0^o, 18^o). An extensive literature review on the determination of the physical properties (k, μ, ρ, Cp) of nanofluids is given in this paper. Multilayer Perceptron (MLP), one of theartificial neural network (ANN) methods, was used to determine the most agreeable physical propertiesof TiO_2 nanofluids among correlations. The inputs ofthe ANN analyses were the correlations of physical properties, the average temperature and velocity of water in the test tubes, and the nanoparticle concentrations, while the outputs were shear stress, friction factor, heat flux, convective heat transfer coefficient, and pressure drop. After obtaining the best combination of physical properties of TiO_2 nanofluids from the ANN analyses, the numerical model was validated by means of a CFD program,with the experimental smooth tube data as a case study; it was also validatedas a simulation studyfor several micro-fin tubes through a CFD program. This paper shows temperature, pressure, and velocity distributions in the investigated tubes; in addition, average and local experimental, theoretical, and numerical values in the smooth and micro-fin tubes are compared with oneanother in terms of friction factors, shear stresses, convective heat transfer coefficients, and pressure drops, according to various nanoparticle concentrations.

Keywords: Heat transfer coefficient, Pressure drop, ANN, Nanofluid, Single-phase flow, CFD.

1. INTRODUCTION

Thermal conductivity is an important parameter that expresses the heat transfer performance of a heat transfer fluid. Due to their low thermal conductivity, conventional heat transfer fluids (e.g. water, oil, ethylene glycol mixtures) restrict the enhancement of performance and compactness in heat exchangers used in the electronic, automotive, and aerospace industries. One solution for improving the thermal conductivity of a fluid is to suspend small solid particles in the fluid. Since the thermal conductivity of solid metals is higher than that of fluids, the suspended particles are expected to be able to increase thermal conductivity and heat transfer performance. Experimental studies on the thermal conductivity of nanofluids have been performed by many researchers. Slurries are formed by adding metallic, non-metallic and polymeric particles to fluids. Due to the large size of these suspended particles (on the millimeter scale), problems such as abrasion and clogging can occur. For this reason, such large particles cannot offer a workable solution for heat transfer enhancement. Recently, progress in manufacturing technologies has made possible the production of particles on the nanometer scale (i.e., particle diametersranging from 10 to 100 nm). These smaller-sized particles allow uniform and stable suspensions to form; thus, nanofluidsprovide higher heat transfer enhancement than do existing techniques. The first continuous studies on the use of particles of nanometer dimension were conducted by a research group at the Argonne National Laboratory approximately a decade ago. Choi [1] was likely the first researcher who called the fluids with nanometer particles 'nano-fluids'. The term 'nanofluid' thus refers to a two-phase mixture usually composed of a continuous liquid phase and of dispersed nanoparticles in suspension.

Xuan and Li [2] stated that nanofluids are easily fluidized and can almostbe considered a fluid due to their tiny particle size, despite their character as atwo-phase mixture. For this reason, nanofluid flow can be treated as a single-phase flow. Maxwell [3] assumed that the fluid phase and the particles are in thermal equilibrium and move at the same velocity under certain conditions,given the ultra-fine and lowvolume fraction of the solid particles. Advantages of a single-phase flow include its simplicity and its lowerrequired computational time. It should be emphasizedthat physical properties of nanofluids have a strong impact on experimental, numerical, and theoretical solutions. The most well-known nanoparticles are Al_2O_3, CuO, TiO_2, each of which is used, together with the base fluids of water and ethylene glycol, in the experimental work of many researchers. Across the range ofparticle sizes and types of base fluids, the enhancement of thermal conductivity has beenachievedunder all experimental conditions with these nanoparticles.

The following paragraph summarizes some of the recent studies presented by researchers on the flow of nanofluids. The review paper of Daungthongsuk and Wongwises [4] summarized published resultson the forced convective heat transfer of nanofluids inboth experimental and numerical investigation. Daungthongsuk and Wongwises [5] reported that the thermal conductivity of nanofluids increased with increasing nanofluid temperatures and, conversely, that the viscosity of nanofluids decreased with increasing nanofluid temperatures. Duangthongsuk and Wongwises [6] studied the differences between using measured and computed thermophysical

*Address correspondence to this author at the Heat and Thermodynamics Division, Department of Mechanical Engineering, Yildiz Technical University (YTU), Yildiz, Besiktas, Istanbul 34349, Turkey; Tel: +9 0212 3832819; Fax: +9 0212 2616659; E-mail: dalkilic@yildiz.edu.tr

1875-6786/13 $58.00+.00

properties to describe the heat transfer performance of TiO_2-water nanofluids; they concluded that measuring the thermophysical properties of nanofluids is an important way to address the transport behavior of nanofluids.Duangthongsuk and Wongwises [7] also conducted an experimental study on the heat transfer performance and pressure drop results of TiO_2-water nanofluids under a turbulent flow regimen. Their results indicated that the dispersion of nanoparticles into the base liquid increases the thermal conductivity and viscosity of the nanofluids, and that this augmentation increases with increasing particle concentrations. Daungthongsuk and Wongwises [8] further reported their study on the forced convective heat transfer and flow characteristics of a nanofluid consisting of water and 0.2vol.%TiO_2 nanoparticles. According to their results, the heat transfer coefficient of the nanofluid increases with an increase in the mass flow rate of the hot water and nanofluid; increases with a decrease in the nanofluid temperature; and does not significantly respond to the temperature of the heating fluid. Duangthongsuk and Wongwises [9] also studied the role of thermophysical properties models in the prediction of convective heat transfer coefficientsin low concentration nanofluids. They reported that precise values for thermal and physical properties such as specific heat, viscosity, and thermal conductivity are required in order to study the heat transfer behavior of the nanofluids. Daungthongsuk *et al*. [10] presented an experimental study on the heat transfer and pressure drop characteristics of Al_2O_3-water nanofluids flowing through a microchannel heat sink (MCHS). The study investigated the effects of the Reynolds number and of particle concentrations on the heat transfer and flow behavior of the nanofluids. Results indicatedan increase in the heat transfer performance of MCHS both with an increase in the Reynolds number and with an increase in particle concentration. Suriyawong and Wongwises [11] studied the nucleate pool-boiling heat transfer of TiO_2-water nanofluids experimentally. Nanofluids with varying concentrations of 0.00005, 0.0001, 0.0005, 0.005, and 0.01vol.% were employed in their study. The experiments explored the effects of nanofluid concentrations and of the heating and roughnessof the surface material on the nucleate pool-boiling characteristics and on the heat transfer coefficient under ambient pressure. In the case ofaheated copper surface tested at a concentration of 0.0001vol.%, results showed a higher nucleate pool-boiling heat transfer coefficient than was obtained with the base fluid. Trisaksri and Wongwises [12] investigated the nucleate pool-boiling heat transfer of a refrigerant-basednanofluid at different nanoparticle concentrations and pressures. TiO_2 nanoparticles were mixed with the refrigerant HCFC 141b at 0.01, 0.03 and 0.05vol.%, and pool-boiling experiments on nanofluids were compared tofindings on the base refrigerant. Results indicated that the nucleate pool-boiling heat transfer deteriorated with increasing particle concentrations, especially at high heat fluxes.

This paragraph summarizes some of the recent studies presented on the CFD analyses of in-tube flows. Dalkilic *et al*. [13-14] presented theoretical flow models for homogeneous and separated flows applied to in-tube condensation to predict the pressure drop characteristics of R134a. Numerical analyses were performed by means of a CFD program to determine average and local homogeneous wall shear stresses and friction factors [15]. Refrigerant-side total pressure drops, frictional pressure drops, friction factors, and wall shear stresses were determined within a ±30% error band. Demir *et al*. [16] numerically investigated laminar and turbulent forced convection flows of a nanofluid consisting of water and Al_2O_3 particles in a horizontal smooth tube with constant wall temperature. Their CFD15 results demonstrated a heat transfer enhancement due to the presence of the nanoparticles in the fluid. Demir *et al*. [17] studied numerically the single-phase forced convection heat transfer characteristics of TiO_2 nanofluids in a double-tube counter-flow heat exchanger. In their paper, they used Palm *et al*.'s [18] correlations to determine the thermophysical properties of the nanofluids. Their CFD [15] results indicateda heat transfer enhancement due to the presence of the nanoparticles in the fluid,agreeing with the results of the experimental study used in the validation process for the numerical model. Agra *et al*. [19] investigated the heat transfer and pressure drop characteristics of smooth, corrugated, and helically finned tubes by using Fluent CFD software [15] and Gambit software [15] to plot and mesh models of the test tubes. The problem under investigation was a two-dimensional (axisymmetric), steady forced turbulent convection flow of water flowing inside straight and enhanced circular tubes. Their paper compared numerical results with experimental data and with the Blasius equation. It was seen that the Fluent CFD [15] program predicted the experimental data more accurately than did the Blasius equation.

The following paragraph summarizes some of the recent studies presented on the artificial intelligence analyses of in-tube flows. Balcilar *et al*. [20] used computational numerical methods such as artificial neural networks (ANNs) to determine the compatibility of the most suitable coefficients of the correlations with the majority of experimental data; Balcilar *et al*. [21] and Bolat *et al*. [22] studied heat transfer characteristics in their analyses by means of ANNs. The inputs of the ANNs are the measured values of test sections such as mass flux, heat flux, temperature differences between the tube wall and the saturation temperature, and average vapor quality, while the outputs are the experimental condensation heat transfer coefficient and the pressure drop measured in the analysis. Balcilar *et al*. [23-24] investigated the nucleate pool-boiling heat transfer characteristics of TiO_2 nanofluids to determine the effects of the important parameterson the heat transfer coefficient, and also to formreliable empirical correlations based on the neural network analysis. Balcilar *et al*. [25] predicted the condensation and evaporation pressure drops of R32, R125, R410A, R134a, R22, R502, R507a, R32/R134a (25/75 by wt%), R407C, and R12, flowing inside various horizontal smooth and micro-fin tubes, by means of the numerical techniques of ANNs and of non-linear least squares (NLS). Total pressure drops within in-tube condensation and in-tube evaporation tests were modeled using the ANN method of multi-layer perceptron (MLP) with a 12-40-1 architecture. In light of cross-validation tests of 1485 evaporation and condensation data points,the average error rate of this method was 7.085%.

For some time now, many studies have concentrated on proposing a model to predict the heat transfer enhancement of nanofluids. It should be noted, however, that there has not yet been a paper on the investigation of the proper physical properties of nanofluids by ANN analyses. In the remainder of this paper, the most agreeable physical properties (k, μ, ρ, c_p) of nanofluids will be analyzed through experimental data, making use ofnearly all correlations in the current literature. To this end, two ANN models with different input values were developed using experimental results to determine the most suitable physical properties among these correlations. Smooth and micro-fin tubes were drawn in SOLIDWORKS [26] software and then imported into ANSYS Fluent [27] software for CFD analysis. Prior to thesimulation of the micro-fin tubes in the CFD program, the smooth-tube model was validated using the agreeable physical properties obtained from ANN analyses and experimental data from the forced convection of TiO_2nanofluids, which were calculated and measured for heat transfer coefficients and pressure drops. Temperature distributions, pressure and velocity of the inner surface and of the fluids at the inlet and outlet sections of the tube, friction factors, wall shear stresses, pumping powers and particle concentrations, local heat transfer coefficients, and pressure drops along the tubes were also obtained from the numerical study for smooth and micro-fin tubes. Last of all,this paper demonstrates a heat transfer enhancement and an increase in pressure drop and pumping power due to the presence of the nanofluids and the micro-fin tubes.

2. SAMPLE PREPARATION

In the present study, nanofluids provided by a commercial source (DEGUSSA, VP Disp. W740x) were used as working fluid. The fluid mixture was composed of TiO_2 nanoparticles with an average diameter of 21 nm dispersed in water. The original particle concentration was 40 wt.%. In order to produce other required particle volume fractions, dilution with water and stirring action were employed. An ultrasonic vibrator was used to sonicate the solution continuously for about 2 h in order to break down the agglomeration of the nanoparticles. The desired volume concentrations used in this study were 0.2%, 0.6%, and 1.0%, with pH values of 7.5, 7.1, and 7.0, respectively. From these pH values it can be seen that the solution chemistry of nanofluids is nearly neutral. A transmission electron microscope (TEM) was used to approximate the size of the primary nanoparticles. As Fig. (**1**) shows, it is clear that the primary size of the nanoparticles was approximately spherical, with an average diameter of around 21 nm.

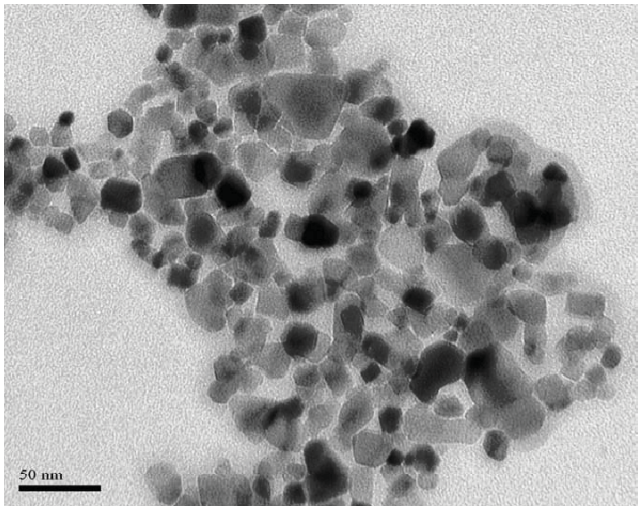

Fig. (1). TEM image of dispersed TiO_2 nanoparticles in water [From Duangthongsuk and Wongwises [6], with permission from Elsevier].

3. EXPERIMENTAL APPARATUS

The experimental system used in the present study is shown schematically in Fig. (**2a**). It consisted mainly of a test section, two receiver tanks, a magnetic gear pump, a hot water pump, a cooler tank, a hot water tank, and a collection tank. The test section was a 1.5 m long counter-flow horizontal double-tube heat exchanger with nanofluid flowing inside the tube and hot water flowing in the annular. The inner tube was made from smooth copper tubing with a 9.53 mm outer diameter and a 0.7 mm thickness, while the outer tube was made from PVC tubing and has a 33.9 mm outer diameter and a 3 mm thickness. The test section was thermally isolated from its upstream and downstream sections by plastic tubes in order to reduce the heat loss along the axial direction. The differential pressure transmitter and the T-type thermocouple were mounted at both ends of the test section to measure the nanofluid's pressure drop and bulk temperature,respectively. Thermocouples were mounted in sets of three, equally spaced around the tube circumference, at different longitudinal positions along the surface of the inner tube wall. The inlet and exit temperatures of the hot water were measured using T-type thermocouples inserted directly into the flow. The 60 L receiver tanks,made of stainless steel, stored the nanofluid and hot water leaving the test section. The cooler tank had a 4.2 kW cooling capacity, and a thermostat was used to keep the nanofluid temperature constant. As with the cooler tank, a 3 kW electric heater with a thermostat was installed to keep the temperature of the hot water constant. The nanofluid flow rate was controlled by adjusting the rotation speed of the magnetic gear pump. The hot water flow rate was measured by a rotameter, while the nanofluid flow rate wascalculated from the exact time required for the entire mass of nanofluid to be discharged. For each pump speed, five measurements were taken. Averagesare given for all data in the present study.

A portable programmable calibrator was used to calibrate all T-type thermocouples, with a maximum precision of 0.1 °C. The nanofluid mass flow rates were determined by electronic balance, with an uncertainty of ±0.0006 kg. Maximum uncertainty of the nanofluid mass flow rate was evaluated at 2.2%; this was taken into account in calculating the uncertainty of the Nusselt number.

The uncertainty of the hot water mass flow rate was evaluated $\pm$7% (full scale). As noted above, the uncertainty of the measured Nusselt number can readily be seen to depend on measurements of temperature, nanofluid flow rate, and hot water flow rate. The uncertainty of the measured Nusselt number was evaluated using the root mean sum square method, and was found to be 5%.

During the test run, wall temperatures of the test section, mass flow rates of the hot water and nanofluid, and the inlet and exit temperatures of the hot water and nanofluid were measured.

A view of the geometrical parameters of the micro-fin tubes is given in Fig. (**2b**). The dimensional parameters of the investigated tubes are given in Table **4**.

4. DATA REDUCTION

4.1. Thermal and Physical Properties of Nanofluids

The determination of nanofluid properties is known to be a widespread pursuit in current research. Some correlations have been developed toward this end by Williams *et al*. [28]. The measurement of physical properties has been undertaken by several researchers within the literature,including Rea *et al*. [29] and Duangthongsuk and Wongwises [7].

Tables **1**, **2**, and **3** provide a summary of the current literature on almost all empiricalcorrelations for nanofluid dynamic viscosity [30-53], thermal conductivity [3, 18, 54-68], and specific heat capacity at constant pressure [3, 54, 69-70], respectively.

It should be noted that the density of the nanofluid was calculated from Pak and Cho's [48] correlation, as follows:

$$\rho_{nf} = \rho_s.\phi + (1-\phi).\rho_w \tag{1}$$

4.2. Governing Dimensionless Numbers, Heat Flux, the Heat Transfer Coefficient, and the Nusselt Number

As test fluid flows through ducts, the heat transfer surface surrounds and guides the stream, and the convection process is said to be internal. The velocity distribution in a duct has two distinct regions in laminar flow: first, the entrance region, where the walls are lined by successive boundary layers, and second, farther downstream, the fully developed region, where longitudinal velocity is independent of position along the duct. It is assumed that duct geometry does not change with longitudinal position. The flow through a straight duct ceases to be laminar when the Reynolds number (Re) exceeds approximately 2300, and the turbulent flow becomes fully developed hydrodynamically and thermally after a relatively short entrance distance [71].

The Reynolds number (Re) and the Prandtl number are used in theoretical analysis [18]; the particle volume fraction (φ) and the ratios k_p/k_{bf} and Cp_p/Cp_{bf} are used to characterize the problem, and can be calculated as follows:

$$\mathrm{Re} = \frac{2Q}{\pi d\nu} \tag{2}$$

$$\mathrm{Pr} = \frac{C_p\mu}{k} \tag{3}$$

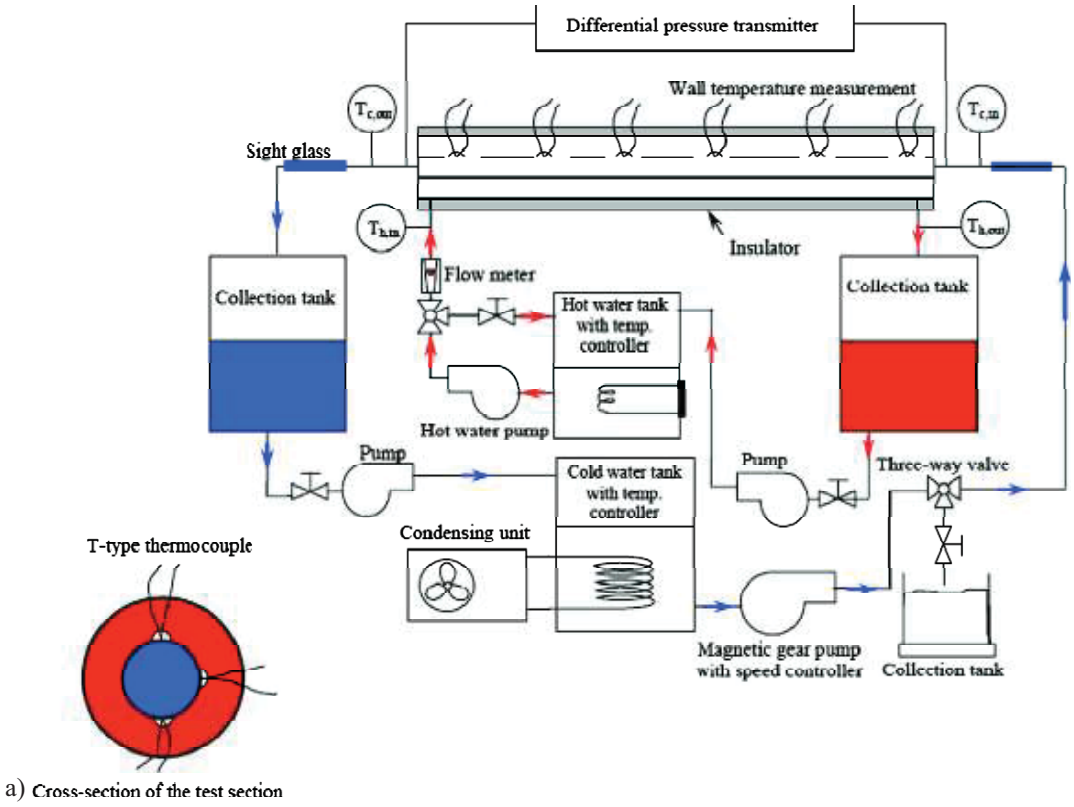

Fig. (2). Schematic diagram of the experimental apparatus (**a**) [From Duangthongsuk and Wongwises [6], with permission from Elsevier] and view of geometrical parameters of micro-fin tubes (**b**).

In the fully developed region, the friction factor is defined as in the laminar flow:

$$f = \frac{64}{\mathrm{Re}} \tag{4}$$

Petukhov [72] discovered a formula for the friction factor in turbulent flow, as follows:

$$f = (0.970 \ln \mathrm{Re} - 1.64)^{-2} \tag{5}$$

By using the Darcy friction factor, wall shear stress can be calculated as below:

$$\tau = \frac{f \rho V_{avg}^2}{8} \tag{6}$$

Table 1. Some Dynamic Viscosity Correlations of Nanofluids in Literature

Researcher	Correlation
(1) Einstein [30]	$\mu_{eff} = (1 + 2.5\varphi)\mu_f$
(2) Brinkman [31]	$\mu_{eff} = \mu_{bf}(1 - \varphi)^{2.5}$
(3) Batchelor [32]	$\mu_{eff} = (1 + \eta\varphi + k_H\varphi^2)\mu_f = (1 + 2.5\varphi + 6.2\varphi^2)\mu_f$
(4) Graham [33]	$\mu_{eff} = (1 + 2.5\varphi)\mu_f + \left[\frac{4.5}{(h/r_p)(2+h/r_p)(1+h/r_p)^2}\right]\mu_f$
(5) Kitano *et al*. [34]	$\mu_{eff} = \mu_{bf}\left[1-(\varphi-\varphi_m)\right]^{-2}$
(6) Bicerano *et al*. [35]	$\mu_{nf} = \mu_{bf}\left[1+\eta\phi+k_H\phi^2)\right]$
(7) Wang *et al*. [36]	$\mu_{nf} = \mu_{bf}\left[1+7,3\phi+123\phi^2\right]$
(8) Tseng and Chen [37]	$\mu_{nf} = \mu_{bf}\,0,4513e^{0,6965\phi}$
(9) Chen *et al*. [38]	$\mu_{nf} = \mu_{bf}\left[1+10,6\phi+(10,6\phi)^2\right]$
(10)-(11) Nguyen *et al*. [39]	$\mu_{nf} = \mu_{bf}\,0,904e^{0,1482\phi}$ $\mu_{nf} = \mu_{bf}(1 + 0,025\phi + 0,015\phi^2)$
(12) Khanafer and Vafai [40]	$\mu_{nf} = \mu_{bf}(1,0538 + 0,1448\phi - 3,363x10^{-3}T - 0,0147\phi + 6,735x10^{-5}T^2 - 1,337\frac{\phi}{T})$
(13) Duanghongsuk and Wongwises [5]	$\mu_{nf} = \mu_{bf}(1,013 + 0,092\phi + 0,015\phi^2)$
(14) Vand [41]	$\mu_{nf}=\mu_{bf}e^{2.5\phi+2.7\phi^2/(1-0.609\phi)}$
(15) Mooney [42]	$\mu_{nf} = \mu_{bf}e^{(\frac{2.5*\phi_m*\phi}{1-\phi})}$
(16)-(17) Krieger [43-44]	$\mu_{nf} = \mu_{bf}(\frac{\phi_m}{1-\phi})^a$ $\mu_{nf} = \mu_{bf}(\frac{\phi_m}{1-\phi})^{1.82}$
(18) Frankel and Acrivos [45]	$\mu_{nf} = \mu_{bf}1.125(\frac{\phi}{\phi_m})^{1/3}/(1-(\frac{\phi}{\phi_m})^{1/3})$
(19) Miler *et al*. [46]	$\mu_{nf} = \mu_{bf}(537.42\phi - 0.188)$
(20) Chow [47]	$\mu_{nf} = \mu_{bf} * (e^{\frac{2.5*\phi}{1-\phi}}) + (A*\phi^2)/(1 - A*\phi^2*\phi_m)$
(21) Pak and Cho [48]	$\mu_{nf} = \mu_{bf}(108.2\phi^2 + 5.45\phi + 1)$

(Table 1) Contd….

Researcher	Correlation
(22) Liu [49]	$\mu_{nf} = \mu_{bf}((\frac{1-\phi}{\phi_m})^2 + (\frac{k_1 - 2}{\phi_m})\phi + (\frac{k_2 - 6}{\phi_m^2})\phi^2)$
(23)-(24) Wang *et al*. [50]	$\mu_{nf} = \mu_{bf}(123\phi^2 + 7.3\phi + 1)$ $\mu_{nf} = \mu_{bf}(306\phi^2 - 0.19\phi + 1)$
(25) Davalos *et al*. [51]	$\mu_{nf} = \mu_{bf}(6.17\phi^2 + 2.5\phi + 1)$
(26)-(27) Putra *et al*. [52]	$\mu_{nf} = 2.9x10^{-7}xT^2 - 2x10^{-4}xT + 3.4x10^{-2}$ for %1 $\mu_{nf} = 3.4x10^{-7}xT^2 - 2.3x10^{-4}xT + 3.9x10^{-2}$ for %4
(28) Tang *et al*. [53]	$\mu_{nf} = 2.761x10^{-6}xe^{1713/T}$

Table 2. Some Thermal Conductivity Correlations of Nanofluids in Literature

Researcher	Correlation
(1) Maxwell [3]	$k_{nf}=k_f * \frac{k_p+2k_f+2\phi(k_p-k_f)}{k_p+2k_f-\phi(k_p-k_f)}$
(2) Hamilton and Crosser [54]	$k_{nf}=k_f * \frac{k_p+(n-1)k_f-(n-1)\phi(k_f-k_p)}{k_p+(n-1)k_f+\phi(k_f-k_p)}, n=\frac{3}{\Psi}, \Psi=\frac{\phi\rho_f}{\rho_p+\phi\rho_f-\phi\rho_p}$
(3) Hui *et al*. [55]	$k_{nf}=\frac{1}{4}[(3\phi-1)k_p+(2-3\phi)k_f]+\frac{k_p}{4}\sqrt{\Delta},$ $\Delta=(3\phi-1)^2(\frac{k_p}{k_f})^2+(2-3\phi)^2+2(2+9\phi-9\phi^2)(\frac{k_p}{k_f})$
(4) Xuan and Li [56]	$k_{nf}=k_f \frac{k_p+2k_f-2\phi(k_f-k_p)}{k_p+2k_f+\phi(k_f-k_p)}$
(5) Yu and Choi [57]	$k_{nf}=k_f * \frac{k_{pe}+2k_f+2\phi(k_{pe}-k_f)(1+\beta)^3}{k_{pe}+2k_f-\phi(k_p-k_f)(1+\beta)^3}$, $\beta=\frac{h}{r}$, h<10nm,β=0.1
(6) Godson *et al*. [58]	$k_{nf} = 0.9692\phi + 0.9508$
(7) Prasher *et al*. [59]	$k_{nf}=k_f \frac{1+A\phi\ Re^m\ Pr^{0,333}*(1+2\alpha)+2\phi(1-\alpha)}{(1+2\alpha)-\phi(1-\alpha)}$, $\alpha=\frac{2R_bk_f}{d_p}$, A=40000 ,m=2.5 , $R_b=0.77.10^{-8}$
(8) Koo and Kleinstreuer [60]	$k_{nf}=k_{MG}+5\times10^4\ \beta\phi\rho_p\ C_p\sqrt{\frac{K_B\ T}{\rho_p D}}\ f(T,\phi)$, $k_{MG}=k_f\left(1+\frac{3\phi\left(\frac{k_p}{k_f}-1\right)}{\left(\frac{k_p}{k_f}+2\right)-\phi\left(\frac{k_p}{k_f}-1\right)}\right)$ $f(T,\phi)=(-6.04\phi+0.4705).T+(1722.3\phi-134.63), \beta=0.0137(100\phi)^{-0.8229} \rightarrow \phi\le 1\%$
(9)-(10) Li and Peterson [61]	$k_{nf}=k_f+k_f(0.764\phi-0.0187\ (T-273.15)-0.462)$ For Al_2O_3 $k_{nf}=k_f+k_f(3.761\phi+0.0179\ (T-273.15)-0.307)$ For CuO
(11)-(12) Palm [18]	Al_2O_3 $\left(\begin{array}{l} k_{nf}=0.003352T-0.3708 \text{ For } \phi=\%1 \\ k_{nf}=0.004961T-0.8078 \text{ For } \phi=\%4 \end{array}\right)$
(13)-(14) Maiga *et al*. [62]	$k_{nf}=k_f(4.97\phi^2+2.72\phi+1)$ For Al_2O_3 $k_{nf}=k_f(28.905\phi^2+2.827\phi+1)$ For CuO

(Table 2) Contd….

Researcher	Correlation
(15) Bhattacharya *et al*. [63]	$k_{nf}=k_p\phi+(1-\phi)k_f$
(16) Buongiorno [64]	$k_{nf}=k_f\ (1+7.47\phi)$
(17) Kim *et al*. [65]	$k_{nf}=0.65+4{,}864\times10^{-7}T^3$
(18) Timofeeva *et al*. [66]	$k_{nf}=k_f(1+3\phi)$
(19) Chon *et al*. [67]	$k_{nf}=k_f\ .(1+64.7\phi^{0.746}\ (d_f/d_p\ )^{0.369}(k_p/k_f)^{0.747}Re^{1.2321}\ Pr^{0.9955})$ $Pr=\frac{\mu}{\rho_{BF}\alpha},Re=\frac{\rho_{BF}Vd_p}{\mu}=\frac{\rho_{BF}K_BT}{3\pi\mu^2L_{BF}},\mu=2.414\times10^{-5}\times10^{(\frac{247}{T-140})}$
(20) Murshed *et al*. [68]	$k_{nf}=\frac{k_f(1+0.27\phi^{4/3}\ (\frac{k_p}{k_f}-1)(1+\frac{0.52\phi}{1-\phi^{1/3}}\ (\frac{k_p}{k_f}-1)}{1+\phi^{4/3}\ (\frac{k_p}{k_f}-1)(\frac{0.52}{1-\phi^{1/3}}+0.27\phi^{1/3}+0.27)}$

Table 3. Some Specific Heat Capacity Correlations of Nanofluids in Literature

Researcher	Correlation
(1) Maxwell [3]	$Cp_{nf}=(1-\varphi)Cp_{nf}(1+2.5\varphi_p)\mu_f$
(2) Hamilton and Crosser [54]	$Cp_{nf}=\frac{\phi.\rho_s.Cp_s+(1-\phi).\rho_w.Cp_w}{\rho_{nf}}$
(3) Yang *et al*. [69]	$\frac{Cp_{eff}}{Cp_f}=(1-\phi)+\phi\frac{Cp_n}{Cp_f}$
(4) Yu *et al*. [70]	$Cp_{nf}=\frac{\varphi(p_s)Cp_s+(1-\varphi).(\rho.c_p)}{\varphi\rho_p+(1-\varphi).\rho_{bf}}$

Because of viscous effects, pressure loss occurs, and is expressed for all types of fullydeveloped internal flows as follows:

$$\Delta P_L=f\frac{L}{D}\frac{\rho V_{avg}^2}{2} \quad (7)$$

When a pressure drop occurs, the pumping power required to overcome flow resistance can be determined as follows:

$$W_P=\dot{Q}.\Delta P \quad (8)$$

Heat flux in the test section is determined as follows:

$$q"=\frac{m_wC_{p,w}(T_i-T_o)}{\pi dL} \quad (9)$$

The heat transfer coefficient of the base fluid and the nanofluid can be calculated as follows:

$$h=\frac{q"}{(T_w-T_{f,m})} \quad (10)$$

The Nusselt numberfor the base fluid and the nanofluid can be calculated as follows:

$$Nu=\frac{hd}{k} \quad (11)$$

4.3. Numerical method - CFD Approach

The ANSYS Fluent program [15] is commonly used software in CFD analysis, and a detailed description of its mathematical models can be found in the Fluent User's Guide. The program uses a technique based on control volume theory to convert governing equations into algebraic equations so that they can be solved numerically, providing a significant research solution [27]. The control volume technique works by integrating the governing equations for each control volume, and then by discretizing the equations that conserve each quantity based on the control volume.

Classic single-phase conservation equations found a solution in the control volume approach, since governing equations could be given numerical solutions after being converted into a set of algebraic equations. This addressed some of the entailments of governing equations, including convection terms, diffusion terms, and other quantities, which were not properly addressed in a second-order upwind scheme. All scalar values and velocity components are calculated at the center of control volume interfaces, where grid

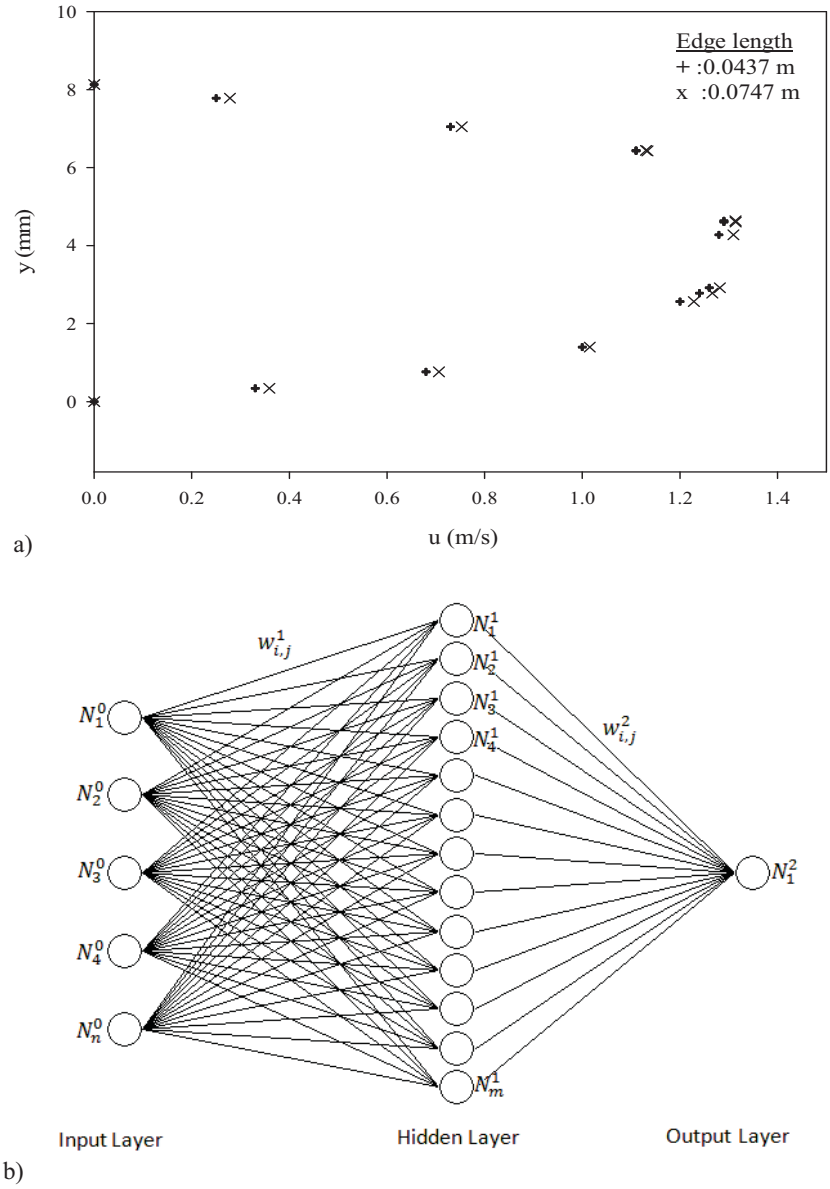

Fig. (3). Achieving the grid independency for velocity profiles at Re=8895.2 (**a**) and schematic representation of MLP (**b**) for the numerical part of the study.

schemes are used extensively. The Semi-Implicit Method for Pressure Linked Equations (SIMPLE) was used to pair pressure and velocity. A point-implicit (Gauss-Seidel) linear equation solver, in conjunction with an algebraic multigrid method, was employed in the Fluent CFD program [15] to solve the linear systems resulting from discretization schemes. k-ε turbulence models were chosen in the viscous model. Residuals were thoroughly monitored during the iterative process, and all solutions were considered to have converged when the residuals for each governing equation fell below 10^{-6}. Boundary conditions were defined for the velocity inlet at the pipe inlet and for the pressure outlet at the pipe exit; turbulence intensity and hydraulic diameter were defined for the turbulence parameters. Constant heat flux was applied to the pipe surface. To show grid-independent solutions, two different edge lengths were used in the tetrahedrons grid type for Re=8895.2. Fig. (**3a**) shows the velocity profile distributions of the two, which are nearly identical.

4.4. Numerical Method- ANN Approach

An artificial neural network (ANN) is an information-processing system that has certain performance characteristics in common with biological neural networks. Artificial neural networks have been developed as generalizations of mathematical models of human cognition or neural biology, based on the assumptions as follows [73].

- Information processing occurs at many simple elements called neurons
- Signals are passed between neurons over connection links
- Each connection link has an associated weight, which, in a typical neural net, multiplies the signal transmitted
- Each neuron applies an activation function (usually non-linear) to its net input (sum of weighted input signals) to determine its output signal.

The ANN is the most widely used model, and is able to find linear and non-linear relationships between input and output patterns. To find a relationship between input and output sets, well-known training sets are first used to generalize concerning a relationship. Once a generalization is made, the ANN tries to predict the outputs of a new test set. The performance metrics of the ANN are measured by the quality of its test set predictions. There are many types of ANN in function approximation literature, including the Multi-Layer Perceptron (MLP), the Radial Basis Functions Networks (RBFN), the Generalized Regression Neural Network (GRNN), and the decision-making system based on human 'fuzzy logic', the ANN Artificial Neural Fuzzy Inference System (ANFIS).

4.4.1. Multi-layer Perceptron

A multilayer perceptron (MLP) is a feedforward artificial neural network model that maps sets of input data onto a set of appropriate output. An MLP consists of multiple layers of nodes in a directed graph, with each layer fully connected to the next one. Except for the input nodes, each node is a with a nonlinear activation function. MLP utilizes a supervised learning technique called back propagation for training the network [74-75].

The MLP consists of three different layers, the input layer, the hidden layer, and the output layer. The input layer's neuron number and the output layer's neuron number are equal to the dimensions of the input variables and output variables, respectively. The number of the hidden layer and the number of any hidden layer's neuron may be manipulated at will; if the number of the hidden layer and any hidden layer's neuron increases, then the non-linear feature of the model will increase as well. A schematic representation of the MLP model is shown in Fig. (**3b**).

Let Nbe the number of input parameters used for the estimation of displacement, and M the neuron number in the hidden layer;let the inputs of the MLP (0^{th} layer outputs) be shown as $\left\{N_1^0, N_2^0, ...N_n^0\right\}$, the output values of the hidden layer (1^{st} layer outputs) as $\left\{N_1^1, N_2^1, ...N_m^1\right\}$, the output values of the output layer (2^{nd} layer outputs, predicted value) as N_1^2, the connection weight of the i^{th} neuron of the input layer to the j^{th} neuron of the hidden layer as $w_{i,j}^1$, the j^{th} neuron of the l^{st} layer's bias value as b_j^l, andthe l^{st} layer's transfer function as f_l ;the j^{th} neuron of the l^{st} layer's output is then calculated as in Eq. (12):

$$N_j^l = f_l\left(b_j^l + \sum_i N_i^{l-1}.w_{i,j}^l\right) \tag{12}$$

In the literature, there are many different kinds of transfer functions,including purelin, tansig, logsig, and so on. If the training output set is shown by D, then the error function of the prediction is calculated as in Eq. (13):

$$J = \frac{1}{2}\sum\left(N^{out} - D\right)^2 \tag{13}$$

The optimization method appliedin Eq. (12) in order to find the w and b values, and to yield a minimum value of J, is called the MLP learning algorithm. The mean of training calculates optimal w and b values by way of the training set. The Gradient Descent, Gradient Descent with Momentum, Conjugate Gradient, Quasi-Newton, and Levenberg-Marquardt methods are well-known learning algorithmswithin the literature.

4.4.2. Validation and Performance Metrics

Validation is a supervised learning method using data points obtained from experiments, and must be performed in order to gauge the success of learning algorithms. The most well-known validation methods are the hold-out, the k-fold cross, and the leave-one-out cross-validation methods.

In the k-fold cross-validation method, n number data obtained from experimentationare divided randomly into k number sets,each data cluster having equal elements and each being numbered from 1 to k.

$$\upsilon_i \in \{1,2,..k\} \qquad i=1..n \tag{14}$$

Data whose υ_i values are equal to 1 are first placed in the test set, while data whose υ_i values are different from 1 are placed in the training set. The suggested method is then to train using the training set and to examine using the test set. The researcher's next step is to send data with a υ_i value of 2 to the test set and data with υ_i values different from 2 to the training set. The method is repeated once again with a new training set and a new testing set, and the process continues until all folds are tested [76].

To determine the most appropriate inputs for this process, the mean squared error (MSE) and the coefficient of correlation determination (R) metrics are used as performance criteria for the validation sets. If n is the number of experimental data, y is the value of the experiment, and $\hat{y}$ is the prediction of the MLP, then the formulations of MSE and R are shown in Eq. (15) and Eq. (16), respectively.

$$mse = \frac{1}{n}\sum_{i=1}^{n}\left(y_i - \hat{y}_i\right)^2 \tag{15}$$

$$R = \frac{n.\sum(y.\hat{y}) - \sum(\hat{y}).\sum(y)}{\sqrt{\left(n.\sum y^2 - \left(\sum y\right)^2\right).\left(n.\sum \hat{y}^2 - \left(\sum \hat{y}\right)^2\right)}} \tag{16}$$

4.4.3. Application of Multi-Layer Perceptron

To simulate the behavior of liquids flowing inside a pipe, CFD software processes 7 different inputs: the physical properties of nanofluids (k,μ,C_p,ρ),volume fraction, and the average temperature and velocity of the water. This simulation produces the outputs $h,\tau,\Delta P$, and Q. These outputs are maximally compatible with the experimental data, defined in the literature in terms of 20 different thermal conductivity correlations, 28 different dynamic viscosity correlations, and 4 different specific correlations of heat at constant pressure. To determine which combination of these correlations should be used, all of the possibilities can be tested individually. So many options can so prolong the simulation process as to make it infeasible; if the MLP model can simulate CFD software, however, finding relationships between the inputs and outputs of the CFD software within acceptable limits, the MLP model can be used instead of CFD software to determine the best input combination.

Because the CFD software requires 7 inputs and produces 4 outputs, the MLP requires 7 input neurons and 4 output neurons. In practice, the selected architecture of MLP has only 1 hidden layer with 5 neurons, as shown in Fig. (**3b**).; the MLP also has an available 7-5-4 architecture. The back-propogation model can be used, along with the Levenberg-Marquardt methods,as a learning algorithm. The transfer functions of the hidden layer (1st layer) and the output layer (2nd layer) are tansig and purelin, respectively, shown in Eq. (17):

$$f(x) = \frac{2}{1+e^{-2x}} - 1 \qquad f(x) = x \tag{17}$$

The validation process was performed by the 2-fold cross-validation method, using data groups according to test results and R criteria.

5. RESULTS AND DISCUSSION

The commercial software package ANSYS Fluent [27] was employed in the numerical study. Investigated tubes were plotted in the SolidWorks program [26], and were imported to ANSYS Geometry as shown in Fig. (**4a**) and Fig. (**4b**). After the investigated tubes were imported to ANSYS Geometry, they were forwarded for meshing in the ANSYS Meshing program. The mesh influences the accuracy, convergence, and speed of the solution. Furthermore, the time required to create a mesh model often represents a significant portion of the time required to acquire results from the solutions; this means that the better and more automated the meshing tools, the better the solution. The mesh performed for the investigated tubes is shown in Fig. (**4c**) and Fig. (**4d**).

Two different ANN models were developed to determine the best combination of physical properties for the TiO_2 nanofluid. The inputs of the ANN model 1 analyses were the correlations of physical properties, the average temperature and velocity of water in the test tube, and the nanoparticle concentration, while the outputs of the analyses were shear stress, friction factor, heat flux, convective heat transfer coefficient, and pressure drop. The inputs of the ANN model 2 analyses were the correlations of physical properties and the inlet and outlet temperature and velocity of the water in the test tube, while the outputs were the convective heat transfer coefficient and the pressure drop. The success of the ANN models are represented in Table **5**. The changes inthe numerical and experimental results ofthe ANN models are shown in Figs. (**5a** and **5b**) and (Figs. **6a** and **6b**). All results seemed to be successful within the ±5% deviation band. The most substantiated correlations were obtained from the ANN 1 model for the physical properties (k, μ, Cp) of nanofluids. They are given below:

$$k_{nf}=k_p\phi+(1-\phi)k_f \quad (18)$$

$$\mu_{nf}=\mu_{bf}(306\phi^2-0.19\phi+1) \quad (19)$$

$$Cp_{nf}=(1-\phi)Cp_{nf}(1+2.5\phi_p)\mu_f \quad (20)$$

These equations were obtained from ANN results; Eq. (18) is the thermal conductivity correlation of Bhattacharya *et al*. [63], numbered 15 in Table **2**; Eq. (19) is the viscosity correlation of Wang *et al*. [50], numbered 24 in Table **1**; and Eq. (20) is the heat capacity correlation of Maxwell [3], numbered 1 in Table **3**.

The validation process for numerical models is performed by means of the experimental data [6], as shown in Fig. (**7**) regarding heat transfer characteristics. Fig. (**7**) clearly demonstrates that the numerical model of ANSYS Fluent [27] is in substantialagreement with experimental values [6] in the calculation of the heat transfer coefficient (within a ±25% range) and of the pressure drop (within a ±10% range) for the in-tube single-phase flow of pure water and nanofluid with TiO_2 volume concentrations of 0.2, 0.6, and 1%. Table **6** further shows error rates of less than 1.56% and 2.02% between experimental and numerical temperatures at the outlet section and at the surface, respectively. It should be noted that experimental and numerical studies are conducted for Re numbers between 4516 and 15681 and for surface heat fluxes between 7233 and 13340 W m^{-2}.

The velocity of the fluid in contact with the pipe wall is essentially zero, and it increases with increasing distance from the wall. The velocity profile depends upon the surface condition of the pipe wall;a smoother wall results in a more uniform velocity profile than does a rough pipe wall. The pressure of the fluid in contact with the pipe wall is likewise small, and likewise increases with increasing distance from the wall. The pressure of the fluid has its maximum value at the entrance of pipe and decreases with increasing distance from the entrance. The temperature of the fluid has its maximum value on the wall, since a constant heat flux is applied to the pipe surface. The temperature of the fluid has its minimum value at the entrance of pipe and increases with increasing distance fromthe entrance, due to the constant heat flux. The ANSYS Fluent CFD [27] program was used in numerical analyses to develop velocity, pressure, and temperature profiles at various locations, and was applied to φ=1% to the smooth tube (Fig. **8**), to the micro-fin tube with a helix angle of 0º (Fig. **9**), and to the micro-fin tube with a helix angle of 18º (Fig. **10**).

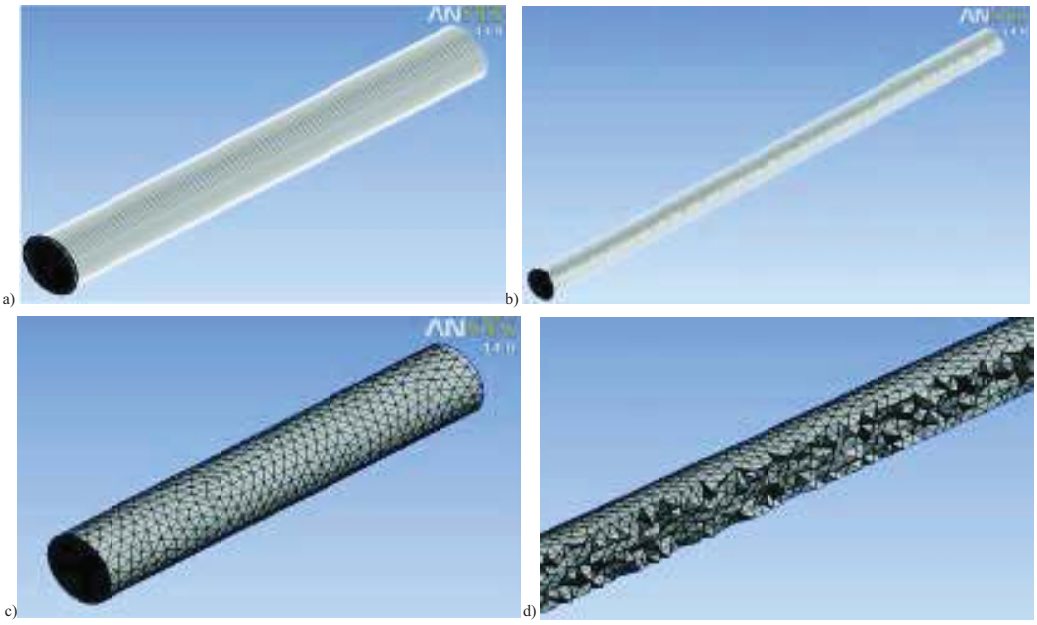

Fig. (4). Views of different helix angles of micro-fin tubes 0º (**a**), 18º (**b**), and views of meshing (**c**) and detailes of meshing (d) for smooth tube.

Table 4. Geometrical Parameters of the Investigated Tubes

Tubes	Smooth	Micro-fin 1	Micro-fin 2
a(°)	-	0	18
Θ(°)	-	36	36
e (mm)	-	0.435	0.435
p (mm)	-	0.378	0.378
n_f	-	60	60
s (mm)	-	0.293	0.293
di (mm)	8.13	8.13	8.13
do (mm)	9.13	9.13	9.13
L (m)	1.5	1.5	1.5
A (mm^2)	38311.7	92180.86	96210

Table 5. The Best Inputs Obtained from ANN Analyses and Numbered in Tables 1-2-3

k ($W\ m^{-1}K^{-1}$)	μ ($kg\ m^{-1}s^{-1}$)	c_p ($J\ kg^{-1}K^{-1}$)	R^2
12	24	1	0.967465
10	10	2	0.963421
6	7	2	0.961502
12	11	2	0.960374
13	8	1	0.958547
16	9	2	0.958514
14	27	2	0.958276
5	3	2	0.957927
11	11	3	0.957073
1	7	2	0.956864

a-) considering the determination of shear stress, friction factor, heat flux, convective heat transfer coefficient and pressure drop as outputs (ANN model 1)

k ($W\ m^{-1}K^{-1}$)	μ ($kg\ m^{-1}s^{-1}$)	c_p ($J\ kg^{-1}K^{-1}$)	R^2
18	2	2	0.99290234
6	21	2	0.99105436
11	1	4	0.99006633
15	1	2	0.98885878
6	1	1	0.98860543
19	26	3	0.9881786
7	12	1	0.98806904
8	28	2	0.98798953
6	7	2	0.98795459
16	2	4	0.98774095

b-) considering the determination of pressure drop and convective heat transfer coefficient as outputs (ANN model 2)

Table 6. Comparison of Experimental and Numerical Temperatures at Outlet Section and at Surface Using Pure Water with 0.2%, 0.6% and 1% TiO_2 Particles Data [4]

Concentration (%)	$T_{o,exp}$(°C)	$T_{o,num}$(°C)	Error Rate (%)	$T_{s,exp}$(°C)	$T_{s,num}$(°C)	Error Rate (%)
Pure water	26.6	26.9	1.26	27.4	27.8	1.45
0.2 %	27.0	27.4	1.52	27.85	28.4	1.97
0.6 %	27.2	27.6	1.56	28.13	28.7	2.02
1 %	27.0	27.4	1.45	27.75	28.2	1.62

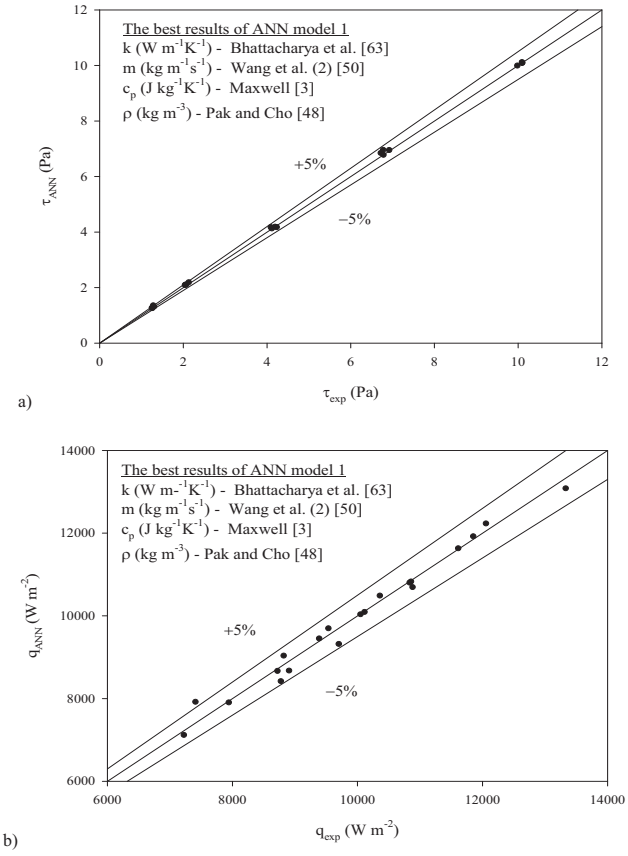

Fig. (5). The best results of ANN model 1 regarding with the shear stress (**a**) and heat flux (**b**).

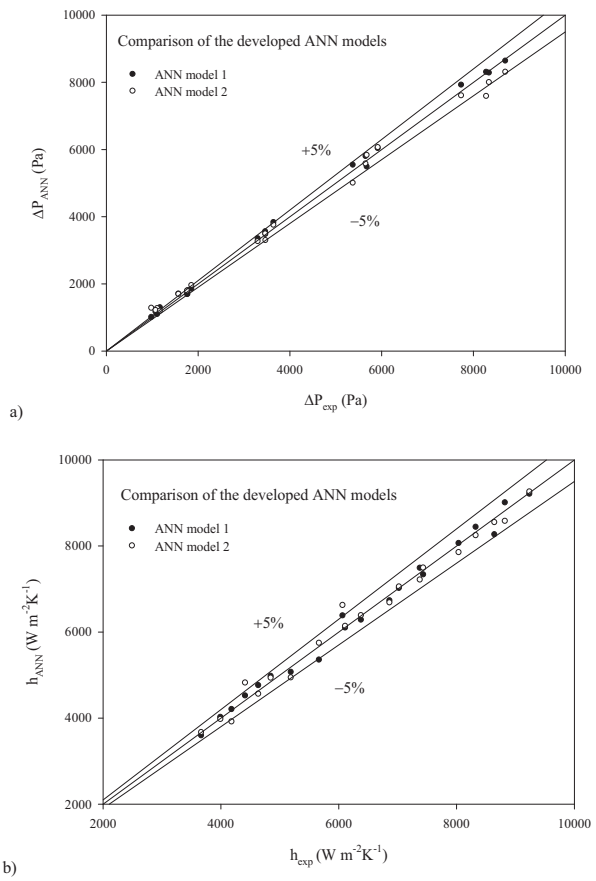

Fig. (6). Comparison of the developed ANN models regarding with the pressure drop (**a**) and convective heat transfer coefficient (**b**).

The variation in the local heat transfer coefficients along the pipe length for the flow of pure water, and for the nanofluids with different particle weight concentrations inside the smooth tube, are shown in Fig. (**11a**). This figure indicates that the additionof solid nanoparticles to the pure water did in fact lead to an increase in the local heat transfer coefficient for the flow inside the smooth tube. As has been shown before, the addition of nanoparticles improves the thermal conductivity of the base fluid. The convective heat transfer enhancement from the nanofluid may be due to an increase in thermal conductivity or to the random movement and dispersion of nanoparticles in the nanofluid. Disordered movements of the solid particles in the flow will alsoupset the thermal boundary layer formation on the tube wall surface, causing the development of the thermal boundary layer to lag and higher heat transfer coefficientsto obtain at the thermal entrance region. Here too, it appears that adding nanoparticles will improve the local heat transfer coefficient in a fluid flow. At higher weight concentrations of nanofluids, both the thermal conductivity of the TiO_2-water mixture and the disturbance effect of the solid nanoparticles will increase; nanofluids with higher weight concentrations will therefore haveeven higher convective heat transfer coefficients.

Fig. (**11b**) further demonstrates that nanofluids display better heat transfer performance when they flow inside micro-fin tubes with helix angles of 0º and 18º than when they flow insidesmooth tubes. The results clearly indicate that the highest heat transfer coefficientswere obtained for micro-fin tubeswith a helix angle of 18º and a volume concentration of 1%; these results are compatible withother current findings in the literature. (Fig. **11c**), furthermore, compares heat transfer coefficients between smooth and micro-fin tubes, and shows that the heat transfer coefficients of micro-fin tubeswith a helix angle of 18º are higher those of than micro-fin tubeswith a helix angle of 0º at nearly the same Reynolds numbers,

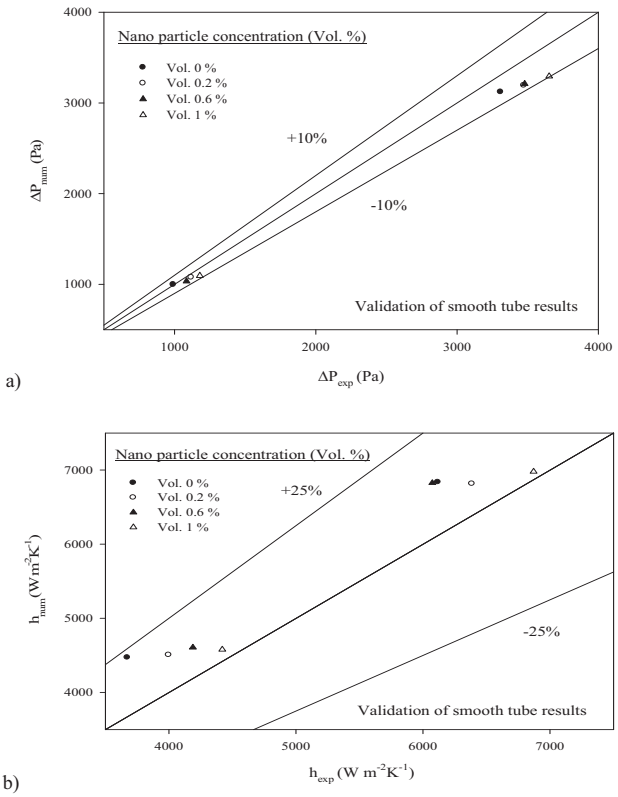

Fig. (7). Comparison of experimental and numerical pressure drops (**a**) and heat transfer coefficients (**b**) and using pure water with 0.2%, 0.6% and 1% TiO_2 particles data [6].

heat flux, and volume concentrations along the pipe. Similarly, the heat transfer coefficients of micro-fin tubes with a helix angle of 0º are higher than those of the smooth tubes.

Fig. (**12a**) shows a remarkable increase in the pressure drop of nanofluids with 0.2, 0.6, and 1 wt.% particle concentrations compared to pure water when flowing inside smooth and micro-fin tubes. This trend tends to continue for nanofluids at higher weight fractions. This is due to the fact that suspending solid particles in a fluid generally increases dynamic viscosity relative to the base fluid. Since viscosity stands in direct relation to pressure drop, the higher viscosity naturally leads to an increased pressure drop. Experimental results show that the pressure drop of micro-fin tubes with a helix angle of 18º is higher than that of micro-fin tubes with a helix angle of 0º. Moreover, the pressure drop of micro-fin tubes with a helix angle of 0º is higher than that of the smooth tubes. More exactly, the pressure drop of micro-fin tubes with a helix angle of 18º is 21.5% higher than that of smooth tubes, and the pressure drop of micro-fin tubes with a helix angle of 0º is 15.5% higher than that of smooth tubes at φ=1%.

From Fig. (**12b**), it is evident that the friction factor increases with increasing concentrations of nanoparticles because of the rise in working fluid viscosity. As was previously observed, nanofluids in smooth tubes with concentrations of 0.2%, 0.6%, and 1% provide friction factors higher than those of base fluids by 1.5, 5.1, and 5.8%, respectively. Similarly, nanofluids in micro-fin tubes with a helix angle of 18º, and with concentrations of 0.2%, 0.6%, and 1%, provide friction factors higher than those of base fluids by around 0.33%, 2.2% and 3.2%, respectively. It can be observed from Fig. (**12c**) that wall shear stress increases with the increasing volume concentration of the nanoparticles; the Reynolds number of the flow also increases as the inclusion of nanoparticles raises the viscosity of the mixture.

As the numbers indicate, nanofluids in smooth tubes with concentrations of 0.2%, 0.6%, and 1% induced a wall shear stress higher than that of the base fluid by around 2.2, 2.7% and 5.2%, respectively. Likewise, nanofluids in micro-fin tubes with a helix angle of 18º, and with concentrations of 0.2%, 0.6% and 1%, induced a wall shear stress higher than that of the base fluid by around 1%, 1.2%, and 4.2%, respectively. According to Fig. (**12c**), the wall shear stress of micro-fin tubes with a helix angle of 18º is 21.1% higher than that of smooth tubes, and the wall shear stress of micro-fin tubes with a helix angle of 0º is 3.77% higher at φ=0.6 % than that of smooth tubes. Fig. (**12d**) shows, finally, a remarkable increase in pumping power due to the increase in the pressure drop of the nanofluid in a large cross-section of the micro-fin tubes. The results show that the pumping power of micro-fin tubes with a helix angle of 18º is higher than that of micro-fin tubes with a helix angle of 0º; similarly, the pumping power of micro-fin tubes with a helix angle of 0º is higher than that of smooth tubes. In all, the characteristics of in the sub-figures of Fig. (**12**) are found to be compatible with other current findings in the literature.

6. CONCLUSION

This study investigated the heat transfer characteristics of pure water and of a water-TiO_2 mixture flowing inside smooth tubes, as a validation study, and inside micro-fin tubes, as a simulation study, with various volume concentrations investigated for forced flow conditions using two- dimensional governing equations. The conclusions of this study can be outlined as follows:

- The heat transfer coefficient was slightly increased with increasing nanofluid volume concentration.
- Micro-fin tubes with helix angles of 0° and 18° enhanced the heat transfer coefficient significantly under the same flow conditions, yielding at φ=1% mean heat transfer coefficients higher than those of smooth tubes by 23.5% and 32.5%, respectively.
- Compared to micro-fin tubes with a helix angle of 0°, the mean heat transfer coefficient and pressure drop of micro-fin tubes with a helix angle of 18° increased at φ=1% by 11.8% and 7.55%, respectively.
- Nanofluids with concentrations of 0.2%, 0.6%, and 1% in micro-fin tubes with a helix angle of 18º yielded friction factors higher than those of the base fluid by approximately 0.33%, 2.2%, and 3.2%, respectively.
- The wall shear stress of micro-fin tubeswith a helix angle of 18º was 21.1% higher at φ=0.6% than those of smooth tubes, and the wall shear stress of micro-fin tubeswith a helix angle of 0º was 3.77% higher than that of smooth tubes.
- The pumping power of micro-fin tubeswith a helix angle of 18º was 68.8% higher at φ=1% than that of smooth tubes and 11.5% higher than that of micro-fin tubeswith a helix angle of 0º.
- Nanofluids at higher volume concentrations showed both higher heat transfer enhancement and higher pressure drop. Therefore, judicious decisions should be taken to select a nanofluid that will balance the heat transfer enhancement and the pressure drop penalty.

As this study has also found, the proven tools of computational fluid dynamics (CFD) will make it feasible for researchers to analyze different geometrical configurations and various nanofluids without needing to perform additional experimental studies, once they have performed their validation process on the experimental data.

a)

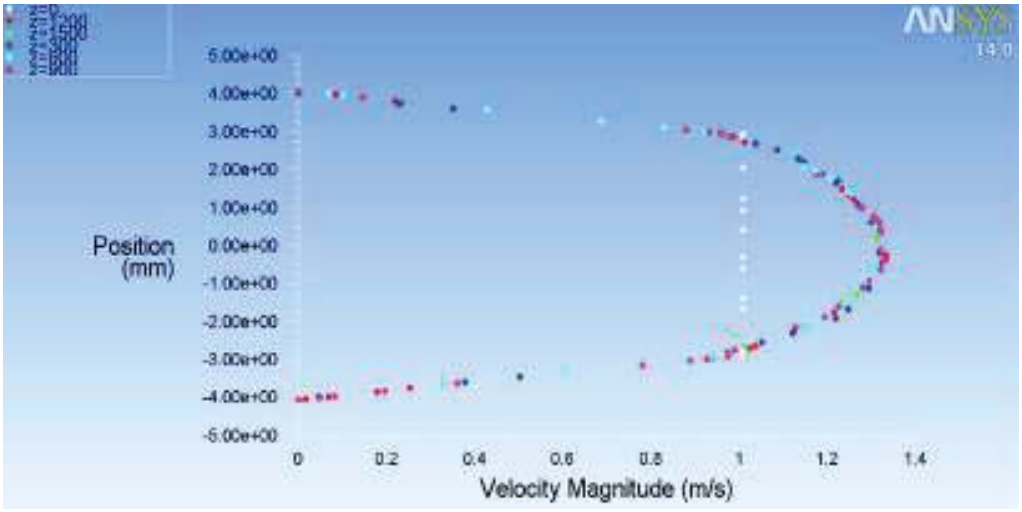

b)

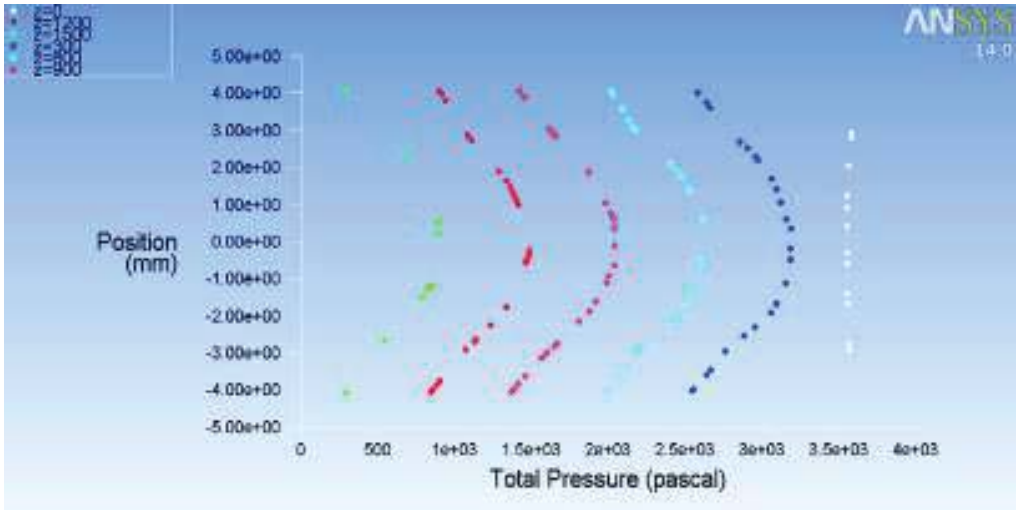

c)

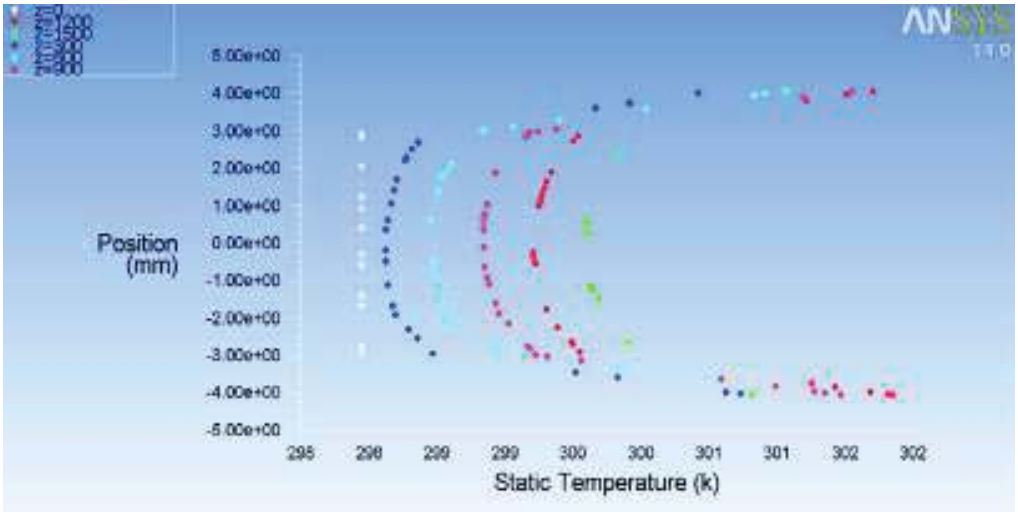

Fig. (8). Velocity profile (**a**), pressure profile (**b**) and temperature profile (**c**) at various locations in smooth tube.

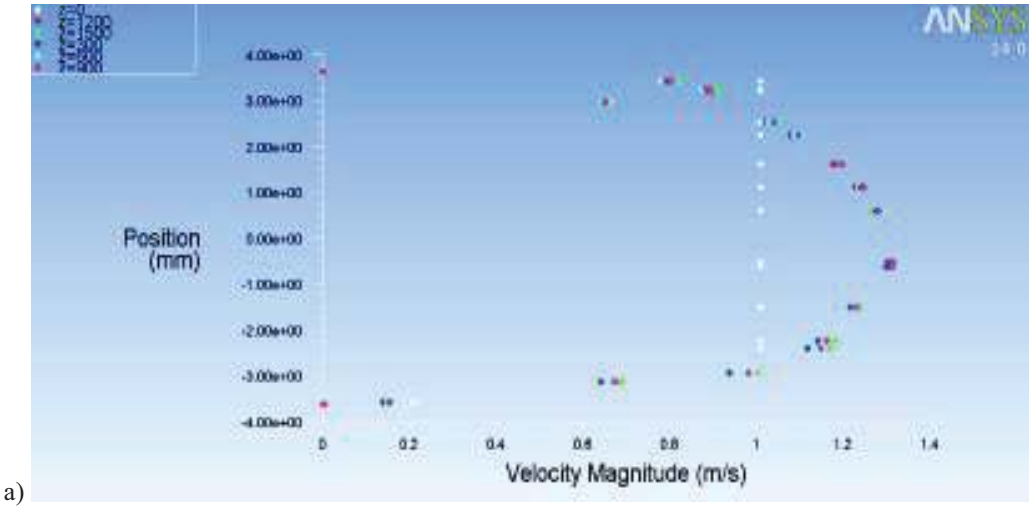

a)

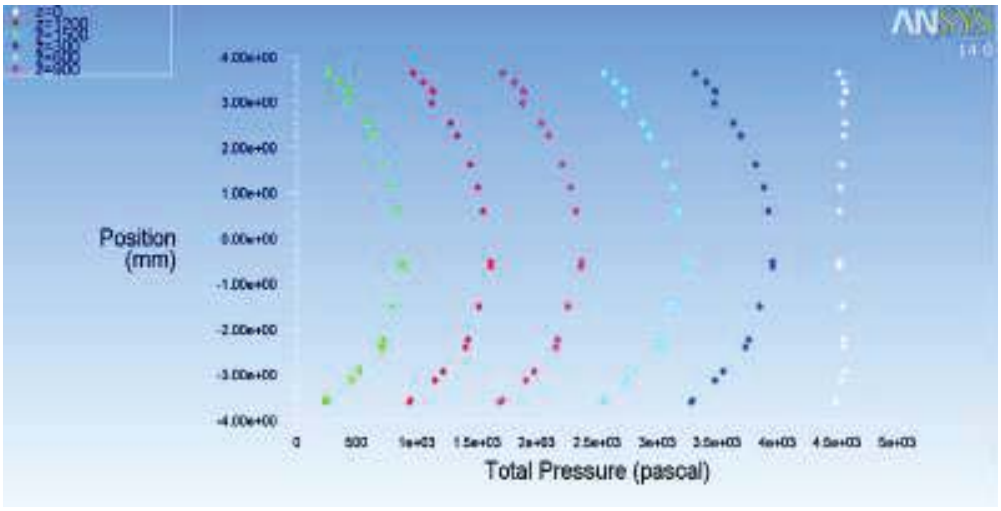

b)

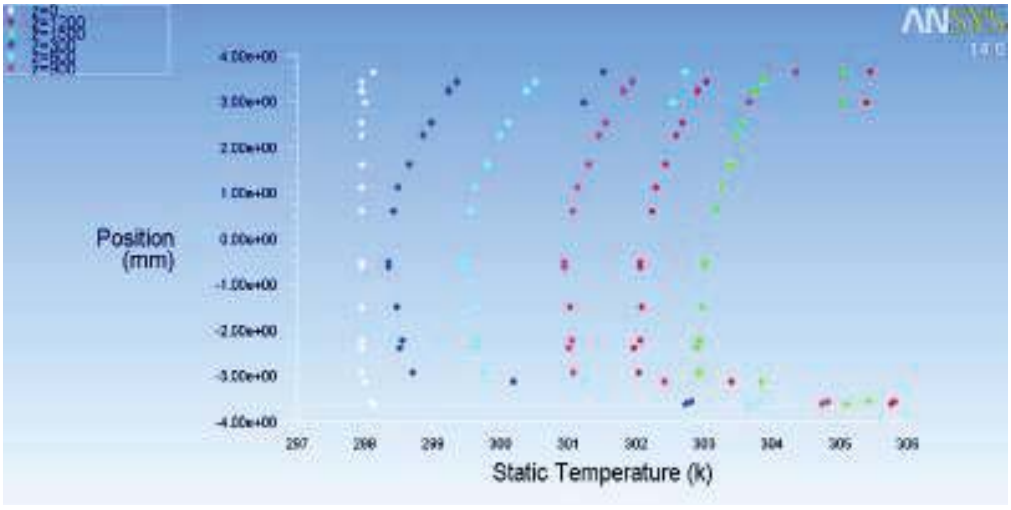

c)

Fig. (9). Velocity profile (**a**), pressure profile (**b**) and temperature profile (**c**) at various locations in micro-fin tube having helix angle 0º.

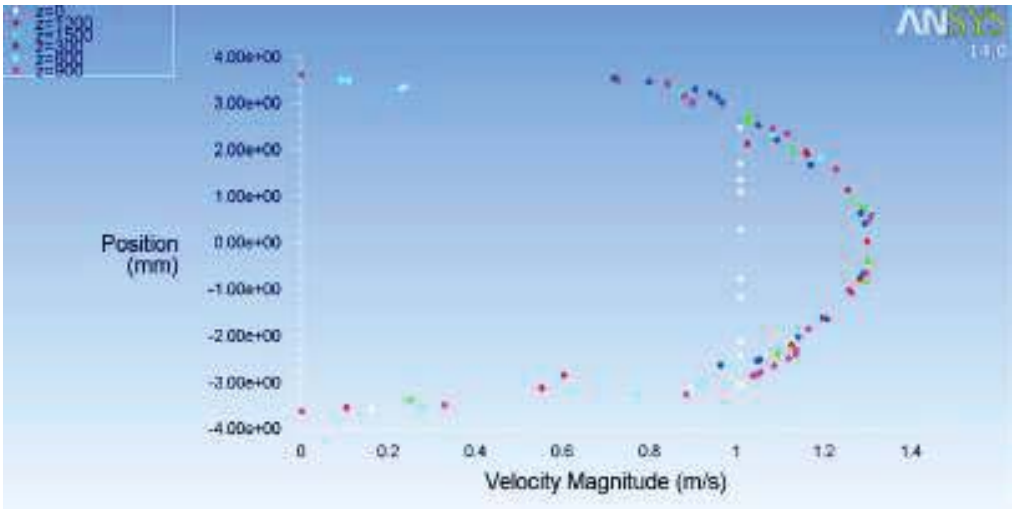

a)

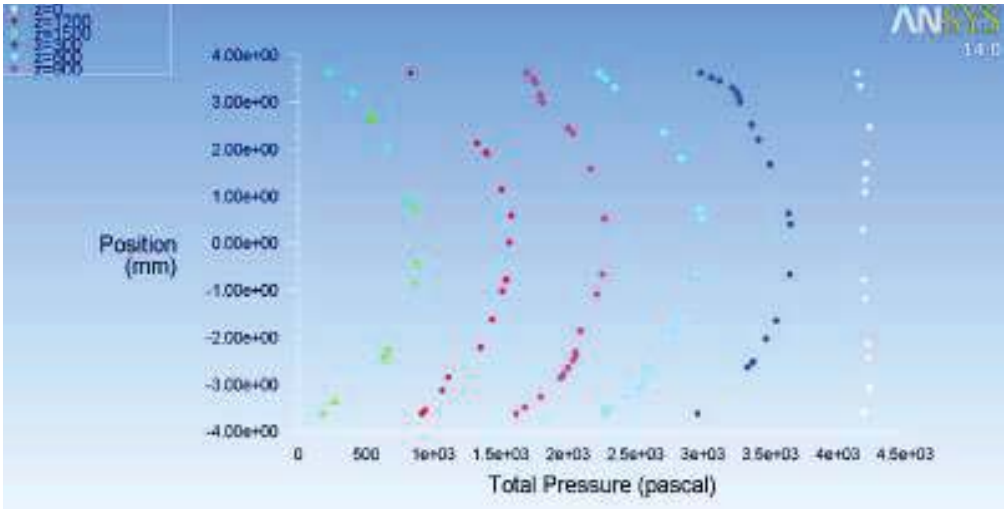

b)

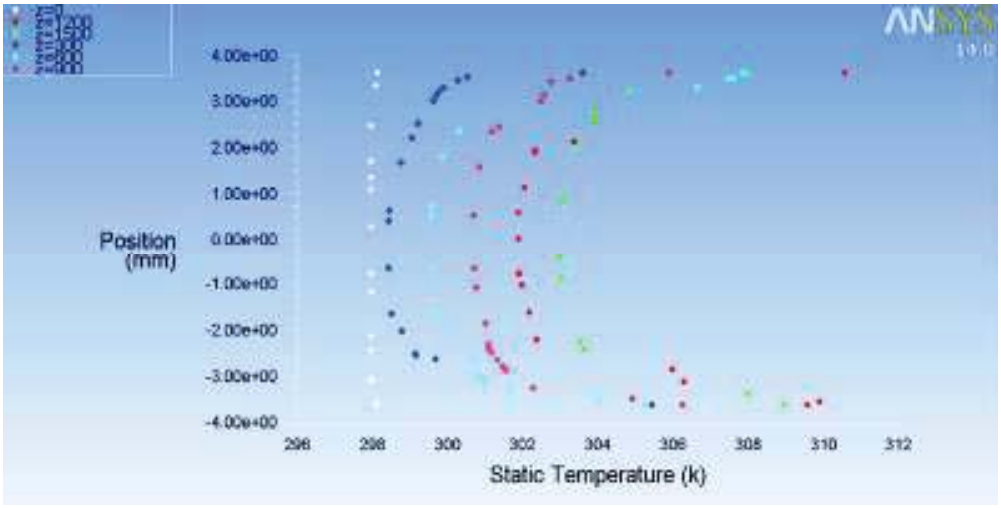

c)

Fig. (10). Velocity profile (**a**), pressure profile (**b**) and temperature profile (**c**) at various locations in micro-fin tube having helix angle 18º.

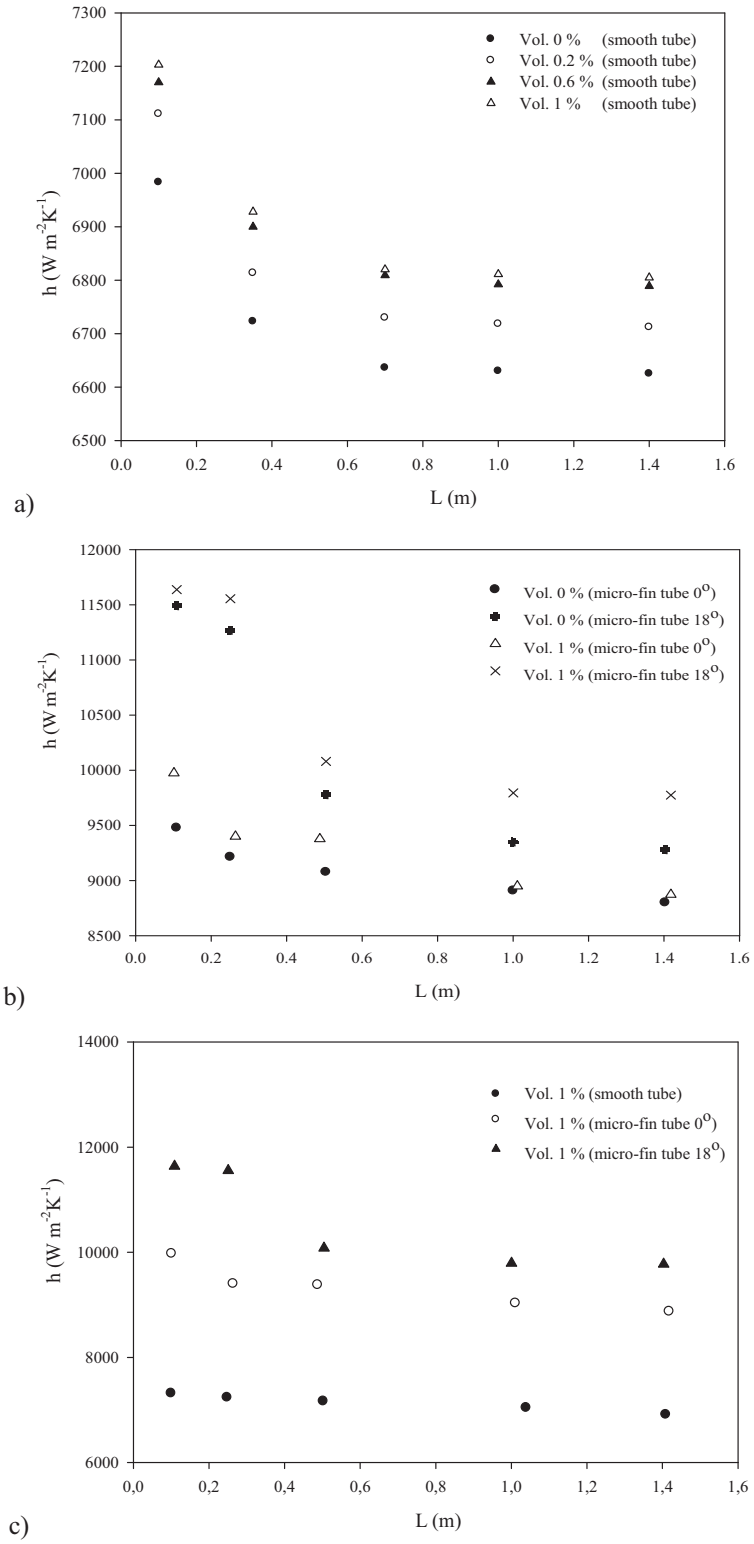

Fig. (11). Variations in heat transfer coefficient of smooth tube (**a**), micro-fin tubes (**b**) and smooth-micro-fin tubes (**c**) on volume concentration along the tube length.

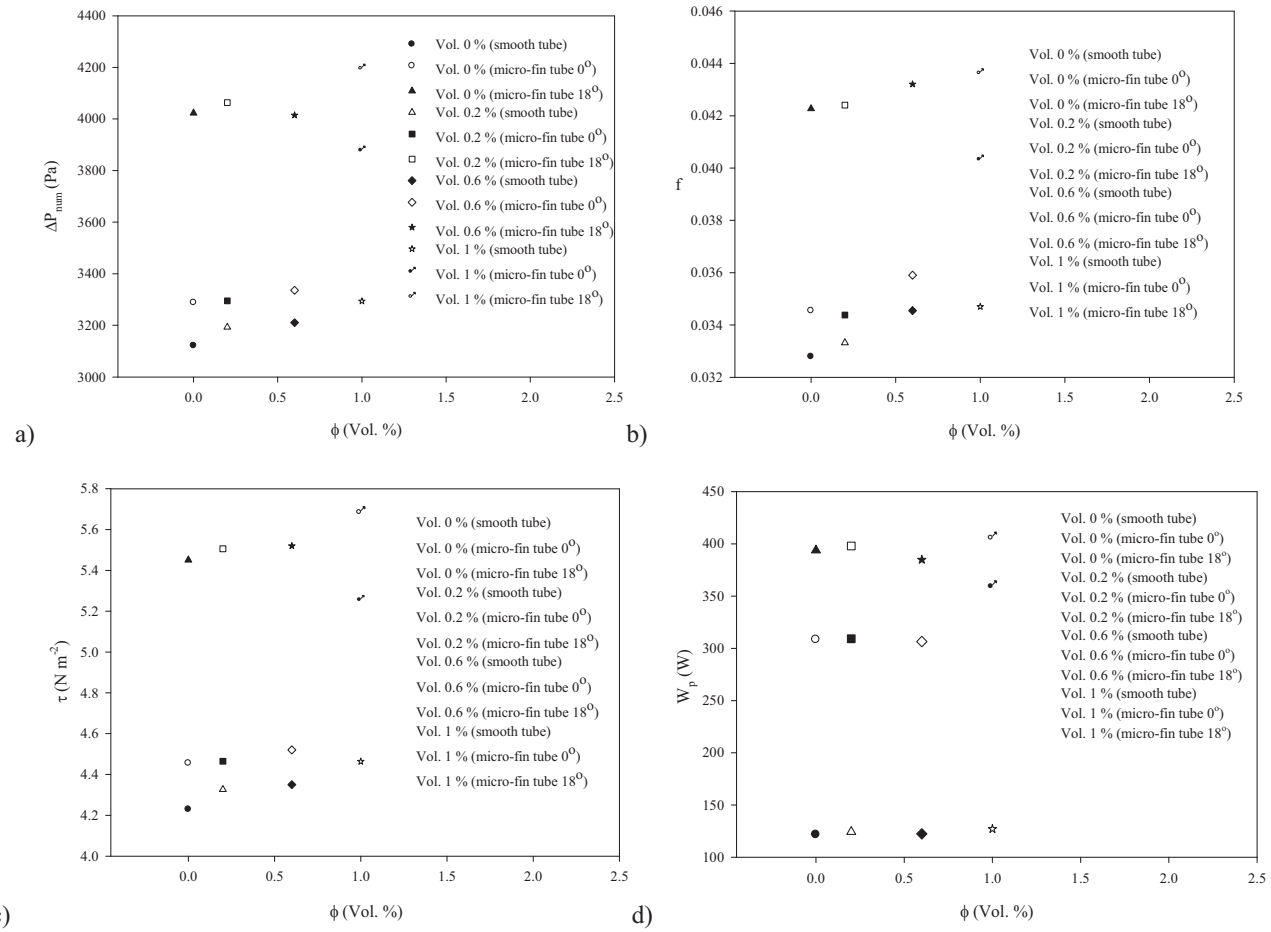

Fig. (12). Variations in pressure drop (**a**), friction factor (**b**), wall shear stress (**c**) and pumping power (**d**) of smooth tube and micro-fin tubes on different volume.

CONFLICT OF INTEREST

The authors confirm that this article content has no conflicts of interest.

ACKNOWLEDGEMENTS

The authors would like to express their appreciation to the Thailand Research Fund (TRF) and The National Research University Project for providing financial support for this study. Especially, the First author wishes to thank KMUTT for providing him with a Postdoctoral fellowship. The authors also wish to thank DEGUSSA AG, Germany for the valuable donation of the nanoparticles used in the present study. This research has been supported by Yıldız Technical University Scientific Research Projects Coordination Department. Project Number: 29-06-01-01.

NOMENCLATURE

Cp	=	Specific heat [J $kg^{-1}K^{-1}$]
d	=	Internal tube diameter [m]
h	=	Heat transfer coefficient [W $m^{-2}K^{-1}$]
k	=	Thermal conductivity [W $m^{-1}K^{-1}$]
k_H	=	Huggins coefficient.
L	=	Length of test tube [m]
m	=	Mass flow rate [kg s^{-1}],
Nu	=	Nusselt number
ΔP	=	Pressure drop [Pa]
Pr	=	Prandtl number
Re	=	Reynolds number
Q	=	Heat transfer rate [W]
q"	=	Heat flux [W m^{-2}]
T	=	Temperature [°C]
μ	=	Dynamic viscosity [Pa.s]
ρ	=	Density [kg m^{-3}]
τ	=	Shear stress [N m^{-2}]
φ	=	Volume fraction [%]
$φ_m$	=	maximum particle packing fraction
ν	=	Kinematic viscosity [m^2 s^{-1}]
m	=	Mass [kg]
f	=	Friction factor
W	=	Work [J]
P	=	Pressure [Pa]
A	=	Area [m^2]
u	=	Average velocity [m/s]
n	=	Number of fins

e = Height of fin [m]
p = Distance between micro-fins [m]
Q = Flow rate

SUBSCRIPTS

avg = Average
bf = Base fluid
nf = Nano fluid
exp = Experimental
ext = External
f = Fluid
h = Hot
i = Inlet
m = Mean
nf = Nanofluid
num = Numerical
p = Particle
r = Radius of particle
s = Surface
o = Outlet
w = Water

REFERENCES

[1] Choi, U.S. Enhancing thermal conductivity of fluids with nanoparticles. *ASME FED,* **1995**, *66*, 99-103.

[2] Xuan, Y.; Li, Q. Heat transfer enhancement of nanofluids. *Int. J. Heat Fluid Fl.*, **2000**, *21*, 58-64.

[3] Maxwell, J.C. *Electricity and Magnetism*.; Clarendon Press: Oxford UK, **1873**.

[4] Daungthongsuk, W.; Wongwises, S. A critical review of convective heat transfer of nanofluids. *Renew. Sustain. Energy Rev.,* **2007**, *11*, 797-817.

[5] Duangthongsuk, W.; Wongwises, S.Measurement of temperature-dependent thermal conductivity and viscosity of TiO_2-water nanofluids. *Exp. Therm. Fluid Sci.*, **2009**, *32*, 706-714.

[6] Duangthongsuk, W.; Wongwises, S. Comparison of the effects of measured and computed thermophysical properties of nanofluids on heat transfer performance. *Exp. Therm. Fluid Sci.*, **2010**, *34*, 616-624.

[7] Duangthongsuk, W.; Wongwises, S. An experimental study on the heat transfer performance and pressure drop of TiO_2-water nanofluids flowing under a turbulent flow regime. *Int. J. Heat Mass Trans.,* **2010**, *53*, 334-344.

[8] Duangthongsuk, W.; Wongwises, S. Heat transfer enhancement and pressure drop characteristics of TiO2-water nanofluid in a double-tube counter flow heat exchanger. *Int. J. Heat Mass Tran.*, **2009**, *52*, 2059-2067.

[9] Duangthongsuk, W.; Wongwises, S. Effect of thermophysical properties models on the predicting of the convective heat transfer coefficient for low concentration nanofluid. *Int. Commun. Heat Mass.,* **2008**, *35*, 1320-1326.

[10] Duangthongsuk, W.; Dalkilic, A.S.; Wongwises, S. Convective heat transfer of Al2O3-water nanofluids in a microchannel heat sink. *Curr. Nanosci.,* **2012**, *8,* 317-322.

[11] Suriyawong, A.; Wongwises, S., Nucleate pool boiling heat transfer characteristics of TiO_2-water nanofluids at very low concentrations. *Exp. Therm. Fluid Sci.*, **2010**, *34*, 992-999.

[12] Trisaksri, V.; Wongwises, S. Nucleate pool boiling heat transfer of TiO2–R141b nanofluids. *Int. J. Heat Mass Trans.*, **2009**, *52*, 1582-1588.

[13] Dalkilic, A.S.; Kürekci, N.A.; Wongwises, S. Effect of void fraction and friction factor models on the prediction of pressure drop of R134a during downward condensation in a vertical tube. *Heat Mass Transfer*., **2012**, *48*, 123-139.

[14] Dalkilic, A.S.; Kürekci, N.A.; Wongwises , S. Prediction of two-phase friction factor of refrigerants inside a horizontal tube using CFD analysis for the homogeneous condensation flow.*ASME-JSME-KSME Joint Fluids Engineering Conference, ASME-JSME-KSME.*, **2011**, *July 24-29*, Japan.

[15] Fluent release 6.2.16, Fluent Incorporated, **2005.**

[16] Demir, H.; Dalkilic, A.S.; Kurekci , N.A.; Kelesoglu, B.; Wongwises, S. A numerical investigation of nanofluids forced convection flow in a horizontal smooth tube. *Int. Heat Transfer Con.* ASME. , **2010**, *August 8-13*, USA.

[17] Demir, H.; Dalkilic, A.S.; Kurekci , N.A.; Kelesoglu, B.; Wongwises, S., Numerical investigation on the single phase forced convection heat transfer characteristics of TiO_2nanofluids in a double-tube counter flow heat exchanger. *Int. Commun. Heat Mass.,* **2011**, *38*, 218-228.

[18] Palm, S.J.; Roy, G.; Nguyen, C.T. Heat transfer enhancement with the use of nanofluids in radial flow cooling systems considering temperature-dependent properties. *Appl. Therm. Eng.*, **2006**, *26*, 2209-2218.

[19] Ağra, Ö.; Demir, H.; Atayılmaz, Ş.Ö.; Kantaş, F.; Dalkılıç, A.S. Numerical investigation of heat transfer and pressure drop in enhanced tubes. *Int. Commun. Heat Mass.,* **2011**, *38*, 1384-1391.

[20] Balcılar, M.; Dalkılıç, A.S.; Bolat, B.; Wongwises, S. Investigation of empirical correlations on the determination of condensation heat transfer characteristics during downward annular flow of R134a inside a vertical smooth tube using artificial intelligence algorithms. *J. Mec. Sci. Technol.,* **2011**, *25*, 2683-2701.

[21] Bolat, B.; Balcilar , M.; Dalkilic, A.S.; Wongwises, S. Optimization of the relationship between the two-phase friction factor and Reynolds equivalent number model by the means of Genetic Algorithm. *ASME/JSME 8th Thermal Engineering Joint Conference. ASME.,* **2011**, *March 13-17*, Hawaii.

[22] Balcilar, M.; Dalkilic, A.S.; Wongwises S. Artificial neural network (ANN) techniques for the determination of condensation heat transfer characteristics during downward annular flow of R134a inside a vertical smooth tube.*Int. Commun. Heat Mass.,* **2011**, *38*, 75-84.

[23] Balcilar, M.; Dalkilic, A.S.; Wongwises S. Determination of condensation heat transfer characteristics of R134a by means of artificial intelligence method. *International Mechanical Engineering Congress and Exposition, ASME*., **2010,** *November 12-18*, USA.

[24] Balcilar, M.; Dalkilic, A.S.; Suriyawong, A.; Yiamsawas , T.; Wongwises, S. Investigation of pool boiling of nanofluids using artificial neural networks and correlation development techniques. *Int. Commun. Heat Mass.,* **2012**, *39*, 424-431.

[25] Balcilar, M.; Dalkilic, A.S.; Agra, O.; Atayilmaz, S.O.; Wongwises, S. A correlation development study on the prediction of pressure drop during condensation and evaporation of various refrigerants in horizontal smooth and micro-fin tubes. *Int. Commun. Heat Mass.,* **2012**, *39*, 937-944.

[26] SolidWorks, SolidWorks Corporation, 300 Baker Avenue, Concord, MA 01742. Available from: http://www.solidworks.com/.

[27] ANSYS Fluent, ANSYS Inc., 10 Cavendish Court Lebanon, NH 03766 Available from: http://www.ansys.com/.

[28] Williams, W.C.; Buongiorno, J.; Hu, L.W. Experimental investigation of turbulent convective heat transfer and pressure loss of alumina/water and zirconia/water nanoparticle colloids (nanofluids) in horizontal tubes. *J. Heat Transf*., **2008**, *130*, 042412.

[29] Rea, U.; McKrell, T.; Hu, L.; Buongiorno, J. Laminar convective heat transfer and viscous pressure loss of alumina-water and zirconia-water nanofluids.*Int. J. Heat Mass Tran.,* **2009**, 52, 2042-2048.

[30] Einstein, A. Eineneuebestimmung der moleküldimensionen.*Ann Phys-Newyork***., 1906**, *324*, 289-306.

[31] Brinkman, H. The viscosity of concentrated suspensions and solutions.*J. Chem. Phys.*, **1952**, *20*, 571-581.

[32] Batchelor, G. The effect of brownian motion on the bulk stress in a suspension of spherical particles.*J. Fluid Mech.,* **1977**, *83*, 97-117.

[33] Graham, A.L. On the viscosity of suspensions of solid spheres.*J. ApplSci Res*., **1981**, *37*, 275-286.

[34] Kitano, T.; Kataoka, T.; Shirota, T. An empirical equation of the relative viscosity of polymer melts filled with various inorganic fillers. *The Journal RheologicaActa*., **1981** , *20*, 207-209.

[35] Bicerano, J.; Douglas, J.F.; Brune, D.A. Model for the viscosity of particle dispersions. *J. Macromol Sci-Rev. M.,* **1999**, *39*, 561-642.

[36] Wang, X.; Xu, X.; Choi, S.U.S. Thermal conductivity of nanoparticle–fluid mixture. *J.Thermophys Heat Tr.*, **1999**, *13*, 474-480.

[37] Tseng, W.J.; Chen, C.N. Effect of polymeric dispersant on rheological behavior of nickel-terpineol suspensions.*Mat. Sci. Eng.A-Struct*, **2003**, *347*, 145-153.

[38] Chen, H.; Ding, Y.; He, Y.; Tan, C. Rheological behaviour of ethylene glycol based titanianofluids. *Chem. Phys. Lett.*, **2007**, *444*, 333-337.

[39] Nguyen, C.; Desgranges, F.; Roy, G.; Galanis, N.; Mare, T.; Boucher, S.; Anguemintsa, H. Temperature and particle-size dependent viscosity data for water-based nanofluids-hysteresis phenomenon. *Int. J. Heat Fluid Fl.*, **2007**, *28*, 1492-1506.

[40] Khanafer, K.; Vafai, K. A critical synthesis of thermophysical characteristics of nanofluids.*Int. J. Heat Mass Tran.*, **2011**, *54*, 4410-4428.

[41] Vand , V. Viscosity of solutions and suspensions I. Theory, *J. Phys. Colloid Chem.*, **1948**, *52*, 277-299.

[42] Mooney, M. The viscosity of a concentrated suspension of spherical particles. *J. Coll. Sci. Imp. U. Tok***., 1951**, 6-8.

[43] Krieger , I. M.; Dougherty, T. J. A mechanism for non-newtonian flow in suspensions of rigid spheres. *J. Rheol.*, **1959**, *3*, 137-152.
[44] Krieger, I.M. Rheology of monodisperse lattices., *Adv. Colloid Interfac.*, **1972**, *3*, 111-136.
[45] Frankel, N.A.; Acrivos, A. On the viscosity of a concentrated suspension of solid spheres. *Chem. Eng. Sci.*, **1967**, *22*, 847-853.
[46] Miller, A.; Gidaspow, D.; Dense, D. Vertical gas-solid flow in a pipe. *AIChE journal*, **1992**, *38*, 1801-1815.
[47] Chow , T.S. Viscosities of concentrated dispersions.*Phys. Rev. E.*, 1993, *48*, 1977-1983.
[48] Pak, B.C.; Cho, Y.I. Hydrodynamic and heat transfer study of dispersed fluids with submicron metallic oxide particles.*Exp. Heat Transfer.*, **1998**, *11*, 151-170.
[49] Liu, S. Particle dispersion for suspension flow. *Chem. Eng. Sci.*, **1999**, *54*, 873-891.
[50] Wang, X.; Xu, X. Choi S.U.S., Thermal conductivity of nanoparticle-fluid mixture, *J. Thermophys. Heat Tr.*, **1999**, *13*, 474-480.
[51] Davalos, L.A.; Orozco, L.A.; Castillo, L.F. Del. Hydrodynamic behavior of suspensions of polar particles. *Encycl. Surf. Colloid Sci.*, **2002**, *4*, 2375-2396.
[52] Putra, N.; Roetzel, W.; Das, S.K. Natural convection of nano-fluids.*Heat Mass Transfer*., **2003**, *39*, 775-784.
[53] Tang, G.Y.; Yang, C.; Chai, J.C.Gong, H.Q. Joule heating effect on electroosmotic flow and mass species transport in a microcapillary. *Int. J. Heat Mass Trans.*, **2004**, *47*, 215-227.
[54] Hamilton, R.L.; Crosser , O.K. Thermal conductivity of heterogeneous two component systems.*Ind. Eng. Chem.*, **1962**, *1*, 187-191.
[55] Hui , P.M.; Zhang, X.; Markworth , A.J.; Stroud, D. Thermal conductivity of graded composites: numerical simulations and an effective medium approximation. *J. Mater. Sci.*, **1999**, *34*, 5497-5503.
[56] Xuan, Y.; Li , Q. Heat transfer enhancement of nanofluids.*Int. J. Heat Fluid Fl.*, **2000**, 21, 58-64.
[57] Yu, W.; Choi, S.U.S. The role of interfacial layers in the enhanced thermal conductivity of nanofluids: a renovated Maxwell model. *J. Nanopart. Res.*, **2003**, *5*, 167-171.
[58] Godson, L.; Raja, B.; Mohan, D. Lal; Wongwises, S. Experimental investigation on the thermal conductivity and viscosity of silver-deionized water nanofluid. *Exp. Heat Transfer.*, **2010**, *23*, 317-332.
[59] Prasher, R.; Bhattacharya, P.; Phelan, P.E. Thermal conductivity of nanoscale colloidal solutions (nanofluids). *Phys. Rev. Lett.*, **2005**, *94*, 025901-1–025901-4.
[60] Koo, J.; Kleinstreuer, C. A new thermal conductivity model for nanofluids. *J. Nanopart. Re.,* **2004**, *6,* 577-588.
[61] Li, C.H.; Peterson, G.P. Experimental investigation of temperature and volume fraction variations on the effective thermal conductivity of nanoparticle suspensions (nanofluids). *J. Appl. Phys.*, **2006**, 99-084314.
[62] Maiga, S.E.B.; Nguyen, C.T.; Galanis, N.; Roy, G. Heat transfer behaviours of nanofluids in a uniformly heated tube. *Superlattice Microst.*, **2004**, *35*, 543-557.
[63] Bhattacharya, P.; Saha, S.K.; Yadav, A.; Phelan, P.E.; Prasher, R.S. Brownian dynamics simulation to determine the effective thermal conductivity of nanofluids. *J. Appl. Phys.,* **2004**, *95*, 6492-6494.
[64] Buongiorno, J. Convective transport in nanofluids. *J. Heat Transf.*, **2006**, *128*, 240-251.
[65] Kim, D.; Kwon, Y.; Cho, Y.; Li, C.; Cheong, S.; Hwang, Y.; Lee, J.; Hong, D.; Moon, S. Convective heat transfer characteristics of nanofluids under laminar and turbulent flow conditions.*Curr. Appl. Phys.*, **2009**, *9 (2)*, 119-123.
[66] Elena, V.; Timofeeva, V.; Gavrilov, N.A.; McCloskey, J.M.; Tolmachev, Y.V. Thermal conductivity and particle agglomeration in alumina nanofluids: Experiment and Theory. *Phys. Rev. E.*, **2007,** *76*, 061203.
[67] Chon, C.H.; Kihm, K.D.; Lee, S.P.; Choi, S.U.S. Empirical correlation finding the role of temperature and particle size for nanofluid (Al_2O_3) thermal conductivity enhancement. *Appl. Phys. Lett.*, **2005**, 87.
[68] Murshed, S.M.S.; Leong, K.C.; Yang, C. A. model for predicting the effective thermal conductivity of nanoparticles–fluid suspensions. *Int. J. Nanosci.*, **2006**, *5*, 23-33.
[69] Yang, Y.; Zhang, Z.G.; Grulke, E.A.; Anderson, W.B.; Wu, G. Heat transfer properties of nanoparticle-in-fluid dispersions (nanofluids) in laminar flow.*Int. J. Heat Mass Trans.,* **2005**, 1107-1116
[70] Yu , W.; France, D.M.; Routbort, J.L.; SUS., Choi., Review and comparison of nanofluid thermal conductivity and heat transfer enhancements. *Heat Transfer Eng.*, **2008**, *29 5*, 432-460.
[71] Bejan, A.; Tsatsaronics, G.; Moran, M. Thermal design and optimization, Wiley-Interscience Publication:**1996**.
[72] Petukhov, B. S. Heat transfer and friction in turbulent referred to in handbook of single-phase convective pipe flow with variable physical properties. In Heat Transfer, ed. T. F. Irvine and J. P.New York: Wiley Interscience, 1987. Hartnett, Vol. 6, Academic Press:New York, **1970.**
[73] Fausett, L., *Fundamentals of Neural Networks, Architectures, Algorithms, and Application; Prentice-HallInc. Press*, **1994**.
[74] Rosenblatt , F., *Principles of Neurodynamics: Perceptrons and the Theory of BrainMechanisms*; Washington DC: Spartan Books, **1961**.
[75] Rumelhart D.E., G. E., Hinton, R.J., Williams, *Learning internal representations by error propagation.In D. E. Rumelhart& J. L. McClelland (Eds.), Parallel Distributed Processing1*, **1986**, pp. 318-362.
[76] Alpaydin, E.*Introduction to Machine Learning*, (T. Dietterich, C. Bishop, D. Heckerman, M. Jordan, & M. Kearns, Eds.) Machine Learning , **2004**, *56*, pp.387-99.

Received: August 22, 2012 **Revised: October 16, 2012** **Accepted: October 25, 2012**

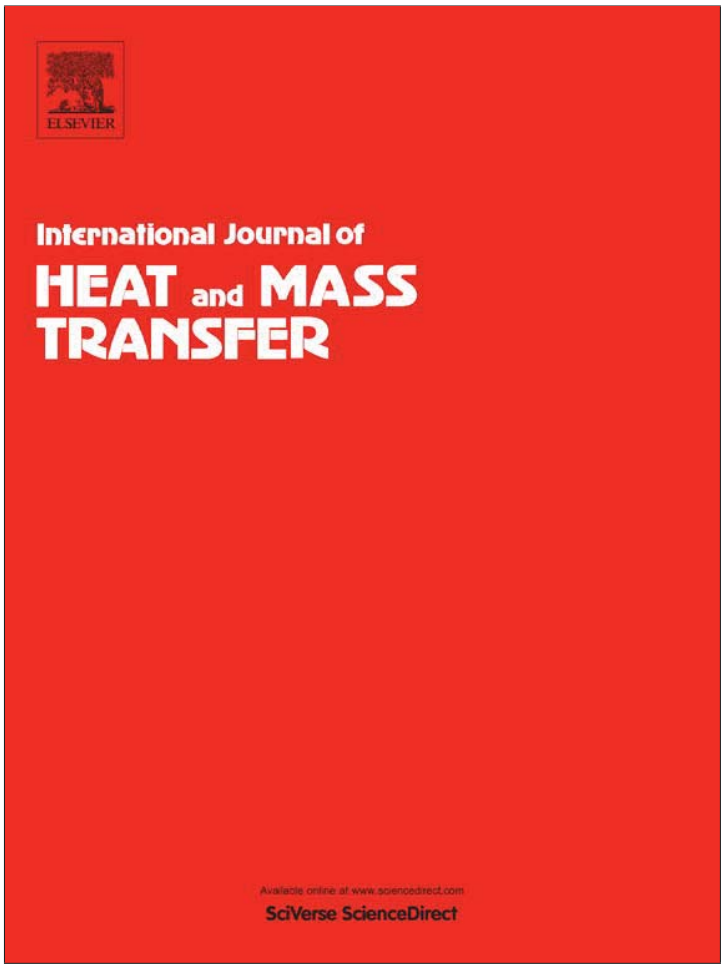

(This is a sample cover image for this issue. The actual cover is not yet available at this time.)

International Journal of Heat and Mass Transfer 60 (2013) 201–209

Contents lists available at SciVerse ScienceDirect

International Journal of Heat and Mass Transfer

journal homepage: www.elsevier.com/locate/ijhmt

Heat transfer performance of screen mesh wick heat pipes using silver–water nanofluid

Lazarus Godson Asirvatham [a,*], Rajesh Nimmagadda [a], Somchai Wongwises [b,c]

[a] Department of Mechanical Engineering, Karunya University, Coimbatore 641 114, Tamil Nadu, India
[b] Fluid Mechanics, Thermal Engineering and Multiphase Flow Research Lab (FUTURE), Department of Mechanical Engineering, Faculty of Engineering, King Mongkut's University of Technology Thonburi,126 Bangmod, Tongkru, Bangkok 10140, Thailand
[c] The Academy of Science, The Royal Institute of Thailand, Sanam Suea Pa, Dusit, Bangkok 10300, Thailand

ARTICLE INFO

Article history:
Received 3 May 2012
Received in revised form 6 November 2012
Accepted 10 November 2012

Keywords:
Silver
De-ionized water
Nanofluid
Thermal resistance
Evaporation and condensation heat transfer coefficients
Dry-out condition

ABSTRACT

This study presents the improvement in heat transfer performance of a heat pipe using silver nanoparticles dispersed in DI (De-Ionized) water. The nanoparticles suspended in conventional fluids have superior heat transfer capability due to improved thermal conductivity. The heat pipes are tested for heat inputs ranging from 20 W to 100 W in five steps, which is suitable for removing heat from power transistors in electronics and processors in computers. The effect of various operational limits and test parameters such as heat inputs, volume fraction, vapour temperature on the thermal resistance, evaporation and condensation heat transfer coefficients, are experimentally investigated. The tested silver nanoparticles volume concentration ranged from 0.003% to 0.009% with average nanoparticle diameter of 58.35 nm. The experimental results are evaluated in terms of performance metrics by direct measurement of vapour temperatures in the centre core of heat pipe. A substantial reduction in thermal resistance of 76.2% is observed for 0.009 vol.% concentration of silver nanoparticles. Further an enhancement in the evaporation heat transfer coefficient of 52.7% is observed for the same concentration. The use of nanoparticles enhances the operating range of heat pipe by 21% compared with that of DI water.

1. Introduction

Heat pipes and their applications in thermal management have been studied for decades. They constitute an efficient compact tool to dissipate substantial amount of heat from various engineering systems including electronics cooling [1,2] like computers, laptop notebooks etc. In fact, virtually every notebook computer manufactured today uses at least one heat pipe assembly, typically designed to carry 30 W of power. The results of reports from various researchers [3] concludes that the conventional working fluids such as DI water, methanol etc. in heat pipes possess limited heat transport capabilities which arises due to working fluid transport properties. To overcome these limitations, the thermo physical properties of working fluid have to be improved. An innovative way to enhance liquid thermal conductivity is the dispersion of highly conductive solid nanoparticles within the base fluid. This new generation of conductive fluids with nanoparticles is referred to as nanofluid [4,5]. Taehyun Cho et al. [6] investigated thermal conductivity of fluids suspended with silver nanoparticles. The observation concludes an improvement in thermal conductivity by 10%, 16% and 18% for respective concentrations of 1000, 5000 and 10000 ppm.

Das et al. [7] investigated the increase in thermal conductivity with temperature and volume fraction for Al_2O_3 and CuO nanoparticles dispersed in water. The increase in effective thermal conductivity of nanofluids between 20 and 40 °C is found to be 15% for each type nanofluid. It was observed that in comparison with distilled water, the addition of nanoparticles gives a better enhancement with temperature for low volume fraction of particles. Terekhov et al. [8] reviewed experimental and theoretical results on heat transfer mechanism in nanofluids and concluded significant divergences in data of different researchers and possible reasons for this divergence. Lee et al. [9] used transient hot wire method to measure thermal conductivities of oxide nanofluids. The results shows that nanofluids have higher thermal conductivity than base fluid and the enhancement observed is 5%–60% increment in thermal conductivity for volume fraction ranging from 0.1% to 5%. Paisarn Naphon et al. [10] experimentally investigated titanium nanofluids on heat pipe thermal efficiency. The heat pipes with the de-ionic water, alcohol, and nanofluids (alcohol and nanoparticles) are tested. The titanium nanoparticles with diameter of 21 nm are used in the present study. Effects of percentage charge amount of working fluid, heat pipe tilt angle and percentage

* Corresponding author. Tel.: +91 422 2614430; fax: +91 422 2615615.
E-mail addresses: godson@karunya.edu, godasir@yahoo.co.in (L.G. Asirvatham), rajesh.mech335@gmail.com (R. Nimmagadda), somchai.won@kmutt.ac.th (S. Wongwises).

0017-9310/$ - see front matter © 2012 Elsevier Ltd. All rights reserved.
http://dx.doi.org/10.1016/j.ijheatmasstransfer.2012.11.037

Nomenclature

A	surface area (m^2)
C_p	specific heat (J/kg K)
d	outer diameter (m)
h	heat transfer coefficient (W/m^2 K)
K	thermal conductivity (W/m K)
L	length (m)
m	mass flow rate (kg/s)
Q	heat load (W)
q	heat flux (kW/m^2)
R	thermal resistance (°C/W)
ΔT	temperature difference (°C)
$\overline{T}$	average temperature (°C)
U	uncertainty

Subscript

A	adiabatic
C	condenser
CT	condenser temperature
CW	cooling water
c/s	cross-sectional
E	evaporator
EC	evaporator and condenser
ET	evaporator temperature
eff	effective
H.P	heat pipe
Inlet	inlet to condenser
nf	nanofluid
p	particle
Surf	surface
Vap	vapour
vs	vapour and surface
w	water

Greek Symbols

φ	volume fraction
ρ	density (kg/m^3)
μ	dynamic viscosity (kg/m-s)
Δ	increment

nanoparticles volume concentrations on the thermal efficiency of heat pipe are considered. For the heat pipe with 0.10% nanoparticles volume concentration, the thermal efficiency is 10.60% higher than that with the base fluid.

Riehl [11] has observed that a higher heat transfer coefficient can be seen when using nanoparticles in water under low heat input conditions. Tsaia et al. [12] investigated the influence of particle size on the heat pipe thermal performance. The study is based on the structural characteristics of gold nanoparticles of various sizes dispersed in aqueous solution on heat pipe thermal resistance. The thermal resistance of heat pipe ranges from 0.17 to 0.215 °C/W with different nanoparticle solutions. Furthermore, the thermal resistance of the heat pipes with nanoparticle solution is lower than that with DI water. Shafahi et al. [3] used a two-dimensional analysis to study the thermal performance of a cylindrical heat pipe using Al_2O_3, CuO, and TiO_2 nanoparticles suspended in water as the working fluid. The existence of optimum mass concentration to improve heat transfer performance is obtained as 5%, 15% and 7% for Al_2O_3, CuO, and TiO_2 respectively. It was found that smaller nanoparticles with particle diameter of 10 nm have a more pronounced effect on the temperature gradient along the heat pipe when compared to 40 nm. Kang et al. [13] used dilute dispersion of silver nano particles in pure water as working fluid in a circular heat pipe. The diameters of the nano particles used are 10 and 35 nm, respectively. The results showed that the nanofluid as working fluid in heat pipe can transport heat up to 70 W and is higher than pure water by about 20 W. Do et al. [14] investigated the effect of water-based Al_2O_3 nanofluids on the thermal performance of circular screen mesh wick heat pipes. The volume fraction of the nanoparticles used are 1 and 3 vol.%. It is found that the thermal resistance at the evaporator-adiabatic section decreases by 40% when using nanofluid with volume fraction of 3.0 vol.%. It is also shown that the use of water based Al_2O_3 nanofluids enhances the maximum heat transport rate of heat pipes. Do and Jang [15] evaluated the thermal performance of a heat pipe with rectangular grooved wick using water-based Al_2O_3 nanofluid. They found that the thin porous coating layer formed by nanoparticles is the key effect for higher heat transfer. The results showed the feasibility of enhancing the thermal performance up to 100% although water-based Al_2O_3 nanofluids with the concentration less than 1.0% is used as working fluid.

Yang et al. [16] carried out an experiment to study the heat transfer performance of a horizontal micro-grooved heat pipe using CuO–water nanofluids. Mass concentration of CuO nanoparticles ranging from 0.5 to 2.0 wt.% having the average diameter of 50 nm and the operating pressure varying from 7.45, 12.38 and 19.97 kPa, are respectively used. The experimental results showed that the CuO–water nanofluids can improve the thermal performance of the heat pipe at optimum mass concentration of 1 wt.%. Under an operating pressure of 7.45 kPa, the heat transfer coefficients of the evaporator can be averagely enhanced by 46% and the CHF (critical heat flux) can be maximally enhanced by 30% compared with those of the heat pipe using DI water. Guo-Shan Wang et al. [17] have carried out an experimental study on thermal performance of a cylindrical miniature grooved heat pipe using aqueous CuO nanofluids for two different operating conditions. One was the steady operating processes with constant cooling conditions and the other was the unsteady start up processes with constant cooling conditions. The start up characteristics of the heat pipe using nanofluids was especially compared with that of the heat pipe using water. The experimental results are useful for designing miniature grooved heat pipes using nano-fluids as the working liquid. It was found that the thermal performance of the heat pipe had a remarkable increase by adding CuO nanoparticles into the base liquid. For unsteady start-up process, substituting the nanofluid for water as the working fluid, cannot only improve the thermal performance, but also reduce significantly the start-up time. The total heat resistance was reduced by 50% and heat removal capacity increases by 40% for nanofluid based heat pipe when compared with that of heat pipe using water. Park et al. [18] and Shung-Wen Kang et al. [19] also observed in another study that silver nanofluid grooved heat pipe thermal performance was higher than that for a conventional grooved heat pipe with water as working fluid.

It is found from the above mentioned literature [10,12,13] that all the researchers have observed an enhancement in the thermal performance of heat pipes using nanofluids. It is also observed that most of the previous investigations have been performed with high concentrations of metal oxide nanoparticles [3,14–16]; and very little amount of work has been carried out with the use of pure metal nanoparticles in predicting the thermal performance of heat pipes. It is also reported that use of high concentration

nanoparticles will block the wick due to the deposited nanoparticles and causes more resistance on the returning fluid to reach from condenser to evaporator. This eventually results in early evaporator dry out and causes heat pipe failure. Moreover, the earlier experiments have been performed by measuring only the wall temperature to evaluate the heat transfer performance of heat pipes. Interestingly, it is observed from the present study that there exist 5.8 °C difference between the wall and vapour temperatures measured at the core of the evaporator. Hence, there is a need to analyze the performance of heat pipes by considering the effect of the temperature difference between the wall and the vapour core which have never before appeared in the open literature. Therefore, the present study aims to experimentally analyze the thermal performance of heat pipe using low volume concentration (0.003%, 0.006% and 0.009%) of pure metal (silver) nanoparticles by measuring both the vapour and wall temperatures at the same time in all the three regions. The effect of heat load on the quantities such as thermal resistance, axial temperature distribution, evaporation, condensation heat transfer coefficients, effective thermal conductivity etc. are experimentally analyzed on the basis of vapour core and wall temperatures are discussed and presented.

2. Experimentation

2.1. Experimental setup

The schematic layout of test facility to measure the effect of nanoparticle concentration on the performance of heat pipe is shown in Fig. 1. The test section is made up of copper with outer diameter and length as 10 and 180 mm, respectively. The wall thickness, lengths of evaporator section, adiabatic section and condenser section of the heat pipes are 0.5, 50, 50 and 80 mm, respectively. Two layers of copper wick with a wire diameter of 0.105 mm and mesh number 100/inch is wrapped inside the heat pipe. 30% of the total volume of the heat pipe is charged with working fluid to completely saturate the wick. The condenser section of the het pipe was inserted horizontally into a cooling chamber made up of acrylic material. The test set up also consists of a pump and flow meter (with an uncertainty of ±10 ml) to circulate cooling water at a constant flow rate of 260 ml per minute through the condenser section. A constant temperature chilled water bath is used to maintain the inlet temperature of the circulating cooling water at 24 °C for all the test sections at various heat loads to obtain performance accuracy. The temperatures of the cooling water circulating through the condenser section are recorded by using two T-type thermocouples fixed at inlet and outlet of the condenser. A total of eight thermo couple sensors with T-type thermocouples of uncertainty ±0.5 °C are fixed along the test section include two in evaporator, three in adiabatic and three in condenser section, respectively. These sensors will directly measure the vapour temperature which is passing through the centre core of the heat pipe from evaporator section to condenser section. The evaporator and condenser surface temperatures are measured by fixing four T-type thermocouples two on each section.

The heat input to the heat pipe is applied using a digital wattmeter (with an uncertainty of ±0.5 W) connected to an electric heater wounded on the evaporator section. A 220 V A.C supply is used to energize the heater. The evaporator and adiabatic sections of the heat pipe are completely insulated using glass wool to minimize the heat loss. The temperature readings of the test section are recorded by connecting thermo couples to data logger [Model-(DA 100-13-1F), Yokogawa-N 200]. The entire data acquisition system is monitored and controlled by using a P.C.

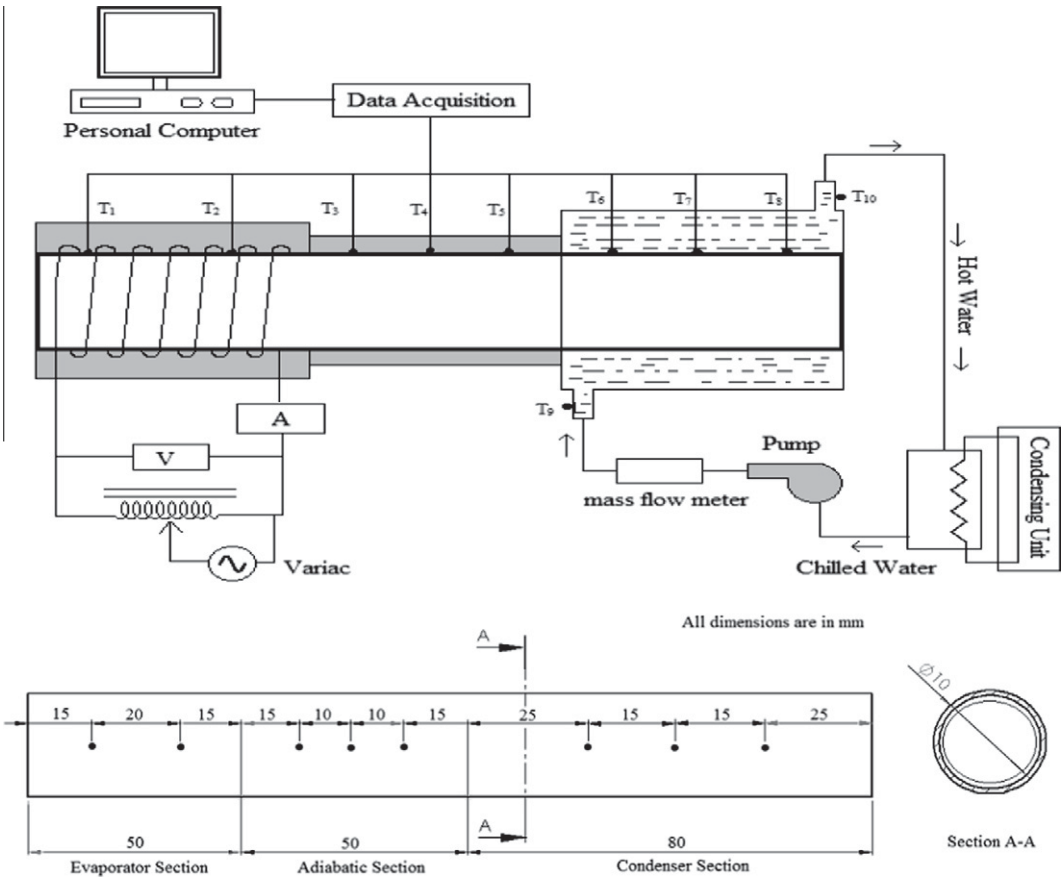

Fig. 1. Schematic diagram of the experimental apparatus.

2.2. Experimental procedure

2.2.1. Nanofluid preparation

The nanoparticles used in the present study is silver (manufactured by Sigma Aldrich; The Product Number - 576832, Silver nano-powder, <100 nm, 99.5% metals). A two step method is used to prepare silver–water nanofluid. The nanoparticles are mixed directly with De-ionized water without addition of any surfactant. The nanofluids are sonicated well for about 1 h in an ultra sonicator at sound frequencies of 50–60 kHz to ensure uniform and stable dispersion of nanoparticles in base fluid. The silver nanoparticles are further characterized by using scanning electron microscope (SEM) and particle size analyzer to study the size distribution and morphology. Fig. 2 shows the SEM image of 0.009 vol.% concentration of silver nanoparticles taken at 45,000X magnification. The size of the nanoparticles is marked in the SEM image. It is found that the size of the silver nanoparticles vary from 51 nm to 67 nm in some places. It is clearly seen that the nanoparticles are well dispersed with certain level of agglomeration. It is also observed that the size of the agglomerated nanoparticles exceed 100 nm in some places. Hence, the agglomerated nanoparticles are finely grinded in a ball grinder before adding to base fluid for sonication. Similarly, the size of the silver nanoparticles is measured using the particle size analyzer and shown in Fig. 3. It is clearly observed from the figure that the majority of the nanoparticles have the average size of 110–120 nm with an intensity of 13% and it is also seen from the peak that 10% of the nanoparticles have the size varying between 40 and 60 nm with 1.5% intensity. This justifies the average size of the silver nanoparticles used for the present study.

2.2.2. Experimental test

The experiments are conducted using four identical heat pipes in horizontal orientation which are fabricated as per mentioned dimensions. One of the heat pipes is filled with De-ionized water and remaining three heat pipes are filled with three different concentrations of silver–water nanofluid. The tests on all the four heat pipes are conducted under identical operating conditions such as constant flow rate and inlet temperature of the cooling water circulating through the condenser section. The power supply was turned on and the heater was energized with a heat load of 20 W. The steady state vapour temperature reading as well as surface temperature reading is recorded using data acquisition system. The input heat load is incremented gradually in equal steps from 20 W to beyond 100 W until dry out condition is reached.

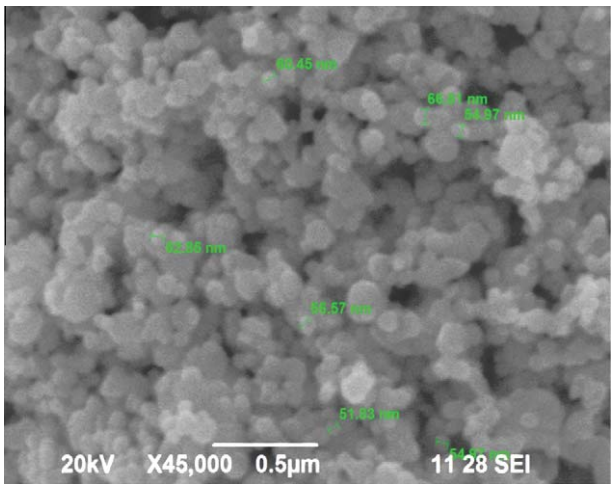

Fig. 2. SEM image of 0.009 vol.% concentration of silver nanoparticles.

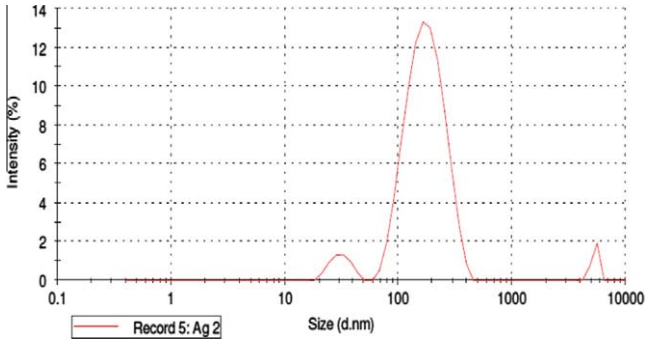

Fig. 3. Size distribution by intensity of the silver nanoparticles.

The heat input at which dry out condition is observed is assumed as maximum heat transport capability of heat pipe. At this condition the vapour temperature difference between evaporator and condenser abruptly increases.

2.3. Thermo physical properties of nanofluid

The thermo-physical properties of silver water nanofluid are calculated as follows.

The density is calculated from Pak and Cho [21] using the following equation:

$$\rho_{nf} = \varphi\rho_p + (1-\varphi)\rho_w \tag{1}$$

The specific heat is calculated from Xuan and Roetzel [22] as follows:

$$(\rho C_p)_{nf} = \varphi(\rho C_p)_p + (1-\varphi)(\rho C_p)_w \tag{2}$$

where $(\rho C_p)_{nf}$ is the heat capacity of the nanofluid, $(\rho C_p)_p$ is the heat capacity of the nanoparticles and $(\rho C_p)_w$ is the heat capacity of the base fluid.

The other properties such as viscosity and thermal conductivity are measured using the following equations proposed by the present authors. The detailed measurement techniques and procedure are given elsewhere [23] in a published literature for reference

$$\frac{\mu_{nf}}{\mu_w} = (1.005 + 0.497\varphi - 0.1149\varphi^2) \tag{3}$$

$$\frac{K_{nf}}{K_W} = (0.9692\varphi + 0.9508) \tag{4}$$

2.4. Data reduction

$$R_{H,P} = \frac{\overline{T}_{E,Vap} - \overline{T}_{C,Vap}}{Q} \tag{5}$$

The thermal resistance of heat pipe ($R_{H,P}$) is defined as the ratio of vapour temperature difference measured between evaporator and condenser ($\overline{T}_{E,Vap} - \overline{T}_{C,Vap}$) to the applied heat load (Q)

$$h_C = \frac{Q}{A_C \Delta T_C} \quad \text{where } A_C = \pi d_C L_C, \quad \Delta T_C = \overline{T}_{C,Vap} - \overline{T}_{C,Surf} \tag{6}$$

The condenser heat transfer coefficient (h_C) is defined as the ratio of heat load (Q) to the product of condenser surface area (A_C) and the temperature difference (ΔT_C) between vapour ($\overline{T}_{C,Vap}$) and surface ($\overline{T}_{C,Surf}$) in the condenser region. In the condenser region the vapour temperature ($\overline{T}_{C,Vap}$) is higher than the surface temperature ($\overline{T}_{C,Surf}$) due to heat rejection

$$h_E = \frac{Q}{A_E \Delta T_E} \quad \text{where } A_E = \pi d_E L_E, \quad \Delta T_E = \overline{T}_{E,Surf} - \overline{T}_{E,Vap} \tag{7}$$

The evaporator heat transfer coefficient (h_E) is defined as the ratio of applied heat load (Q) to the product of evaporator surface area (A_E) and the temperature difference (ΔT_E) between surface ($\overline{T}_{E,Surf}$) and vapour ($\overline{T}_{E,Vap}$) in the evaporator region. In the evaporator region the surface temperature ($\overline{T}_{E,Surf}$) is higher than the vapour temperature ($\overline{T}_{E,Vap}$) due to heat addition

$$K_{eff} = \frac{1}{A_{c/s,H,P} R_{H,P}} \quad \text{where } A_{c/s,H,P} = \frac{\pi}{4} d^2 \tag{8}$$

The effective thermal conductivity of heat pipe is defined as the inverse of product of cross sectional area of the heat pipe ($A_{c/s,H,P}$) and the thermal resistance of heat pipe ($R_{H,P}$).

2.4.1. Uncertainty analysis of measured parameters

$$\frac{\Delta Q}{Q} = \left[\left(\frac{\Delta V}{V}\right)^2 + \left(\frac{\Delta I}{I}\right)^2 + \left(\frac{\Delta L_E}{L_E}\right)^2 + \left(\frac{\Delta d_E}{d_E}\right)^2 \right]^{1/2} \tag{9}$$

Uncertainty in heat flux is calculated using Eq. (9). It is calculated based on the uncertainties in the applied voltage (ΔV), applied current (ΔI) to the heater coil. It also includes the uncertainties in the measured length (ΔL_E) and diameter (Δd_E) of the evaporator region over which heater coil is wrapped. The least count of the vernier calipers used to measure this length and diameter is taken as the uncertainty value

$$\frac{\Delta R}{R} = \left[\left(\frac{\Delta Q}{Q}\right)^2 + \left(\frac{\Delta(\Delta T)}{\Delta T_{EC}}\right)^2 \right]^{1/2} \tag{10}$$

Uncertainty in calculated thermal resistance is done using the Eq. (10). It depends on uncertainty in heat applied (ΔQ) and uncertainty in the measured temperature difference between evaporator and condenser ($\Delta(\Delta T)$). The actual temperature difference measured is found to be (ΔT_{EC})

$$\frac{\Delta h}{h} = \left[\left(\frac{UQ}{Q}\right)^2 + \left(\frac{U\Delta T}{\Delta T_{VS}}\right)^2 \right]^{1/2} \tag{11}$$

Uncertainty in the calculated heat transfer coefficient is made using Eq. (11). The calculation is done by taking into consideration all the uncertainties in the parameters on which heat transfer coefficient depends. The various uncertainties on which this heat transfer coefficient depends are uncertainty in the applied heat load (UQ) and uncertainty in the measured temperature difference between surface and vapour ($U\Delta T$). All these calculations are done to eliminate the experimental errors and the obtained results are taken from a standardized experimental test facility. The maximum uncertainties in thermal resistance and heat transfer coefficient are found to be 5.57% and 6.64%.

3. Results and discussion

The experiments are conducted for various heat loads (20, 40, 60, 80, 100 W) with heat pipes kept in horizontal position. The vapour temperatures as well as the surface temperature readings are recorded using thermocouples connected to a data acquisition system. The experimental results are compared between base fluid and nanofluid for all the concentrations and the enhancement in heat transfer performance with respect to concentration, heat load, thermo physical properties etc. are discussed in the following sub sections. Many day-to-day experiments have been conducted with the base fluid to check the repeatability in the experimental readings and found that the deviation between day1 and day2 reading is found to be less than 1.4%. The operating conditions of all the heat pipes such as evaporator heat load, cooling water inlet temperature and circulation rate are maintained constant for effective comparison of the results. Table 1 gives the experimental conditions chosen for the present study.

Table 1
Experimental conditions.

Working fluid charged (ml)	Q (W)	m_{CW} (kg/s)	$T_{CW,Inlet}$ (°C)
3.5	20	4.3333×10^{-3}	24
	40	4.3333×10^{-3}	24
	60	4.3333×10^{-3}	24
	80	4.3333×10^{-3}	24
	100	4.3333×10^{-3}	24

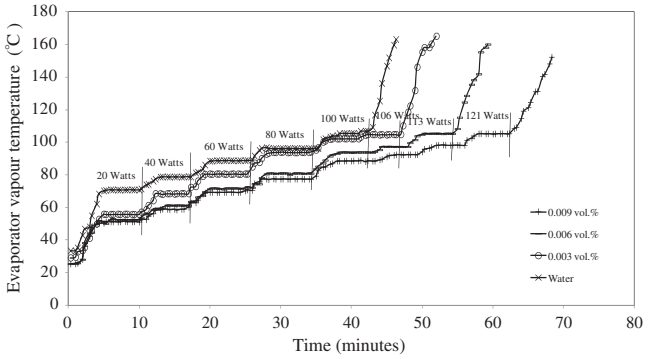

Fig. 4. Vapour temperature in the evaporator with respect to time in minutes.

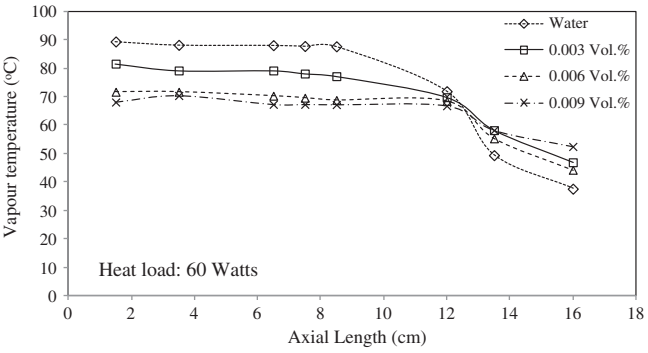

Fig. 5. Vapour temperature distribution with respect to axial length.

The vapour temperature in the evaporator section as a function of time for various heat loads and concentrations are shown in Fig. 4. It is observed that the steady state has been attained approximately after 15–20 min. The steady state temperature reading is taken for the analysis and data reduction. The dry out condition is observed beyond 100 W for heat pipes with DI water as working fluid. The vapour temperature reading decreases with the increase in concentration of nanofluid. This drop in temperature increases the operating range of heat pipe beyond 100 W, with nanofluid. It is also seen that for 0.003 and 0.006 vol.%, dry out is observed near 106 and 113 W. Whereas for heat pipe with 0.009 vol.% the dry out appears beyond 121 W. This shows that an increment of 21% in heat transfer capability is observed by using nanofluid as working fluid in heat pipe. The vapour temperature distribution along the axial length of the heat pipe for heat load of 60 W is shown in Fig. 5. It is clearly seen that a reduction in vapour temperature is observed by using nanofluids due to high thermal

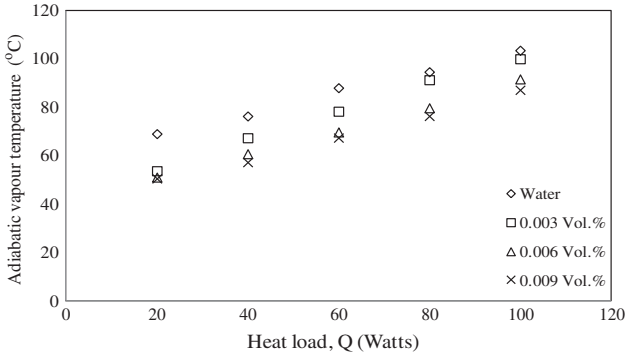

Fig. 6. Variation in adiabatic vapour temperature as a function of heat load.

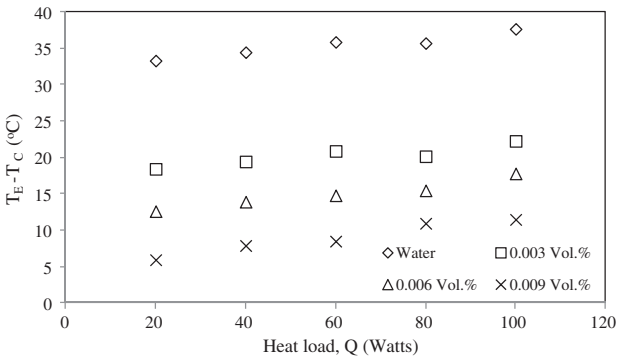

Fig. 8. Evaporator and condenser vapour temperature difference as a function of heat load.

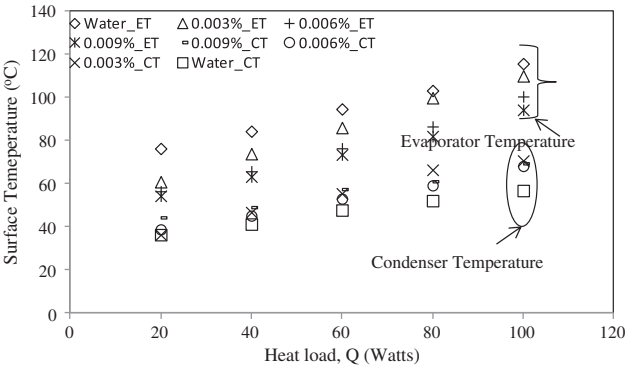

Fig. 7. Evaporator and condenser surface temperature as a function of heat load.

conductivity of silver nanoparticles. This reduces the vapour temperature inside the heat pipe. 19.5 °C temperature difference is observed in the evaporator for maximum concentration of the heat pipe when compared with DI water. Subsequent slight drop in vapour temperature is also observed in condenser section for a constant cooling water flow rate at constant inlet temperature. A slight drop of 1–2 °C is observed between evaporator and adiabatic chamber due to losses. The low vapour temperature for constant heat input indicates that an increment in the operating range of the heat load when compared with that of base fluid heat load.

The adiabatic vapour temperature as a function of heat load is shown in Fig. 6. It is observed from the figure that the adiabatic vapour temperature which is also called as operating temperature of heat pipe increases as heat load on the evaporator section increases and decreases as volume concentration of nanoparticles in base fluid increases. The reduction in this temperature indicates an effective heat transfer capability due to addition of additives in base fluid. 21.54% reduction is observed in case of heat pipe operating with 0.009 vol.% concentration. This increases the operating range of the heat pipe beyond 100 W which is the maximum heat load in the case of water based heat pipe. Similarly a reduction of 9.49% and 18.25% is observed respectively for 0.003 and 0.006 vol.% concentration when compared to heat pipe operating with water. The surface temperatures of evaporator and condenser with respect to various heat loads are shown in Fig. 7. The evaporator surface temperature increases with increment in heat load and decreases with increment in volume concentration of nanoparticles. This reduction in surface temperature enhances and aids faster cooling rate of the heat dissipating components. It is found that for the maximum volume concentration of 0.009%, the decrement in the evaporator surface temperature is 21 °C for input heat load of 60 W. Similarly the evaporator surface temperatures of heat pipes with volume concentration of 0.003% and 0.006% is reduced by 8.6 and 18.2 °C when compared to heat pipe with DI water. The lowering of the evaporator surface temperature with the increase in the volume concentration of nanoparticles permits the heat pipe with additional heat flow rate before reaching dry out condition. It is also found that the increase in volume concentration of nanoparticles in base fluid increases the condenser surface temperature due to effective heat rejection in condenser section.

The temperature difference between evaporator and condenser as a function of heat load is shown in Fig. 8. It is observed that the temperature difference between evaporator and condenser gradually decreases with respect to the increase in the concentration level of nano particles for a given heat load. It is found that for a constant temperature difference between evaporator and condenser the use of nanofluid allows the heat pipe to operate under larger heat loads. It is also seen that the temperature difference reduces by 72.57%, 56.39% and 42% respectively for 0.009, 0.006 and 0.003 vol.% of silver water nanofluid when compared to heat pipe operating with DI water. This reduction in temperature difference enhances an increment in heat transport capability of heat pipe. The reason for this is that the nanoparticles suspended in water forms a porous coating in the evaporator region. This increases the surface roughness and cause enhancement in the bubble formation, growth and collapse. The porous coating formed on the screen mesh wick eventually increases the evaporator heating surface and leads to high heat transfer. It also increases the pumping capability of the wick. Researchers like Kim et al. [24] and Yang et al. [16] indicated that the formation of coating layer by nanoparticles reduces the contact angle and increases the surface wettability and surface roughness. It is observed that the porous coating layer formed on the wick surface reduces the evaporator vapour temperature by increasing the evaporator heating surface. It also increases the wick capillary pumping ability and eventually induces liquid suction due to capillary wicking into the evaporator region, which enhances the maximum heat transport rate This eventually reduces the vapour temperature difference between evaporator and condenser.

The thermal resistances of the heat pipes are calculated based on the vapour temperatures to quantitatively evaluate the thermal performance of heat pipes using silver–water nanofluids. As shown in Fig. 9 the thermal resistances of heat pipes using both the base fluid and nanofluids are high at low heat loads as thick liquid film resides in the evaporator section. However the thermal resistance decreases rapidly as heat load increases. This reduction in thermal resistance of heat pipes using silver–water nanofluid is more when compared with that of the heat pipe operating with DI water. 40% reduction in thermal resistance is observed for 0.003 vol.% silver nanofluid when compared with that of DI water. It is also observed

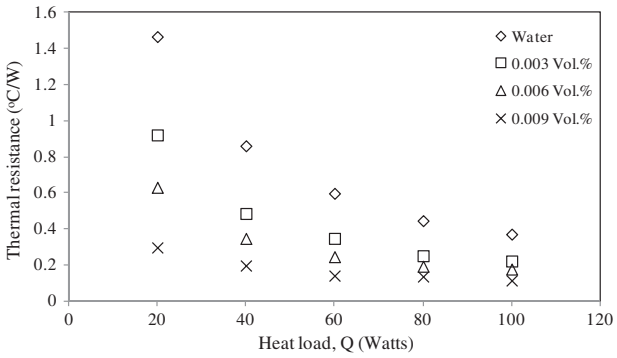

Fig. 9. Variation in thermal resistance as a function of heat load.

that this reduction in thermal resistance gradually increases as concentration of nanoparticles in base fluid increases. However for the maximum concentration of 0.009 vol.% of silver nanofluid, 76% reduction in thermal resistance is observed when compared with DI water. The thin porous coating layer formed by nanoparticles, not only improve the maximum heat transport rate but also significantly reduce the thermal resistance of the heat pipe using nanofluids is considered to be the main reason for the decrease in the thermal resistance of the heat pipe. Similar results have also been observed by Do et al. [14].

In order to check formation of the porous coating layer by addition of silver nanoparticles in the screen mesh wick surface of the evaporator region, a SEM image has been taken with the plain wick and the one with the addition of nanoparticles after conducting the experiments. The Fig. 10(a), shows the SEM image of the plain screen mesh wick surface without adding the nanoparticles. It is observed from the figure that the walls of the wick surface are found to be smooth and does have any pores or coating. However, the Fig. 10(b) shows the SEM image of the screen mesh wick surface with 0.009 vol.% of silver–water nanofluids. It clearly seen from the figure that there exists the porous coating layer which is formed by silver nanoparticles on the wick surface. This observation shows evidence for the formation of the thin porous coating layer at screen mesh wick of the evaporation region. The coating layer on the mesh wick surface provides an additional evaporating surface where high heat transfer rates occur. This drastically reduces the thermal resistance of the mesh wicked heat pipe and increases the capillary pumping ability to pull the liquid to the mesh wick surface. This leads to the enhancement in the heat transport rate of the of the heat pipe when using the silver–water nanofluid. The effective thermal conductivity of heat pipes with respect to various heat loads is shown in Fig. 11. It is clearly seen that the effective thermal conductivity of heat pipe increases with respect to heat load and concentration. The enhancement observed is 73.5% for 0.009 vol.% concentration of silver–water nanofluid. This concludes effective heat transfer is possible through the heat pipes employed with nanofluids. Similarly the heat pipes operating with 0.003 and 0.006 vol.% gives 42.4% and 56.8% increment in conductivity when compared with water based heat pipe.

The evaporation heat transfer coefficient as a function of heat flux is shown in Fig. 12. It is found that the evaporation heat transfer coefficients of heat pipe with silver–water nanofluid is higher when compared with that of the heat pipe with DI water for the same heat flux. The increment in nanoparticles volume concentration in base

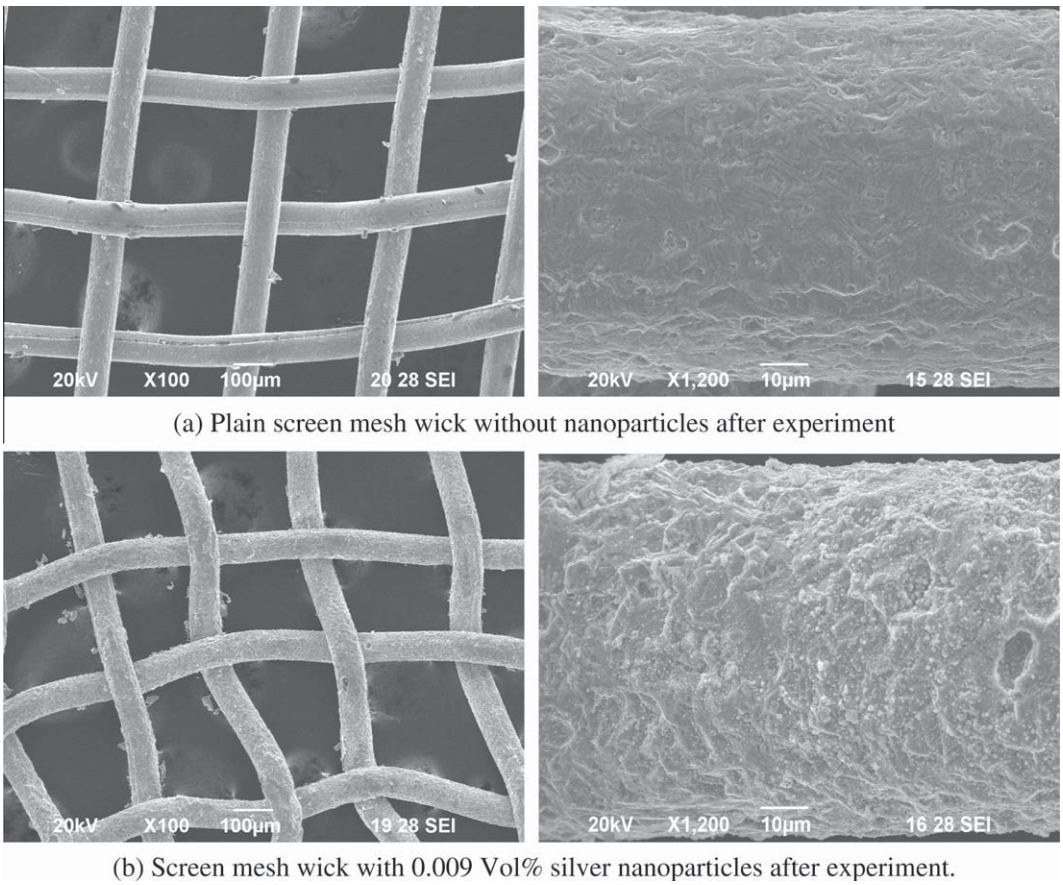

Fig. 10. SEM image of the screen mesh wick surface (a) plain screen mesh wick without nanoparticles after experiment; (b) Screen mesh wick with 0.009 vol.% silver nanoparticles after experiment.

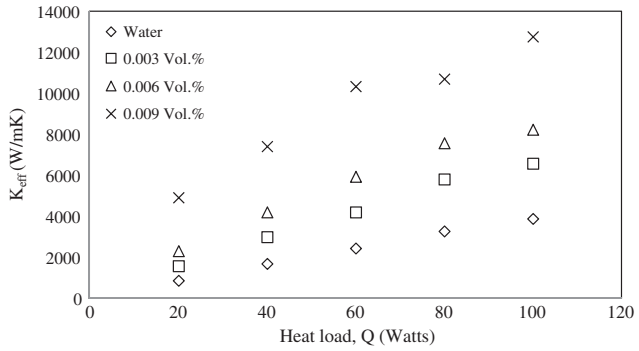

Fig. 11. Effective thermal conductivity of heat pipe as a function of heat load.

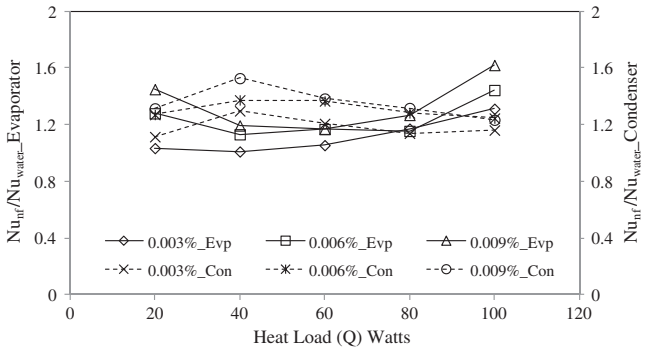

Fig. 13. Nusselt number ratio of evaporator and condenser as a function of heat load.

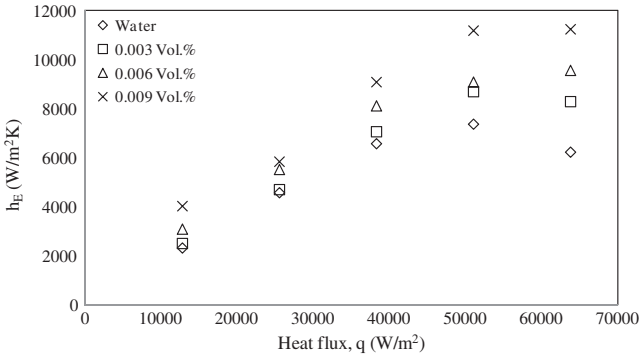

Fig. 12. Evaporation heat transfer coefficient with respect to the heat flux.

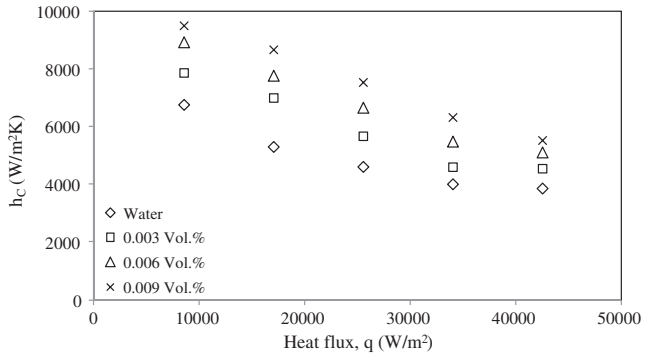

Fig. 14. Condensation heat transfer coefficient with respect to the heat flux.

fluid increases the evaporation heat transfer coefficient. For 0.009 vol.%, concentration an increment of 52.7% in evaporation heat transfer coefficient is observed experimentally when compared to heat pipe with DI water. It is mainly due to less temperature difference between the evaporator surface and vapour core. This concludes that the effective heat transfer is possible through heat pipes employed with nanofluids as working fluid. It is also found and clearly observed from Fig. 12 that the evaporation heat transfer coefficient of DI water based heat pipe decreases as the heat flux increases beyond 50 kW/m^2 due to reaching out of partial dry out condition. The reason for this is that the evaporator region is completely filled with vapour, since the optimum heat transport capacity of heat pipe is reached near 100 W; the heat pipe tends to move closer to the dry-out condition. Due to this partial dry out condition the temperature difference between evaporator surface and vapour increases and tends the heat transfer coefficient to decrease. However, for heat pipes with silver water nanofluid, the evaporation heat transfer coefficient still increases beyond the heat flux of 50 kW/m^2 because of higher heat transport capability employed with the presence of nanoparticles. From the observed results it is significantly seen that the presence of nanoparticles decreases the wall and the vapour temperatures which in turn increases the operating range of the pipe to higher heat flux when compared with that of the DI water.

The Nusselt number ratio of evaporator and condenser drawn respectively in the primary and secondary axis against heat load is shown in Fig. 13. It is observed that the Nusselt number ratio of both evaporator and condenser increases with the increase in the volume concentration of silver nanoparticles. At higher heat load the Nusselt number ratio for evaporator is found to be higher when compared with that of condenser Nusselt number ratio. As Nusselt number is a dimensionless parameter which depends on heat transfer coefficient, thermal conductivity of working fluid and characteristic length. It is found that at low heat load say for example (40 W) the Nusselt number ratio of condenser is more when compared with that of the evaporator. The reason is that the temperature difference (ΔT) between the wall surface and vapour core in the evaporator is high at low heat load and the temperature difference between the vapour core and the wall surface is less in the condenser section. This increases the heat transfer coefficient in the condenser which is directly proportional to the Nusselt number ratio at low heat loads and the inverse effect is found in the case of evaporator.

The condensation heat transfer coefficient as a function of heat flux is shown in Fig. 14. It is found that at low heat flux say for example (12 kW/m^2) the condensation heat transfer coefficient is more when compared with that of the evaporation heat transfer coefficient. The reason is that the temperature difference (ΔT) between the wall surface and vapour core in the evaporator is high at low heat flux and the temperature difference between the vapour core and the wall surface is less in the condenser section. Also the surface area of the condenser is more than the evaporator; since the length is 1.5 times the length of the evaporator section. As the heat flux increases the (ΔT) in evaporator decreases due to the formation of large number of small nucleation sites by the nanoparticle layer deposited on the heating surface. This eventually increases the evaporation heat transfer coefficient. However in condenser the (ΔT) increases with respect to heat flux, which results in a decrement in the condensation heat transfer coefficient. A similar trend of results has also been observed and reported in the published literature by Liu et al. [20]. Meantime, on an average the enhancement of the condensation heat transfer coefficient is also quite similar to that of the evaporation heat transfer coefficient for the same nanofluid. On the other hand, the condensation heat transfer coefficient curves has the similar trend for both water

and nanofluids at the present operating pressure, that describes actually a heat transfer characteristic of the convective condensation. The mode of heat transfer in evaporator and condenser is convective. The main reasons for the enhancement of heat transfer effect of nanofluid based heat pipes are:

1. The highly conductive nanoparticles in base fluid will increase the effective thermal conductivity of nanofluid.
2. During heat pipe operation, the working fluid travels through the porous wick and the nanoparticles present in it forms a coating layer on the wick and on the heating surface. This enhances the heat transfer effect of heat pipe.
3. The random motion (Brownian motion) of nanoparticles in base fluid causes the particles to collide with each other and with particles of DI water. This will enhance the heat transfer effect by convection. This Brownian motion is significant at higher temperatures.

4. Conclusion

The heat transfer performance of heat pipe using silver–water nanofluid with volume concentrations of 0.003%, 0.006% and 0.009% is experimentally investigated. It is clearly seen that by using silver–water nanofluid, the operating range of heat pipe increases beyond 100 W which is the maximum heat transport range for DI water based heat pipe. The dry out condition is observed near 106, 113 and 121 W respectively for 0.003, 0.006 and 0.009 vol.% concentrations. It is also observed that the thermal resistance of heat pipe decreases with the use of silver–water nanofluid, which in turn increases the effective thermal conductivity by 42.4%, 56.8% and 73.5% respectively for 0.003, 0.006, 0.009 vol.% concentrations. It is also observed that the evaporation and condensation heat transfer coefficients increases with the increases in the concentration of silver nanoparticles. Similarly, the difference between evaporator wall temperature and vapour temperature near a heat load of 60 W is observed to be 5.8, 5.4, 4.7 and 4.2 °C respectively for DI water, 0.003, 0.006 and 0.009 vol.% concentrations of the silver nanoparticles indicating the improved performance of heat pipes.

Acknowledgements

The authors would like to thank Mr. Seelan, Mr. P. Augustine and Mr. Jeyakumar of Karunya University for helping in the fabrication of the experimental test facility. The third author would like to thank the Thailand Research Fund for the supporting.

References

[1] Mariya Ivanova, Yvan Avenas, Christian Schaeffer, Jean-Bernard Dezord, Juergen Schulz-Harder, Heat pipe integrated in direct bonded copper (DBC) technology for cooling of power electronics packaging, IEEE Trans. Power Electron. 21 (6) (2006) 1541–1547.

[2] R. Sonan, S. Harmand, J. Pelle, D. Leger, M. Fakès, Transient thermal and hydrodynamic model of flat heat pipe for the cooling of electronics components, Int. J. Heat Mass Transfer 51 (25–26) (2008) 6006–6017.

[3] Maryam Shafai, Vincenzo Bianco, Kambiz Vafai, Oronzio Manca, An investigation of the thermal performance of cylindrical heat pipes using nanofluids, Int. J. Heat Mass Transfer 53 (2010) 376–383.

[4] S.U.S. Choi, Enhancing thermal conductivity of fluids with nanoparticles, ASME FED 231 (1995) 99–105.

[5] S. Kakac, A. Pramuanjaroenkij, Review of convective heat transfer enhancement with nanofluids, Int. J. Heat Mass Transfer 52 (2009) 3187–3196.

[6] Taehyun cho, Ilhyun Baek, Jonghee Lee, Sangdo Park, Preparation of nanofluids containing suspended silver particles for enhancing fluid thermal conductivity of fluids, J. Ind. Eng. Chem. 11 (3) (2005) 400–406.

[7] S.K. Das, N. Putra, P. Thiesen, W. Roetzel, Temperature dependence of thermal conductivity enhancement for nanofluids, J. Heat Transfer 125 (2003) 567–574.

[8] V.I. Terekhov, S.V. Kalinina, V.V. Lemanov, The mechanism of heat transfer in nanofluids, state of the art (review). Part 1. Synthesis and properties of nanofluids, Thermophys. Aeromech. 17 (1) (2010).

[9] S. Lee, S.U.S. Choi, S. Li, J.A. Eastman, Measuring thermal conductivity of fluids containing oxide nanoparticles, J. Heat Transfer 121 (1999) 280–289.

[10] Paisarn Naphon, Pichai Assadamongkol, Teerapong Borirak, Experimental investigation of titanium nanofluids on the heat pipe thermal efficiency, Int. Commun. Heat Mass Transfer 35 (10) (2008) 1316–1319.

[11] R.R. Riehl, Analysis of loop heat pipe behavior using nanofluid, in: Heat Powered Cycles International Conference (HPC), New Castle, UK, 2006, Paper: 06102.

[12] C.Y. Tsaia, H.T. Chiena, P.P. Dingb, B. Chanc, T.Y. Luhd, P.H. Chena, Effect of structural character of gold nanoparticles in nanofluid on heat pipe thermal performance, Mater. Lett. 58 (2004) 1461–1465, http://dx.doi.org/10.1016/j.matlet.2003.10.009.

[13] S. Kang, W. Wei, S. Tsai, C. Huang, Experimental investigation of nanofluids on sintered heat pipe thermal performance, Appl. Therm. Eng. 29 (5–6) (2009) 973–979.

[14] K. Do, H. Ha, S. Jang, Thermal resistance of screen mesh wick heat pipes using the water-based Al_2O_3 nanofluids, Int. J. Heat Mass Transfer 53 (25–26) (2010) 5888–5894.

[15] K.H. Do, S.P. Jang, Effect of nanofluids on the thermal performance of a flat micro heat pipe with a rectangular grooved wick, Int. J. Heat Mass Transfer 53 (9–10) (2010) 2183–2192.

[16] X.F. Yang, Z. Liu, J. Zhao, Heat transfer performance of a horizontal micro grooved heat pipe using CuO nanofluid, J. Micromech. Microeng. 18 (3) (2008) 035038.

[17] Guo-Shan Wang, Bin Song, Zhen-Hua Liu, Operation characteristics of cylindrical miniature grooved heat pipe using aqueous CuO nanofluids, Exp. Therm. Fluid Sci. 34 (8) (2010) 1415–1421.

[18] K.H. Park, W.H. Lee, K.W. Lee, I.H. Baek, S.H. Rhi, D.R. Shin, Study on the operating characteristics in small size heat pipe using nanofluids, in: Proceedings of the Third IASME/WSEAS International Conference on Heat Transfer, Thermal Engineering and Environment, Corfu Greece, August 20–25 (2005) pp. 106–109.

[19] Shung-Wen Kang, Wei-Chiang Wei, Sheng-Hong Tsai, Shih-Yu Yang, Experimental investigation of silver nanofluid on heat pipe thermal performance, Appl. Therm. Eng. 26 (17–18) (2006) 2377–2382.

[20] Zhen-Hua Liu, Yuan-Yang Li, Ran Bao, Compositive effect of nanoparticle parameter on thermal performance of cylindrical micro-grooved heat pipe using nanofluids, Int. J. Therm. Sci. 50 (2011) 558–568.

[21] Bock Choon Pak, I. Young Cho, Hydrodynamic and heat transfer study of dispersed fluids with sub-micron metallic oxide particles, Exp. Heat Transfer 11 (2) (1998) 151–170.

[22] Yimin Xuan, Wilfried Roetzel, Conceptions for heat transfer correlation of nanofluids, Int. J. Heat Mass Transfer 43 (19) (2000) 3701–3707.

[23] L. Godson, B. Raja, D. Mohan lal, S. Wongwises, Experimental investigation of thermal conductivity and viscosity of silver-deionized water nanofluid, Exp. Heat Transfer 23 (4) (2010) 317–332.

[24] H.D. Kim, J. Kim, M.H. Kim, Experimental studies on CHF characteristics of nanofluids at pool boiling, Int. J. Multiphase Flow 33 (2007) 691–706.

JOURNAL OF THERMOPHYSICS AND HEAT TRANSFER
Vol. 27, No. 1, January–March 2013

Entropy Generation Between Two Rotating Cylinders with Magnetohydrodynamic Flow Using Nanofluids

Omid Mahian*
Islamic Azad University, 91735 Mashhad, Iran
Shohel Mahmud†
University of Guelph, Guelph, Ontario N1G 2W1, Canada
and
Somchai Wongwises‡
King Mongkut's University of Technology Thonburi, Bangmod, Bangkok 10140, Thailand

DOI: 10.2514/1.T3908

The flow between two cylinders where one or both of the cylinders rotate has many practical applications such as swirl nozzles, rotating electrical machines, rotating disks, standard commercial rhymesters, and chemical and mechanical mixing equipment. In this paper, the effect of using TiO_2-water nanofluid ($\phi \leq 2\%$) on entropy generation between two corotating cylinders in the presence of magnetohydrodynamic flow is investigated. An analytical approach is applied to solve the simplified governing equations in the cylindrical coordinate system. To calculate the thermal conductivity and viscosity of the nanofluid, two correlations, which are based on the experimental data, are used. The velocity field is obtained as modified Bessel functions, and then, using the expansions of these Bessel functions with three terms, the temperature field and, subsequently, the entropy generation rate are estimated. The results are presented for various parameters, including the entropy generation number (N_S), Bejan number (Be), Hartmann number (M), Brinkman number (Br), and a group parameter ($\frac{\Omega}{Br}$). From the results, it is concluded that, at low Brinkman numbers (depending on the value of $\frac{\Omega}{Br_f}$), the average entropy generation number $(N_S)_{ave}$ decreases with the increase in nanoparticle volume fraction.

Nomenclature

Be	=	Bejan number
Br	=	Brinkman number
B_0	=	constant magnetic flux density
C_p	=	specific heat
E	=	electric field
Ec	=	Eckert number
J	=	electric current
k	=	thermal conductivity
M	=	Hartmann number
N_F	=	entropy generation number, fluid friction
N_H	=	entropy generation number, heat transfer
N_m	=	entropy generation number, magnetohydrodynamic flow
N_S	=	entropy generation number, total
$N_{S,a}$	=	augmentation entropy generation number
Pr	=	Prandtl number
Q	=	electric charge density
R	=	dimensionless radius
r	=	radius
$\dot{S}'''_{\text{gen}}$	=	entropy generation rate
T	=	temperature
u	=	peripheral velocity
$\boldsymbol{V}$	=	velocity vector
α	=	thermal diffusivity
Γn	=	constants of integration, $n = 1 \times$ to $\times$ 12
θ	=	dimensionless temperature
λ	=	velocity ratio
μ	=	dynamic viscosity
Π	=	radius ratio
ρ	=	density
ϕ	=	volume fraction of nanoparticles
Ω	=	dimensionless temperature difference
ω	=	angular velocity
$\forall$	=	volume

Subscripts

ave	=	average (overall value)
f	=	base fluid
nf	=	nanofluid
0	=	value at the inner cylinder
1	=	value at the outer cylinder

Received 27 February 2012; revision received 29 May 2012; accepted for publication 31 May 2012; published online 29 November 2012.

*Graduate Student, Young Researcher's Club, Mashhad Branch; omid.mahian@gmail.com (Corresponding Author).
†Assistant Professor, School of Engineering.
‡Professor, Fluid Mechanics, Thermal Engineering, and Multiphase Flow Research Laboratory (FUTURE), Department of Mechanical Engineering, Faculty of Engineering.

I. Introduction

IN THE last three decades, many studies have been conducted on the analysis of the second law of thermodynamics with the aim of entropy generation minimization to improve the performance of thermal engineering systems. Bejan [1,2] investigated the different effective factors behind entropy generation in heat transfer engineering, in which the destruction of useful energy (exergy) of a system occurs through entropy generation. Recently, Naterer and Camberos [3] presented past analytical methods of entropy generation minimization to numerical simulations involving more complex configurations and experimental measurement techniques. Of course, it should be noted that some researchers during the analysis of heat exchangers concluded that the minimum entropy generation is not always related to the optimal performance. Therefore, the parameter of heat exchanger effectiveness should be considered to examine the real performance of heat exchanges for avoiding the entropy generation paradox [4–7].

In recent years, various methods have been used to improve the performance of thermal engineering systems. One of these methods is using a nanofluid as the working fluid in heat transfer devices.

Nanofluid is the name given to a fluid in which nanometer-sized particles (1–100 nm) are suspended [8]. The enhancement of heat transfer using nanofluids is a relatively new field within the past decade. Currently, research groups worldwide are focusing on the properties of various nanofluids and their applications in different thermal engineering systems and devices [9]. For more recent studies on nanofluids, readers can refer to some research articles and review papers in which various models to calculate the thermophysical properties of nanofluids and their applications are reviewed [10–14]. Relatively little information is currently available on the effects of flow and heat transfer of nanofluids on entropy generation.

Here, the main studies concerning the second-law analysis of the flow and heat transfer of nanofluids are presented. Singh et al. [15] conducted an analytical analysis of entropy generation due to the flow and heat transfer of water-alumina nanofluids in different regimes within channels (with different sizes), including microchannels, minichannels, and conventional channels. Their results indicated that there is an optimum channel type in which entropy generation is minimized. They also found that using a water-alumina nanofluid with high viscosity in microchannels with laminar flow, as well as in minichannels and conventional channels with turbulent flow, is not beneficial. Li and Kleinstreuer [16] numerically investigated entropy generation due to the steady laminar flow of pure water and water-CuO nanofluids in trapezoidal microchannels. They determined that using nanofluids with very low particle loading reduces entropy generation at low Reynolds numbers. Feng and Kleinstreuer [17] considered the flow of an alumina-water nanofluid with heat transfer in a parallel disk system. They found that the total entropy generation rate decreases with an increase in the volume fraction of nanofluid.

Moghaddami et al. [18] analytically studied entropy generation due to water-Al_2O_3 and ethylene gylcol-Al_2O_3 nanofluid flow inside a circular pipe with constant heat flux for both laminar and turbulent regimes. Their results revealed that adding a volume fraction of nanofluids is effective only when irreversibility caused by heat transfer is dominant. Concerning the turbulent flow of water-Al_2O_3 nanofluid, they concluded that adding nanoparticles only for Reynolds numbers smaller than 40,000 decreases entropy generation, whereas for Reynolds numbers bigger than 80,000, entropy generation becomes higher in magnitude. Shahi et al. [19] studied numerically entropy generation due to the natural convection cooling of a heat source within a cavity filled by water-Cu nanofluid, in which the heat source can be mounted at different positions on the walls of the cavity. They investigated the effects of the Rayleigh number, nanoparticle concentration, and the position of the heat source on entropy generation. Esmaeilpour and Abdollahzadeh [20] investigated entropy generation numerically due to the natural convection of Cu-water nanofluids with a volume fraction from 0 to 10% inside a two-dimensional wavy enclosure. Their results showed that, with the addition of nanoparticles to a base fluid, the entropy generation rate decreases. Bianco et al. [21] presented a numerical analysis of the turbulent forced-convection flow of water-Al_2O_3 nanofluids inside a square tube with constant and uniform wall heat flux. They determined analytically the optimum Reynolds number at which entropy production becomes smallest. Recently, Falahat and Vosough [22] investigated entropy generation through a coiled tube heat exchanger with uniform wall heat flux conditions in both laminar and turbulent regimes using water-Al_2O_3 nanofluid. They obtained the optimum conditions based on the entropy generation sense for both laminar and turbulent regimes.

A review of the literature shows that there is no analytical report concerning the effect of using nanofluids on entropy generation between two concentric rotating cylinders in the presence of magnetohydrodynamic (MHD) flow. The flow between two cylinders where one or both of the cylinders rotate has many practical applications, such as swirl nozzles, rotating electrical machines, rotating disks, standard commercial rhymesters, and chemical and mechanical mixing equipment. In addition, the flow and heat transfer in annuli, where the outer cylinder rotates and the inner one is stationary, is an important research subject in many engineering applications, such as in the petroleum, food, and automobile industries [23,24].

Yilbas [23] conducted an entropy generation analysis for a rotating outer cylinder and differentially heated isothermal boundary condition assuming a linear velocity distribution in the annuli. Mahmud and Fraser [24,25] investigated entropy generation inside the cylindrical annular space with different boundary conditions. They simplified and solved governing equations in cylindrical coordinates to obtain analytical expressions for dimensionless entropy generation and the Bejan number as a function of the parameters involved in the problem. In another work, Mirzazadeh et al. [26] focused on entropy generation induced by the flow of a nonlinear viscoelastic fluid between concentric rotating cylinders.

Using an external magnetic field is of significant importance in many industrial applications, particularly as a control mechanism in material manufacturing [27]. In addition, the study of flow and heat transfer in a closed cavity or a channel in the presence of a magnetic field is important because of engineering applications such as the cooling of nuclear reactors, MHD micropumps, electronic packages, and microelectronic devices. In the past decade, the study of MHD flow and its effect on entropy generation in related systems has received extensive attention because of its importance in industry, as mentioned previously. Some works that investigated the effect of MHD flow on entropy generation for various flows and geometries are mentioned.

Salas et al. [28] analyzed the second law for MHD induction devices such as electromagnetic pumps and electrical generators. Ibanez et al. [29] optimized the operation conditions for an alternate MHD generator based on the global entropy generation rate. Mahmud et al. [30] studied the effect of a transverse magnetic field on entropy generation inside a vertical channel made of two parallel plates by considering mixed convection inside the channel. Later, Tasnim et al. [31] considered the same problem for porous media. Mahmud and Fraser [32] investigated the second law analytically for a mixed convection–radiation interaction in a vertical porous channel in the presence of MHD flow. Mahmud and Fraser [33] examined the problem of entropy generation in a fluid-saturated porous cavity for laminar natural convection heat transfer where the magnetic field is assumed to act along the direction of the force of gravity.

Ibanez and Cuevas [34] applied the approach of entropy generation minimization by considering joule dissipation, heat conduction, and viscosity to optimize the MHD flow between two infinite parallel walls with limited electrical conductivity. Mahmud and Fraser [35] presented a general relation for entropy generation for a single-plate thermoacoustic system that was exposed to a transverse magnetic field. Ibanez and Cuevas [36] considered a stationary buoyant MHD flow of a liquid metal immersed in a magnetic field through a vertical rectangular duct with thin conducting or insulating walls.

Arikoglu et al. [37] investigated the effect of slip and joule dissipation on entropy generation in a single rotating disk in the presence of MHD flow by a seminumerical analytical solution method, in which the magnetic field is constant and acts only in the axial direction. In addition, the effect of a magnetic field on entropy generation in a microchannel was investigated by Ibanez and Cuevas [38].

As mentioned, the aim of this study is to investigate the effect of using nanofluids on entropy generation between two rotating cylinders in the presence of MHD flow. The governing equations in cylindrical coordinates are simplified and analytically solved using isothermal boundary conditions to obtain the average entropy generation in the annulus.

II. Description of the Problem

The geometry of the cylindrical annulus considered is indicated in Fig. 1. A Newtonian nanofluid fills the gap between the inner and outer cylinders, which are of radii r_0 and r_1 and with constant surface temperatures of T_0 and T_1, respectively. The inner and outer cylinders can rotate with constant angular velocities of ω_0 and ω_1, respectively. A magnetic field (B_0) constantly acts in parallel to the axial direction

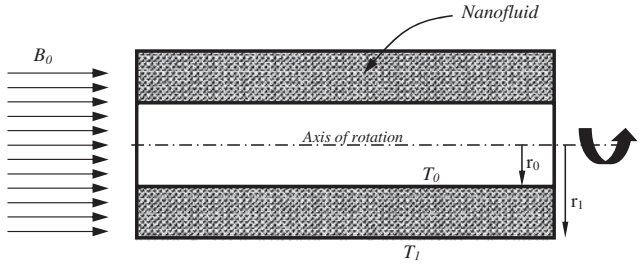

Fig. 1 Schematic diagram of the problem under consideration.

of the cylinders while the flow between the cylinders is laminar and steady.

It is assumed that the fluid and nanoparticles are in thermal equilibrium and that no slip occurs between them. It should be remarked that, in practical situations, most nanofluids used for enhancement of heat transfer are made up of very fine particles, normally less than 40 nm. Hence, the nanofluids can be considered to behave like a conventional, homogeneous, single-phase fluid [39]. Also, the thermophysical properties of the nanofluid are assumed to be constant. In the present work, TiO_2-water nanofluid is considered in the analysis.

III. Problem Formulation and Analysis

A. First Law Analysis

With the assumption of no relative axial motion between the cylinders and ignoring the radial velocity component compared to the tangential one, the momentum equation in cylindrical coordinates is simplified as follows:

$$\left(\frac{\partial^2 u_\theta}{\partial r2}+\frac{1}{r}\frac{\partial u_\theta}{\partial r}-\frac{u_\theta}{r^2}\right)-\frac{\sigma B_0^2}{\mu_{\rm nf}}u_\theta=0 \tag{1}$$

where u_θ is the tangential velocity component and σ is the fluid's electrical conductivity. The energy equation disregarding the convection term becomes (see Jiji [40] for details)

$$\frac{k_{\rm nf}}{r}\frac{\partial}{\partial r}\left(r\frac{\partial T}{\partial r}\right)=-\mu_{\rm nf}\left(\frac{\partial u_\theta}{\partial r}-\frac{u_\theta}{r}\right)^2 \tag{2}$$

The boundary conditions for the momentum and energy equations are as follows:

$$\begin{aligned} &r=r_0\colon\ u_\theta=u_0=r_0\omega_0 \quad \text{and} \quad T=T_0\\ &r=r_1\colon\ u_\theta=u_1=r_1\omega_1 \quad \text{and} \quad T=T_1 \end{aligned} \tag{3}$$

To calculate the thermal conductivity ($k_{\rm nf}$) and viscosity ($\mu_{\rm nf}$) of the nanofluid, the Duangthongsuk and Wongwises equations [41], which are based on experimental results, are considered as follows:

$$\frac{k_{\rm nf}}{k_f}=1.0204+0.0249\phi \tag{4}$$

$$\frac{\mu_{\rm nf}}{\mu_f}=1.013+0.092\phi-0.015\phi^2 \tag{5}$$

In the previous relation, ϕ is the volume fraction of nanoparticles, and k_f and μ_f are the thermal conductivity and viscosity of the base fluid, respectively. It should be stated that Eqs. (4) and (5) are valid for 0.2–2 vol % of TiO_2-water nanofluid. These relations are obtained for 25° C, but in this work, the properties of nanofluids are assumed to be independent of temperature.

Using the following dimensionless parameters and considering the outer cylinder as the reference,

$$\begin{aligned} &R=\frac{r}{r_1},\quad U=\frac{u_\theta}{r_1\omega_1},\quad \theta=\frac{T-T_1}{T_0-T_1},\quad \Pi=\frac{r_0}{r_1},\\ &\lambda=\frac{\omega_0}{\omega_1}\quad Pr_f=\frac{\mu_f C_{p,f}}{k_f},\quad Ec_f=\frac{(r_1\omega_1)^2}{C_{p,f}\Delta T},\quad M^2=\frac{\sigma B_0^2}{\mu_f}r_1^2 \end{aligned} \tag{6}$$

The governing equations in dimensionless form can be expressed as follows: Momentum equation:

$$\begin{aligned} &R^2\frac{\partial^2 U}{\partial R^2}+R\frac{\partial U}{\partial R}-\left[1+\left(\frac{\mu_f}{\mu_{\rm nf}}\right)M^2R^2\right]U=0 R=\Pi\colon\ U=\Pi\lambda\\ &R=1\colon\ U=1 \end{aligned} \tag{7}$$

Energy equation:

$$\begin{aligned} &\frac{1}{R}\frac{\partial}{\partial R}\left(R\frac{\partial\theta}{\partial R}\right)=-Ec_f Pr_f\left(\frac{\mu_{\rm nf}}{\mu_f}\right)\left(\frac{k_f}{k_{\rm nf}}\right)\left(\frac{\partial U}{\partial R}-\frac{U}{R}\right)^2\ \ R=\Pi\colon\ \theta=1\\ &R=1\colon\ \theta=0 \end{aligned} \tag{8}$$

where M is the Hartmann number, Ec_f is the Eckert number, and Pr_f is the Prandtl number. By noting that the multiplication of $(\mu_f/\mu_{\rm nf})$ by M^2 is a positive quantity, and then by considering $H^2=(\mu_f/\mu_{\rm nf})M^2$, the solution of the momentum equation is obtained as follows:

$$U(R)=\Gamma_1 I_1(HR)+\Gamma_2 K_1(HR) \tag{9}$$

where $I_1(HR)$ is known as the modified Bessel function of the first kind, of order 1, and $K_1(HR)$ as the modified Bessel function of the second kind, of order 1. The constants of integration Γ_1 and Γ_2 can be calculated while applying the boundary conditions; therefore, the constants are obtained as follows:

$$\begin{aligned} \Gamma_1&=\frac{\Pi\lambda K_1(H)-K_1(H\Pi)}{I_1(H\Pi)K_1(H)-K_1(H\Pi)I_1(H)}\\ \Gamma_2&=\frac{\Pi\lambda I_1(H)-I_1(H\Pi)}{K_1(H\Pi)I_1(H)-I_1(H\Pi)K_1(H)} \end{aligned} \tag{10}$$

To find the temperature field from Eq. (8), the expansions of the Bessel functions $I_1(HR)$ and $K_1(HR)$, with three terms, are used as follows:

$$\begin{aligned} I_1(HR)&\cong\frac{1}{2}HR+\frac{(HR)^3}{16}+\frac{(HR)^5}{384}\\ K_1(HR)&\cong\frac{1}{HR}+\left[\frac{1}{2}\ln\left(\frac{HR}{2}\right)-\frac{1}{4}(-2\gamma+1)\right](HR)\\ &\quad+\left[\frac{1}{16}\ln\left(\frac{HR}{2}\right)-\frac{1}{32}\left(\frac{5}{2}-2\gamma\right)\right](HR)^3 \end{aligned} \tag{11}$$

in which

$$\gamma\approx 0.57722\ldots$$

By substituting the values of $I_1(HR)$ and $K_1(HR)$ for the expansions in the velocity distribution equation [Eq. (9)], and using the new velocity distribution in Eq. (8), the temperature gradient that is required in the entropy generation analysis is given as follows:

$$\frac{\partial\theta}{\partial R}=\frac{\Gamma_3}{R}+\left(\frac{\mu_{\rm nf}}{\mu_f}\right)\left(\frac{k_f}{k_{\rm nf}}\right)\frac{Br_f}{R}\times\left[\begin{array}{l}2\Gamma_2^2\ \ln\left(\frac{HR}{2}\right)+\frac{2\Gamma_2^2}{H^2R^2}+\Gamma_5(HR)^6\ \ln\left(\frac{HR}{2}\right)\\+\Gamma_6(HR)^6-\frac{1}{384}\Gamma_2^2(HR)^6\left[\ln\left(\frac{HR}{2}\right)\right]^2\\+\Gamma_7(HR)^2+\Gamma_8(HR)^4-\frac{1}{32}\Gamma_2^2(HR)^4\ \ln\left(\frac{HR}{2}\right)\\+\Gamma_9(HR)^8-\frac{1}{3072}\Gamma_1\Gamma_2(HR)^8\ \ln\left(\frac{HR}{2}\right)-\frac{1}{92{,}160}(HR)^{10}\Gamma_1^2\end{array}\right]\tag{12}$$

In this equation, Br_f is the Brinkman number that is the multiplication of Ec_f by Pr_f. Also, Γ_3 is the constant of integration and the constants Γ_5 to Γ_9 are in terms of Γ_1, Γ_2, and γ as follows:

$$\begin{aligned}\Gamma_5&=\frac{11}{2304}\Gamma_2^2-\frac{1}{192}\Gamma_1\Gamma_2-\frac{1}{192}\Gamma_2^2\gamma\\\Gamma_6&=\frac{11}{2304}\Gamma_2^2\gamma+\frac{7}{2304}\Gamma_1\Gamma_2-\frac{1}{384}\Gamma_2^2\gamma^2-\frac{1}{384}\Gamma_1^2\\&\quad-\frac{125}{55,296}\Gamma_2^2-\frac{1}{192}\Gamma_1\Gamma_2\gamma\\\Gamma_7&=\frac{1}{4}\Gamma_2^2\gamma-\frac{7}{16}\Gamma_2^2+\frac{1}{4}\Gamma_1\Gamma_2\\\Gamma_8&=\frac{1}{32}\Gamma_2^2-\frac{1}{32}\Gamma_2^2\gamma-\frac{1}{48}\Gamma_1\Gamma_2\\\Gamma_9&=\frac{7}{24,576}\Gamma_1\Gamma_2-\frac{1}{3072}\Gamma_1\Gamma_2\gamma-\frac{1}{3072}\Gamma_1^2\end{aligned}$$

Therefore, the temperature field is given by integrating Eq. (12) as follows:

$$\theta=\Gamma_4+\Gamma_3\ \ln(R)\quad+\left(\frac{\mu_{\rm nf}}{\mu_f}\right)\left(\frac{k_f}{k_{\rm nf}}\right)Br_f\left\{\begin{array}{l}\Gamma_{10}(HR)^6+\Gamma_{11}(HR)^8+\Gamma_{12}(HR)^4+\frac{1}{2}\Gamma_7(HR)^2-\frac{1}{921{,}600}\Gamma_1^2(HR)^{10}\\+\Gamma_2^2\left[\ln\left(\frac{HR}{2}\right)\right]^2-\frac{\Gamma_2^2}{(HR)^2}+\frac{1}{6}\Gamma_5\ \ln\left(\frac{HR}{2}\right)(HR)^6-\frac{1}{2304}\Gamma_2^2\left[\ln\left(\frac{HR}{2}\right)\right]^2(HR)^6\\+\frac{1}{6912}\Gamma_2^2\ \ln\left(\frac{HR}{2}\right)(HR)^6-\frac{1}{128}\Gamma_2^2\ \ln\left(\frac{HR}{2}\right)(HR)^4-\frac{1}{24{,}576}\Gamma_1\Gamma_2\ \ln\left(\frac{HR}{2}\right)(HR)^8\end{array}\right\}\tag{13}$$

The constants of integration Γ_3 and Γ_4 will be readily obtained using isothermal boundary conditions. To conserve space, the expressions for Γ_3 and Γ_4 are not presented here due to length constraints. Constants Γ_{10}, Γ_{11}, and Γ_{12} are given as follows:

$$\Gamma_{10}=-\frac{1}{36}\Gamma_5+\frac{1}{6}\Gamma_6-\frac{1}{41,472}\Gamma_2^2\quad\Gamma_{11}=\frac{1}{8}\Gamma_9+\frac{1}{196,608}\Gamma_1\Gamma_2$$
$$\Gamma_{12}=\frac{1}{4}\Gamma_8+\frac{1}{512}\Gamma_2^2$$

B. Entropy Generation Analysis

In the presence of a magnetic field, the local volumetric entropy generation rate can be expressed as follows (see [37] with a similar analysis):

$$\dot{S}'''_{\rm gen}=\frac{k_{\rm nf}}{T_1^2}[\nabla T]^2+\frac{\mu_{\rm nf}}{T_1}\phi+\frac{1}{T_1}[(J-QV)(E+V\times B)]\tag{14}$$

where

$$J=\sigma(E+V\times B)\tag{15}$$

In Eq. (14), ϕ is viscous dissipation, J is the electric current, Q is the electric charge density, V is the velocity vector, E is the electric field, and B is the magnetic induction. Assuming that QV is negligible compared with J, and disregarding E in comparison with $V\times B$, the entropy production rate [Eq. (14)] decreases in this case to

$$\dot{S}'''_{\rm gen}=\frac{k_{\rm nf}}{T_1^2}\left(\frac{\partial T}{\partial r}\right)^2+\frac{\mu_{\rm nf}}{T_1}\left[r\frac{\partial}{\partial r}\left(\frac{u}{r}\right)\right]^2+\frac{\sigma B_0^2}{T_1}u^2\tag{16}$$

Equation (16) shows that entropy generation is due to three effects: a conductive effect ($k_{\rm nf}$), a viscous effect ($\mu_{\rm nf}$), and a magnetic effect (B_0). Defining N_S as the entropy generation number, the dimensionless form of Eq. (16) can be expressed as follows:

$$\begin{aligned}N_S&=\frac{\dot{S}'''_{\rm gen}}{\left(\frac{\mu_{\rm nf}\omega_1^2}{T_1}\right)}=\frac{\Omega}{Br_f}\left(\frac{k_{\rm nf}}{k_f}\right)\left(\frac{\mu_f}{\mu_{\rm nf}}\right)\left(\frac{\partial\theta}{\partial R}\right)^2+\left(R\frac{\partial}{\partial R}\left(\frac{U}{R}\right)\right)^2+H^2U^2\\&=N_H+N_F+N_M\end{aligned}\tag{17}$$

where Ω is the dimensionless temperature difference, which equals $\Delta T/T_1$. On the right side of Eq. (17), the first term ($=N_H$) is the local entropy generation due to heat transfer irreversibility, the second term ($=N_F$) is the local entropy generation due to fluid friction irreversibility, and the last term ($=N_M$) is the local entropy generation due to the magnetic field. To calculate the entropy generation number N_S in Eq. (17), the terms N_F and N_M are determined directly by using Eq. (9) without any approximation, unlike the term N_H, in which the temperature gradient is obtained using approximation.

To evaluate the irreversibility distribution, the parameter Be (Bejan number), which is the ratio of entropy generation due to heat transfer to the overall entropy generation [42], is defined as follows:

$$Be=\frac{N_H}{N_H+N_F+N_M}\tag{18}$$

The Bejan number varies from 0 to 1. Subsequently, $Be=0$ reveals that the irreversibility due to fluid friction and magnetic field dominates, whereas $Be=1$ indicates that the irreversibility due to heat transfer is dominant. It is obvious that $Be=0.5$ is the case in which the irreversibility due to heat transfer is equal to fluid friction and magnetic field contributions in the entropy production.

The volumetric averaged entropy generation rate, $(N_S)_{\rm ave}$, can be obtained using Eq. (17) as follows:

$$(N_S)_{\rm ave}=\frac{1}{\forall}\int_{\forall}N_S\,{\rm d}\forall=\frac{2}{(1-\Pi^2)}\int N_S R\,{\rm d}R\tag{19}$$

or

$$(N_S)_{\rm ave}=\frac{2}{(1-\Pi^2)}\int(N_H+N_F+N_M)R\,{\rm d}R\tag{20}$$

From this relation, it is possible to evaluate the contributions of heat transfer, fluid friction, and the magnetic field in the averaged entropy

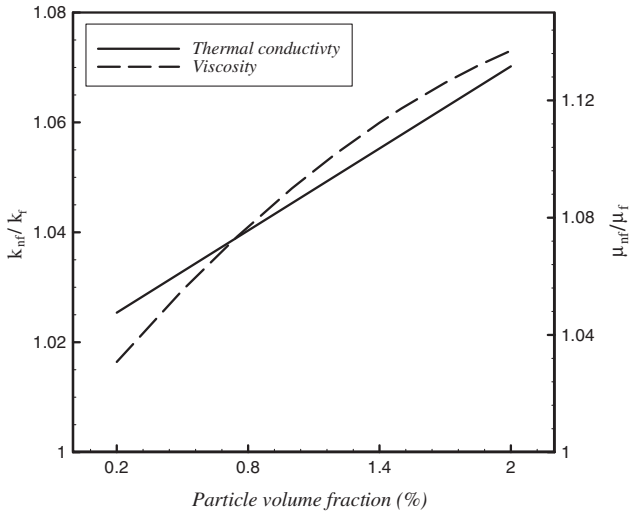

Fig. 2 Variations of the thermal conductivity and viscosity ratios with particle volume fraction.

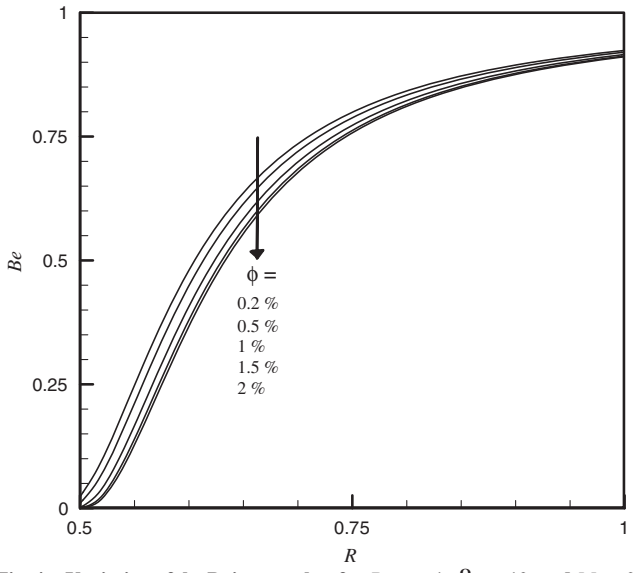

Fig. 4 Variation of the Bejan number for $Br_f = 1$, $\frac{\Omega}{Br_f} = 10$, and $M = 0$ at different nanoparticle volume fractions.

generation. It should be noted that, in practical applications, the inner cylinder is assumed at rest, and therefore the velocity ratio ($\lambda = \frac{\omega_0}{\omega_1}$) becomes zero. It is also assumed that the radius ratio ($\Pi = \frac{r_0}{r_1}$) is equal to 0.5.

IV. Results and Discussion

Figure 2 shows the variations of the thermal conductivity ratio ($\frac{k_{nf}}{k_f}$) and the viscosity ratio ($\frac{\mu_{nf}}{\mu_f}$) of the nanofluid with the particle volume fraction for TiO_2-water nanofluid. It was observed that, as the particle volume fraction increased up to 2 vol %, the thermal conductivity and viscosity increased by ~7 and ~14%, respectively.

The variation of the entropy generation number (N_S) with radial distance (R) is shown in Fig. 3 for $Br_f = 1$, $\frac{\Omega}{Br_f} = 10$, $M = 0$, and volume fraction (ϕ) from 0.2 to 2%. The figure reveals that the temperature and velocity gradients are highest on the inner cylinder, whereas the minimum gradients occur on the outer cylinder. As shown, with the increase in volume fraction, the entropy generation number falls in the gap due to the decreasing temperature gradients in the annulus. In this case, the temperature gradients decrease, because with an increase in the volume fraction the effective thermal conductivity increases. Consequently, the thermal conductance in the gap enhances, and the irreversibility due to heat transfer decreases. It also is seen that the decreasing tendency in the entropy generation number is more obvious between $\phi = 0.5\%$ to $\phi = 1\%$ compared with $\phi = 1.5\%$ to $\phi = 2\%$. This is because the effects of viscosity and fluid friction are higher at high volume fractions than at low volume fractions; therefore, the decreases in entropy generation decrease.

The variation of the Bejan number with radial distance is displayed in Fig. 4 for the same conditions of Fig. 3. As shown in Fig. 4, the Bejan number falls in the annulus in response to an increase in the particle volume fraction. This phenomenon can be described by considering the definition of the Bejan number in Eq. (18). When the particle volume fraction increases, the effective viscosity in the annulus increases; hence, the irreversibility due to fluid friction (N_F) increases. Thus, Be decreases with an increase in N_F, because N_F is in the denominator of Eq. (18). On the other hand, increasing the volume fraction leads to the increase of effective thermal conductivity; hence, the irreversibility due to heat transfer (N_H) decreases. Therefore, the Bejan number decreases due to the increase in nanoparticle loading, and the Bejan number is maximized on the

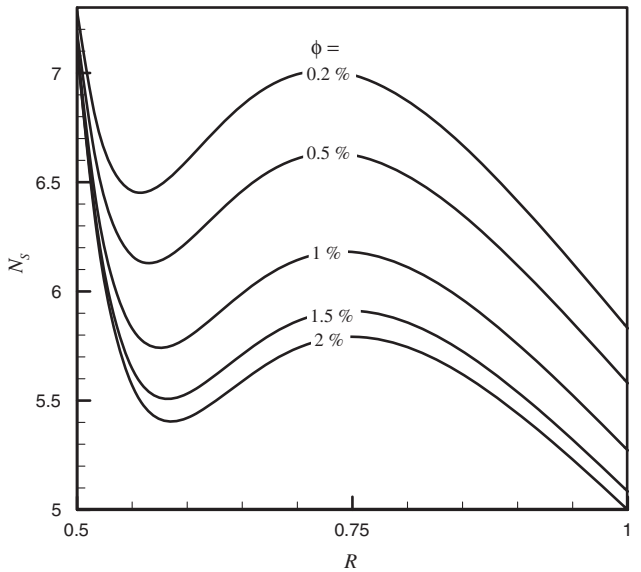

Fig. 3 Variation of the entropy generation number for $Br_f = 1$, $\frac{\Omega}{Br_f} = 10$, and $M = 0$ at different nanoparticle volume fractions.

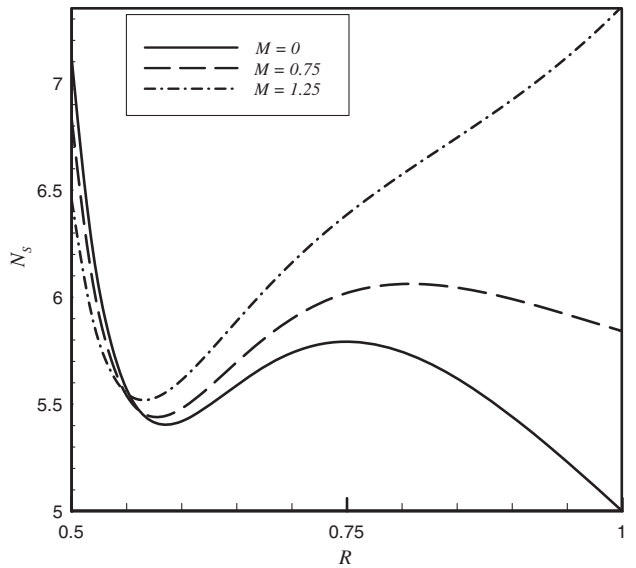

Fig. 5 Variation of the entropy generation number for $Br_f = 1$, $\frac{\Omega}{Br_f} = 10$, $\phi = 2\%$, and different values of the Hartmann number.

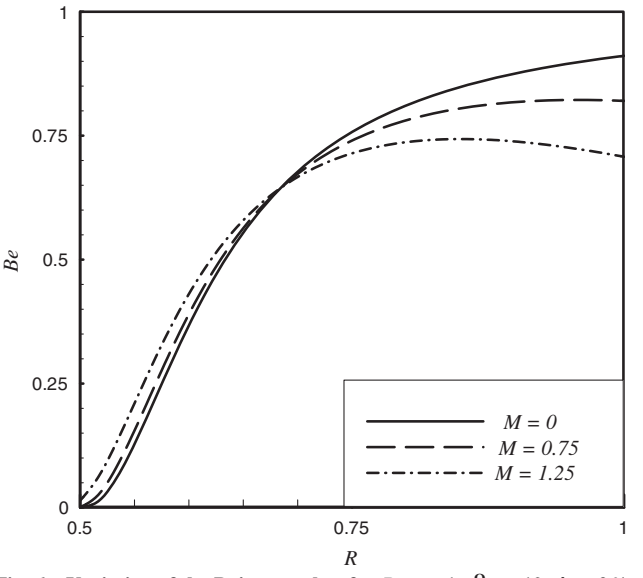

Fig. 6 Variation of the Bejan number for $Br_f = 1$, $\frac{\Omega}{Br_f} = 10$, $\phi = 2\%$, and different values of the Hartmann number.

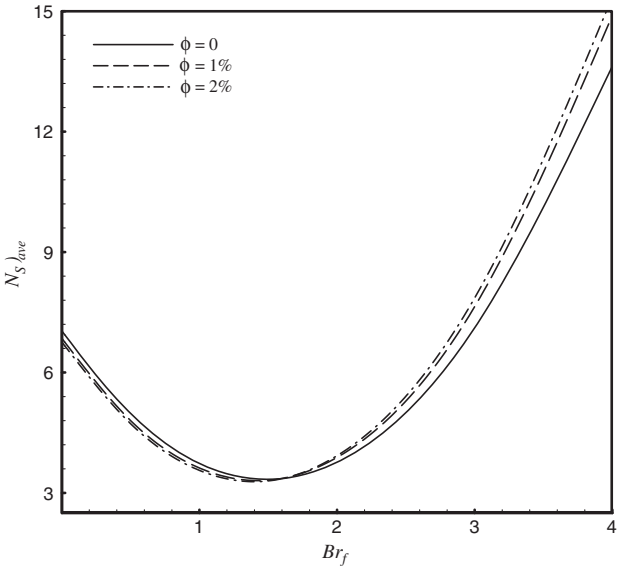

Fig. 8 Effect of nanoparticle loading on the average entropy generation number at different Brinkman numbers for $\frac{\Omega}{Br_f} = 1$.

outer cylinder. This indicates that in regions near the outer cylinder, the contribution of heat transfer to entropy generation is greater than in other regions.

The variation of the entropy generation number with radial distance is indicated in Fig. 5 for $Br_f = 1$, $\frac{\Omega}{Br_f} = 10$, $\phi = 2\%$, and three different values of the Hartmann number. It was found that the entropy generation number in the vicinity of the inner cylinder decreased a little with an increase in the Hartmann number from 0 to 1.25, whereas, with movement toward the outer cylinder, the entropy generation number increased with the increasing intensity of the magnetic field. In other words, as the Hartmann number increases, the gradients near the outer cylinder increase. In this case, an enhanced magnetic field leads to a decrease in the fluid velocity, and consequently, the boundary layer thickness in the annulus decreases. This leads to the increases in the velocity gradients.

Figure 6 shows the variation of the Bejan number with radial distance for the same conditions of Fig. 5. It was observed that an increase in the Hartmann number decreased the contribution of heat transfer in entropy generation near the outer cylinder; thus, Be decreased. In addition, it was found that because high values of shear stresses and high viscous dissipations are dominant near the inner cylinder, the Bejan number tends toward zero.

In this section, the effect of different parameters on average entropy generation is investigated. The effect of particle loading on the average entropy generation number at different Brinkman numbers from 0.001 to 4 is illustrated in Fig. 7 for $\frac{\Omega}{Br_f} = 0.1$ and $M = 1$. For $Br_f \leq 2.7$, the average entropy generation number decreased with an increase in ϕ; for $Br_f > 2.7$, $(N_S)_{\text{ave}}$ increases with the nanoparticle loading. The Brinkman number determines the relative significance between dissipation effects and fluid conduction effects (see White [43]). At high Brinkman numbers, the dissipation effects dominate conduction effects; hence, an increase in particle volume fraction is more effective in the irreversibility due to fluid friction, and consequently the average entropy generation increases. It also is shown that there is an optimum Brinkman number at which the average entropy generation is minimized. This optimum point can be obtained readily by the following relation:

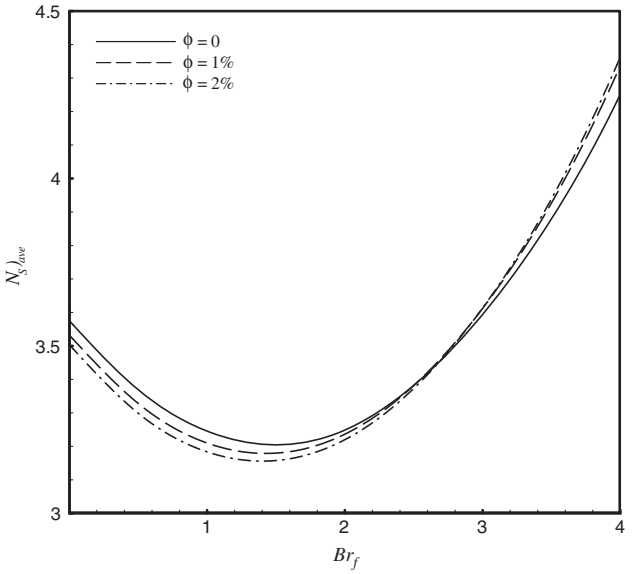

Fig. 7 Effect of nanoparticle loading on the average entropy generation number at different Brinkman numbers for $\frac{\Omega}{Br_f} = 0.1$.

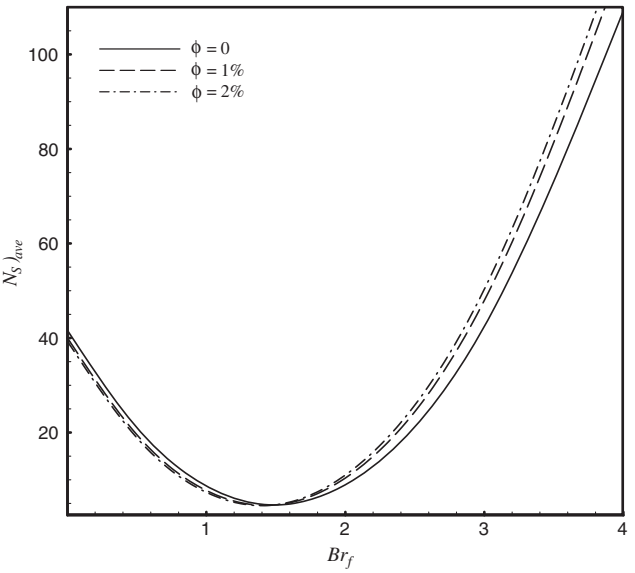

Fig. 9 Effect of nanoparticle loading on the average entropy generation number at different Brinkman numbers for $\frac{\Omega}{Br_f} = 10$.

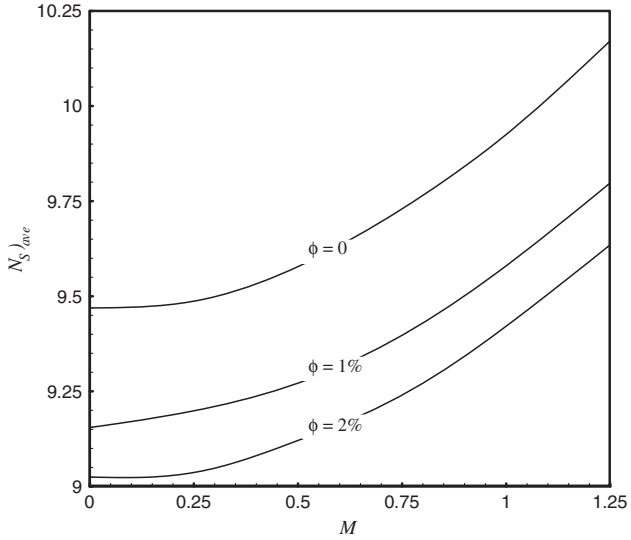

Fig. 10 Variation of the average entropy generation number with the Hartmann number for $Br_f = 0.1$ and $\frac{\Omega}{Br_f} = 2$.

$$\frac{(\partial N_S)_{\text{ave}}}{\partial Br_f} = 0 \quad \text{or} \quad \frac{\partial(\int_{0.5}^{1} N_S R \, dR)}{\partial Br_f} = 0 \tag{21}$$

The optimum Brinkman number is approximately equal to 1.5.

Figures 8 and 9 present the variation of $(N_S)_{\text{ave}}$ with the Brinkman number for $M = 1$, $\frac{\Omega}{Br_f} = 1$, and $\frac{\Omega}{Br_f} = 10$. In these two cases, as in the previous case, the optimum Brinkman number at which entropy generation is minimized is approximately 1.5. However, unlike the previous case, the range of the Brinkman number at which increasing ϕ results in decreasing$(N_S)_{\text{ave}}$ decreases from 2.7 to 1.5. With increasing $\frac{\Omega}{Br_f}$, the average entropy generation increases, as expected.

The results of Figs. 7–9 have significance for industrial applications as follows. When the Brinkman number is small and the outer cylinder rotates at low speed, the addition of nanoparticles leads to a reduction in entropy generation of the system. By contrast, the addition of nanoparticles is not recommended when the outer cylinder rotates at high speeds.

The variation of the average entropy generation number with the Hartmann number is presented in Fig. 10 for $Br_f = 0.1$ and $\frac{\Omega}{Br_f} = 2$. As mentioned in the previous section, the average entropy generation decreases for Brinkman numbers of less than 1.5 with an increase in the nanoparticle volume fraction. This fact also is shown in Fig. 10. The decreasing tendency in entropy generation is more obvious between $\phi = 0$ and $\phi = 1\%$, because the viscous dissipation effects are smaller at lower particle volume fractions. Hence, the addition of nanoparticles leads to more reduction in entropy generation.

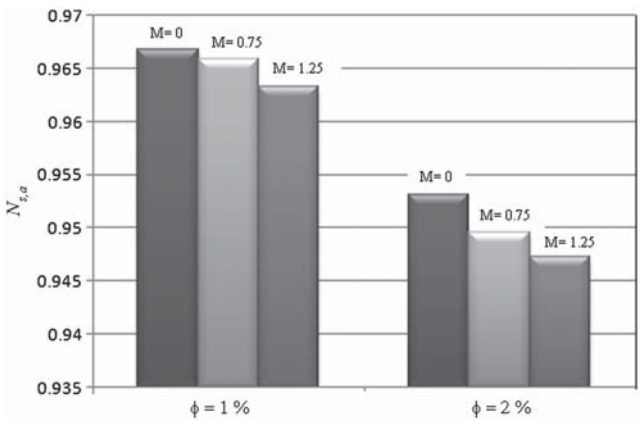

Fig. 11 Augmentation entropy generation number for $Br_f = 0.1$ and $\frac{\Omega}{Br_f} = 2$.

It also is shown in the figure that, with the augmentation of the magnetic field, the average entropy generation increases. The presence of the magnetic field makes a resistive force similar to the drag force, which acts in the opposite direction of fluid movement. This reduces the fluid velocity, leads to the increase in viscous dissipation, and results in more internal heating of the working fluid. Consequently, there is an increase of the entropy generation. As shown, the profiles of $(N_S)_{\text{ave}}$ for different values of ϕ are parallel and regular.

The proper effect of the augmentation method (here, adding nanoparticles) on the thermodynamic performance of the thermal system can be appraised by comparing the irreversibility before and after using the augmentation method. For this purpose, the augmentation entropy generation number is defined as follows [22]:

$$N_{S,a} = \frac{N_S}{N_{S,0}} \tag{22}$$

where $N_{S,0}$ indicates the degree of irreversibility when the volume fraction is zero (distilled water). According to Eq. (22), adding nanoparticles is advantageous with respect to the second law of thermodynamics when $N_{S,a}$ values are less than 1. Figure 11 presents the variation of augmentation entropy generation number at different Hartmann numbers and volume fractions (1 and 2%) for the conditions of Fig. 10. The figure shows that the augmentation entropy generation decreases with an increase in volume fraction and the Hartmann number. Therefore, for this case, the following suggestion can be given. With respect to the second law of thermodynamics, adding nanoparticles to the working base fluid is more justifiable with increasing intensity of magnetic field than in the case in which the magnetic field is poor.

V. Conclusions

An analytical analysis of the second law of thermodynamics is presented to investigate the effect of using TiO_2-water nanofluid (up to 2 vol %) on entropy generation between two rotating cylinders in the presence of magnetohydrodynamic flow. The governing equations in a cylindrical coordinate system are simplified and solved to obtain analytical expressions for the velocity and temperature fields and, consequently, the entropy generation rate. To calculate the thermophysical properties of the nanofluid, including thermal conductivity and viscosity, the Duangthongsuk and Wongwises models, which are based on experimental data, have been used. The results for the local entropy generation analysis reveal that entropy generation is highest near the inner cylinder due to the maximum gradients of velocity and temperature. In addition, with an increase in the Hartmann number (magnetic field), entropy generation in the vicinity of the inner cylinder decreases, whereas in other regions, the entropy generation number is raised. The results show that, at low Brinkman numbers (depending on the value of $\frac{\Omega}{Br_f}$), the average entropy generation number decreases with the addition of nanoparticle volume fraction. It also was found that the increase in the Hartmann number results in an increase in the average entropy generation number. Hence, with respect to the second law of thermodynamics, using nanofluids for the flow between two rotating cylinders in the presence of a magnetohydrodynamic field is suggested only at low Brinkman numbers.

Acknowledgments

The third author would like to thank the Thailand Research Fund and the National Research University Project for support.

References

[1] Bejan, A., "Second-Law Analysis in Heat Transfer and Thermal Design," *Advances in Heat Transfer*, Vol. 15, 1982, pp. 1–58. doi:10.1016/S0065-2717(08)70172-2

[2] Bejan, A., *Entropy Generation Minimization*, CRC Press, Boca Raton, FL, 1996.

[3] Naterer, G. F., and Camberos, J. A., *Entropy Based Analysis and Design of Fluids Engineering Systems*, CRC Press, Boca Raton, FL, 2008.
[4] Shah, R. K., and Skiepko, T., "Entropy Generation Extrema and their Relationship with Heat Exchanger Effectiveness—Number of Transfer Unit Behavior for Complex Flow Arrangements," *Journal of Heat Transfer*, Vol. 126, No. 6, 2004, pp. 994–1002. doi:10.1115/1.1846694
[5] Guo, Z. Y., Liu, X. B., Tao, W. Q., and Shah, R. K., "Effectiveness–Thermal Resistance Method for Heat Exchanger Design and Analysis," *International Journal of Heat and Mass Transfer*, Vol. 53, Nos. 13–14, 2010, pp. 2877–2884. doi:10.1016/j.ijheatmasstransfer.2010.02.008
[6] Guo, J., and Xu, M., "The Application of Entransy Dissipation Theory in Optimization Design of Heat Exchanger," *Applied Thermal Engineering*, Vol. 36, 2012, pp. 227–235. doi:10.1016/j.applthermaleng.2011.12.043
[7] Cheng, X., and Liang, X., "Computation of Effectiveness of Two-Stream Heat Exchanger Networks Based on Concepts of Entropy Generation, Entransy Dissipation and Entransy-Dissipation-Based Thermal Resistance," *Energy Conversion and Management*, Vol. 58, 2012, pp. 163–170. doi:10.1016/j.enconman.2012.01.016
[8] Yu, W., France, D. M., Routbort, J. L., and Choi, S. U. S., "Review and Comparison of Nanofluid Thermal Conductivity and Heat Transfer Enhancements," *Heat Transfer Engineering*, Vol. 29, No. 5, 2008, pp. 432–460. doi:10.1080/01457630701850851
[9] Yu, W., France, D. M., Smith, D. S., Singh, D., Timofeeva, E. V., and Routbort, J. L., "Heat Transfer to a Silicon Carbide/Water Nanofluid," *International Journal of Heat and Mass Transfer*, Vol. 52, Nos. 15–16, 2009, pp. 3606–3612. doi:10.1016/j.ijheatmasstransfer.2009.02.036
[10] Trisaksri, V., and Wongwises, S., "Critical Review of Heat Transfer Characteristics of Nanofluids," *Renewable and Sustainable Energy Reviews*, Vol. 11, No. 3, 2007, pp. 512–523. doi:10.1016/j.rser.2005.06.005
[11] Duangthongsuk, W., and Wongwises, S., "A Critical Review of Convective Heat Transfer of Nanofluids," *Renewable and Sustainable Energy Reviews*, Vol. 11, No. 5, 2007, pp. 797–817. doi:10.1016/j.rser.2005.06.005
[12] Godson, L., Raja, B., Mohan Lal, D., and Wongwises, S., "Enhancement of Heat Transfer Using Nanofluids—An Overview," *Renewable and Sustainable Energy Reviews*, Vol. 14, No. 2, 2009, pp. 629–641. doi:10.1016/j.rser.2009.10.004
[13] Saidur, R., Leong, K. Y., and Mohammad, H. A., "A Review on Applications and Challenges of Nanofluids," *Renewable and Sustainable Energy Reviews*, Vol. 15, No. 3, 2011, pp. 1646–1668. doi:10.1016/j.rser.2010.11.035
[14] Khanafer, K., and Vafai, K., "A Critical Synthesis of Thermophysical Characteristics of Nanofluids," *International Journal of Heat and Mass Transfer*, Vol. 54, Nos. 19–20, 2011, pp. 4410–4428. doi:10.1016/j.ijheatmasstransfer.2011.04.048
[15] Singh, P. K., Anoop, K. B., Sundararajan, T., and Das, S. K., "Entropy Generation Due to Flow and Heat Transfer in Nanofluids," *International Journal of Heat and Mass Transfer*, Vol. 53, Nos. 21–22, 2010, pp. 4757–4767. doi:010.1016/j.ijheatmasstransfer.2010.06.016
[16] Li, J., and Kleinstreuer, C., "Entropy Generation Analysis for Nanofluid Flow in Microchannels," *Journal of Heat Transfer*, Paper 122401, Vol. 132, No. 12, 2010
[17] Feng, Y., and Kleinstreuer, C., "Nanofluid Convective Heat Transfer in a Parallel-Disk System," *International Journal of Heat and Mass Transfer*, Vol. 53, No. 21–22, 2010, pp. 4619–4628. doi:10.1016/j.ijheatmasstransfer.2010.06.031
[18] Moghaddami, M., Mohammadzade, A., and Varzane Esfehani, S. A., "Second Law Analysis of Nanofluid Flow," *Energy Conversion and Management*, Vol. 52, No. 2, 2011, pp. 1397–1405. doi:10.1016/j.enconman.2010.10.002
[19] Shahi, M., Mahmoudi, A. H., and Raouf, A. H., "Entropy Generation Due to Natural Convection Cooling of a Nanofluid," *International Communications in Heat and Mass Transfer*, Vol. 38, No. 7, 2011, pp. 972–983. doi:10.1016/j.icheatmasstransfer.2011.04.008
[20] Esmaeilpour, M., and Abdollahzadeh, M., "Free Convection and Entropy Generation of Nanofluid Inside an Enclosure with Different Patterns of Vertical Wavy Walls," *International Journal of Thermal Sciences*, Vol. 52, 2012, pp. 127–136. doi:10.1016/j.ijthermalsci.2011.08.019
[21] Bianco, V., Nardini, S., and Manca, O., "Enhancement of Heat Transfer and Entropy Generation Analysis of Nanofluids Turbulent Convection Flow in Square Section Tubes," *Nanoscale Research Letters*, Vol. 6, 2011, p. 252. doi:10.1186/1556-276X-6-252
[22] Falahat, A., and Vosough, A., "Effect of Nanofluid on Entropy Generation and Pumping Power in Coiled Tube," *Journal of Thermophysics and Heat Transfer*, Vol. 26, No. 1, 2012, pp. 141–146. doi:10.2514/1.T3771
[23] Yilbas, B. S., "Entropy Analysis of Concentric Annuli with Rotating Outer Cylinder," *International Journal of Exergy*, Vol. 1, No. 1, 2001, pp. 60–66. doi:10.1016/S1164-0235(01)00011-5
[24] Mahmud, S., and Fraser, R. A., "Second Law Analysis of Heat Transfer and Fluid Flow Inside a Cylindrical Annular Space," *International Journal of Exergy*, Vol. 2, No. 4, 2002, pp. 322–329. doi:10.1016/S1164-0235(02)00078-X
[25] Mahmud, S., and Fraser, R. A., "Analysis of Entropy Generation Inside Concentric Cylindrical Annuli with Relative Rotation," *International Journal of Thermal Sciences*, Vol. 42, No. 5, 2003, pp. 513–521. doi:10.1016/S1290-0729(02)00051-0
[26] Mirzazadeh, M., Shafaei, A., and Rashidi, F., "Entropy Analysis for Non-Linear Viscoelastic Fluid in Concentric Rotating Cylinders," *International Journal of Thermal Sciences*, Vol. 47, No. 12, 2008, pp. 1701–1711. doi:10.1016/j.ijthermalsci.2007.11.002
[27] Jery, A. E., Hidouri, N., Magherbi, M., and Brahim, A. B., "Effect of an External Oriented Magnetic Field on Entropy Generation in Natural Convection," *Entropy*, Vol. 12, No. 6, 2010, pp. 1391–1417. doi:10.3390/e12061391
[28] Salas, H., Cuevas, S., and Haro, M. L., "Entropy Generation Analysis of Magnetohydrodynamic Induction Devices," *Journal of Physics D: Applied Physics*, Vol. 32, No. 20, 1999, pp. 2605–2608. doi:10.1088/0022-3727/32/20/304
[29] Ibanez, G., Cuevas, S., and Haro, M. L., "Optimization Analysis of an Alternate Magnetohydrodynamic Generator," *Energy Conversion and Management*, Vol. 43, No. 14, 2002, pp. 1757–1771. doi:10.1016/S0196-8904(01)00133-9
[30] Mahmud, S., Tasnim, S. H., and Mamun, M. A. H., "Thermodynamic Analysis of Mixed Convection in a Channel with Transverse Hydromagnetic Effect," *International Journal of Thermal Science*, Vol. 42, No. 8, 2003, pp. 731–740. doi:10.1016/S1290-0729(03)00040-1
[31] Tasnim, S. H., Mahmud, S., and Mamun, M. A. H., "Entropy Generation in a Porous Channel with Hydromagnetic Effect," *Energy*, Vol. 2, No. 4, 2002, pp. 300–308. doi:10.1016/S1164-0235(02)00065-1
[32] Mahmud, S., and Fraser, R. A., "Mixed Convection-Radiation Interaction in a Vertical Porous Channel: Entropy Generation," *Energy*, Vol. 28, No. 15, 2003, pp. 1557–1577. doi:10.1016/S0360-5442(03)00154-3
[33] Mahmud, S., and Fraser, R. A., "Magnetohydrodynamic Free Convection and Entropy Generation in a Square Porous Cavity," *International Journal of Heat and Mass Transfer*, Vol. 47, Nos. 14–16, 2004, pp. 3245–3256. doi:10.1016/j.ijheatmasstransfer.2004.02.005
[34] Ibanez, G., and Cuevas, S., "Optimum Wall Conductance Ratio in Magnetoconvective Flow in a Long Vertical Rectangular Duct," *International Journal of Thermal Science*, Vol. 47, No. 8, 2008, pp. 1012–1019. doi:10.1016/j.ijthermalsci.2007.09.003
[35] Mahmud, S., and Fraser, R. A., "The Thermoacoustic Irreversibility for a Single-Plate Thermoacoustic System," *International Journal of Heat and Mass Transfer*, Vol. 49, Nos. 19–20, 2006, pp. 3448–3461. doi:10.1016/j.ijheatmasstransfer.2006.02.051
[36] Ibanez, G., and Cuevas, S., "Optimum Wall Conductance Ratio in Magnetoconvective Flow in a Long Vertical Rectangular Duct," *International Journal of Thermal Science*, Vol. 47, No. 8, 2008, pp. 1012–1019. doi:10.1016/j.ijthermalsci.2007.09.003
[37] Arikoglu, A., Ozkol, I., and Komurgoz, G., "Effect of Slip on Entropy Generation in a Single Rotating Disk in MHD Flow," *Applied Energy*, Vol. 85, No. 12, 2008, pp. 1225–1236. doi:10.1016/j.apenergy.2008.03.004
[38] Ibanez, G., and Cuevas, S., "Entropy Generation Minimization of a MHD (Magnetohydrodynamic) Flow in a Microchannel," *Energy*, Vol. 35, No. 10, 2010, pp. 4149–4155. doi:10.1016/j.energy.2010.06.035

[39] Mansour, R. B., Galanis, N., and Nguyen, C. T., "Effect of Uncertainties in Physical Properties on Forced Convection Heat Transfer with Nanofluids," *Applied Thermal Engineering*, Vol. 27, No. 1, 2007, pp. 240–249. doi:10.1016/j.applthermaleng.2006.04.011
[40] Jiji, L. M., *Heat Convection*, Springer-Verlag, Berlin, 2006.
[41] Duangthongsuk, W., and Wongwises, S., "Measurement of Temperature-Dependent Thermal Conductivity and Viscosity of TiO_2 Water Nanofluids," *Experimental Thermal and Fluid Science*, Vol. 33, No. 4, 2009, pp. 706–714. doi:10.1016/j.expthermflusci.2009.01.005
[42] Paoletti, S., Rispoli, F., and Sciubba, E., "Calculation of Exergetic Losses in Compact Heat Exchanger Passages," *American Society of Mechanical Engineers, Advanced Energy Systems Division*, Vol. 10, No. 2, 1980, pp. 21–29.
[43] White, F. M., *Viscous Fluid Flow*, McGraw–Hill, New York, 1974.

HVAC&R Research (2013) **19**, 159–174

ISSN: 1078-9669 print / 1938-5587 online
DOI: 10.1080/10789669.2012.751812

Taylor & Francis
Taylor & Francis Group

Numerical simulation of refrigerants flowing through short-tube orifices during flashing process

KITTI NILPUENG[1,2] and SOMCHAI WONGWISES[2,3,*]

[1]*Department of Mechanical Engineering, South East Asia University, Bangkok 10160, Thailand*
[2]*Fluid Mechanics, Thermal Engineering and Multiphase Flow Research Lab (FUTURE), Department of Mechanical Engineering, Faculty of Engineering, King Mongkut's University of Technology Thonburi, Bangmod, Bangkok 10140, Thailand*
[3]*The Academy of Science, The Royal Institute of Thailand, Sanam Suea Pa, Dusit, Bangkok 10300, Thailand*

A numerical simulation for calculating the flashing flow characteristics of refrigerants inside short-tube orifices is presented. The refrigerant flow behaviors along short-tube orifices are separated into three sections: subcooled liquid region, metastable liquid region, and two-phase region. Annular two-phase flow pattern is developed from the mass, energy, and momentum equation. The present simulation is corroborated by comparison with the experimental data. The selection charts are also presented to estimate the refrigerant mass flow rate along short-tube orifices in practical applications.

Introduction

Expansion device is one of four main parts of refrigeration system. The functions are two-fold: (1) to reduce the refrigerant pressure from high pressure in condenser to low pressure in evaporator and (2) to control the refrigerant flow rate from the condenser to the evaporator. Short-tube orifice is a constant-restriction type of expansion device commonly used in domestic and automobile air conditioners. It is a short and narrow tube with length-to-diameter ratio of 3–20 and lengths of 10–13 mm (0.394–0.512 in.) for domestic air conditioners. Length-to-diameter ratio and diameter of short-tube orifices are 21–35 mm (0.827–1.378 in.) and 1–2 mm (0.039–0.079 in.) for automobile air conditioners (ASHRAE 1998). The benefits of using short-tube orifices are low starting torque of the compressor, high reliability, low cost, and simplicity. However, it is found that to obtain the optimum air conditioner performance, the refrigerant flow inside the short-tube orifice should be choked. Moreover, after the size of a short-tube orifice is selected to install into an air-conditioning system, it will be suitable for only one design condition. This means that the refrigerant flow rate and pressure drop cannot be satisfied under different operating conditions. Therefore, a design tool for estimating the refrigerant mass flow rate along the short-tube orifice at a given operating condition is very necessary.

During the past decades, the numerical analysis on the refrigerant flashing flow through short-tube orifices has been reported in the publications. It is separated into two classifications: semi-empirical models and theoretical models. Semi-empirical models are generated in the form of simple equations with the correction factor created from experimental data. It was found that a single-phase orifice equation (ASME 1971) has been proposed by most previous researchers as follows:

$$\dot{m} = CA\sqrt{\frac{2\rho(P_{up} - P_{down})}{(1-\beta^4)}}. \tag{1}$$

As shown in Equation 1, it was found that the mass flow rate was a function of downstream pressure (P_{down}), upstream pressure (P_{up}), short-tube orifice flow area (A), upstream density (ρ), and the orifice diameter-to-tube diameter ratio (β). The correction factor, which was combined in the single-phase orifice equation, was presented into two forms: orifice constant correlation (C) and downstream pressure correlation. The first one was dependent on the difference of upstream pressure and downstream pressure, downstream vapor quality, ratio of length to diameter, and degree of subcooling (Mei 1982; Pasqua 1953; Tu et al. 2006). The other one was dependent on the ratio of length to diameter, upstream temperature, downstream pressure, and upstream pressure (Aaron and Domanski 1990; Kim 1993; Kim et al. 2002; Liu et al. 2004). A generalized mass flow rate correlation of alternative refrigerant through short-tube orifices was proposed in few publications (Choi et al. 2004). The correlation in power law form, which was included with dimensionless parameters, was generated and proposed. Buckingham Pi theorem was used to create the dimensionless parameters.

Although the semi-empirical models can be used to calculate the refrigerant mass flow rate through short-tube orifices, they cannot be used to indicate the physical meaning of refrigerant flow mechanism; the accuracy of the models are valid only over the testing conditions. Therefore, theoretical

Received June 14, 2012; accepted November 9, 2012
Kitti Nilpueng, D.Eng, is lecturer and researcher. **Somchai Wongwises, PhD, Dr-Ing**, is professor.
*Corresponding author e-mail: somchai.won@kmutt.ac.th

models have been proposed to simulate the characteristic of refrigerant through short-tube orifice by some researchers. Eight critical flow models were compared with the experimental data of HCFC-22 and HFC-134a by Kim and O'Neal (1995). These models were divided into three classes: homogeneous equilibrium models (HEMs), nonhomogeneous equilibrium models (NEMs), and homogeneous frozen models (HFMs). A comparison between the experimental data and calculated results of models showed that the HFM gave the best agreement except at outlet qualities below 0.06. A nonequilibrium two-fluid model, which consisted of mass, momentum, and energy equations for each phase, was represented for predicting the refrigerant flow behavior through short-tube orifices by Yang and Zhang (2005). Based on the measured mass flow rates of HFC-134a, CFC-12, HCFC-22, HFC-410A, and HFC-407C, it was found that the two-fluid model gave an acceptable prediction with a deviation of $\pm 20\%$. However, in the case of supercritical carbon dioxide (CO_2), Zhang and Yang (2005) reported that the difference of interphase temperature and velocity in two-phase region between gas and liquid were small. Therefore, the nonhomogeneous and nonequilibrium flow behavior inside the short-tube orifice was insignificant. They also concluded that the accuracy of the two-fluid model was similar to that of the HEM. The fluid-dynamic flow characteristic of CO_2 through short-tube orifices was simulated by Garcia-Valladares (2006). He developed the governing equations from the continuity equation, energy equation, entropy equation, and momentum equation. The simulation has been solved by a finite volume formulation. The numerical results showed good acceptance with the measured results.

As mentioned above, it is observed that the theoretical model is more attractive than the semi-empirical model because it can show the physical meaning of the refrigerant along the short-tube orifice. However, the theoretical model is rather difficult to solve when it includes the complicated equations and correlations. As a result, only a few research works have been reported and it is still not clear which one is the best.

The objective of this research work is to develop the numerical model for estimating the flashing flow of refrigerant along the short-tube orifice. The assumptions of metastable liquid flow and annular flow pattern in a two-phase section are applied in this model. The numerical results of refrigerant flow rate and distribution of pressure inside a short tube orifice are verified with the experimental data. Moreover, the short-tube orifice selection charts are presented to estimate the refrigerant mass flow rate along short-tube orifices in practical applications.

Mathematical modeling

The refrigerant flow behavior inside a short-tube orifice is shown diagrammatically in Figure 1. It is separated into three sections: subcooled liquid region, metastable liquid region, and two-phase region. To simulate the refrigerant flow behavior along the short-tube orifice, a present model is developed from the mass, energy, and momentum equation with the following assumptions:

- one dimensional steady flow;
- adiabatic flow; and
- the short-tube orifice diameter and surface roughness is constant.

Subcooled liquid region

As shown in Figure 1, the steady flow energy equation for subcooled liquid region (points 1–3) can be expressed as:

$$\frac{P_1}{\rho_1 g} + \frac{V_1^2}{2g} + z_1 = \frac{P_3}{\rho_3 g} + \frac{V_3^2}{2g} + z_3 + h_L. \tag{2}$$

For an incompressible fluid ($\rho_2 \cong \rho_3 = \rho_L$), the continuity equation is written as:

$$\dot{m} = \rho_2 V_2 A = \rho_3 V_3 A = \rho V A, \tag{3}$$

where h_L is the head loss due to the sudden contraction and friction of the tube wall. It is determined by the following equation:

$$h_L = k\frac{V^2}{2g} + f_{sp}\frac{L}{D}\frac{V^2}{2g}, \tag{4}$$

where k is the entrance loss coefficient and f_{sp} is the friction factor for single-phase flow. It is calculated from the Colebrook

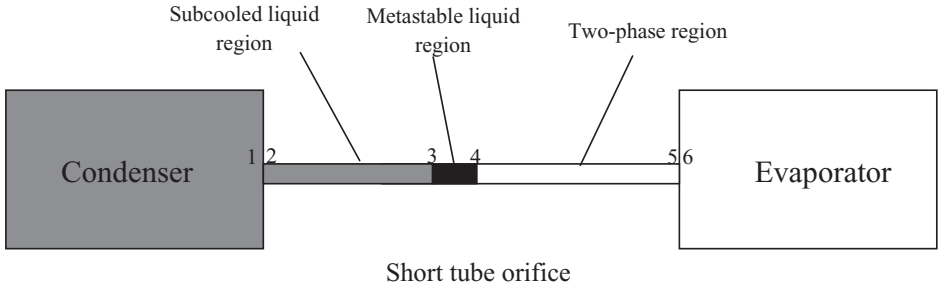

Fig. 1. Schematic diagram a short-tube orifice (color figure available online).

formula as follows:

$$\frac{1}{\sqrt{f_{sp}}} = 1.14 - 2\log\left[\frac{\varepsilon}{D} + \frac{9.3}{\mathrm{Re}\sqrt{f_{sp}}}\right], \quad (5)$$

where

$$\mathrm{Re} = \rho V D/\mu. \quad (6)$$

For a horizontal short-tube orifice ($z_2 = z_3$), substituting Equation 4 into Equation 2, the subcooled liquid length can be estimated from:

$$L_{sub} = \left[(P_1 - P_3)\frac{2}{\rho V^2} - (k+1)\right]\frac{D}{f_{sp}}, \quad (7)$$

where P_3 is the saturation pressure corresponding to the upstream temperature.

Metastable liquid region

The experimental data from prior studies (Kim 1993; Nilpueng and Wongwises 2009) show that even the pressure was decreased lower than the saturation pressure; the refrigerant inside the short-tube orifice was liquid. This indicates that the inception of vaporization is delayed. This flow phenomenon is defined as metastable liquid flow. Considering the length of the metastable liquid region (points 3–4) in Figure 1, it can be calculated based on the steady flow energy equation as follows:

$$L_{mt} = \left[\frac{2}{\rho V^2}(P_3 - P_4)\right]\frac{D}{f_{sp}}, \quad (8)$$

where P_4 is the actual pressure of vaporization. In this model, two empirical correlations of actual pressure of vaporization (P_υ) are applied as follows:

- *Chen et al. correlation* (Chen et al. 1990):
  The Chen et al. correlation was developed based on the flow of R12 through capillary tubes for predicting the actual pressure of vaporization. In this study, it is applied as follows:

$$\frac{(P_s - P_\upsilon)\sqrt{kT_s}}{\sigma^{3/2}} = 0.679\left(\frac{\upsilon_G}{\upsilon_G - \upsilon_L}\right)\mathrm{Re}^{0.914} \times \left(\frac{\Delta T_{sub}}{T_c}\right)^{-0.208}\left(\frac{D}{D'}\right)^{-3.18}, \quad (9)$$

  where D' is the reference length ($\sqrt{kT_s/\sigma}\times 10^4$), T_c is the refrigerant critical temperature, and k is the Boltzman constant (1.380662×10^{-23}). The thermodynamic properties are determined at saturation condition.
- *Lackme correlation* (Lackme 1979):

$$P_\upsilon = k_1 P_s, \quad (10)$$

  where the average value of k_1 ($k_1 = 0.93$) is applied in this study.

Two-phase region

The model is developed from the separated flow model presented by Collier and Thome (1996). The flow pattern of the vapor core is covered by the liquid film (annular flow) is applied in this model (Wongwises and Suchatawat 2002). The governing equations of annular flow are developed from the mass, energy, and momentum equation. The continuity equation for two-phase flow is presented in the following relationship:

$$\frac{d\dot{m}_L}{dz} + \frac{d\dot{m}_G}{dz} = \frac{d\dot{m}}{dz} = 0. \quad (11)$$

The momentum equation for each phase can be expressed as:

$$\frac{d(\dot{m}_L V_L)}{dz} = -\tau_{Lw}C_{Lw} + \tau_i C_i - A_L\frac{dP}{dz} + V_L\frac{d\dot{m}_L}{dz}, \quad (12)$$

$$\frac{d(\dot{m}_G V_G)}{dz} = -\tau_i C_i - A_G\frac{dP}{dz} + V_G\frac{d\dot{m}_G}{dz}. \quad (13)$$

The momentum transfer between liquid and vapor is:

$$\tau_i C_i + V_L\frac{d\dot{m}_L}{dz} - \tau_i C_i + V_G\frac{d\dot{m}_G}{dz} = 0. \quad (14)$$

Combining Equations 12 and 13 by using the relation of the momentum transfer between liquid and vapor (Equation 14), the following is obtained:

$$\frac{d(\dot{m}_L V_L + \dot{m}_G V_G)}{dz} = -\tau_{Lw}C_{Lw} - (A_L + A_G)\frac{dP}{dz}. \quad (15)$$

If Equation 15 is rearranged with the following basic relationships:

$$G = \frac{\dot{m}}{A} = \rho V = \frac{V}{\upsilon}, \quad \dot{m}_G = GAx, \dot{m}_L = GA(1-x),$$
$$\alpha = \frac{A_G}{A}, (1-\alpha) = \frac{A_L}{A}, \quad V_G = \frac{Gx}{\rho_G\alpha}, V_L = \frac{G(1-x)}{\rho_L(1-\alpha)},$$

then it can be written as:

$$-\left(\frac{dP}{dz}\right) = \frac{\tau_{Lw}C_{Lw}}{A} + G^2\frac{d}{dz}\left[\frac{x^2\upsilon_G}{\alpha} + \frac{(1-x)^2\upsilon_L}{(1-\alpha)}\right]. \quad (16)$$

The two-phase frictional pressure gradient is calculated by using the Lockhart Martinelli correlation as follows:

$$\left(\frac{dP_F}{dz}\right)_{TP} = \frac{\tau_{Lw}C_{Lw}}{A} = \phi_L^2\left(\frac{dP_F}{dz}\right)_L. \quad (17)$$

The two-phase multiplier is:

$$\phi_L^2 = 1 + \frac{C}{X} + \frac{1}{X^2}. \quad (18)$$

The value of constant C depends on the flow condition of the gas and liquid phase. It is varied from 5 to 20. The Martinelli parameter can be expressed as:

$$X^2 = \frac{(dP_F/dz)_L}{(dP_F/dz)_G}, \tag{19}$$

when

$$\left(\frac{dP_F}{dz}\right)_L = \frac{2f_L G_L^2}{\rho_L D}, \tag{20}$$

$$\left(\frac{dP_F}{dz}\right)_G = \frac{2f_G G_G^2}{\rho_G D}. \tag{21}$$

The void fraction is expressed in the following equation:

$$\alpha = \frac{x\upsilon_G}{(1-x)\upsilon_L S + x\upsilon_G}. \tag{22}$$

In this equation, three empirical correlations of slip ratio, which are used to indicate the difference between liquid and vapor velocities, are considered as follows:

- *Chisholm correlation* (Chisholm 1973):

$$S = \left[1 - x\left(1 - \frac{\rho_L}{\rho_G}\right)\right]^{1/2}. \tag{23}$$

- *Miropolskiy et al.* correlation (Miropolskiy et al. 1970):

$$S = 1 - \frac{13.5(1 - P/P_c)}{Fr_L^{5/12}\mathrm{Re}_L^{1/6}}, \tag{24}$$

where

$$Fr_L = G^2\upsilon_L^2/gD \quad \text{and} \quad \mathrm{Re}_L = GD/\mu_L.$$

- *Zivi correlation* (Zivi 1964):

$$S = \left(\frac{\rho_L}{\rho_G}\right)^{1/3}. \tag{25}$$

As shown in Equation 16, the accelerational pressure gradient, which is the last term of the equation, can be expanded as:

$$\begin{aligned}\frac{\mathrm{d}}{\mathrm{d}z}\left[\frac{x^2\upsilon_\mathrm{G}}{\alpha} + \frac{(1-x)^2\upsilon_\mathrm{L}}{(1-\alpha)}\right] &= \frac{\mathrm{d}x}{\mathrm{d}z}\left\{\left[\frac{2x\upsilon_\mathrm{G}}{\alpha} - \frac{2(1-x)\upsilon_\mathrm{L}}{(1-\alpha)}\right]\right.\\ &\left.+\left(\frac{\partial\alpha}{\partial x}\right)_P\left[\frac{(1-x)^2\upsilon_\mathrm{L}}{(1-\alpha)^2} - \frac{x^2\upsilon_\mathrm{G}}{\alpha^2}\right]\right\}\\ &+\frac{\mathrm{d}P}{\mathrm{d}z}\left\{\left[\frac{x^2}{\alpha}\frac{\mathrm{d}\upsilon_\mathrm{G}}{\mathrm{d}P} + \frac{(1-x)^2}{(1-\alpha)}\frac{\mathrm{d}\upsilon_\mathrm{L}}{\mathrm{d}z}\right]\right\}\\ &+\left(\frac{\partial\alpha}{\partial P}\right)_x\left[\frac{(1-x)^2\upsilon_\mathrm{L}}{(1-\alpha)^2} - \frac{x^2\upsilon_\mathrm{G}}{\alpha^2}\right].\end{aligned} \tag{26}$$

Therefore, Equation 16 can be expressed as:

$$A_1\left(-\frac{\mathrm{d}P}{\mathrm{d}z}\right) - A_2\left(\frac{\mathrm{d}x}{\mathrm{d}z}\right) = B_1, \tag{27}$$

where

$$\begin{aligned}A_1 &= 1 + G^2\left\{\left[\frac{x^2}{\alpha}\frac{\mathrm{d}\upsilon_\mathrm{G}}{\mathrm{d}P} + \frac{(1-x)^2}{(1-\alpha)}\frac{\mathrm{d}\upsilon_\mathrm{L}}{\mathrm{d}z}\right]\right.\\ &\left.+\left(\frac{\partial\alpha}{\partial P}\right)_x\left[\frac{(1-x)^2\upsilon_\mathrm{L}}{(1-\alpha)^2} - \frac{x^2\upsilon_\mathrm{G}}{\alpha^2}\right]\right\},\\ A_2 &= G^2\left\{\left[\frac{2x\upsilon_\mathrm{G}}{\alpha} - \frac{2(1-x)\upsilon_\mathrm{L}}{(1-\alpha)}\right]\right.\\ &\left.+\left(\frac{\partial\alpha}{\partial x}\right)_P\left[\frac{(1-x)^2\upsilon_\mathrm{L}}{(1-\alpha)^2} - \frac{x^2\upsilon_\mathrm{G}}{x^2}\right]\right\},\\ B_1 &= \frac{\tau_{Lw}C_{Lw}}{A}.\end{aligned}$$

Based on the assumptions of adiabatic flow, steady state steady flow, no energy transfer by work, and horizontal short-tube orifice, the liquid and vapor energy equations are expressed as:

$$\begin{aligned}\frac{d}{dz}\left[\dot{m}_L\left(h_L + \frac{V_L^2}{2}\right)\right] &= -q''_{Lw}C_{Lw} + q''_i C_i + \tau_i V_i C_i\\ &+\left(h_L + \frac{V_L^2}{2}\right)\frac{d\dot{m}_L}{dz},\end{aligned} \tag{28}$$

$$\begin{aligned}\frac{d}{dz}\left[\dot{m}_G\left(h_G + \frac{V_G^2}{2}\right)\right] &= -q''_i C_i - \tau_i V_i C_i\\ &+\left(h_G + \frac{V_G^2}{2}\right)\frac{d\dot{m}_G}{dz}.\end{aligned} \tag{29}$$

At the interface between liquid and vapor, the conservation of energy is written as:

$$\begin{aligned}q''_i C_i + \tau_i V_i C_i + \left(h_L + \frac{V_L^2}{2}\right)\frac{d\dot{m}_L}{dz} - q_i C_i - \tau_i V_i C_i\\ +\left(h_G + \frac{V_G^2}{2}\right)\frac{d\dot{m}_G}{dz} = 0.\end{aligned} \tag{30}$$

Combining Equations 28 and 29 with using the relationship of energy at the interfacial (Equation 30), the following is obtained:

$$\frac{d}{dz}(\dot{m}_G h_G + \dot{m}_L h_L) + \frac{d}{dz}\left[\dot{m}_G\frac{V_G^2}{2} + \dot{m}_L\frac{V_L^2}{2}\right] = -q''_{Lw}C_{Lw}. \tag{31}$$

In this work, the energy transfer by heat from the tube wall to liquid film is neglected ($q''_{Lw} \approx 0$). This is because the axial conduction along the wall is very slight (Chisholm 1973).

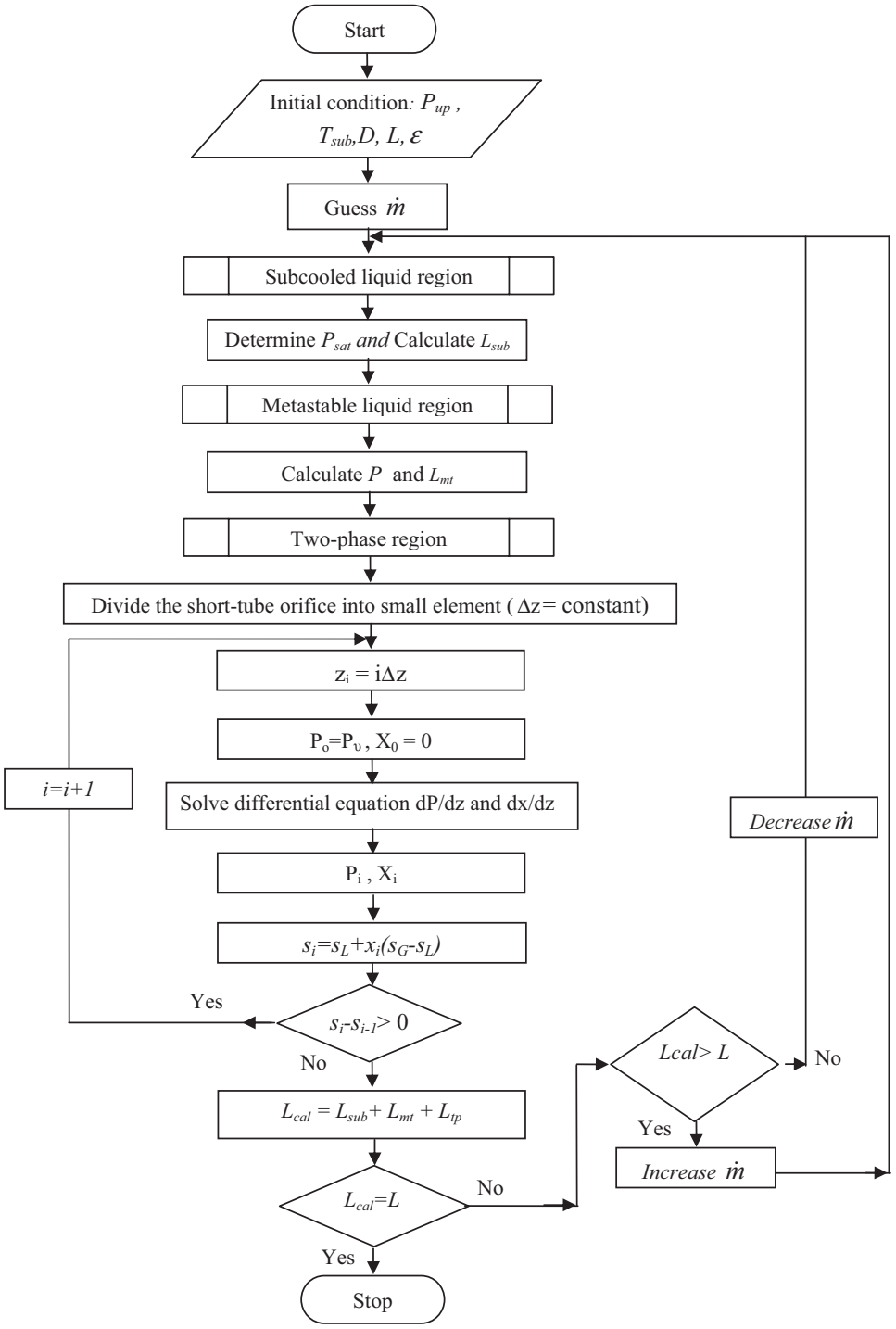

Fig. 2. Flow chart for calculating the critical mass flow rate inside short-tube orifice.

Substituting the basic two-phase relationship into Equation or 31, it can be expressed as:

$$\frac{d}{dz}\left[(GAx)h_G + GA(1-x)\,h_L\right] + \frac{1}{2}\frac{d}{dz}\left[GAx\,V_G^2 + GA(1-x)\,V_L^2\right] = 0 \qquad (32)$$

$$x\frac{dh_G}{dz} + h_G\frac{dx}{dz} + (1-x)\frac{dh_L}{dz} - h_L\frac{dx}{dz} + \frac{1}{2}\left[2xV_G\frac{dV_G}{dz} + V_G^2\frac{dx}{dz} + 2(1-x)V_L\frac{dV_L}{dz} - V_L^2\frac{dx}{dz}\right] = 0, \qquad (33)$$

Table 1. Testing conditions of the experimental data.

Refrigerant	Short-tube orifice diameter (mm)	Short-tube orifice diameter (in.)	Short-tube orifice length (mm)	Short-tube orifice length (in.)	Upstream pressure (kPa)	Upstream pressure (psi)	Degree of subcooling (°C)	Degree of subcooling (°F)	Downstream pressure (kPa)	Downstream pressure (psi)
HFC-134a										
• Kim (1993)	1.097–1.731	0.043–0.068	9.48–24.47	0.037–0.963	890–1459	129.1–211.6	2.8–13.9	5.04–25.02	310–483	44.9–70.1
• Singh et al. (2001)	1.22–1.71	0.048–0.067	13.1–38.4	0.515–1.512	1020–2140	147.9–310.4	0.6–24.5	1.08–44.1	3.4–5.2	49.3–75.4
• Nilpueng and Wongwises (2009)	0.961–1.2	0.037–0.047	10–20	0.394–0.787	900–1300	130.5–188.6	1–12	1.8–21.6	300–400	43.5–58.0
HFC-407C										
• Payne and O'Neal (1998)	1.097–1.94	0.043–0.076	12.68–25.39	0.499–0.999	1526–2273	221.3–329.6	0.28–11.28	0.50–20.3	630–770	91.4–111.7
HFC-410A										
• Payne and O'Neal (1999)	1.097–1.983	0.043–0.078	12.67–25.57	0.498–1.01	2130–3179	308.9–461.1	0.479–11.18	0.862–20.12	800–1100	116.0–159.5
• Kim et al. (2005)	1.097–1.799	0.043–0.071	12.7	0.5	2349–2617	340.7–379.6	1.792–11.03	3.225–19.85	772–1274	111.9–184.8

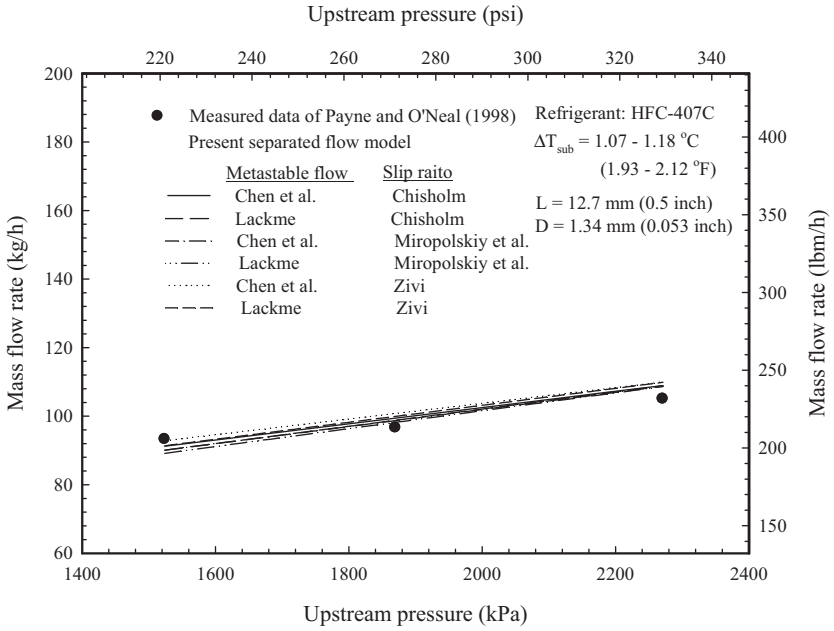

Fig. 3. Comparison of the numerical results with the measured mass flow rate at different upstream pressure.

where

$$\frac{dV_G}{dz} = G\left[\frac{x}{\alpha}\frac{d\upsilon_G}{dP}\frac{dP}{dz} + \frac{\upsilon_G}{\alpha}\frac{dx}{dz} - \frac{x\upsilon_G}{\alpha^2}\left(\left(\frac{\partial\alpha}{\partial P}\right)_x\frac{dP}{dz} + \left(\frac{\partial\alpha}{\partial x}\right)_p\frac{dx}{dz}\right)\right] \tag{34}$$

and

$$\frac{dV_L}{dz} = G\left\{\frac{1}{(1-\alpha)}\left[(1-x)\frac{d\upsilon_L}{dP}\frac{dP}{dz} - \upsilon_L\frac{dx}{dz}\right] + \frac{(1-x)\upsilon_L}{(1-\alpha)^2}\left[\left(\frac{\partial\alpha}{\partial P}\right)_x\frac{dP}{dz} + \left(\frac{\partial\alpha}{\partial x}\right)_p\frac{dx}{dz}\right]\right\}. \tag{35}$$

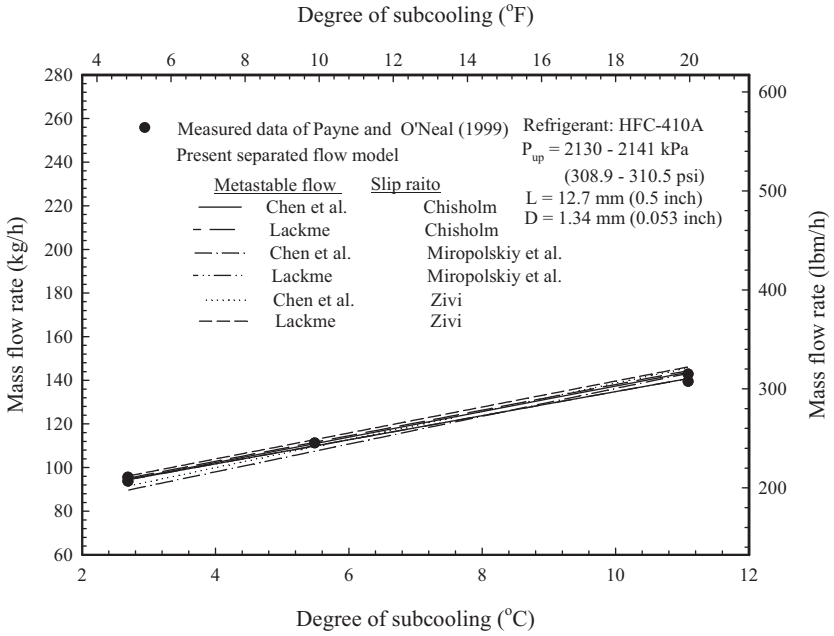

Fig. 4. Comparison of the numerical results with the measured mass flow rate at different degree of subcooling.

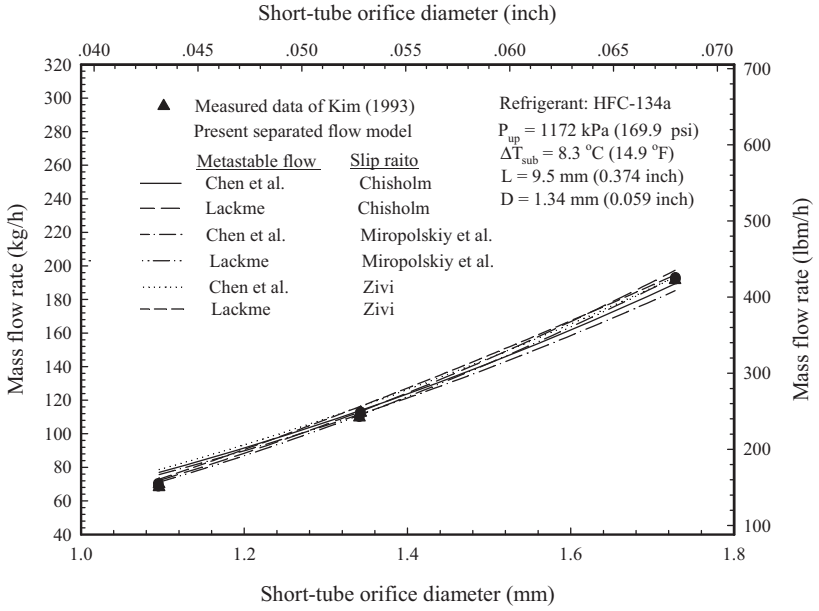

Fig. 5. Comparison of the numerical results with the measured mass flow rate at different short-tube orifice diameter.

Substituting Equations 34 and 35 into Equation 33 gives the following:

$$
\begin{aligned}
&(h_G - h_L)\frac{dx}{dz} + x\frac{dh_G}{dP}\frac{dP}{dz} + (1-x)\frac{dh_L}{dP}\frac{dP}{dz} + Gx\left(\frac{Gx\upsilon_G}{\alpha}\right)\\
&\times\left[\frac{x}{\alpha}\frac{d\upsilon_G}{dP}\frac{dP}{dz} + \frac{\upsilon_G}{\alpha}\frac{dx}{dz} - \frac{x\upsilon_G}{\alpha^2}\left(\left(\frac{\partial\alpha}{\partial P}\right)_x\frac{dP}{dz}\right.\right.\\
&\left.\left.+\left(\frac{\partial\alpha}{dx}\right)_p\frac{dx}{dz}\right)\right] + \frac{1}{2}\left[\frac{Gx\upsilon_G}{\alpha}\right]^2\frac{dx}{dz} + (1-x)G\\
&\times\left[\frac{G(1-x)\upsilon_L}{1-\alpha}\right]\left\{\frac{(1-x)}{(1-\alpha)}\frac{d\upsilon_L}{dP}\frac{dP}{dz} - \frac{\upsilon_L}{1-\alpha}\frac{dx}{dz}\right.\\
&\left.+\frac{(1-x)\upsilon_L}{(1-\alpha)^2}\left[\left(\frac{\partial\alpha}{\partial P}\right)_x\frac{dP}{dz} + \left(\frac{\partial\alpha}{\partial x}\right)_p\frac{dx}{dz}\right]\right\}\\
&-\frac{1}{2}\left[\frac{G(1-x)\upsilon_L}{1-\alpha}\right]^2\frac{dx}{dz} = 0. \qquad (36)
\end{aligned}
$$

Therefore, Equation 36 can be written as:

$$A_3\left(-\frac{dP}{dz}\right) - A_4\left(\frac{dx}{dz}\right) = B_2, \qquad (37)$$

where

$$
\begin{aligned}
A_3 = &\left\{x\frac{dh_G}{dP} + (1-x)\frac{dh_L}{dP} + \frac{G^2x^3\upsilon_G}{\alpha^2}\frac{d\upsilon_G}{dP}\right.\\
&+\frac{G^2(1-x)^3\upsilon_L}{(1-\alpha)^2}\frac{d\upsilon_L}{dP}\\
&\left.-\left[\frac{G^2x^3\upsilon_G^2}{\alpha^3} - \frac{G^2(1-x)^3\upsilon_L^2}{(1-\alpha)^3}\right]\left(\frac{\partial\alpha}{\partial P}\right)_x\right\},\\
A_4 = &\left\{(h_G - h_L) + \frac{3}{2}\frac{G^2x^2\upsilon_G^2}{\alpha^2} - \frac{3}{2}\frac{G^2(1-x)^2\upsilon_L^2}{(1-\alpha)^2}\right.\\
&\left.-\left[\frac{G^2x^3\upsilon_G^2}{\alpha^3} - \frac{G^2(1-x)^3\upsilon_L^2}{(1-\alpha)^3}\right]\left(\frac{\partial\alpha}{\partial x}\right)_P\right\}, \quad B_2 = 0.
\end{aligned}
$$

Table 2. Mean absolute deviations between measured and calculated mass flow rate with different correlations.

	Actual pressure of vaporization correlation	Slip ratio correlation	HFC-134a (%)	HFC-407C (%)	HFC-410A (%)
1.	Chen et al.	Chisholm	8.32	12.94	16.67
2.	Chen et al.	Miropolskiy et al.	8.89	12.45	16.16
3.	Chen et al.	Zivi	9.13	14.10	17.68
4.	Lackme	Chisholm	9.03	12.20	15.43
5.	Lackme	Miropolskiy et al.	9.02	11.74	14.83
6.	Lackme	Zivi	9.08	13.19	16.41

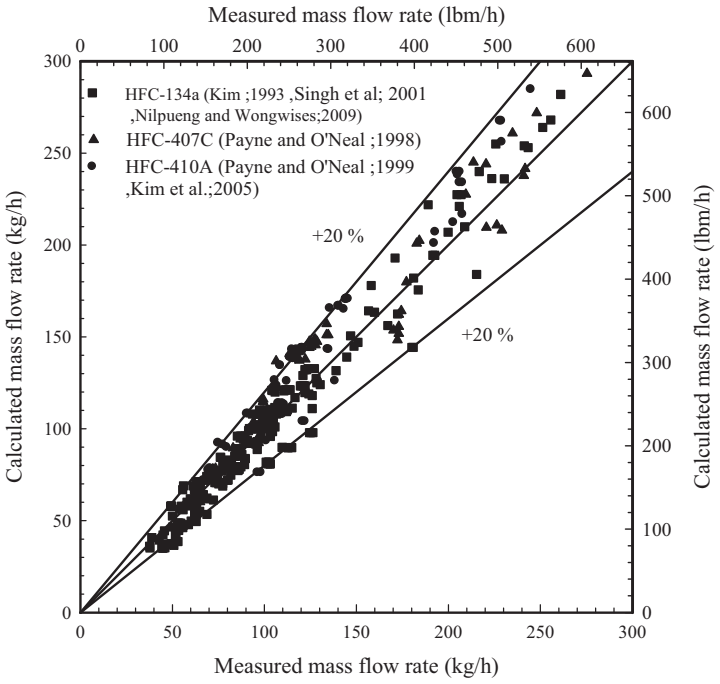

Fig. 6. Measured mass flow rateversus calculated massflow rate obtained from present model with Lackme (1979) and Miropolskiy et al. (1970) correlation.

According to Equations 27 and 37, the system of differential and equations is solved by the following equations:

$$-\frac{dP}{dz} = \frac{A_4 B_1 - A_2 B_2}{A_1 A_4 - A_2 A_3} \tag{38}$$

$$\frac{dx}{dz} = \frac{A_3 B_1 - A_1 B_2}{A_1 A_4 - A_2 A_3}. \tag{39}$$

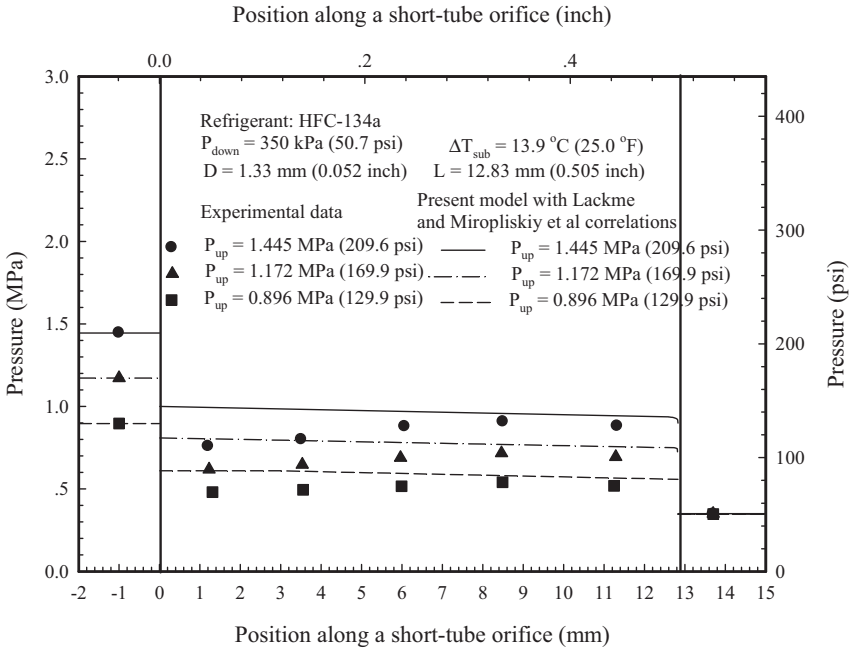

Fig. 7. Comparison of measured pressure distribution with numerical results at different upstream pressure.

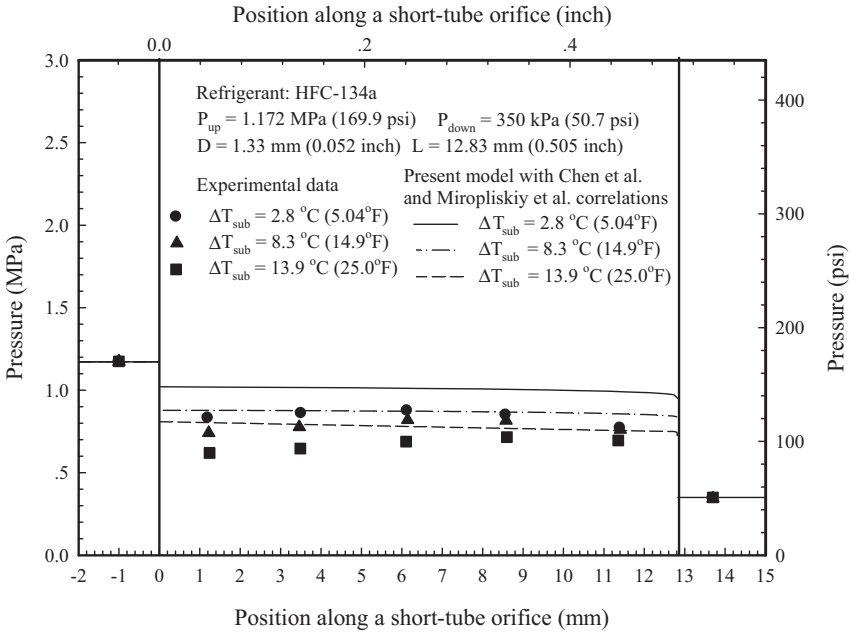

Fig. 8. Comparison of measured pressure distribution with numerical results at different degree of subcooling.

Solution method

The calculation procedure of the mass flow rate inside the short-tube orifice is presented by using the flow chart as shown in Figure 2. The thermodynamic properties and initial conditions, including upstream pressure, diameter, length, and degree of subcooling are specified. The thermodynamic properties of refrigerants are computed as a function of the pressure by using REFPROP (McLinden et al. 1998). As described above, the refrigerant flow behavior inside the short-tube orifice is separated into three sections, subcooled liquid region, metastable liquid region, and two-phase region. The surface roughness of drawn brass ($\varepsilon = 0.0000015$ m [0.0000049 ft.]) is assumed and used for Equation 5. To calculate the subcooled liquid length, the saturation pressure corresponding to the inlet temperature and friction factor obtained from the Colebrook equation are determined and applied into Equation 7. Similarly, the metastable liquid length is calculated by using Equation 8 with the correlation of actual pressure of vaporization. In this study, two correlations of actual vapor pressure obtained from Lackme (1979) and Chen et al. (1990) are considered. In the case of a two-phase region, short-tube orifice length is separated into numerous sections. The refrigerant pressure, which is calculated at the ending of the metastable liquid flow, is the initial condition of two-phase flow region. The fourth-order Runge-Kutta method is used to solve the system of differential equations, which are presented by Equations 38 and 39. The computation of each section is run until the choked flow phenomenon is appeared. Under choked flow condition, the refrigerant velocity reaches sonic speed and the entropy at the exit plane is equal to the maximum value. To verify the appearance of choked flow, the entropy increment at the exit plane of tube is inspected. That is, the choked flow occurs as the entropy increment is negative. The entropy of two-phase flow of each section can be estimated by:

$$s_i = s_L(1 - x_i) + s_G x_i. \tag{40}$$

After the choked flow appears, the length of the two-phase region can be calculated by:

$$L_{tp} = \Delta z n, \tag{41}$$

where n is number of sections. Therefore, the calculated length is the summation of lengths in the subcooled liquid region, metastable liquid region and two-phase flow:

$$L_{cal} = L_{sub} + L_{mt} + L_{tp}. \tag{42}$$

To obtain the critical mass flow rate under a given short-tube orifice length, the iteration procedure is done until the calculated length (L_{cal}) and the actual length are equal. That is, as the calculated length is higher than the actual length, the mass flow rate is increased. Conversely, the mass flow rate decreases when the calculated length is less than the actual length.

Results and discussion

To confirm the accuracy of the present model, the numerical results of mass flow rate and distribution of pressure inside the short-tube orifice are compared with the experimental data under choked flow conditions. The present model with three correlations of slip ratio (Chisholm 1973; Miropolskiy et al. 1970; Zivi 1964) and two correlations of actual pressure of vaporization (Chen 1990; Lackme 1979) are proved. The experimental data, which are used to validate the numerical results,

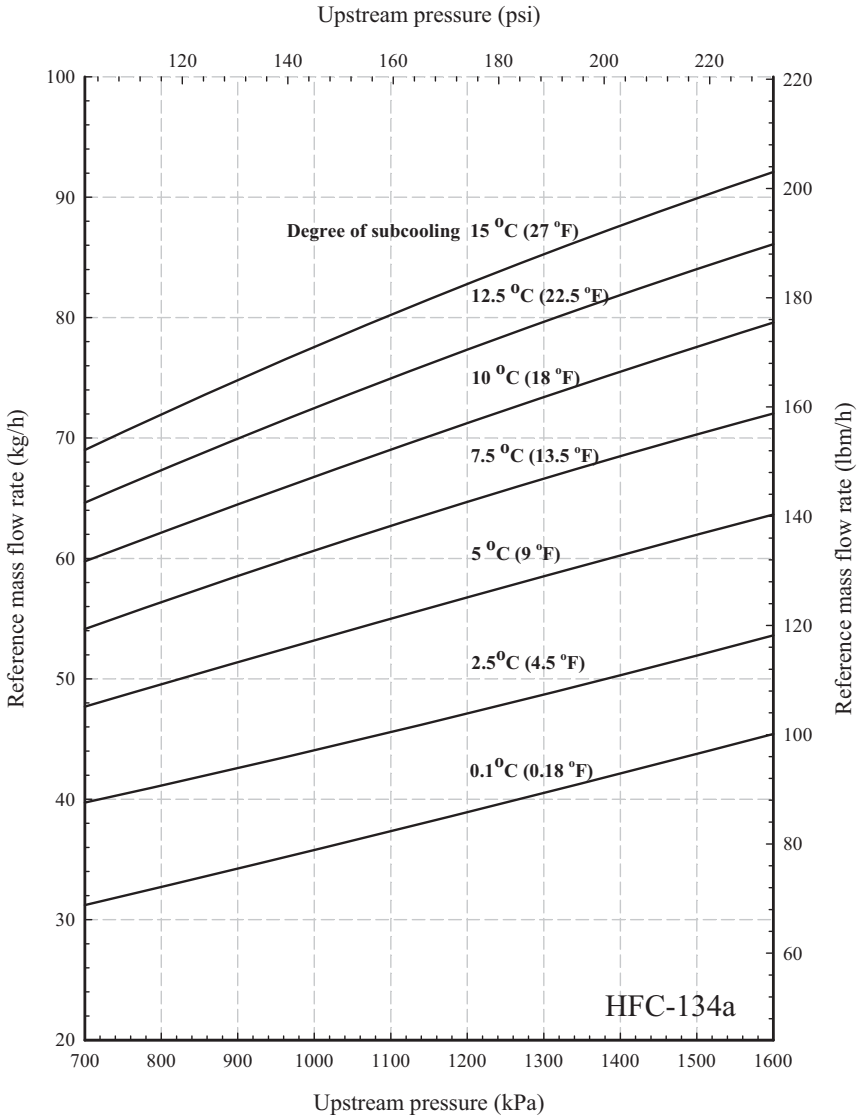

Fig. 9. Short-tube orifice selection chart generated from the present model for HFC-134a ($D = 1.1$ mm (0.043 in.) and $L = 12.7$ mm (0.5 in.)).

include 279 data points for HFC-134a (Kim 1993; Nilpueng and Wongwises 2009; Singh et al. 2001), 122 data points for HFC-407C (Payne and O'Neal 1998), and 95 data points for HFC-410A (Payne and O'Neal 1999; Kim et al. 2005). The testing conditions of experimental data are listed in Table 1.

The comparisons between the experimental and calculated mass flow rate at different upstream pressures are presented in Figure 3. It is found that the calculated results show good agreement with the experimental data, especially, the model with correlations of Lackme (1979) and Miropolskiy et al. (1970), which gives the MAD (mean absolute deviation) of 4.78%. It is also clear that the mass flow rate obtained from the present model increases in direct proportion as the upstream pressure is increased. This is because, based on the numerical results, the difference of pressure across the short-tube orifice is increased as the upstream pressure increases. This leads to an increase of mass flow rate. On the other hand, it is also observed that the upstream density is decreased when the upstream pressure is increased which results in the decrease of mass flow rate. However, the influence of the difference of pressure across the short-tube orifice dominates the influence of refrigerant density, which results in an increase of the refrigerant flow rate. In addition, based on the calculations in the present model, it is found that the prediction of underpressure (*Ps* - *Pv*) obtained from Lackme correlation is higher than that obtained from Chen correlation, about 42.5%.

Figure 4 shows the effect of degree of subcooling on the mass flow rate by comparing the experimental data with the numerical results. The tendency of calculated mass flow rate and experimental results is consistent. The prediction of the present model using Chen et al. (1990) and Miropolskiy et al. (1970) correlations gives the smallest mean absolute deviation (MAD), which is 1.32%. The numerical results indicate that the mass flow rate proportionally enhanced when the degree

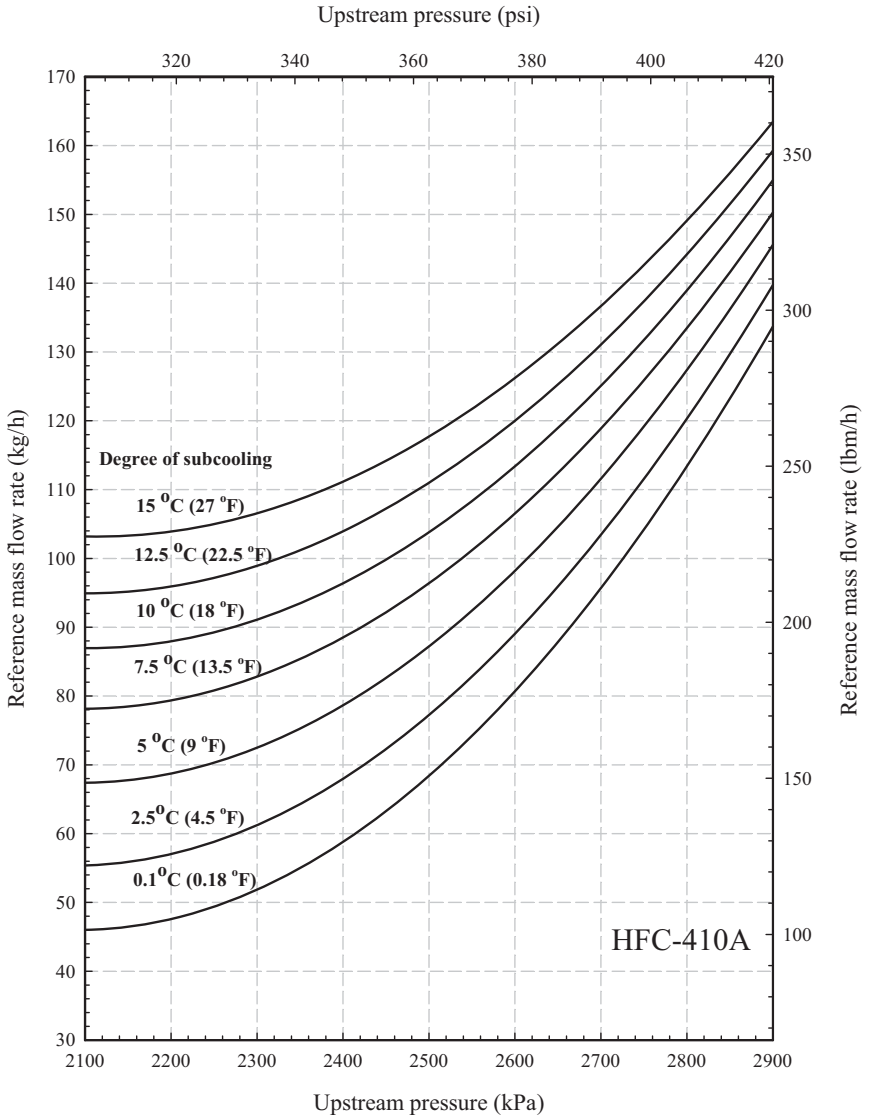

Fig. 10. Short-tube orifice selection chart generated from thepresent model for HFC-410A ($D = 1.1$ mm (0.043 in.) and $L = 12.7$ mm (0.5 in.)).

of subcooling increased. This is because the increase of degree of subcooling results in an increase of upstream density and the difference of pressure across the short-tube orifice, which results in an increase of mass flow rate.

The influence of short-tube orifice diameter on the mass flow rate is presented in Figure 5. It is found that the mass flow rate is strongly increased by enlarging short-tube orifice diameter. This is because the increase of diameter results in an increase of cross-sectional flow area. All of the calculated results give acceptable predictions compared with the measured data. However, the proposed model with Chen et al. (1990) and Miropolskiy et al. (1970) correlation shows the best prediction with MAD of 4.52%.

As mentioned above, the tendency of numerical results is estimated and compared with the experimental data at different sizes of short-tube orifice and working conditions. However, to verify the accuracy of the model at the same condition, the MAD between the numerical results and all experimental data is also examined. Based on the 496 data points of experimental results of HFC-134a, HFC-407C, and HFC-410A, the MAD of mass flow rate are estimated as showed in Table 2. It is found that the present model with Chen et al. (1990) and Chisholm (1973) gives the best prediction for HFC-134a, whereas the present model with Lackme (1979) and Miropolskiy et al. (1970) gives the best prediction for HFC-407C and HFC-410A. However, for all refrigerant types, the present model with the correlations of Lackme (1979) and Miropolskiy et al. (1970) shows the best calculation with MAD of 11.86%. In addition, the calculated results from the model with Lackme (1979) and Miropolskiy et al. (1970) correlations is compared with the measured mass flow rate (Figure 6). It is found that the present model can describe 98.2% of mass flow rate within

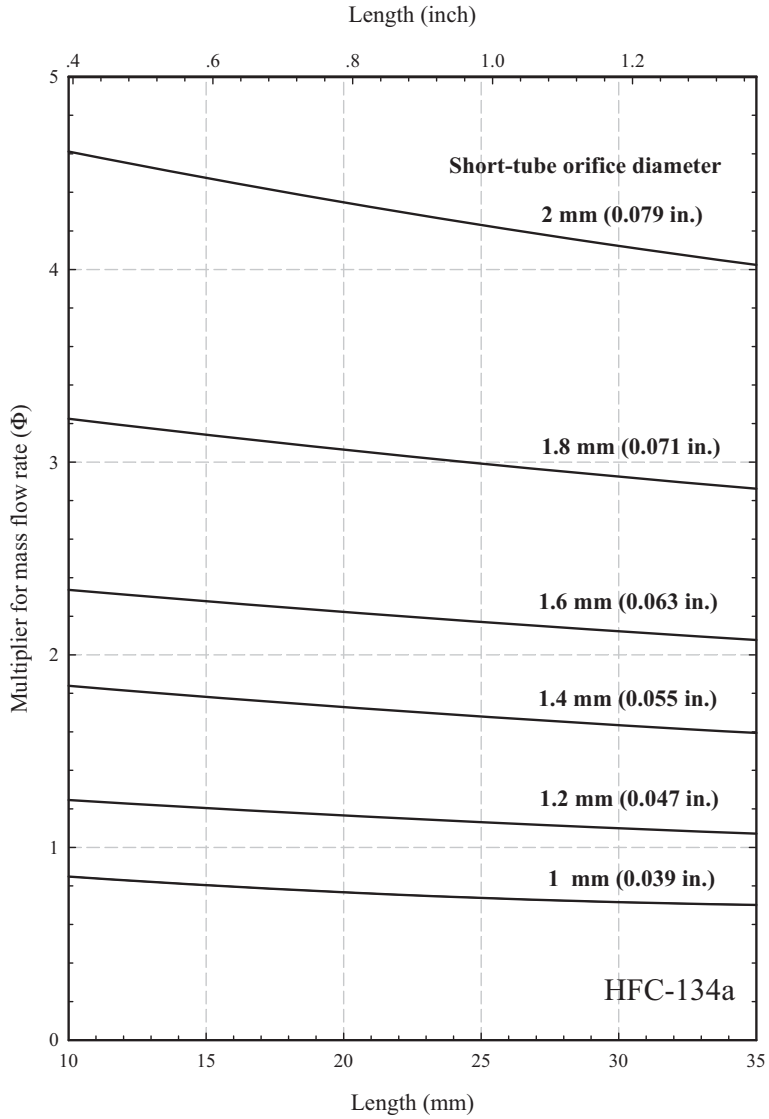

Fig. 11. Multiplier for mass flow rate to be applied to Figure 9 for other diameter and lengths of short-tube orifice.

±20%. Comparing the accuracy of this model with the two-fluid model (Yang and Zhang 2005), it is found that, for the two-fluid model, the relative deviations of 94% data are within 20%. This indicates that the relative deviation obtained from both models is similar. However, it can be noted that the two-fluid model is rather complicated when it is included with the six governing equations.

Figure 7 depicts the relationship between the pressure distribution and upstream pressure obtained from experimental data and the present model with the correlation of Lackme (1979) and Miropolskiy et al. (1970). The average of pressure distribution along the short-tube orifice is enhanced with increasing the upstream pressure. It is also discovered that the pressure decreases suddenly at the inlet, while it slightly increases over a short length and gradually decreases thereafter inside the short-tube orifice. This phenomenon indicates that the vena contracta occur inside the short tube- orifice. The reasons for the variation of pressure inside the short-tube are due to the increase of flow area after the vena contracta, and wall shear stress. In the model, the equation of head loss at the inlet section indicates the loss of flow due to sudden contraction after the refrigerant flow past the inlet section. However, the model does not include the flow behavior at the vena contracta. As a consequence, the variation of pressure obtained from numerical model is inconsistent with experimental results at the vena contracta, whereas it agrees with experimental results after the vena contracta. The large pressure drop at the outlet section can be explained by choked flow phenomenon. Under the choked flow condition, the pressure at the exit plane reaches the infinity value. In addition, the numerical results give an average overestimation of 9.54%. It is also found that the calculated mass flow rate shows good agreement with the experimental data with a MAD of 3.12%.

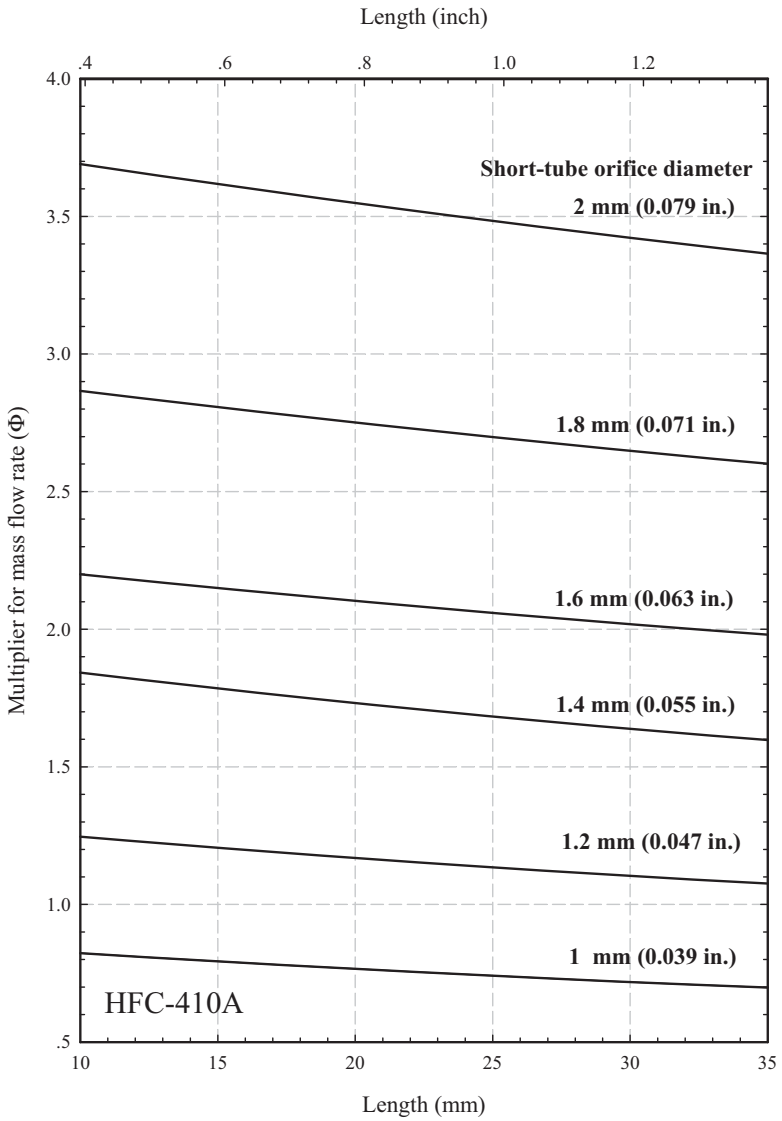

Fig. 12. Multiplier for mass flow rate to be applied to Figure 10 for other diameter and lengths of short-tube orifice.

The comparison of pressure distribution inside the short-tube orifice obtained from numerical and experimental results at different degrees of subcooling are shown in Figure 8. The present model gives an average over-prediction of 11.98%. It can be seen that the increase of degree of subcooling results in the decrease of average pressure along the short-tube orifice. This is due to, based on the numerical calculation, the difference of upstream and critical pressure, and upstream density is increased as the degree of sub-cooling is increased. These effects result in an increase of the refrigerant velocity. Therefore, the average refrigerant pressure along the short-tube orifice decreases. In addition, the predicted mass flow rate agrees well with the experimental data and gives the MAD of 2.64%.

In order to utilize the present numerical model in practical applications, the selection charts, which are generated for various condenser pressures and degree of sub-cooling at given short-tube orifice diameters and lengths, are presented for HFC-134a and HFC-410A. The proposed charts are similar to the rating chart for flow through capillary tube developed by ASHRAE (1998). For a short-tube orifice having a diameter of 1.1 mm (0.043 in.) and a length of 12.7 mm (0.5 in.), the mass flow rate can be estimated directly from selection charts (Figures 9 and 10) by specifying the condenser pressures and degree of subcooling. However, under the different size of diameter and length, the multiplier obtained from correction charts is required (Figures 11 and 12). Based on the proposed selection charts, the MAD of the mass flow rate is 9.48% and 16.04% for HFC-134a and HFC-410A, respectively.

Conclusion

The numerical simulation for calculating the flashing flow of refrigerant along the short-tube orifices is presented. The

precision of the present model is verified with 496 data points of experimental results of HFC-134a, HFC-407C, and HFC-410A. The results show that the calculated mass flow rate and pressure distribution through the short-tube orifice give reasonable agreement with the experimental data. The proposed model with the correlation of Lackme (1979) and Miropolskiy et al. (1970) shows the best prediction with MAD of 11.86%. This implied that the proposed model with appropriate correlations of slip ratio and actual vapor pressure can be used to calculate the refrigerant flow characteristic inside the short-tube orifice. Moreover, based on the present model with Lackme (1979) and Miropolskiy et al. (1970) correlations, the selection charts are also proposed to calculate the refrigerant mass flow rate along short-tube orifices.

Acknowledgments

The present study is supported by the Thailand Research Fund, the Office of the Higher Education Commission, and the National Research University Project whose guidance and assistance are gratefully acknowledged.

Nomenclature

A = cross section area of tube, m^2 (ft^2)
C = circumference of tube, m (ft)
D = diameter of tube, m (ft)
f = friction factor
g = gravitational acceleration, m/s^2 (ft/s^2)
G = mass flux, kg/m^2 s (lbm/ft^2 s)
h = specific enthalpy, J/kg (Btu/lbm)
L = length, m (lbm)
$\dot{m}$ = mass flow rate, kg/s (lbm/s)
P = pressure, Pa (psi)
q'' = heat flux, W/m^2 (Btu/lbm^2 h)
Re = Reynolds number
S = slip ratio
s = specific entropy, J/kg K (Btu/lbm ^oR)
T = temperature, K (^oR)
V = velocity, m/s (ft/s)
x = vapor quality
z = horizontal position, m (ft)

Greek symbols

α = void fraction
ε = wall roughness, m (ft)
μ = dynamic viscosity, kg/m s (lb s/ft^2)
ρ = density, kg/m^3 (lbm/ft^3)
σ = surface tension, N/m (lb/ft)
τ = shear stress, N/m^2 (lb/ft^2)
υ = specific volume, m^3/kg (ft^3/lbm)

Subscripts

G = vapor phase
L = liquid phase
in = inlet condition
i = liquid-vapor interface
Lw = liquid-wall interface
mt = metastable region
s = saturated condition
sp = single-phase
sub = subcooling
tp = two-phase
v = vaporization

References

Aaron, A.A.20, and P.A. Domanski. 1990. Experimentation analysis and correlation of refrigerant-22 flow through short tube restrictors. *ASHRAE Transactions* 96:729–42.

ASHRAE. 1998. *ASHRAE Handbook*—Refrigeration, chap. 45. Atlanta, GA: ASHRAE.

ASME. 1971. *Fluid Meters—Their Theory and Application*. New York: American Society of Mechanical Engineers.

Chen, Z.H., R.Y. Li, S.Lin, and Z.Y. Chen. 1990. A correlation for metastable flow of refrigerant 12 through capillary tubes. *ASHRAE Transactions* 96:550–4.

Chisholm, D. 1973. Pressure gradient due to friction during the flow of evaporating two-phase mixture in smooth tube and channel. *International Journal of Heat and Mass Transfer* 16:347–58.

Choi, J., J.T. Chung, and Y. Kim. 2004. A generalized correlation for two-phase flow of alternative refrigerants through short tube orifices. *International Journal of Refrigeration* 27:393–400.

Collier, J.G., and J.R. Thome. 1996. *Convective Boiling and Condensation, 3rd ed.* Oxford University Press, New York.

Garcia-Valladares, O. 2006. Numerical simulation of trans-critical carbon dioxide (R744) flow through short tube orifices. *Applied Thermal Engineering* 144–51.

Kim, Y. 1993. Two-phase flow of HFC134a and HCFC22 through short tube orifices. Ph.D. Thesis, Texas A&M University, College Station, TX.

Kim, Y., and D.L. O'Neal. 1995. A comparison of critical flow models for estimating two-phase flow of HCFC22 and HFC134a through short tube orifices. *International Journal of Refrigeration* 18:447–55.

Kim, Y.C., W.V. Payne, D.L. O'Neal, and M. Farzad. 2002. Refrigerant flow through flexible short tube orifices. *HVAC&Research* 8:179–90.

Kim, Y., V. Payne, J. Choi, and P. Domanski. 2005. Mass flow of R410A through short tube working near the critical point. *International Journal of Refrigeration* 28:547–53.

Lackme, C. 1979. Incompleteness of the flashing of supersaturated liquid and sonic ejection of the produced phases. *International Journal of Multiphase Flow* 5:131–41.

Liu, J.P., Y.M. Niu, J.P. Chen, Z.J. Chen, and X. Feng. 2004. Experimental and correlation of R744 two-phase flow through short tubes. *Experimental Thermal and Fluid Science* 28:565–73.

McLinden, M.O., S.A. Klein, and E.W. Lemmon. 1998. REFPROP-thermodynamic and transport properties of refrigerant and refrigerant mixtures. NIST Standard Reference Database, Version 6.01.

Mei, V.C. 1982. Short-tube refrigerant flow restrictors. *ASHRAE Transactions* 88:157–69.

Miropolskiy, Z.L., R.I. Shneyerova, and A.I. Karamysheva. 1970. Vapour void fraction in steam fluid mixture flowing in heated and unheated channels. *International Heat Transfer Conference, Paris, France, August 31–September 5,* paper B4.75.

Nilpueng, K., and S. Wongwises. 2009. Experimental investigation of two-phase flow characteristics of HFC-134a through short-tube orifices. *International Journal of Refrigeration* 32:854–64.

Pasqua, P.F. 1953. Metastable flow of Freon-12. *Refrigeration Engineering* 61:1084–8.

Payne, W.V., and D.L. O'Neal. 1998. Mass flow characteristics of R407C through short-tube orifices. *ASHRAE Transactions* 104:197–209.

Payne, W.V., and D.L. O'Neal. 1999. Multiphase flow of refrigerant 410A through short tube orifices. *ASHRAE Transactions* 105: 66–74.

Singh, G.M., P.S. Hrnjak, and C.W. Bullard. 2001. Flow of refrigerant R134a through orifice tubes. *HVAC&R Research* 7: 245–62.

Tu, X., P.S. Hrnjak, and C.W. Bullard. 2006. Refrigerant 134a liquid flow through micro-scale short tube orifices with/without phase change. *Experimental Thermal and Fluid Science* 30:253–62.

Wongwises, S., and M. Suchatawat. 2002. A simulation for predicting the refrigerant flow characteristics including metastable region in adiabatic capillary tubes. *International Journal of Energy Research* 27:93–109.

Yang, L., and C.-L. Zhang. 2005. Two-fluid model of refrigerant two-phase flow through short tube orifice. *International Journal of Refrigeration* 28:419–27.

Zhang, C-L., and L. Yang. 2005. Modeling of supercritical CO_2 flow through short tube orifice. *Journal of Fluid Engineering, Transactions of ASME* 127:1194–8.

Zivi, S.M. 1964. Estimation of steady-state steam void fraction by means of the principle of minimum entropy production. *ASME Journal of Heat Transfer* 86:247–52.